



## City Research Online

### City, University of London Institutional Repository

---

**Citation:** Ong, C.F. (1992). Computer-aided design of tension structures. (Unpublished Doctoral thesis, City University London)

This is the accepted version of the paper.

This version of the publication may differ from the final published version.

---

**Permanent repository link:** <https://openaccess.city.ac.uk/id/eprint/7994/>

**Link to published version:**

**Copyright:** City Research Online aims to make research outputs of City, University of London available to a wider audience. Copyright and Moral Rights remain with the author(s) and/or copyright holders. URLs from City Research Online may be freely distributed and linked to.

**Reuse:** Copies of full items can be used for personal research or study, educational, or not-for-profit purposes without prior permission or charge. Provided that the authors, title and full bibliographic details are credited, a hyperlink and/or URL is given for the original metadata page and the content is not changed in any way.

# COMPUTER-AIDED DESIGN OF TENSION STRUCTURES

Submitted by Chee Fatt Ong

for the degree of Ph.D.

at the Department of Civil Engineering,

City University, London.

September, 1992.

020252523

## Contents

	<u>Page</u>
Acknowledgements	(v)
Abstract	(vi)
<b>PART I</b>	
1. General introduction to tension structures	
1.1 Introduction	1
1.2 Structural performance as a function of form	5
1.2.1 Behaviour under load	5
1.2.2 Dynamic behaviour	6
1.3 An overview of Parts I, II and III of this thesis	7
1.3.1 Part I	7
1.3.2 Part II	7
1.3.3 Part III	8
2. Review of numerical solution methods	
2.1 Introduction	10
2.2 Element stiffness relations	11
2.3 Iterative solution methods	16
2.3.1 Newton-Raphson method	16
2.3.2 Modified Newton-Raphson method	17
2.3.3 Secant stiffness method	19
2.4 Incremental solution methods	20
2.5 Explicit analyses	23
2.5.1 Minimisation methods	23
2.5.1.1 Gradient vector	25
2.5.1.2 Method of Steepest Descent	28
2.5.1.3 Conjugate Gradient method	29
2.5.1.4 Scaling and transformation of energy surface	29
2.5.2 Relaxation methods	33
3. Dynamic relaxation analysis of tension structures	
3.1 Introduction	38
3.2 Physical basis	38
3.3 Method formulation	39
3.3.1 Basic equations	39
3.3.2 Numerical stability	41
3.3.3 Viscous damping constant	46
3.3.4 Kinetic damping	47
3.3.5 Natural stiffness relations	50
3.4 Conclusions	58
4. Compression and bending elements incorporated into the DR scheme	
4.1 Introduction	59

4.2	Moment-curvature relations	60
4.3	Non-linear effects	67
4.4	Boundary conditions	71
4.5	Implementation into the dynamic relaxation analysis	71
4.6	Other considerations	73
4.7	Numerical results and comparisons	75
4.8	Conclusions	80

## PART II

5.	Definition of surface shapes and their differential geometry	
5.1	Introduction	82
5.2	Base vectors on a surface	84
5.3	The metric tensor and the first fundamental form	86
5.4	Associated tensors	88
5.5	The coefficients of the second fundamental form	88
5.6	Principal curvatures, Gaussian curvature and mean curvature	89
5.7	Spherical image	90
5.8	Faceted surface	92
5.9	The Gauss equations and the Christoffel symbols	93
5.10	The Gauss' theorem and the Codazzi equations	93
5.11	Fundamental theorem of surface theory	95
5.12	Comments on the Gaussian curvature	95
5.13	Geodesic coordinates	96
5.14	How does Gaussian curvature distort the fabric?	99
5.15	Membrane equilibrium equations	101
5.16	Form-finding and cutting patterns determination	104
5.17	Conclusions	106
6.	Numerical form-finding and fabrication patterning	
6.1	Introduction	108
6.2	Review of solution methods available for the form-finding	109
6.2.1	Non-linear displacement analysis	109
6.2.2	Siev-Eidelman method	109
6.2.3	Force density method	111
6.2.4	Least squares method	112
6.2.4.1	Overdetermined least squares solution method	114
6.2.4.2	Underdetermined least squares solution method	115
6.2.5	Optimisation method	116
6.2.6	Iterative smoothing method	117
6.2.7	Combined approach	118
6.3	Form-finding by the dynamic relaxation method	118
6.3.1	<u>Cable nets</u>	119
6.3.1.1	Geodesic nets	119
6.3.1.2	Uniform mesh nets	122
6.3.1.3	Principal curvature nets	122
6.3.1.4	Momentless compression boundaries	123



	<u>Page</u>
6.3.2 Membrane structures	123
6.3.3 Air-supported structures	127
6.4 Fabrication patterning	129
6.5 Behaviour under load	130
6.6 Conclusions	131
 7. Interactive design of tension structures	
7.1 Introduction	133
7.2 Underlying philosophy	134
7.3 The design process	138
7.4 Project manager	139
7.5 File manager	139
7.6 Graphic display	140
7.7 Node control	143
7.8 Topology	145
7.9 Mesh generation	153
7.10 Element generation	155
7.11 Fixity	157
7.12 Elastic properties	159
7.13 Stress/force and elastic controls	161
7.13.1 Membrane elements	161
7.13.2 Line elements	163
7.14 Boundary control	165
7.15 Analysis	167
7.16 Loading definition	170
7.17 Patterning	173
7.18 Cloth width adjustments	179
7.19 Structure visualisation	186
7.20 Further visualisation options	193
7.21 Beam elements	202
7.22 Fabrication geometry	210
7.23 Post-processing	213
7.24 Listing	215
7.25 Conclusions	216

### PART III

 8. Loadings: static and dynamic	
8.1 Introduction	219
8.2 Design loads	219
8.2.1 Snow loads	221
8.2.2 Wind loads	222
8.2.2.1 Gust spectrum	222
8.2.2.2 Quasi-static wind loads	224
8.2.2.3 Fluctuating wind loads	228
8.3 Conclusions	229

	<u>Page</u>
9. <u>Dynamic responses of tension structures</u>	
9.1 Introduction	231
9.2 A brief review of available solution schemes	234
9.2.1 The mode superposition method	235
9.2.2 The direct step-by-step time integration methods	235
9.3 Dynamic analysis by an explicit numerical scheme	237
9.4 Visco-elastic material behaviour	238
9.5 Incremental procedure to account for on/off buckling	241
9.6 Pneumatic stiffness and damping	245
9.7 Added mass effects	246
9.8 Basic assumptions	248
9.9 Potential flow theory	250
9.10 Solution of the Laplace equation	253
9.11 Kinetic energy considerations	261
9.12 A diaphragm embedded in an infinite rigid plane	262
9.13 A shallow pneumatic dome	266
9.14 A generalised discrete source method	269
9.15 Comparison of $\Psi_{ij}$ coefficients calculated numerically and analytically	276
9.16 The shallow pneumatic dome and its imaginary mirror image	281
9.17 Explicit dynamic analysis with added mass calculations	283
9.18 Numerical examples and discussions	286
9.18.1 Static load analysis	289
9.18.1.1 Centrally applied load	289
9.18.1.2 Asymmetrically applied load	290
9.18.2 Dynamic analysis	293
9.18.2.1 Centrally unloaded dome	297
9.18.2.2 Asymmetrically unloaded dome	311
9.19 The dynamic response in the presence of wind	315
9.20 Summary and conclusions	319
10. Summary, conclusions and recommendations	
10.1 Summary and conclusions	324
10.2 Recommendations	330
References	332

## Acknowledgements

I would like to thank the many people who have helped and advised during my research and preparation of this thesis.

I am particularly grateful to Dr. Michael Barnes for his guidance and supervision throughout my studies and research at City University especially his 'lessons' on many occasions on how simple and practical engineering solutions can be found.

I would like to express my appreciation to Dr. David Wakefield in his role as the industrial supervisor during the (1988-1990) period of the Teaching Company Scheme between City University and Buro Happold, for his support and successful management of the scheme.

I am very grateful to Dr. Chris Williams of the School of Architecture and Building Engineering, University of Bath for his patience and advice on chapters 5 and 9 of this thesis. In addition, my thanks to the Computer Unit of the University of Bath for use of their computer facilities.

I must thank Hilda Iu for all her invaluable help throughout the duration of my research at City University especially in the preparation of the figures included in this thesis.

Further thanks are due to Buro Happold, and in particular Colin, Angus, Paul, Richard and Grant for their assistance and use of their facilities in the preparation of this thesis.



## Abstract

This thesis consists of three parts. Part I (chapters 1-4) gives a review and description of the basis for the numerical modelling of tension structures. The discussion in Part I leads to the conclusion of a need for an interactive design procedure for tension structures which is the subject under consideration in Part II (chapters 5-7). In the design of tension structures, an area which requires special attention is the dynamic response often initiated by the action of a natural wind. In Part III (chapters 8 and 9), this area is examined in detail and a strategy is proposed to give an improved modelling of dynamic response. The numerical procedure developed is assessed by comparison with previously reported test results for a pneumatic dome.

Chapter 1 gives a general introduction to tension structures, and their main characteristics and behaviour are briefly described. From both the structural and architectural points of view, tension structures (classified as either prestressed cable nets or doubly curved membranes) do offer a number of benefits which arise from their characteristics and behaviour. The different types of cable nets which can be constructed are outlined, and various possible types of membrane structures and membrane materials which can be used are described. In addition, the form-finding and load analysis stages in the design process of tension structures are briefly discussed. An overview of Parts I, II and III of this thesis is also included.

As a result of the flexible nature of a tension structure, large deformations often occur under loads acting normal to the surface. In addition, the coated woven fabrics exhibit material non-linearities, ie. the material properties vary under loads. In other words, a full non-linear structural analysis accounting for both material and geometric non-linearities is required in order to give a realistic modelling of the behaviour of a tension structure. Chapter 2 reviews numerical methods which have been widely reported for dealing with non-linear structural analysis. From the review, it will be noted that the dynamic relaxation (DR) method is well suited to solving the highly non-linear problems which occur particularly in the case of tension structures.

The dynamic relaxation method with a finite element idealisation of the structure is chosen as the solution scheme for all the analysis work in this thesis, and a detailed description of the method is given in chapter 3. Features of the method which are particularly useful for the design of tension structures are:

- (a) the effective decoupling of the equations of compatibility and equilibrium which allows complex material properties modelling and the use of slip cables, etc., and
- (b) the use of a 'kinetic' damping procedure which permits gross changes in support geometries to be made during interactive form-finding without the possibility of numerical instability.

Although the main surface spanning elements may be purely tensile, many tension structures will employ compression and bending elements for their support. For example, as a means of providing support to a large span tension structure, a compression boundary is considered to be an efficient alternative to tension anchorages. In a sense, a compression boundary is complimentary to the tension elements in the structure as these elements also act as supports to the compression boundary. This gives the advantage of a compression boundary comprising of slender sections. The compression boundary is modelled as a series of beam elements. The moment-curvature equations of a beam element expressed in the form of natural stiffness relations, are developed in chapter 4. In addition, the non-linearities, both geometric and material, and boundary conditions which can be dealt with by the beam elements are considered. An outline is given of the implementation of the beam elements using the dynamic relaxation method. Included in chapter 4 are also the results to test problems which have been set up in order to validate the underlying theory and implementation of the beam elements.

As tension structures often exhibit complex surface curvatures, a study of surfaces, their properties and behaviour is appropriate, and useful in the understanding of concepts applied in the design process. This study is the subject of chapter 5 which focusses on the relevant topics of differential geometry. A few useful ideas from differential geometry form the basis of certain procedures implemented into the form-finding and patterning stages being considered in chapter 6. The derivation of the equilibrium equations for a surface when acted on by applied loads is also given in chapter 5.

The discussion in chapter 6 is about the stages of form-finding and static load analysis in the design process. A review of the available solution methods for the form-finding problem are given in this chapter. In these methods, the solution can be for either the unknown geometry or unknown stresses, or both. The adopted approach in this thesis is to solve for the unknown equilibrium geometry given the stress distributions, and initial and boundary conditions. The controls which can be used during form-finding to achieve the desired geometries of cable nets and membrane structures are discussed. The equilibrium geometry derived from the form-finding stage has to be subsequently evaluated for its performance under loads at the load analysis stage. After an equilibrium geometry which behaves satisfactorily under loads has been achieved, the corresponding cutting patterns are developed in the case of membrane structures.

Recent advances in interactive computer graphics technology have made it possible to develop a fully interactive CAD system for tension structures. The development of such a CAD system is the subject of discussion in chapter 7. The CAD system integrates together the form-finding, load analysis and fabrication patterning stages, resulting in a continuous design process. It demonstrates how the various concepts discussed in Part I of this thesis fit together within an interactive environment implemented with an effective and functional user interface. It is illustrated in chapter 7 how such a user interface has been achieved. The CAD system fully exploits the capabilities



offered by the available computer hardware such that the computations involved during analysis of the structure, in generation of surface shaded graphic images and so on, can be executed at very high speeds. As a result, the CAD system can respond quickly to the user and is thus consistent with the interactive nature of the design process. The discussion in chapter 7 also provides an insight into the various procedures involved throughout the design process. The CAD system has produced a number of benefits of which the main one is the saving in design time which has been achieved. As the CAD system is highly user friendly, only a short learning period is required, thus enabling it to be used more widely among designers. The CAD system also serves as a useful tool for the communication of ideas between the engineer and the architect. In the design of a tension structure unlike that of a conventional building, there is often close cooperation between the engineer and the architect right from the early stages of conceptual development.

In chapter 8, the possible loads which may act on a tension structure during its service life are considered. These loads are applied to the structure at the load analysis stage in the design process. In most cases, the design loads are those due to snow and wind. An accurate assessment of the loads is essential in order to achieve a structurally sound and economic design. In addition, it should be possible to represent the loads in a form which can be easily applied in the structural analysis. The considerations which are involved in the assessments of the snow and wind loads are outlined.

The dynamic responses of tension structures which result from the action of a natural wind or initiated by other means is considered in chapter 9. A tension structure when set into motion causes additional mass, stiffness and damping terms to be generated. A brief review of the available solution schemes for the dynamic analysis of structures in general is outlined. These solution schemes include the mode superposition method and the direct step-by-step time integration methods. In this chapter, the explicit central difference time integration method is the adopted solution scheme for the dynamic analysis of tension structures. The creep effects which arise from the visco-elasticity present in most membrane materials are also considered. A strategy based on the Voigt-Kelvin model is used to calculate for the accumulated creep strains. An outline is given of an incremental procedure to allow for the on/off element buckling which occurs during dynamic analysis. The internal air stiffening effect due to changes in internal volume and pressure of an air-supported structure as it deforms during dynamic analysis, <sup>are</sup> is also considered. X

When a membrane undergoes vibrations, the surrounding air attached to the membrane is mobilised into motion as well. This in turn gives rise to the added mass effects. It is the main aim in chapter 9 to develop a means of modelling the added mass effects and for this purpose, an approach based on the potential flow theory has been formulated. The basic assumptions and concepts of the potential flow theory which are relevant to the approach are outlined. In the approach, it is required to solve the Laplace equation and the solution can be in terms of either a distribution of sources or doublets over the membrane. In this case, a distribution of sources are used to calculate the

kinetic energy of the surrounding air when set into motion. An indication of the added mass effects is given by the ratio of the kinetic energy of the surrounding air to the kinetic energy of the vibrating membrane. The mechanics which are involved in the determination of this ratio known as the added mass coefficient, are outlined. The proposed approach is applied to investigate the dynamic response of an air-supported dome and some encouraging results are obtained.

A summary of the work discussed in previous chapters is given in chapter 10 which also includes the main conclusions of this thesis. The discussions in previous chapters suggest that there are various areas in which further research work can be pursued and these areas are outlined in chapter 10.



## Part I

### Chapter 1

#### General introduction to tension structures

##### 1.1 Introduction

There are many examples of tension structures both in nature, such as soap films and spider webs, as well as man-made structures. The traditional examples of tension structures were the tents used by nomads and armies, and the large tents used for circuses and exhibitions. These tents were designed by craftsmen rather than architects. In addition, natural materials were used in their construction and generally, only single curvatures or none at all was present. One of the earliest modern tension structures to be constructed on a grand scale is the saddle shaped roof for the Raleigh Arena in North Carolina in 1952 designed by Mathew Norwicks with Fred Severud. This monument was a tremendous source of inspiration to many architects and in particular, two who had developed the basic principles behind the Raleigh Arena roof to produce unique and even more striking large span spaces, ie. Saarinen's Yale ice hockey rink in 1956 and Kenzo Tange's two Tokyo Olympic stadia in 1961. Since those early days, many advances have been made in the design of tension structures in terms of analysis methods, materials and construction techniques.

Frei Otto has been principally responsible for the full development of the architectural possibilities of tension structures. The Raleigh Arena had also greatly inspired Frei Otto into exploring the idea of surface stressed structures as a means of providing cover. From the mid-1950s, he made exhaustive studies of small scale models using nets, cables, soap bubbles and elastic membranes simply to realise the huge possibilities of shapes which could be generated. As a result, Frei Otto had acquired an understanding of the behaviour of tension structures which was far ahead of the engineer's ability to provide suitable design solutions for turning his small models into large scale reality. His earliest projects consisted mainly of relatively small scale tents and it was not until the mid-1960s that the spans rose above 40m. Among the impressive list of well known tension structures in which Frei Otto was involved are the German Federal Pavilion for Expo '68 in Montreal and the Munich Olympic Stadium.

A tension structure offers a number of attractive features. It can be classified as soft architecture as opposed to the hard architecture of conventional reinforced concrete and steel buildings. There is clearly a growing awareness among architects of the large vocabulary of surface forms which can be achieved with tension structures. They appeal to many architects as a means of expressing their innovations to cover or use open spaces to great effect or possibly to provide contrast with surrounding conventional 'hard' buildings. The inherent beauty of the free-form curved surfaces exhibited by tension

structures combined with their lightness of feel, and the quality of space and light obtainable underneath are factors which make them attractive options.

A tension structure as the name suggests, derives its load carrying capacity mainly from the constituent tension elements and a key element is its surface curvature. A flat piece of membrane has to deform and provide a component of the tension in the membrane to resist any applied loads. An element in tension is the most efficient structural element since the full section can be stressed to the design strength. There is no need to design the section for flexure or buckling. Another characteristic of tension structures is their light weight, in general due to their thin or small sections. As a result, possible savings can be gained in terms of the structure itself and supporting components which transmit loads from the structure to the ground. In addition, tension structures can offer economic cover over areas with very large, clear spans. As there are many elements of a tension structure which are prefabricated components, the erection time and thus, on-site construction costs can be reduced. Being light and flexible, a tension structure can also more readily adapt to extreme conditions such as earthquakes.

In general, tension structures are technically difficult to design and offer challenges to the architects, engineers and other specialists involved. The complex behaviour of tension structures is beyond the grasp of most architects except perhaps the most technically equipped. Consequently, this calls for far greater influence of the structural engineer in the design than is the case for conventional buildings. The engineer becomes involved right from the early stages of conceptual development alongside the architect.

The modern day tension structure can be properly engineered to exploit advances in materials and analysis methods. These structures differ from traditional tents in the following aspects [129] :

- they are much more durable,
- they are often very large,
- they cannot be designed purely from practical experience,
- they use higher strength materials,
- they should be wrinkle free,
- they should not flap about,
- they are expected not to fail.

There are two broad categories of tension structures, namely cable nets and membrane or fabric structures. Cable nets are often used to provide cover over large spans, supporting a variety of materials as cladding; these materials may include concrete, timber, coated fabrics and glass. There are various types of cable nets which can be constructed, ie. uniform mesh, geodesic and principal curvature nets. A uniform mesh cable net typically has a 0.5m spacing so that it is safe to work on. The best known uniform mesh cable net is the roof over the stands of the Munich Olympic Stadium. A uniform mesh cable net is prejointed at the slack state so that the internode spacing is constant except for those adjacent to boundaries or internal supports. A



geodesic net is also known as a minimal net in which the cables over the net surface each takes a path of minimum length, with constant tension throughout its length. The intersections between cables over the surface are jointed only after pretensioning. A principal curvature net is one in which the cables follow lines of principal curvature over the surface. This results in quadrilateral meshes which are plane and suitable for glazing (provided sufficient shearing flexibility is allowed at the junction of panels).

For membrane structures, the woven fabric material used consists of two sets of crossing yarns with one set in the warp direction and the other set in the fill direction of the fabric material. A flexible coating (such as PVC) is then applied which provides some shearing stiffness and weather protection to both the structural fabric and the building interior. The prestresses are applied in the warp and fill directions of the fabric material. This is to avoid large and unpredictable strains in the bias direction of the fabric material. There are various forms of membrane structures which can be constructed. Within a defined boundary, a membrane structure prescribed with a uniform prestress (ie. equal warp and fill prestresses) gives rise to a minimal surface an example of which is the soap film. A minimal surface has the least possible surface area and the minimum strain energy. It is possible to modify the surface by changing the ratio of prestresses in the warp and fill directions until the desired form is obtained. The form of a membrane structure is also strongly influenced by the types of supports and boundaries used in the structure, which may be beams, walls, arches, or boundary and/or ridge cables. As can be easily demonstrated with a soap film, a membrane cannot be supported by a point. At a mast point in general, there will be two ridge cables, sometimes three or four, which transfer the stresses in the membrane to the mast. For a conical membrane structure, there are often a large number of radial cables coming together at the mast. An example of a membrane structure in which ring supports are used is the series of 40m×40m tent covers over the Hajj Pilgrim's terminal at Jeddah in Saudi Arabia. A compression ring beam can also be used to provide support as in the case of the Raleigh Arena and the Calgary Olympic Stadium. A further form of membrane structure is the air-supported or pneumatic structure in which the membrane is prestressed by an internal pressure so that the tensile prestress is sufficiently high not to be reduced to zero by external loads. A fan is needed to maintain the internal pressure, which can be raised in limited periods, and access has to be through some form of air lock to prevent loss of internal pressure. The internal pressure does not have to be large as the membrane is lightweight. Air-supported structures provide a very economic structural type of enclosure of large spans for instance, to provide a roof over a stadium in the case of the Silverdome Stadium at Pontiac, USA.

There is a range of industrial fabrics which can be used for the membrane material. The commonly used coated fabrics are PVC-coated polyester, teflon-coated glass fibre and silicone-coated glass fibre. The PVC is a versatile coating which can be applied to all base cloths. Although the polyester base cloth has strength, it degrades with time through reactions mainly to ultra-violet light and rainwater. This degradation hardens the coating and makes it brittle. In a



well-stressed tension structure, the fabric does not flex much and this is not a problem. Unfortunately, the appearance suffers with discoloration and dirt retention, and this usually determines the end point of the fabric. The PVC-coated polyester fabric has a useful life of about 10-15 years after which it needs to be replaced.

Teflon-coated glass fibre was developed about 20 years ago to overcome the disadvantages of the PVC-coated polyester. It is translucent and, while initially buffcoloured, it soon bleaches white and is self cleansed by the action of rain and wind. It can also be stressed up to a high degree and is inherently fire resistant. Neither the glass base cloth nor the teflon coating degrade in sunlight. However, the strength of this material is reduced by damage from creasing during fabrication and installation, and by the consequent possibility of ingress of water into the fibres (wicking). Consequently, the fabric needs to be patterned, fabricated and installed with great care bearing in mind the difficulties in handling and folding the fabric. Silicone coating also offers excellent durability and is more flexible, and so does not suffer from mechanical damage due to handling/folding. The silicone-coated glass fibre is however seamed by gluing, which requires the skills of a specialist fabricator. Moreover, the seams can tend to degrade with time. For this reason, the most frequently used material for permanent structures (typically with a 30-year life) is teflon-coated glass fibre. Both the teflon-coated and silicone-coated glass fibres result in a cost per square metre of finished fabric equal to about three times that of the PVC-coated polyester. As a result, owners usually prefer to use the PVC-coated polyester fabric and replace it every ten years or so.

From a purely structural viewpoint of fabric, in addition to fire resistance, robustness against abrasion and tearing, dimensional stability and resistance to ageing with time, biaxial stress-strain characteristics become very significant in the accurate patterning of engineered forms. As well as construction stretch which is different in the warp and fill directions, fabric suffers from crimp interchange and in the case of polyester fabrics, creep. Construction stretch and creep are allowed for in the patterning of the fabric by compensating the patterns so that they stretch out to their correct size under prestress. Under typical levels of prestress (for example, uniform values in warp and fill of 2 kN/m for PVC-coated polyester or 5 kN/m for teflon-coated glass fibre), the 'stretch' in the fill direction may be 4% and in the warp direction perhaps -1%. This is because the fill yarns straighten out and the crimp in the weave goes into the warp. This effect is called 'crimp interchange' and accounts for much of the extension of glass fibre fabrics where the fibres themselves are fairly stiff.

For either a cable net or a membrane structure of woven fabric construction, there are two sets of cables or yarns which ideally would follow the lines of principal curvature so that they have opposing curvature. For a woven fabric, this may conflict with the need for simplicity and economy in the cutting and jointing pattern. The most practical alternative, which does not entail distortion of the weave, is to base fabric cutting patterns on geodesic lines

over the surface. The surface is prestressed in order to ensure structural stability and to provide adequate stiffness against deflection. When acted on by applied loads, the resulting stresses in the surface are given by the prestresses combined with the stresses due to elastic deformations.

## **1.2 Structural performance as a function of form**

The form of a cable net or membrane structure cannot be chosen arbitrarily. Due to the lack of flexural stiffness, the surface shape and the internal stresses must interact to satisfy equilibrium at all times. The form of the structure has to meet this requirement and such a form is developed at the form-finding stage in the design process. A detailed account of the form-finding stage is given in chapter 6. During form-finding, a prestressed equilibrium form is developed which satisfies the design requirements from both the structural and architectural points of view.

### **1.2.1 Behaviour under load**

The form of the structure derived from form-finding needs to be evaluated in terms of its performance when subject to possible loads which may act upon it during its useful life. These loads may be the structure self-weight, wind, snow and so on. The accurate definition of the wind and snow loads is of great importance. However, these are notoriously hard to predict when each structure can have a highly individual and complex shape. The wind load often constitutes the most significant loading for the design in which uplift generally dominates. The downward loads are taken by the sagging set of tendons and the upward loads by the hogging tendons (the tendons here refer to either cables in the case of cable nets or yarns in the woven fabric material for membrane structures). The tension along any particular tendon remains sensibly constant so local high pressures are taken by the surface deflecting. This means that a stressed surface is a load averaging system; the maximum tension in a particular sagging tendon is caused by the maximum average downward pressure in the area of the tendon.

As a result of the flexible nature of tension structures, large deformations often occur under loads acting normal to the surface. In some cases, the loads themselves will be deformation dependent. Within the limits tolerated by the chosen cladding system, large deformations are acceptable provided they are not accompanied by severe local changes in shape or excessive in-plane shear distortions. The ponding problem may arise as result of large deformations in the absence of proper drainage away from the deflected pocket. If this happens, additional rain or melt water will run into the pocket which will become larger and larger until the fabric tears or the supporting structure collapses. By ensuring that there are no flat horizontal areas over the surface, the ponding problem may be avoided. For canopy structures which are used primarily in the summer, it is sensible to install drainage grommets in areas where ponding can occur. Furthermore, the resulting stresses from the load



analysis should be checked, and the form of the structure may in turn need to be revised in order to reduce or eliminate the inadequacies of its performance under loads. It may be required to increase the prestress levels in order to limit the deflections. On the other hand, a change of curvature which means a change in prestress ratios, may be the preferred solution.

### 1.2.2 Dynamic behaviour

Generally, the lightweight and flexibility of tension structures makes them susceptible to dynamic loading due to wind. Tension structures have natural frequencies of vibration which could interact with the wind to produce fairly large oscillations. In practice, these wind induced oscillations are made structurally acceptable by the very high material damping and adequate prestressing. For large structures, the dynamic behaviour may be studied by aeroelastic model testing in a boundary layer wind tunnel in which the turbulent boundary layer is suitably modelled. A detailed discussion of the dynamic response of tension structures, is given later in chapter 9.

Wind tunnel tests are carried out in order to determine the pressure coefficients, examine the frequencies of vortex shedding from bluff edges and detect possible aeroelastic instabilities. In the case of Munich Olympic Stadium for example, following wind tunnel testing, the edge rim was shaped to avoid dynamic excitation of the structure by buffeting vortices [10]. The wind pressure coefficients, and in the case of an air-supported structure, the internal volume and pressure will change significantly with deformations. The variations of internal pressure give rise to an air stiffening effect. Consequently, the fundamental modes and frequencies of an air-supported structure may differ radically from those predicted by theory which does not account for the variations in internal pressure.

A tension structure when set into vibrations can also give rise to secondary interactions between the structure and the surrounding or enclosed air which increases the virtual mass of the surface structure due to added/attached air mass effect. The wind/structure interaction may also lead to additional aerodynamic forces. These additional forces may produce further structural deformations which then lead to further aerodynamic forces. This interaction may tend to become smaller until a condition of stable equilibrium is reached or conversely may lead to instability. Such responses constitute an aeroelastic behaviour. As a result, the dynamic analysis of tension structures is a complex aeroelastic problem. At present, the practical solution to this complex problem is the wind tunnel testing of an aeroelastic model of the actual structure. In chapter 9, an attempt has been made to devise a numerical approach for predicting the dynamic response of tension structures. This approach is still under development and further work is needed in order to eventually achieve a realistic alternative to the wind tunnel testing.

For the (current) routine design of most tension structures however, it is usual to employ equivalent quasi-static wind loading for the analysis of the structure.

### **1.3 An overview of Parts I, II and III of this thesis**

#### **1.3.1 Part I**

Physical modelling used to be the primary means of designing tension structures. For cable nets, simple physical models can be constructed from wire meshes and small cable clamps, and such models have been used by Frei Otto to design the German Federal Pavilion for Expo '68 in Montreal. The physical models of membrane structures can be made from soap films and stretch fabric of one form or another such as lycra. Although physical models are useful for the qualitative study of form, concept and visual assessment, it is difficult to extract quantitative design data such as forces, stresses and component geometries from the physical models due to their fragile nature and the problems associated with taking accurate measurements on them.

The numerical modelling methods were developed to overcome the difficulties associated with physical modelling. Part I of this thesis gives a review of these numerical methods which can be classified into iterative methods, incremental methods, minimisation methods and relaxation methods. It will be shown that the dynamic relaxation (DR) method (ie. an explicit relaxation method which involves central difference integration) has a few advantages that make it well suited for dealing with tension structures. Consequently, the dynamic relaxation method is the chosen numerical modelling method in this thesis.

#### **1.3.2 Part II**

The adopted approach for form-finding using the dynamic relaxation method differs radically from the usual methods of structural design and analysis. In conventional structures, the engineer will propose a trial form of the structure and then analyse it for various loading conditions to determine the resulting stresses. This procedure when applied to tension structures which typically have complex, doubly curved surfaces is faced with the difficulty of having to describe such surfaces before the loads can be applied. In general, mathematical representations do not exist for arbitrary surface geometries. In the adopted approach, this process is reversed, ie. stresses (or prestresses) are specified a priori and the resulting form is then determined. This offers an efficient and effective means of achieving the form which meets the architectural and structural requirements. A trial and error procedure will consequently be required in the solution for the desired form. This in turn leads to the need for interactive computer-aided design (CAD) of tension structures. The same numerical model is also used for the load analysis and



for establishing the cutting patterns and cable lengths. In other words, the whole design is made into a continuous process.

In Part II of this thesis, the development of a fully interactive CAD system for tension structures is discussed in detail. This development was carried out over the 2-year period (1988-1990), when I was on a Teaching Company Scheme (TCS) set up between Buro Happold and City University. This CAD system is now in operation for actual project work at the Lightweight Structures Division of Buro Happold. The CAD system has been developed to fully exploit the capabilities offered by the computer hardware which in this case is a Hewlett-Packard HP9000/350 workstation, such that the computations involved during the analysis of the structure, in the generation of surface shaded graphic images and so on, can be executed at very high speeds. The CAD system can therefore respond quickly to the user. The various stages such as form-finding, load analysis and patterning involved in the design process have been integrated together into the CAD system. The need for such an interactive CAD system is justified from the number of benefits it has brought to the design process as outlined in chapter 7. The success of the CAD system depends to a large extent on the implementation of an effective human user interface. In the discussion given in Part II of this thesis, it will be clearly illustrated how such a user interface has been achieved. The discussion will also provide an insight into the various procedures which are involved throughout the design process.

### 1.3.3 Part III

It has already been mentioned earlier that the dynamic response of tension structures is a complex aeroelastic problem due to the presence of aerodynamic effects. There is no available solution method for the dynamic analysis of a tension structure which takes all the aerodynamic effects into account. This problem can only be approximately solved at present by aeroelastic model testing in a boundary layer wind tunnel. An aeroelastic model has scaled mass, stiffness and damping values which reflect the corresponding properties of the real structure. The deflections and strains of the aeroelastic model are measured directly during the wind tunnel testing. According to Williams [136, 137], even the most rudimentary aeroelastic model test is more accurate and should be used rather than a sophisticated rigid model test followed by non-linear dynamic analysis. This is because the results from the wind tunnel testing of a rigid model will be unrealistic as the rigid model is unable to account for the aerodynamic effects and aeroelastic phenomena such as divergence and flutter. However, aeroelastic model construction may be difficult and the whole procedure of aeroelastic model testing in a boundary layer wind tunnel can be very costly and justifiable perhaps only in the design of a very large structure.

Consequently, there is a need to develop a numerical approach which can at least conservatively predict the dynamic response of tension structures. This will give the advantage of much economy in terms of the design costs and



time. In addition, such an approach may be more readily applicable in the routine design of most tension structures. The numerical approach should be sufficiently general, accurate and reliable for it to be considered as a suitable alternative to the wind tunnel testing of an aeroelastic model. The emphasis in Part III of this thesis is on the effort to develop such a numerical approach. Under investigation in this case is the dynamic response of an air-supported dome. An approach based on the potential flow theory has been proposed to account for the aerodynamic effect due to the 'attached' air mass mobilised by the vibrating membrane of the dome. Although further work is needed in order to account for the aerodynamic damping and air momentum effects, at least an effort has been made to improve the modelling of dynamic response of tension structures.

## Chapter 2

### Review of numerical solution methods

#### 2.1 Introduction

As mentioned in chapter 1, there is a need to use numerical modelling methods in the design of tension structures due to the inadequacies of physical modelling. This chapter presents a review of the numerical solution methods which are available.

It was also pointed out in chapter 1 that due to the flexible nature of tension structures, large deformations often occur under loads acting normal to the surface. In some cases, the loads themselves will be deformation dependent. In addition, the materials from which tension structures are constructed such as the coated woven fabrics, exhibit non-linear material behaviour, ie. the material properties vary under loads. In order to give a realistic modelling of the behaviour of tension structures, the solution method should take into account the above mentioned geometric and material non-linearities.

Indeed, analytic solutions are available only for tension structures of simple and regular configurations such as soap film bubbles, spherical, cylindrical and hyperbolic paraboloid shells. Leonard [91] had developed a perturbation method for predicting the behaviour of air-supported 'shell' of revolution during the inflation phase. It involves superposing an infinite set of asymptotically converging linear solutions to approximate the non-linear equation for the inflated shell. However, limitations arise when irregular shapes, and peculiar boundary and loading conditions are encountered. As a result, the analytic approach is not sufficiently general for wide practical applications.

The analytic solutions treat the tension structure as a whole continuum. In the numerical approach however, the tension structure is discretised into finite elements and analysed as a discrete system. There has been much research into discrete methods of analysis. In general, the discrete methods can be classified into the following categories, ie.

- iterative methods, (MATRIX)
- incremental methods,
- minimisation methods, } (VECTOR)
- relaxation methods.

Both the iterative and incremental methods are implicit schemes as they require setting up the overall or tangent stiffness matrix of the structure. On the other hand, the minimisation and relaxation methods are explicit schemes because the current displacements are updated from the previous displacement vector without the need for an overall stiffness matrix. Hence, the computer memory requirements are much less than for implicit schemes.

All these methods can cope with geometric non-linearities in tension structures provided all elements remain in tension and the applied loads are not functions of deformations. In methods which use matrix formulations, the occurrences of singular stiffness matrices have to be avoided. It may be necessary to impose controls in order to limit the deflections at any iterative or increment step as excessive deflections can lead to divergence of solution. In the presence of material non-linearities, on/off non-linearities such as element slackening or applied loads which are functions of deformations, a path dependent solution becomes inevitable and thus, requires the use of an incremental method, or a combination of incremental and iterative, minimisation or relaxation methods.

Before proceeding to review the above mentioned numerical methods, the element stiffness relations of the link or cable element will be briefly discussed. The intention is to examine the tangent stiffness in the case of large displacements, and emphasise the difference between the small strain and large strain formulations. The principle applies similarly to the membrane and beam elements.

## 2.2 Element stiffness relations

In figure 2.1 is a two-dimensional system with a single cable element with elastic modulus  $E$  and cross-sectional area  $A$ .

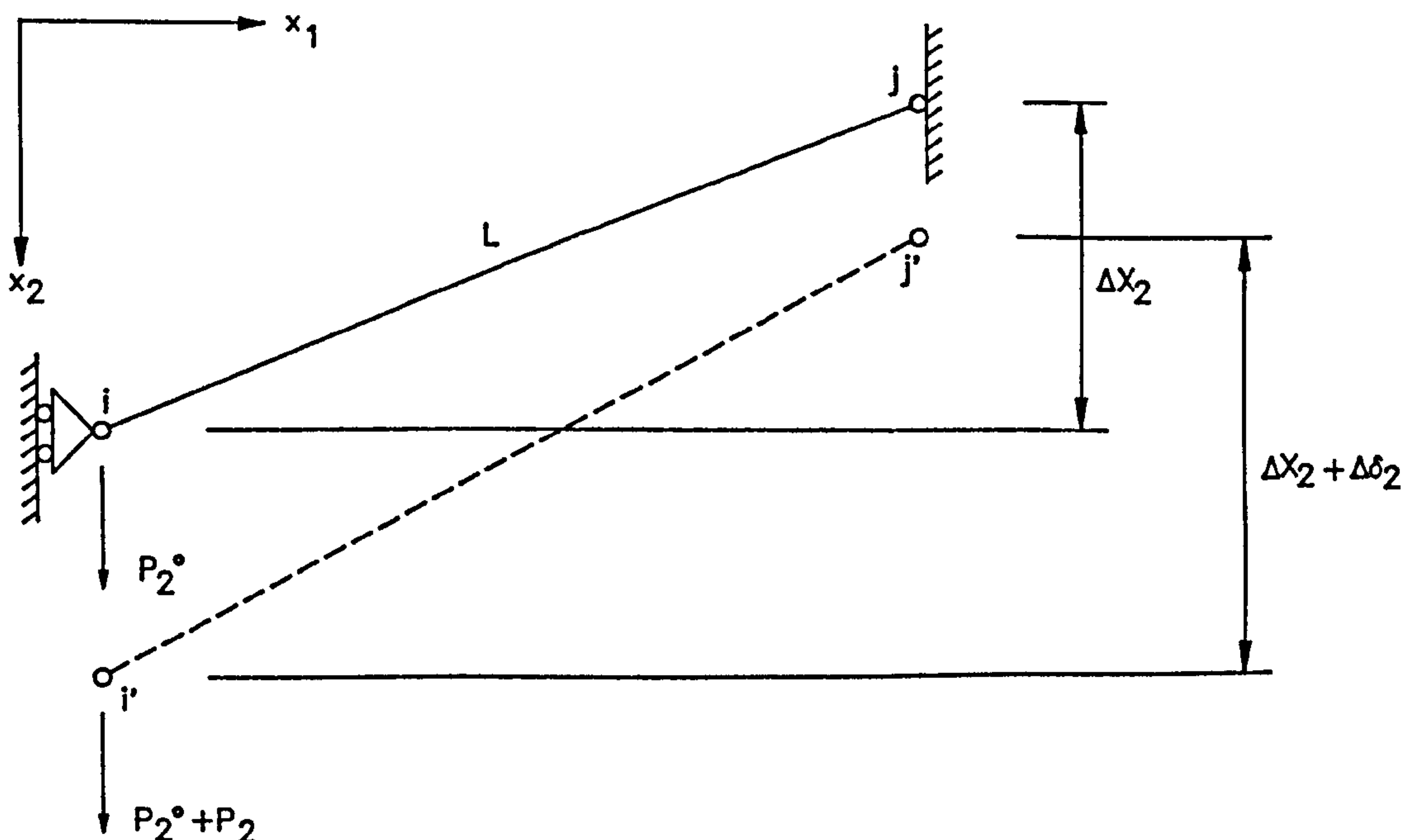


Figure 2.1

In the initial state,  $P_2^0$  is the force which produces a tension  $T$  in the element of length  $L$ . Resolving in the  $x_2$ -direction,

$$T \frac{\Delta X_2}{L} = P_2^0 \quad (2.2.1)$$

where  $\Delta X_2 = x_{2i} - x_{2j}$ , and  $x_{2i}$  and  $x_{2j}$  are respectively the  $x_2$  coordinates of nodes  $i$  and  $j$ .

Under an additional force  $P_2$ ,

$$(T + \Delta T) \frac{(\Delta X_2 + \Delta \delta_2)}{L + e} = P_2^0 + P_2 \quad (2.2.2)$$

in which  $\Delta \delta_2 = \delta_{2i} - \delta_{2j}$ , and  $\delta_{2i}$  and  $\delta_{2j}$  are respectively the  $x_2$  displacements of nodes  $i$  and  $j$ ,  $e$  refers to the element extension and  $\Delta T$  the increase in tension.

Furthermore,

$$\begin{aligned} L^2 &= \sum_{j=1}^2 (\Delta X_j)^2, \\ (L + e)^2 &= \sum_{j=1}^2 (\Delta X_j + \Delta \delta_j)^2, \\ \Rightarrow L^2 + 2Le + e^2 &= \sum_{j=1}^2 (\Delta X_j^2 + 2\Delta X_j \Delta \delta_j + \Delta \delta_j^2). \end{aligned} \quad (2.2.3)$$

By neglecting second order terms, equation (2.2.3) reduces to

$$\begin{aligned} 2Le &= \sum_{j=1}^2 2\Delta X_j \Delta \delta_j, \\ \Rightarrow e &= \sum_{j=1}^2 \frac{2\Delta X_j}{L} \Delta \delta_j \end{aligned} \quad (2.2.4)$$

$$\text{and} \quad \Delta T = \frac{EA}{L} \sum_{j=1}^2 \frac{2\Delta X_j}{L} \Delta \delta_j. \quad (2.2.5)$$



In addition,

$$\begin{aligned}
 \frac{\Delta X_i + \Delta \delta_i}{L + e} &= \frac{\frac{\Delta X_i}{L} + \frac{\Delta \delta_i}{L}}{1 + \frac{e}{L}} = \left(\frac{\Delta X_i}{L} + \frac{\Delta \delta_i}{L}\right) \left(1 + \frac{e}{L}\right)^{-1} \\
 &= \left(\frac{\Delta X_i}{L} + \frac{\Delta \delta_i}{L}\right) \left[1 - \frac{e}{L} + \left(\frac{e}{L}\right)^2 - \dots\right] \\
 &\approx \frac{\Delta X_i}{L} - \frac{\Delta X_i}{L} \left(\frac{e}{L}\right) + \frac{\Delta \delta_i}{L}.
 \end{aligned} \tag{2.2.6}$$

Using equations (2.2.1) and (2.2.6), equation (2.2.2) becomes on expansion (ignoring second order terms)

$$\Delta T \frac{\Delta X_2}{L} + T \left[ \frac{\Delta \delta_2}{L} - \frac{\Delta X_2}{L} \left(\frac{e}{L}\right) \right] = P_2, \tag{2.2.7}$$

and using equations (2.2.4) and (2.2.5), equation (2.2.7) then becomes

$$\begin{aligned}
 \left(\frac{EA}{L}\right) \frac{\Delta X_2}{L} \sum_{j=1}^2 \left(\frac{\Delta X_j}{L}\right) \Delta \delta_j + \frac{T}{L} \left[ \Delta \delta_2 - \frac{\Delta X_2}{L} \sum_{j=1}^2 \left(\frac{\Delta X_j}{L}\right) \Delta \delta_j \right] &= P_2, \\
 \Rightarrow P_2 &= \left(\frac{EA}{L}\right) \frac{\Delta X_2}{L} \left(\frac{\Delta X_1}{L} \Delta \delta_1 + \frac{\Delta X_2}{L} \Delta \delta_2\right) + \frac{T}{L} \left[ \Delta \delta_2 - \frac{\Delta X_2}{L} \left(\frac{\Delta X_1}{L} \Delta \delta_1 + \right. \right. \\
 &\quad \left. \left. \frac{\Delta X_2}{L} \Delta \delta_2 \right) \right] \\
 &= \frac{EA}{L} \left(\frac{\Delta X_1}{L}\right) \left(\frac{\Delta X_2}{L}\right) \Delta \delta_1 + \frac{EA}{L} \left(\frac{\Delta X_2}{L}\right) \left(\frac{\Delta X_2}{L}\right) \Delta \delta_2 - \frac{T}{L} \left(\frac{\Delta X_1}{L}\right) \left(\frac{\Delta X_2}{L}\right) \Delta \delta_1 + \\
 &\quad \frac{T}{L} \left[ 1 - \left(\frac{\Delta X_2}{L}\right) \left(\frac{\Delta X_2}{L}\right) \right] \Delta \delta_2. \tag{2.2.8}
 \end{aligned}$$

The stiffness components in equation (2.2.8) form a row in the element stiffness matrix. Resolving in the  $x_1$ -direction, the remaining components can similarly be derived. The element stiffness relations in matrix form are written as follows-

$$\{P\} = [K]\{\Delta \delta\} = ([K_e] + [K_g])\{\Delta \delta\} \tag{2.2.9}$$

in which  $\{P\} = \begin{bmatrix} P_1 \\ P_2 \end{bmatrix}$ ,  $\{\Delta \delta\} = \begin{bmatrix} \Delta \delta_1 \\ \Delta \delta_2 \end{bmatrix}$ ,



$[K_e] = \frac{EA}{L} \begin{bmatrix} l^2 & lm \\ ml & m^2 \end{bmatrix}$  is the elastic stiffness,

$$[K_g] = \frac{T}{L} \begin{bmatrix} (1-l^2) & -lm \\ -ml & (1-m^2) \end{bmatrix} \text{ is the geometric stiffness,} \quad (2.2.10)$$

with  $l = \frac{\Delta X_1}{L} = \cosine \text{ of angle between the element and the } x_1\text{-axis,}$

and  $m = \frac{\Delta X_2}{L} = \cosine \text{ of angle between the element and the } x_2\text{-axis.}$

The elastic stiffness relates to deformations of the element while the geometric stiffness is associated with changes in geometry of the element with element taken as a rigid body.

Alternatively, if in equation (2.2.2),  $e$  is taken to be negligible (ie. assuming 'small strain' stiffness relations), then

$$\begin{aligned} \frac{\Delta X_2 + \Delta \delta_2}{L + e} &\approx \frac{\Delta X_2}{L} + \frac{\Delta \delta_2}{L}, \\ \Rightarrow (T + \Delta T) \left( \frac{\Delta X_2}{L} + \frac{\Delta \delta_2}{L} \right) &= P_2^0 + P_2, \end{aligned} \quad (2.2.11)$$

and ignoring the second order terms in equation (2.2.11),

$$P_2 = \Delta T \frac{\Delta X_2}{L} + T \frac{\Delta \delta_2}{L}. \quad (2.2.12)$$

Substituting equation (2.2.5) into equation (2.2.11),

$$\begin{aligned} P_2 &= \frac{\Delta X_2}{L} \left( \frac{EA}{L} \right) \sum_{j=1}^2 \left( \frac{\Delta X_j}{L} \Delta \delta_j \right) + \frac{T}{L} \Delta \delta_2 \\ &= \frac{EA}{L} (lm \Delta \delta_1 + m^2 \Delta \delta_2) + \frac{T}{L} \Delta \delta_2. \end{aligned} \quad (2.2.13)$$

Obviously, in large displacement analysis where element strains become significantly large, it is more appropriate to use equation (2.2.8) instead of equation (2.2.13).

The equivalent element stiffness relations in three-dimension can similarly be set up. In the general case of  $k$  link elements joining at node  $a$ , and from equation (2.2.8), the equilibrium equation for node  $a$  in the  $x_i$ -direction ( $i = 1, 2, 3$ ) is then given by

$$\sum_k \left\{ \left[ \frac{EA \Delta X_i}{L} \sum_{j=1}^3 \left( \frac{\Delta X_j}{L} \Delta \delta_j \right) \right] + \frac{T}{L} \left[ \Delta \delta_i - \frac{\Delta X_i}{L} \sum_{j=1}^3 \left( \frac{\Delta X_j}{L} \Delta \delta_j \right) \right] \right\}_k = P_i. \quad (2.2.14)$$

Equation (2.2.14) can be written for all nodes in the entire structure in the following matrix form, ie.

$$[K_o]\{\Delta\delta\} = \{P\} \quad (2.2.15)$$

where  $[K_o]$  is the overall stiffness matrix, and the  $T$ ,  $\Delta X_i$  and  $L$  terms in  $[K_o]$  refer to the prestress state. On the other hand, when considering the incremental loading,

$$[K_T]\{\Delta\delta\} = \{\Delta P\} \quad (2.2.16)$$

in which  $[K_T]$  is the tangent stiffness matrix, and the  $T$ ,  $\Delta X_i$  and  $L$  terms in  $[K_T]$  refer to the previous displaced state.

As for the element in figure 2.1 defined by nodes  $i$  and  $j$ , the three-dimensional element stiffness relations in matrix form within a global  $x_1$ -,  $x_2$ - and  $x_3$ -axis system are given by

$$\{P\} = [K]\{\delta\} = ([K_E] + [K_G])\{\delta\} \quad (2.2.17)$$

$$\text{in which } \{P\} = \begin{bmatrix} P_{1i} \\ P_{2i} \\ P_{3i} \\ P_{1j} \\ P_{2j} \\ P_{3j} \end{bmatrix}, \quad \{\delta\} = \begin{bmatrix} \delta_{1i} \\ \delta_{2i} \\ \delta_{3i} \\ \delta_{1j} \\ \delta_{2j} \\ \delta_{3j} \end{bmatrix},$$

$$\text{the elastic stiffness } [K_E] = \begin{bmatrix} k_e & -k_e \\ -k_e & k_e \end{bmatrix} \text{ where } [k_e] = \frac{EA}{L} \begin{bmatrix} l^2 & lm & ln \\ ml & m^2 & mn \\ nl & nm & n^2 \end{bmatrix},$$

$$\text{the geometric stiffness } [K_G] = \begin{bmatrix} k_g & -k_g \\ -k_g & k_g \end{bmatrix} \text{ where } [k_g] = \frac{T}{L} \begin{bmatrix} (1-l^2) & -lm & -ln \\ -ml & (1-m^2) & -mn \\ -nl & -nm & (1-n^2) \end{bmatrix} \quad (2.2.18)$$

with  $l, m$  as defined before and  $n = \frac{\Delta X_3}{L} = \cosine \text{ of angle between the element and the } x_3\text{-axis.}$

Siev [122] first derived the equilibrium equations in equation (2.2.14) with element stiffnesses as given by equation (2.2.18).

In the case of large displacement analysis with 'small strains' assumption, the above stiffness relations apply except that  $[k_g]$  is now given by

$$[k_g] = \frac{T}{L} \begin{bmatrix} 1 & 0 & 0 \\ 0 & 1 & 0 \\ 0 & 0 & 1 \end{bmatrix}. \quad (2.2.19)$$

This approach has been used by Turner, et. al. [130] to solve problems which involve truss and triangular plane stress elements.

With the above brief discussion establishing the element stiffness relations, the various available iterative solution methods are next outlined.

### 2.3 Iterative solution methods

The 3 iterative solution methods which will be discussed here include the Newton-Raphson, modified Newton-Raphson and secant stiffness methods.

#### 2.3.1 Newton-Raphson method

The Newton-Raphson method is most widely used for solving problems with geometric non-linearities because it provides a stable solution process. This method has been applied to form-finding and static analysis of tension structures by Argyris [3], Baron [21], Haug [67, 68], Knudson [83], Poskitt [116] and Siev [122].

The basic mechanics of this method can be summarised as follows-

- (1) Apply full load and solve  $[K_0]\{\delta\} = \{P\}$  for the displacements  $\{\delta\}$ .
- (2) The out-of-balance or residual forces are then given by (at a particular node in direction  $i$ )

$$R_i = P_{Ti} - \sum_k \left\{ (T + \Delta T) \frac{(\Delta X_i + \Delta \delta_i)}{L + e} \right\}_k \quad (2.3.1)$$

where  $P_{Ti}$  is the total applied load.

- (3) With the displacements and tensions known from step (1), the tangent stiffness relations are reset to form  $[K_T]$ .
- (4) Apply out-of-balance or residual nodal forces (as a load increment or decrement) and determine deflection increments  $\{\Delta\delta\}$  from



$$[K_T]\{\Delta\delta\} = \{R\}, \quad (2.3.2)$$

$$\text{and } \{\delta\} = \{\delta\} + \{\Delta\delta\}. \quad (2.3.3)$$

(5) Return to step (2) and iterate through steps (2) → (4) until convergence is reached (ie. when the residual forces become very low).

The Newton-Raphson method as applied to a single degree of freedom system having a 'stiffening' behaviour is illustrated in figure 2.2 while the case of 'softening' behaviour is shown in figure 2.3.

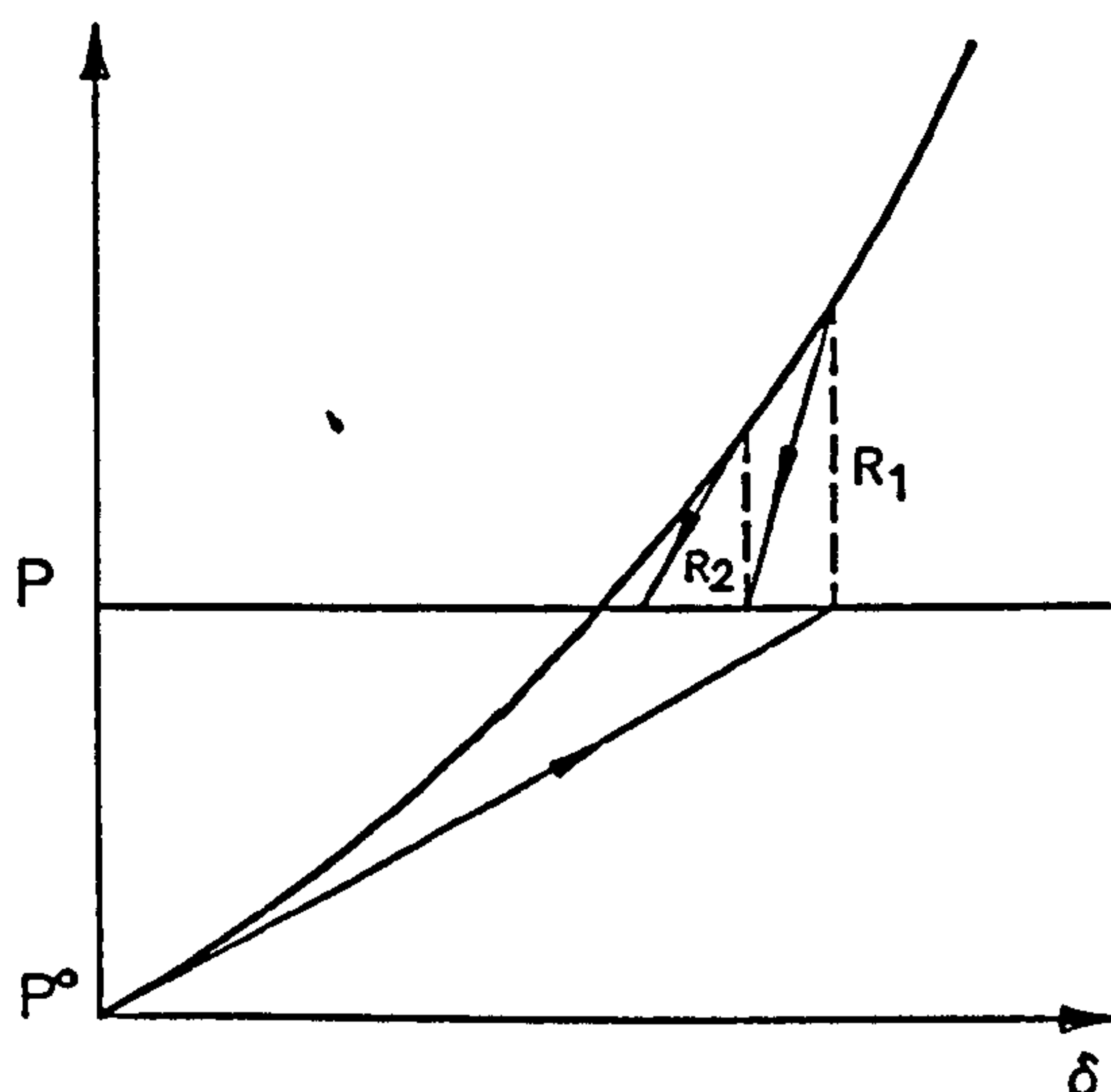


Figure 2.2 (Stiffening)

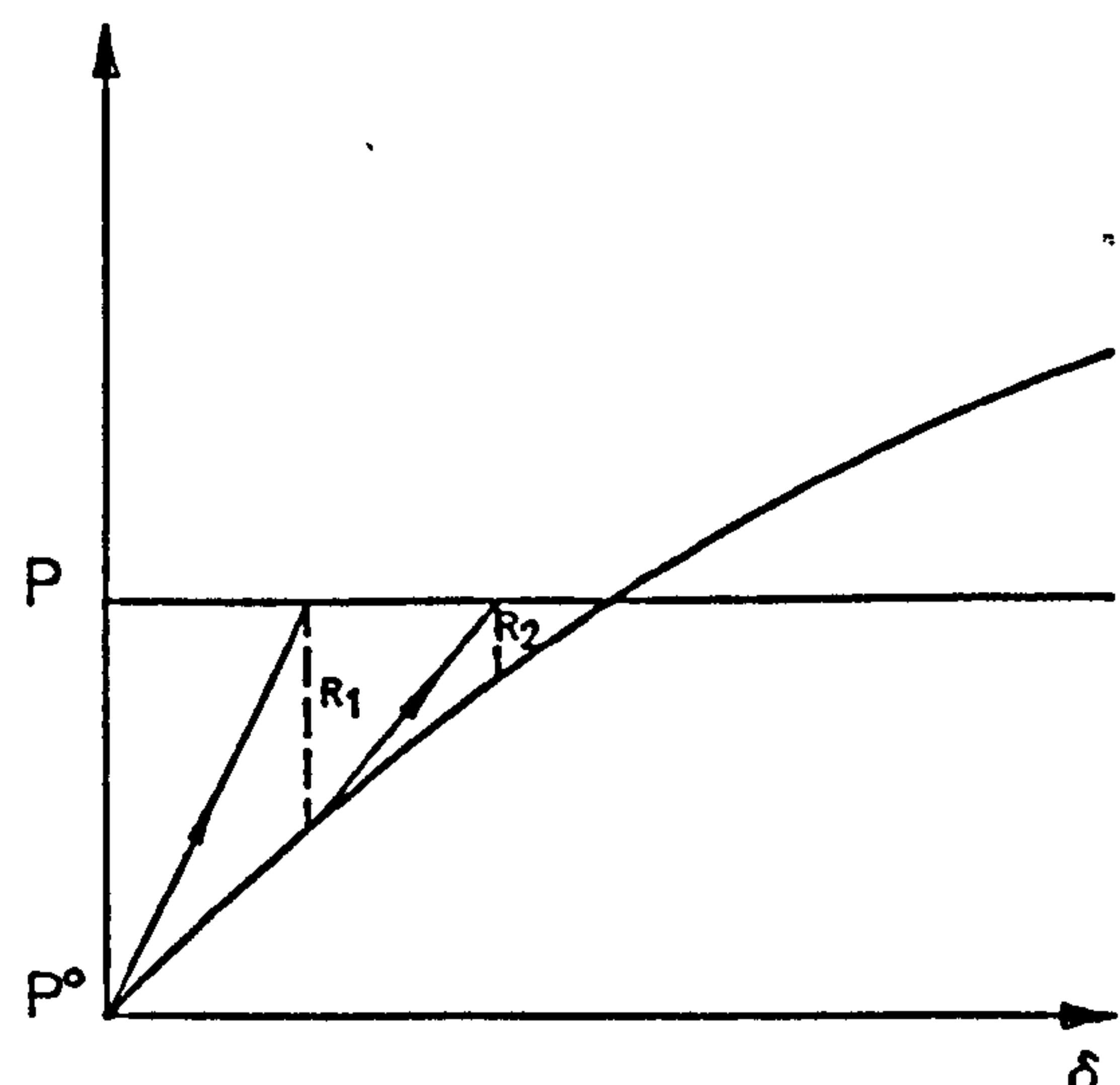


Figure 2.3 (Softening)

A system with 'stiffening' behaviour is most representative of tension structures. In situations where the diagonal stiffness terms are close to zero, the deflection increments have to be scaled down to restrict them within upper limits [67]. In addition, the Newton-Raphson method has a disadvantage that  $[K_T]$  needs to be reset and solved at each iteration step. During the solution process for the displacements, it is preferable to use Gaussian elimination for solving the simultaneous sets of equations.

### 2.3.2 Modified Newton-Raphson method

As the name suggests, this method is basically similar to the Newton-Raphson method mentioned above except that now  $[K_0]$  is used throughout the solution process (or reset only at infrequent intervals). As a result, there are fewer computations when compared to the standard Newton-Raphson method. In fact, the modified Newton-Raphson method is suitable only for problems where non-linearities are not too extreme. Consequently, this method is not ideal for dealing with tension structures. In addition, convergence is less rapid than for the Newton-Raphson method. The method

as used in the case of stiffening and softening systems are shown in figures 2.4 and 2.5 respectively.

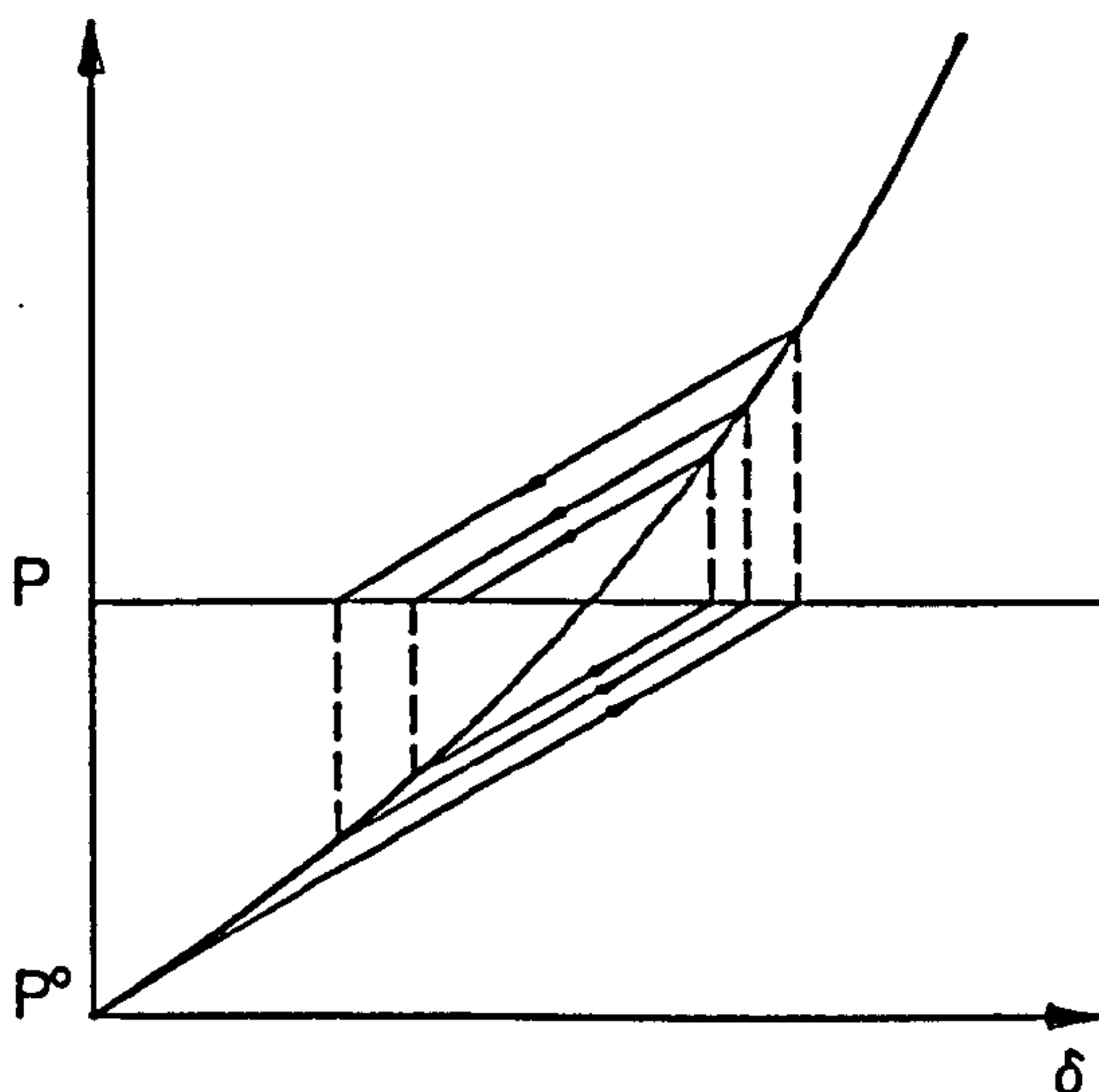


Figure 2.4 (Stiffening)

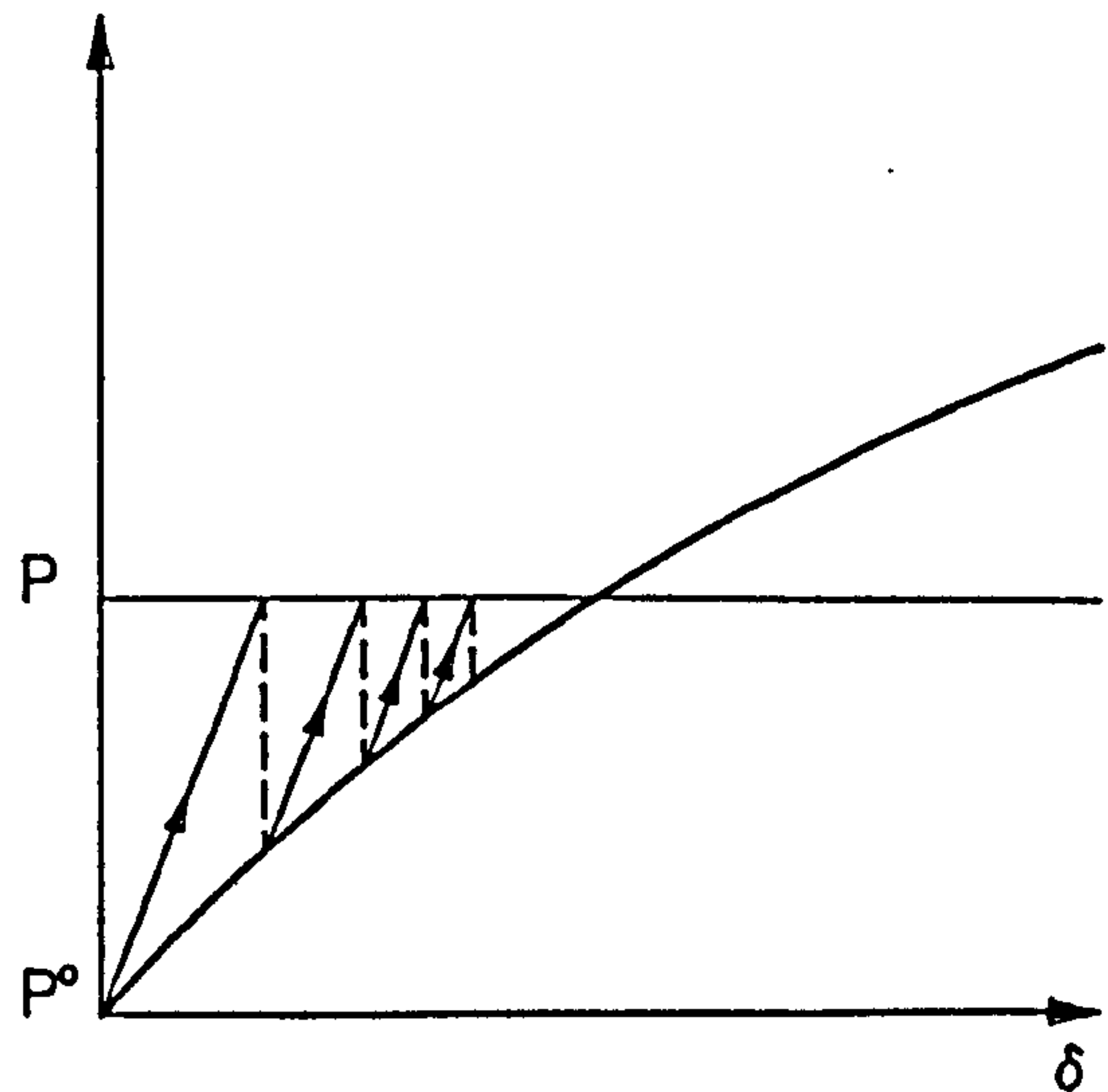


Figure 2.5 (Softening)

In this method, the initial stiffness matrix is (inverted and then) held constant throughout. A variation is to reset the stiffness matrix at infrequent intervals having a fixed number of iterations within each interval. Besides this modification, the method is similar to the standard Newton-Raphson method, ie. as in section 2.3.1, follow steps (1), (2), (4) and (5), skip step (3) or execute it only at infrequent intervals.

$$\{\delta\} = [K_0]^{-1}\{P\} \Rightarrow \{R\} \Rightarrow \{\Delta\delta\} = [K_0]^{-1}\{R\}. \quad (2.3.4)$$

Figure 2.5 shows that a geometrically softening system always produces a converged solution. For a stiffening system which is highly non-linear, an initial out-of-balance force which is too large may lead to divergence of the solution process as shown in figure 2.6. In the case of tension structures, typical working loads may already be too large and result in divergence. A possible cure is to use a fictitious stiffness matrix  $[K_0']$  in which the stiffness terms are artificially increased. Mollman and Mortensen [98] have applied this strategy which they called 'simplified Newton-Raphson' to the solution of prestressed networks as shown in figure 2.6. The modified Newton-Raphson method in total displacement form is illustrated in figure 2.7 in

which  $\bar{R}_i$  stands for the absolute value of the residual force at the  $i$ th iteration.

Furthermore, it is realised that the residuals in successive iterations oscillate about the converged position. Hence, a possible improvement is to adopt

$$\{\delta\}^{q+1} = [K_0]^{-1}\left\{P + \frac{R^q + R^{q-1}}{2}\right\} \quad (2.3.5)$$

at iteration  $q$  as proposed by Krishna [88] and can lead to much increase in the convergence rate.

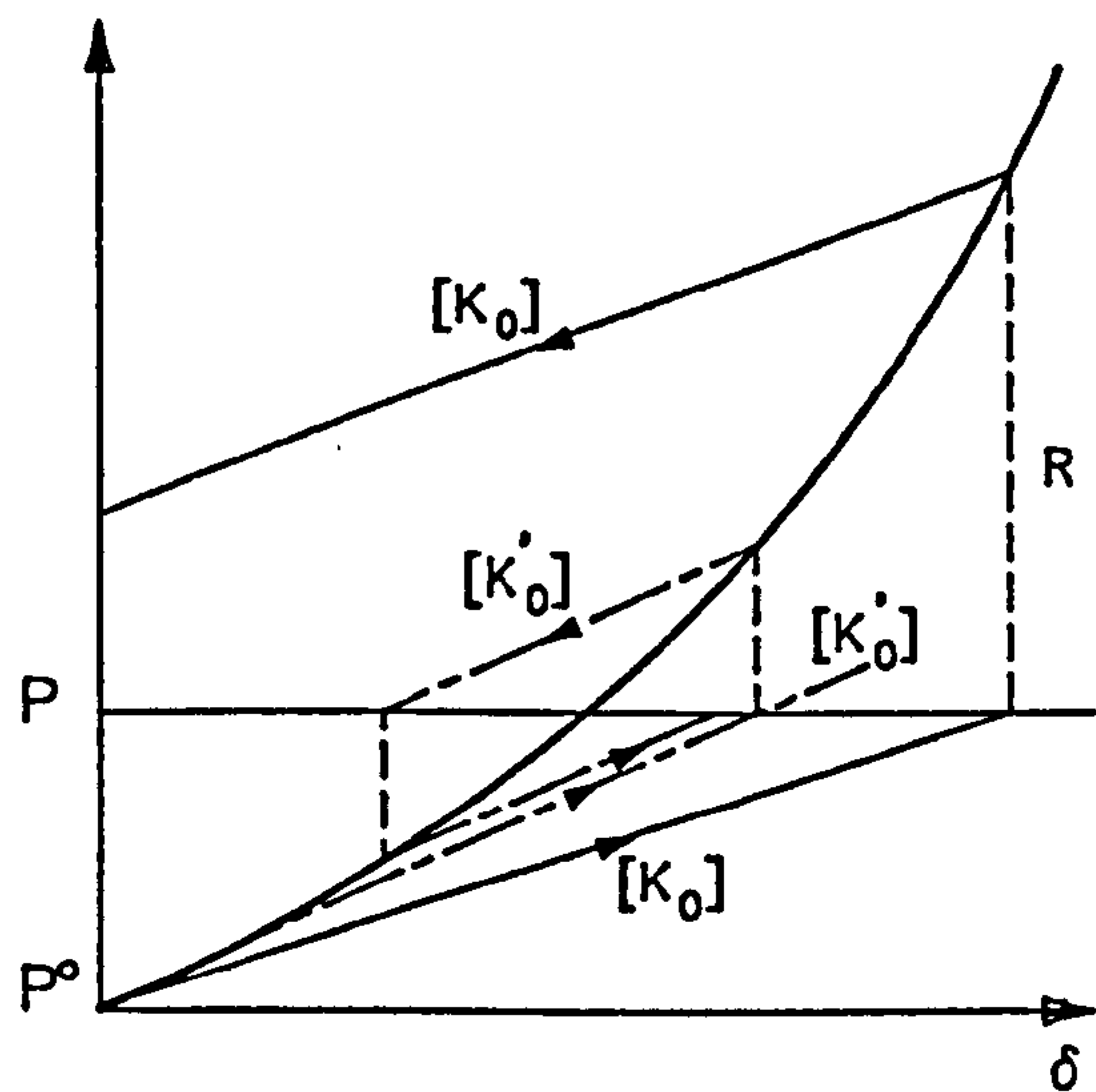


Figure 2.6

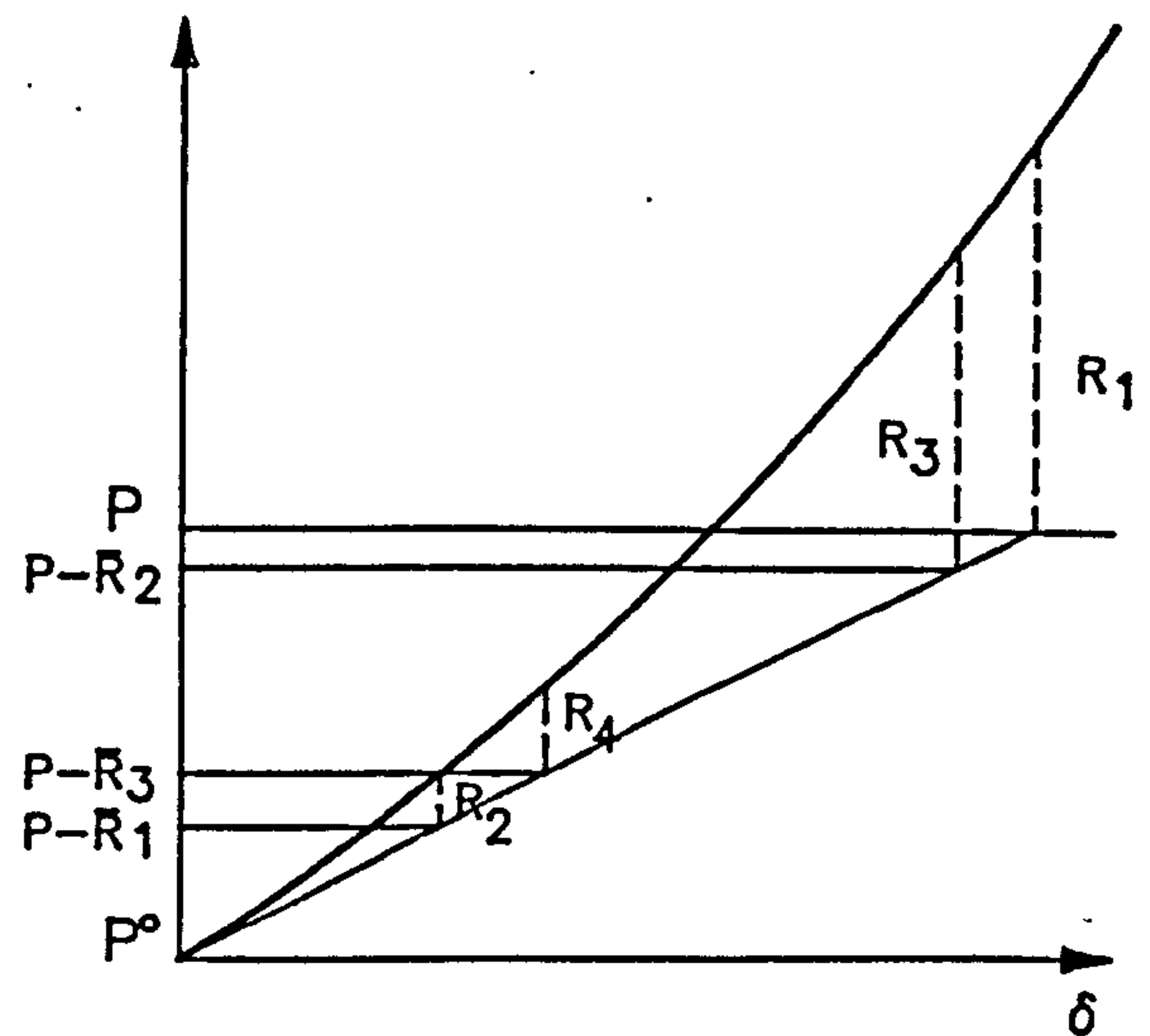


Figure 2.7

### 2.3.3 Secant stiffness method

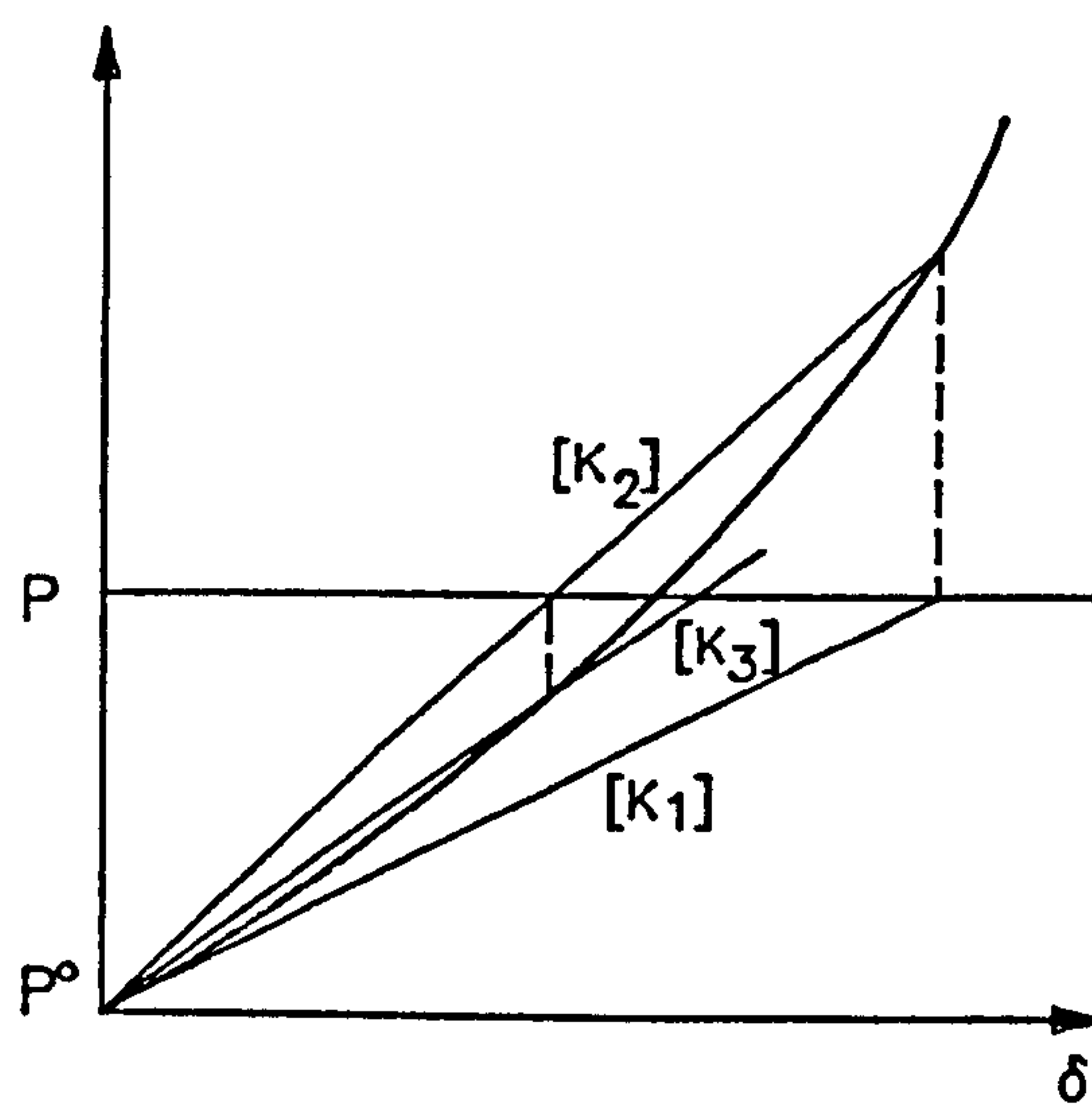


Figure 2.8

The secant stiffness method is demonstrated in figure 2.8 and uses the relation

$$[K_s]^q \{\delta\}^{q+1} = \{P\} \quad (2.3.6)$$

in which the secant stiffness matrix  $[K_s]^q = [K_l] + [K_{nl}]^q$  with  $[K_l]$  being a linear matrix and  $[K_{nl}]^q$  a non-linear function of displacements. Hence, the  $[K_{nl}]^q$  is



reset during each iteration while  $[K_1]$  remains constant. The iterative procedure is applied in the total displacement form.

This method has been used to investigate cable and truss structures by Baron and Venkatesan [21]. The secant stiffness method has the advantage of being able to cope with element slackening. In situations with a few members going slack, it is useful to have a combination of the secant and modified Newton-Raphson methods.

In general, all matrix iterative methods may be written in the form of a recurrence equation as follows-

$$\{\delta\}^{q+1} = \{\delta\}^q + ([K]^q)^{-1} \{R\}^q \quad (2.3.7)$$

in which if

- (a)  $[K]^q = [K_T]^q$  gives the Newton-Raphson method,
- (b)  $[K]^q = [K_0]$  gives the modified Newton-Raphson method,
- (c)  $[K]^q = [K_s]^q$  gives the secant stiffness method.

## 2.4 Incremental solution methods

For structures having both material and geometric non-linearities, a path dependent solution is expected as  $[K_T]$  becomes a function of current geometry and possibly current stress levels as well. The path dependent solutions are also required when dealing with on/off non-linearities such as element slackening, and when applied loads are functions of displacements. In solving path-dependent problems, the true solution path is only obtained by applying the full load in sufficiently small increments which is the basis of the incremental method, ie.

$$[K_T]\{\Delta\delta\} = \{\Delta P\}. \quad (2.4.1)$$

The structure is assumed to behave linearly within each load increment. In other words, the method is equivalent to solving a succession of linear problems with the tangent stiffness reset at each load increment.

The incremental methods can be grouped under two categories as follows-

- (1) Purely incremental solution in which the equilibrium state is not fully achieved and the solution itself tends to deviate away from the true load-deflection behaviour.

- (2) Incremental solution with correction steps to ensure full equilibrium is achieved within each load increment and as such, known as 'self-correcting' methods.

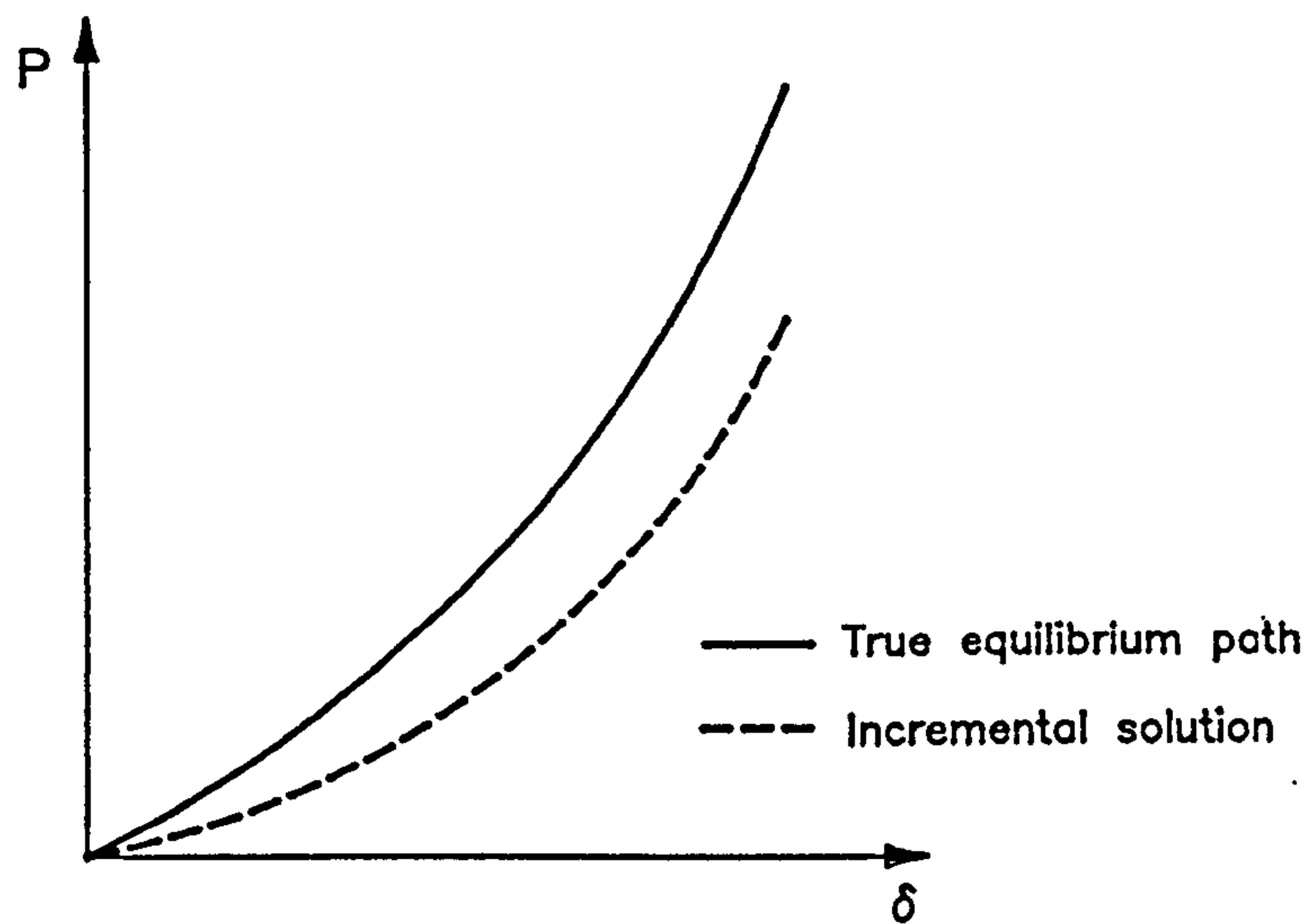


Figure 2.9

An example which comes under category (1) is the Euler method which in fact is the simplest form of incremental solution [78]. This method is based on the Euler forward difference approximation and thus, equation (2.4.1) is set up at the start of each load increment. Although the Euler method is popular in use, it tends to deviate rapidly from the true solution path. Improved results, at the expense of additional computation, are possible by taking  $[K_T]$  not at the beginning but near the mid-point of each load increment, corresponding to a second order Runge-Kutta procedure [62]. Another obvious possibility is to apply large load increments over linear regions but smaller increments with increasing non-linearity as proposed by Bergan and Soriède [26].

The tendency of methods from category (1) to deviate from the true solution path is eliminated in methods from category (2) by using self-correcting procedures. The simplest self-correcting method is to apply the current residual forces to the next load increment. This is equivalent to one cycle of the Newton-Raphson iteration followed by a simple Euler increment using the same  $[K_T]$  as for the iteration. With more iterations within each load increment, a closer approximation to the true equilibrium path is obtained. When iterating within each load step,  $[K_T]$  may either be reset at each iteration or remains constant throughout. The former corresponds to the Newton-Raphson method while the later is the modified Newton-Raphson method.

As a summary, the four possible solution methods are as follows- (see figure 2.10)

- (1) incremental solution,
- (2) incremental solution with correction for residual forces from previous load step,

- (3) Newton-Raphson iteration,
- (4) modified Newton-Raphson iteration.

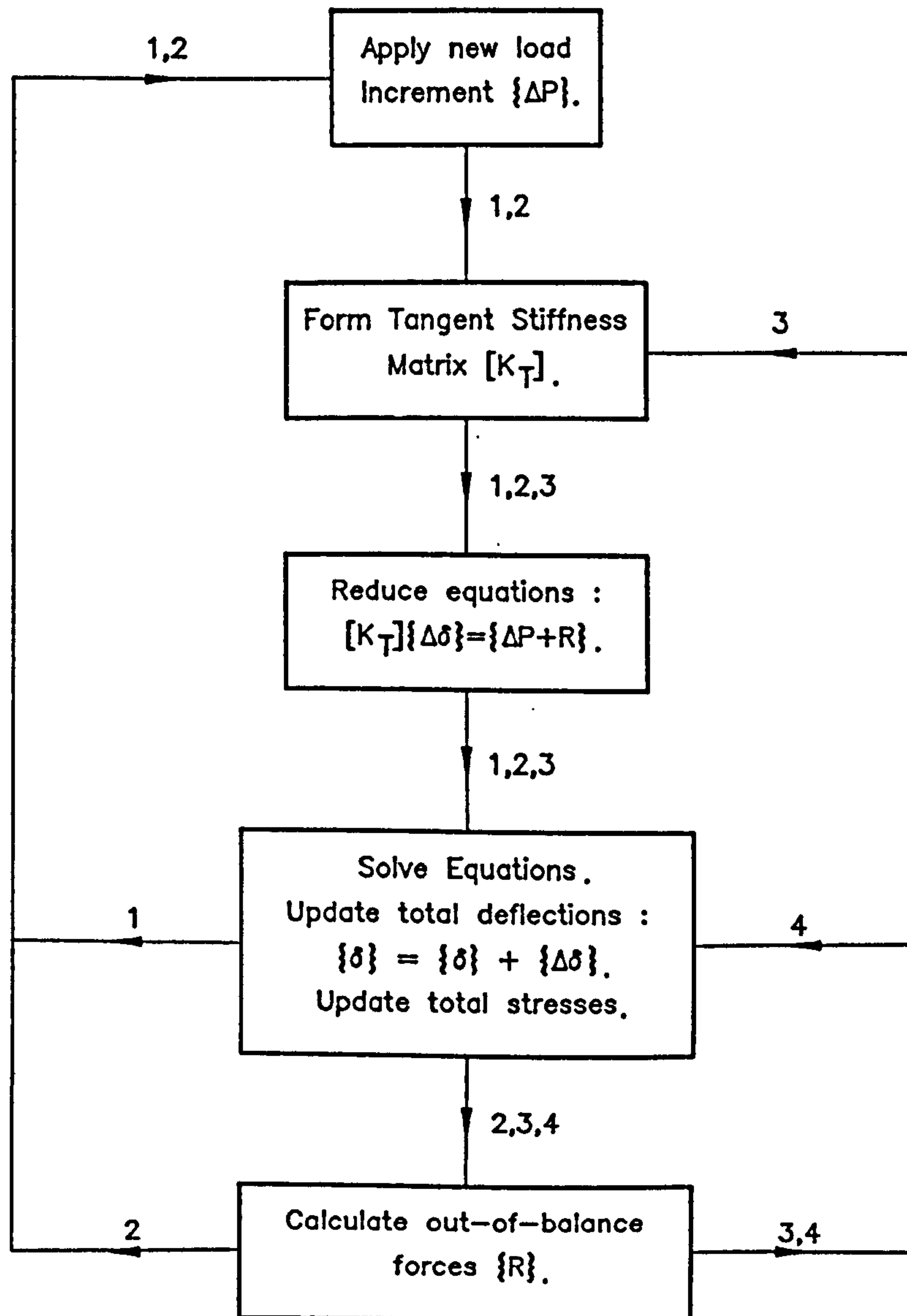


Figure 2.10

For the incremental solution in (2), either (3) or (4) may be applied to the iterations within each load increment until equilibrium is achieved. The choice of solution method relies mainly upon the type and level of non-linearity in each problem. In the presence of extreme geometric and material non-linearities, a combination of (2), (3) and (4) may be needed. If only material non-linearities are present, method (2) alone may suffice. Further factors to be considered are the loading level and stress-strain history. For instance, as load increments are applied up to the point of linear behaviour, an iterative solution is suitable and for the non-linear region beyond, an incremental solution is appropriate.



As mentioned earlier, the convergence of incremental methods can be increased by taking  $[K_T]$  at the mid-point of the load increment instead of at the beginning. This may be implemented by extrapolating previously known deflections or using an averaged tangent stiffness.

Greenberg [62] investigating the inelastic behaviour of cable structures up to failure, adopted a scheme of averaging the main diagonal stiffness terms  $K_{ii}$  to correct the deflections at each cycle. The process in use is outlined as follows-

- (1) Form  $[K_T]$  based on current conditions and store the  $K_{ii}$  terms.
- (2) Apply load increments  $\Delta P$  and solve for linearised deflections and tensions.
- (3) Update the modulus of elasticity for individual members according to their stresses from (2).
- (4) Form  $K_{ii}'$  coefficients based on new geometry and elastic moduli.
- (5) Revise deflections:  $\delta_i = \frac{K_{ii}' + K_{ii}}{2K_{ii}'} \times \delta_i$
- (6) Determine residual forces based on revised geometry and return to (1).
- (7) Iterate from (1) → (6) until residuals fall within acceptable limits.
- (8) Proceed to next load increment if all element strains are less than the ultimate strain permitted for the material and return to (1).
- (9) Repeat (1) → (8) until ultimate load is reached.

In step (3), a continuous exponential function is assumed to model the stress-strain behaviour of steel cables over the inelastic region.

## 2.5 Explicit analyses

As opposed to implicit methods, an explicit solution scheme does not involve forming the overall or tangent stiffness matrix. The generally known explicit methods can be grouped into two categories, ie. the minimisation methods and the relaxation methods.

### 2.5.1 Minimisation methods

The physical basis of minimisation methods is to establish the equilibrium state by minimising the total potential energy function  $W$  with respect to all the possible displacements  $\{\delta\}$  in which

$$W = U + V \quad (2.5.1)$$

where  $U$  is the strain or potential energy due to internal forces and  $V$  the potential energy (ie. given by  $\{\delta\}^T \cdot \{P\}$ ) due to applied forces  $\{P\}$  assumed independent of displacements  $\{\delta\}$ .

The direct minimisation techniques such as the random search or Monte-Carlo method make use of the objective function  $W$  only in the solution process. These methods do not require explicit evaluation of any partial derivatives of  $W$ . Mallett, et. al. [94, 95] have applied direct minimisation to solving non-linear structural problems with varying success. Many of the direct search methods lack convergence proofs and result in premature convergence. However in structural problems, the preferred methods are generally the gradient methods of minimisation which have in their solutions in addition to the objective function  $W$  itself, values of partial derivatives of  $W$  with respect to independent variables as well as information from previous iterations.

Basically, minimisation methods use the idea that in moving from point  $x_i$  a distance of  $d_i$  along the direction  $\phi_i$  such that

$$x_{i+1} = x_i + d_i \phi_i, \quad (2.5.2)$$

results in the value of function  $F$  at the new point  $x_{i+1}$  being smaller, ie.

$$F(x_{i+1}) < F(x_i). \quad (2.5.3)$$

Given a function  $F(x)$  in a system with  $n$  degrees of freedom, for which all the first partial derivatives  $\frac{\partial F}{\partial x_i}$  ( $i = 1, \dots, n$ ) exist at all points, a necessary condition for a minimum to exist is given by

$$\frac{\partial F}{\partial x_1} = \frac{\partial F}{\partial x_2} = \dots = \frac{\partial F}{\partial x_i} = 0. \quad (2.5.4)$$

The objective function  $W$  may be taken as an energy surface in  $n$ -dimensional space. Provided the energy surface is convex and the initial state lies on the surface, a solution may be found by searching along a descent direction in  $n$ -dimensional space until the minimum in that particular direction is located. The search continues along a different descent direction and the process repeated until the global minimum of  $W$  is achieved. The displacement vector  $\{\delta\}$  is updated iteratively using the general relation, ie.

$$\{\delta\}^{q+1} = \{\delta\}^q + S^q \{V\}^q \quad (2.5.5)$$

at iteration  $q$  in which  $\{V\}^q$  is the gradient vector (ie. vector of descent directions) and  $S^q$  is a scalar steplength representing an incremental distance in the descent/search direction. An essential feature of all gradient minimisation methods is the linear search in the descent direction to find the optimum steplength to descent in that direction. Normalisation of  $\{V\}^q$  is not necessary, as it merely has the effect of scaling the steplength  $S^q$ . As the

analysis procedure is explicit, no stiffness matrix operations are needed and thus, has the advantage of much reduced memory requirements in the computer.

The descent direction vector  $\{V\}$  can be found by various first or second order gradient methods in which the minimum along a particular direction is determined at each stage of iteration by expressing  $W$  as a polynomial in  $S$  and then, finding the  $S$  which minimises the polynomial. The first order methods have principally been developed and applied by Buchholdt [Refs. 29 → 39] to the analysis of a wide range of cable network problems. The second order gradient methods use the second derivatives of  $W$  and the one most often used is the Newton-Raphson method (an implicit technique). This has been used as such with a steplength control by Buchholdt [35]. The second partial derivatives of  $W$  with respect to  $\{\delta_i\}$  lead to stiffness matrix relationships.

Furthermore, it has been shown that the energy surface of a cable network is convex if all members of the network remain in tension [31]. This is not, however a necessary condition and it is possible for some members to go slack temporarily while moving along the descent direction. During the form-finding process, convergence difficulties may perhaps be experienced as a result.

### 2.5.1.1 Gradient vector

The total potential energy of a structural idealisation with  $K$  elements can be written as

$$W = \sum_{k=1}^K U_k - \{P\}^T \{\delta\} \quad (2.5.6)$$

in which  $U_k$  is the strain energy of element  $k$  and  $\{\delta\}$  the true displacement vector.

The exact expression for the gradient vector  $\left\{ \frac{\partial W}{\partial \delta_i} \right\}$  was derived by Buchholdt [31]. A detailed discussion can also be found in [133]. The derivative of the total potential energy function  $W$  with respect to a displacement  $\delta_i$  at any node  $a$  in direction  $i$  represents the out-of-balance forces in that direction, ie. (the proof can be found in [31], [115] and [133])

$$g_i = \frac{\partial W}{\partial \delta_i} = \sum_k \left\{ (T + \Delta T) \frac{(\Delta X_i + \Delta \delta_i)}{L + e} \right\}_k - P_{Ti} \quad (2.5.7)$$



in which the summation applies to all links  $k$  joining node  $a$  to adjacent nodes  $b$ , and

$$\Delta X_{ik} = X_{ia} - X_{ib} \quad , \quad \Delta \delta_{ik} = \delta_{ia} - \delta_{ib}. \quad (2.5.8)$$

The vector of out-of-balance forces  $\{g\}$  in the global coordinate system has the direction of greatest increase of the total potential energy for the displacement vector  $\{\delta\}$  and

$$\{g\} = -\{R\} \quad (2.5.9)$$

where  $\{R\}$  is the vector of current out-of-balance forces acting on nodes within the structure.

The strain energy in any element  $k$ ,  $U_k$  may be expressed as

$$U_k = \int T_k de_k = \int (T^0 + \frac{EA}{L}e)_k de_k = T_k^0 e_k + \frac{EA}{2L_k} e_k^2. \quad (2.5.10)$$

If the element strain  $e_k$  corresponds to the displacement state  $\{\delta'\}$  at any point along the current descent direction, then

$$\{\delta'\} = \{\delta\} + S\{V\} \quad (2.5.11)$$

and for element  $k$  with end nodes  $i$  and  $j$ ,

$$\begin{aligned} (L + e)_k^2 &= \sum_{m=1}^3 [(X_{mj} + \delta_{mj} + SV_{mj}) - (X_{mi} + \delta_{mi} + SV_{mi})]^2 \\ &= \sum_{m=1}^3 (\Delta X_m + \Delta \delta_m + S\Delta V_m)^2 \\ &= [(\Delta X) + (\Delta \delta) + S(\Delta V)]^T [(\Delta X) + (\Delta \delta) + S(\Delta V)] \end{aligned} \quad (2.5.12)$$

in which  $\Delta X_m = X_{mj} - X_{mi}$ ,  $\Delta \delta_m = \delta_{mj} - \delta_{mi}$ ,  $\Delta V_m = V_{mj} - V_{mi}$ ,  
 $X_{mi}$ ,  $X_{mj}$  = initial coordinates of nodes  $i$  and  $j$  respectively.

On expanding equation (2.5.12) and neglecting  $e_k^2$  (ie. assume  $e_k \ll L_k e_k$ ),

$$\begin{aligned} e_k &= \frac{1}{L} [(\Delta X)^T \{\Delta \delta\} + \frac{\{\Delta \delta\}^T \{\Delta \delta\}}{2}] + ((\Delta X)^T \{\Delta V\} + \{\Delta V\}^T \{\Delta \delta\})S + \\ &\quad \left( \frac{\{\Delta V\}^T \{\Delta V\}}{2} \right) S^2] \\ &= \frac{1}{L} (a_1 + a_2 S + a_3 S^2). \end{aligned} \quad (2.5.13)$$

By substituting equation (2.5.13) into equation (2.5.10) for the element strain energy, Buchholdt [31] produced a polynomial of fourth order in steplength  $s$  for the total potential  $W$  as follows-

$$W = c_1 s^4 + c_2 s^3 + c_3 s^2 + c_4 s + c_5. \quad (2.5.14)$$

Furthermore, the total potential energy at iteration  $(q+1)$  is then given by

$$\begin{aligned} W^{q+1} &= \sum_{k=1}^K U_k - \{P\}^T \{\delta\}^{q+1} \\ &= \sum_{k=1}^K U_k - \{P\}^T \{\delta\}^q - s \{P\}^T \{V\}^q \\ &= \sum_{k=1}^K (T_k^0 e_k + \frac{EA}{2L_k} e_k^2) - \{P\}^T \{\delta\}^q - s \{P\}^T \{V\}^q. \end{aligned} \quad (2.5.15)$$

By substituting equation (2.5.13) into equation (2.5.15) and comparing the coefficients of  $s, s^2, s^3$ , etc. with equation (2.5.14),

$$\begin{aligned} c_1 &= \sum \frac{EA a_3^2}{2L^3}, & c_2 &= \sum \frac{EA a_2 a_3}{L^3}, \\ c_3 &= \sum \left[ \frac{T^0}{L} a_3 + \frac{EA}{2L^3} (a_2^2 + 2a_1 a_3) \right], \\ c_4 &= \sum \left[ \frac{T^0}{L} a_2 + \frac{EA}{L^3} a_1 a_2 \right] - \{P\}^T \{V\}, \\ c_5 &= \sum \left[ \frac{T^0}{L} a_1 + \frac{EA}{2L^3} a_1^2 \right] - \{P\}^T \{\delta\}, \end{aligned} \quad (2.5.16)$$

where the summation is for each element within the structure.

For a minimum value of the total potential in equation (2.5.14),

$$\frac{\partial W}{\partial s} = 4c_1 s^3 + 3c_2 s^2 + 2c_3 s + c_4 = 0 \quad (2.5.17)$$

and solve the resulting cubic equation either analytically or iteratively using Newton's approximation for the smallest positive root which gives  $s^q$ .

The displacement vector is then updated, ie.

$$\{\delta\}^{q+1} = \{\delta\}^q + s^q \{V\}^q. \quad (2.5.18)$$

The minimisation process is repeated until the out-of-balance forces (or gradient vector) are negligible and the equilibrium state attained.

### 2.5.1.2 Method of Steepest Descent

The steepest descent method is the simplest first gradient method. According to this method [32],

$$\{V\} = -\{g\} = \{R\}. \quad (2.5.19)$$

$$\text{Thus, } \{\delta\}^{q+1} = \{\delta\}^q + S^q\{R\}^q. \quad (2.5.20)$$

Each descent direction is pursued until  $W$  is minimised locally and the method follows a zig-zag descent path towards convergence as shown in figure 2.11.

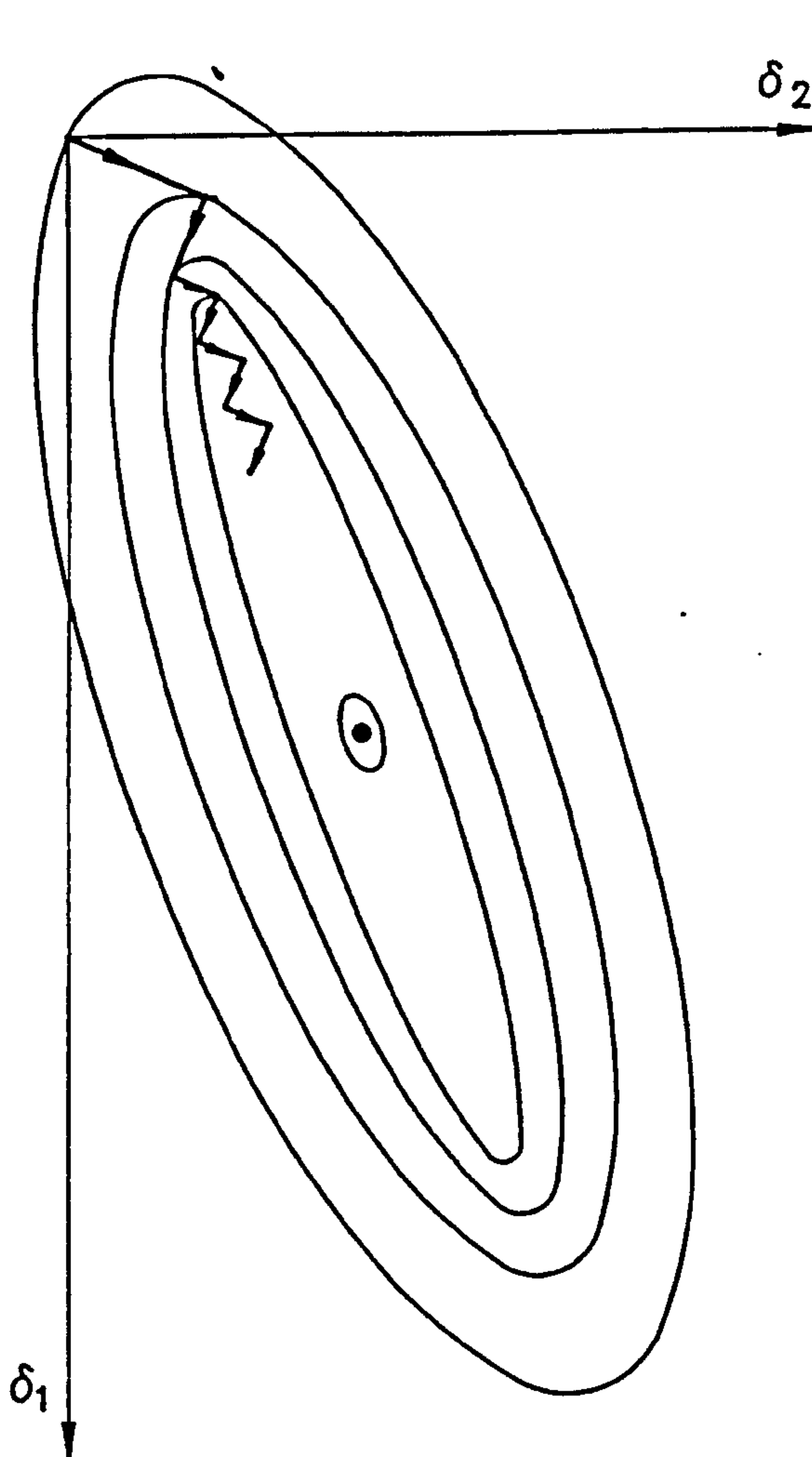


Figure 2.11

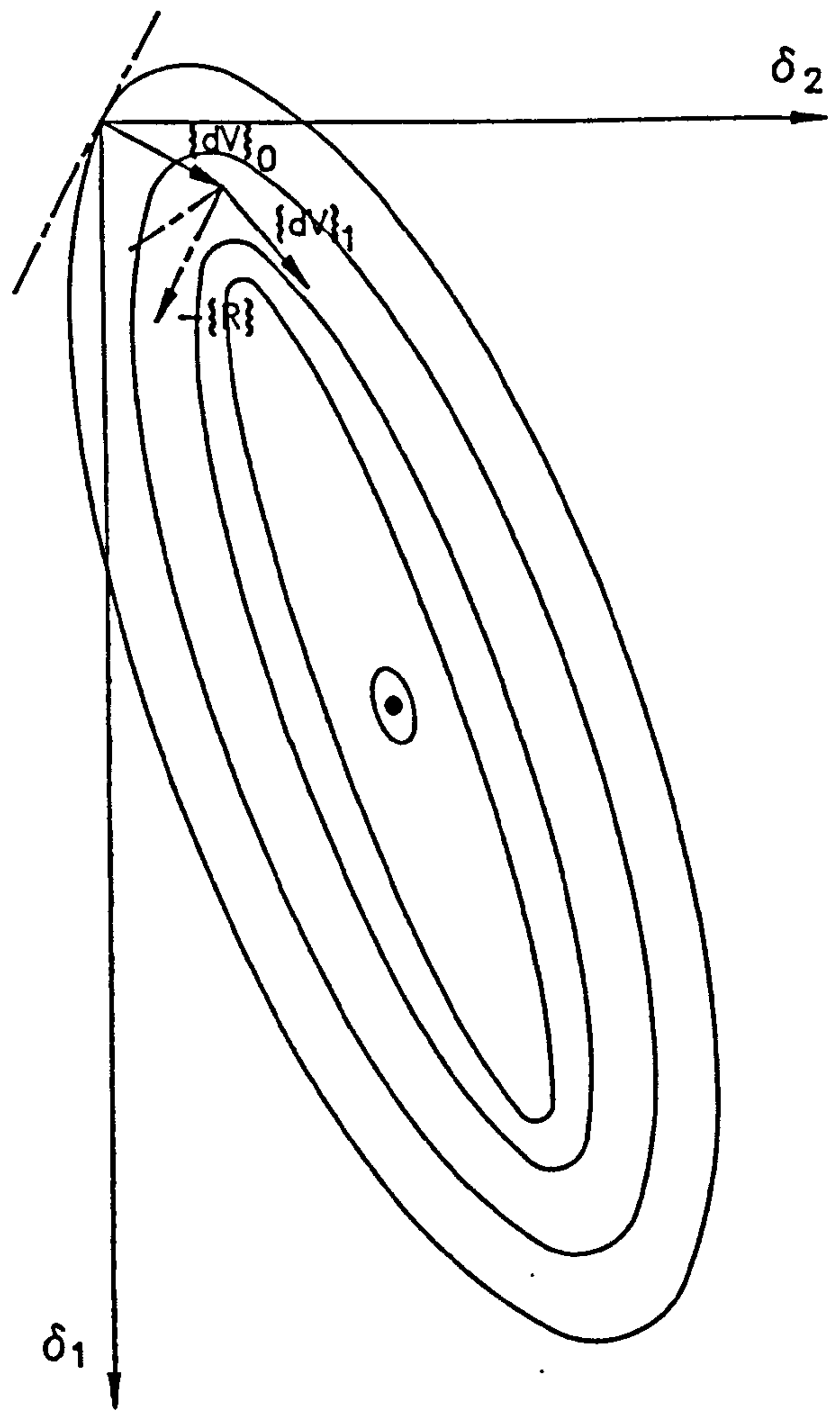


Figure 2.12

The steepest descent method has several disadvantages which make it impractical for many problems. The zig-zag path of the steepest descent



method results in very slow convergence. A possible improvement is to use a relaxed steplength, ie.

$$\{\delta\}^{q+1} = \{\delta\}^q + \lambda S^q \{R\}^q \quad (2.5.21)$$

with a relaxation factor  $0 < \lambda < 1$ . It is not possible to make an analytical prediction of the optimum value of  $\lambda$  to use. However, for a small cable network analysis, with  $(0.05 < \lambda < 0.95)$  the number of iterations to convergence are reduced to between 5% and 25% of those needed using the full steplength [133].

### 2.5.1.3 Conjugate Gradient method

The most effective first order gradient technique is based on conjugate gradients as developed by Hestenes and Stiefel [73] for solving sets of linear equations. A pair of conjugate vectors have the following property, ie.

$$\{V\}_i^T [K] \{V\}_j = 0 \quad (\text{for } i \neq j), \quad (2.5.22)$$

and Fletcher and Reeves [56] have shown that, for constant  $[K]$ ,

$$\beta^q = \frac{\|R^{q+1}\|^2}{\|R^q\|^2} \quad \text{in which } \|R^q\|^2 = \{R\}^T \{R\}. \quad (2.5.23)$$

and the recurrence relation for the descent direction of the conjugate gradient method is given by

$$\{V\}^{q+1} = \{R\}^{q+1} + \beta^q \{V\}^q. \quad (2.5.24)$$

Conjugate descent directions have been set without direct reference to the system matrix  $[K]$ . For a linear problem with  $n$  degrees of freedom, exact convergence is obtained within  $n$  iterations [56]. However, for non-linear problems when  $[K]$  does not remain constant, convergence may take longer as the descent directions are now only approximately conjugate.

The first descent vector (or first few) is taken in the direction of steepest descent. Subsequently, the previous descent vector is given a weighting  $\beta^q$  in determining the current vector. Graphically, for a structure with two degrees of freedom  $\delta_1$  and  $\delta_2$ , the conjugate gradient technique is illustrated in figure 2.12 [38].

### 2.5.1.4 Scaling and transformation of energy surface

The convergence rate of the conjugate gradient method depends on the condition number of the associated stiffness matrix, defined as the ratio of the

highest to lowest eigenvalues of the matrix. In the case of a two degree of freedom system, these eigenvalues are inversely proportional to the squares of the lengths of the axes forming the elliptic contours of the total potential energy surface. When the condition number is large, the potential ellipses are long and narrow implying slow convergence. As the condition number approaches unity, the total potential contours change towards a circular profile and the convergence rate increases [38]. The condition number is a measure of the ill-conditioning of the system of equations.

In order to improve the convergence of the conjugate gradient method, the contour lines can be transformed to result in the potential ellipses changing towards a circular profile. This is achieved by replacing the actual displacement vector  $\{\delta\}$  with a scaled vector  $\{u\}$  such that

$$\{\delta\} = [H]\{u\} \quad (2.5.25)$$

where  $[H]$  is a diagonal scaling matrix.

The total potential energy written in matrix notation is as follows-

$$W = \frac{1}{2}\{\delta\}^T[K_T]\{\delta\} - [P]^T\{\delta\}. \quad (2.5.26)$$

Substituting equation (2.5.25) into equation (2.5.26),

$$\begin{aligned} W &= \frac{1}{2}\{u\}^T[H]^T[K_T][H]\{u\} - [P]^T[H]\{u\} \\ &= \frac{1}{2}\{u\}^T[K_T']\{u\} - [P]^T[H]\{u\} \end{aligned} \quad (2.5.27)$$

in which  $[K_T'] = [H]^T[K_T][H]$ .

The scaled gradient vector is then given by

$$\left\{\frac{\partial W}{\partial u}\right\} = [H]\left\{\frac{\partial W}{\partial \delta}\right\} \quad (2.5.28)$$

and the scaled descent direction  $\{V'\}$  is incremented as follows-

$$\{V'\}^{q+1} = -\left\{\frac{\partial W}{\partial u}\right\}^{q+1} + \beta^q\{V'\}^q \quad (2.5.29)$$

(similar as for conjugate gradient technique with no scaling).

The optimal steplength  $s$  along the descent direction towards a minimum potential value (ie.  $\frac{\partial W}{\partial s} = 0$ ) is then solved for.

$$\{u\}^{q+1} = \{u\}^q + s^q \{V'\}^q. \quad (2.5.30)$$

Subsequently, the scaled displacement vector  $\{u\}$  is updated as given by equation (2.5.30). The above process is re-iterated until the scaled residual forces  $\left\{\frac{\partial W}{\partial u}\right\} = 0$  and the actual displacements are then given by  $\{\delta\} = [H]\{u\}$ .

Furthermore, Wakefield [133] extended Buchholdt's gradient minimisation method in order to account for arbitrary element strains. Buchholdt made an assumption of small strains (ie.  $e_k \ll L_k e_k$ ) in deriving the fourth order polynomial in  $s$  given by equation (2.5.14). For compatibility reasons, the same approximation should apply in the definition of the gradient vector. Otherwise, unsatisfactorily high residual forces may result at convergence or even complete divergence may occur. The work by Wakefield [133] on the exact gradient minimisation for arbitrary cable strains based upon the scaled conjugate gradient approach is briefly outlined as follows-

$$\{X^s\} = \{X^0\} + \{u'\} + s\{V'\} \quad (2.5.31)$$

in which  $\{X^s\}$  are the nodal coordinates at a point along the current scaled descent direction and  $\{X^0\}$  are the initial coordinates. As mentioned earlier, the idea is to find the smallest positive value of  $s$  which minimises the total potential energy of the structure.

In addition, for an element  $k$ ,

$$e_k^s = e_k + e_k' \quad (2.5.32)$$

in which  $e_k = L_k^c - L_k$ ,

$L_k^c$  = current length at point  $\{X^0 + u'\}$ ,

$L_k$  = initial length,

$e_k'$  = element extension due to displacement along the current descent direction,

$e_k^s$  = current total element extension.

With  $\Delta$  denoting the difference between values at end nodes  $i$  and  $j$  of element  $k$ ,

$$L_k^{c2} = \{\Delta X_k^0 + \Delta u_k'\}^T \{\Delta X_k^0 + \Delta u_k'\},$$



$$(L_k^c + e_k')^2 = \{\Delta X_k^0 + \Delta u_k' + s\Delta V'\}^T \{\Delta X_k^0 + \Delta u_k' + s\Delta V'\},$$

$$2L_k^c e_k' + e_k'^2 = 2s\{\Delta V'\}^T \{\Delta X_k^0 + \Delta u_k'\} + s^2\{\Delta V'\}^T \{\Delta V'\}. \quad (2.5.33)$$

Assuming  $((e_k')^2 \ll L_k e_k')$  leads to

$$e_k' = \frac{s}{L_k^c} \{\Delta V'\}^T \{\Delta X_k^0 + \Delta u_k'\} + \frac{s^2}{2L_k^c} \{\Delta V'\}^T \{\Delta V'\}$$

$$= a_2' s + a_3' s^2.$$

$$\Rightarrow e_k^s = a_1' + a_2' s + a_3' s^2 \text{ where } a_1' = e_k. \quad (2.5.34)$$

The trick here is that unlike Buchholdt's method, the approximation of neglecting  $(e_k')^2$  does not affect the final solution as  $(e_k^s \rightarrow e_k)$  when  $(e_k' \rightarrow 0)$  at the convergence stage.

Subsequently, by substituting equation (2.5.34) into equation (2.5.10), the element strain energy is now given as follows-

$$U_k = T_k^0(a_1' + a_2' s + a_3' s^2) + \frac{EA}{2L_k}(a_1' + a_2' s + a_3' s^2)^2. \quad (2.5.35)$$

Furthermore, by substituting equation (2.5.35) into equation (2.5.6), the total potential energy of the system as a fourth order polynomial in  $s$  is again derived, ie.

$$W = c_1' s^4 + c_2' s^3 + c_3' s^2 + c_4' s + c_5' \quad (2.5.36)$$

in which  $c_1' = \sum \alpha (a_3')^2$ ,  $c_2' = \sum \alpha 2a_2' a_3'$ ,  $c_3' = \sum \beta a_3' + \alpha ((a_2')^2 + 2a_1' a_3')$ ,

$$c_4' = \sum (\beta a_2' + \alpha 2a_1' a_2') - \{P\}^T \{V'\}, \quad c_5' = \sum (\beta a_1' + \alpha (a_1')^2) - \{P\}^T \{u'\}, \quad (2.5.37)$$

where  $\alpha = \frac{EA'}{2L_k} = \frac{(EA + T_k^0)}{2L_k}$ ,  $\beta = T_k^0$  and the summation is for all elements in the structure.

In the limit, when true equilibrium is obtained, no approximations have been made in calculating either the gradient vector or the polynomial coefficients. This formulation now accounts for arbitrary element strains. It has been successively applied in the solution of cable network problems [133]. In situations where significant strains may develop, the above scheme is the suitable choice for the solution.

If the scaling matrix  $[H]$  is such that  $[K_T']$  is symmetric with all the diagonal elements approximately unity and off diagonal terms close to zero, then  $[K_T']$  will yield almost equal eigenvalues implying a condition number close to unity. However, this is not possible in practice. A diagonal matrix  $[H]$  such that

$$h_{ii} = \sqrt{\frac{1}{k_{ii}}} \quad (2.5.38)$$

results in  $[K_T']$  having a leading diagonal of unity and improved convergence is achieved as the off-diagonal terms tend towards zero. The choice of a diagonal scaling matrix means least additional computer storage and is compatible with the explicit nature of the scheme. The individual scaling terms can be set on an element by element basis without having to form the overall stiffness matrix. A much increased convergence rate has been demonstrated by Buchholdt [38] when applying the scaled conjugate gradient method to cable networks and proved by far more efficient than the Newton-Raphson method, method of relaxed steepest descent and conjugate gradient method without scaling.

## 2.5.2 Relaxation methods

According to Varga [132], there are three basic explicit iterative methods, ie. the Point-Jacobi, Gauss-Seidel and Successive Over-Relaxation methods. All these methods can be applied as direct iterative solutions of fully or partly uncoupled equations and thus, suitable for solving non-linear problems.

The objective is to solve equations in the following form, ie.

$$[K_T]\{\delta\} = \{P\} \quad (2.5.39)$$

where  $[K_T]$  is the overall or tangent stiffness matrix and may be written as

$$[K_T] = [L + D + U] \quad (2.5.40)$$

in which  $[D]$  is the main diagonal of  $[K_T]$ , and  $[L]$  and  $[U]$  are respectively the remaining lower and upper triangular portions of  $[K_T]$ . Multiplying equation (2.5.39) by  $[D]^{-1}$  leads to

$$\begin{aligned} [D]^{-1}[K_T]\{\delta\} &= [D]^{-1}\{P\}, \\ \Rightarrow [K_T']\{\delta\} &= \{P'\} \quad \text{where } [K_T'] = ([L'] + [I] + [U']). \end{aligned} \quad (2.5.41)$$

Therefore,

$$\{\delta\}^{q+1} = \{P'\} - ([L'] + [U'])\{\delta\}^q,$$

$$\Rightarrow \{\delta\}^{q+1} - \{\delta\}^q = \{P'\} - [K_T']\{\delta\}^q. \quad (2.5.42)$$

A general form of the basic iterative method can be written as follows-

$$\{\delta\}^{q+1} - \{\delta\}^q = [H](\{P'\} - [K_T']\{\delta\}^q) \quad (2.5.43)$$

and if  $[H] = [I]$ , the resulting method is the Point-Jacobi method,  
 if  $[H] = ([I] + [L])^{-1}$ , the resulting method is the Gauss-Seidel method,  
 if  $[H] = \omega([I] + \omega[L])^{-1}$ , the resulting method is the Successive Over-Relaxation method where  $\omega$  is a relaxation parameter.

Equation (2.5.43) may be further expressed in the following form

$$\begin{aligned} \{\delta\}^{q+1} &= [H](\{P'\} + ([I] - [H][K_T'])\{\delta\}^q, \\ \Rightarrow \{\delta\}^{q+1} &= [H]\{P'\} + [M]\{\delta\}^q \end{aligned} \quad (2.5.44)$$

with matrix  $[M]$  being the characteristic matrix of the iterative method.

In the Point-Jacobi method, the first step is to assume the unknown vector  $\{\delta\}$  equal to the diagonal of  $[K_T']$ , ie.  $[I]$ . A new estimate of  $\{\delta\}$  is then calculated from the recurrence equation, ie.

$$\begin{aligned} \{\delta\}^{q+1} &= [I]\{P'\} + ([I] - [I][K_T'])\{\delta\}^q \\ &= \{P'\} + ([I] - [K_T'])\{\delta\}^q. \end{aligned} \quad (2.5.45)$$

In the Gauss-Seidel method, the components of  $\{\delta\}^{q+1}$  which have been computed are substituted back into the recurrence equation to obtain the remaining components. The recurrence equation is expressed as follows, ie.

$$\{\delta\}^{q+1} = ([I] + [L])^{-1}\{P'\} + ([I] - ([I] + [L])^{-1}[K_T'])\{\delta\}^q. \quad (2.5.46)$$

Furthermore, a relaxation or accelerating parameter  $\omega$  can be applied to either the simultaneous (Point-Jacobi) or successive (Gauss-Seidel) relaxation methods. In the case of the Point-Jacobi scheme, it follows that

$$\{\delta\}^{q+1} - \{\delta\}^q = \omega(\{P'\} - [K_T']\{\delta\}^q). \quad (2.5.47)$$

The accelerated form of the Gauss-Seidel scheme leads to the Successive Over-Relaxation method, ie.

$$\{\delta\}^{q+1} - \{\delta\}^q = \omega([I] + \omega[L])^{-1}(\{P'\} - [K_T']\{\delta\}^q). \quad (2.5.48)$$



With  $1 < \omega < 2$ , this method produces the highest convergence rate compared with the Point-Jacobi and Gauss-Seidel methods [10]. All the above iterative methods are explicit schemes, ie. each degree of freedom is solved in the uncoupled form. Alternatively, solution in a partly uncoupled form with main diagonal submatrix operations node by node is also possible as illustrated in the case of the Point-Jacobi method here.

At node  $i$  (with  $n$  degrees of freedom), the relaxation equation is

$$\{\delta_i\}^{q+1} = \{P_i'\} + ([I] - [K_{Ti}']^c)\{\delta_i\}^q \quad (2.5.49)$$

in which  $\{\delta_i\} = n$  displacement components at node  $i$ ,

$\{P_i'\} = n$  applied load components at node  $i$ ,

$[K_{Ti}']^c = (n \times n)$  tangent stiffness submatrix based on the current geometry at iteration  $q$ .

Therefore, the relaxation process is simultaneous at node  $i$ . In the fully uncoupled form, the relaxation equation may be expressed as follows, ie.

$$\{\delta_i\}^{q+1} = \{P_i'\} + ([I] - [K_{di}']^c)\{\delta_i\}^q \quad (2.5.50)$$

in which  $[K_{di}']^c$  is a diagonal matrix of the current direct tangent stiffness components. However, this approach may result in convergence difficulties.

In the case of the Gauss-Seidel or SOR scheme, there is a need to perform matrix inversion at each node and iteration for the partly uncoupled implementation. It is possible that the matrix may become singular at some stage of this process. There is no need for matrix inversion in the fully uncoupled form of the solution scheme. On the other hand, in a fully uncoupled solution, the occurrence of situations such as cable slackening or co-planar elements may result in zero diagonal  $K_{di}'$  terms leading to infinite deflection increments. Hence, conditional deflection controls are needed.

The above relaxation methods have not been widely applied to the analysis of tension structures [10]. In contrast, the more recently developed method known as dynamic relaxation (DR) has been applied successfully to the form-finding and static analysis of many built tension structures [4, 5, 8, 10, 21, 115, 133]. Dynamic relaxation is an uncoupled simultaneous iterative procedure which has the following recurrence relationship, ie.

$$\{\delta\}^{q+1} = \{\delta\}^q + \alpha(\{\delta\}^{q+1} - \{\delta\}^q) + \gamma\{R\}^q \quad (2.5.51)$$

where the factors  $\alpha$  and  $\gamma$  are chosen to optimise the convergence. The method is much suited to handle highly non-linear problems such as on/off non-linearities as any temporary loss of element stiffness does not lead to infinite deflection increments. Dynamic relaxation was first proposed by Day

[53] to solve problems involving a portal frame, a skew plate and a thick steel cylinder under internal pressure loading.

With  $\{\epsilon\}$  being a vector of errors between the current and true deflections, and

$$\{\epsilon\}^{q+1} = \lambda \{\epsilon\}^q, \quad (2.5.52)$$

the parameter  $\lambda$  therefore measures the change in magnitude of errors between successive iterations and used as an indication of convergence rates of DR compared with the basic iterative methods as follows-

Simultaneous Methods	Successive Methods
<u>Point-Jacobi</u> $\lambda = \frac{p-1}{p+1}$	<u>Gauss-Seidel</u> $\lambda = \left(\frac{p-1}{p+1}\right)^2$
<u>Dynamic Relaxation</u> $\lambda = \frac{\sqrt{p}-1}{\sqrt{p}+1}$	<u>Successive Over-Relaxation</u> $\lambda = \left(\frac{\sqrt{p}-1}{\sqrt{p}+1}\right)^2$

Figure 2.13

in which  $p = \sqrt{\frac{b}{a}}$  = condition number of the stiffness matrix, and  $a$  and  $b$  are respectively the numerical values of the smallest and largest eigenvalues of the stiffness matrix of the structure being considered.

The above comparison is due to Lynch [93] and valid only for linear structures with tri-diagonal stiffness matrices. The table shows that SOR is twice as fast as dynamic relaxation and that the same relationship exists between Gauss-Seidel and Point-Jacobi methods.

Finally, any of the above iterative methods may be stated in the form of a minimisation problem as discussed earlier, ie.

$$\{\delta\}^{q+1} = \{\delta\}^q + s^q \{V\}^q. \quad (2.5.5)$$

Dynamic relaxation is shown to be a dynamic implementation of a first order gradient method in [133].

From the above discussion, it can be seen that the explicit schemes are in general well suited for solving non-linear problems. When a load increment is applied, an explicit scheme usually needs no more effort for a non-linear

problem than for a linear one, whereas an implicit scheme often requires several iterations with each iteration being a complete solution to an equivalent linear problem.

In the comparative study of all the methods mentioned above applied to tension structures, the conclusion is that the dynamic relaxation method is the most efficient explicit scheme and compared in efficiency with the implicit Newton-Raphson method [115]. Furthermore, the dynamic relaxation method has a few advantages which make it highly suited to be applied to the form-finding and load analysis of tension structures. The main advantages are summarised below.

Firstly, the equilibrium and compatibility conditions are uncoupled within the dynamic relaxation method. As a result, complex stress-strain relations such as stress as a polynomial function of strain, can be readily implemented. In addition, the on/off buckling of elements which can often occur during the analysis of a tension structure, can be handled without difficulty. The stiffness relations can also be considered at the element level without the need for an overall stiffness matrix of the structure.

Secondly, the kinetic damping procedure instead of viscous damping when introduced into the dynamic relaxation method, ensures stability in the event of high residuals which may arise suddenly during radical adjustments to the numerical model at the form-finding stage. In the case of local adjustments, the disturbances are rapidly dissipated without propagation through the entire model.

A full account of the above features of the dynamic relaxation method is given in chapter 3.



## Chapter 3

### Dynamic relaxation analysis of tension structures

#### 3.1 Introduction

From the review of numerical methods in chapter 2, it is noted that the dynamic relaxation (DR) method which is an explicit numerical scheme, has a few advantages which make it well suited to deal with the highly non-linear analysis of tension structures, and is therefore the chosen solution scheme for all the analysis work in this thesis.

The dynamic relaxation method as the name itself suggests, is applicable strictly to situations where the analysis is for the static equilibrium state of a structure. However, the explicit numerical scheme which forms the basis of the dynamic relaxation method, can also be applied to the dynamic analysis of tension structures which will be considered in chapter 9. In this chapter, the dynamic relaxation method as applied to the form-finding and static load analysis of tension structures is considered, and an outline is given of the basic mechanics of the method, and the controls needed to make it into an automated and efficient procedure.

#### 3.2 Physical basis

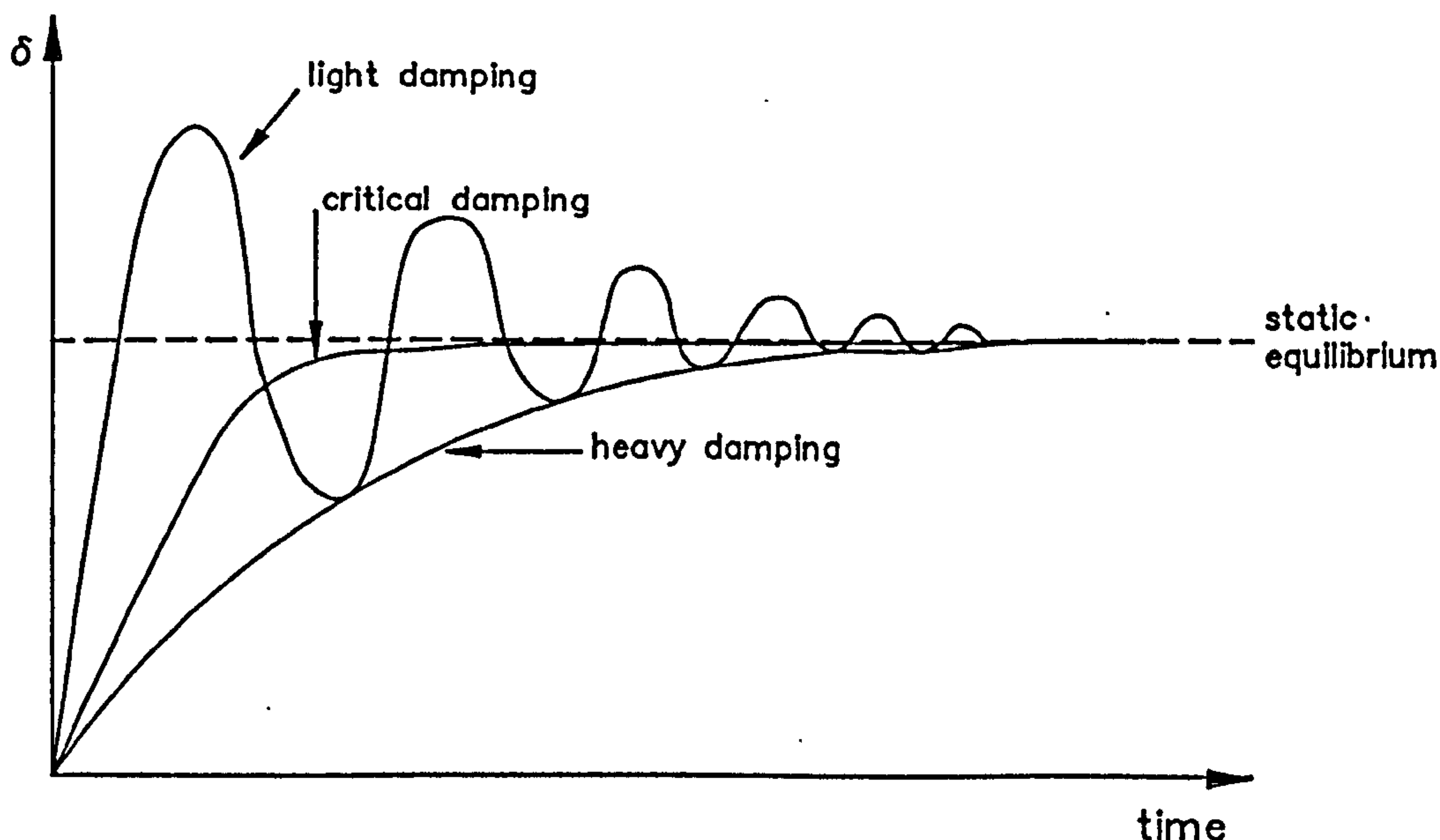


Figure 3.1

The physical basis of the dynamic relaxation method is that a structure in its initial state is allowed to vibrate and under imposed high fictitious damping, the structure will eventually reach a static equilibrium state which then gives

the required solution (see figure 3.1). During the solution process, the vibrations of the structure are traced in small time steps, and artificial controls such as fictitious masses and fictitious elastic properties can be used to improve the convergence rate of the solution process. Instead of using viscous damping, a kinetic damping procedure which will be described in further detail later on, can also be used to control the solution process.

### 3.3 Method formulation

The dynamic relaxation method can be implemented in two possible ways, ie. one based on finite differences and the other based on finite elements. The finite difference approach involves the setting up of a two-way finite difference grid over the structure concerned and then solving the corresponding simultaneous sets of equations; hence, enormous computational effort is required especially when a fine grid is used. In the analysis of structures which are discretised into finite elements, it is more appropriate to use the dynamic relaxation method implemented on the basis of finite elements instead of finite differences, and such an approach is adopted in this thesis. As will be described later, this approach can be developed into an efficient solution procedure for dealing with tension structures.

#### 3.3.1 Basic equations

In the dynamic relaxation method, the governing equation is the Newton's second law of motion, ie.

$$\text{Force} = \text{Mass} \times \text{Acceleration}, \quad (3.3.1)$$

and for the motion in the  $x$ -direction at node  $i$ , equation (3.3.1) can in turn be written as

$$P_{xi} - K_{xi}\delta_{xi} - C_{xi}'\dot{\delta}_{xi} = M_{xi}\ddot{\delta}_{xi} \quad (3.3.2)$$

in which  $P_{xi}$  = externally applied loads at node  $i$  in direction  $x$ ,

$K_{xi}$  = stiffness term at node  $i$  in direction  $x$ ,

$C_{xi}'$  = viscous damping constant at node  $i$ ,

$M_{xi}$  = mass at node  $i$ , and

$\delta_{xi}$ ,  $\dot{\delta}_{xi}$ ,  $\ddot{\delta}_{xi}$  = total displacement, velocity and acceleration  
respectively of node  $i$  in direction  $x$ .

The term  $(P_{xi} - K_{xi}\delta_{xi})$  gives the residual force  $R_{xi}$  at node  $i$  in the  $x$ -direction. The element masses in the structural idealisation are assumed to be lumped at the nodes. The relation given in equation (3.3.2) applies equally for the motions in the  $y$ - and  $z$ -directions.

Equation (3.3.2) can then be written for any time  $t$  as follows-

$$R_{xi}^t = M_{xi} \dot{V}_{xi}^t + C_{xi}' V_{xi}^t \quad (3.3.3)$$

in which  $V_{xi}^t = \dot{\delta}_{xi}^t$ , ie. the velocity of node  $i$  in direction  $x$  at time  $t$ , and

$\dot{V}_{xi}^t = \ddot{\delta}_{xi}^t$ , ie. the acceleration of node  $i$  in direction  $x$  at time  $t$ .

Expressing equation (3.3.3) in the central finite difference form for a small time step  $\Delta t$  gives

$$R_{xi}^t = \frac{M_{xi}}{\Delta t} (V_{xi}^{t+\Delta t/2} - V_{xi}^{t-\Delta t/2}) + \frac{C_{xi}'}{2} (V_{xi}^{t+\Delta t/2} + V_{xi}^{t-\Delta t/2}). \quad (3.3.4)$$

As given in equation (3.3.4), the residual forces are calculated at successive time intervals  $0, \Delta t, 2\Delta t, \dots, t-\Delta t, t, t+\Delta t, \dots$  etc., and the nodal velocities are determined for the mid-points of these time intervals.

Equation (3.3.4) can then be rearranged to give a recurrence equation for the nodal velocity at time  $(t + \Delta t/2)$  as follows-

$$V_{xi}^{t+\Delta t/2} = V_{xi}^{t-\Delta t/2} \left( \frac{M_{xi}/\Delta t - C_{xi}'/2}{M_{xi}/\Delta t + C_{xi}'/2} \right) + R_{xi}^t \left( \frac{1}{M_{xi}/\Delta t + C_{xi}'/2} \right). \quad (3.3.5)$$

The damping factor  $C_{xi}'$  may be more conveniently defined as  $C_{xi}' = M_{xi}(C/\Delta t)$ . In addition, the damping per unit mass ( $C/\Delta t$ ) may be assumed as constant throughout the structure.

Equation (3.3.5) then becomes

$$V_{xi}^{t+\Delta t/2} = A V_{xi}^{t-\Delta t/2} + B_{xi} R_{xi}^t \quad (3.3.6)$$

where  $A = \left( \frac{1 - C/2}{1 + C/2} \right)$ , ie. a constant for the structure, and

$$B_{xi} = \frac{\Delta t}{M_{xi}} \left( \frac{1}{1 + C/2} \right), \text{ ie. a constant for node } i \text{ in direction } x. \quad (3.3.7)$$

The total  $x$ -deflection of node  $i$  at time  $(t + \Delta t)$  is then given by

$$\delta_{xi}^{t+\Delta t} = \delta_{xi}^t + \Delta t V_{xi}^{t+\Delta t/2}. \quad (3.3.8)$$



The velocities and deflections in the  $y$ - and  $z$ -directions can be similarly calculated. The current displaced geometry of the whole structure at time  $(t + \Delta t)$  can then be obtained. Subsequently, the current nodal residuals  $R_{xi}^{t+\Delta t}$  can be determined as follows-

$$R_{xi}^{t+\Delta t} = P_{xi} + \sum_m \left( \frac{\Delta X}{L} \right)_m T_m^{t+\Delta t} \quad (3.3.9)$$

in which the summation is for all members  $m$  (links or sides of membrane elements) meeting at node  $i$ ,  $(\Delta X/L)_m$  is the current direction cosine between member  $m$  and the  $x$ -axis, and  $T_m$  is the current tension in member  $m$ . The iteration then returns to equation (3.3.6) for the next time step. The process continues until the analysis converges to within a specified criterion given by the maximum allowable current residuals in the structure.

At the start of the analysis (ie. time  $t = 0$ ), it is assumed that  $V_{xi}^{t=0} = 0$ , thus

$$-V_{xi}^{-\Delta t/2} = V_{xi}^{\Delta t/2} \quad (3.3.10)$$

and using this relation in equation (3.3.6) leads to

$$V_{xi}^{\Delta t/2} = \frac{B_{xi}}{(1 + A)} R_{xi}^{t=0} \quad (3.3.11)$$

For a structure initially in equilibrium, then  $R_{xi}^{t=0} = P_{xi}$ , ie. the applied nodal loads.

It can be seen that the equilibrium condition in equation (3.3.9) is separated from the compatibility condition in equation (3.3.8) which is characteristic of an explicit vector scheme such as the dynamic relaxation method. These two conditions will be consistent with each other to give a unique solution at the point of convergence.

### 3.3.2 Numerical stability

As the dynamic relaxation method is an explicit scheme, it is only conditionally stable, ie. the use of a time step  $\Delta t$  which exceeds a critical value will lead to numerical instability. According to Barnes [10], the true critical time interval lies within the following bounds, ie.

$$\sqrt{\frac{2M_i}{S_i}} \leq \Delta t_{crit} \leq \sqrt{\frac{4M_i}{S_i}} \quad (3.3.12)$$

in which  $S_i$  is the direct stiffness of node  $i$  relative to all adjacent nodes.

Another expression for the critical time interval was derived from the direct comparison of the dynamic relaxation method with the Frankel's method by Cassell and Hobbs [43], and is given as follows-

$$\Delta t^2 \leq \frac{4M_i}{(a + b)} \quad (3.3.13)$$

where  $a$  and  $b$  are respectively the smallest and largest eigenvalues of the stiffness matrix associated with the structure being considered, and from the Gershgorin's bound theorem

$$|b| \leq b_g = \max_i \sum_{j=1}^n |S_{ij}| \quad (3.3.14)$$

in which  $S_{ij}$  are the elements of the stiffness matrix, and the maximum value of the sum for each row  $i$  is taken. As is often the case that  $(a \ll b)$  and hence,  $|a + b| \leq b_g$  which in turn leads to

$$\Delta t^2 \leq \frac{4M_i}{b_g}. \quad (3.3.15)$$

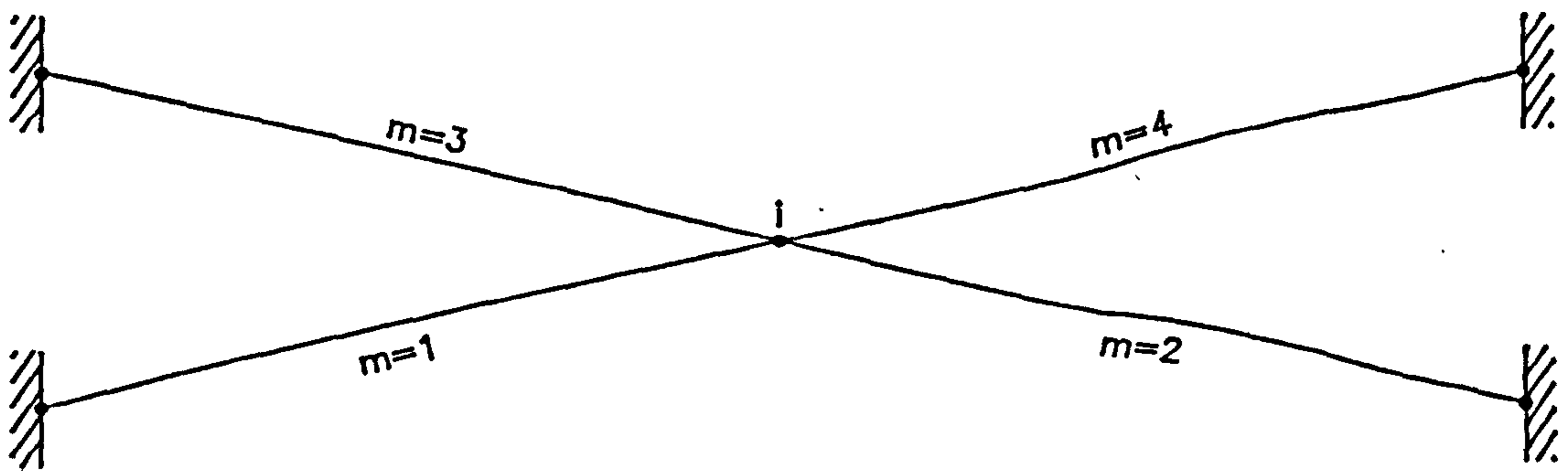


Figure 3.2

During form-finding, gross changes in geometry may occur and members joining a particular node could become aligned in a single direction. In such a case, the greatest possible stiffness is given by

$$S_{imax} = \sum_m \left[ \frac{EA}{L_o} + \frac{T}{L_c} \right]_m \quad (3.3.16)$$

summed over all members  $m$  meeting at node  $i$  (see figure 3.2), and  $(EA/L_o)$  is the axial elastic stiffness and  $(T/L_c)$  is the geometric stiffness of the member.

This value of  $S_{imax}$  should be used when setting the time step  $\Delta t$  to be used for the analysis.

For a uniform mesh net, the  $S_{i\max}$  comprises mainly of the component  $(EA/L_0)$  and with little contribution from  $(T/L_c)$ . The term  $(T/L_c)$  is relevant in some form-finding situations such as that of geodesic nets where the  $EA$  values may be set to zero. The current link lengths  $L_c$  may also change significantly during the analysis. Typically, the crossing links may bunch together resulting in some link lengths being much shorter than the values used in the calculation of  $S_{i\max}$ . Hence, the geometric stiffness term in equation (3.3.16) has to be factored accordingly. For the form-finding of triangular membrane elements with specified stresses, a similar factor has to be applied to the geometric stiffness terms to allow for both reduction in element sizes and changes of aspect ratios.

As the eventual solution of a dynamic relaxation analysis is given by the static equilibrium state, the nodal masses used in the analysis do not change the final solution but only influence the solution path to convergence; this suggests the possibility of using fictitious nodal masses as a means of improving the convergence rate.

Fictitious masses were first used in dynamic relaxation by Otter, Cassell and Hobbs [113]. For non-linear problems, Cassell and Hobbs [43] updated the fictitious masses at discrete intervals during the analysis. The Gershgorin bounds were used for calculating these masses, and separation of the linear and non-linear components means that only the latter needs to be updated. Frieze, Hobbs and Dowling [59], and Turvey [131] used fictitious masses in their large deflection analysis of plates. In addition, Frieze [58] found that fictitious masses based on elastic rigidities alone lead to convergence although plastic behaviour was present in his dynamic relaxation analysis of elasto-plastic buckling of thin walled rectangular sections. In these investigations, the additional computational effort involved in the updating of non-linear fictitious mass components may more than offset the benefit of increased convergence rate.

By using fictitious masses, the time step required for a stable solution can be optimised in order to produce an increased convergence rate, and the following equation [10]

$$M_i = \frac{\Delta t^2}{2} S_i \quad (3.3.17)$$

is used for this purpose. Using equation (3.3.17), the nodal mass at node  $i$  which ensures numerical stability for a chosen time interval  $\Delta t$ , can be calculated. In addition, it is most desirable if the fictitious nodal masses can be adjusted to achieve the situation of approximately equal stiffness/mass ratios (and thus, the critical time intervals) at all nodes of the structure. As a result of the gross geometry changes which may occur during form-finding, the nodal mass in each of the three coordinate axes directions may be set using the greatest possible stiffness at any node as follows-



$$M_{xi} = M_{yi} = M_{zi} = \frac{\Delta t^2}{2} S_{imax}. \quad (3.3.18)$$

It may be convenient to choose the time interval  $\Delta t = 1$  and then use equation (3.3.18) to calculate for the corresponding fictitious nodal masses. However, as mentioned earlier, a factor has to be applied to the geometric stiffness term of  $S_{imax}$  and experience is needed to decide on the appropriate factor to use. The value of this factor can be wide ranging and may require regular adjustments during analysis to maintain the optimum convergence rate. On some occasions, trial and error may be required to establish such a factor.

Alternatively, the required set of fictitious mass components at any node  $i$  can be calculated as follows [17, 133]-

$$\begin{aligned} [M_i] &= \frac{\Delta t^2}{2} [T_i]^T [S_i] [T_i] \\ &= \frac{\Delta t^2}{2} [S_i]^* \end{aligned} \quad (3.3.19)$$

in which  $[M_i]$  is a  $(3 \times 3)$  block mass matrix,  $[S_i]$  is a diagonal matrix of principal direct stiffness components, and  $[T_i]$  is a transformation matrix relating the principal stiffness directions of node  $i$  to the global coordinate system for the structure. Hence, this is equivalent to having diagonal mass matrices in the local coordinate system of node  $i$  (coincident with the principal stiffness directions) which results in an optimum time interval for the solution process. However, although the number of time steps to convergence are minimised, the additional computation involved favour the use of a diagonal mass matrix factored appropriately to account for the coupling effects.

Subsequently, the lumped (diagonal) nodal masses of node  $i$  may be calculated as follows-

$$\{M_i'\} = \frac{\Delta t^2}{2} \{S_i'\} \quad (3.3.20)$$

where the equivalent direct stiffness components  $\{S_i'\}$  are derived from  $[S_i]^*$ , and a possible scheme of finding  $\{S_i'\}$  is given by

$$S_j' = \alpha S_{jj} \quad (3.3.21)$$

in which  $S_{jj}$  is the diagonal term of  $[S_i]^*$  for the  $j$ th degree of freedom at the node. If the nodal principal stiffnesses coincide with the global coordinate system, setting  $(\alpha=1)$  will suffice to produce a stable solution. However, this is not commonly the case and a value of  $(\alpha>1)$  is required in order to avoid

the onset of numerical instability. Using ( $\alpha=2$ ) in the dynamic relaxation analysis of a wide range of pin and rigid jointed structures (both planar and spatial), satisfactory results have been obtained by Wakefield [133]. On the other hand, if the principal direct stiffness directions are close to the global coordinate system as in a shallow network, the estimated mass components will then be over conservative.

An alternative suggestion for calculating  $S_j'$  is given by

$$S_j' = \alpha \sum_{k=1}^n |S_{jk}| \quad (3.3.22)$$

where  $n$  is the number of degrees of freedom and  $S_{jk}$  are the terms in row  $j$  of  $[S_i]^*$ .

Furthermore, a minimum value may be set for the coefficients of  $\{S_i'\}$  as follows-

$$S_j' \geq \beta S_{i_{\max}}' \quad (3.3.23)$$

where  $S_{i_{\max}}'$  is the maximum coefficient in  $\{S_i'\}$ . The case of ( $0.05 < \beta < 0.1$ ) has been used successfully in the dynamic relaxation analysis of both pin and rigid jointed structures by Wakefield [133]. In form-finding where gross deformations may occur, it may be necessary to use a higher value of  $\beta$  such as 1.0.

The three methods of control for fictitious nodal masses outlined above can be summarised as follows-

- (1) diagonal mass matrices with coefficients based on leading diagonal direct stiffness terms (equation (3.3.21)),
- (2) diagonal mass matrices with coefficients based on row sums of the direct stiffness matrix (equation (3.3.22)),
- (3) square mass matrices (equation (3.3.19)).

Wakefield [133] applied the above methods of control to a pretensioned network with rigid boundaries and compared their efficiencies in terms of number of iterations and solution times to convergence. The square mass matrices in (3) above have been shown to often lead to the case of least number of iterations and solution times to convergence, and that the scheme in (1) is the least efficient. However, more storage requirements are demanded by the square mass matrices. Subsequently, it is suggested that the diagonal mass matrix with row sums of stiffness terms in (2) is the preferred choice for general applications. For the example considered, this scheme often



takes only slightly longer solution times than the case of square mass matrices, and keeps the computer program simple and reduces storage requirements. This scheme is also readily implemented as an automatic control of the fictitious nodal masses. By choosing the appropriate  $\alpha$  and  $\beta$  parameters at the start of the analysis and it is usual to use values which are within the following ranges, ie.  $(1.0 < \alpha < 2.0)$  and  $(0.05 < \beta < 1.0)$ , a stable solution will be attained in most cases. Hence, this scheme is adopted for the task of calculating the fictitious nodal masses in all subsequent analysis.

A brief mention here about the dynamic behaviour of a low rise air-supported dome. Of primary interest may be the displacements normal to the membrane surface but the critical time interval for numerical stability is governed by the higher in-plane membrane stiffness. With a square mass matrix, it is allowable at the level of local coordinates to impose high fictitious principal mass components for the in-plane motions and use the actual mass values for the out-of-plane motions. Within the local coordinate system, the in- and out-of-plane motions are decoupled and this idea leads to an optimum time step for the out-of-plane motions having real mass values meanwhile ensuring that the in-plane motions are numerically stable. Consequently, in this case, the principal stiffnesses and their corresponding coordinate transformations have to be worked out in order to set up the square mass matrices with the correct scaling of the principal mass values in the global coordinate system.

For nodes with six degrees of freedom (ie. three translations and three rotations), the square mass matrices remain  $(3 \times 3)$  as the numerical stabilities of the translational and rotational vibrations are decoupled.

### 3.3.3 Viscous damping constant

The true structural damping should be used when modelling the dynamic behaviour. The low level of damping in a bare network will have little effect on the resulting maximum dynamic stresses and frequency response. On the other hand, the corresponding influence of the high level of damping in a clad network will be much more significant.

For static solutions, a high fictitious damping is imposed to achieve the final steady equilibrium state. If critical damping is used, then monotonic convergence will be ensured. However, a slightly sub-critical damping produces more rapid convergence and bounds to the true equilibrium state are obtained as well. From a trial analysis (ie. undamped or lightly damped), the fundamental frequency  $f$  of the structure can be found from the deflection-time trace. Alternatively, the frequency can be determined from a trace of total kinetic energy given by an undamped trial analysis. The kinetic energy varies at twice the fundamental frequency and such an approach also gives a clearer indication of the fundamental frequency. An estimate of the critical damping constant is then given by



$$C_{\text{crit}} = 4\pi f\Delta t. \quad (3.3.24)$$

In some instances however, the critical viscous damping factor may be difficult to estimate [115].

### 3.3.4 Kinetic damping

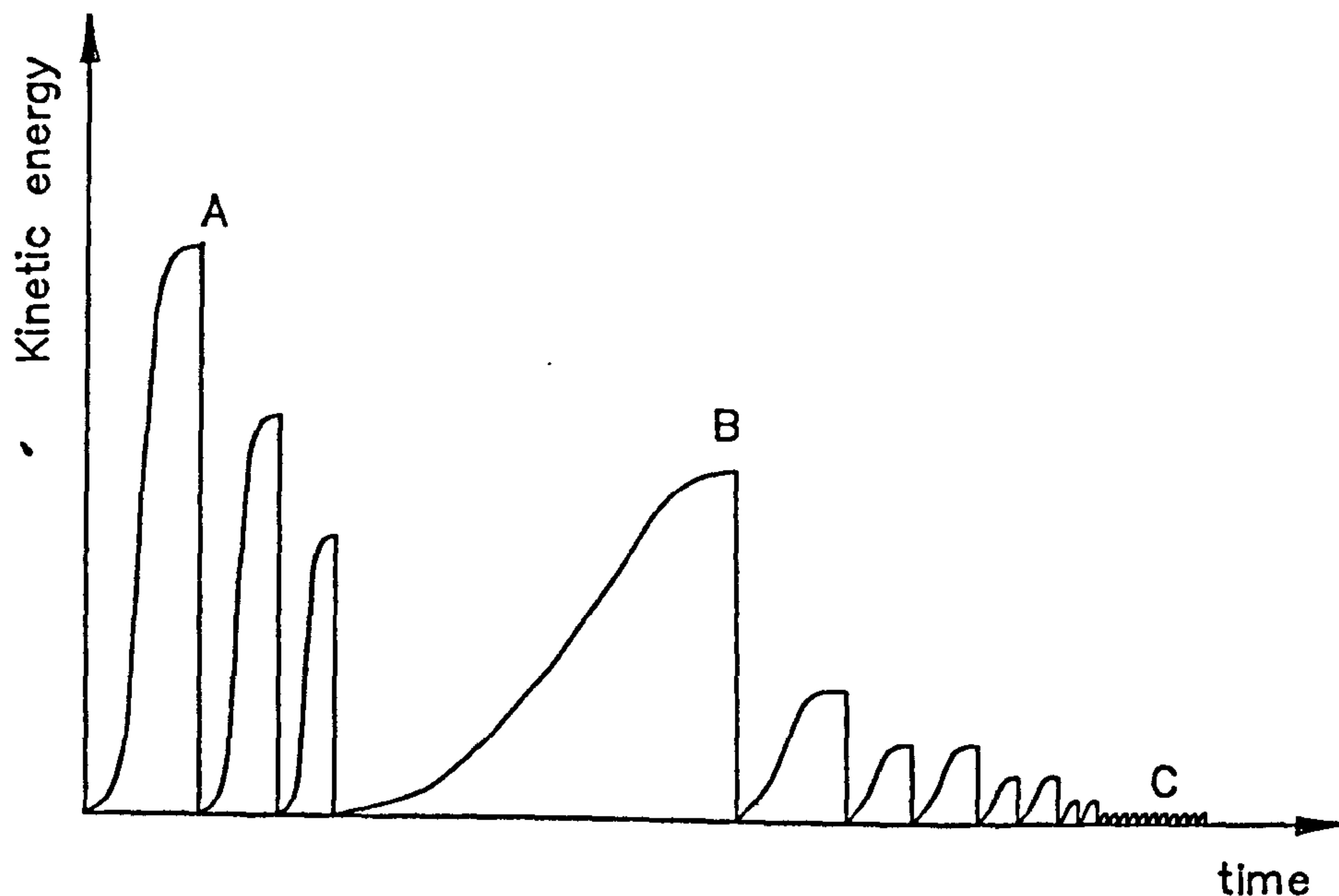


Figure 3.3

It is possible to use dynamic relaxation with zero viscous damping and the concept of kinetic damping introduced in its place instead. As a result, there is no need for a prior determination of the damping constant. The underlying basis of kinetic damping is that as an oscillating body passes through its static equilibrium state, its total kinetic energy reaches a local maximum. Barnes, et. al. [9] found that the scheme of dynamic relaxation with kinetic damping is generally stable and rapidly convergent when dealing with large local disturbances. Under this scheme, the total kinetic energy is traced during the undamped motion of the structure. Upon the detection of a local energy peak, all current nodal velocities are set to zero. The process is then restarted from the current geometry and continued through further (generally decreasing) peaks until the energy of all modes of vibration has been dissipated and the structure attains its static equilibrium. A kinetic energy trace typical of that produced in most cases is given above in figure 3.3 and often representative of the form-finding of a cable net or prestressed membrane structure with inaccurate initial geometry. The initial energy peaks (A) are a result of the high frequency modes caused by large residual forces in boundary or point support regions. The energy peaks which follow (ie. B) relate to the overall structural form and lowest frequency modes. As the converged solution is within reach, the low energy peaks (C) occur rapidly as a result of slight in-plane motions. This scheme allows form or shape adjustments which may be

local changes to boundary geometry, surface topology, cable tensions or specified stresses in membrane elements, without the propagation of these disturbances to those regions further away. The out-of-balance forces due to the form adjustments are rapidly equilibrated locally.

From equation (3.3.7), and with  $C_{xi}' = 0$ ,

$$A = 1 \quad \text{and} \quad B_{xi} = \frac{\Delta t}{M_{xi}},$$

and equation (3.3.6) then becomes

$$\{V\}^{t+\Delta t/2} = \{V\}^{t-\Delta t/2} + \Delta t [M]^{-1} \{R\}^t \quad (3.3.25)$$

written in vector form for the entire structure. Subsequently,

$$KE^{t+\Delta t/2} = \frac{1}{2} (\{V\}^{t+\Delta t/2})^T [M] \{V\}^{t+\Delta t/2} \quad (3.3.26)$$

where  $KE$  denotes the current total kinetic energy of the structure and the updated coordinates at time  $(t + \Delta t/2)$  are given by

$$\{\delta\}^{t+\Delta t} = \{\delta\}^t + \Delta t \{V\}^{t+\Delta t/2}. \quad (3.3.27)$$

The condition  $(KE^{t+\Delta t/2} < KE^{t-\Delta t/2})$  signals the presence of a local energy peak. The velocities must then be set to zero and the coordinates adjusted from  $\{\delta\}^{t+\Delta t}$  to  $\{\delta\}^{t^*}$  where  $t^*$  is the time at which the true peak occurs. The coordinates  $\{\delta\}^{t^*}$  can be found by fitting a quadratic polynomial through the current ( $C$ ) and two previous kinetic energy values ( $A$  and  $B$ ) as shown in figure 3.4 which in turn leads to

$$\Delta t^* = \Delta t \frac{E}{(E - D)} = \Delta t q \quad (3.3.28)$$

where  $E = (C - B)$  and  $D = (B - A)$ . From figure 3.4, the conditions  $(B > A)$  and  $(C < B)$  mean that the local peak occurs within the time interval  $(t \rightarrow t - \Delta t)$ .

From equation (3.3.28), the values of  $q$  which correspond to specific cases are as given below

$$\begin{aligned} (B = C) &\Rightarrow q = 0, \\ (A = C) &\Rightarrow q = \frac{1}{2}, \\ (A = B) &\Rightarrow q = 1. \end{aligned} \quad (3.3.29)$$

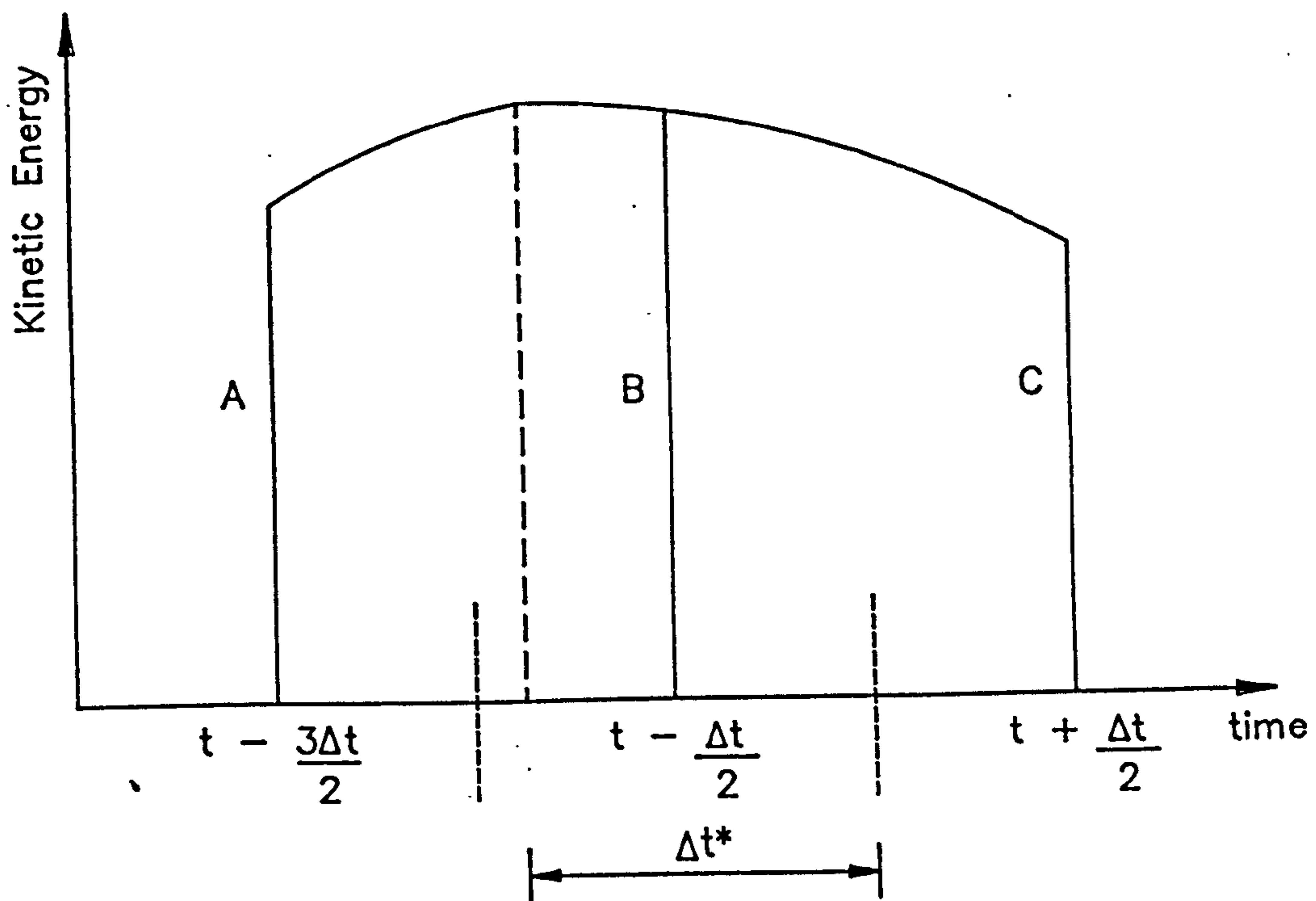


Figure 3.4

As the coordinates have been updated using average velocities (at mid-points of time intervals), they should be reset according to the same scheme. The velocities  $\{V\}^{t+\Delta t/2}$  apply over the time interval  $(t \rightarrow t+\Delta t)$  while the velocities  $\{V\}^{t-\Delta t/2}$  apply over the time interval  $(t-\Delta t \rightarrow t)$ . Thus,

$$\{\delta\}^{t^*} = \{\delta\}^{t+\Delta t} - \Delta t \{V\}^{t+\Delta t/2} - \Delta t^* \{V\}^{t-\Delta t/2} \quad (3.3.30)$$

From equations (3.3.25), (3.3.28) and (3.3.30),

$$\{\delta\}^{t^*} = \{\delta\}^{t+\Delta t} - \Delta t(1+q)\{V\}^{t+\Delta t/2} + \Delta t^2 [M]^{-1} q \{R\}^t \quad (3.3.31)$$

As a simplification, if the energy peak is assumed to occur at time  $(t-\Delta t/2)$ , then  $q = \frac{1}{2}$  in equation (3.3.31).

The process is restarted with the velocities at the mid-point of the first time step given by

$$\{V\}^{\Delta t/2} = \frac{\Delta t}{2} [M]^{-1} \{R\}^{t=0} \quad (3.3.32)$$

Subsequently, the velocities are updated according to equation (3.3.25) in order to search for the next energy peak. The whole process continues until the analysis converges to within a specified tolerance.



Hence, the kinetic damping procedure together with automatic control of nodal mass components, ensures numerical stability in the event of suddenly imposed high residuals which occur frequently during form adjustments.

### 3.3.5 Natural stiffness relations

As indicated earlier on, the nodal residual forces are calculated at every iteration step of the dynamic relaxation method. Consequently, an efficient procedure for calculating the nodal residual forces will greatly enhance the computational speed of the solution process. In these calculations, it is desirable to use the least amount of matrix operations and for the sizes of any matrices involved to be as small as possible. In addition, matrix inversions are to be avoided as singularities may arise under certain circumstances. These features can be found in a procedure which uses natural stiffness relations.

In the solutions of non-linear transient problems, a scheme based on natural stiffness relations has been used for the efficient derivation of nodal residual forces by Belytschko, et. al. [24]. A local element or coordinate system is set up with one node of the element as the origin and the axes directions are then defined by another node. The local coordinates are thus free to translate and rotate with the element as the structure deforms.

The natural stiffness approach uses the basic displacements or strain measures which are the smallest number of geometric parameters necessary to completely describe the deformed/strained state of the element not due to any rigid body motion [99]. The element natural stiffness relates the basic displacements to the corresponding set of basic or natural member forces.

In the case of a cable/strut element, the basic displacement is the axial extension of the element. Argyris [2] first suggested a natural stiffness matrix for the constant strain triangular membrane element relating the tensions to extensions along the three sides of the element as shown in figure 3.5. A dynamic relaxation scheme which uses such a natural stiffness matrix has been applied to the form-finding and static analysis of prestressed membrane structures by Barnes [13, 15, 16, 17, 18]. This approach leads to the most efficient calculation of nodal residual forces and minimum computer storage requirements for most elements. More importantly, it simplifies the use of on/off or other non-linear stress-strain relations. Basically, the process involves a few simple steps outlined as follows-

- (1) set up the coordinate transformation matrix,
- (2) compute basic displacements from the global nodal coordinates,
- (3) compute natural forces from the basic displacements using either linear or non-linear natural stiffness relations,
- (4) natural forces transformed to global coordinate system and added to nodal residual forces.

For the cable element  $m$ , the natural stiffness relation at time  $(t + \Delta t)$  is given by

$$T_m^{t+\Delta t} = T_m^s + \left(\frac{EA}{L_0}\right)_m^s \Delta L_m^{t+\Delta t} \quad (3.3.33)$$

in which  $T_m^s$  and  $\left(\frac{EA}{L_0}\right)_m^s$  are respectively the initial specified tension and axial elastic stiffness of the cable element, and  $\Delta L_m^{t+\Delta t}$  is the extension of cable element (from the initial state) at time  $(t + \Delta t)$ . The value of  $T_m^{t+\Delta t}$  found is then substituted into equation (3.3.9) to obtain the nodal residual forces. Both the terms  $T_m^s$  and  $\left(\frac{EA}{L_0}\right)_m^s$  are available controls for making shape adjustments during form-finding. Furthermore, element buckling (ie. the cable has become slack) is modelled by simply setting zero values to both  $T_m^s$  and  $\left(\frac{EA}{L_0}\right)_m^s$ .

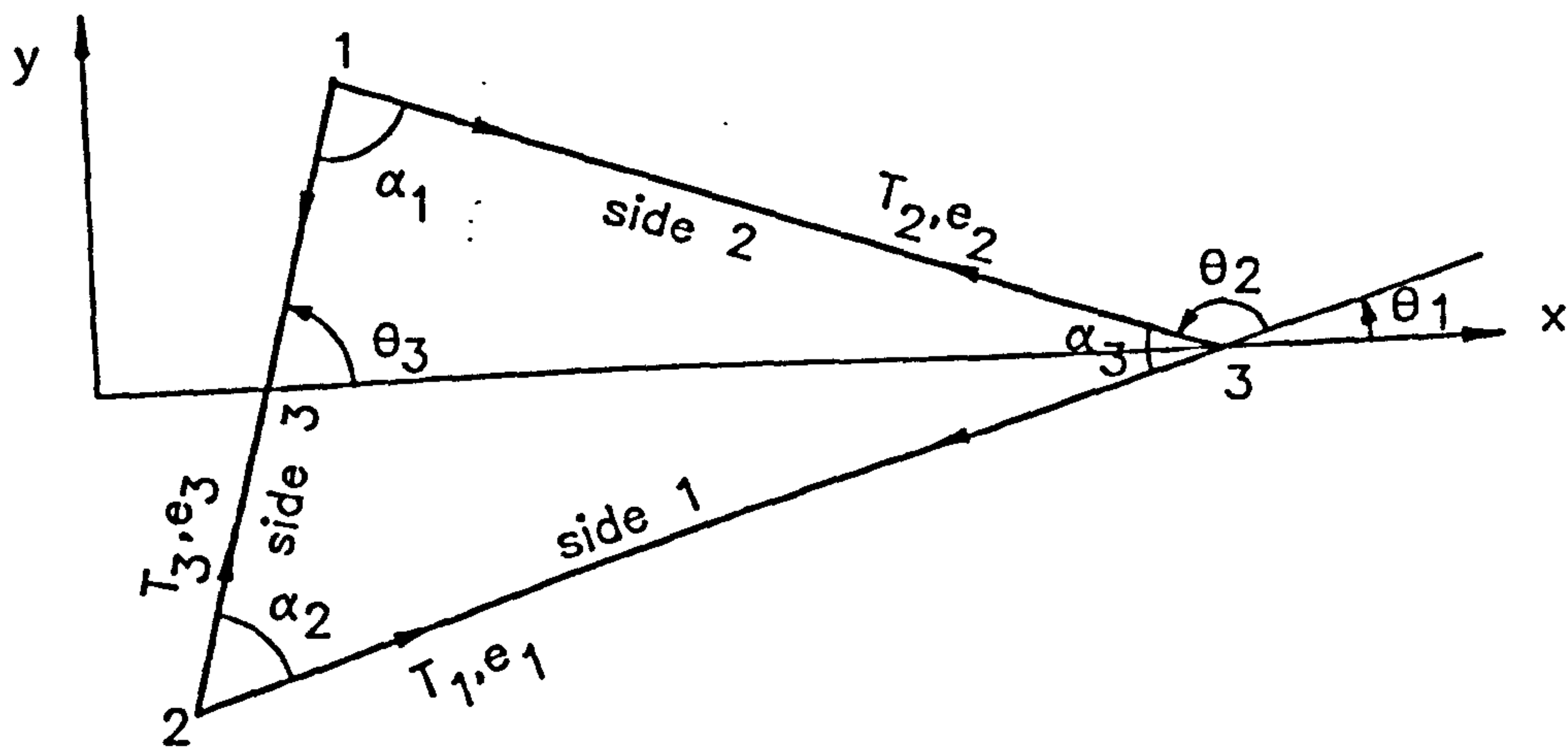


Figure 3.5

For the constant strain triangular membrane element as shown in figure 3.5, the natural stiffness relation is given by

$$\{T\} = \{T\}^s + [K]\{e\} \quad (3.3.34)$$

in which  $[K]$  is the  $(3 \times 3)$  element natural stiffness matrix,

$$\{T\} = \begin{bmatrix} T_1 \\ T_2 \\ T_3 \end{bmatrix}, \quad \{T\}^s = \begin{bmatrix} T_1^s \\ T_2^s \\ T_3^s \end{bmatrix}, \quad \{e\} = \begin{bmatrix} e_1 \\ e_2 \\ e_3 \end{bmatrix}, \quad (3.3.35)$$

and  $T_i$ ,  $T_i^s$ ,  $e_i$  are respectively the current tension, initial specified tension and extension from the initial state along side  $i$  of the element for  $i = 1, 2, 3$ .

Consider the transformation of element strains from the directions of the local element  $x$ - and  $y$ -axes as shown in figure 3.5 to along each side of the element. The strains are assumed constant along each side and hence, throughout the element. Applying the law of strain transformations, the strain along side 1 is then given by

$$\epsilon_1 = \epsilon_x \cos^2 \theta_1 + \epsilon_y \sin^2 \theta_1 + \gamma_{xy} \cos \theta_1 \sin \theta_1 \quad (3.3.36)$$

where  $\epsilon_x$ ,  $\epsilon_y$  and  $\gamma_{xy}$  are the element constant strains, and  $\theta_1$  is the inclination of side 1 to the local  $x$ -axis (measured anti-clockwise from  $x$ -axis to side 1). The strains along sides 2 and 3 of the element can be similarly determined. In matrix form, the strains along each side of the element is then given by

$$\{\epsilon\} = [A]\{\epsilon_{xy}\}, \quad (3.3.37)$$

or in expanded form

$$\begin{bmatrix} \epsilon_1 \\ \epsilon_2 \\ \epsilon_3 \end{bmatrix} = \begin{bmatrix} a_1 & b_1 & c_1 \\ a_2 & b_2 & c_2 \\ a_3 & b_3 & c_3 \end{bmatrix} \begin{bmatrix} \epsilon_x \\ \epsilon_y \\ \gamma_{xy} \end{bmatrix} \quad (3.3.38)$$

in which  $a_i = \cos^2 \theta_i$ ,  $b_i = \sin^2 \theta_i$  and  $c_i = \cos \theta_i \sin \theta_i$  for  $i = 1, 2, 3$ , and

$$\begin{bmatrix} \epsilon_1 \\ \epsilon_2 \\ \epsilon_3 \end{bmatrix} = \begin{bmatrix} e_1/l_1 \\ e_2/l_2 \\ e_3/l_3 \end{bmatrix}. \quad (3.3.39)$$

in which  $e_i$  and  $l_i$  are respectively the extension and initial length of side  $i$ .

$$\text{Thus,} \quad \{\epsilon_{xy}\} = [A]^{-1}\{\epsilon\} = [G]\{e\} \quad (3.3.40)$$

$$\text{in which} \quad [G] = \frac{1}{|A|} \begin{bmatrix} (b_2 c_3 - b_3 c_2)/l_1 & (b_3 c_1 - b_1 c_3)/l_2 & (b_1 c_2 - b_2 c_1)/l_3 \\ (a_3 c_2 - a_2 c_3)/l_1 & (a_1 c_3 - a_3 c_1)/l_2 & (a_2 c_1 - a_1 c_2)/l_3 \\ (a_2 b_3 - a_3 b_2)/l_1 & (a_3 b_1 - a_1 b_3)/l_2 & (a_1 b_2 - a_2 b_1)/l_3 \end{bmatrix} \quad (3.3.41)$$

and  $|A|$  is the determinant of  $[A]$ .



Furthermore, the element stresses are related to the strains in the following manner

$$\{\sigma_{xy}\} = [D]\{\epsilon_{xy}\}, \quad (3.3.42)$$

or in expanded form

$$\begin{bmatrix} \sigma_x \\ \sigma_y \\ \tau_{xy} \end{bmatrix} = \begin{bmatrix} d_{11} & d_{12} & 0 \\ d_{21} & d_{22} & 0 \\ 0 & 0 & d_{33} \end{bmatrix} \begin{bmatrix} \epsilon_x \\ \epsilon_y \\ \gamma_{xy} \end{bmatrix} \quad (3.3.43)$$

where  $d_{11}$ ,  $d_{12}$ ,  $d_{21}$  and  $d_{33}$  are the material orthotropic elastic constants which constitute the elasticity matrix  $[D]$  corresponding to the local element  $x$ - and  $y$ -axes.

For an isotropic material,

$$d_{11} = d_{22} = \frac{E}{(1 - \nu^2)}, \quad d_{12} = d_{21} = \frac{\nu E}{(1 - \nu^2)}, \quad d_{33} = \frac{E}{2(1 + \nu)} \quad (3.3.44)$$

in which  $\nu$  is the Poisson's ratio and  $E$  is the Young's modulus of the membrane material.

On the other hand, for a linear elastic material which is anisotropic in an orthogonal sense, the stress-strain relationship is given by

$$\epsilon_x = \frac{\sigma_x}{E_x} - \nu_y \frac{\sigma_y}{E_y}, \quad (3.3.45)$$

$$\epsilon_y = -\nu_x \frac{\sigma_x}{E_x} + \frac{\sigma_y}{E_y} \quad (3.3.46)$$

where  $E_x$ ,  $E_y$  are respectively the moduli of elasticity in the  $x$ - and  $y$ -directions, and  $\nu_x$ ,  $\nu_y$  are respectively the Poisson's ratios in the  $x$ - and  $y$ -directions.

Multiplying equation (3.3.45) by  $\nu_x$  and adding the resulting equation to equation (3.3.46) gives

$$\nu_x \epsilon_x + \epsilon_y = \frac{\sigma_y}{E_y} (1 - \nu_x \nu_y). \quad (3.3.47)$$

Hence, 
$$\sigma_x = \frac{E_x}{(1 - \nu_x \nu_y)} (\epsilon_x + \nu_y \epsilon_y), \quad \sigma_y = \frac{E_y}{(1 - \nu_x \nu_y)} (\nu_x \epsilon_x + \epsilon_y). \quad (3.3.48)$$

Subsequently, the  $[D]$  matrix for an orthotropic material is given by

$$[D] = \begin{bmatrix} E_x/(1 - \nu_x \nu_y) & \nu_y E_x/(1 - \nu_x \nu_y) & 0 \\ \nu_x E_y/(1 - \nu_x \nu_y) & E_y/(1 - \nu_x \nu_y) & 0 \\ 0 & 0 & d_{33} \end{bmatrix} \quad (3.3.49)$$

where  $d_{33}$  is the shear rigidity which is normally less than 1/15 of the rigidity in tension.

By the Maxwell's reciprocal theorem, the moduli of elasticity and Poisson's ratios are interrelated as follows-

$$\frac{\nu_x}{E_x} = \frac{\nu_y}{E_y}. \quad (3.3.50)$$

Substituting equation (3.3.40) into equation (3.3.42) leads to

$$\{\sigma_{xy}\} = [D][G]\{e\}. \quad (3.3.51)$$

The element stiffness relations are then given by

$$\begin{aligned} \{F\} &= [[G]^T [D] [G] V] \{e\} \\ &= [K] \{e\} \end{aligned} \quad (3.3.52)$$

where  $\{F\}$  = element side forces,

$\{e\}$  = element side extensions,

$[K]$  =  $(3 \times 3)$  element stiffness matrix,

and  $V$  = volume of element given by  $(A \times t)$  with  $A$  and  $t$  being the element surface area and thickness respectively.

For form-finding in which the prescribed membrane stresses are held constant at  $\{\sigma\}^s$ , the element side tensions  $\{F\}$  can then be calculated as follows-

$$\{F\} = V[G]^T \{\sigma\}^s. \quad (3.3.53)$$

The shear modulus of the coated fabric material is generally very low (ie.  $d_{33} \approx 0$ ) which means that the resulting shear stresses will be negligible (ie.  $\tau_{xy} \approx 0$ ) and can thus be ignored in most cases. In addition, the local element x- and y-axes can be set coincident with the material principal directions, ie. the warp and fill directions respectively, and with side 1 of the element taken to

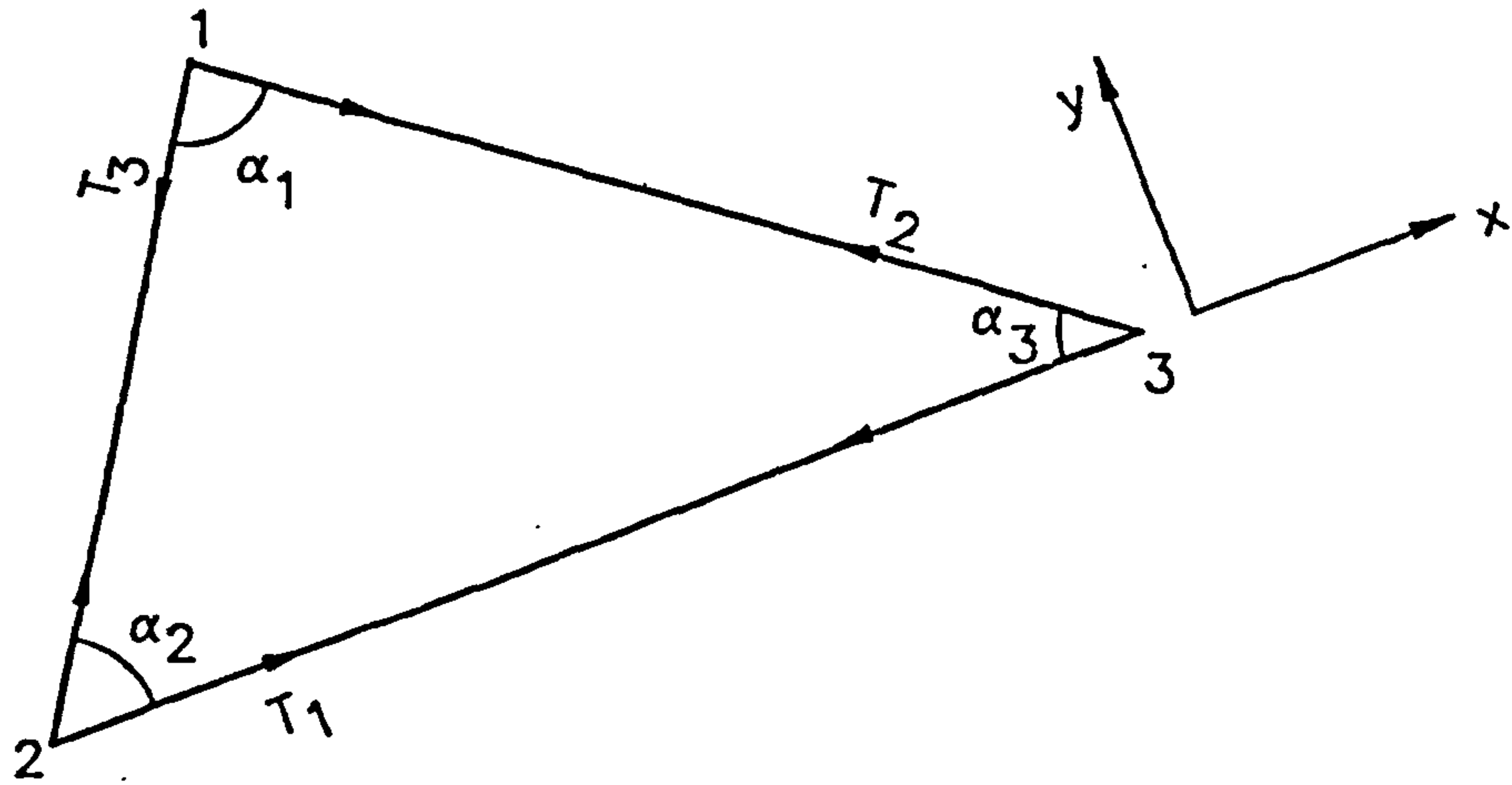


Figure 3.6

be along the warp direction, ie.  $\theta_1 = 0$  as shown in figure 3.6. As a result, the tension in any side  $i$  can be written in the following much simplified form [17, 18]

$$T_i = \frac{\sigma_y l_i}{2 \tan \alpha_i} \quad (3.3.54)$$

except for side 1 if  $(\sigma_x \neq \sigma_y)$ , then

$$T_1 = \frac{\sigma_y l_1}{2 \tan \alpha_1} + \frac{A}{l_1} (\sigma_x - \sigma_y). \quad (3.3.55)$$

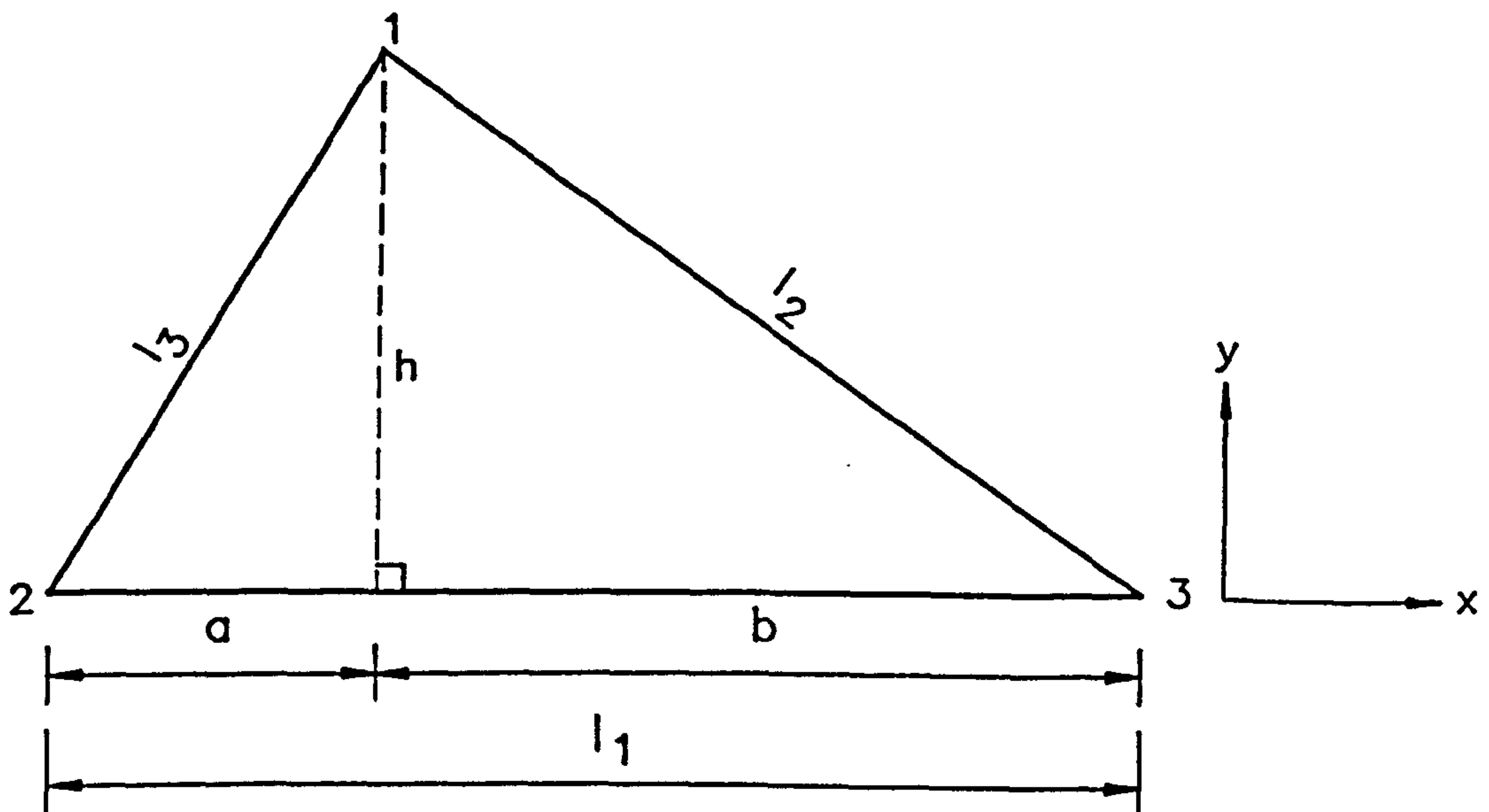


Figure 3.7



If the shear stresses are to be taken into account, then their contributions to the side tensions are given as follows [20]

$$\begin{aligned} T_1 &= \frac{\tau_{xy}(l_2^2 - l_3^2)}{2l_1} = \frac{\tau_{xy}(b - a)}{2}, \\ T_2 &= -\frac{\tau_{xy}l_2}{2}, \quad T_3 = \frac{\tau_{xy}l_3}{2} \end{aligned} \quad (3.3.56)$$

in which the  $a, b, l_1, l_2$  and  $l_3$  terms are as defined in figure 3.7.

In equations (3.3.54) and (3.3.55), the membrane stresses are forces per unit width and for simple orthotropic stress-strain relations, are given by

$$\begin{aligned} \sigma_x &= \sigma_x^s + d_{11}\epsilon_x + d_{12}\epsilon_y, \\ \sigma_y &= \sigma_y^s + d_{12}\epsilon_x + d_{22}\epsilon_y \end{aligned} \quad (3.3.57)$$

where  $\sigma_x, \sigma_y$  are the current principal stresses,

$\sigma_x^s, \sigma_y^s$  are the initial prestresses, and

$d_{11}, d_{22}, d_{12}$  are the material orthotropic elastic constants.

In addition, the shear stress  $\tau_{xy}$  is given by

$$\tau_{xy} = d_{33}\gamma_{xy}. \quad (3.3.58)$$

The element strains in equation (3.3.57) can in turn be calculated in the following manner

$$\epsilon_x = \frac{l_1}{l_1^s} - 1, \quad \epsilon_y = \frac{Al_1^s}{A^s l_1} - 1 \quad (3.3.59)$$

where  $A^s$  and  $l_1^s$  are respectively the element area and length of side 1 (parallel to x-axis) in the initial or prestressed state, and  $A$  and  $l_1$  are the corresponding values in the current state.

Furthermore, the shear strain  $\gamma_{xy}$  can in turn be found as shown in figure 3.8, ie.

$$a = l_3 \cos \alpha_2,$$

$$\delta = a - \left(\frac{a^s}{l_1^s}\right)l_1,$$

$$\gamma_{xy} = \tan^{-1}\left(\frac{\delta}{h}\right) \approx \frac{\delta}{h} \quad (3.3.60)$$

in which again the above terms are for the current state except for those with the superscript 's' which are values in the initial or prestressed state.

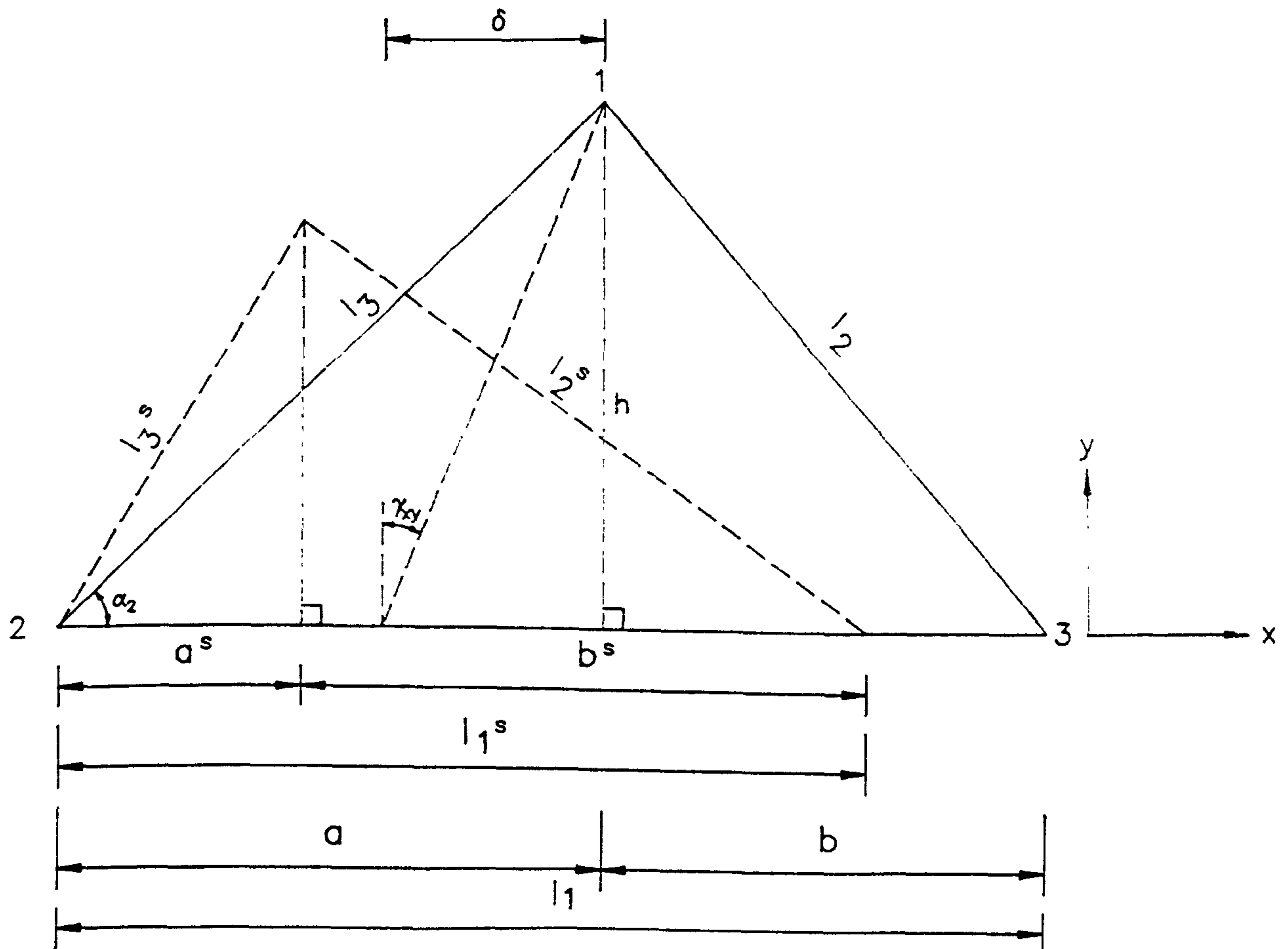


Figure 3.8

As a useful feature of the dynamic relaxation method, the strain components in equations (3.3.59) and (3.3.60) are updated independently of the stresses in equations (3.3.57) and (3.3.58) instead of being coupled as in matrix methods. This enables the modelling of more complex stress-strain relations such as stresses as polynomial functions of strains, slip cables and on/off non-linearities, and also simplifies the inclusion of physical controls in the form-finding and static analysis stages. With the buckling of the membrane elements considered only in the principal weave (x- and/or y-) directions, the buckling of the real membrane will be closely approximated bearing in mind the generally very low shear stiffness of the fabric material. It is also noted that geometric non-linearity is automatically accounted for with the element strains in equations (3.3.59) and (3.3.60) calculated from the current updated geometry of the structure.

### 3.4 Conclusions

In this chapter, the basic mechanics of the dynamic relaxation method are outlined in relation to its application to the form-finding and static analysis of tension structures in which the solution is for the static equilibrium state of the structure concerned. The method has a clear underlying physical basis. With an image of the structure in its current geometry displayed on the computer screen and the image updated at regular intervals during the analysis, any signs of physical instabilities in the structure can be easily detected and often their causes are easily identifiable as well. The method is also relatively simple in terms of its underlying theory and implementation into a computer program.

As the dynamic relaxation method is basically an explicit numerical scheme, it is only numerically stable on condition that a time step less than a critical value is used. By using fictitious nodal masses, the time step required for a stable solution can be optimised in order to produce an increased convergence rate. A strategy which gives an automated control of the fictitious nodal masses is adopted. In this strategy, a diagonal matrix of fictitious masses is used at each node and this matrix is factored appropriately to account for the coupling effects between the various degrees of freedom at each node. As an alternative to viscous damping, the kinetic damping procedure is used to control the solution path to convergence, and this procedure is effective in dealing with high residuals which can often arise suddenly during radical changes to the numerical model. Furthermore, the natural stiffness relations are used in the calculations for the natural forces from the corresponding basic displacements. The natural forces are then transformed to the global coordinate system and added to the nodal residual forces. This proves an efficient means of deriving the nodal residual forces and hence, greatly enhances the computational speed of the overall solution process. In the method, geometric non-linearity is automatically accounted for. Another useful feature of the method is the effective decoupling of the equations of compatibility and equilibrium which allows the modelling of complex material properties, slip cables and on/off non-linearities, and simplifies the inclusion of physical controls in the form-finding and static analysis stages. Finally, the reasons for choosing the dynamic relaxation method as the preferred solution scheme are therefore clear from the above discussion.



## Chapter 4

### Compression and bending elements incorporated into the DR scheme

#### 4.1 Introduction

The idea of a structure comprising of tension elements being stabilised by a compression boundary becomes obvious in a simple example such as the bicycle wheel. In this case, the bicycle spokes all in tension are bound by the rim which is in compression. On a much larger scale, compression ring beams have been used as boundary supports for tension structures such as the Raleigh Arena and the Calgary Olympic Stadium. It is an excellent alternative to provide compression boundaries as opposed to the more obvious choice of tension anchorages as support means for large span tension structures. The tension elements in such structures act as elastic supports for the compression boundaries and thus, slender sections can be used in these boundaries.

From both the studies by Mollmann [99] and Samuelli Ferretti, et. al. [120], it is concluded that when the flexibility of the compression boundary of a tension structure is ignored, then large enough errors are introduced into the analysis of the structure to invalidate the results produced. This is particularly so if the stiffness of the boundary is relatively low compared with that of the tension structure it supports. By modelling the compression boundary using compression (or strut) and/or bending (or beam) elements, the flexibility and thus, finite deformations of the boundary can be properly accounted for. This in turn will enable a realistic modelling of the interaction between the boundary and the tension structure. The compression elements are used in situations where compressive forces are to be resisted in the absence of any bending moment. On the other hand, where bending moments are to be resisted, the beam elements should be used, and compressive forces can also be taken as axial loads in the elements.

The case of prestressed cable structures with compression boundary supports has been studied by Mollmann [99] using a finite element displacement analysis based on the Newton-Raphson method, by Buchholdt, Das and Al-Hilli [38] using the conjugate gradient method, and by Wakefield [133] using the dynamic relaxation method. In the study by Wakefield [133], it is shown that the dynamic relaxation method can cope with the beam elements with equal ease and efficiency as for the tension elements, and is also more efficient than the scaled conjugate gradient method. An extension of the approach used by Wakefield [133] is discussed in this chapter. It is convenient to adopt this approach for modelling the beam elements as the dynamic relaxation method is the chosen solution scheme in this thesis.

A detailed description of the dynamic relaxation method as applied to the tension elements has already been given in chapter 3, and the method can be applied equally to the compression elements with the consideration of allowing compressive forces in these elements, bearing in mind that the

tension elements will buckle under compression. Although only minor adjustments will be needed, more consideration is required when applying the dynamic relaxation method to the beam elements. Hence, the discussion in this chapter will be mainly concerned with the implementation of the beam elements using the dynamic relaxation method.

## 4.2 Moment-curvature relations

The compression boundary can be modelled as a series of initially straight beam elements. As shown in figure 4.1, each beam element in space has six basic displacements with corresponding natural forces. The basic displacements and natural forces are defined relative to a local axes system in which the  $x$ -axis is along the direction from node  $i$  to node  $j$  of the element, and the corresponding  $y$ - and  $z$ -axes set up to give a right-handed coordinate system. The  $y$ - and  $z$ -axes are chosen to coincide with the principal axes for the element cross-section.

The six basic displacements indicated in figure 4.1(a) are as follows-

- $e$  : the axial displacement along the  $x$ -axis,
- $\theta_{xji}$  : the torsional displacement along the  $x$ -axis,
- $\theta_{yi}$  : the rotational displacement about the  $y$ -axis at node  $i$ ,
- $\theta_{yj}$  : the rotational displacement about the  $y$ -axis at node  $j$ ,
- $\theta_{zi}$  : the rotational displacement about the  $z$ -axis at node  $i$ ,
- $\theta_{zj}$  : the rotational displacement about the  $z$ -axis at node  $j$ .

The corresponding natural forces of the element as shown in figure 4.1(b) are given by

$$\{m_i\} = \begin{Bmatrix} m_{xi} \\ m_{yi} \\ m_{zi} \end{Bmatrix}, \quad \{m_j\} = \begin{Bmatrix} m_{xj} \\ m_{yj} \\ m_{zj} \end{Bmatrix},$$

in which  $m_{xi}$ ,  $m_{yi}$  and  $m_{zi}$  are the moments at node  $i$  about the local  $x$ -,  $y$ - and  $z$ -axes respectively with similar moments at node  $j$ , and

$$\{p_i\} = \begin{Bmatrix} p_{xi} \\ p_{yi} \\ p_{zi} \end{Bmatrix}, \quad \{p_j\} = \begin{Bmatrix} p_{xj} \\ p_{yj} \\ p_{zj} \end{Bmatrix},$$

in which  $\{p_i\} = -\{p_j\}$ , and  $p_{xi}$ ,  $p_{yi}$  and  $p_{zi}$  are the forces at node  $i$  in the directions of the local  $x$ -,  $y$ - and  $z$ -axes respectively with similar forces at node  $j$ .

The above basic displacements and natural forces are related to their corresponding values in the global axes system by a transformation matrix. The current position and orientation of the beam element can be established

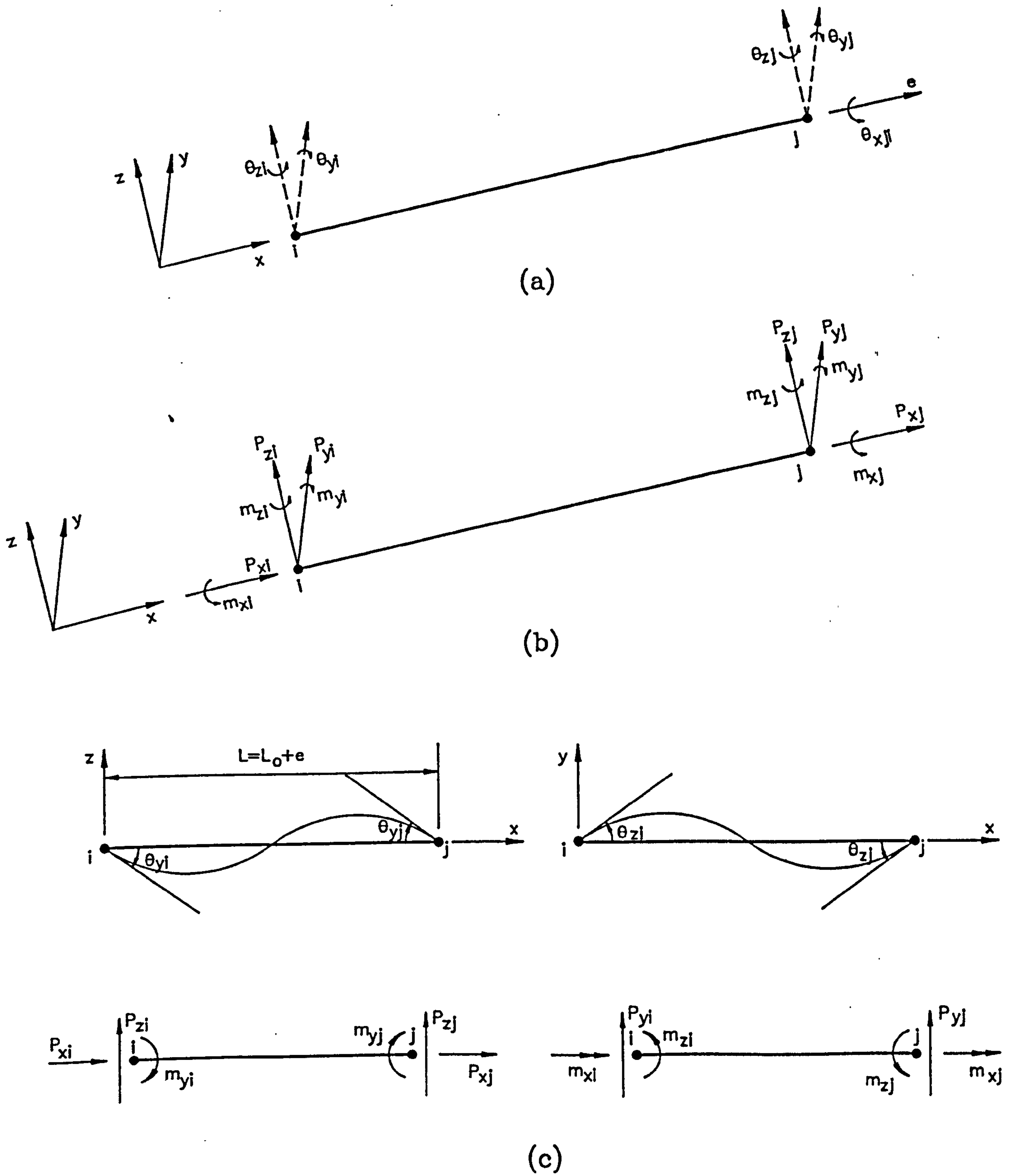


Figure 4.1 Basic displacements and natural forces



from the current global node coordinates  $\{X\}$ . However, the rotational displacements are derived relative to an initial state defined at the start of the analysis.

The basic displacements are related to the natural forces of the beam element by the following equations

$$\begin{Bmatrix} m_{yi} \\ m_{yj} \end{Bmatrix} = \frac{EI_y}{L} \begin{bmatrix} 4 & 2 \\ 2 & 4 \end{bmatrix} \begin{Bmatrix} \theta_{yi} \\ \theta_{yj} \end{Bmatrix}, \quad (4.2.1)$$

$$\begin{Bmatrix} m_{zi} \\ m_{zj} \end{Bmatrix} = \frac{EI_z}{L} \begin{bmatrix} 4 & 2 \\ 2 & 4 \end{bmatrix} \begin{Bmatrix} \theta_{zi} \\ \theta_{zj} \end{Bmatrix}, \quad (4.2.2)$$

$$m_{xi} = -m_{xj} = -\frac{GJ}{L} \theta_{xji}, \quad (4.2.3)$$

$$p_{xi} = -p_{xj} = -\frac{EA}{L_0} e, \quad (4.2.4)$$

$$p_{yi} = -p_{yj} = \frac{(m_{zi} + m_{zj})}{L}, \quad (4.2.5)$$

$$p_{zi} = -p_{zj} = -\frac{(m_{yi} + m_{yj})}{L}, \quad (4.2.6)$$

$$L = L_0 + e, \quad (4.2.7)$$

in which  $E$ ,  $G$ ,  $A$ ,  $L$  and  $L_0$  denote the Young's modulus, shear modulus, cross-sectional area, current length and slack or initial length respectively, and  $I_y$  and  $I_z$  are the principal second moments of area about the local  $y$ - and  $z$ -axes respectively, and  $J$  is the polar second moment of area. The moments about the local  $x$ -axis are torsional moments, and the moments about the local  $y$ - and  $z$ -axes are bending moments. The forces in the direction of the local  $x$ -axis are axial thrusts, and the forces in the directions of the local  $y$ - and  $z$ -axes are shear forces.

The current position of the beam element in space is given by the current node coordinates at the two ends of the element. However, the exact orientation of the principal cross-section is only known with the definition of an additional variable, ie. the  $\beta_0$  angle as shown in figure 4.2. A plane which contains the local  $x$ -axis (ie. the axis along the direction from node  $i$  to node  $j$  of the beam element) and the global  $z$ -axis such as the  $i, j, k$  plane in figure 4.2, can be formed. In the case of a beam element which lies parallel to the global  $z$ -axis, the plane containing the local  $x$ -axis and the global  $y$ -axis can be taken instead. The  $\beta_0$  angle is defined as the angle between the  $i, j, k$  plane and the local  $z$ -axis of the beam element.

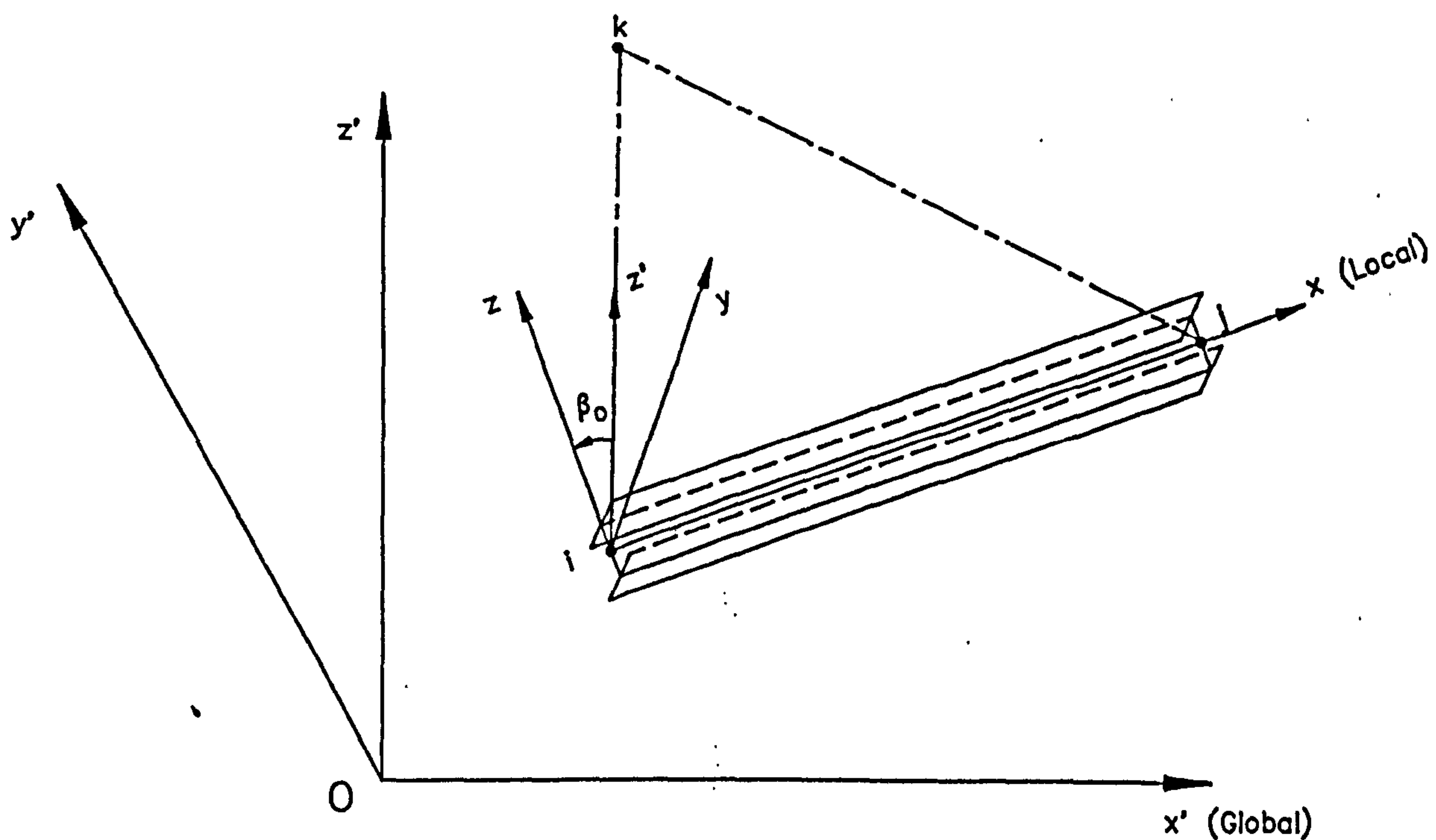


Figure 4.2

Furthermore, it is assumed that there is a linear variation of torsional displacements along the local  $x$ -axis. The current orientation angle  $\beta$  is then given by the sum of the specified  $\beta_0$  angle and the average of the torsional displacements at nodes  $i$  and  $j$  of the element, ie.

$$\beta = \beta_0 + \frac{(\theta_{xi} + \theta_{xj})}{2} \quad (4.2.8)$$

in which  $\theta_{xi} = [l \ m \ n]\{\theta_i\}$ , and  $\{\theta_i\}$  are the global nodal rotational displacements, and  $l, m$  and  $n$  are the direction cosines of the current local  $x$ -axis. With the  $\beta$  angle known, the local right-handed axes of the beam element can then be uniquely defined, and the transformation matrix  $[T]$  between the local and global axes can in turn be found. Subsequently,

$$\{X\} = [T]\{X'\} \quad (4.2.9)$$

in which  $\{X\}$  and  $\{X'\}$  are the local and global node coordinates respectively, and

$$[T] = \begin{bmatrix} l_1 & m_1 & n_1 \\ l_2 & m_2 & n_2 \\ l_3 & m_3 & n_3 \end{bmatrix} \quad (4.2.10)$$



with  $l_1$ ,  $m_1$  and  $n_1$  being the direction cosines between the local  $x$ -axis and the global  $x$ -,  $y$ - and  $z$ -axes respectively, and so on. On the other hand,

$$\{X'\} = [T]^T\{X\}. \quad (4.2.11)$$

In addition, the transformation matrix  $[T]$  is used to relate the local translational displacements to their global equivalents as shown below

$$\begin{Bmatrix} \Delta u \\ \Delta v \\ \Delta w \end{Bmatrix} = \begin{Bmatrix} u_j - u_i \\ v_j - v_i \\ w_j - w_i \end{Bmatrix} = [T] \begin{Bmatrix} x'_{ji} - x'_{oji} \\ y'_{ji} - y'_{oji} \\ z'_{ji} - z'_{oji} \end{Bmatrix}, \quad (4.2.12)$$

in which  $u_i$ ,  $v_i$  and  $w_i$  are the translational displacements at node  $i$  in the directions of the current local  $x$ -,  $y$ - and  $z$ -axis respectively with similar displacements at node  $j$ , and

$$x'_{ji} - x'_{oji} = (x'_j - x'_i) - (x'_{oj} - x'_{oi}) = (x'_j - x'_{oj}) - (x'_i - x'_{oi}), \quad (4.2.13)$$

with  $x'_{oi}$  and  $x'_i$  being the initial and current global  $x$  coordinates of node  $i$  and so on. The initial global coordinates correspond to the position of the beam element when first defined and thus, these coordinates have to be stored for subsequent use in equation (4.2.12).

In order to account for the rigid body motions of the beam element when determining the rotational displacements from the global nodal rotations, two sway angles, ie.  $\phi_{yji}$  and  $\phi_{zji}$  have to be calculated for bending about the local  $y$ - and  $z$ -axes respectively. In figure 4.3, the local  $x_o$ -,  $y_o$ - and  $z_o$ -axes define the beam element in its initial state with end nodes at  $i_o$  and  $j_o$  whereas the local  $x$ -,  $y$ - and  $z$ -axes define the element in its current state with end nodes at  $i$  and  $j$ . The beam element undergoes local translational displacements of  $\Delta u$ ,  $\Delta v$  and  $\Delta w$  in going from its initial to its current state. Let  $v_a$  be the vector along the local  $x_o$ -axis (ie. from node  $i_o$  to node  $j_o$ ) of the beam element,  $v_c$  be the vector along the local  $x$ -axis (ie. from node  $i$  to node  $j$ ) of the element, and  $v_y$  be the unit vector in the direction of the local  $y$ -axis of the element. Due to the  $\Delta v (= v_j - v_i)$  displacement in the local  $x$ - $y$  plane, and

$$v_b = v_a + \Delta v v_y, \quad (4.2.14)$$

and the  $\Delta w (= w_j - w_i)$  displacement in the local  $x$ - $z$  plane, it follows that

$$\phi_{yji} = \cos^{-1} \left( \frac{v_b \cdot v_c}{|v_b| |v_c|} \right), \quad (4.2.15)$$



For the calculation of the sway angle  $\phi_{zji}$ , consider figure 4.4 in which the same notation as described above for figure 4.3 is used and with  $v_z$  being the unit vector in the direction of the local z-axis of the beam element. Due to the  $\Delta w (= w_j - w_i)$  displacement in the local x-z plane, and

and the  $\Delta v (= v_j - v_i)$  displacement in the local  $x$ - $y$  plane, it follows that

For the case of  $(\Delta v < 0)$  as shown in figure 4.4, the sway angle  $\phi_{zji}$  (for bending about the local z-axis) has a negative sense.

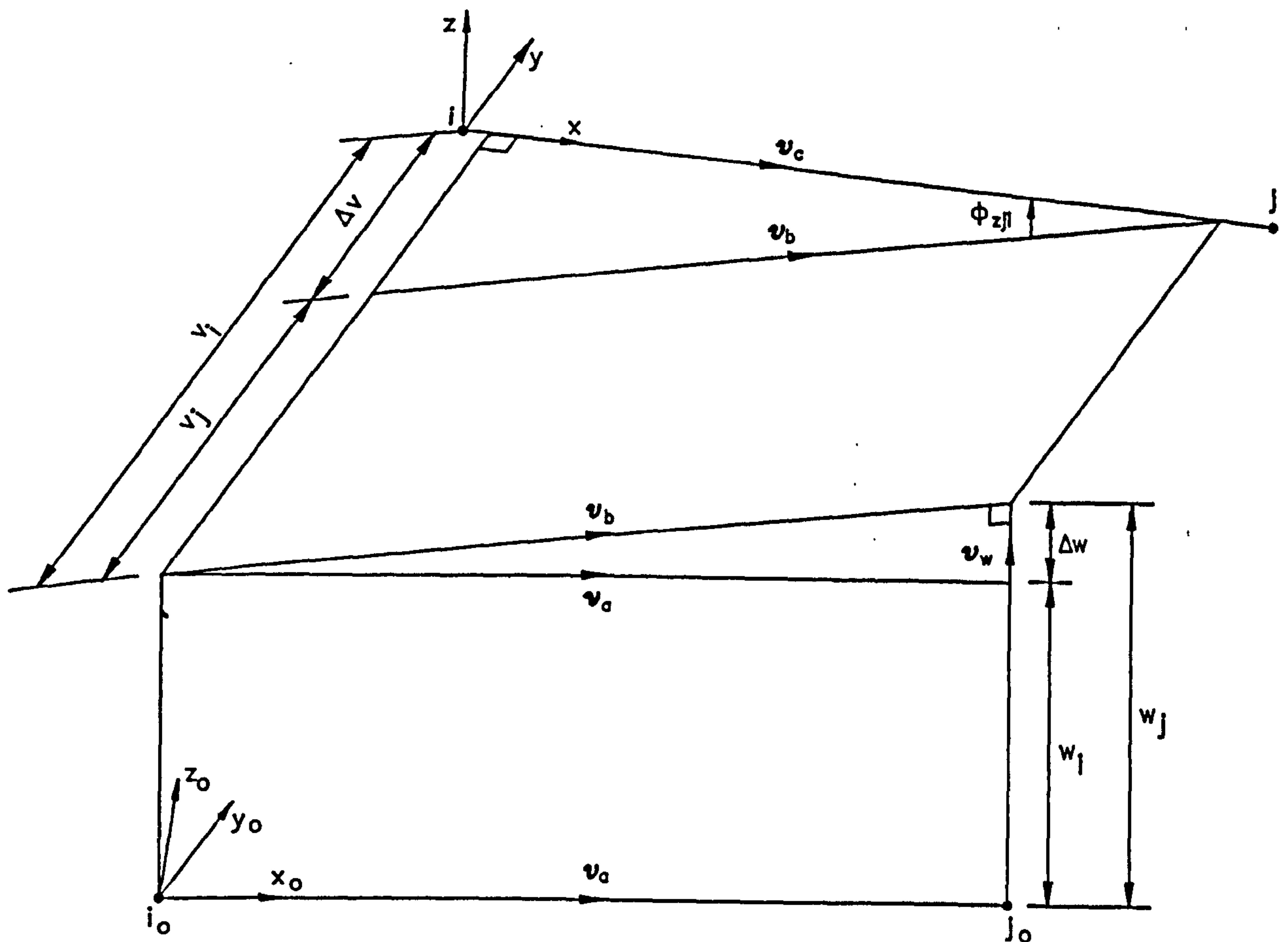


Figure 4.4

Subsequently, the components of global nodal rotations in the local axes system of the element in its current state can be found as follows-

$$\{\Theta\}_i = [T]\{\Theta'\}_i,$$

$$\Rightarrow \begin{Bmatrix} \Theta_{xi} \\ \Theta_{yi} \\ \Theta_{zi} \end{Bmatrix} = \begin{bmatrix} l_1 & m_1 & n_1 \\ l_2 & m_2 & n_2 \\ l_3 & m_3 & n_3 \end{bmatrix} \begin{Bmatrix} \Theta'_{xi} \\ \Theta'_{yi} \\ \Theta'_{zi} \end{Bmatrix}, \quad (4.2.18)$$

in which  $\{\Theta\}_i$  and  $\{\Theta'\}_i$  are the rotations at node  $i$  in the local and global senses respectively, and the same applies at node  $j$ ;  $\Theta_{xi}$ ,  $\Theta_{yi}$  and  $\Theta_{zi}$  are the rotations at node  $i$  about the local  $x$ -,  $y$ - and  $z$ -axis respectively, and so on.

The local rotational displacements of the element are in turn given by the following equations

$$\theta_{xji} = \Theta_{xj} - \Theta_{xi},$$

$$\theta_{yi} = \Theta_{yi} - \phi_{yji}, \quad \theta_{yj} = \Theta_{yj} - \phi_{yji},$$

$$\theta_{zi} = \Theta_{zi} - \phi_{zji}, \quad \theta_{zj} = \Theta_{zj} - \phi_{zji}. \quad (4.2.19)$$

The current length  $L$  can be calculated from the current global coordinates of nodes  $i$  and  $j$  of the element, and the axial displacement  $e$  can then be obtained from equation (4.2.7). With the basic displacements determined, the natural stiffness relations given in equations (4.2.1) to (4.2.6) can in turn be used to solve for the natural forces acting on the element. A transformation process can subsequently be applied to the natural forces to give their components in the global axes system, ie.

$$\{m_i'\} = [T]^T\{m_i\}, \quad \{p_i'\} = [T]^T\{p_i\} \quad (4.2.20)$$

in which  $\{m_i'\}$  and  $\{m_i\}$  are the global and local moments respectively at node  $i$ , and  $\{p_i'\}$  and  $\{p_i\}$  are the global and local direct forces (ie. axial and shear forces) respectively at node  $i$ . These global moments and direct forces can then be subtracted from their corresponding residual force vectors at node  $i$ , and the contributions of global forces from all elements connected to node  $i$  have to be taken into account. The same steps also apply at node  $j$  of the beam element concerned.

### 4.3 Non-linear effects

The beam elements are developed to cope with a number of non-linear effects. Firstly, the non-linear effect due to the influence of axial force on the linear moment-curvature relations given in equations (4.2.1) and (4.2.2) can be accounted for by using the  $s$  and  $c$  stability functions in the following manner, ie.

$$\begin{Bmatrix} m_{yi} \\ m_{yj} \end{Bmatrix} = \frac{EI_y}{L} \begin{bmatrix} s & sc \\ sc & s \end{bmatrix} \begin{Bmatrix} \theta_{yi} \\ \theta_{yj} \end{Bmatrix} \quad (4.3.1)$$

and similarly for bending about the  $z$ -axis. The stability functions can be expressed in the form of a power series as derived by Livesley, et. al. [92] and are given by the following equations

$$s = 3\phi_2 + \phi_1, \quad (4.3.2)$$

$$sc = 3\phi_2 - \phi_1, \quad (4.3.3)$$

and with  $\rho = P/P_E$ , ie. the ratio of current to Euler compressive forces,



$$\phi_1 = \frac{(64 - 60\rho + 5\rho^2)}{(16 - \rho)(4 - \rho)} - \sum_{n=1}^{n=7} \frac{a_n \rho^n}{2^{3n}}, \quad (4.3.4)$$

$$\phi_2 = \frac{\pi^2 \rho}{12(1 - \phi_1)}, \quad (4.3.5)$$

and

$$\begin{aligned} a_1 &= 1.57973627, & a_2 &= 0.15858587, \\ a_3 &= 0.02748899, & a_4 &= 0.00547540, \\ a_5 &= 0.00115281, & a_6 &= 0.00024908, \\ a_7 &= 0.00005452. \end{aligned} \quad (4.3.6)$$

The above expressions apply equally to bending about the local  $y$ - or  $z$ -axis, and can cope with either tensile or compressive axial forces by simply using the correct sign in each case. In addition, the case of zero axial force poses no problem. Alternative expressions have been derived for the stability functions in which the presence of either tensile or compressive axial forces are dealt with in separate equations as given in [45], which become indeterminate for zero axial force.

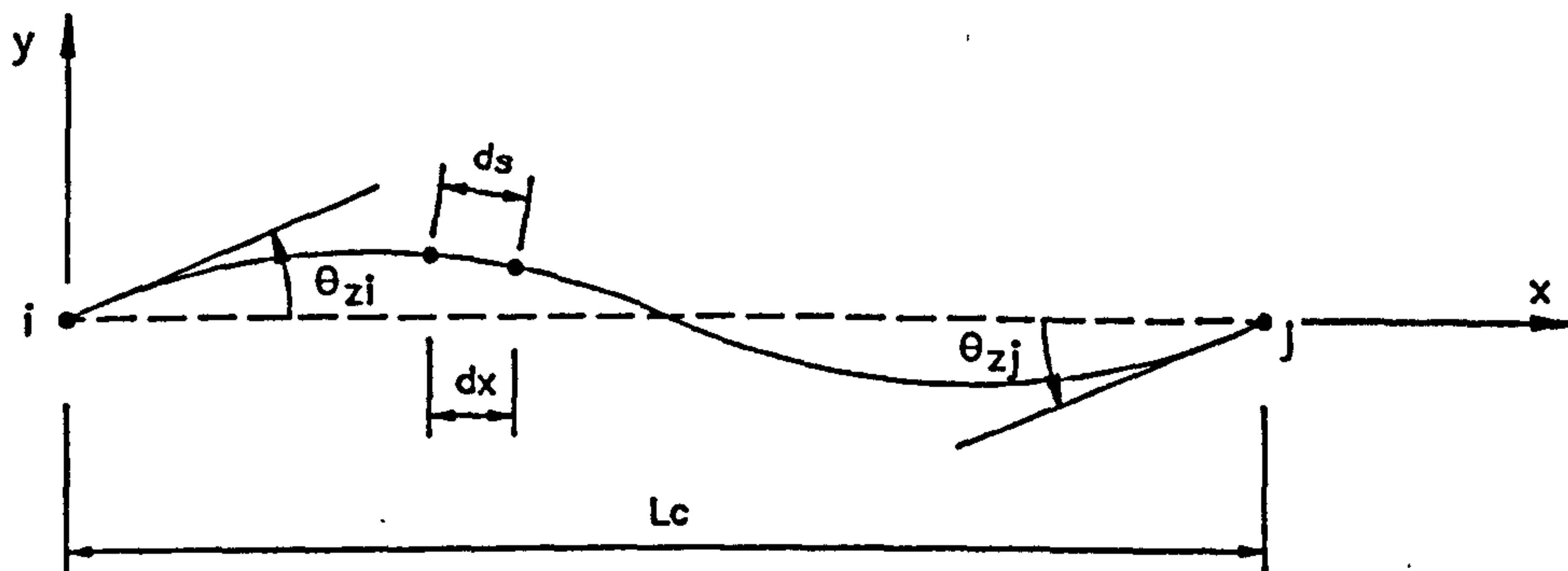


Figure 4.5

The non-linear effect of element bowing on the axial displacement has been considered by both Saafan [119] and Wakefield [133]. This effect is modelled by using correction factors, and their derivation given below is taken from the account by Wakefield [133]. For a beam element in space, bending and thus, bowing can occur in both the local  $x$ - $z$  and  $x$ - $y$  planes. First, consider the bowing effect in the  $x$ - $y$  plane as shown in figure 4.5. The axial displacement of the beam element can be expressed in the following form

$$\Delta L = e + \Delta_B \quad (4.3.7)$$

in which  $e$  is due to the axial elastic deformation, and from equation (4.2.4),  $e = -\frac{p_{xi}L_0}{EA}$ , and  $\Delta_B$  is given by the difference between the arc length  $L_a$  and the chord length  $L_c$ . Subsequently,

$$\Delta_B = \int_0^{L_c} (ds - dx), \quad (4.3.8)$$

in which  $ds = \sqrt{dx^2 + dy^2}$  and thus,

$$\Delta_B = \int_0^{L_c} \left[ \sqrt{1 + \left(\frac{dy}{dx}\right)^2} - 1 \right] dx. \quad (4.3.9)$$

Applying binomial expansion to equation (4.3.9) and neglecting the fourth and higher order terms, gives

$$\Delta_B = \int_0^{L_c} \frac{1}{2} \left(\frac{dy}{dx}\right)^2 dx. \quad (4.3.10)$$

On solving equation (4.3.10), the following results are obtained as given in [119], ie.

$$\Delta_B = L_c [b_1(\theta_{zi} + \theta_{zj})^2 + b_2(\theta_{zi} - \theta_{zj})^2],$$

$$\text{in which } b_1 = \frac{s(1+c)(sc-2)}{8\pi}, \quad b_2 = \frac{c}{8(1+c)}. \quad (4.3.11)$$

In order to account for the bowing effects in both the local  $x$ - $z$  and  $x$ - $y$  planes, the  $ds$  term in equation (4.3.8) is now replaced by  $ds = \sqrt{dx^2 + dy^2 + dz^2}$  and in turn leads to

$$\Delta_B = \int_0^{L_c} \left[ \sqrt{1 + \left(\frac{dy}{dx}\right)^2 + \left(\frac{dz}{dx}\right)^2} - 1 \right] dx \quad (4.3.12)$$

$$\approx \int_0^{L_c} \frac{1}{2} \left[ \left( \frac{dy}{dx} \right)^2 + \left( \frac{dz}{dx} \right)^2 \right] dx. \quad (4.3.13)$$

Consequently, the bowing effects in each of the local  $x$ - $z$  and  $x$ - $y$  planes can be found separately and then their results summed to give the  $\Delta_B$  term in equation (4.3.7).

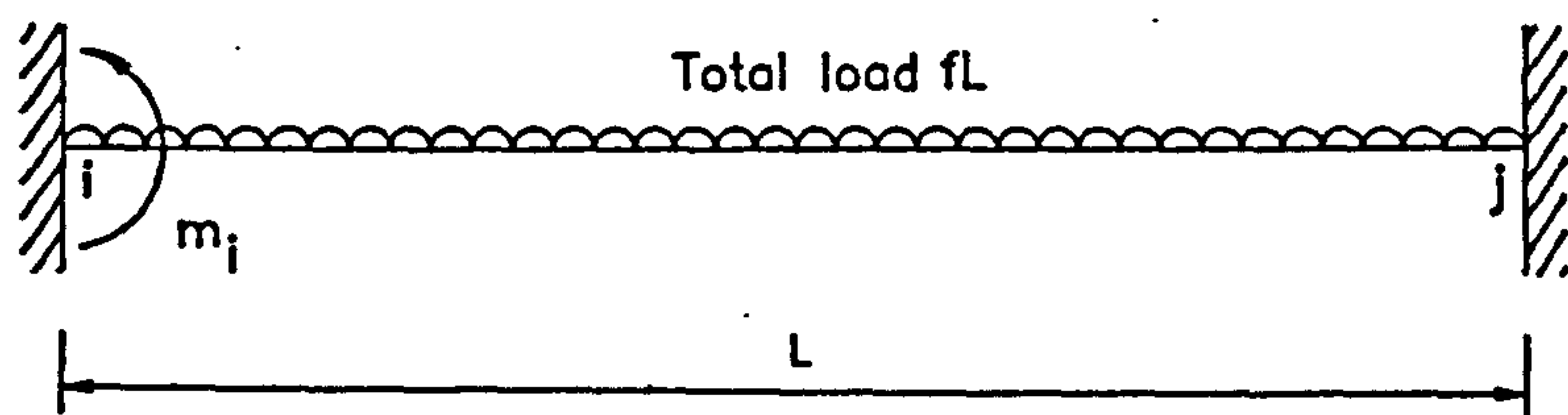


Figure 4.6

A further consideration is the influence of axial force on the fixed-end moments due to the distributed loading on the element. In the case of a uniformly distributed load as shown in figure 4.6, the fixed-end moment  $m_i$  is given by

$$m_i = r \frac{fL^2}{12} \quad (4.3.14)$$

in which  $r = \frac{3}{\rho^2} (1 - \rho \cot \rho)$  (4.3.15)

as given in [45]. However, in the case of zero axial force when  $r$  should be 1, equation (4.3.15) becomes indeterminate. Hence, it is better to use an expression for  $r$  which assumes the following form [133]

$$r = \frac{6}{s(1 + c)} \quad (4.3.16)$$

where the case of zero axial force causes no problem. In addition, equation (4.3.16) can be shown to be equivalent to equation (4.3.15).

In the dynamic relaxation analysis which uses the kinetic damping procedure, it is convenient to update the non-linear effects of the stability functions, element bowing and influence of axial force on the fixed-end moments, and also reset the beam element stiffnesses when an energy peak is detected.



#### 4.4 Boundary conditions

In order for the analysis to produce any meaningful result, the appropriate boundary conditions have to be prescribed. These boundary conditions can be assigned through restraints on any of the three rotational and three translational degrees of freedom at each node connected to a beam element. For instance, the fixed-ended or encastred boundary condition at a node is prescribed by ensuring that there are no rotational and translational displacements at that node.

Consider the case where a few beam elements are connected to a common node  $i$ . It may be required to impose a pin-ended or zero moment condition to node  $i$  of a beam element with nodes  $i$  of the other beam elements still moment resisting. This situation can be modelled by prescribing an end release to node  $i$  of the beam element where the pin-ended condition is imposed. An end release can be prescribed to impose a pin-ended condition for bending about any of the local  $x$ -,  $y$ - and  $z$ -axes.

Subsequently, the natural stiffness relations for a beam element can be written as follows-

$$\begin{Bmatrix} m_{yi} \\ m_{yj} \end{Bmatrix} = \begin{bmatrix} a & b \\ b & a \end{bmatrix} \begin{Bmatrix} \theta_{yi} \\ \theta_{yj} \end{Bmatrix} \quad (4.4.1)$$

in which  $m_{yi}$  and  $m_{yj}$  are the moments about the local  $y$ -axis at nodes  $i$  and  $j$  of the element respectively,  $\theta_{yi}$  and  $\theta_{yj}$  are the corresponding rotational displacements, and  $a$  and  $b$  are the corresponding stiffness terms. Using equation (4.4.1), it can be shown that

with an end release at node  $i$ , then  $m_{yi} = 0 \Rightarrow \theta_{yi} = -\frac{b}{a}\theta_{yj}$ , and

with an end release at node  $j$ , then  $m_{yj} = 0 \Rightarrow \theta_{yj} = -\frac{b}{a}\theta_{yi}$ .

The above procedure applies similarly for bending about the local  $z$ -axis. Hence, an end release is modelled by simple adjustment of the appropriate rotational displacement.

#### 4.5 Implementation into the dynamic relaxation analysis

Within the dynamic relaxation scheme, the beam elements are handled in a similar manner as the tension elements discussed in chapter 3. Only a few modifications pertaining to the beam elements need to be considered.

The rotational degrees of freedom are treated as decoupled from as well as in a similar manner as the translational degrees of freedom. As a result, two



(3×3) mass matrices are set up for each node connected to a beam element, ie. a (3×3) mass matrix each for the rotations and translations. It has been shown by Wakefield [133] that numerically stable solutions can be achieved in this way. This approach leads to a more efficient solution in terms of computational effort compared with forming a (6×6) mass matrix to account for the three rotations and three translations at each node connected to a beam element. The mass matrices are derived from the principal nodal stiffnesses of the beam element (see equation (3.3.19) of chapter 3). For each beam element, the principal nodal stiffnesses for the translational and rotational degrees of freedom are given by

$$\begin{aligned}
 [S_T] &= \begin{bmatrix} EA/L & 0 & 0 \\ 0 & 12EI_z/L^3 & 0 \\ 0 & 0 & 12EI_y/L^3 \end{bmatrix}, \\
 [S_R] &= \begin{bmatrix} GJ/L & 0 & 0 \\ 0 & 4EI_y/L & 0 \\ 0 & 0 & 4EI_z/L \end{bmatrix}
 \end{aligned} \tag{4.5.1}$$

respectively. In the dynamic relaxation scheme, the mass matrices are considered relative to the global axes system. However, the principal nodal stiffness directions (coincident with the local axes of the element) are generally different from those of the global axes. Hence, transformations have to be applied to the principal nodal stiffnesses in equation (4.5.1) to obtain their components in the global axes system (see equation (3.3.19)), ie.

$$\begin{aligned}
 [S_T]' &= [T]^T [S_T] [T], \\
 [S_R]' &= [T]^T [S_R] [T]
 \end{aligned} \tag{4.5.2}$$

in which  $[S_T]'$  and  $[S_R]'$  are the respective transformed square (3×3) matrices of the principal nodal stiffnesses. These square stiffness matrices are then used in the assessment of the nodal masses which will ensure numerical stability in the dynamic relaxation analysis. Subsequently, the row sums of these transformed matrices are taken as contributions to the corresponding components of nodal masses for nodes  $i$  and  $j$  of the beam element. The basis of such a step has already been discussed in section (3.3.2) of chapter 3. Furthermore, various factors are applied to the nodal masses in order to account for possible deviations in the stiffnesses calculated from equations (4.5.1) and (4.5.2) as the analysis proceeds. The stiffnesses which may arise from geometric deformations of the beam elements (ie. geometric stiffnesses) and thus, their contributions to the nodal masses are insignificant in most cases. Consequently, it is adequate to assess the nodal masses for beam elements on the basis of their elastic stiffnesses alone.

#### 4.6 Other considerations

It is also useful for the beam elements to be implemented with facilities related to plane of symmetry and model reflection. In the case where symmetry is present in the structure, a plane of symmetry may be defined so that only part of the structure is used in the form-finding as well as analysis under a symmetric loading. However, the full structure may be required in the analysis under an asymmetric loading. The form of the part structure which is stored in the database after the form-finding, can then be reflected about the plane of symmetry to produce the full structure. Hence, there is no need to use the full structure in the form-finding and all load analyses.

For a node which lies in a plane of symmetry, the coordinates and rotations at this node are constrained to remain in the plane. The nodal residual vector for the translational degrees of freedom is also constrained to lie within the plane of symmetry. On the other hand, the nodal residual vector for the rotational degrees of freedom is required to remain normal to the plane.

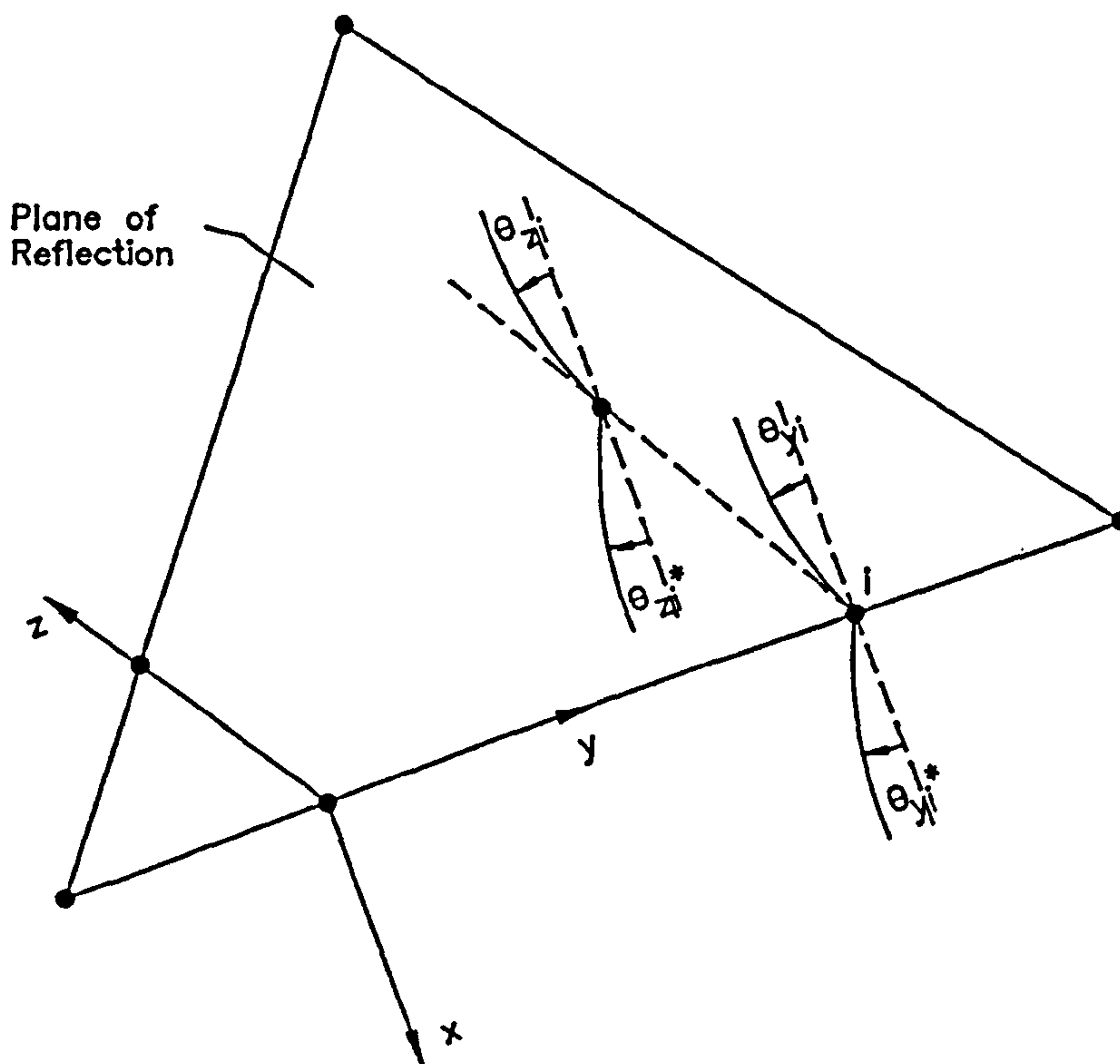


Figure 4.7

A plane of reflection can be defined in the structure as shown in figure 4.7. By reflecting the structure about this plane, additional elements can be generated as a result. Figure 4.7 illustrates the transformations which apply to the rotations at any node  $i$  lying in the plane on reflection about the plane. The '\*' superscript indicates a nodal rotation after reflection about the plane while a rotation before reflection has no superscript. In figure 4.7, a local  $x$ -,  $y$ - and  $z$ -axes system is set up such that the  $x$ -axis is normal to the reflection plane



while the  $y$ - and  $z$ -axes lie within the plane. At any node  $i$ , the rotation about the local  $x$ -axis should remain the same before and after reflections about the plane (ie.  $\theta_{xi} = \theta_{xi}^*$ ). On the other hand, the rotations about the local  $y$ -axis before and after reflections should be symmetrical about the plane (ie.  $\theta_{yi} = -\theta_{yi}^*$ ). Similarly, the rotations about the local  $z$ -axis before and after reflections should be equal but in opposite senses (ie.  $\theta_{zi} = -\theta_{zi}^*$ ). The above transformations on the rotations at node  $i$  on passing through the reflection plane can be summarised as follows

$$\begin{Bmatrix} \theta_{xi} \\ \theta_{yi} \\ \theta_{zi} \end{Bmatrix} \Rightarrow \begin{Bmatrix} \theta_{xi}^* \\ -\theta_{yi}^* \\ -\theta_{zi}^* \end{Bmatrix}. \quad (4.6.1)$$

Next, consider any node  $j$  in space, and

$$\{ \theta_j \}' = [T] \{ \theta_j \} \quad (4.6.2)$$

in which  $\{ \theta_j \}'$  are the rotations at node  $j$  in the global axes system,  $\{ \theta_j \}$  are the components of the rotations in the local axes system of the reflection plane, and  $[T]$  is the transformation matrix between the global and local axes systems. It follows from equation (4.6.1) that

$$\{ \theta_j \}^* = \begin{bmatrix} 1 & 0 & 0 \\ 0 & -1 & 0 \\ 0 & 0 & -1 \end{bmatrix} \{ \theta_j \} \quad (4.6.3)$$

in which  $\{ \theta_j \}^*$  are the resulting rotations on passing  $\{ \theta_j \}$  through the reflection plane. The  $\{ \theta_j \}^*$  rotations are then transformed back to their components in the global axes system, ie.

$$\{ \theta_j \}^R = [T]^T \{ \theta_j \}^* \quad (4.6.4)$$

in which  $\{ \theta_j \}^R$  are the global rotations at node  $j$  after reflection about the plane. Hence, from equations (4.6.2), (4.6.3) and (4.6.4),

$$\{ \theta_j \}^R = [T_R] \{ \theta_j \}' \quad (4.6.5)$$

$$\text{in which } [T_R] = [T]^T \begin{bmatrix} 1 & 0 & 0 \\ 0 & -1 & 0 \\ 0 & 0 & -1 \end{bmatrix} [T]. \quad (4.6.6)$$

Equation (4.6.5) is used to transform the rotations at node  $j$  when reflected about a plane. This seems an efficient and elegant way of accomplishing such

a task. The remaining nodal rotations in the structure can similarly be operated on using equation (4.6.5).

Additional node coordinates and beam elements are also generated on reflection about the plane, and the mechanics involved are quite straightforward.

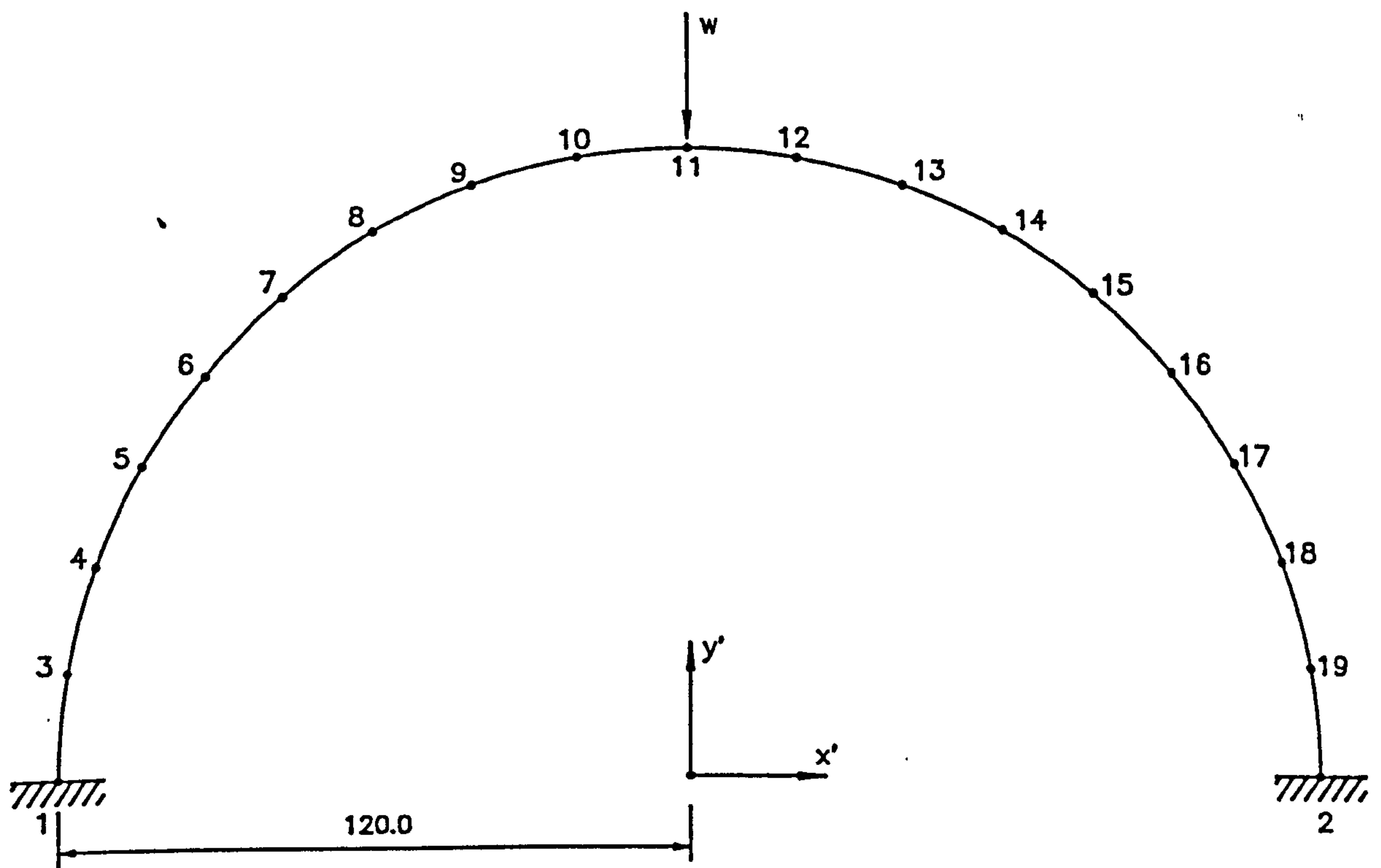
#### 4.7 Numerical results and comparisons

The beam elements formulated as described in this chapter, have been incorporated into a module as part of an interactive computer-aided design system for tension structures which will be discussed in chapter 7. A validation exercise was carried out to ensure that the module did not produce unexpected results. Furthermore, the user interface was checked for its effectiveness and that it was performing as desired. For the above purposes, the module was applied to the solution of two test problems and the results obtained are compared with published solutions.

Firstly, the module was used to analyse the semi-circular arch problem shown in figure 4.8. The result of load ( $w$ ) versus vertical displacement of node 11 given by the module is compared in figure 4.9 with that obtained by Wakefield [133], and the two sets of results agree closely.

In addition, the module was used to analyse the highly non-linear problem of an inclined portal framework subjected to asymmetric loading shown in figure 4.10. The results of load ( $w$ ) versus translational  $x$ -,  $y$ - and  $z$ -displacements of node 12 given by the module are compared in figure 4.11 with those obtained by Wakefield [133], and there is good agreement between the two sets of results.

Furthermore, the user interface developed for the module is highly interactive and versatile, and seems to behave as expected.



$$EA = 3.0 \times 10^7, \quad GJ = 0.0, \\ EI_{y'} = EI_{z'} = 2.5 \times 10^6.$$

Figure 4.8



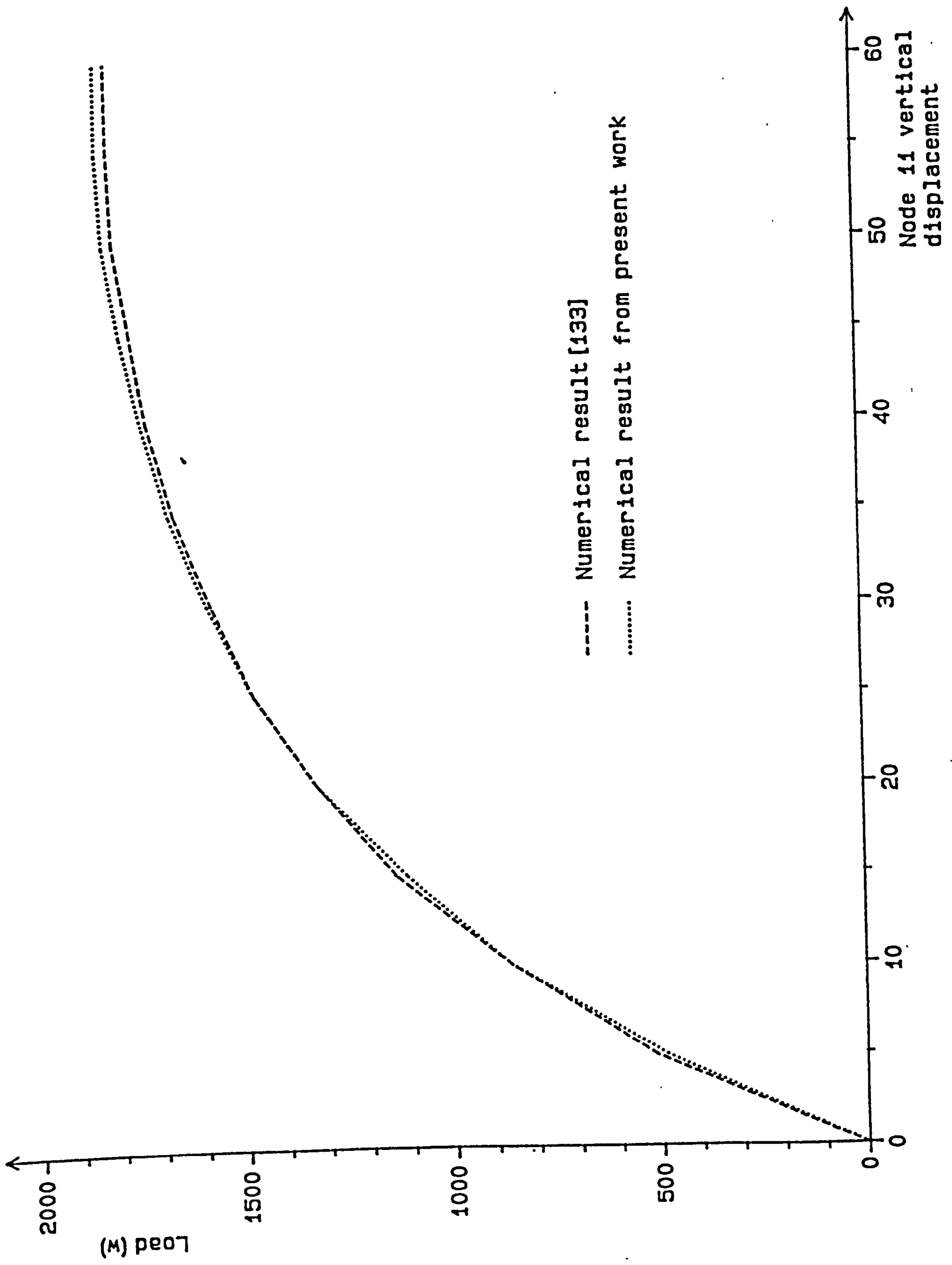


Figure 4.9 Numerical results from non-linear analysis of semi-circular arch

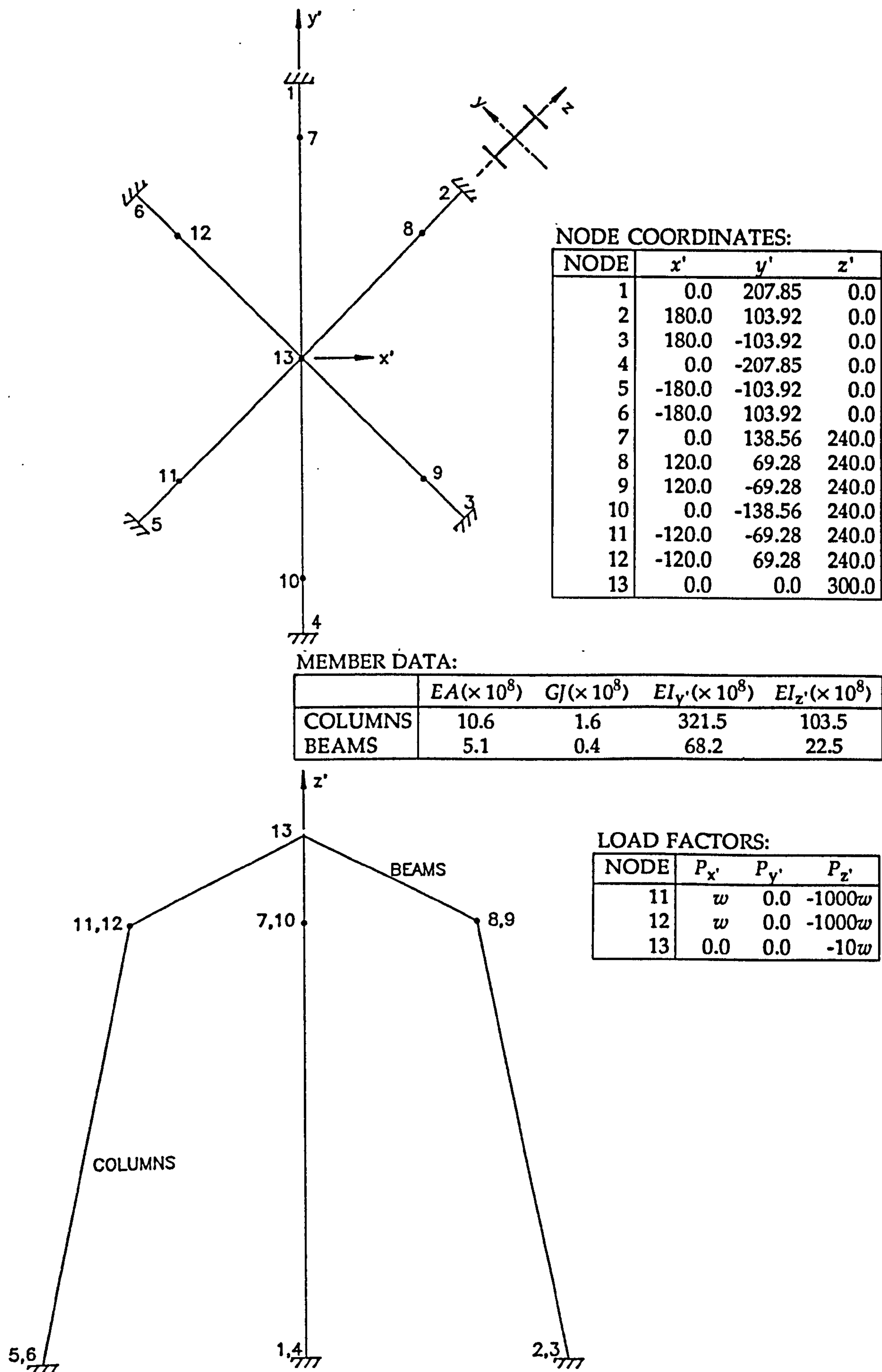


Figure 4.10

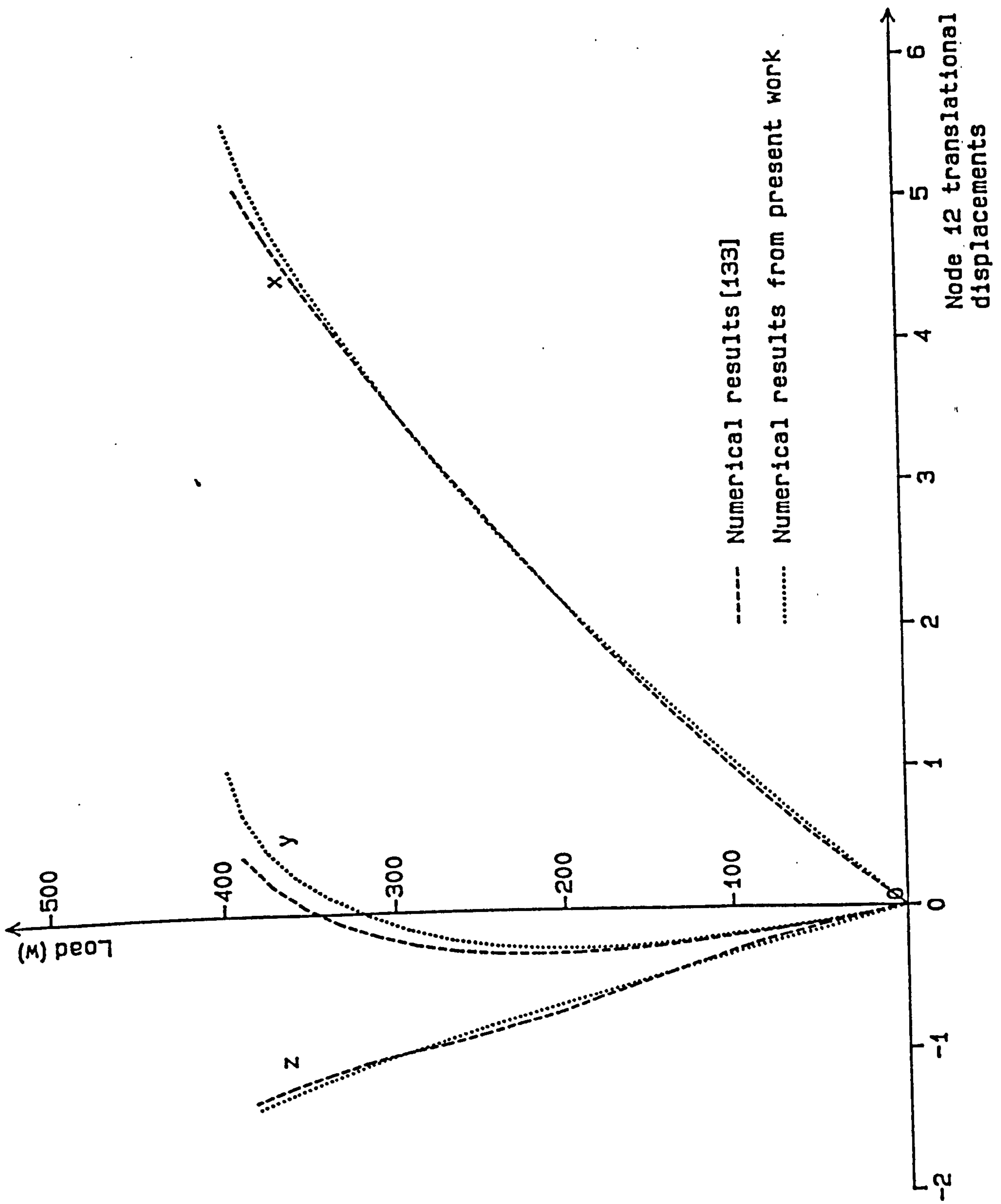


Figure 4.11 Numerical results from non-linear analysis of inclined portal frame



## 4.8 Conclusions

In this chapter, the implementation of the beam elements using the dynamic relaxation scheme is discussed. These elements can be used to model the compression boundaries of tension structures. A compression boundary can prove to be an efficient alternative to tension anchorages as a means of providing support to a large span tension structure. By using beam elements, the flexibility of the compression boundary and thus, the interaction between the boundary and the tension structure can be properly accounted for.

The moment-curvature relations of the beam element are derived on the basis of the natural stiffness relations. Hence, a local axes system is set up for each element which in turn requires first defining the orientation of the principal cross-section of the element by means of the  $\beta_0$  angle. The transformation matrix between the local and global axes system can subsequently be found. This transformation matrix is used to relate the local displacements and forces to their global components. In calculating the rotational displacements about the local  $y$ - and  $z$ -axes, the corresponding sway angles have to be taken into account. The position of the beam element when first defined is required when determining the two sway angles. The beam elements are developed to cope with a few non-linear effects. The  $s$  and  $c$  stability functions are used to account for the non-linear effect due to the influence of axial force on the moment-curvature relations. The non-linear effects caused by element bowing in the local  $x$ - $z$  and  $x$ - $y$  planes, and the influence of axial force on the fixed-end moments due to a uniformly distributed load acting on the element, are also accounted for. As the kinetic damping procedure is used in the dynamic relaxation scheme, these non-linear effects are conveniently updated when an energy peak is detected. The element stiffnesses and node coordinates are also reset at this point to be consistent with the current geometry. Hence, any geometric non-linearity is automatically taken into account. The boundary conditions can be assigned through restraints on any or combination of the three rotations and three translations at each node connected to a beam element. An end release can also be prescribed to impose a pin-ended condition for bending any of the local axes, and which will require simple adjustment of the appropriate rotational displacement. The mass matrices are derived from the principal nodal stiffnesses of the beam element. For each node of the element, a  $(3 \times 3)$  mass matrix is set up for the rotational degrees of freedom separately from the  $(3 \times 3)$  mass matrix for the translational degrees of freedom. This is because the rotational degrees of freedom are treated as decoupled from as well as in a similar manner as the translational degrees of freedom in the dynamic relaxation scheme. The beam elements are also implemented with useful facilities related to plane of symmetry and model reflection, and an efficient means of reflecting nodal rotations about a plane is developed. Only minor modifications to the dynamic relaxation scheme developed in chapter 3 are required in order to accommodate the beam elements, and the resulting scheme provides an efficient means for dealing with tension structures which are bounded by compression boundary supports. The beam elements formulated as described in this chapter, have been incorporated into a module as part of

an interactive computer-aided design system for tension structures which will be discussed in chapter 7. This module was used to solve two test problems and the results obtained agree closely with the published solutions.



## Part II.

### Chapter 5

#### Definition of surface shapes and their differential geometry

##### 5.1 Introduction

A tension structure can assume many different forms a majority of which will exhibit a doubly curved surface. For instance, consider the doubly curved surface of a sphere where any point on the surface has two principal normal curvatures, ie. the maximum and minimum normal curvatures at that point. A description of the principal normal curvatures for a general surface is given in the discussion on differential geometry which follows. It will be shown that the product of the two principal normal curvatures at any point on a surface give the Gaussian curvature at the point. In addition, the principal radius of curvature =  $1/(\text{principal curvature})$ .

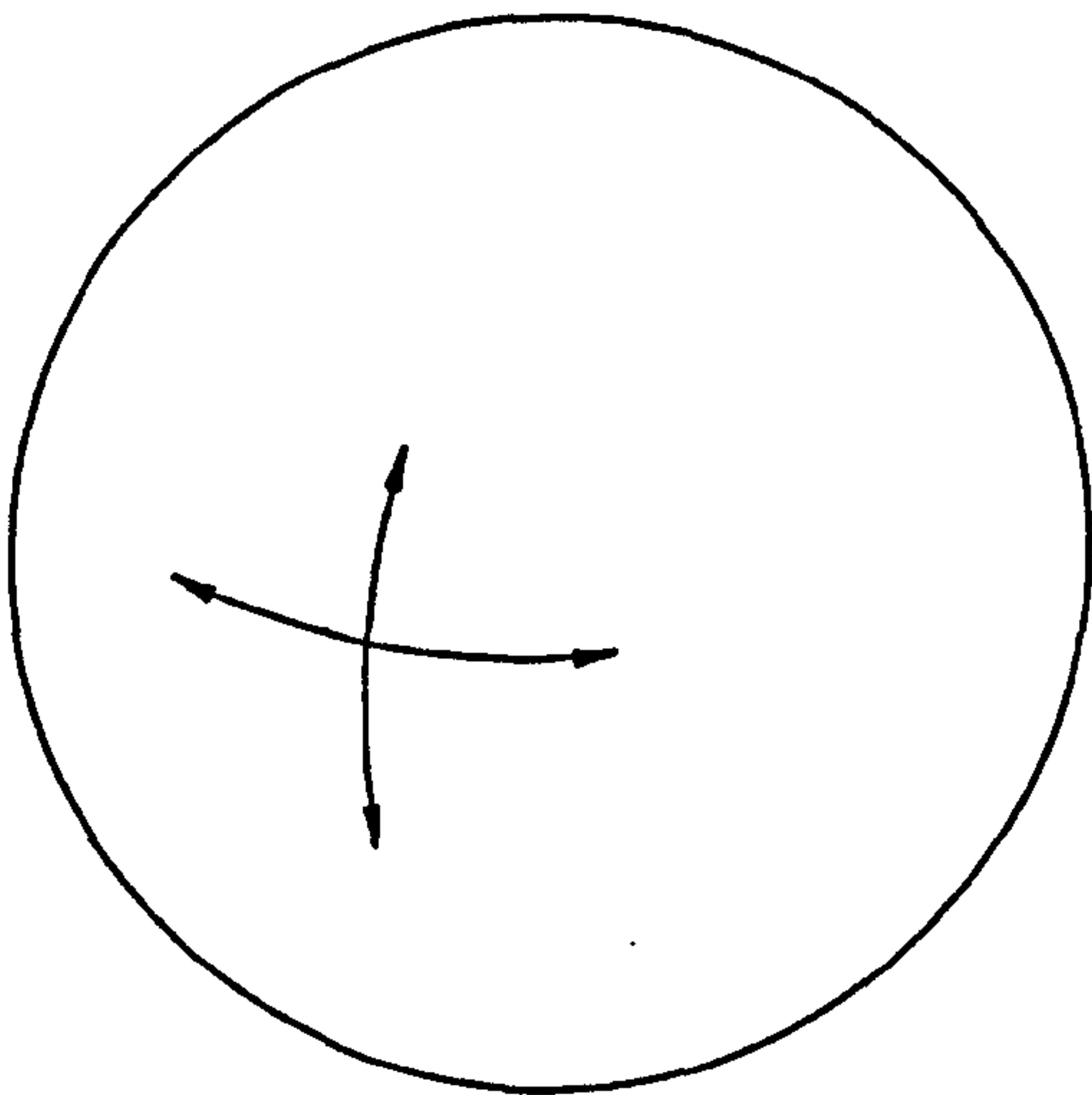


Figure 5.1

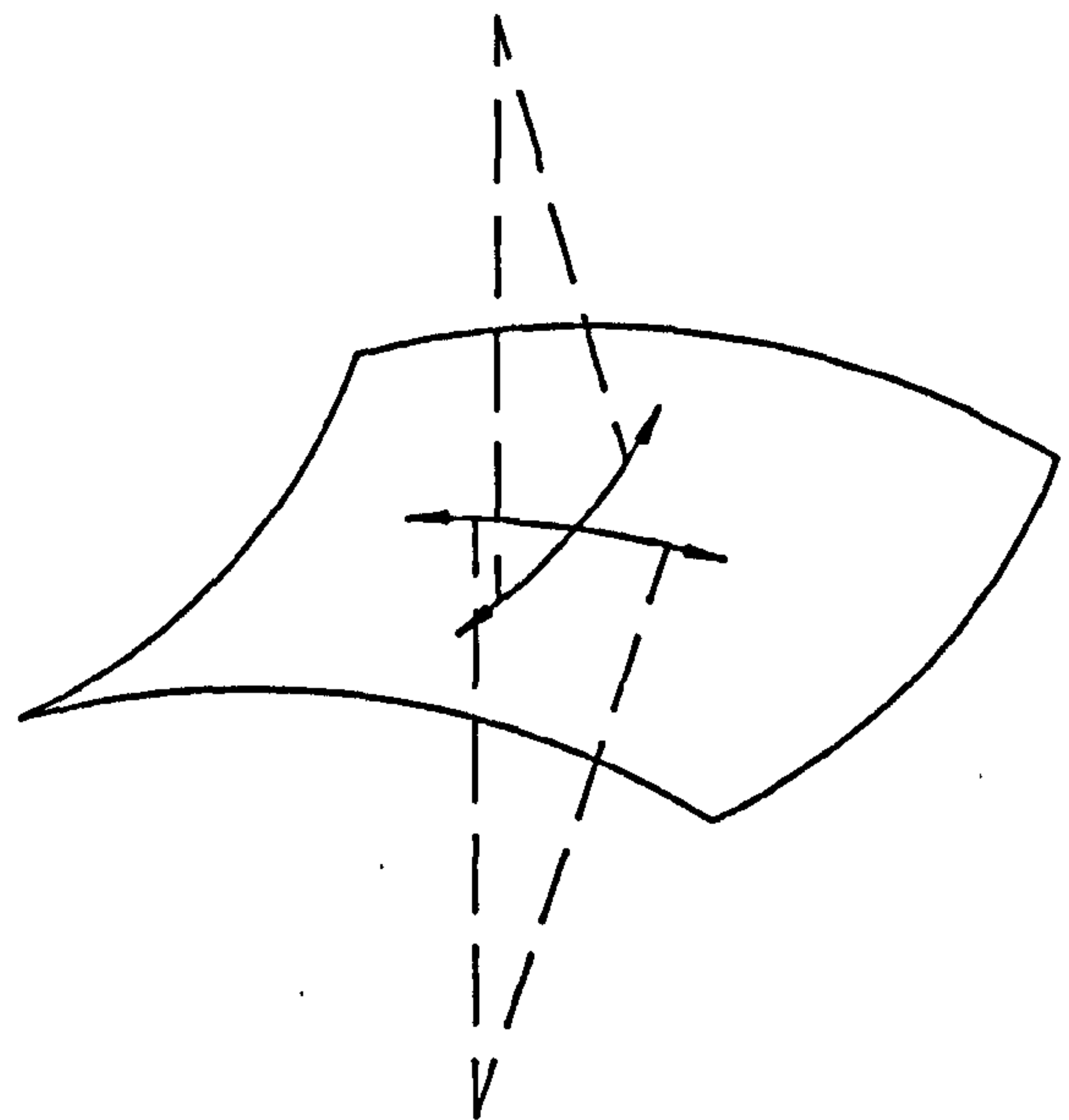


Figure 5.2

A surface with the centres of principal curvatures on the same side of the surface is known as a synclastic surface as shown in figure 5.1. In other words, a synclastic surface has a positive Gaussian curvature. On the other hand, an anticlastic surface is one in which the centres of principal curvature are on opposite sides of the surface as shown in figure 5.2. An anticlastic surface has therefore a negative Gaussian curvature. For a singly curved surface such as that of a cylinder, the Gaussian curvature is zero as although there is a principal curvature in the circumferential direction, the curvature along the axis is zero. Hence, the Gaussian curvature is a useful means of defining a surface shape, and is discussed in further detail later on together with other interesting geometric relationships for a surface in general. This will provide



an insight into the characteristics of the complex surface curvatures often found in a tension structure.

In the design of a tension structure, the task is to achieve a surface geometry which has been defined by say the architect to satisfy certain requirements such as function, aesthetic, space and clearance. In many cases, it is not feasible to simply propose a surface geometry for a tension structure and be sure that the proposed geometry can actually be built. It needs to be established if the proposed geometry can achieve equilibrium and thus, physically attainable. This is essentially the role of the form-finding stage.

In general, a tension structure is flexible both in the plane of the surface and in bending. Hence, the surface changes shape with relatively little change in membrane stresses when subjected to applied loads. This change in shape contributes to an increase in stiffness of the surface known as the initial or geometric stiffness. Most high strength materials are relatively stiff. The required in-plane flexibility is achieved by using two sets of crossing cables in a cable net or two sets of crossing yarns (the warp and fill yarns) in a woven coated fabric. The in-plane strains can then occur by relative rotation of the two sets of cables or yarns. It will be shown later that the crossing cables or yarns undergo relative rotation in order to achieve the Gaussian curvature of the surface. In a coated fabric, the amount of relative rotation of the yarns is more limited and therefore the fabric panels are usually shaped before being sewn, welded or glued together to form the surface.

A tension structure if properly designed should have a surface which will always remain in tension. Due to the high in-plane stiffness but almost negligible flexural stiffness present, a tension structure can only resist tensile membrane stresses. The tensile prestress is chosen to give sufficient stiffness under low loads and avoid loss of tension under most working conditions. It is often acceptable to have localised loss of tension in one direction under extreme conditions leading to wrinkling of the surface without damaging it. The stresses in a surface increase directly with the radius of curvature of the surface. Hence, flat areas in a surface should be avoided in a well designed tension structure. With a lower prestress, the lower will be the membrane stresses, foundation loads and so on, and therefore the cost.

The surface geometry is related to the membrane stresses in the surface by the equilibrium considerations. The derivations of the membrane equilibrium equations for a surface subjected to applied loads are outlined later in this chapter. The unknowns in the solution of the equilibrium equations can either be the stresses or geometry of the surface. At the form-finding stage, the surface is generally pretensioned with a stress distribution. Due to the generally lightweight nature of a tension structure, it is often convenient to ignore the self-weight of the structure. During form-finding, no design loads such as the wind and snow loads are applied to the structure. These loads are considered only in the load analysis stage which follows after the form-finding. For an air-supported structure however, the inflation pressure has to be considered during the form-finding. There are several solution methods



which can be used for the form-finding and a review of these methods is given in chapter 6. In these methods, the solution can be for either the surface geometry, stress distribution or both. The adopted approach in this thesis for the form-finding of a membrane structure is to solve for the surface geometry given a prescribed stress distribution and boundary conditions. The tensile prestresses are applied in the warp and fill directions of a fabric panel. This is to avoid large and unpredictable strains in the bias direction of the fabric panel. In addition, the condition of seam lines of fabric panels following geodesic paths over the surface is imposed during the form-finding. This has the advantage of producing cutting patterns which minimise the wastage of the fabric roll from which they will be fabricated. The proof of this will be given later in this chapter.

The subject of differential geometry is the study of space curves and surfaces, and a good understanding of the various ideas mentioned above requires some knowledge of differential geometry. A discussion of the relevant topics of differential geometry will be given in this chapter. From the discussion, it will become clear how differential geometry provides the basis for certain procedures which are applied in the form-finding and fabrication patterning stages which will be discussed in chapter 6.

The theory of differential geometry has been well established with most of the contributions being made during the last two centuries. The French mathematician, Monge (1746-1818) and the German mathematician, Gauss (1777-1855) can be considered the founders of differential geometry of curves and surfaces. In 1828, Gauss [60] wrote a classic paper on this subject which discussed many of the ideas which will be considered in the following sections. The application of differential geometry to the field of tension structures is largely credited to much work by Williams [134, 135, 138, 139, 140] of the University of Bath.

It is customary to use tensors in the discussion of differential geometry and the tensor notation used here is based upon that as described in Green and Zerna [61].

## 5.2 Base vectors on a surface

Firstly, a convention is adopted for notations used in the discussion to follow. Unless otherwise stated, Latin indices stand for the numbers 1,2,3 and Greek indices indicate the numbers 1,2 only. If an index is repeated twice, terms with the indices are summed over the range of the index. This summation convention applies unless stated otherwise. In addition, letters in bold represent vectors.

The position vector of a point in space is given by

$$\mathbf{R} = \mathbf{r} + \theta^3 \mathbf{a}_3 \quad (5.2.1)$$

where  $r = r(\theta^1, \theta^2)$

$$= x^1(\theta^1, \theta^2)l_1 + x^2(\theta^1, \theta^2)l_2 + x^3(\theta^1, \theta^2)l_3$$

$$= x^k l_k \quad (5.2.2)$$

in which  $x^k$  are cartesian coordinates and  $l_k$  are unit vectors in the directions of the cartesian axes system.

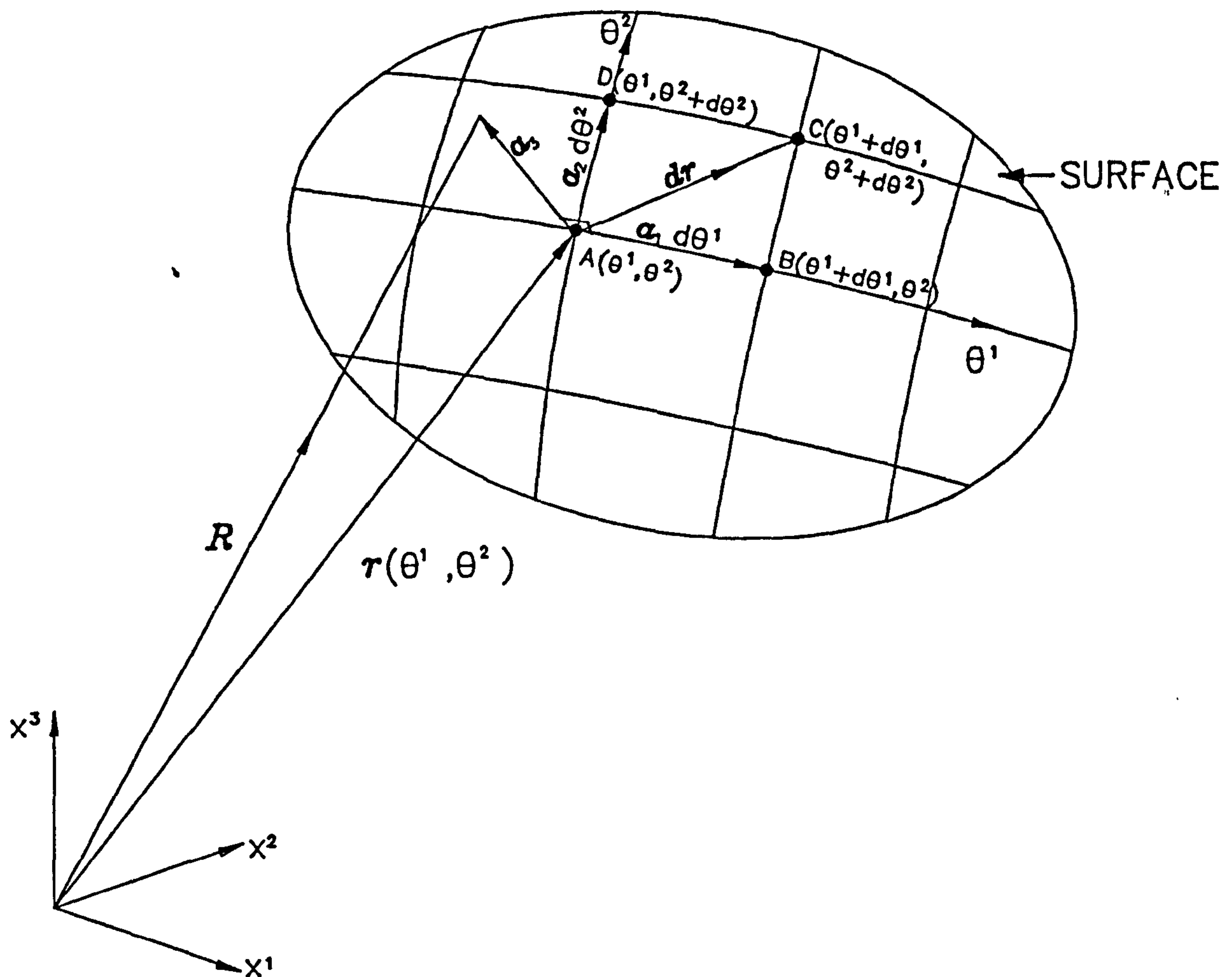


Figure 5.3

Lines  $\theta^1 = \text{constant}$  and  $\theta^2 = \text{constant}$  are coordinate curves on the surface. As such,  $(\theta^1, \theta^2)$  forms a system of curvilinear coordinates on the surface.

Any point on the surface is located by  $r(\theta^1, \theta^2)$ . Subsequently, two sets of base vectors can be defined at the point  $r(\theta^1, \theta^2)$ , ie. the covariant base vectors  $a_k$  and contravariant base vectors  $a^k$ . The covariant base vectors  $a_k$  are defined as follows



$$\mathbf{a}_\alpha = \frac{\partial \mathbf{r}}{\partial \theta^\alpha} = \mathbf{r}_{,\alpha}. \quad (5.2.3)$$

At  $\mathbf{r}(\theta^1, \theta^2)$ ,  $\mathbf{a}_1$  and  $\mathbf{a}_2$  are tangential to the coordinate curves  $\theta^1 = \text{constant}$  and  $\theta^2 = \text{constant}$  respectively, thus lying in the local plane of the surface. Generally,  $\mathbf{a}_1$  and  $\mathbf{a}_2$  are not unit vectors. Furthermore,  $\mathbf{a}_3$  is a unit vector normal to this plane and given by

$$\mathbf{a}_3 = \frac{\mathbf{a}_1 \times \mathbf{a}_2}{|\mathbf{a}_1 \times \mathbf{a}_2|}. \quad (5.2.4)$$

The covariant base vectors  $\mathbf{a}_k$  and contravariant base vectors  $\mathbf{a}^k$  are related as follows

$$\begin{aligned} \mathbf{a}^\alpha \cdot \mathbf{a}_\beta &= \delta_\beta^\alpha = 0 \quad (\alpha \neq \beta) \\ &= 1 \quad (\alpha = \beta, \beta \text{ not summed}) \end{aligned} \quad (5.2.5)$$

in which  $\delta_\beta^\alpha$  are the Kronecker deltas and  $\mathbf{a}^3 = \mathbf{a}_3$ .

Hence,  $\mathbf{a}^1$  and  $\mathbf{a}^2$  lie in the same local plane as the covariant base vectors. In addition,  $\mathbf{a}^1$  and  $\mathbf{a}^2$  are perpendicular to  $\mathbf{a}_2$  and  $\mathbf{a}_1$  respectively.

### 5.3 The metric tensor and the first fundamental form

The components of a tensor sometimes have superscripts and sometimes subscripts but the total number of indices is equal to the order of the tensor. A scalar is a zeroth order tensor and a vector is a first order tensor. Examples of second order tensors are the stress and strain tensors.

On the surface, it is possible to define a set of second order metric tensors  $a_{\alpha\beta}$  (ie. with two indices) as follows

$$a_{\alpha\beta} = \mathbf{a}_\alpha \cdot \mathbf{a}_\beta \quad (5.3.1)$$

and they are symmetric, ie.

$$a_{\alpha\beta} = a_{\beta\alpha}. \quad (5.3.2)$$

Similarly, the contravariant equivalents are given by

$$a^{\alpha\beta} = a^{\beta\alpha} = \mathbf{a}^\alpha \cdot \mathbf{a}^\beta. \quad (5.3.3)$$

It can also be shown that

$$a_{\alpha} = a^{\beta} a_{\beta\alpha} = a_{\alpha\beta} a^{\beta} \quad (5.3.4)$$

$$a^{\alpha} = a^{\alpha\beta} a_{\beta}. \quad (5.3.5)$$

As shown in figure 5.3, let the vector  $\vec{AC}$  (ie. the line element of the surface) be  $dr$ , ie.

$$dr = a_1 d\theta^1 + a_2 d\theta^2 = a_{\alpha} d\theta^{\alpha} \quad (5.3.6)$$

and the length of  $dr$  is given by  $ds$  as follows

$$ds = |dr| = \sqrt{dr \cdot dr}, \quad (5.3.7)$$

$$\begin{aligned} \Rightarrow ds^2 &= dr \cdot dr \\ &= a_{\alpha} d\theta^{\alpha} \cdot a_{\beta} d\theta^{\beta} \\ &= a_{\alpha\beta} d\theta^{\alpha} d\theta^{\beta} \end{aligned} \quad (5.3.8)$$

in which  $d\theta^{\alpha}$  and  $d\theta^{\beta}$  are contravariant surface tensors of order one.

Equation (5.3.8) expresses the first fundamental form of the surface which is concerned with lengths on the surface.

The following relationship holds between  $a^{\beta\lambda}$  and  $a_{\lambda\alpha}$ , ie.

$$\begin{aligned} a^{\beta\lambda} a_{\lambda\alpha} &= \delta_{\alpha}^{\beta} = 0 \quad (\alpha \neq \beta) \\ &= 1 \quad (\alpha = \beta, \beta \text{ not summed}) \end{aligned} \quad (5.3.9)$$

in which  $\delta_{\alpha}^{\beta}$  are the Kronecker deltas for the surface.

Using the above relation, it can be shown that

$$a^{11} = \frac{a_{22}}{a}, \quad a^{12} = a^{21} = -\frac{a_{12}}{a}, \quad a^{22} = \frac{a_{11}}{a} \quad (5.3.10)$$

where  $a = |a_{\alpha\beta}| = a_{11}a_{22} - (a_{12})^2$ . In addition,  $\sqrt{a} d\theta^1 d\theta^2$  defines the area of surface element  $ABCD$  in figure 5.3.

#### 5.4 Associated tensors

The indices of tensors of any order can be lowered or raised by applying certain rules. The tensor is multiplied by  $a_{\alpha\beta}$  or  $a^{\alpha\beta}$  and then summation over the repeated indices. For instance,

$$\begin{aligned} A^{\alpha}_{\cdot\beta} &= A_{\mu\beta} a^{\mu\alpha}, \\ A^{\cdot\alpha}_{\beta} &= A^{\mu\alpha} a_{\mu\beta}, \\ A_{\alpha\beta} &= A^{\mu}_{\cdot\beta} a_{\alpha\mu} = A^{\cdot\mu}_{\alpha} a_{\beta\mu}, \\ A^{\alpha\beta} &= A^{\alpha}_{\cdot\mu} a^{\beta\mu} = A^{\cdot\beta}_{\mu} a^{\alpha\mu}. \end{aligned} \quad (5.4.1)$$

The dot indicates the order of the indices. If  $A_{\alpha\beta}$  is symmetric, ie.  $A_{\alpha\beta} = A_{\beta\alpha}$ , then

$$A^{\alpha}_{\cdot\beta} = A^{\cdot\alpha}_{\beta} = A^{\alpha}_{\beta}, \quad (5.4.2)$$

and the dot being unnecessary. The above rules can be applied to tensors of any order. Tensors obtained in this fashion are termed associated tensors.

Similarly, the surface tensors of order two, ie.  $b_{\alpha\beta}$  and  $b^{\alpha\beta}$  satisfy the above rules. Thus,  $b_{\alpha\beta}$  and  $b^{\alpha\beta}$  are associated surface tensors and they are symmetric as well.

#### 5.5 The coefficients of the second fundamental form

As shown in figure 5.3, due to the small displacement  $d\mathbf{r}$  on the surface, the unit normal will change by  $d\mathbf{a}_3$ . The component of  $d\mathbf{a}_3$  in the direction of  $d\mathbf{r}$  gives the normal curvature in the direction of  $d\mathbf{r}$ . The component of  $d\mathbf{a}_3$  perpendicular to  $d\mathbf{r}$  gives the twist of the surface in the direction of  $d\mathbf{r}$ . Also,  $d\mathbf{a}_3$  lies in the tangent plane of the surface and is given by

$$d\mathbf{a}_3 = \mathbf{a}_{3,\alpha} d\theta^\alpha. \quad (5.5.1)$$

The second fundamental form of the surface is given by the scalar product

$$\begin{aligned} d\mathbf{r} \cdot d\mathbf{a}_3 &= \mathbf{a}_\alpha d\theta^\alpha \cdot d\mathbf{a}_3 = \mathbf{a}_\alpha \cdot d\mathbf{a}_3 d\theta^\alpha \\ &= -b_{\alpha\beta} d\theta^\alpha d\theta^\beta \end{aligned} \quad (5.5.2)$$



where  $b_{\alpha\beta} = b_{\beta\alpha} = -a_{\alpha} \cdot a_{3,\beta} = -a_{\beta} \cdot a_{3,\alpha} = a_{\alpha,\beta} \cdot a_3 = a_{\beta,\alpha} \cdot a_3$  (as  $a_{\alpha} \cdot a_3 = 0$ ). (5.5.3)

Subsequently, the normal curvature in the direction of  $dr$  is given by

$$k_n = -\frac{\text{2nd fundamental form}}{\text{1st fundamental form}}$$

$$= -\frac{dr \cdot da_3}{dr \cdot dr}. \quad (5.5.4)$$

Thus, the normal curvature is only dependent on the direction of  $dr$ , ie. on the ratio  $d\theta^2/d\theta^1$ .

### 5.6 Principal curvatures, Gaussian curvature and mean curvature

At each point on the surface, there are two values of  $d\theta^2/d\theta^1$  which correspond to the maximum and minimum normal curvatures. This condition arises when  $da_3$  is parallel to  $dr$ , ie. there is no twist of the surface in the direction of  $dr$ ;

$$da_3 + kdr = 0,$$

$$\Rightarrow (-b_{\alpha\beta}a^{\alpha} + ka_{\beta})d\theta^{\beta} = 0. \quad (5.6.1)$$

Scalar multiplying by  $a^{\mu}$  and for non-trivial solution, ie.  $d\theta^{\beta} \neq 0$ , the determinant

$$\begin{vmatrix} -b_{\beta}^{\mu} + k\delta_{\beta}^{\mu} \end{vmatrix} = 0. \quad (5.6.2)$$

Solving gives

$$k = \frac{(b_1^1 + b_2^2) \pm \sqrt{A}}{2} \quad (5.6.3)$$

where  $A = b_1^1 b_1^1 - 2b_1^1 b_2^2 + b_2^2 b_2^2 + 4b_2^1 b_1^2$ .

The two values of  $k$  correspond to the minimum and maximum values of normal curvature, ie. the two principal normal curvatures at a point on the surface. On substitution into equation (5.6.1), each  $k$  results in a ratio of  $d\theta^2/d\theta^1$  which defines a principal direction on the surface. The resulting two principal directions are orthogonal to each other. If the two values of  $k$  are

the same at a point, then all directions at that point are principal directions. Lines on the surface which follow the principal directions are called lines of curvature. Furthermore, the product of the two principal normal curvatures give the Gaussian curvature  $K$  at the point, ie.

$$\begin{aligned}
 K &= k_{(1)}k_{(2)} \\
 &= b_1^1 b_2^2 - b_2^1 b_1^2 = \frac{1}{2}(b_\alpha^\alpha b_\beta^\beta - b_\alpha^\beta b_\beta^\alpha) \\
 &= \frac{b_{11}b_{22} - (b_{12})^2}{a_{11}a_{22} - (a_{12})^2}
 \end{aligned} \tag{5.6.4}$$

$$\text{Also, } R_{(1)} = \frac{1}{k_{(1)}}, \quad R_{(2)} = \frac{1}{k_{(2)}} \tag{5.6.5}$$

where  $R_{(1)}, R_{(2)}$  are the principal radii of curvatures.

$$\begin{aligned}
 \text{In addition, } H &= \frac{k_{(1)} + k_{(2)}}{2} \\
 &= \frac{b_1^1}{2} + \frac{b_2^2}{2} = \frac{b_\alpha^\alpha}{2} \\
 &= \frac{a_{11}b_{22} - 2a_{12}b_{12} + a_{22}b_{11}}{2(a_{11}b_{22} - (a_{12})^2)}
 \end{aligned} \tag{5.6.6}$$

in which  $H$ , the mean curvature is the mean of the two principal curvatures. A surface with  $H = 0$  is known as a minimal surface. The surfaces of a sphere and a cylinder are examples of surfaces with constant mean curvature.

## 5.7 Spherical image (see figure 5.4)

By applying the rule of parallel normals, points on a general surface can be mapped to points on a sphere of unit radius. The corresponding points on the sphere form the spherical image. A curve on a surface and its spherical image both have the same normal for all points along the curve. As such, all points on a planar surface map to a spherical image of a single point.

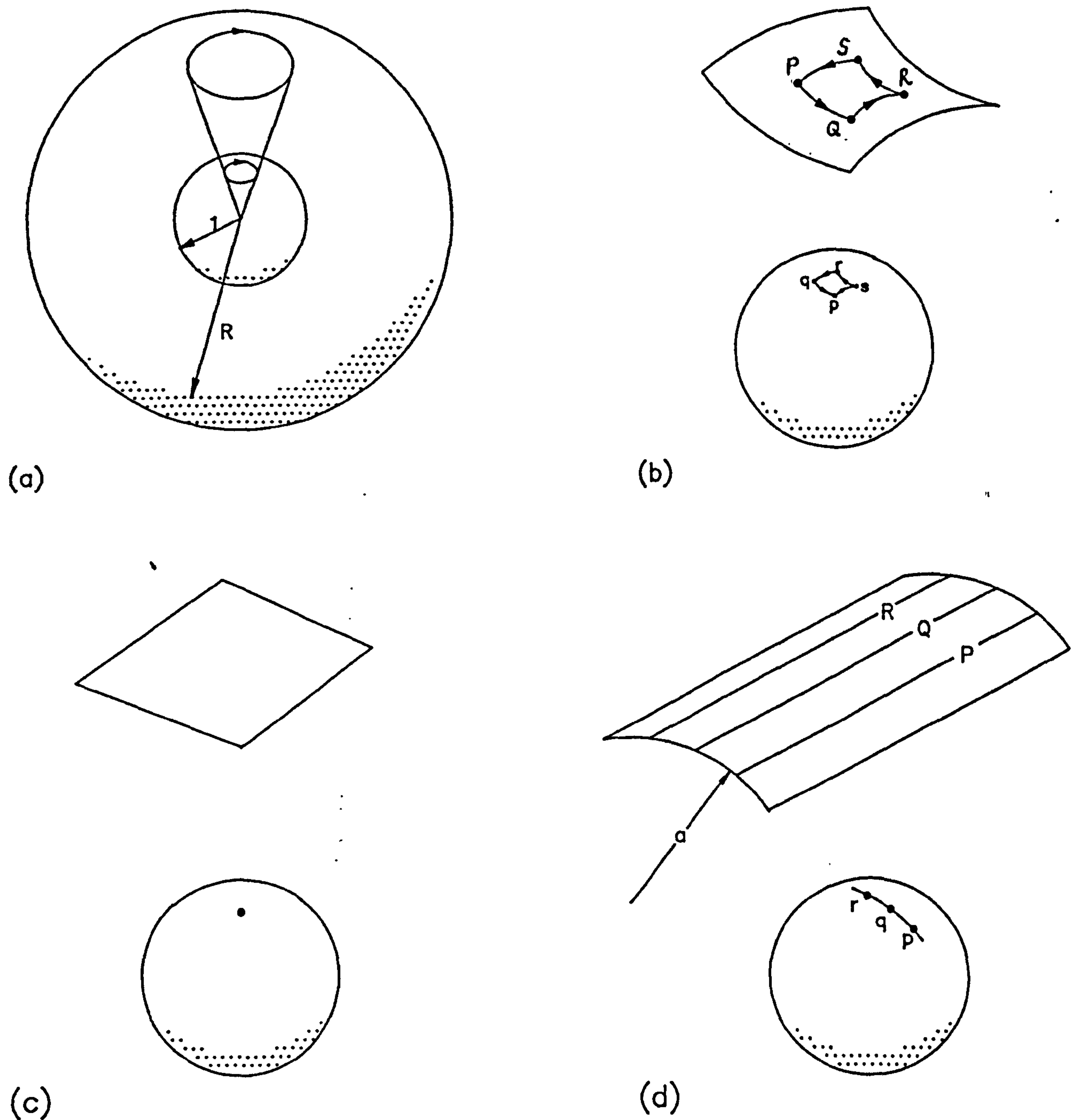


Figure 5.4

Using the idea of spherical image, Gauss derived the following formula for the Gaussian curvature, ie.

$$\text{Gaussian curvature} = \frac{\text{area of spherical image}}{\text{area of region of surface}} \quad (5.7.1)$$

As mentioned earlier, an elemental area of the general surface is given by  $dA = (a_{11}a_{22} - (a_{12})^2)^{1/2} d\theta^1 d\theta^2$ . For the corresponding area of the spherical image, substitute  $a_{\alpha\beta}$  with



$$a_{3,\alpha} a_{3,\beta} = a^{\mu\eta} b_{\mu\alpha} b_{\eta\beta} = a_{\mu\eta} b_{\alpha}^{\mu} b_{\beta}^{\eta} \quad (5.7.2)$$

in the expression for  $dA$ . This leads to equation (5.7.1).

### 5.8 Faceted surface (see figure 5.5)

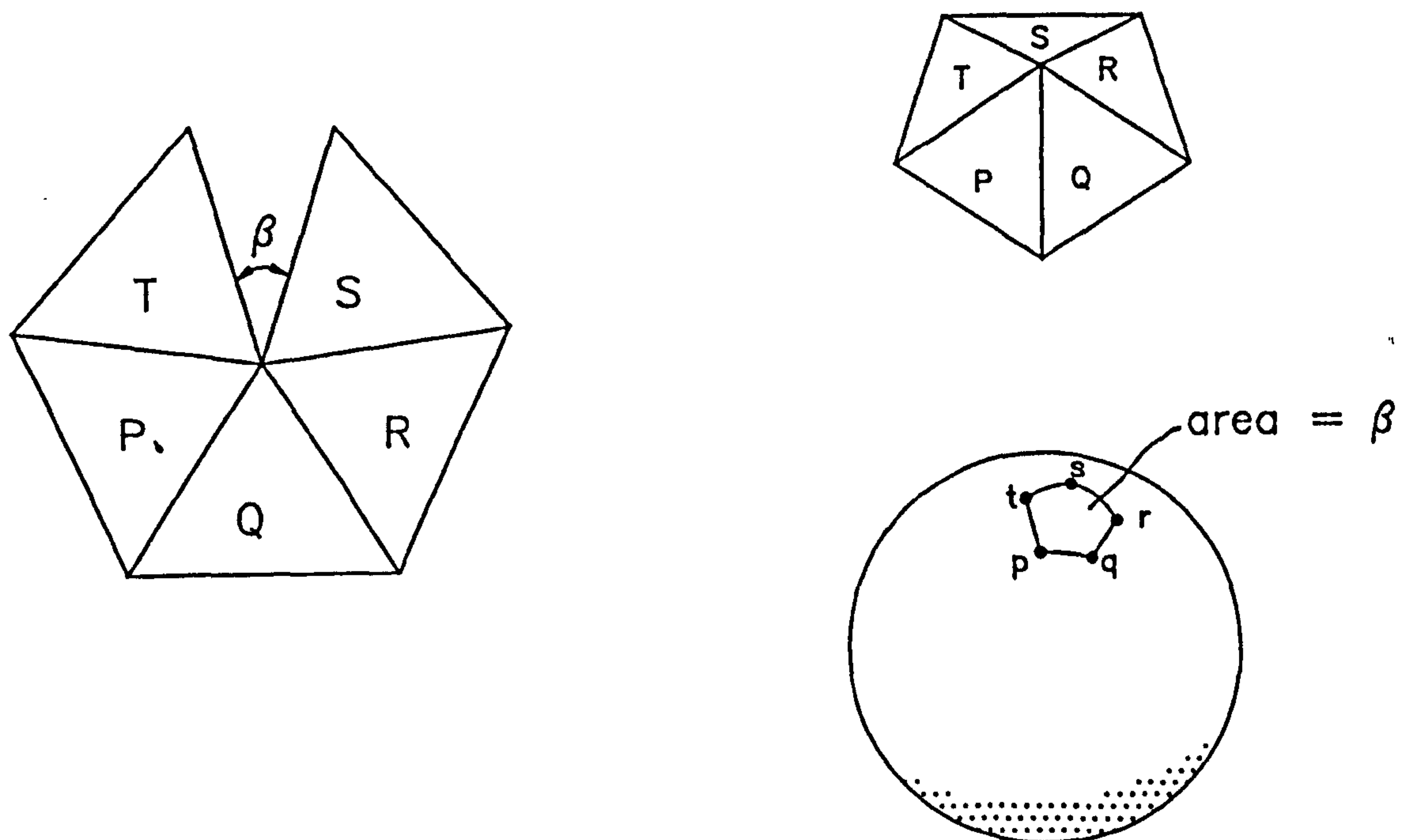


Figure 5.5

In a numerical solution, the surface will be represented by planar triangular elements. In other words, all over the surface are planar faces or facets joined together at nodes/vertices. Subsequently, an expression for Gaussian curvature relevant to this faceted surface representation is useful. It can then be shown that the area of spherical image is equal to the solid angle of embrace which in turn equals the angular defect at the vertex. The angular defect at a vertex is taken as  $(2\pi - \text{sum of interior angles of faces meeting at the vertex})$ . Hence,

$$\text{Gaussian curvature} = \frac{\text{angular defect at a vertex}}{\text{area associated with the vertex}} \quad (5.8.1)$$

in which the area associated with the vertex  $= \frac{1}{3}(\text{sum of areas of triangles meeting at the vertex})$ . As a result, it can be seen that the effects of surface curvature and thus, Gaussian curvature are concentrated at nodes on the surface.

## 5.9 The Gauss equations and the Christoffel symbols

The Gauss equations are given by

$$a_{\alpha'\beta} = \Gamma_{\alpha\beta}^{\mu} a_{\mu} + b_{\alpha\beta} a_3 \quad (5.9.1)$$

where  $\Gamma_{\alpha\beta}^{\mu}$  are called the Christoffel symbols of the second kind.

Also,  $\Gamma_{\alpha\beta}^{\mu} = \Gamma_{\beta\alpha}^{\mu}$ . (5.9.2)

In general, the Christoffel symbols are not components of a tensor. They do not follow the transformation rule for tensors under a change of surface coordinates. Scalar multiplying equation (5.9.1) by  $a^{\eta}$  leads to

$$\begin{aligned} \Gamma_{\alpha\beta}^{\eta} &= a^{\eta} \cdot a_{\alpha'\beta} \\ &= a^{\mu\eta} a_{\mu} \cdot a_{\alpha'\beta} \\ &= a^{\mu\eta} \Gamma_{\alpha\beta\mu} \end{aligned} \quad (5.9.3)$$

where  $\Gamma_{\alpha\beta\mu}$  are the Christoffel symbols of the first kind and

$$\Gamma_{\alpha\beta\mu} = a_{\mu} \cdot a_{\alpha'\beta} = \frac{1}{2} (a_{\mu\beta',\alpha} + a_{\mu\alpha',\beta} - a_{\alpha\beta',\mu}). \quad (5.9.4)$$

## 5.10 The Gauss' Theorem and the Codazzi equations

The coefficients of the first and second fundamental forms, ie.  $a_{\alpha\beta}$  and  $b_{\lambda\rho}$  respectively are required to satisfy further equations. These equations are the Gauss-Codazzi equations.

Using the Gauss equations (equation (5.9.1)), it can be shown that

$$\begin{aligned} K &= \frac{b_{11}b_{22} - (b_{12})^2}{a_{11}a_{22} - (a_{12})^2} \\ &= \frac{[a_{12,12} - \frac{1}{2}(a_{11,22} + a_{22,11}) - \Gamma_{11}^{\lambda} \Gamma_{22}^{\rho} a_{\lambda\rho} + \Gamma_{12}^{\lambda} \Gamma_{12}^{\rho} a_{\lambda\rho}]}{[a_{11}a_{22} - (a_{12})^2]}. \end{aligned} \quad (5.10.1)$$

It is noted from equations (5.9.3) and (5.9.4) that  $\Gamma_{\alpha\beta}^{\lambda}$  can be expressed in terms of the metric tensor and its derivatives only. Therefore, equation (5.10.1) proves that the Gaussian curvature can be expressed in terms of the metric tensor and its derivatives only. Equation (5.10.1) represents the Gauss' theorem (or Gauss' theroma egregium) which shows that the Gaussian curvature of a surface is a bending invariant. Note that there is also a completely separate Gauss' integral theorem. If a surface is bent but not stretched, shrunk or torn, the Gaussian curvature at each point on the surface is unchanged. This bending leaves the distance between two points on the surface, measured along a curve on the surface, unchanged and the angle between two tangent directions at a point remains constant. Deformation of this kind is termed inextensional deformation. In the case of a finite element surface representation, inextensional deformation implies no change in the side lengths and thus, internal angles of the triangular elements. Generally, for a complete simply-connected surface, an inextensional bending deformation cannot take place without cutting out a portion of the surface.

In the Gauss equations (equation (5.9.1)), with  $\beta=1$  and differentiating with respect to  $\theta^2$  should be equivalent to setting  $\beta=2$  and differentiating with respect to  $\theta^1$ . This is due to the order of partial differentiation being immaterial. Scalar multiplying by  $a_3$  then leads to the following equations

$$\Gamma_{\alpha 1}^{\lambda} b_{\lambda 2} + b_{\alpha 1,2} = \Gamma_{\alpha 2}^{\lambda} b_{\lambda 1} + b_{\alpha 2,1}, \quad (5.10.2)$$

$$b_{\alpha 1,2} - b_{\alpha 2,1} = \Gamma_{\alpha 2}^{\lambda} b_{\lambda 1} - \Gamma_{\alpha 1}^{\lambda} b_{\lambda 2}. \quad (5.10.3)$$

$$\text{For } \alpha=1, \quad b_{11,2} - b_{12,1} = \Gamma_{12}^1 b_{11} + \Gamma_{12}^2 b_{21} - \Gamma_{11}^1 b_{12} - \Gamma_{11}^2 b_{22}. \quad (5.10.4)$$

$$\text{For } \alpha=2, \quad b_{21,2} - b_{22,1} = \Gamma_{22}^1 b_{11} + \Gamma_{22}^2 b_{21} - \Gamma_{21}^1 b_{12} - \Gamma_{21}^2 b_{22}. \quad (5.10.5)$$

Letting  $\theta^2 \equiv v$ ,  $\theta^1 \equiv u$ ,  $b_{11} \equiv e$ ,  $b_{12} \equiv b_{21} \equiv f$ ,  $b_{22} \equiv g$ ,

equation (5.10.4) becomes

$$\frac{\partial e}{\partial v} - \frac{\partial f}{\partial u} = e\Gamma_{12}^1 + f(\Gamma_{12}^2 - \Gamma_{11}^1) - g\Gamma_{11}^2, \quad (5.10.6)$$

and equation (5.10.5) becomes

$$\frac{\partial f}{\partial v} - \frac{\partial g}{\partial u} = e\Gamma_{22}^1 + f(\Gamma_{22}^2 - \Gamma_{12}^1) - g\Gamma_{12}^2. \quad (5.10.7)$$



Equations (5.10.4) and (5.10.5) are the two Codazzi equations. Using the notation of covariant differentiation as in [61], the Codazzi equations can also be written as

$$b_{\alpha\mu} |_{\beta} = b_{\alpha\mu\beta} - \Gamma_{\alpha\beta}^{\eta} b_{\eta\mu} - \Gamma_{\mu\beta}^{\eta} b_{\alpha\eta}. \quad (5.10.8)$$

From equation (5.10.8), it can be seen that covariant derivatives are tensors. Also, the covariant derivative of the metric tensor is zero. In equation (5.10.8), with  $\mu=1$  and  $\beta=2$ , it can be shown that

$$b_{\alpha 1} |_2 = b_{\alpha 2} |_1 \quad (5.10.9)$$

is equivalent to equation (5.10.2). Equations (5.10.2) or (5.10.9) (for  $\alpha=1$  and  $\alpha=2$ ) are the two Codazzi equations.

### 5.11 Fundamental theorem of surface theory

According to the fundamental theorem of surface theory, if  $a_{\alpha\beta}$  and  $b_{\alpha\beta}$  satisfy the Gauss-Codazzi equations (Gauss theorem and two Codazzi equations) while  $[(a_{11}a_{22} - (a_{12})^2) \neq 0]$ , then a surface with its first and second fundamental forms given by  $a_{\alpha\beta}d\theta^{\alpha}d\theta^{\beta}$  and  $-b_{\alpha\beta}d\theta^{\alpha}d\theta^{\beta}$  respectively is uniquely determined. The Gauss-Codazzi equations are effectively compatibility equations which ensure that the surface 'fits together'. This surface is uniquely determined except for its overall position and orientation in space. In other words, when the position and orientation of  $\mathbf{a}_1$  and  $\mathbf{a}_2$  at a point on the surface are known, the remainder of the surface can then be determined or grown away from that point.

In a numerical solution using the dynamic relaxation method, compatibility conditions are automatically satisfied since the Cartesian coordinates of each node are updated until they conform to the surface geometry of an equilibrium form.

### 5.12 Comments on the Gaussian curvature

The concept of Gaussian curvature as applied to thin shell structures in general of which tension structures are a sub-class is briefly discussed here. A thin shell structure resists applied loads by a combination of 'bending' and 'membrane' actions. On the other hand, tension structures achieve their load-carrying capacity through 'membrane' action alone. Calladine [41] has done much work into the behaviour of thin shell structures. He considers a thin shell conceptually as consisting of two distinct but coincident stretching and bending surfaces. Under loads, bending effects take place in the bending surface while in-plane actions take place in the stretching surface. For

compatibility reason, the two surfaces have to deform equally. This criterion is satisfied if the Gaussian curvature at corresponding points on the two surfaces is the same whether initially or in the deformed state. Consequently, the change in Gaussian curvature of the stretching surface is due to in-plane deformation as indicated in equation (5.7.1). For the bending surface, the change in Gaussian curvature is caused by bending which in turn modify the principal curvatures in equation (5.6.4). This compatibility condition completes the set of governing equations to solve the problem. It can be seen that the Gaussian curvature can be based upon a two-dimensional view of in-plane deformation in the stretching surface as well as a three-dimensional view of flexure in the bending surface.

### 5.13 Geodesic coordinates

In many instances, due to high Gaussian curvature of the surface, it is required to shape the fabric panels in order to account for the surface curvature. Also, it is obviously desirable for each fabric panel to make optimum use of the fabric roll. This is achieved by aligning centre lines of the fabric panels and hence, the seam lines to follow geodesic paths over the surface.

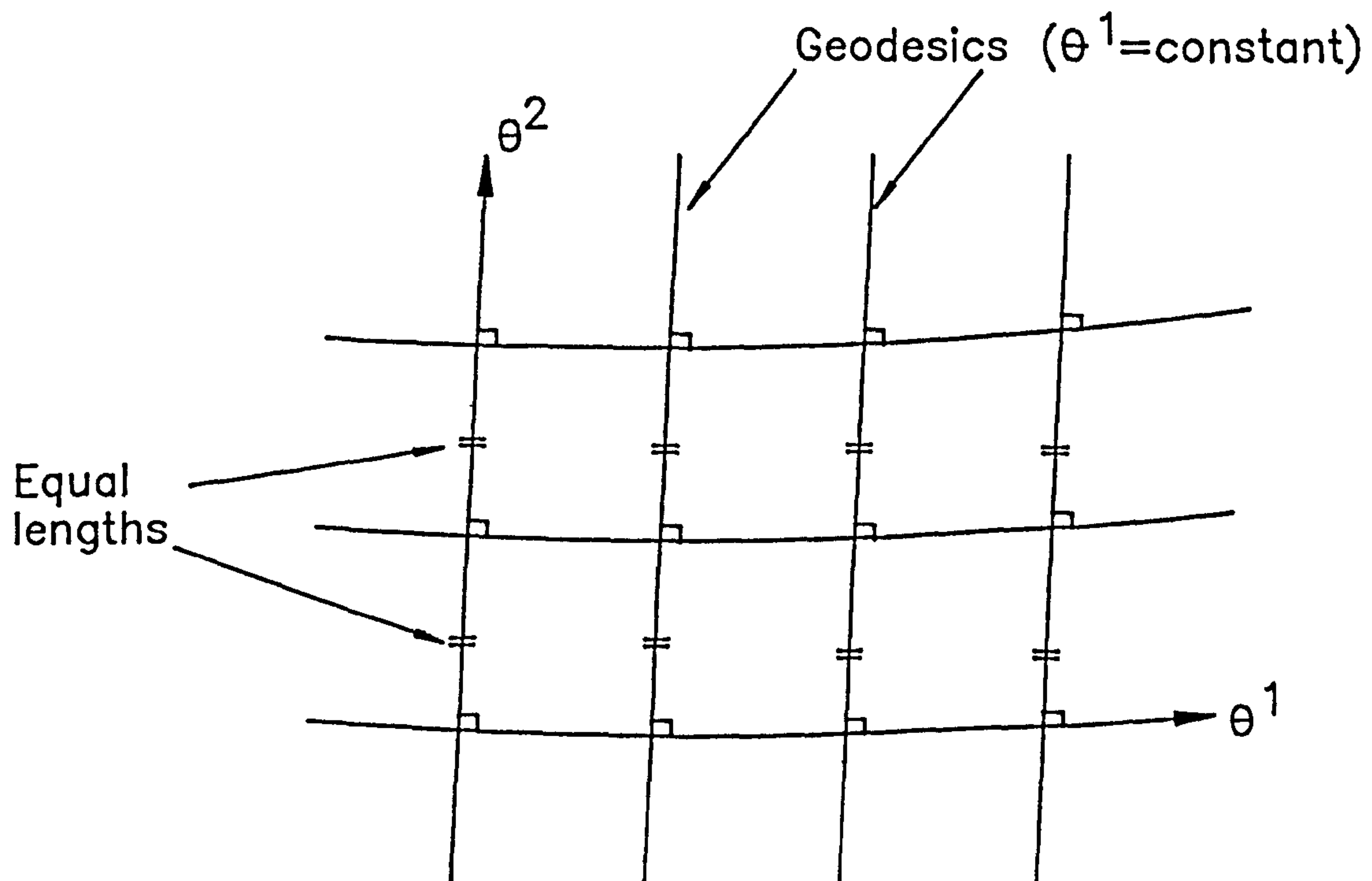


Figure 5.6

A geodesic is a curve on the surface, of zero geodesic curvature (ie. the curvature when looking at the curve along a normal to the surface). There exists a geodesic in every direction through every point on a surface and that a geodesic is uniquely defined by a starting point and a starting direction. If the lines  $\theta^1 = \text{constant}$  are the geodesics, a set of lines  $\theta^2 = \text{constant}$  can be



drawn orthogonal to each geodesic to form a  $\theta^1, \theta^2$  coordinate system on the surface as shown in figure 5.6. For fabric panels which are not too wide, a coordinate system can be set up such that the warp and fill directions of each panel follow the paths of geodesics and their orthogonal trajectories respectively over the surface. The seam lines arranged to coincide with the warp directions become geodesics on the surface. In the prestress state, the principal tensile stresses are applied in the warp and fill directions of the panels. In this way, large and unpredictable deformations in the bias direction of the fabric panel can be avoided. In other words, the condition of applied principal tensile stresses following the sense of the geodesic coordinate system is imposed on the form-finding process. This requirement is not necessary but does offer a convenient and flexible approach of producing different surface forms the choice of which can be enormous. Furthermore, many tension structures have been successfully designed and built in this way. Obviously, other approaches can be used in achieving a desired surface geometry and this is an area where further thoughts or investigations can be pursued.

It follows that for zero geodesic curvature,

$$a_{2,2} \cdot a_1 = a_{12,2} - \frac{1}{2} a_{22,1} = 0. \quad (5.13.1)$$

As  $a_{12} = 0$  and taking the lines  $\theta^1 = \text{constant}$  as geodesics, then

$$a_{22,1} = 0.$$

Hence,  $a_{22}$  is a function of  $\theta^2$  only and can always be chosen as a constant, say 1.

With  $a_{12} = 0, a_{22} = 1, \Gamma_{\alpha\beta}^\eta = a^\eta \cdot a_{\alpha\beta},$

the Gauss theorem (equation (5.10.1)) becomes

$$\begin{aligned} K &= \frac{[a_{12,12} - \frac{1}{2}(a_{11,22} + a_{22,11}) - \Gamma_{11}^\lambda \Gamma_{22}^\rho a_{\lambda\rho} + \Gamma_{12}^\lambda \Gamma_{12}^\rho a_{\lambda\rho}]}{[a_{11}a_{22} - (a_{12})^2]} \\ &= -\frac{1}{2} \frac{a_{11,22}}{a_{11}} + \frac{1}{4} \left( \frac{a_{11,2}}{a_{11}} \right)^2 \\ &= -\frac{1}{\sqrt{a_{11}}} \frac{\partial^2 \sqrt{a_{11}}}{\partial \theta^{22}}. \end{aligned} \quad (5.13.2)$$



As shown in figure 5.7, with the seam lines aligned along geodesics on the surface,  $w$  taken as the distance between two adjacent geodesics (ie.  $= \sqrt{a_{11}}$ ) and  $s$  the distance along the geodesics, and for a reasonably narrow panel, equation (5.13.2) then becomes

$$K = -\frac{1}{w} \frac{d^2 w}{ds^2}. \quad (5.13.3)$$

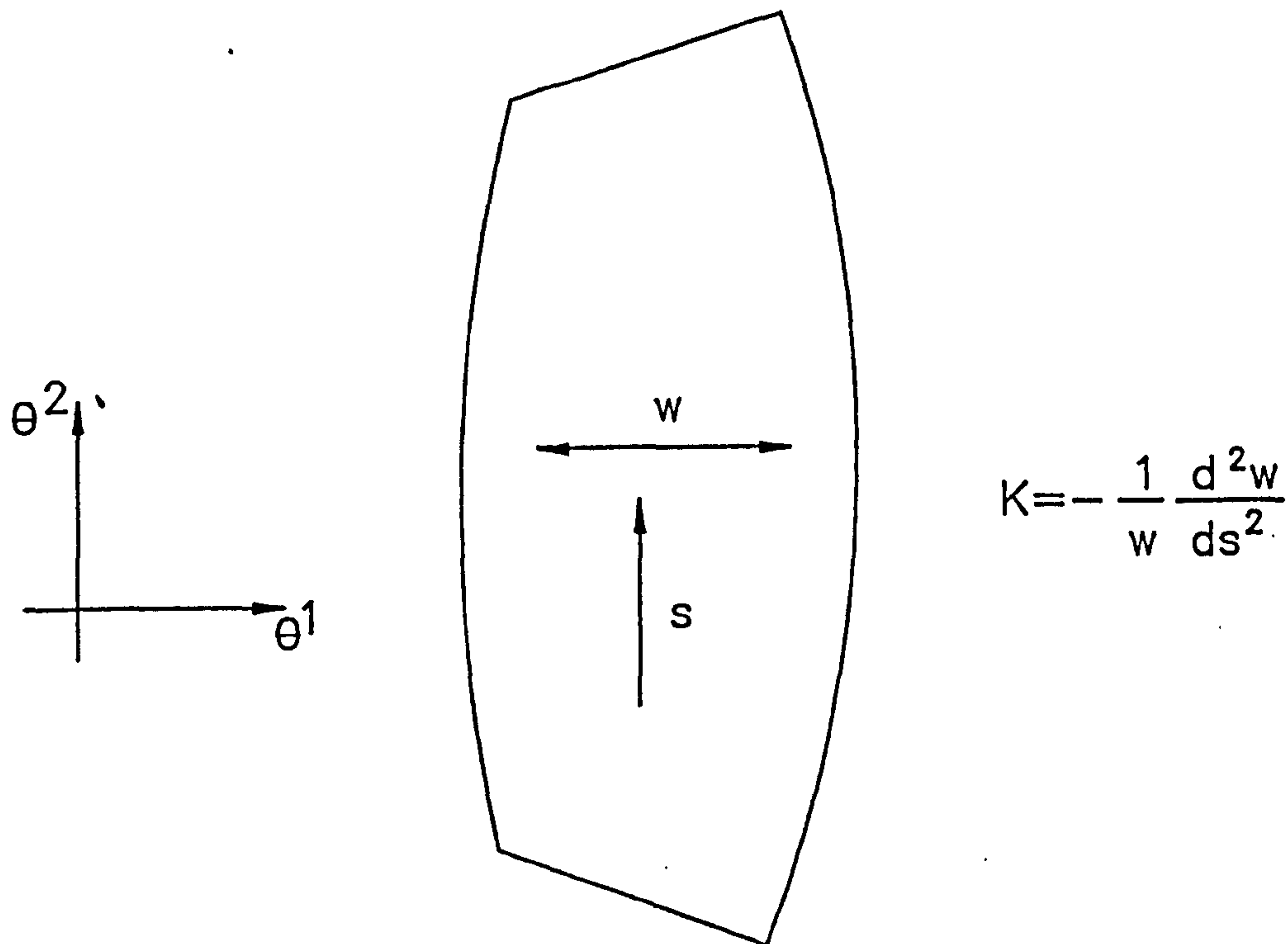


Figure 5.7

Equation (5.13.3) shows the relationship between the width of a fabric panel and the Gaussian curvature at a point on the surface. If  $K > 0$  (ie. a synclastic surface), the fabric panel will be on 'convex' both sides and if  $K < 0$  (ie. an anticlastic surface), then both sides will be 'concave'. For  $K = 0$  (ie. a singly curved surface such as that of a cylinder), the sides can be straight or parallel and the surface is developable. A developable surface can be unfolded onto a plane without affecting its Gaussian curvature.

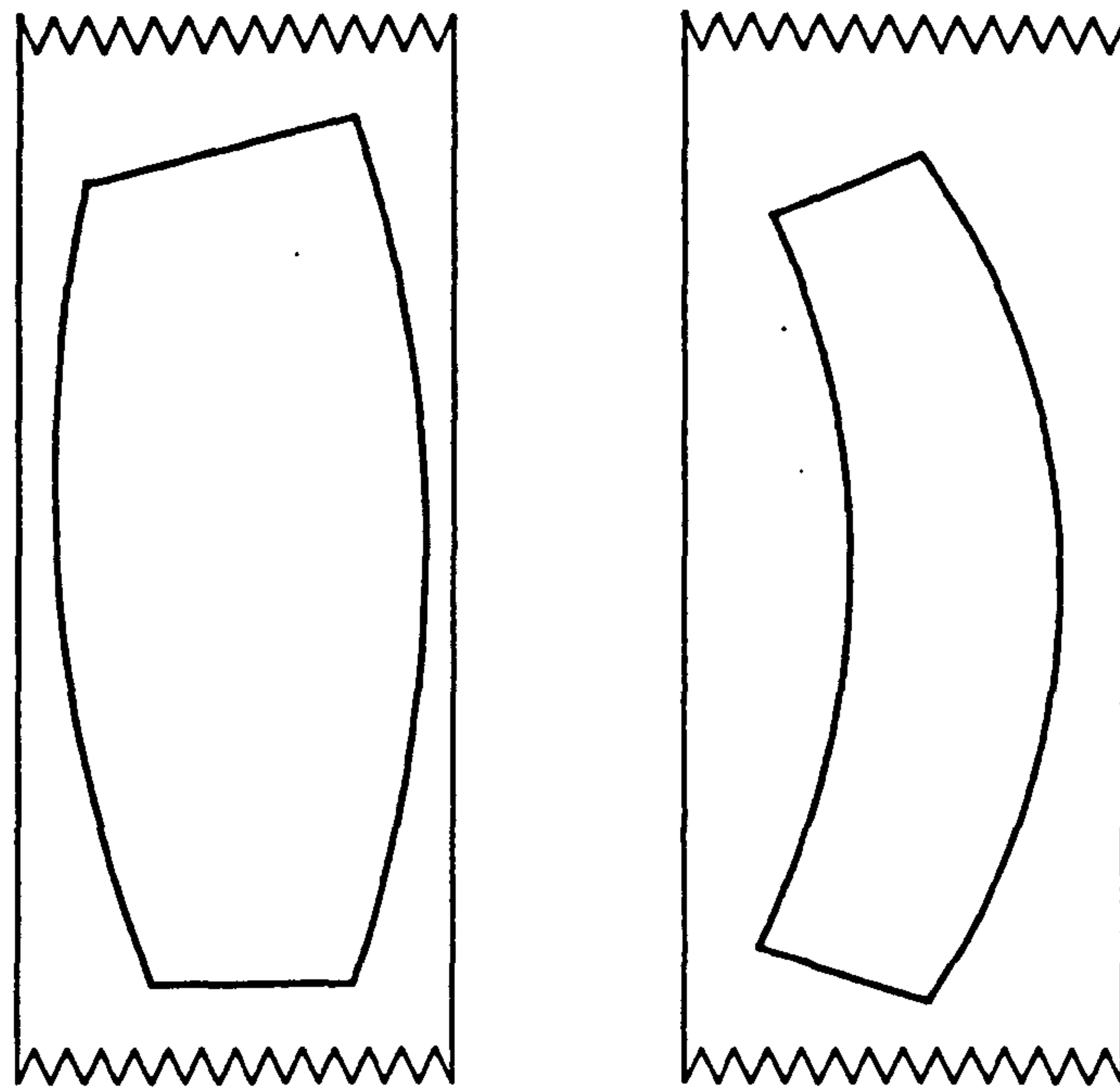


Figure 5.8

#### 5.14 How does Gaussian curvature distort the fabric?

In order to take up the Gaussian curvature of the surface, the fabric panels have to distort in their own plane as well as undergo bending. The fact that the fabric panels have been shaped before being sewn or welded together reduce but do not eliminate the distortions that will take place. In a finite element discretisation, planar triangular elements are used to approximate the surface. Each fabric panel is made of a sequence of triangular elements. Consequently, the actual surface curvature over the interior of a planar triangular element itself is not accounted for. Due to their flexibility, the fabric panels can then distort to give a smooth curvature over the surface. This in-plane flexibility is achieved by having two sets of crossing cables in a cable net or crossing warp and fill yarns in a woven fabric. It will be shown that a fabric panel will distort by angle change between the warp and fill yarns. This relationship between the distortion of a fabric panel and the Gaussian curvature is examined in the following discussion.

Assume a constant mesh coordinate system as shown in figure 5.9 with the warp and fill yarns in the  $\theta^1$  and  $\theta^2$  directions respectively. It is taken that  $a_{11} = a_{22} = 1$ , and therefore

$$\begin{aligned}
 a_{12} &= \mathbf{a}_1 \cdot \mathbf{a}_2 \\
 &= |\mathbf{a}_1| |\mathbf{a}_2| \cos \alpha \\
 &= \cos \alpha.
 \end{aligned}
 \tag{5.14.1}$$

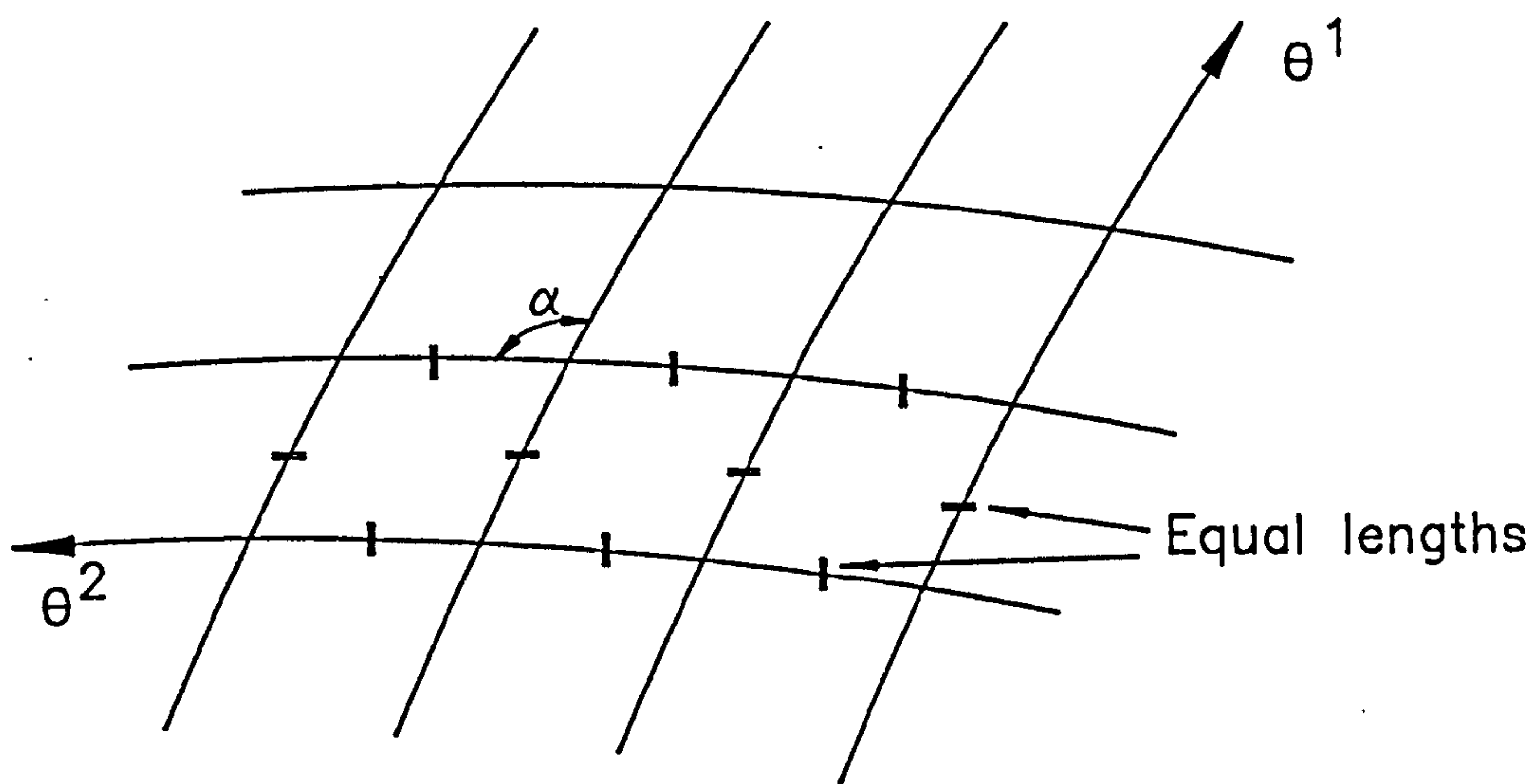


Figure 5.9

From the Gauss equations (equation (5.9.1)),

$$\begin{aligned} \Gamma_{11}^1 &= -\frac{a_{12}a_{12,1}}{1-(a_{12})^2}, & \Gamma_{11}^2 &= \frac{a_{12,1}}{1-(a_{12})^2}, \\ \Gamma_{12}^1 &= \Gamma_{12}^2 = 0, \\ \Gamma_{22}^1 &= \frac{a_{12,2}}{1-(a_{12})^2}, & \Gamma_{22}^2 &= -\frac{a_{12}a_{12,2}}{1-(a_{12})^2}. \end{aligned} \quad (5.14.2)$$

It follows that the Gauss' theorem (equation (5.10.1)) then becomes

$$\begin{aligned} K &= \frac{a_{12,12}(1-(a_{12})^2) + a_{12}a_{12,1}a_{12,2}}{[1-(a_{12})^2]^2} \\ &= -\frac{1}{\sin\alpha} \frac{\partial^2 \alpha}{\partial \theta^1 \partial \theta^2}. \end{aligned} \quad (5.14.3)$$

Hence, relative rotation of the warp and fill yarns has to take place in order to satisfy the Gaussian curvature and contribute to most of the distortion of the fabric panels. In addition, the condition of  $(a_{11} = a_{22})$  corresponds to an equal mesh cable net if the elastic extensions of the cables are neglected. Consequently, an equal mesh net with two sets of orthogonal wires when flat, undergoes a continuous change in angle between the wires in the  $\theta^1$  and  $\theta^2$  directions as given in equation (5.14.3) during erection to achieve the Gaussian curvature of the surface.



### 5.15 Membrane equilibrium equations

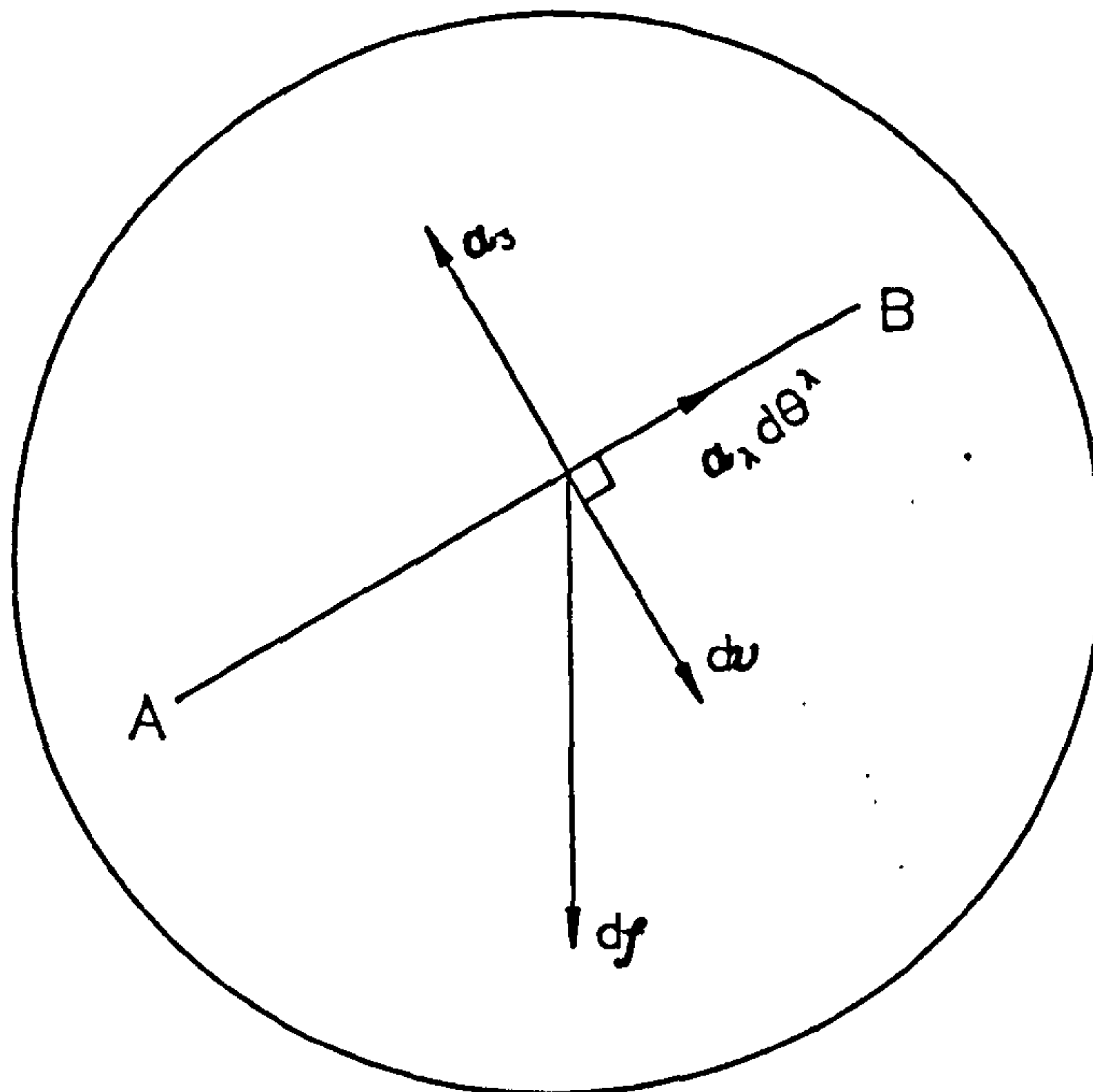


Figure 5.10

First of all, for an imaginary cut in the surface as shown in figure 5.10,  $dv$  denotes a vector in the local plane of the surface perpendicular to the cut. The magnitude of  $dv$  gives the length of the cut. Due to the membrane stresses in the surface, at the cut is a force  $df$  in the local plane of the surface. The bending stiffness is assumed to be zero and as such, there are no shear forces perpendicular to the surface. From figure 5.10,

$$dv = dv^\alpha a_\alpha = dv_\alpha a^\alpha, \quad (5.15.1)$$

$$\begin{aligned} df &= df^\alpha a_\alpha = df_\alpha a^\alpha \\ &= n^{\alpha\beta} dv_\alpha a_\beta \end{aligned} \quad (5.15.2)$$

where  $n^{\alpha\beta}$  (a second order tensor) are the membrane stress resultants.

The vector along  $AB$  in figure 5.10 is  $a_\lambda d\theta^\lambda$  and thus,

$$dv_\alpha a^\alpha = \epsilon_{\alpha\beta} a^\alpha d\theta^\beta \quad (5.15.3)$$

in which the  $\epsilon$  tensors for the surface,  $\epsilon_{\alpha\beta}$  and  $\epsilon^{\alpha\beta}$  are given by

$$\begin{aligned} \epsilon_{12} &= -\epsilon_{21} = \sqrt{a}, \quad \epsilon^{12} = -\epsilon^{21} = \frac{1}{\sqrt{a}}, \\ \epsilon_{11} &= \epsilon_{22} = \epsilon^{11} = \epsilon^{22} = 0. \end{aligned} \quad (5.15.4)$$

Consider an element of surface  $ABCD$  in equilibrium under the action of forces as shown in figure 5.11. The force across  $BC$  is given by  $n^{1\beta}a_\beta\sqrt{a}d\theta^2$  and the force across  $DC$  is given by  $n^{2\beta}a_\beta\sqrt{a}d\theta^1$ . In general,  $n^{\alpha\beta}$  are not equal to the forces per unit width in the membrane since  $a_{11}, a_{12}$  and  $\sqrt{a}$  are not generally equal to 1.

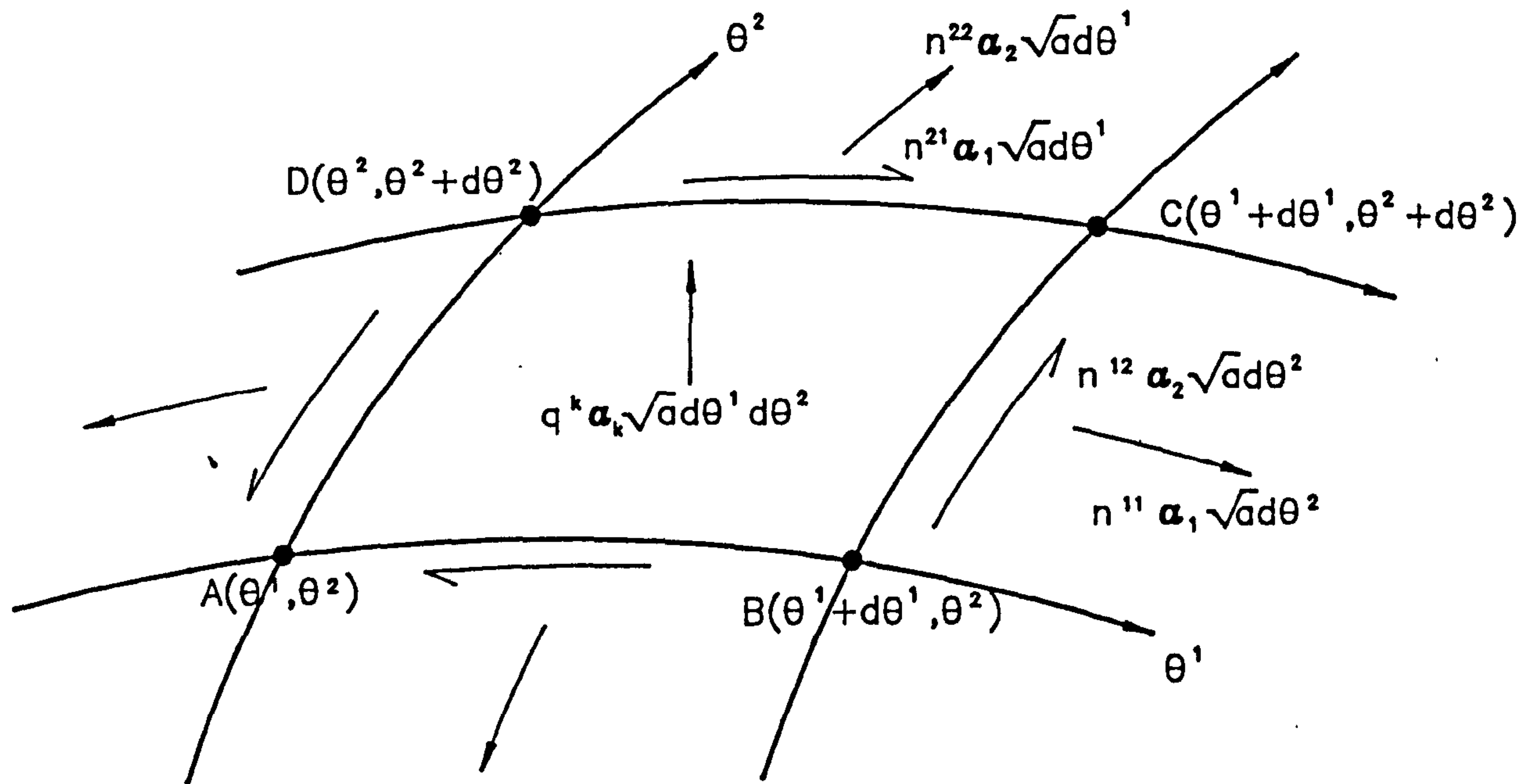


Figure 5.11

In addition,

$$p^k a_k = p^1 a_1 + p^2 a_2 + p^3 a_3 \quad (5.15.5)$$

is the external load including self-weight, any inflation pressure or inertia effects applied to the membrane per unit area. The load applied to  $ABCD$  is then given by

$$p^k a_k \sqrt{a} d\theta^1 d\theta^2 \quad (5.15.6)$$

as the area of  $ABCD$  is  $\sqrt{a} d\theta^1 d\theta^2$ .

By taking moments about the normal to the surface, it can be shown that  $n^{\alpha\beta}$  is symmetric, ie.

$$n^{\alpha\beta} = n^{\beta\alpha}. \quad (5.15.7)$$

The net force crossing  $BC$  and  $AD$  is

$$\frac{\partial}{\partial \theta^1} [n^{1\beta} a_{\beta} \sqrt{a} d\theta^2] d\theta^1 \quad (5.15.8)$$

and that across CD and AB is

$$\frac{\partial}{\partial \theta^2} [n^{2\beta} a_{\beta} \sqrt{a} d\theta^1] d\theta^2. \quad (5.15.9)$$

By adding all the forces acting on the element, the following relationship is obtained, ie.

$$\frac{\partial}{\partial \theta^{\alpha}} [n^{\alpha\beta} a_{\beta} \sqrt{a}] + p^k a_k \sqrt{a} = 0. \quad (5.15.10)$$

Using the Gauss equations (equation (5.9.1)), equation (5.15.10) can then be written as

$$n^{\alpha\beta}_{,\alpha} a_{\beta} + n^{\alpha\beta} \Gamma^{\lambda}_{\alpha\beta} a_{\lambda} + n^{\alpha\beta} b_{\alpha\beta} a_3 + \frac{1}{2} n^{\alpha\beta} a_{\beta} \frac{a_{,\alpha}}{a} + p^k a_k = 0. \quad (5.15.11)$$

These equations are similar to those in [61] except that in [61], the notation of the covariant derivative is used.

Consider the special case of a geodesic coordinate system with

$$a_{12} = 0, \quad a_{22} = 1, \quad a = a_{11}a_{22} - (a_{12})^2 = a_{11},$$

and the principal stresses (warp and fill) in the membrane to be in the directions of the coordinate axes (ie.  $n^{12} = 0$ ). The membrane is subjected to inflation pressure  $p$  and no other loads are applied.

By scalar multiplying the equilibrium equation (ie. equation (5.15.11)) by  $a_1$ ,  $a_2$  and  $a_3$ , the following equations are obtained, ie.

$$\underline{a_1} \Rightarrow (n^{11}a_{11})_{,1} = 0, \quad (5.15.12)$$

$$\underline{a_2} \Rightarrow (\sqrt{a_{11}}n^{22})_{,2} - n^{11}a_{11}(\sqrt{a_{11}})_{,2} = 0, \quad (5.15.13)$$

$$\underline{a_3} \Rightarrow n^{11}b_{11} + n^{22}b_{22} + p = 0. \quad (5.15.14)$$

With equations (5.15.12) and (5.15.13) expressed in terms of the principal membrane stresses in the fabric given by



$$\sigma_{(1)} = n^{11}a_{11}, \quad \sigma_{(2)} = n^{22}a_{22} = n^{22}, \quad (5.15.15)$$

and then on integrating gives

$$\int \frac{\partial \sigma_{(1)}}{\partial \theta^1} d\theta^1 = \sigma_{(1)} = f(\theta^2), \quad (5.15.16)$$

and

$$\begin{aligned} \int \frac{\partial [\sigma_{(2)} \sqrt{a_{11}}]}{\partial \theta^2} d\theta^2 &= \int f(\theta^2) \frac{\partial (\sqrt{a_{11}})}{\partial \theta^2} d\theta^2, \\ \Rightarrow \quad \sigma_{(2)} &= f(\theta^2) - \frac{1}{\sqrt{a_{11}}} \int \sqrt{a_{11}} \frac{df(\theta^2)}{d\theta^2} d\theta^2 + \frac{F(\theta^1)}{\sqrt{a_{11}}} \end{aligned} \quad (5.15.17)$$

Thus, the state of stress in the membrane is defined by the two functions of integration,  $f(\theta^2)$  and  $F(\theta^1)$  which in turn determine the surface of the structure. By setting  $f(\theta^2) = \text{constant}$  and  $F(\theta^1) = 0$ , uniform surface tension such as in a soap film will result. With  $f(\theta^2) = \text{constant}$  and  $F(\theta^1) \neq 0$ , the state of stress is that of a soap film with a set of tensioned threads which will automatically form geodesics on the surface.

The equilibrium equations of the surface subjected to applied loads (ie. equations (5.15.12), (5.15.13) and (5.15.14)) relate the stresses in the surface to its geometry, and the unknowns in these equations can either be the stresses or geometry of the surface. One approach is to determine the stresses given the geometry, applied loads such as internal pressure for air-supported structures and boundary conditions. This approach may be relevant in a situation such as where the solution is for the equilibrium geometry of a principal curvature net. However, the numerical approach is often to define the applied stresses and boundary conditions, and calculate the resulting geometry of the surface.

## 5.16 Form-finding and cutting patterns determination

Form-finding is the derivation of a surface geometry which satisfies the prescribed initial and boundary conditions. At this stage, no loads are applied except for internal pressure in the case of air-supported structures and may be self-weight. Obviously, a form requirement for tension structures is that all principal stresses in the surface should be tensile. A numerical procedure for the simultaneous form-finding and production of cutting patterns can be conveniently set up [134, 135, 138]. First, a finite element mesh is generated over the surface. The initial coordinates of the nodes are immaterial and hence, it is usual to start with a flat mesh. The ends of geodesics or seam lines are defined. A stress distribution based upon choice of the functions  $F(\theta^1)$  and

$f(\theta^2)$  is applied. This leads to principal stresses in the warp and fill directions of fabric yarns which coincide with a geodesic coordinate system. For air-supported structures, the inflation pressure is also specified. A numerical method such as dynamic relaxation can then be used in the solution which needs to satisfy two criteria, ie.

- (1) the seam lines follow geodesic paths,
- (2) at each node, equilibrium in the direction normal to the surface.

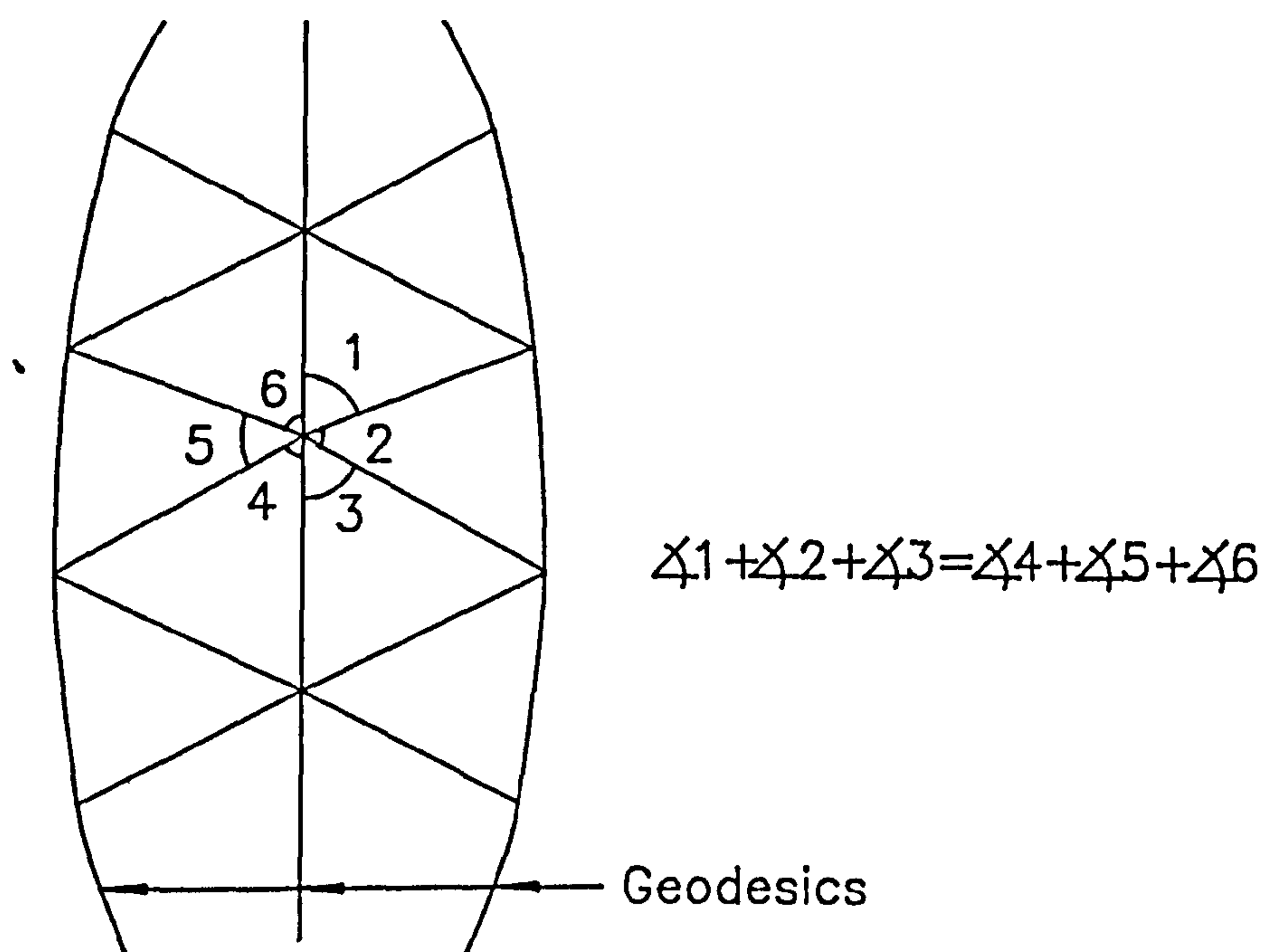


Figure 5.12

As shown above, the in-plane equilibrium of the surface is automatically satisfied by using a stress distribution dependent on the functions,  $F(\theta^1)$  and  $f(\theta^2)$ . In addition, it is desirable for nodes to be evenly spaced along each geodesic to prevent them bunching together. Subsequently, geodesic paths over the surface can be achieved in two ways, ie.

- (1) imposing the geometric condition of (angle 1 + angle 2 + angle 3) = (angle 4 + angle 5 + angle 6) at each node along a seam line as shown in figure 5.12. This implies a straight line in the plane of the surface at the common node which is a valid definition of a geodesic. Also, the distances between nodes along the seam line are set to be equal.
- (2) specifying a constant tension value all along the seam line. A constant tension string will automatically find a shortest path between its starting node and last node, over the surface and thus, define a geodesic. At each node along the seam line, the component of tension normal to the surface



is ignored. In this way, the specified tension makes no contribution to equilibrium in the direction normal to the surface. Consequently, the above mentioned two criteria are thereby satisfied. As a variation, the condition of constant tension coefficient may be imposed. A tension coefficient is the ratio of the constant tension to the length between two adjacent nodes along the seam line. A constant tension coefficient leads to evenly spaced nodes along the seam line.

In the dynamic relaxation analysis, iterations which involve moving nodes to satisfy the above criteria are carried out. Once an equilibrated form which fulfills the criteria is reached, it is a simple operation of taking each panel bound by geodesics and flattening out the folds between adjacent members in the sequence of triangular elements within the panel, to produce the cutting pattern. Furthermore, the maximum allowable width for each cutting pattern is limited by the width of the fabric roll. The control over the maximum width for each cutting pattern is achieved through shuffling the ends of geodesics during the form-finding.

In general, iterations within the form-finding process converge fairly quickly except for large numerical models. Peculiar boundary conditions may also prolong the form-finding. The production of cutting patterns is a quick and direct geometric exercise. However, analysis under applied loads usually takes much longer as both the stresses and geometry of the surface are being solved for at the same time.

The numerical implementation of simultaneous form-finding and determination of cutting patterns on the basis of the dynamic relaxation solution scheme will be discussed in further detail in chapter 6, and its incorporation into an interactive computer-aided design system for membrane structures will be considered in chapter 7.

## 5.17 Conclusions

A proper understanding of form-finding and fabrication of cutting patterns requires some knowledge of differential geometry. This becomes more apparent when the mechanics of form-finding and patterning are discussed in further detail in chapter 6. The various ideas discussed in this chapter such as the Gaussian curvature, geodesics and so on, provide a valuable basis for understanding the geometry and behaviour of surfaces in general. On a broader basis, a knowledge of or familiarity with tensors is also useful for the future research of many classic literatures such as reference [61] where the tensor notation is commonly used.

It is shown that by imposing the condition of seam lines following geodesic paths over the surface during the form-finding of a membrane structure, fabric panels which optimise the width use of a fabric roll will be achieved. In addition, the warp and fill yarns in a fabric panel will undergo distortions by continuously changing the angle between them in order to achieve the



Gaussian curvature of the surface. The derivation of the equilibrium equations of the surface subjected to applied loads, is also given. These equations express the relationships between the stresses in the surface and its geometry.

## Chapter 6

### Numerical form-finding and fabrication patterning

#### 6.1 Introduction

The distinct stages in the design process of tension structures include the form-finding, load analysis (and fabrication patterning for fabric/membrane structures) and detailed design. During the form-finding, the objective is to derive a suitable form, ie. a surface geometry in equilibrium with the corresponding stress distribution in the surface. In the load analysis stage, the form will then be analysed for the possible loads which may act upon it during its useful life. If the load analysis gives satisfactory results, this will be followed by the fabrication patterning stage for membrane structures. In this stage, the corresponding cutting patterns are developed so that the fabric can be tailored to give the required geometry when prestressed. The final stage is the detailed design of the supporting steelwork, connections and so on.

As mentioned in chapter 5, in the solution of the membrane equilibrium equations during the form-finding, the unknowns can either be the membrane stresses or geometry of the surface. Hence, this gives rise to two basic approaches which can be used for the form-finding, ie. in one approach, the solution is for the stresses in the surface given the surface geometry and boundary conditions while in the other approach, the solution is for the surface geometry given the stresses in the surface and boundary conditions. A number of solution methods for the problem of form-finding have been reported and a review of these methods is given below. In general, these methods fall into either one of two approaches. There are also methods in which the equilibrium equations are solved for the unknown geometry and unknown stresses in the surface. In these methods, the solution of the equilibrium equations can be carried out using a scheme such as the implicit Newton-Raphson method or the explicit dynamic relaxation method. A highly flexible and efficient numerical procedure for the form-finding of tension structures will be described later in this chapter. This procedure involves the use of the dynamic relaxation method to solve for the unknown equilibrium geometry given the stress distributions and boundary conditions. The controls which can be used during form-finding to achieve the desired geometries of cable nets and membrane structures will be discussed. Further detail on the fabrication patterning and load analysis stages in the design process, will also be given.

In some literature [69], form-finding is also known as 'shape-finding'. However, the problem is only one of shape-finding in cases where the solution is for an equilibrium geometry given the stress distribution in the surface. Another name which has been used for the form-finding problem is the term 'initial equilibrium problem' suggested by Haber [63].



## 6.2 Review of solution methods available for the form-finding

### 6.2.1 Non-linear displacement analysis

Argyris, Angelopoulos and Bichat [3], and Haug and Powell [69] have considered the form-finding of cable nets by means of non-linear displacement analysis. Haug and Powell [69] have also extended the analysis to include membrane structures. The analysis uses the following basic equation, ie.

$$([K_l] + [K_g])\{\delta\} = \{R\} \quad (6.2.1)$$

in which  $[K_l]$  and  $[K_g]$  are respectively the linear and geometric stiffness matrices,  $\{\delta\}$  is the vector of nodal displacements relative to the current state,  $\{R\}$  is the vector of nodal residual forces.

The non-linear behaviour of these structures require the use of Newton-Raphson iterations in the analysis. Fictitious values can be used for the material elastic properties. With a zero elastic modulus, the influence of the  $[K_l]$  term in equation (6.2.1) becomes nil. The element stiffness then comes entirely from the  $[K_g]$  term. This allows stress values to be prescribed in each element and starting from an arbitrary trial shape, the analysis can then proceed to find the final surface shape. On the other hand, large elastic moduli can be used to control dimensional changes in the elements of the structure such as to keep accurate wire mesh spacing in a cable net for construction purposes. However, the resulting stresses may be very large and become impractical. Hence, a compromise may be needed between the control of element stresses and dimensions by adjusting the values of elastic moduli in equation (6.2.1). In this approach, the solution is for either the unknown surface shape or unknown internal stresses or both.

### 6.2.2 Siev-Eidelman method

This method suggested by Siev and Eidelman [123] is rather restrictive in terms of the structures to which it can be applied. It can only cope with cable nets in which the horizontal equilibrium is already satisfied and only the vertical equilibrium is to be solved for. Hence, each cable in the net has to lie in a single vertical plane, ie. assumes a straight line in plan projection.

Each cable consists of a series of linear elements. A constant horizontal component of the axial force in each cable is imposed to satisfy the horizontal equilibrium requirement. Hence, at an interior node of the net, a cable element can only contribute to the residual force acting in the vertical direction. Horizontal equilibrium along the boundary of the structure is imposed by having fixed support conditions or a funicular plan form for the



boundary geometry. In addition, only applied loads if any in the vertical direction are permitted.

The process begins with the cable net being defined by a straight line plan grid. Each cable is then given a horizontal force component and the vertical coordinates of the support points specified. Subsequently, the vertical loads are applied to the nodes and the solution is then to solve for the vertical coordinates of each interior node which lead to vertical equilibrium.

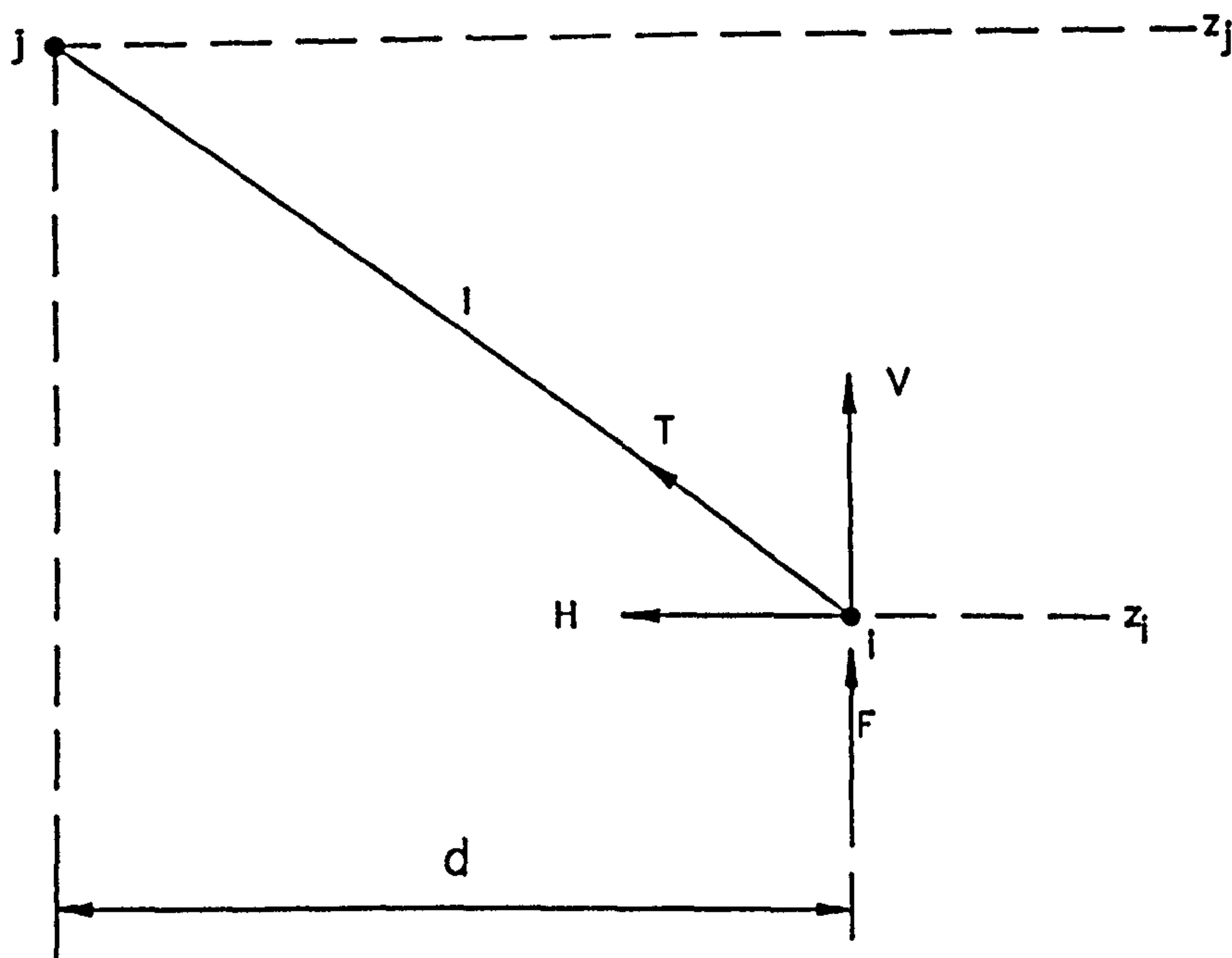


Figure 6.1

Consider a typical cable element with end nodes  $i$  and  $j$  as shown in figure 6.1. The axial, horizontal and vertical forces in the element are denoted by  $T$ ,  $H$  and  $V$  respectively. The vertical applied load at node  $i$  is  $F$ . The element has a length  $l$  with the horizontal component of  $l$  being  $d$ . Thus,

$$V = H \frac{(z_j - z_i)}{d} \quad (6.2.2)$$

in which  $z_i$  and  $z_j$  are the  $z$  coordinates of nodes  $i$  and  $j$  respectively. For vertical equilibrium at node  $i$ ,

$$F + \sum_k \left[ \frac{H}{d} (z_j - z_i) \right]_k = 0 \quad (6.2.3)$$

summed over all elements  $k$  meeting at node  $i$ . All of the variables in equation (6.2.3) are known except for the  $z$  coordinates. Similarly, the vertical equilibrium at all remaining unsupported nodes is considered and all these equations assembled into a matrix form followed by the solution for the  $z$  coordinates. The complete geometry of the structure is then defined with

these  $z$  coordinates determined. Subsequently, the length of each cable element is calculated and in turn, the element axial force found directly as follows

$$T_k = \left(\frac{H}{d}\right)_k l_k. \quad (6.2.4)$$

In this method, it is somewhat difficult to control both the cable forces and surface shape. With a constant horizontal force for each cable, there is undesirable variation in the axial cable force if the slope of the cable varies significantly. As only straight line cable grids are allowed, the possible forms of the cable net become limited. In addition, the method cannot be applied directly to membrane structures.

### 6.2.3 Force density method

Schek [121] proposed the force density method which improves on a few aspects of the Siev-Eidelman method. No restrictions are imposed on the interior geometry of the cable net and free edge conditions are allowed. The applied loads on the structure may take any form. The method solves for the surface shape and internal stress distribution which result in equilibrium.

From figure 6.1,

$$V = T \frac{(z_j - z_i)}{l} \quad (6.2.5)$$

and the vertical equilibrium at node  $i$  is then given by

$$F + \sum_k \left[ \frac{T}{l} (z_j - z_i) \right]_k = 0 \quad (6.2.6)$$

summed over all elements  $k$  meeting at node  $i$ . The term  $(T/l)$  is known as the force density of the cable element. Similar equations can be written for equilibrium in the  $x$ - and  $y$ -directions in terms of force densities and the corresponding node coordinates. These equations can in turn be written in matrix form as follows

$$[D]\{x\} = \{F\} \quad (6.2.7)$$

in which  $[D]$  is a matrix of element force densities,  $\{x\}$  is a vector of unknown  $x$ ,  $y$  and  $z$  node coordinates and  $\{F\}$  is a vector of nodal loads in the  $x$ -,  $y$ - and  $z$ -directions. Equation (6.2.7) is considered at all unsupported nodes, and with the applied loads and force densities for individual elements specified, the unknown node coordinates can then be solved for. Subsequently, the length of each cable element is calculated and the axial force in turn determined from the prescribed force density, ie.



$$T_k = \left(\frac{T}{l}\right)_k l_k. \quad (6.2.8)$$

In this method, the solution is for the surface shape and internal stress distribution. The initial choice of force densities offers little clue as to the surface shape and stress pattern which will eventually result. It is often that highly irregular geometries with undesirable stress distribution are obtained. Various schemes which constrain the solution to achieve equal element lengths or uniform stresses have been suggested by Schek [121]. In addition, the method cannot be applied directly to membrane structures.

An extension of the force density method is the assumed geometric stiffness method proposed by Haber [63] and applicable to structures other than cable nets. The basic equation in this approach by Haber [63] is

$$[K_g]\{x\} = \{F\} \quad (6.2.9)$$

in which  $[K_g]$  is the updated Lagrangian geometric stiffness matrix,  $\{x\}$  is the vector of node coordinates and  $\{F\}$  is the vector of nodal loads. Unlike the standard stiffness relations, equation (6.2.9) is solved for the equilibrium node coordinates instead of the node displacements. In the case of a cable element, the geometric stiffness matrix is simply the element force density. Equation (6.2.9) is non-linear since  $[K_g]$  is a function of the unknown coordinates.

In this approach, the geometric stiffness matrix for each element is prescribed and the node coordinates are then solved for directly. With the node coordinates determined, the equilibrium stresses are then found using the geometric stiffness matrix assumed. The process is iterated until the final equilibrium shape is obtained. The solution is for the surface shape and internal stress distribution. The terms of  $[K_g]$  may lack design significance and either the surface shape or stress distribution is difficult to predict from the values of these terms. In addition, the form of  $[K_g]$  may be very complex for higher order elements.

#### 6.2.4 Least squares method

The method solves for the stress distribution in equilibrium with a prescribed surface shape subjected to any applied loads. The method as applied to a cable net was proposed by Knudson and Scordelis [84], and Ohyama and Kawabata [109]. A few limitations of the Siev-Eidelman method such as straight line plan cable grids, constant horizontal force components and purely vertical loading, are present in the least squares method by Knudson and Scordelis [84], and Ohyama and Kawabata [109]. Hence, the least squares method here considers equilibrium in the vertical direction only. In this case, the solution is for the horizontal cable force components which will lead to vertical equilibrium. Equation (6.2.3) gives the vertical equilibrium at a node but now with all the variables known except for the horizontal force components.



Rearranging equation (6.2.3) and with equations for the entire structure then assembled into matrix form leads to

$$[C]\{H\} = \{F\} \quad (6.2.10)$$

in which  $[C]$  is a  $(m \times n)$  matrix assembled from the terms  $((z_j - z_i)/d)$  of the cable elements,  $\{H\}$  is a vector of  $n$  unknown horizontal force components,  $\{F\}$  is a vector of  $m$  vertical nodal loads, and  $m$  and  $n$  being the number of unsupported nodes and cables respectively in the net. With  $m$  generally larger than  $n$ , equation (6.2.10) becomes overdetermined and thus, no exact solutions can be found in most cases. This leads to the search for an approximate solution. Equation (6.2.10) can be rewritten as

$$[C]\{H\} - \{F\} = \{r\} \quad (6.2.11)$$

in which  $\{r\}$  is a vector of out-of-balance vertical nodal forces. The desired solution is to minimise the sum of squares of the out-of-balance forces with respect to changes in the horizontal force components, ie.

$$\frac{\partial(\{r\}^T\{r\})}{\partial\{H\}} = 0 \quad (6.2.12)$$

which in turn simplifies to

$$[C]^T[C]\{H\} = [C]^T\{F\}. \quad (6.2.13)$$

Equation (6.2.13) is solved directly for the horizontal force components. The axial force in each cable element can then found from equation (6.2.4).

The solution obtained is only an approximate one to the vertical equilibrium problem. In order to achieve equilibrium exactly, additional calculations are needed. A non-linear displacement analysis is used by Knudson and Scordelis [84] to make the final adjustment to the surface shape and stress distribution to reach equilibrium.

Haber [63] extended the basic least squares approach to the equilibrium of a general finite element model in terms of a set of unknown generalised stress components. The global equilibrium of a structure is written as follows

$$[A]\{\tau\} = \{F\} \quad (6.2.14)$$

in which  $[A]$  is a  $(r \times s)$  matrix with  $r$  being the number of equilibrium equations and  $s$  the total number of stress components,  $\{\tau\}$  is a vector of  $s$  generalised stress components and  $\{F\}$  is a vector of  $r$  nodal loads. The terms in  $\{\tau\}$  need not have units of stress and may be the horizontal force components, element force densities or axial cable forces. The corresponding terms in  $[A]$  have to be adjusted for compatibility with the terms used in  $\{\tau\}$ .

It is possible to prescribe some of the generalised stress terms or to establish constraint relations between them. This can be done by partitioning the  $p$  independent generalised stresses  $\{\tau_i\}$  from the  $q$  constrained terms  $\{\tau_c\}$ , ie.

$$[[A_i] : [A_c]] \begin{Bmatrix} \{\tau_i\} \\ \dots \\ \{\tau_c\} \end{Bmatrix} = \{F\} \quad (6.2.15)$$

in which  $[A_i]$  is an  $(r \times p)$  matrix and  $[A_c]$  is an  $(r \times q)$  matrix. The  $k$ th constrained stress term  $\tau_{ck}$  may be given by

$$\tau_{ck} = g_k + \sum_j^p h_{kj} \tau_{ij} \quad (6.2.16)$$

in which  $g_k$  is a constant value and  $h_{kj}$  are linear combination terms for the independent stresses  $\tau_{ij}$ . If all the terms  $h_{kj}$  are zero, then  $\tau_{ck}$  is given in terms of  $g_k$  only. The  $q$  constraint equations in matrix form then becomes

$$\{\tau_c\} = \{g\} + [H]\{\tau_i\} \quad (6.2.17)$$

in which  $\{g\}$  is a vector of  $q$  constant terms and  $[H]$  is a  $(q \times p)$  matrix of linear combination terms. Substituting equation (6.2.17) into equation (6.2.15) leads to

$$[\bar{A}]\{\tau_i\} = \{\bar{F}\} \quad (6.2.18)$$

in which  $[\bar{A}]$  is an  $(r \times p)$  matrix. If  $(r > p)$ , then the equations are overdetermined and in general, no exact solution exists. If  $(r < p)$ , the system is underdetermined and no unique solution can be found.

#### 6.2.4.1 Overdetermined least squares solution method

An approximate solution for the generalised stresses is sought and equation (6.2.18) can then be written as

$$[\bar{A}]\{\tau_i\} - \{\bar{F}\} = \{r\} \quad (6.2.19)$$

in which  $\{r\}$  is the vector of residual forces. The least squares technique is applied to minimise the sum of squares of the residuals with respect to  $\{\tau_i\}$  and leads to



$$[\bar{A}]^T[\bar{A}]\{\tau_i\} = [\bar{A}]^T\{\bar{F}\} \quad (6.2.20)$$

which can then be solved directly for the independent generalised stresses. Subsequently, the constrained generalised stresses may be computed from equation (6.2.17).

#### 6.2.4.2 Underdetermined least squares solution method

This method is appropriate if the number of unknown independent generalised stresses exceed the number of equilibrium equations as is often the case with membrane structures in which there are more stress components than in cable nets. In an underdetermined system, there are infinite exact equilibrium solutions for the generalised stresses and the problem then becomes one of finding the optimum solution.

A set of independent generalised stresses  $\{\tau^*\}$  are defined for the structure. In general, as these stresses will not satisfy the equilibrium equations, the actual independent stresses  $\{\tau_i\}$  can be written as the sum of  $\{\tau^*\}$  and a set of stress deviations  $\{\tau_d\}$ , ie.

$$\{\tau_i\} = \{\tau^*\} + \{\tau_d\}. \quad (6.2.21)$$

Substituting equation (6.2.21) into equation (6.2.18) leads to

$$[\bar{A}]\{\tau_d\} = \{\bar{F}\} - [\bar{A}]\{\tau^*\} = \{F^*\} \quad (6.2.22)$$

in which the solution is for the unknown stress deviations. It is desired to obtain the set of stress deviations which have the smallest Euclidean norm. The process of minimising the Euclidean norm will result in a set of actual equilibrium stresses  $\{\tau_i\}$  closest possible to  $\{\tau^*\}$ .

A Lagrange multiplier method is used by Haber [63] as the solution scheme with a functional  $M$  defined as follows

$$M = \{\tau_d\}^T\{\tau_d\} - 2\{\lambda\}^T([\bar{A}]\{\tau_d\} - \{F^*\}) \quad (6.2.23)$$

in which  $\{\lambda\}$  is a vector of Lagrange multipliers. The optimum solution is achieved by minimising  $M$  with respect to the two sets of independent variables  $\{\tau_d\}$  and  $\{\lambda\}$ , thus

$$\delta M(\{\lambda\}) = [\bar{A}]\{\tau_d\} - \{F^*\} = 0, \quad (6.2.24)$$

$$\delta M(\{\tau_d\}) = 2\{\tau_d\} - 2[\bar{A}]^T\{\lambda\} = 0. \quad (6.2.25)$$



From equation (6.2.25),

$$\{\tau_d\} = [\bar{A}]^T\{\lambda\} \quad (6.2.26)$$

and substituting equation (6.2.26) into equation (6.2.22) leads to

$$[\bar{A}][\bar{A}]^T\{\lambda\} = \{F^*\}. \quad (6.2.27)$$

Equation (6.2.27) is solved for the unknown terms in  $\{\lambda\}$  and the stress deviations  $\{\tau_d\}$  then found from equation (6.2.26). The final stresses  $\{\tau_i\}$  can in turn be determined from equation (6.2.21).

In this method, the equilibrium condition is satisfied exactly as given in equation (6.2.24). A reasonable stress pattern often results due to the imposed condition of least deviations from a specified stress distribution.

In the above extended overdetermined and underdetermined least squares approaches by Haber [63], no restrictions are placed on the structural geometries, element types or forms of stress distribution which can be handled. Furthermore, Haber [63] had proposed stress averaging schemes as means of smoothing out areas of highly uneven stress distribution. A smooth stress distribution is sought to replace the original uneven stress distribution, which will result in more or less the same nodal force resultants. Isolated areas of compression may also be eliminated in the process which comprises of two steps. The first step involves averaging stresses at each node on the basis of stresses in elements connected to the node. Subsequently, the new element stresses are given by the average nodal stresses for each element. An iterative cycle may be required to reach a progressively smooth stress distribution. An alternative scheme for achieving a smooth stress distribution may be to adopt a finite element formulation with the element stresses based on interpolation of nodal stresses. The nodal stresses would then become the unknown generalised stresses in equation (6.2.14).

### 6.2.5 Optimisation method

Nakanishi and Namita [102] had proposed this method for use in cable nets. In this case, the solution is for the surface shape and stress distribution. An ideal shape and stress distribution are specified and an optimisation exercise is carried out to best meet these specified criteria. There are four conditions imposed on the optimum solution. The first two conditions require equilibrium be achieved exactly and that all elements will be in tension. The equilibrium condition is satisfied by solving equation (6.2.6) and with positive element force densities, the elements will remain in tension. The force density in equation (6.2.6) may be prescribed. The remaining two conditions are only satisfied approximately. The first of these concerns the surface geometry and involves solving for a set of node coordinates which are closest



possible to a set of specified node coordinates  $\{x^*\}$ . The difference between the actual and the specified coordinates indicates how optimum the solution is. Hence, from equation (6.2.7)

$$\{P\} = [D]^{-1}\{F\} - \{x^*\} \quad (6.2.28)$$

in which  $\{P\}$  is the vector of coordinate differences in terms of force densities.

The final condition is to achieve a set of force densities  $\{T/l\}$  which are closest possible to a set of specified force densities  $\{(T/l)^*\}$ . Hence,

$$\{Q\} = \left\{ \frac{T}{l} \right\} - \left\{ \frac{T^*}{l} \right\} \quad (6.2.29)$$

in which  $\{Q\}$  is the vector of differences between the actual and the specified force densities, indicates the margin to the optimum solution.

The optimisation exercise is performed on the objective function  $J$  defined as follows

$$J = \|[W_1]\{P\}\|^2 + \|[W_2]\{Q\}\|^2 \quad (6.2.30)$$

in which  $[W_1]$  and  $[W_2]$  are diagonal matrices of weighting values. The relative magnitudes of the terms in  $[W_1]$  and  $[W_2]$  indicate if the solution will better meet the imposed shape or force conditions. The only unknown terms in the function  $J$  are the force densities. Consequently, the optimisation exercise becomes the minimisation of  $J$  with respect to the unknown force densities subject to the tension requirement. This task can be executed by means of non-linear programming methods.

In this method, the solution is for the surface shape and internal stress distribution. There is the benefit of apportioning weighting values to compromise between the conflicting requirements of shape and stress distribution. In most cases, the control of one factor has to be relaxed in order to have satisfactory control of another factor. At present, the method has yet to be applied to membrane structures.

#### 6.2.6 Iterative smoothing method

In this method proposed by Haber [63], the stresses are specified directly and the equilibrium shape is then solved for. A set of iterative equations are formulated from the global form of equation (6.2.10). Each unknown node coordinate may be given as a weighted average of the forces acting on the node and the coordinates of the adjacent nodes, ie.



$$x_i = \frac{[F_i - \sum_{j=1}^n (K_g)_{ij} x_j]}{(K_g)_{ii}} \quad \text{for } (j \neq i) \quad (6.2.31)$$

in which  $n$  is the number of node coordinates. Initially, a trial shape is specified with the stress distribution also defined. The geometric stiffness matrix is set up based on current geometry, and equation (6.2.18) then applied to obtain values for the unknown coordinates as an approximate solution. The process is iterated until convergence to an equilibrium shape. As the iterative coordinate averaging is equivalent to a surface smoothing exercise, this method is termed 'iterative smoothing'. The solution is for the surface shape and can deal with any finite element types.

### 6.2.7 Combined approach

The various solution methods outlined above may be combined together into a more flexible design module. A solution method may produce approximate results which are then input into another method to improve on the solution. For instance, the shape adjustment of the iterative smoothing method may be combined with the stress adjustment of a least squares approach. A mathematically defined surface shape may be improved by a few shape adjustment iterations. This updated shape is then used in a least squares method to give an appropriate stress distribution for the shape. If required, these stresses may be passed through a smoothing process. The updated stresses can further be used as input for more shape adjustment iterations. This process is repeated until an acceptable solution for the surface shape and stress distribution are obtained. As a final correction step, the non-linear displacement analysis may be applied.

## 6.3 Form-finding by the dynamic relaxation method

In this thesis, the adopted approach for the form-finding is to solve the equilibrium equations for the unknown surface geometry given the stress distributions and boundary conditions. The solution itself of the equilibrium equations is carried out using the dynamic relaxation method implemented with the kinetic damping procedure. This approach differs radically from the usual methods of structural design and analysis. In conventional structures, the engineer will propose a trial form of the structure and then analyse it for various loading conditions to determine the resulting stresses. This procedure when applied to tension structures which typically have complex, doubly curved surfaces is faced with the difficulty of having to describe such surfaces before the loads can be applied. In general, mathematical representations do not exist for arbitrary surface geometries. In the adopted approach, this process is reversed, ie. stresses (or prestresses) are specified a priori and the resulting form is then determined. This offers an efficient and effective means of achieving the form which meets the architectural and structural requirements. A trial and error procedure will consequently be



required in the solution for the desired form. This in turn leads to the need for interactive computer-aided design (CAD) of tension structures which will be discussed in detail in chapter 7. The same numerical model is also used for the load analysis and for establishing the cutting patterns and cable lengths. In other words, the whole design becomes one continuous process.

The form-finding process will begin with an arbitrary trial form and various controls can then be used to adjust the form until the desired solution is achieved. These form-finding controls which apply to cable nets and membrane structures including air-supported structures, will be described below. In the solution for the equilibrium geometry during the form-finding, pure statics alone is considered without the need to involve the kinematic relationships. Hence, the actual material constitutive properties are not required and fictitious values can be used instead in the form-finding.

By using the kinetic damping procedure, radical adjustments can be made to the numerical model during form-finding without the possibility of numerical instability. This procedure allows local adjustments to be made without the propagation of these disturbances to those regions further away. The out-of-balance forces which arise from the form adjustments are rapidly equilibrated locally.

### 6.3.1 Cable nets

In the numerical model, a cable net is idealised into link or cable elements. The form-finding controls for the cable net include the tension/force and elastic controls which are applied to the cable elements. Under force control, the elastic stiffness of the cable element is set to zero and a tension value prescribed to the element, and the prescribed tension will be adjusted during the form-finding. Under the elastic control, an elastic property and a slack length are prescribed to the cable element, and the prescribed elastic property and/or slack length will be adjusted during the form-finding. In this case, the tension in the element is derived from the elastic extension of the element from its prescribed slack length. These controls as applied to different kinds of cable nets are outlined below.

#### 6.3.1.1 Geodesic nets

Geodesic nets are also known as minimal nets in which the cables over the net surface each takes a path of shortest distance and thus, has minimum length. The tension in each of these cables is constant throughout its length. Consequently, the form-finding control is to set the tensions in all link elements constituting each surface cable to a prescribed value at all stages. The elastic stiffnesses of the surface cables are also set to zero. In other words, the surface cables can slide freely over each other without loss of contact or friction at the nodes. The intersections between the surface cables may be jointed only after pretensioning. For each edge cable if present, tension can

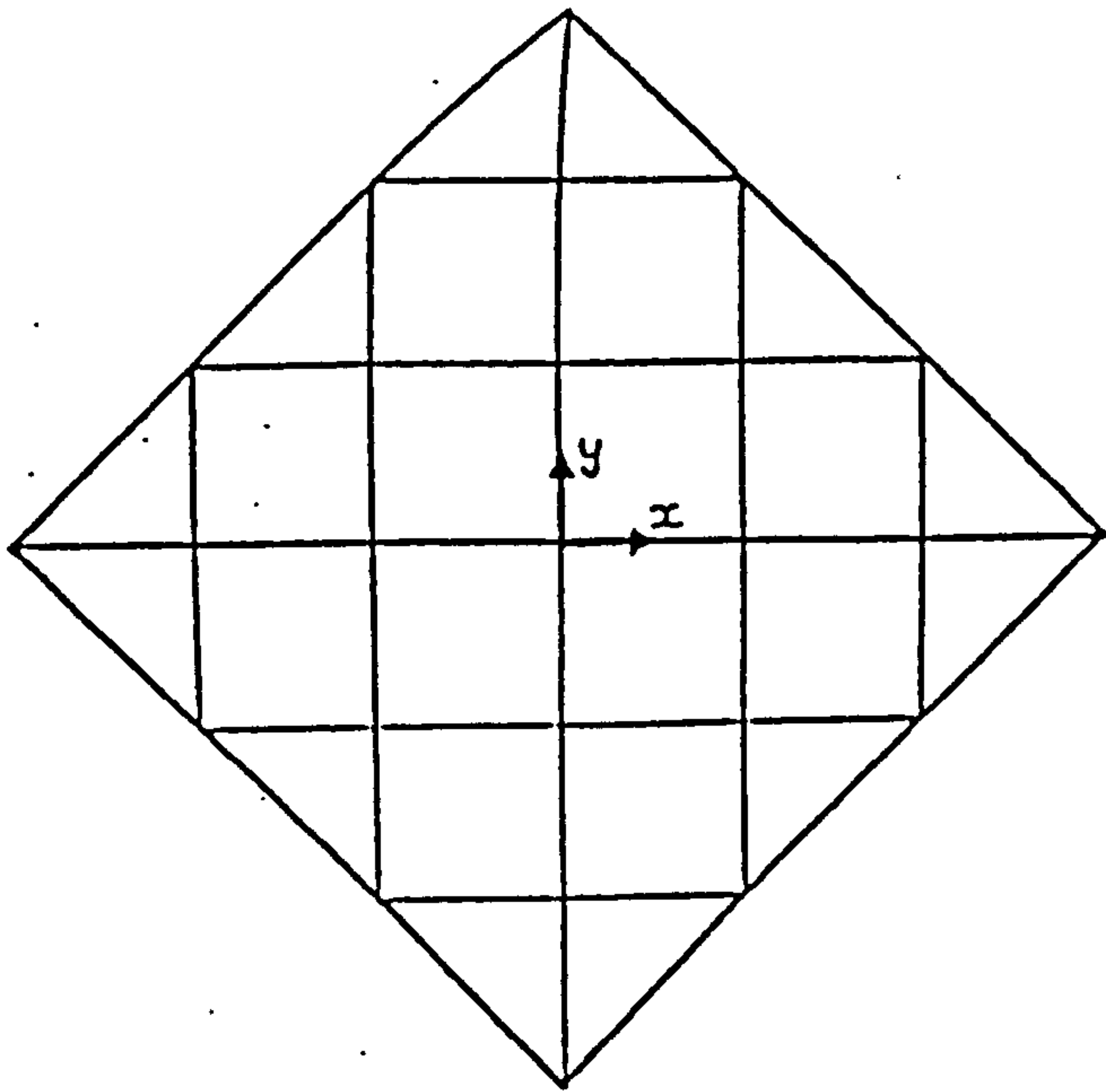


Figure 6.2(a)

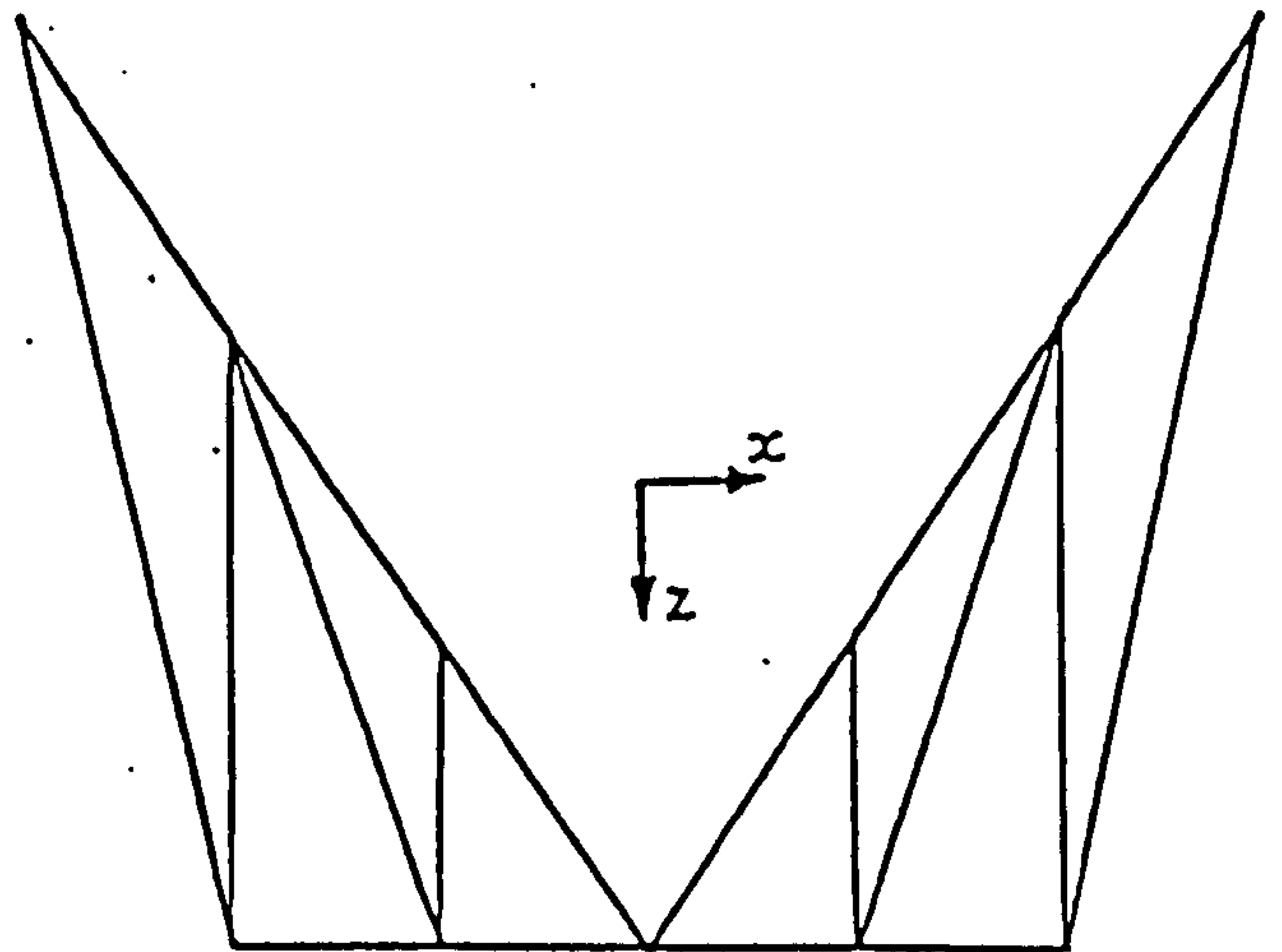


Figure 6.2(b)

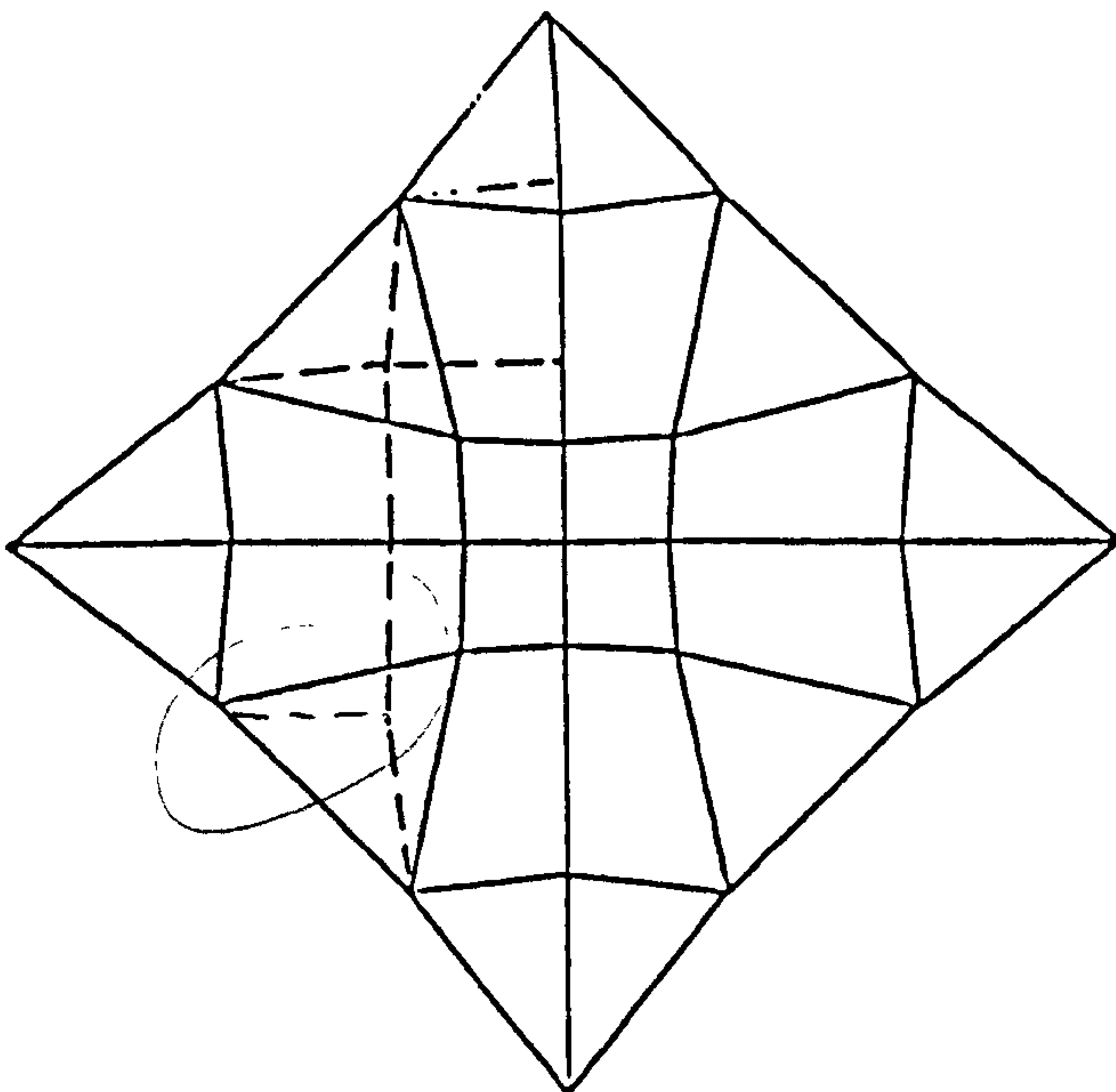


Figure 6.3(a)

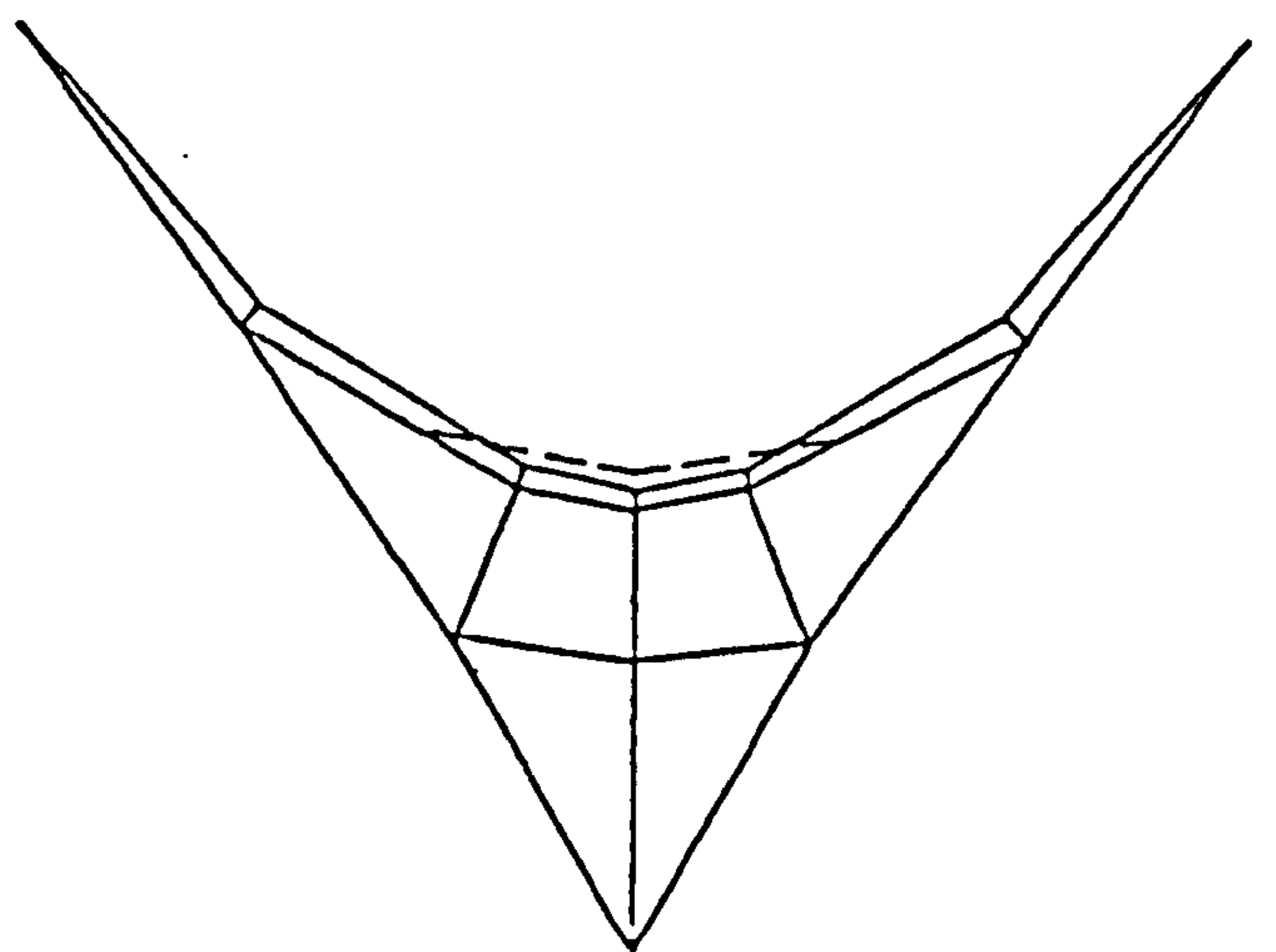


Figure 6.3(b)

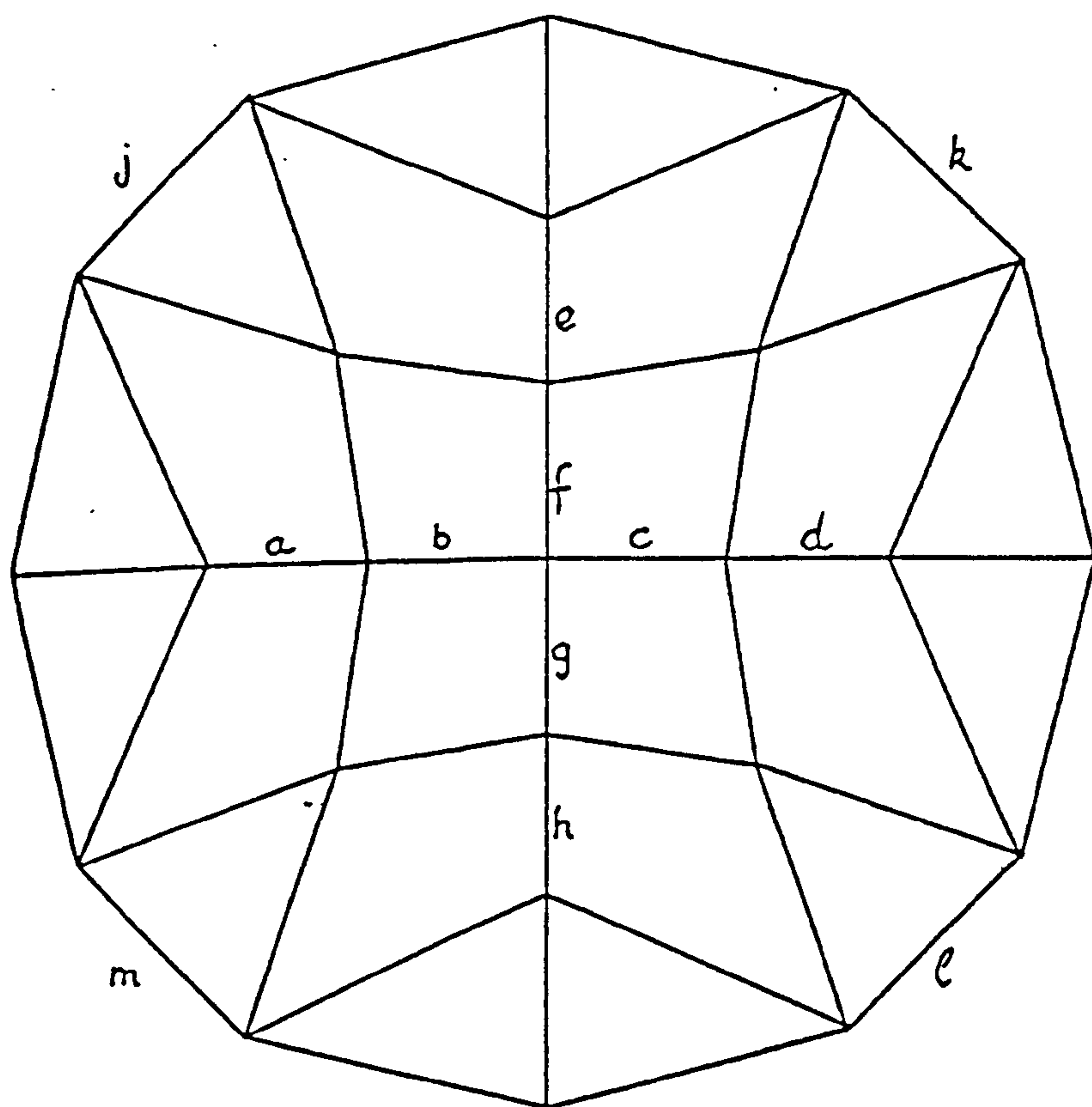


Figure 6.4(a)

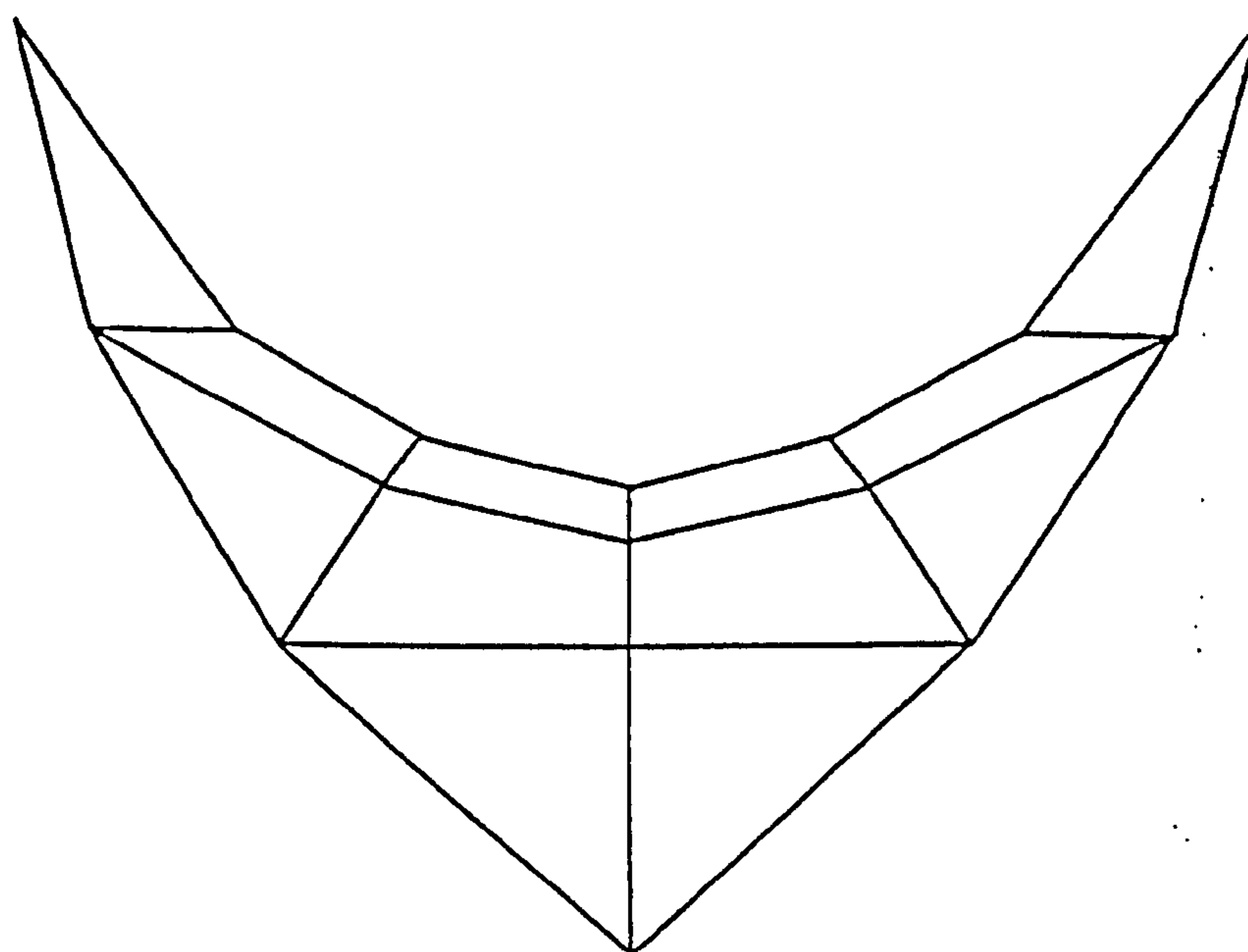


Figure 6.4(b)



only be assigned to one link element with the remaining link elements in the cable being elastically controlled. The form-finding can begin with a highly inaccurate initial geometry as shown in figures 6.2(a) and 6.2(b), and still results in rapid convergence towards the equilibrium geometry of the geodesic net as shown in figures 6.3(a) and 6.3(b). It is noted that the spacing between the surface cables becomes closer towards the central regions of the geodesic net.

#### 6.3.1.2 Uniform mesh nets

Uniform or equal mesh nets have a typical regular spacing of 0.5m so that after erection, workmen can walk on them to fix cladding or so on without too much danger of falling through. The best known uniform mesh net is the roof over the stands of the Munich Olympic Stadium. A number of controls can be used for the form-finding of a uniform mesh net. Changes can be made to the boundary or internal support geometry. At the slack state, the uniform mesh is prejointed so that the internode spacing is constant except for those adjacent to boundaries or internal supports. Realistic values are used for the link stiffnesses in order that changes in internode spacing will be small when the net is stressed up. Links adjacent to boundaries or internal supports may be controlled either by specifying constant tensions in these links or by using low elastic stiffnesses and adjusting their specified slack lengths to achieve the desired geometry. It is often required to use a combination of both controls.

With the initial geometry of a uniform mesh net as shown in figures 6.2(a) and 6.2(b), and using the above mentioned form-finding controls, the equilibrium geometry of the net as shown by the dashed lines in figures 6.3(a) and 6.3(b), is obtained.

Barnes [17] proposed a strategy of laying a two-way grid over the surface of a uniform mesh net which facilitates the data organisation whereby nodes may have to be added or removed during the form-finding. Nodes are identified by two numbers which are values of traverse lines forming the grid and there are arrays for the intercepts of boundaries with the traverse lines.

An approach of using differential geometry to describe the geometries of uniform mesh nets, has been investigated by Williams [138]. However, the assumptions made to simplify the problem limit the applicability of the approach to situations such as for preliminary studies. In addition, the uniform mesh nets which can be dealt with using this approach are only those in shapes like the sphere, hyperbolic paraboloid and right helicoid.

#### 6.3.1.3 Principal curvature nets

According to Williams [138], nets in which the cables follow directions of principal curvature on the surface will spread out in a radial fashion from a mast support. A principal curvature net has the benefit of the quadrilaterals



which formed on its surface being flat simplifying the design of the cladding. The cable tension and spacing increase further away from the mast.

It is not possible to use the dynamic relaxation method for the form-finding of principal curvature nets. This is because there exists no relationship between cable lengths and tensions which will lead automatically to a principal curvature net. Williams [138] has applied differential geometry to produce forms of principal curvature nets and also constant tension coefficient nets.

#### 6.3.1.4 Momentless compression boundaries

In the form-finding of a cable net which is supported by a compression boundary or arch, the beam elements as described in chapter 4 can be used to model the compression boundary. In the case of a momentless compression boundary however, the use of the beam elements may not be necessary. An alternative means of dealing with such a case is described below.

For the cable net shown in figures 6.2(a) and 6.2(b), if the force in the edge cable links is specified as a constant compression, the structure must always become unstable irrespective of starting geometry [10]. This instability can be avoided by reversing all surface cable force components in the calculations of residual forces at the nodes lying along the edge cables which in turn are treated as forming a tension boundary.

With the initial geometry as shown in figures 6.2(a) and 6.2(b), Barnes [10] has used the above scheme to obtain the resulting geometry as shown in figures 6.4(a) and 6.4(b) for a surface to edge force ratio of -1:6. The force in both end links of each boundary was held constant to ensure symmetry with the links ( $j \rightarrow m$ ) being elastically controlled. If the surface system had been entirely geodesic, the structure would have become unstable. However, with elastic stiffnesses assigned to the surface links ( $a \rightarrow h$ ) and constant tensions in the remaining surface links, a stable system can be achieved. Hence, the surface is part geodesic and part elastically controlled. For the same surface:edge force ratio, the geometry can be adjusted by altering the elastic stiffnesses of the links ( $j \rightarrow m$ ) and ( $a \rightarrow h$ ).

#### 6.3.2 Membrane structures

The surface of a membrane structure consists of a series of fabric panels which are sewn or welded together along the common seams between panels. The concept of the geodesic coordinates has already been considered in section (5.13) of chapter 5. The warp and fill directions (which are the material principal directions) of each fabric panel are aligned to follow the paths of geodesics and their orthogonal trajectories respectively over the surface. The seam lines defined to coincide with the warp directions will in turn become

or



geodesics on the surface. This has the advantage of producing fabric panels which will optimise the use of the fabric roll (see figure 5.8).

In the numerical model, each fabric panel is defined by a sequence of triangular membrane elements. As mentioned in section (3.3.5) of chapter 3, the local  $x$ - and  $y$ -axes of each element are set to be coincident with the warp and fill directions respectively, and with side 1 of the element aligned along the warp direction. In the form-finding, all the membrane elements are under stress control, ie. the elastic stiffness of each element is set to zero, and tensile stress values are assigned to the element in both the warp and fill directions. This is to prevent large strains taking place in the bias direction of the fabric panel. Consequently, the condition of applied tensile stresses coincident with the geodesic coordinate system is imposed on the form-finding process. This requirement is not necessary but does offer a convenient and flexible means of achieving different surface forms.

In the modelling of minimal surfaces such as a soap film, a uniform stress distribution is specified, ie. the warp stress  $\sigma_x$  and fill stress  $\sigma_y$  are set equal ( $\sigma_x = \sigma_y$ ) throughout. A minimal surface has zero mean curvature. For a non-uniform stress distribution, the condition of ( $\sigma_x \neq \sigma_y$ ) applies instead. From physical intuition, if more curvature is desired in a certain direction over an area of the surface, the option may be to relax the stress distribution along that direction. Hence, the control of stress distribution offers a means of form adjustments which lead to direct results from the point of view of physical reasoning. By varying the ratio of stresses in the warp and fill directions, the surface geometry is adjusted until the desired result is obtained. In the case of air-supported structures, the inflation pressure has to be specified as well.

The above approach leads to a numerical procedure for the simultaneous form-finding and production of cutting patterns proposed by Williams [138] which has been briefly outlined in section (5.16) of chapter 5. Within this procedure, there are two criteria which have to be satisfied simultaneously, ie.

- (1) the seam lines follow geodesic paths,
- (2) at each node, equilibrium in the direction normal to the surface.

The in-plane equilibrium of the surface is satisfied automatically by using a stress distribution which fulfills certain conditions as outlined in section (5.15). The overall surface form is then governed by the criterion in (2). Subsequently, the criterion in (1) is achieved by geometric adjustments of nodes in the plane of the surface to meet the condition as given in figure 5.12. Alternatively, Haug [71] has suggested a scheme of superimposing a minimal cable net of uniform tension prestress cables over the membrane surface. These cables and thus, the nodes along them will approach geodesic paths over the surface. The tensions in these cables have to be very small so as not to influence the overall surface form. In the case of minimal surfaces with uniform stresses throughout, the minimal cable net leads to no dominating



influence of geodesic patterning in the warp direction. The same situation arises if the fabric stress is higher in the fill than in the warp direction.

Another means of satisfying the criterion in (1) is a modified form of the idea suggested above by Haug [71]. This is to use 'fictitious' slip strings with high tensions compared with the membrane stress resultants as proposed by Barnes [16]. The tensions are constant along these strings and each string will therefore automatically find a shortest path between its starting node and last node, over the surface to define a geodesic. The slip strings are aligned along the warp direction of the fabric, and to account for non-uniform stress conditions along side 1 of each triangular membrane element. At each node along a slip string, the component of tension normal to the surface is ignored. In this way, the specified tension in the string makes no contribution to equilibrium in the direction normal to the surface. In addition, the string tension should not contribute to the residual forces at end nodes of the string which lie on ridge or boundary cables. This results in the geometries of the ridge or boundary cables being controlled only by the membrane stresses and the cable own elastic properties. In other words, these slip or geodesic strings fulfill both the criteria in (1) and (2).

A tension coefficient is the ratio of the tension to the length between two adjacent nodes along the string. As a variation, the condition of constant tension coefficient may be imposed in order to achieve evenly spaced nodes along the string and offers a useful option in situations where nodes tend to bunch together.

The following steps have been proposed by Barnes [17] as the means of imposing the conditions mentioned above on the slip or geodesic strings within the form-finding scheme:

- (1) Begin residual  $\{\bar{R}\}$  calculations with all geodesic strings before any other element type.
- (2) Calculate the average value of surface normal vectors of adjacent triangular membrane elements meeting at a node and Williams [142] suggested applying a weighting to each normal vector which is inversely proportional to the element area (see figure 6.5). This average value is then taken as the surface normal vector at the common node and the unit value of this vector,  $\{\bar{v}_n\}$  found.
- (3) The components of the nodal residual forces normal to the surface,  $R_n$  are then given by  $R_n = \{\bar{v}_n\}^T \{\bar{R}\}$ .
- (4) For each geodesic node, subtract normal component from the global residuals, ie.  $\{\bar{R}\} = \{\bar{R}\} - R_n \{\bar{v}_n\}$ .
- (5) Set nodal residuals along all ridge and boundary cables to zero.



(6) Proceed to residual summation for other element types.

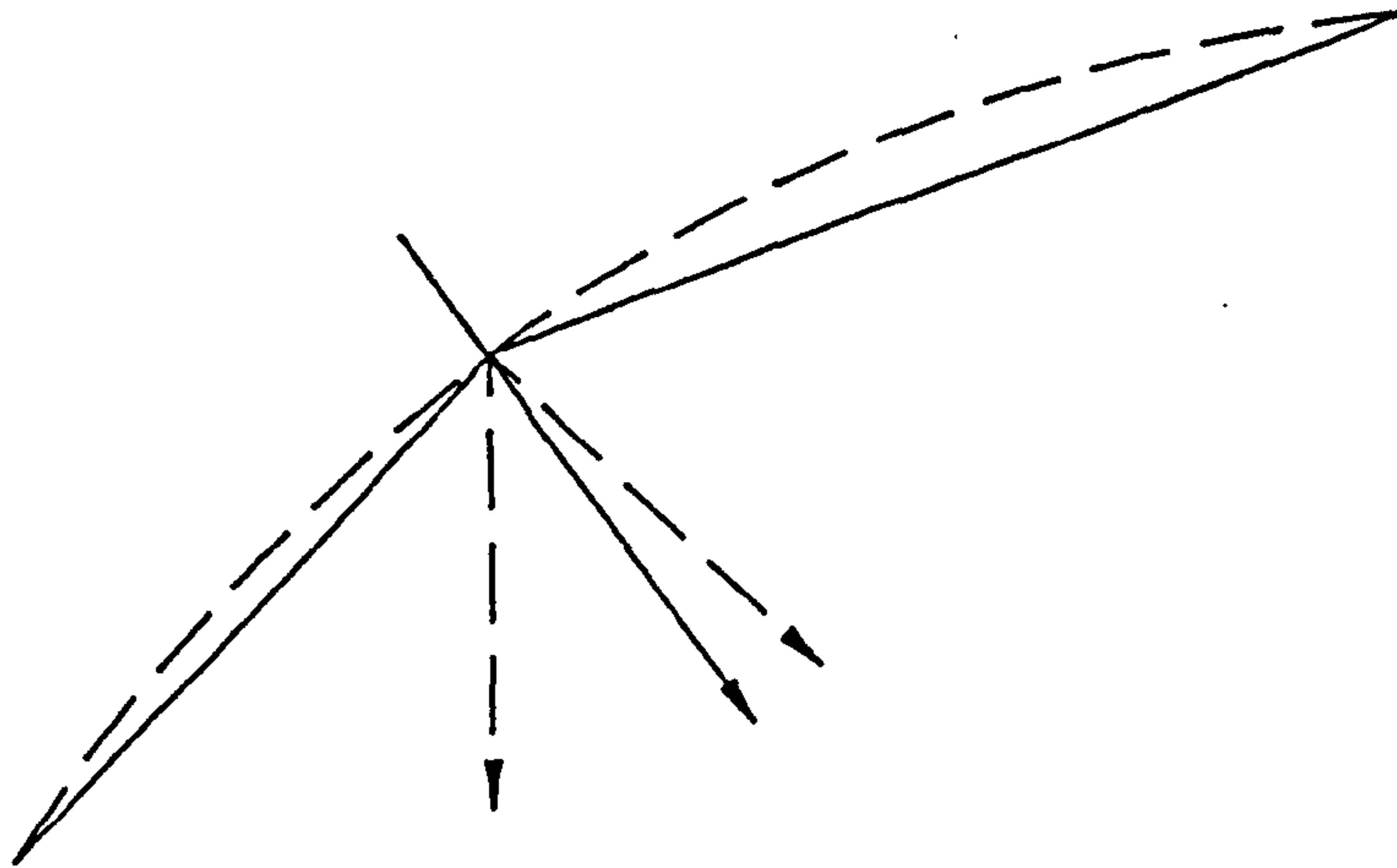


Figure 6.5

The surface form is also a function of the spatial geometries of the ridge and boundary cables used in the membrane structure. Each of these cables is idealised as a series of link or cable elements in the numerical model. The force and elastic controls as used in the cable nets described earlier can equally be applied to the cable elements being considered here. Only one of the constituent elements in a ridge or boundary cable can be given force control with the remaining elements in the cable being elastically controlled. During the form-finding, the force along the cable will be maintained at more or less the value of the specified tension in the force controlled element. The cable geometry is governed by the equilibrium between the membrane stress resultants and the tension along the cable. A simple relationship can be used to approximate the required tension in the cable,  $T$  given the information of desired radius of curvature for the cable,  $R$  and the membrane stress resultants acting along the cable,  $\sigma$  (ie.  $T = R \times \sigma$ ). Hence, a higher cable tension results in the cable having less curvature for the same membrane stress resultants and vice versa. The force control is useful for gross adjustments of the cable geometry towards the desired form.

Under elastic control, the tension along a ridge or boundary cable is derived from the elastic extension of the cable from its initial slack length. Each of the constituent elements in the cable is prescribed with an elastic property and a slack length, and these elastic property and slack length can be adjusted during the form-finding. The curvature of the cable can thus be controlled through these adjustments. For instance, more cable curvature is achieved by using a reduced elastic stiffness in the cable and vice versa. At times, it is required to use a very high element stiffness in order to achieve a stressed length which is as close as desired to a target length. When the stiffness of such an element is much higher than the other stiffnesses in the model, then the increased nodal masses necessary to ensure the numerical stability of the solution for a given time interval will reduce the fundamental frequency of the overall structure and thus, also the rate of convergence of the analysis



[133]. For instance, this problem may arise in the case of a cable girder with short and rigid struts during form-finding to a target element stressed length. A force transfer procedure for handling stiff elements has been proposed by Barnes [10], but it requires the use of over-critical viscous damping to ensure convergence. An alternative suggested by Wakefield [133] involves updating the slack length of a cable element at intervals using a relationship between the element current and required stressed length. In this way, an elastic stiffness may be chosen which is close to that of adjacent elements and thus, results in an improved convergence rate.

In the presence of compression (as indicated by a stressed length which is less than the slack length), the cable element will buckle and the force in the element in turn set to zero. As mentioned in earlier chapters, the dynamic relaxation analysis can cope with on/off element buckling without any difficulty. In situations where compressive forces are to be resisted such as at the mast support, then strut elements will be used. A strut element is similar to a cable element in all respect except that it can take a compressive force. In cases where bending forces are present, then the beam elements as already considered in chapter 4 have to be used.

Another case to consider is the use of the slip cable to model a frictionless cable such as one which slides freely in a fabric sleeve. This is achieved by ensuring that the tension is more or less constant along the slip cable. In the numerical model, the slip cable is idealised as a series of cable elements. Under elastic control, an elastic stiffness and a slack length are assigned to the slip cable. The current length is calculated by adding up the individual current lengths of all the constituent elements. From the difference between the current and slack lengths of the slip cable and using the given elastic property, a tension value can be calculated. This tension is then assigned to each of the constituent elements and will thus be constant along the slip cable. Under force control, a tension value for the slip cable is specified, and the force in an element around mid-point of the slip cable will then be set to this specified tension with the elastic stiffness of the element also set to zero. The remaining elements in the slip cable are elastically controlled given the elastic stiffness and with their individual slack lengths calculated from current coordinates. The forces in all constituent cable elements will then remain approximately at the value of the specified tension for the slip cable. An area where the slip cable may be applicable is in the form-finding of conical membrane structures.

### 6.3.3 Air-supported structures

In 1918, F. W. Lanchester, the British car pioneer patented the design of a tent supported by air. Since then, a number of large scale air-supported stadium roofs have been built mostly in the USA. Apart from the additional factor of inflation pressure, the above discussion on membrane structures applies equally to air-supported structures. The equilibrium equations of a surface subjected to inflation pressure have been derived in section (5.15) of chapter 5.



The form-finding process involves defining the applied stresses, the inflation pressure and boundary conditions, and then finding the surface geometry which satisfies the equilibrium equations.

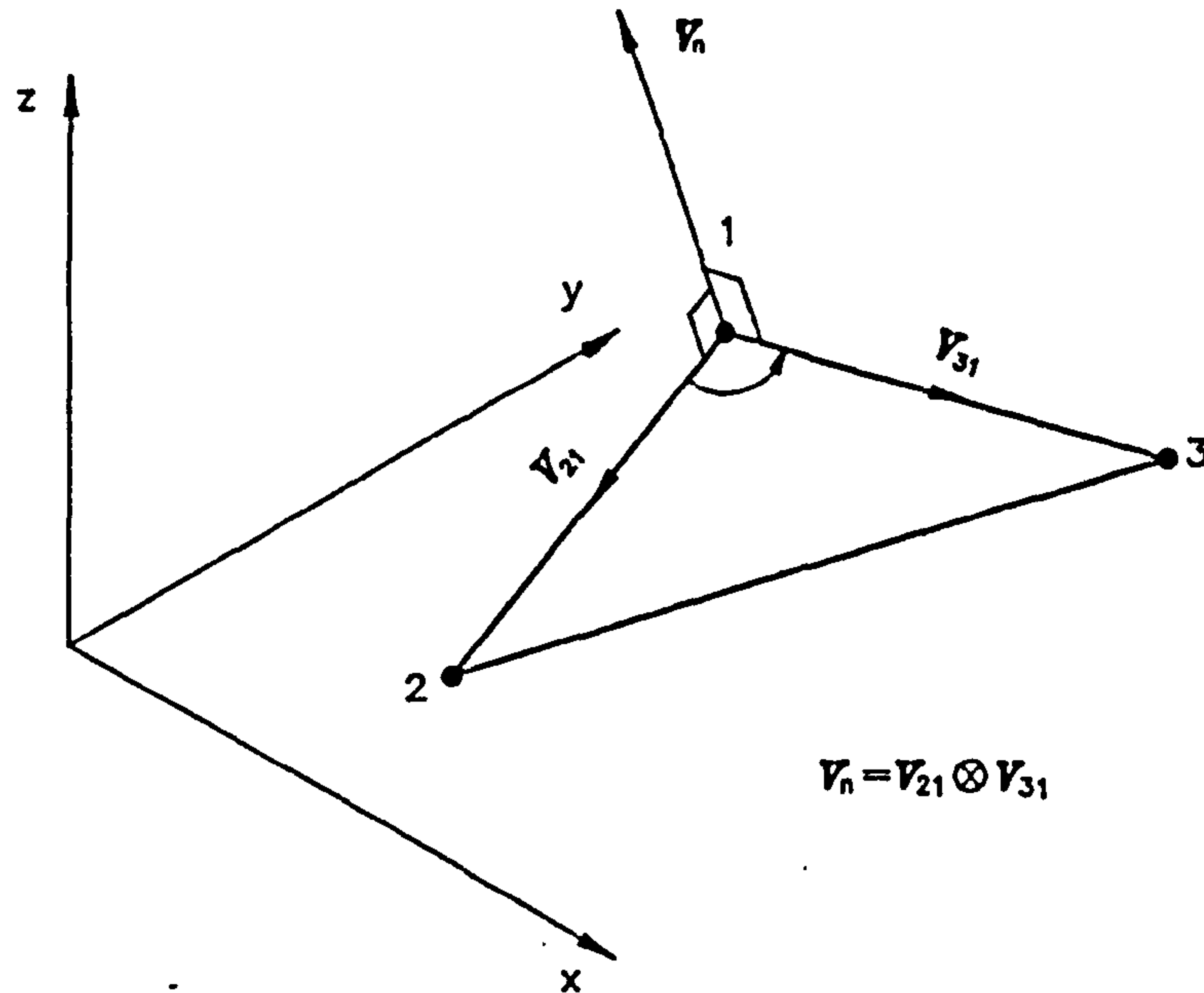


Figure 6.6

Within the dynamic relaxation scheme, the inflation pressure is applied in terms of the equivalent normal nodal forces proportional to the current areas of membrane elements as their shapes vary during the analysis. This is implemented in a simple manner as developed by Barnes [10]. The resolved components of the normal nodal forces can be found in terms of element side vectors without the element areas being calculated explicitly. For a right-handed global coordinate system and with element nodes numbered in an anti-clockwise sense, the out-of-plane normal vector  $v_n$  is given by

$$v_n = v_{21} \otimes v_{31} \quad (6.3.1)$$

in which the  $\otimes$  term stands for a cross product operation, and  $v_{21}$  and  $v_{31}$  are the element side vectors as shown in figure 6.6. This follows that if  $p$  is the inflation pressure, the resolved force components at each node are then given by

$$\begin{Bmatrix} F_x \\ F_y \\ F_z \end{Bmatrix} = \frac{p}{6} v_n = \frac{p}{6} \begin{Bmatrix} y_{21}z_{31} - y_{31}z_{21} \\ x_{31}z_{21} - x_{21}z_{31} \\ x_{21}y_{31} - x_{31}y_{21} \end{Bmatrix} \quad (6.3.2)$$

in which  $F_x$ ,  $F_y$  and  $F_z$  are nodal forces in the global coordinate system, and  $x_{21} = x_2 - x_1$  and so on, with  $x_2$  and  $x_1$  being the  $x$  coordinates of the first and



second nodes respectively in the sequence of node numbering for the element considered.

#### 6.4 Fabrication patterning

The Gaussian curvature of the surface of a membrane structure is often sufficiently large to require the fabric panels to be shaped before being sewn or welded together. Hence, the patterning stage in the design process of membrane structures. Once a suitable form has been found, the cutting patterns can then be developed. It is a direct geometric exercise of taking each fabric panel and flattening out the folds between adjacent members in the sequence of triangular elements within the panel. These cutting patterns will be marked and then cut off from fabric rolls on the shopfloor. As mentioned earlier, the use of geodesic patterning has the advantage of producing cutting patterns which will optimise the use of the fabric roll (see figure 5.8). Furthermore, the physical width of the fabric roll will impose a limit on the maximum width which is allowed for each cutting pattern. Hence, it is required to adjust the cutting patterns until their widths are all within the allowable limit. This can be easily done by moving the ends of the geodesics along the boundary automatically during form-finding [138]. In addition, it may be necessary in some cases to reduce the width of a cutting pattern by splitting it into two smaller ones. A fully interactive module for the width adjustments of cutting patterns has been developed and will be outlined in detail in chapter 7.

The cutting patterns are fabricated in the stress free state. Hence, in order to derive the 'shrunk' geometries of the cutting patterns corresponding to such a state, it is required to apply stretch compensation factors to the cutting patterns developed from the numerical model in the prestress state. These stretch compensation factors are determined from tests carried out on the fabric material. In some areas of the actual structure, it may be difficult to prestress the fabric to the desired levels at the erection stage. Consequently, decompensation factors need to be applied accordingly to portions of the cutting patterns corresponding to these areas.

The patterning procedure accounts for the surface curvature of the model but cannot eliminate the stresses induced as a result of deformations necessary to flatten out the fabric panel. Hence, when the cutting patterns are sewn or welded together and then stressed up to the prestress levels established from the form-finding, the induced stresses mentioned earlier need to be applied in reverse to produce the true stress state in the doubly curved erected patterns. In addition, due to the resistance of the fabric panel to being curved, the surface geometry after erection differs slightly from that obtained during form-finding. However, these deviations in form and stresses from the form-finding values are believed on average to be minimal and thus, discounted.

In sharply curved regions of the surface, it may be sensible to model a fabric panel by two component or coupled half panels. Hence, the element



idealisation of the fabric panel is doubled and a more refined representation of surface curvature across the panel width is achieved as a result. In addition, the profiles at the two ends of the panel are better approximated. At the patterning stage, the two half panels are unfolded, the stretch compensation and/or decompensation factors applied, and their cutting patterns then sheared horizontally across to a straight common seam line between them. Subsequently, these two cutting patterns can be combined together into a single piece for fabrication purposes. The distortion involved in the process can be accommodated due to the in-plane flexibility of the fabric material. On the other hand, in regions of the surface with low curvature, the same process can be applied to produce 'double-width' panels which will make fabrication simpler. A fully interactive module for the above strategy of handling the fabric panels has been developed and will be outlined in chapter 7.

## 6.5 Behaviour under load

The surface geometry established in the form-finding stage has to be analysed for possible loads which may act upon it during its useful life. For this purpose, the stress and force controlled elements employed during form-finding have to be replaced by elastic elements with realistic stiffness values. In the case of membrane elements, the elastic stiffness used should correspond to the appropriate biaxial stress/strain properties for the fabric material. During the load analysis, the prestresses from the form-finding are added to the stresses derived from elastic deformations under loads to give the final stresses.

The design loading may come from the structure self-weight, wind, snow and so on. Due to its lightweight nature, the self-weight of the membrane is often neglected. However, the weights of cables and fittings may have to be considered. The wind loads often constitute the most significant loading for the design. In general, they are applied as surface pressures modified by local coefficients for different areas over the surface. The case of wind uplift is often the dominant one. The wind pressure coefficients may be obtained from wind tunnel tests. However, the validity of wind tunnel testing for the flexible tension structures is questionable. The proper instrumentation of such tests seems difficult because any device attached to the model being tested alters its characteristics considerably. The snow loads are dependent on the amount and nature of snow accumulation over the surface. The snow loads tend to slide down steep slopes and remain on the flatter ones. Furthermore, it is undesirable to have concentrated point loads on the surface. The subject of design loadings for tension structures will be considered in further detail in chapter 8.

After the load analysis, the performance of the structure is evaluated. The resulting deflections or stresses may be over excessive. In addition, potential ponding areas may be identified. The slackening of membrane and cable elements is also possible. Subsequently, it may be required to return to the form-finding stage to improve the form in order to reduce or eliminate the



inadequacies of the structural performance under loads. The prestress levels may have to be increased to limit the deflections. On the other hand, a change of curvature which means a change in prestress ratios, may be the preferred solution. It may be acceptable for small areas of the surface to go temporarily slack under full loading. The condition of no slackened elements at all may be uneconomic. As a result, a criterion of a maximum surface area that is allowed to go slack may be adopted. The problem of ponding can be solved by avoiding flat horizontal areas. With these adjustments made, the modified form will then be analysed again. When satisfactory results are achieved, the forces from the load analysis are used in the structural design of components such as the mast supports, cables, membrane plates, boundary cable clamps and so on. In addition, the fabric with sufficient breaking strength is chosen. In areas where ponding is possible, suitable drainage may be installed.

In general, tension structures have natural frequencies of vibration which could interact with the wind to produce fairly large oscillations. In practice, a properly tensioned structure can reduce the wind induced oscillations and is structurally acceptable in many cases. For large scale structures, the dynamic behaviour may be studied by aeroelastic model testing in a boundary-layer wind tunnel with modelling of the turbulent boundary layer. A detailed discussion of the dynamic behaviour of tension structures will be given later in chapter 9.

During the load analysis, the presence of localised areas of membrane buckling may prevent full convergence from being achieved. This is due to the absence of gradual stress variation from element to element as a result of using constant strain membrane elements. A local rearrangement of the membrane elements may eliminate the problem. Barnes [10] suggested an alternative of a viscous damping approach with the mass components (and hence damping) automatically increased at nodes belonging to buckled elements.

## 6.6 Conclusions

In general, a number of solution methods which have been reported for the form-finding problem fall into either one of two basic approaches, ie. (1) given the surface geometry and boundary conditions, and the equilibrium equations are then solved for the unknown stresses in the surface, and (2) given the stresses in the surface and boundary conditions, and the equilibrium equations are then solved for the unknown surface geometry. There are also methods in which the equilibrium equations are solved for both the unknown stresses in the surface and the unknown surface geometry.

In this thesis, the adopted approach is to use the dynamic relaxation method in solving the equilibrium equations for the unknown surface geometry given the stress distributions and boundary conditions. This approach is highly versatile and applicable in general to most kinds of tension structures. In the form-finding, various controls can be used to adjust the form until the



desired solution is achieved. These form-finding controls as applied to cable nets and prestressed membrane and air-supported structures, are discussed in this chapter. The fabrication patterning and load analysis stages in the design process are also outlined.

From the discussion in this chapter, it is noted that some useful ideas applied in the form-finding process come from areas of differential geometry which have been outlined in detail in chapter 5. The adopted approach for the form-finding involves a trial and error procedure in the solution for the desired form. Hence, it is appropriate to implement this approach with the controls as described in this chapter into an interactive computer-aided design system for tension structures which will be discussed in chapter 7.

## Chapter 7

### Interactive design of tension structures

#### 7.1 Introduction

Until about 1969, tension structures were designed mainly on the basis of physical modelling. Much work in this area has been carried out by Frei Otto at the Institute of Lightweight Structures in Stuttgart. As already discussed in Part I of this thesis, although physical models are useful in the qualitative study of form, concept and visual assessment, quantitative design data is not easily available from them. As a result, there is a need to develop numerical modelling techniques. In addition, it has been shown that the dynamic relaxation method has a few features which are particularly useful for the design of tension structures and is thus the adopted numerical solution method in this thesis. Since the same numerical model is used in the form-finding, load analysis and patterning stages, it is advantageous to integrate all these stages together into one smooth and continuous design process. As mentioned in chapter 6, the adopted approach for the form-finding uses a trial and error procedure in the solution for the desired form. In addition, the form-finding controls used involves form adjustments which will lead to direct effects in a physical sense on the model. Hence, it is easy and useful to assess the impact of previous adjustments which in turn will indicate what further adjustments are required. This suggests the need to implement an interactive strategy for the adopted approach.

From the above considerations, it seems sensible to incorporate the various ideas discussed in earlier chapters into an interactive computer-aided design (CAD) system for tension structures. The development of such a CAD system is the subject of discussion in this chapter, and has been made possible by the availability of powerful hardware with sophisticated graphics capability. The computer software for the CAD system is called 'Tensyl' and was initially developed by Dr. David Wakefield at Buro Happold. Subsequently, as a plan for continued development of the software, a Teaching Company Scheme (TCS) was set up between Buro Happold and City University. A large part of the material in this chapter was produced during the 2-year period (1988-1990) when I was on the TCS. Dr. David Wakefield has also contributed to much development of the software especially at the early stages.

In the CAD system are individual modules for the tasks of form-finding, load analysis and patterning, which are integrated together with a common database. It will be shown later how the CAD system has brought a number of benefits to the design process.



## 7.2 Underlying philosophy

The theory behind the various basic modules of the CAD system has already been outlined in earlier chapters. These modules will be discussed in this chapter with an emphasis on the human user interface aspects. The success of the CAD system depends to a large extent on the implementation of an effective user interface.

The software is written in 'C' programming language and runs within the Unix operating system. The hardware in use is a Hewlett-Packard HP9000/350 workstation with SRX graphics coprocessors and a 19" colour monitor having a 1280×1024 pixel resolution capable of displaying over 16 million colours simultaneously. The 'C' programming language has a few features which make it attractive to be used in the development of a sophisticated CAD system. These features include the data structures, pointers (which are addresses of locations within the memory space) and dynamic memory allocation. The data structures provide a neat way of grouping together information which describes a classification or type. For instance, a data structure may be defined to hold all the variables related to the elastic properties of the membrane elements. With pointers, the data structures and variables stored at various locations within the memory space can be linked together into chains or linked lists. Furthermore, with dynamic memory allocation, the software can allocate and free memory locations depending on the current needs. The Unix operating system also offers some benefits in developing the CAD system. The window and multi-tasking capabilities make it possible to execute a task in a window simultaneously as various tasks in other windows or in the background. In addition, the computational speed of the vast amounts of number crunching involved is increased quite significantly as a result of the floating point accelerator installed into the workstation. The SRX graphics coprocessors implement into hardware the library of graphics routines provided by the Starbase graphics library. These routines are used in the software to generate the graphical images which are displayed on the computer screen. Hence, the generation of these images can be achieved at high speed. This results in a machine which can produce highly realistic graphical images rapidly. In the development of the CAD system, the above mentioned capabilities offered by the hardware are fully exploited.

There are a few principal objectives which form the underlying basis for the development of the CAD system. The software is intended for use within a design office environment. Consequently, it is important that the engineers find the software easy to use, ie. the software should be as user-friendly as is possible. In addition, it is desirable for the software to have a short learning period. Furthermore, it is obviously profitable to reduce the design time as much as possible. In order to fulfill these aims, an effective and functional user interface to the software is essential. A primary factor which contributes towards such an interface is the presence of clarity and consistency throughout.



The user interface has been designed to be fully interactive and based on the concept of the Graphical User Interface (GUI), ie. as much use as possible of graphical images on the screen to inform and guide the user. This involves setting up the CAD system to work within the Window Icon Mouse Pointer (WIMP) environment. The execution and interaction with the CAD system is structured to make use of the accessories such as the windows, icons, mouse and pointers where appropriate. After logging into the workstation, the user can use the Unix operating system to create a number of windows and icons on the screen. An icon is a small picture which represents a closed window. The user can execute an activity or run an application in each window. The operation of the CAD system is initiated by issuing the appropriate command within a window and the user will then enter into the 'master' menu page shown in figure 7.1. Throughout the execution of the CAD system, the screen is divided into areas for the graphics window, menu options and editbox as shown in figure 7.1.

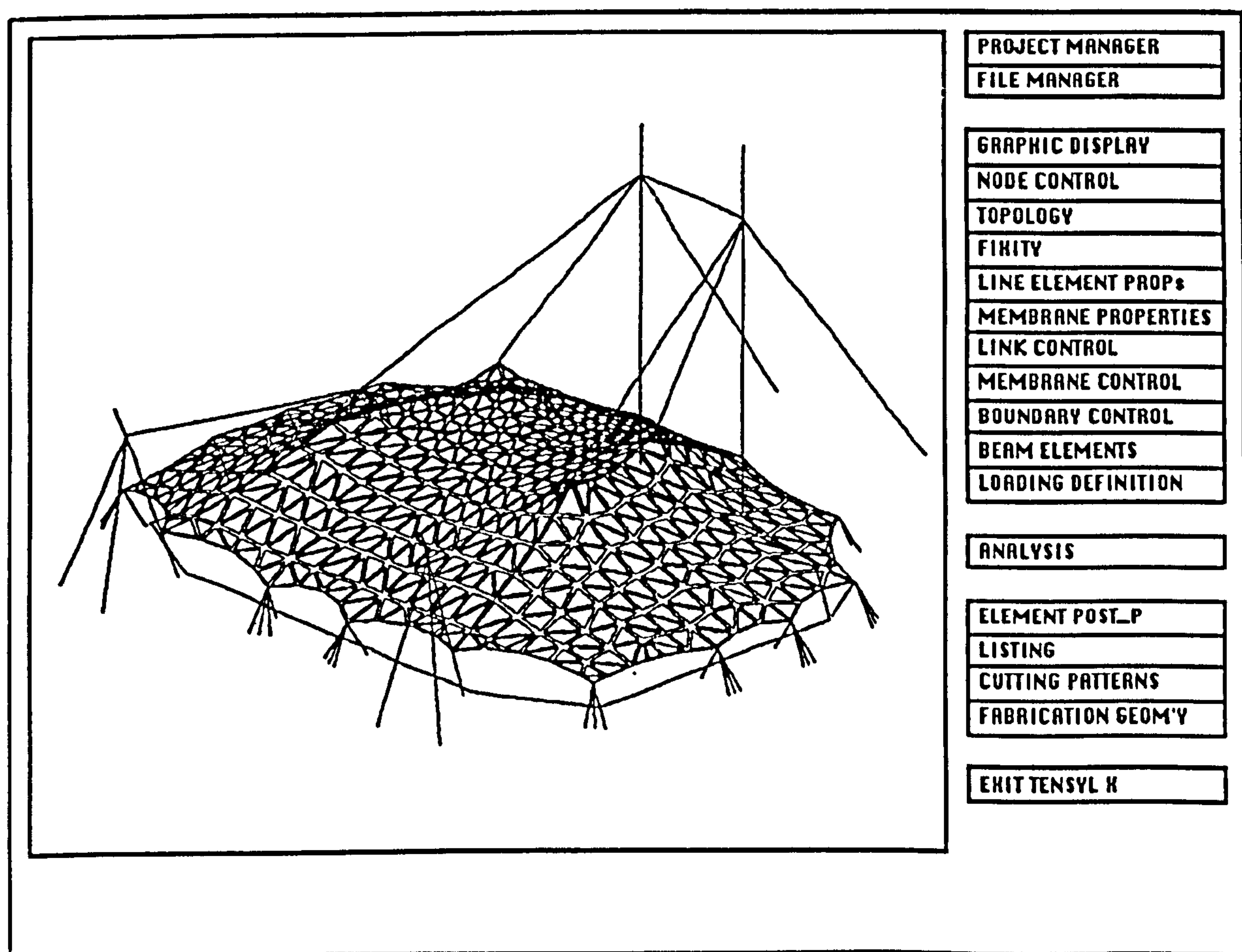


Figure 7.1

A graphical image of the model in its current state is always on display in the graphics window area of the screen. This is because a graphical image is an effective and efficient means of communicating information to the user. It is much easier and thus takes much less time for the user to grasp information which is represented in the form of graphical images rather than texts and numbers. In this respect, there is also much use of colours in the image display to assist the user. Consequently, the user can quickly make an



assessment and respond accordingly to the CAD system. As far as possible, the information of relevance to the current menu page or operation is depicted in the image display. Furthermore, the user can interrogate and interact directly with the graphical image on display in the graphics window. The orientation and angle of view of the model represented by the graphical image is under the direct control of the user. If desired, any part of the graphical image can also be windowed in for a closer inspection.

The CAD system consists of a series of menu pages with each menu page designated for tasks specific to the various stages of the design process. In each menu page, a list of menu options are displayed on the right hand side of the graphics window as shown in figure 7.1. The CAD system is driven by means of interaction with the menu options using a two button mouse with each button assigned to perform specific actions as will be described shortly. A mouse click refers to the press and release of a mouse button. In order to activate a menu option, the user positions the on-screen arrow pointer over the option and then clicks the left mouse button.

A menu option filled in with the red colour indicates that the option is in the active state. A menu option in the non-active (ie. normal) state is indicated by a white option label in a black background. A few menu options are by default in the active state and remain so until they are switched into the non-active state. By activating a menu option in the non-active state, the option is then switched into the active state. In some cases, at the completion of the task associated with a menu option when activated, the option returns to the non-active state. In other cases, by activating a menu option in the non-active state, the option after going into the active state is then switched into another state. In this state, the option label is given a specific colour accordingly, and the option is still in operation and taken to be in the 'on' state. For such a case, the option may indicate that the specific attribute associated with it is switched on, ie. becomes active. This attribute may then be used in conjunction with the operation of another menu option.

By activating the appropriate menu option in the current menu page, the user either initiates the operation associated with the menu option, enters into another menu page or simply as required for the operation which follows. In each of the menu options is an option label. The adopted convention is such that a menu option with a label in upper case can be activated by the user such as to perform a direct operation. The option label itself gives a clue as to the operation associated with the menu option. On the other hand, the user cannot activate a menu option with a lower case label, ie. the option does not have an active state. A lower case label serves to provide for the group of menu options associated with it, an idea about the overall nature of the operations which can be executed using these menu options.

Besides being used to activate a menu option, the left mouse button allows the user to pick the various elements on display in the graphics window. For this purpose, the user may need to enter into the on-screen interaction mode by clicking the right mouse button when appropriate. In this mode, the user



can position the on-screen pointer over any part of an element and the element is then picked by clicking the left mouse button. It is usual for a 'picked' element to be highlighted in red. The user can subsequently exit from the on-screen interaction mode by clicking the right mouse button when appropriate. In addition, the right mouse button can be used to reverse a chain of on-screen actions for instance, to unpick the previous 'picked' elements.

Furthermore, a helpful feature is the varying labels and symbols used for the on-screen pointer to guide the user to the subsequent course of action. Figure 7.2 gives a list of the various forms of the pointer and their associated purposes.

Pointer	Purpose
↑	activate menu option
✕	accept/abort pointer
◆	node pick
◆	membrane pick
◆	link pick
◆	strut pick
◆	boundary pick
◆	field pick
◆	geodesic string pick
◆	cloth pick

Figure 7.2

In most cases, the operation of the CAD system will involve using the arrow pointer to activate a menu option and the arrow pointer will in turn change into the appropriate pointer as given in figure 7.2 for the subsequent actions. For instance, the 'node pick' pointer will suggest to the user that the software awaits the picking of a node on display in the graphics window. For the accept/abort pointer, the user is prompted to confirm a previous action. The user will then respond by either clicking the left mouse button to accept the previous action or clicking the right mouse button to abort the action.



There should be minimum keyboard entries of data and commands with most interaction with the CAD system being executed using the mouse. However, if required, the user will be prompted to enter the data into an editbox displayed beneath the graphics window. In addition, the editbox is used to display supplementary information relevant to the user's current task. On some occasions, the execution of specific operations is controlled from within the editbox. These operations may involve the use of command buttons which are incorporated into the editbox. A command button is activated by placing the arrow pointer over the button followed by a click of the left mouse button.

Finally, if changes whether topological or otherwise have been made to the current model, the database will be automatically updated as the user exits from the current menu page.

### **7.3 The design process**

In general, the design process of a tension structure can be divided into the stages of form-finding, load analysis and patterning. The individual modules for these separate operations are integrated together into the CAD system to make the design process into a smooth and continuous one. A common database is maintained throughout the CAD system so that the user can move conveniently from one stage to another. At the form-finding stage, the aim is to establish an initial equilibrium shape which satisfies the aesthetic and functional requirements of the structure. There is close co-operation between the engineer and the architect at this stage. After achieving the required shape, the model is analysed for the possible loads which may act upon the structure over the period of its design life. If the applied loads cause areas of excessive stresses, wrinkling or structural instability in the model, then it may be necessary to return to the form-finding stage and revise the shape in order to alleviate the problem. When a model which behaves satisfactorily under applied loads is achieved, the data for the production of cutting patterns and fabrication details are processed. The facilities for executing the operations involved in the above mentioned stages of the design process are implemented in the menu options contained within the various menu pages which will be discussed later. In the discussion, the main emphasis will be on the user interface aspects involved in the operations of the menu options. It will show how an effective and functional user interface is implemented into the CAD system.

In the 'master' menu page shown in figure 7.1, the user will exit altogether from the CAD system if the EXIT TENSVL # option is activated, but when any one of the remaining menu options is activated, the user will then enter into a separate menu page to perform specific tasks.



7.4 Project manager

Activate Project:
CURRENT PROJECT
NEW PROJECT

Edit:
ACTIVE PROJ DETAILS

List:
CURRENT PROJECTS
ACTIVE PROJECT LOG

RETURN
--------

Figure 7.3

The PROJECT MANAGER menu page shown in figure 7.3, accessible from the 'master' menu page, is used to manage the various projects previously set up using the software. When a new model is to be set up, the user has to first use the NEW PROJECT option to create a new project title. By activating this option, an editbox as shown below

will then appear beneath the graphics window. The user can enter into the editbox the project title for a new model. The software will then set up a new project directory within the memory of the computer. The future data files for the project will be placed under this directory. At any time, the user can return to this menu page in order to switch from the current project to another. The user can also by activating the RETURN option move back into the 'master' menu page. The menu options in figure 7.3 besides those described above are not functional at present.

Enter REFERENCE NAME of New Project to be Defined ???
--

7.5 File manager

ACTIVE DATA -> FILE
---------------------

Access:
FILE -> ACTIVE DATA

CLEAR ACTIVE DATA
-------------------

Utilities:
LIST DIRCETORY
PRINT ANALYSIS TRACE
COPY FILE
PURGE FILE

RETURN
--------

Figure 7.4

The FILE MANAGER menu page shown in figure 7.4 is where the menu options for the file handling are located. This menu page is accessible from the 'master' menu page. At the various stages of the software execution, the user can access the FILE MANAGER menu page and by activating the ACTIVE DATA -> FILE option, the complete set of data for the current state of the model as stored in the database will then be written into a file created automatically by the software. The current data set in the database is referred to as the active data. A specific number will be assigned to name the file and this file name will be displayed in the editbox beneath the graphics window. The user is required to make a note of this file name. The software will place the file with this name under the project directory for the current model.

Subsequently, if the user needs to return to a previous state of the model, the FILE -> ACTIVE DATA option is available for this purpose. When this option is activated, the user will be prompted to enter a file name into the editbox as shown below, ie.

Enter No of File to be Activated ???
---



which appears beneath the graphics window. The software will open the named file and read into memory the data set stored in the file. This data set in turn becomes the active data of the model. The user will then have as the current state of the model that which is stored in the named file.

The user can continue to work on the model after having the current state of the model written into a file. Furthermore, the user can without worrying make further changes to the model knowing that the model can be returned to its previous state if these changes lead to any undesirable results.

The user can also by activating the RETURN option move back into the 'master' menu page. The menu options in figure 7.4 besides those described above are not functional at present.

## 7.6 Graphic display

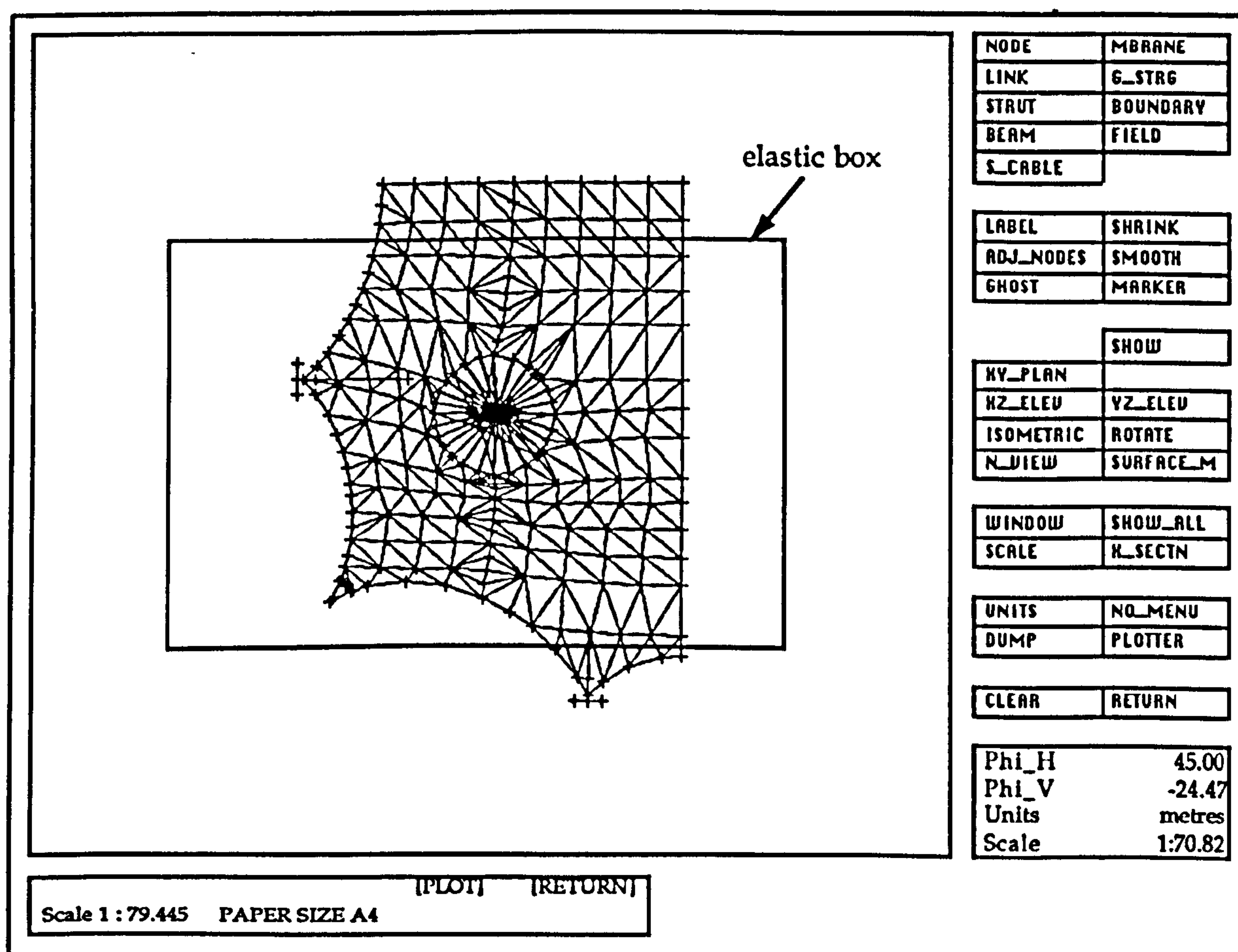


Figure 7.5

The GRAPHIC DISPLAY menu page shown in figure 7.5 provides the menu options which are used to set both the graphics view attributes and element display attributes for the image currently as shown in the graphics window. This menu page is accessible from the 'master' menu page as well as from within most of the other menu pages available in the software. On display in the graphics window area of the screen will be a graphical image of the model in



its current state. The graphical image will always be considered with reference to a right-handed Cartesian coordinate system. The `NO_VIEW` and `NO_MENU` options are not yet functional at the moment.

With an active `HV_PLAN` option, the image shown in the graphics window will correspond to a plan view (ie. the view from above the global  $x-y$  plane) of the model. If instead the `HZ_ELEV`, `VZ_ELEV` or `ISOMETRIC` option is active, then the corresponding global  $x-z$  elevation,  $y-z$  elevation or isometric view of the model will be shown. Furthermore, by activating the `ROTATE` option, an editbox as shown below

Enter Rotations ...	Phi_H	Phi_V
90.00	-90.00	

will then appear beneath the graphics window. The user can directly edit the values of the horizontal and vertical angles currently shown in the editbox. The horizontal angle is an angle in the  $x-y$  plane and is positive when measured in an anti-clockwise sense from the global  $x$ -axis. The vertical angle lies in a plane normal to the  $x-y$  plane and is positive when measured upward from the  $x-y$  plane. These two angles determine the precise angle of view of the model which will be represented in the image shown in the graphics window. As an example, a plan view of the model is equivalent to the case of a horizontal angle of 90.0 degrees and a vertical angle of -90.0 degrees. Hence, using the above options, the user has the means to achieve the desired angle of view of the model.

By activating the `CLEAR` option, the graphics window area of the screen will then be cleared of any graphical image. Subsequently, the user can select the elements to be displayed by activating the appropriate menu options. For instance, with an active `NODE` option and by activating the `SHOW` option, all the nodes in the model will then be displayed in the graphics window. In a similar way, other elements such as the membrane elements and so on, can be selected to be displayed in the graphics window. The elements will be shown in the same colour as that given to the option label for the corresponding menu option when in the 'on' state. For instance, all the nodes will be shown in yellow which is also the colour of the option label for the 'on' `NODE` option. Hence, it is easy to identify from their different colours the various elements currently on display in the graphics window.

Furthermore, the user can also select the attributes which will be used in the graphic display of the different elements in the model. With an active `LABEL` option, the reference numbers of the elements such as the node numbers, the membrane element numbers and so on, will then be shown to label the elements in the graphic display. With an active `SHRINK` option, the membrane elements will be shown in the 'shrunk' mode, ie. slightly apart from each other. Similarly, other elements such as the link elements and so on, can also be shown in the 'shrunk' mode. Furthermore, with an active `MARKER` option, a boundary will be shown with all the nodes lying along the boundary marked with specific symbols. The ends of the boundary will be recognised from their markers which are unlike those given to the remaining nodes along the



along the boundary. The above will similarly apply to the display of a geodesic seam line or slip cable element when the `MARKER` option is active. In addition, an active `GHOST` option means that the elements themselves will not be shown and this option is therefore seldom used. When the `ADJ_NODES` option is active, the elements will then be shown with their nodes labelled with the node numbers.

By default, a boundary will be displayed as a series of lines between the nodes which lie along the boundary. With an active `SMOOTH` option however, a boundary will in turn be displayed as a smooth curve. In this case, a curve will be fitted through the nodes which lie along the boundary. The user can choose if a cubic spline or circular arc will be used for the curve fitting by means of the relevant menu options within the `BOUNDARY CONTROL` menu page which will be described later. In most cases, the cubic spline will be used to derive the smooth curve for the boundary. Similarly, a geodesic seam line or slip cable element will be displayed as a smooth curve when the `SMOOTH` option is active.

By activating the `SCALE` option, an editbox as shown below, ie.

Enter Scale 1 : xxxx (metres) 26.28
--

will then appear beneath the graphics window. The current scale of the image shown in the graphics window will be displayed in the editbox. Subsequently, the user can directly edit the current scale shown and the image will then be shrunk or enlarged accordingly.

The user can also decide on the units in use for the image shown in the graphics window. This requires the use of the `UNITS` option. The horizontal and vertical angles of view, units and scale which currently apply are displayed within a boxed area on the screen as shown in figure 7.5. By default, the software uses the metres units. When the `UNITS` option is activated, the metres units will be switched to the feet units. By activating the `UNITS` option again, the feet units will then be switched back to the metres units.

Furthermore, the `WINDOW` option provides the user with a facility to window in on a specific area of the image shown in the graphics window. When this option is activated, the user will be prompted to first pick a point within the graphics window area. After picking a point, an elastic box will then be drawn with one corner at the first 'picked' point and the diagonally opposite corner at the current position of the arrow pointer. As the user moves the pointer about to define a window, the elastic box will in turn shrink or stretch accordingly. By clicking the left mouse button, the current position of the pointer and the first 'picked' point will then define a window over an area of the image shown in the graphics window. The part of the image which fall within the defined window will then be redrawn enlarged to occupy as much as possible of the graphics window area. In this way, the user can window in on any part of the image in order to have a closer and thus, enlarged view of the image. In fact, the user can continue to window in on an image derived



from a previous windowing exercise. On the other hand, by activating the `SHOW_ALL` option, the image of the entire model will in turn be displayed in the graphics window.

Then, by activating the `DUMP` option, the image as shown in the graphics window will be sent to the laser printer. If instead the `PLOTTER` option is activated, an editbox will then appear beneath the graphics window. On display in the editbox as shown in figure 7.5 will be the parameters such as the plot scale and paper size (ie. A3/A4). The user can directly edit the parameters shown and by activating the [PLOT] button in the editbox, the image in the graphics window will then be sent to the plotter. The image will be plotted according to the parameters set in the editbox.

In addition, there is also the `SURFACE_M` option which provides the facility to show a surface shaded image on the screen (ie. solid modelling). By activating this option, the user will then enter into the `SURFACE_M` menu page which will be fully described later in section 7.19.

If the `RETURN` option is activated, the user will exit from the `GRAPHIC DISPLAY` menu page and return to the previous menu page.

With the menu options as described above, the user has complete control over the image shown in the graphics window. In addition, the user interface in use offers an easy, highly flexible and effective means of achieving the desired image. In fact, the user can enter into the `GRAPHIC DISPLAY` menu page from within most of the other menu pages available in the software. Hence, while working within a separate menu page, the user can access the `GRAPHIC DISPLAY` menu page and use the menu options described above to obtain the desired image on the screen before returning to the current menu page. For instance, the user may need to window in on a specific area of the image or change the angle of view while working in say, the `FIXITY` menu page which will be described later.

## **7.7 Node control**

In the process of setting up a new model, it is customary to first work out the node coordinates of a few system points with reference to a chosen right-handed cartesian coordinate system. The `NODE CONTROL` menu page shown in figure 7.6 provides the means for the user to input these node coordinates into the database of the software. This menu page is accessible from the 'master' menu page. On display in the graphics window of the screen will be a graphical image of the model in its current state. The `RE_PRINT` option serves to refresh the current image display in the graphics window. The `EDIT_VIEW` option enables the user to access the `GRAPHIC DISPLAY` menu page in order to achieve the desired image display in the graphics window.



RE_PAINT	EDIT_VIEW
BACK_UP	RESTORE

NODE	BOUNDARY
ZONE	

HY_PLANE	2N_LINE
3N_PLANE	2N_PLANE
KEYBOARD	

ADD	DELETE
MOVE	CHECK

ALL_NODES	SELECT_N
CLEAR_ALL	PICK_FLD
MOVE	DUPLICATE
NODE_ONLY	ELEM_ALSO
TRANSLATE	ROTATE

LISTING	RETURN
---------	--------

Next, the **NODE** option allows the user to define a new node by specifying the global coordinates of the node. By activating the **ADD** option when both the **NODE** and **KEYBOARD** options are in the active state, the user will then be prompted to enter into the editbox as shown below, ie.

Enter Coords of New Node ... XYZ ???
---

the global  $x$ ,  $y$  and  $z$  coordinates for each of the system points. With each set of global  $x$ ,  $y$  and  $z$  coordinates input through the editbox, the software will automatically create a new node with the specified coordinates. The new node will also be assigned with a node number. Hence, a new node with the specified coordinates will be created at each of the system points. If the right mouse button is clicked instead of entering a set of coordinates into the editbox, the user will then exit from the editbox control. Alternatively, the user can also exit from the editbox control by pressing the 'ESC' button on the

Figure 7.6

keyboard.

By activating the **CHECK** option, the user will be prompted to pick a node and the 'picked' node will be highlighted in red. The current coordinates of the node will also appear in the editbox beneath the graphics window. The user can therefore easily find out the current coordinates of any node in the model. This is necessary since the current node position is always that of the deformed structure under defined prestress or load. If desired, the user can also directly edit the node coordinates shown in the editbox.

Furthermore, the **DELETE** option allows the user to pick and remove a node from the model. The **MOVE** option is used to move a 'picked' node to a new location.

There are also options which operate on a collection of nodes at the same time. These nodes can be picked using the **SELECT\_N** option. If the nodes lying within a field are to be selected, the **PICK\_FIELD** option can be used instead. The **ALL\_NODES** option enables the user to select all the nodes in the model. On the other hand, all the nodes which have been selected previously can also be deselected using the **CLEAR\_ALL** option. Subsequently, the **TRANSLATE** and **ROTATE** options can either apply to the selected nodes themselves if the **MOVE** option is active or to a set of additional nodes which are a duplicate of the selected nodes if the **DUPLICATE** option is active. In addition, with an active **NODE\_ONLY** option, the **TRANSLATE** and **ROTATE** options will then only operate on the corresponding nodes. However, if the **ELEM\_ALSO** option is active instead, the **TRANSLATE** and **ROTATE** options will then apply to the corresponding nodes as well as the elements which are connected to these nodes. When the **TRANSLATE**



option is activated, the user will be prompted to enter into the editbox as shown below, ie.

Enter Structure Translations DX DY DZ ???
--

the appropriate displacements to be applied to the corresponding nodes and/or elements accordingly. These displacements refer to translations in the global x-, y- and z-axes directions. When the **ROTATE** option is activated, the user will be prompted to enter into the editbox as shown below, ie.

TILT_AXIS		X	Y	Z	ANGLE (deg)	[ROTATE]
Pt	T1	0.000000	0.000000	0.000000	0.000	
	T2	1.000000	0.000000	0.000000		[RETURN]

an angle of rotation and the definition of an axis about which the rotation will take place.

The **LISTING** option is used to output to the laser printer the coordinates of all the nodes in the model. By activating the **RETURN** option, the user will then go back to the 'master' menu page. The remaining options in the **NODE CONTROL** menu page not mentioned above are not functional at present.

## 7.8 Topology

The **TOPOLOGY** menu page shown in figure 7.7(a) provides the menu options which enable the user to make topological adjustments to the model. The user will enter into this menu page from the 'master' menu page. On display in the graphics window area of the screen will be a graphical image of the model in its current state. The **RE\_PAINT** option serves to refresh the current image display in the graphics window. The user can access the **GRAPHIC DISPLAY** menu page via the **EDIT\_VIEW** option in order to achieve the desired image display in the graphics window.

For a newly created model, a few system points may have just been defined within the **NODE CONTROL** menu page described above in section 7.7. The user can in turn define a series of boundaries between the system points. In addition, a temporary node may be defined about half-way between two system points. In this way, the initial curvature of the boundary between the two system points can be approximated. A boundary may be used to represent an edge scallop cable or a ridge cable which separates two fields.

With an active **ADD** option and by activating the **BOUNDARY** option, the user can then proceed to define a new boundary. The user can subsequently enter into the on-screen interaction mode by clicking the right mouse button. This is followed by a switch of the on-screen arrow pointer into the 'node pick' pointer. The user can in turn use the 'node pick' pointer to pick a node and the first 'picked' node will be highlighted in red. An elastic line in yellow will always be drawn from the previous 'picked' node to the current location of



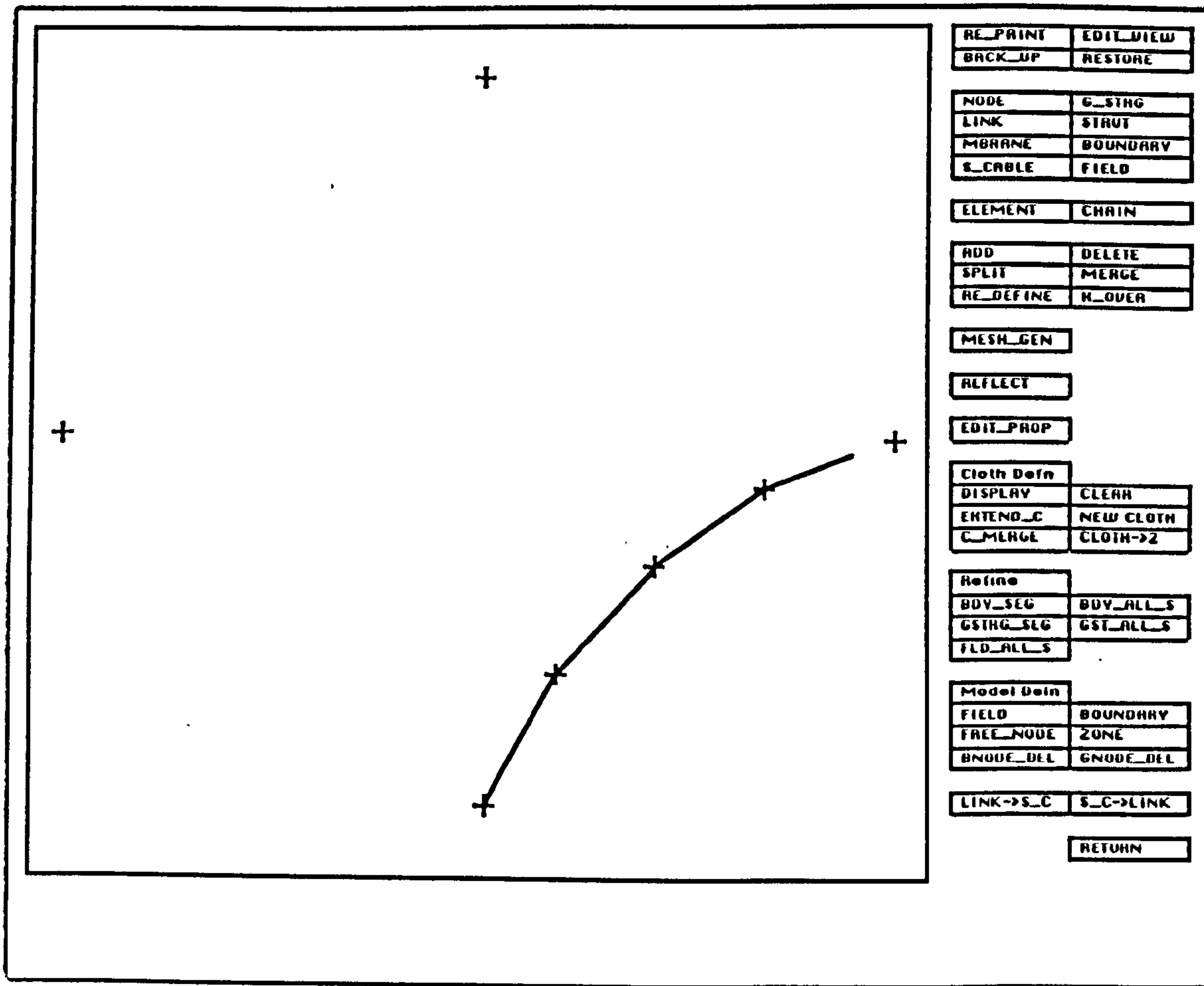


Figure 7.7(a)

the pointer while in the process of picking the next node. In this case, as the user moves the pointer about to pick the second node, the elastic line will shrink or stretch in order to join the current location of the pointer to the first 'picked' node. When the second node is picked, it will similarly be highlighted in red. A line highlighted in red will be drawn from the first to the second 'picked' node. In this way, the user can proceed to pick the remaining nodes which will lie along the boundary currently being defined. The user can also step backward and unpick the nodes which have been picked so far to lie along the boundary currently being defined. For instance, when prompted to pick the fourth node, the user can click the right mouse button instead of picking the fourth node. Subsequently, the highlighted line previously drawn from the second to the third 'picked' node will disappear. The third 'picked' node will be unpicked and the red highlight previously given to the node will be replaced by the normal colour, ie. yellow. If the right mouse button is clicked again, the user will then unpick the second 'picked' node. In this way, the user can step backward along the boundary definition. On the other hand, the user can continue with the node picking until the last node has been picked. Finally, the boundary definition will be completed by picking the last node a second time. The accept/abort pointer will then appear. If the line highlighted in red joining all the 'picked' nodes is accepted, a new boundary will be defined and the definition data of the new boundary automatically set up in the database. The new boundary will be redrawn in its



normal colour, ie. yellow. By repeating the above operations, further new boundaries can be defined in the model.

With an active **DELETE** option and by activating the **BOUNDARY** option, the user can then proceed to delete an existing boundary. The user has to first enter into the on-screen interaction mode by clicking the right mouse button. This is followed by a switch of the on-screen arrow pointer into the 'boundary pick' pointer. The user can in turn use the 'boundary pick' pointer to pick an existing boundary and the 'picked' boundary will be highlighted in red. The accept/abort pointer will then appear. If the 'picked' boundary is accepted, the boundary will then be deleted from the model. By repeating the above operations, further existing boundaries can be removed from the model.

With both the **ADD** and **G\_STRING** options in the active state, the user can perform the task of defining a new geodesic string or seam line. Conversely, when both the **DELETE** and **G\_STRING** options are active, the user can initiate the deletion of an existing geodesic seam line. In both cases, the user interface and the operations involved will be similar to those in the case of the boundary described above. A new geodesic seam line will be shown in the yellow colour.

Furthermore, when both the **ADD** and **S\_CABLE** options are active, the user is ready to define a new slip cable element. Conversely, with both the **DELETE** and **S\_CABLE** options in the active state, the user can proceed with the deletion of an existing slip cable element. In both cases, the user interface and the operations involved will be similar to those in the case of the boundary described above. It is noted that a new slip cable element will given a default set of elastic properties. In addition, the element will be shown in the magenta colour.

When a new link element is to be defined, then both the **ADD** and **LINK** options have to be in the active state. The user can then enter into the on-screen interaction mode by clicking the right mouse button. This is followed by a switch of the on-screen arrow pointer into the 'node pick' pointer. The user can in turn use the 'node pick' pointer to pick a node and the first 'picked' node will be highlighted in red, and the user will then be prompted to pick the second node. At this stage, if the right mouse button is clicked, the first 'picked' node will then be unpicked and the red highlight previously given to the node will be replaced by the normal colour, ie. yellow. On the other hand, when the second node is picked, it will be highlighted in red, and a line highlighted in red will be drawn between the two 'picked' nodes. The accept/abort pointer will then appear. If the highlighted line is accepted, a new link element will then be defined between the two 'picked' nodes and the definition data of the new link element automatically set up in the database. A default set of elastic properties will be assigned to the new link element shown in the green colour. By repeating the above operations, further new link elements can be defined in the model.

When both the **DELETE** and **LINK** options are active, the user is ready to delete an existing link element. The user can then enter into the on-screen interaction



mode by clicking the right mouse button. This is followed by a switch of the on-screen arrow pointer into the 'link pick' pointer. The user can in turn use the 'link pick' pointer to pick a link element and the 'picked' link element will be highlighted in red. The accept/abort pointer will then appear. If the 'picked' link element is accepted, the link element will then be deleted from the model. By repeating the above operations, further link elements can be removed from the model.

With both the `ADD` and `STRUT` options in the active state, the user can perform the task of defining a new strut element. On the other hand, when both the `DELETE` and `STRUT` options are active, the user can initiate the deletion of an existing strut element. In both cases, the user interface and the operations involved will be similar to those in the case of the link element described above. A new strut element will be shown in the magenta colour.

Subsequently, the user can proceed to define a new membrane element when both the `ADD` and `MBRANE` options are active. The user has to first enter into the on-screen interaction mode by clicking the right mouse button. This is followed by a switch of the on-screen arrow pointer into the 'node pick' pointer. The user can in turn use the 'node pick' pointer to pick a node and the first 'picked' node will be highlighted in red, and the user will then be prompted to pick the second node. In this way, the second and the third nodes can be picked, and these two 'picked' nodes will similarly be highlighted in red. If required, the user can also step backward and unpick the nodes which have been picked so far. For instance, when prompted to pick the third node, the user can click the right mouse button instead of picking the third node. The second 'picked' node will then be unpicked and the red highlight previously given to the node will be replaced by the normal yellow colour. If the right mouse button is clicked again, the user will then unpick the first 'picked' node. On the other hand, after picking the third node, it will be highlighted in red, and a triangle highlighted in red will then be drawn between the three 'picked' nodes. The accept/abort pointer will then appear. If the highlighted triangle is accepted, a new triangular membrane element will then be defined between the three 'picked' nodes and the definition data of the new membrane element automatically set up in the database. A default set of elastic properties will be assigned to the new membrane element shown in the cyan colour. It is noted that the three nodes of the new membrane element should have been picked in an anti-clockwise sense when looking from above the model. This is required so that the membrane 'top' surface is consistent with the load directions. In addition, the first and the second 'picked' nodes (ie. which define the first side of the new membrane element) should lie along a geodesic seam line or at least be in a direction as close as possible to that of an adjacent geodesic seam line. By repeating the above operations, further new membrane elements can be defined in the model.

When the user decides to delete an existing membrane element, then both the `DELETE` and `MBRANE` options have to be in the active state. The user has to first enter into the on-screen interaction mode by clicking the right mouse button. This is followed by a switch of the on-screen arrow pointer into the



'membrane pick' pointer. The user can in turn use the 'membrane pick' pointer to pick a membrane element and the 'picked' membrane element will be highlighted in red. The accept/abort pointer will then appear. If the 'picked' membrane element is accepted, the membrane element will then be deleted from the model. By repeating the above operations, further membrane elements can be removed from the model.

Furthermore, the user can also proceed to define a new node when both the `ADD` and `NODE` options are in the active state. The user has to first enter into the on-screen interaction mode by clicking the right mouse button. This is followed by a switch of the on-screen arrow pointer into the 'node pick' pointer. In this case, the user has to pick the three nodes which will define the plane in which the new node will lie. By performing the similar operations as in the case when defining a new membrane element described above, the three nodes will be picked and highlighted in red. These nodes can be any three individual nodes in the model and can also be picked in whatever sense or order. The pointer will then switch into a small cross symbol. When the cross symbol is at the location where the new node will be defined, the user can click the left mouse button. Subsequently, this location will be indicated by a small cross marker coloured in red. The accept/abort pointer will then appear. If the highlighted marker is accepted, a new node will then be defined at the location of the marker. This new node will also lie within the plane defined by the three 'picked' nodes. The definition data of the new node will automatically be set up in the database. By repeating the above operations, further new nodes can be defined in the model.

When both the `DELETE` and `NODE` options are active, the user can initiate the deletion of an existing node. The user has to first enter into the on-screen interaction mode by clicking the right mouse button. This is followed by a switch of the on-screen arrow pointer into the 'node pick' pointer. The user can in turn use the 'node pick' pointer to pick a node, and the 'picked' node and all elements connected to it will be highlighted in red. The accept/abort pointer will then appear. If the 'picked' node is accepted, the node and all the elements connected to it will then be deleted from the model. By repeating the above operations, further nodes can be removed from the model.

After defining the relevant boundaries, the user can proceed to define a new field. For this purpose, both the `ADD` and `FIELD` options have to be in the active state. The user has to first enter into the on-screen interaction mode by clicking the right mouse button. This is followed by a switch of the on-screen arrow pointer into the 'boundary pick' pointer. The user can in turn use the 'boundary pick' pointer to pick a boundary and the 'picked' boundary will be highlighted in red. The user will then be prompted to pick the next boundary. In this way, the user can proceed to pick the remaining boundaries which will define the new field. The user can also step backward and unpick the boundaries which have been picked so far. For instance, when prompted to pick the fourth boundary, the user can click the right mouse button instead of picking the fourth boundary. The third 'picked' boundary will then be unpicked and the red highlight previously given to the boundary will be



replaced by the normal yellow colour. If the right mouse button is clicked again, the user will then unpick the second 'picked' boundary. If necessary, the user can step backward through all the previous 'picked' boundaries. On the other hand, the user can continue with the boundary picking until finally the last boundary is picked to complete the definition of the new field. The last 'picked' boundary should join up with the first 'picked' boundary so that all the 'picked' boundaries will form a closed loop enclosing the field being defined. The definition data of the new field will automatically be set up in the database. Subsequently, all the boundaries enclosing the new field will be redrawn in the green colour. By repeating the above operations, further new fields can be defined in the model.

When both the **DELETE** and **FIELD** options are active, the user can proceed to delete an existing field. The user has to first enter into the on-screen interaction mode by clicking the right mouse button. This is followed by a switch of the on-screen arrow pointer into the 'field pick' pointer. The user can in turn use the 'field pick' pointer to pick a field and all the boundaries enclosing the 'picked' field will be highlighted in red. The accept/abort pointer will then appear. If the 'picked' field is accepted, the field will then be deleted from the model. By repeating the above operations, further existing fields can be removed from the model.

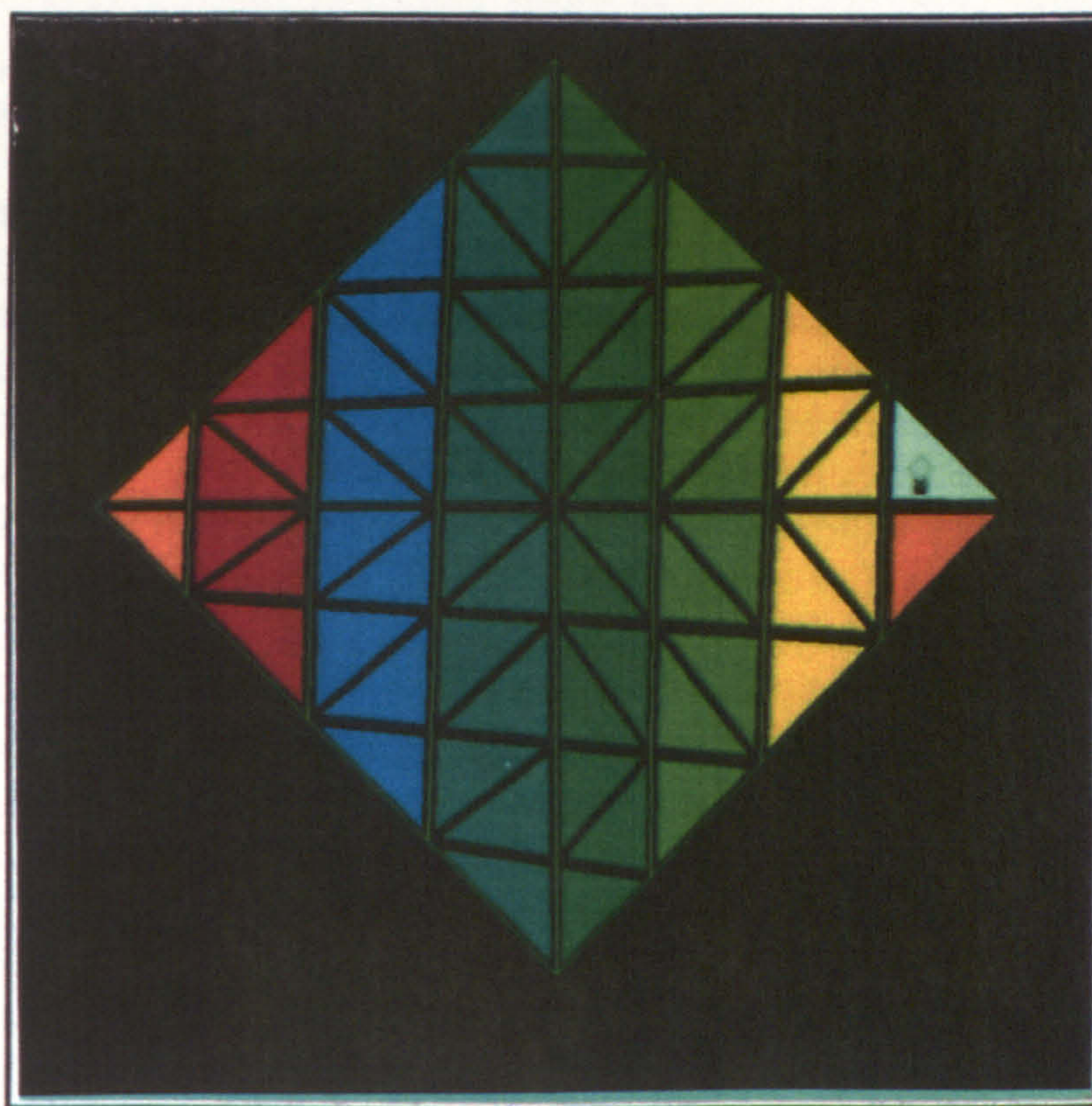


Figure 7.7(b)

Furthermore, the menu options grouped under the **cloth Defn:** label allow the user to perform operations which are specific to cloths. The new membrane elements derived from the mesh generation described later in section 7.9, will be assigned as belonging to the various cloths in the field. By activating the



**DISPLAY** option, all the membrane elements which belong to a cloth will be drawn filled in with the colour designated to the cloth as shown below in figure 7.7(b).

The user can therefore easily check the cloth definitions and decide if any adjustments need to be made. The **EXTEND\_C** option is used to redefine or extend a cloth definition in order to include further membrane elements. When this option is activated, the user will be prompted to pick a cloth. After picking a cloth, the user will be prompted to pick the membrane elements to be included into the definition of the 'picked' cloth. The 'picked' membrane elements will then be drawn filled in with the colour designated to the 'picked' cloth. Furthermore, the **NEW\_CLOTH** option when activated, will enable the user to establish a new definition for a cloth. The user will be prompted to pick all the membrane elements which will constitute a new cloth definition. When a membrane element is picked, it will be drawn filled in with the white colour. After picking the appropriate membrane elements, the user can click the right mouse button and the 'picked' elements will then be redrawn filled in with the colour designated to the cloth. By activating the **CLEAR** option, all the membrane elements in the model will then be redrawn without being filled in and this action is necessary before any one of the other menu options can be used.

If necessary, the **CLOTH->2** option allows the user to split a cloth into two narrower ones. This option has also been implemented within the **ADJUST** menu page. A full outline of this option will be given when the **ADJUST** menu page is described later in section 7.18.

On the other hand, the **C\_MERGE** option is used to achieve the reverse, ie. merging two cloths into one. When this option is activated, the user will be prompted to pick the first cloth and all the sides of the first 'picked' cloth will be highlighted in red. The accept/abort pointer will then appear. If the first 'picked' cloth is accepted, the user will then be prompted to pick the second cloth and all the sides of the second 'picked' cloth will similarly be highlighted in red. It is noted that the second 'picked' cloth should have a side which is shared by the first 'picked' cloth. If the second 'picked' cloth is accepted, the two 'picked' cloths will then be merged together to produce a single cloth. The software will automatically delete the appropriate nodes and elements within the two 'picked' cloths, and generate the new elements for the 'merged' cloth.

Under the **Refine:** label are a group of menu options which are used to refine the topologies of boundaries, geodesic seam lines and cloths. When the **BDY\_ALLS** option is activated, the user will be prompted to pick a boundary. The 'picked' boundary will be highlighted in red and the accept/abort pointer will then appear. If the 'picked' boundary is accepted, the number of segments in the 'picked' boundary will then be doubled. Each successive pair of nodes along a boundary will define a segment. With a doubling of the number of segments, new nodes will be generated along the 'picked' boundary. As a result, the appropriate existing elements will be deleted and replaced with



new ones generated to be consistent with the more refined definition of the 'picked' boundary. These various topological adjustments will be carried out automatically within the software. For the `GST_ALL_S` option, the above actions apply similarly except that this option is used instead to obtain a more refined definition of a geodesic seam line.

On the other hand, the `BDV_SEG` option is used to produce a local refinement of a segment of a boundary. When this option is activated, the user will be prompted to pick a point somewhere along a segment of a boundary. The 'picked' point will be indicated by a small cross symbol highlighted in white. A new node will be generated at the point. The new node will in turn divide the segment into two new and smaller segments. In addition, the appropriate existing elements will be deleted and replaced with new ones generated to be consistent with the two new segments. For the `GST_SEG` option, the above actions apply similarly except that this option is used instead to achieve a local refinement of a segment of a geodesic seam line.

Furthermore, the `LINK->S_C` option provides the user with a means of converting a series of link elements into a slip cable element while the `S_C->LINK` option serves the reverse function, ie. is used to switch a slip cable element into a series of link elements. When the `LINK->S_C` option is activated, the user will be prompted to pick a series of link elements. The 'picked' series of link elements will be highlighted in red and the accept/abort pointer will then appear. If the user accepts, the 'picked' series of link elements will then be converted into a slip cable element. When the `S_C->LINK` option is activated, the user will be prompted to pick a slip cable element. The 'picked' slip cable element will be highlighted in red and the accept/abort pointer will then appear. If the user accepts, the 'picked' slip cable element will then be switched into a series of link elements.

The `REFLECT` option allows the user to reflect the entire model about a specified vertical plane. When this option is activated, the user will be prompted to pick two nodes and the two 'picked' nodes will be highlighted in red. A line highlighted in red will also be drawn between the two 'picked' nodes and the accept/abort pointer will then appear. The highlighted line will represent a vertical plane of reflection. If the highlighted line is accepted, the entire model will then be reflected about the specified vertical plane of reflection.

Under the `Model Deln:` label are a group of menu options which can be used to delete specific items from the model. By activating the `FREE_NODE` option, all the free nodes (ie. nodes not connected to any elements) will be deleted from the model. When the `FIELD` option is activated, the user will be prompted to pick a field, and all the nodes and elements within the 'picked' field will be highlighted in red. The accept/abort pointer will then appear. By clicking the left mouse button, all the nodes and elements within the 'picked' field will then be deleted from the model.

Furthermore, the `BNODE_DEL` option provides a means to perform the intelligent deletion of a node lying along a boundary. When this option is activated, the



user will be prompted to pick a node which lies along a boundary. The 'picked' node will be highlighted in red and the accept/abort pointer will then appear. If the 'picked' node is accepted, the node will be removed from the boundary and the definition data of the boundary will then be revised accordingly. In addition, the elements connected to the 'removed' node will be deleted with the adjacent elements reshuffled accordingly to be consistent with the revised definition of the boundary. In the case of the `GNODE_DEL` option, the above actions apply similarly except that this option is used instead for the intelligent deletion of a node lying along a geodesic seam line.

The user can also by activating the `RETURN` option move back into the 'master' menu page. The operations of the `MESH_GEN` option will be discussed below in section 7.9. The options in the `TOPOLOGY` menu page besides those described above are not functional at present.

As the topological adjustments described above are made to the model, the graphical image display will be updated appropriately to illustrate the effects of these adjustments. Furthermore, these topological adjustments will disturb the equilibrium of the model and this means that the model has to be reanalysed in order to establish its new equilibrium.

## 7.9 Mesh generation

The `MESH_GEN` option in the `TOPOLOGY` menu page shown in figure 7.7(a) provides a mesh generation facility which greatly facilitates the task of generating new elements. This facility allows many new elements to be created all at once instead of having to define each of the new elements individually. Hence, the effort and time needed to set up the entire model will be much reduced. The mesh generation is to be carried out on a field-by-field basis. When the `MESH_GEN` option is activated, the user will be prompted to pick a field. After picking a field, the user will then automatically enter into the `MESH_GEN` menu page shown below in figure 7.8.

Under the `M_Line:` label are the `ADD` and the `DELETE` options. By default, the `ADD` option is active, and the user is ready to sketch a series of mesh lines each of which will begin at one boundary and end at another boundary in order to lay a rough grid over the field which has been picked earlier. There is no restriction on the sense and order of defining the mesh lines. First, the user has to enter into the on-screen interaction mode by clicking the right mouse button. Then, the user will be prompted to pick a point somewhere along one of the boundaries of the field. The first 'picked' point will mark the beginning of a mesh line. The user can continue to pick further points which will define the path of the mesh line across the field. A white line will be drawn to join up all the previous 'picked' points. In addition, an elastic line in white will always be drawn from the most recent 'picked' point to the current location of the pointer while in the process of picking the next point. In this case, as the user positions the pointer to pick the second point, the elastic line will shrink or stretch in order to join the current location of the pointer to the first



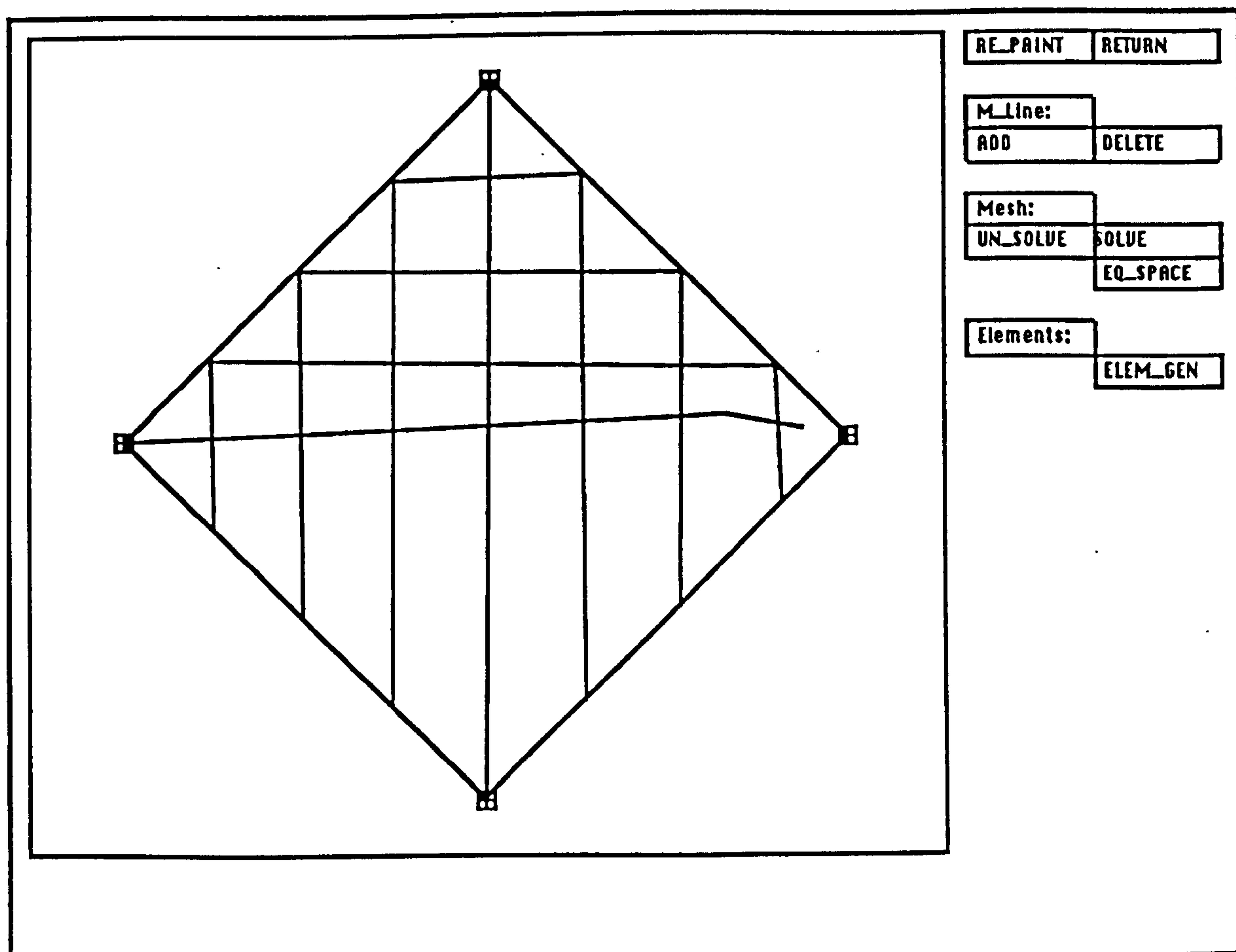


Figure 7.8

'picked' point on a boundary. The user can also step backward and unpick the points which have been picked so far. By clicking the right mouse button, the most recent 'picked' point will then be unpicked and the graphic display of the 'picked' points adjusted accordingly. In this way, further 'picked' points can similarly be unpicked if required. On the other hand, the definition of the mesh line will be completed by picking the last point which should be somewhere along a boundary. The new mesh line will then be shown in the yellow colour. There are a few conditions which may affect the position of the 'picked' point along a boundary where the mesh line will begin or end. If the 'picked' point is very close to the node at either end of the boundary, the point will then snap onto the node. In addition, if the 'picked' point is very close to a node along the boundary which is shared with another field, the point will snap onto the node. Furthermore, if the 'picked' point is very close to the position along the boundary where the beginning or end of another mesh line is, the point will snap onto that position. Hence, if any of the above conditions apply, the position of the first or last 'picked' point will then be determined accordingly. By repeating the above operations, further mesh lines can be defined within the field.

If desired, any of the mesh lines which have been defined can also be removed. This is achieved with an active **DELETE** option. The user has to first enter into the on-screen interaction mode by clicking the right mouse button. This is followed by a switch of the on-screen arrow pointer into the 'mesh



line pick' pointer. The user can in turn use the 'mesh line pick' pointer to pick a mesh line and the 'picked' mesh line will be highlighted in red. The accept/abort pointer will then appear. If the 'picked' mesh line is accepted, the mesh line will then be deleted from the field. By repeating the above operations, further mesh lines can be removed from the field.

After defining a rough grid of mesh lines over the field, the user can activate the `SOLVE` option. The grid will then be 'solved' in order to calculate the initial coordinates of node points at mesh line cross-overs by the weighted interpolation of the end coordinates of these lines. The 'solved' grid of mesh lines will be redrawn in the white colour. The node coordinates calculated will be needed in the generation of new elements which follows. After being solved, the grid of mesh lines can also be 'unsolved' and this is achieved by activating the `UNSOLVE` option. The 'unsolved' grid of mesh lines will be redrawn in the yellow colour.

## 7.10 Element generation

Under the `Elements:` label in the `MESH_GEN` menu page shown in figure 7.8 is the `ELEM_GEN` option which when activated brings the user into the `ELEM_GEN` menu page shown in figure 7.9. The menu options available within this menu page allow the user to decide on the new elements which will be generated from the 'solved' grid of mesh lines established previously within the `MESH_GEN` menu page. The default case is for the `ADD` option to be in the active state.

MESH_GEN	
M_Line:	
FULL	PART
Element:	
LINK	S_CABLE
MBRANE	G_STRG
CLOTH	
ADD	DELETE
L_Prop:	
LAST_PROP	NEW_PROP
NEXT_PROP	

Figure 7.9

Under the `Element:` label are a group of menu options of which the `G_STRG` option is active by default. Subsequently, the user has to enter into the on-screen interaction mode by clicking the right mouse button. The user will then be prompted to pick a mesh line from which a new geodesic seam line will be generated. The 'picked' mesh line will be given a yellow colour. After picking the further mesh lines which will define the new geodesic seam lines, the user can exit from the on-screen interaction mode by clicking the right mouse button. With the `ADD` option still active, the user can choose to activate the `LINK` option and then reenter into the on-screen interaction mode. In this case, the user will pick the mesh lines from which new link elements will be generated, and the 'picked' mesh lines will be shown in green. Furthermore, with both the `ADD` and

`MBRANE` options in the active state, the new membrane elements will be generated from the 'solved' grid of mesh lines when the right mouse button is clicked. The new membrane elements will be shown in the cyan colour.

If required, the user can also undo the actions taken when the `ADD` option is active as described above, by using the `DELETE` option. In the case when both the



**DELETE** and **G\_STRG** options are active, the user can enter into the on-screen interaction mode and pick the mesh lines which are shown in yellow. As described above, a yellow mesh line indicates that the mesh line will be used to generate a new geodesic seam line. In this case, a 'picked' yellow mesh line will be redrawn in white and will in turn play no part in generating a new geodesic seam line. When both the **DELETE** and **LINK** options are active, the user can enter into the on-screen interaction mode and pick the mesh lines which are shown in green. As mentioned above, a green mesh line indicates that the mesh line will be used to generate a series of new link elements. In this case, a 'picked' green mesh line will be redrawn in white and no new link elements will be generated from it. Furthermore, with both the **DELETE** and **MBRANE** options in the active state, the new membrane elements previously generated will be deleted from the field when the right mouse button is clicked. This is followed by an updating of the screen display accordingly.

In the above, when either the **LINK** or **MBRANE** option is active, an editbox will appear beneath the graphics window. On display in the editbox will be the elastic properties which apply either to the link or membrane elements accordingly. With an active **LINK** option, the elastic properties shown in the editbox will consist of the **EA** (ie. modulus of elasticity  $\times$  cross-sectional area) and self-weight values. With an active **MBRANE** option however, the elastic properties shown in the editbox will consist of the moduli of elasticity and Poisson's ratios for the warp and fill directions, shear modulus and self-weight values. By activating the **NEW\_PROP** option, a new set of elastic properties will be created and added to the list of elastic property sets already established in the database. The new set assigned with some default values will be shown in the editbox. If desired, the user can directly edit the values shown in the editbox. When the **LAST\_PROP** option is activated, the previous set in the list of elastic property sets will then be shown in the editbox. By activating the **NEXT\_PROP** option, the next set in the list of elastic property sets will then be shown in the editbox. The set of elastic properties currently shown in the editbox will be taken as the active elastic property set. When the new link or membrane elements are generated as described above, these elements will be given the active elastic property set.

By activating the **MESH\_GEN** option, the user will exit from the **ELEM\_GEN** menu page and return to the **MESH\_GEN** menu page shown in figure 7.8. Subsequently, the user can return to the **TOPOLOGY** menu page shown in figure 7.7(a), and the new link elements and geodesic seam lines will be generated from the 'solved' grid of mesh lines as the user leaves the **MESH\_GEN** menu page. The element generation will affect the definitions of the boundaries which enclose the field. Hence, the definition data of these boundaries will also be adjusted accordingly. Using the various menu options in the **TOPOLOGY** menu page described earlier in section 7.8, the user can if required make further topological adjustments to the new elements derived from the mesh generation.



7.11 Fixity

The proper restraints should be prescribed to the model in order to give a realistic representation of the boundary conditions. The software provides the `FIXITY` menu page shown in figure 7.10 for this purpose. This menu page is accessed from the 'master' menu page. Again, the emphasis is on making the menu and on-screen interactions highly interactive. In the graphics window is a graphical image of the model in its current state. The `RE_PAINT` option serves to refresh the current image display on the screen. If required, the user can access the `GRAPHIC DISPLAY` menu page via the `EDIT_VIEW` option in order to make adjustments to the current view setting for the on-screen image. When a desired view of the image has been obtained or at any time, the user can return to the `FIXITY` menu page. The `DUMP` option is used to send a graphic dump of the on-screen image to the laser printer.

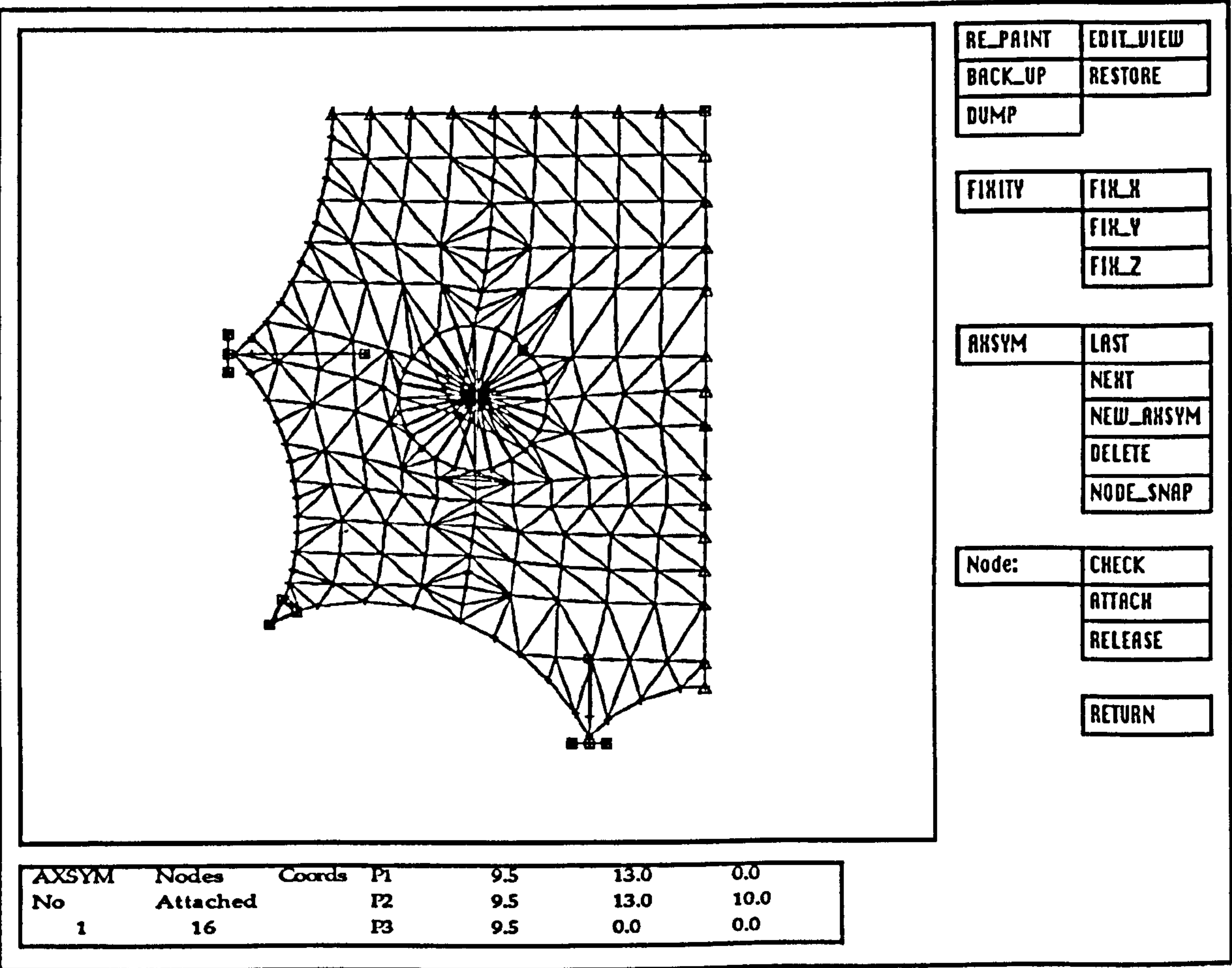


Figure 7.10

There are two means of prescribing the nodal restraints, ie. by using either (i) translational fixities in the global  $x$ -,  $y$ - and  $z$ -directions or (ii) planes of symmetry. In this case, the global  $x$ -direction is taken as the direction of the global  $x$ -axis in the model and so on. By activating the `FIXITY` menu option, the user enters into the mode for option (i). Conversely, the mode for option (ii) corresponds to an active `AHSYM` menu option. In conjunction with these two modes, three further options are available to the user, ie. the `CHECK`, `ATTACH` and



**RELEASE** options all of which are grouped under the **Node:** label. By using the **CHECK** option, the user can inspect the current restraint at a node. The **ATTACH** option is used to prescribe a restraint to a node. The **RELEASE** option is used to delete the current restraint at a node.

The **CHECK**, **ATTACH** and **RELEASE** options all operate through on-screen interaction. The user initiates this interaction by clicking the right mouse button. This is followed by a switch of the on-screen pointer into the 'node pick' pointer. The user can in turn use the 'node pick' pointer to pick a node and the 'picked' node will be highlighted in red. The accept/abort pointer will then appear. To abort the 'picked' node, the user clicks the right mouse button and will then be prompted on the screen for another node pick. By clicking the left mouse button, the user accepts the 'picked' node and the appropriate action for that node will then be executed depending on which is the active option. For instance, in the case of an active **RELEASE** option, the action taken will be the deletion of the current restraint at the 'picked' node. At the completion of the appropriate action, the 'node pick' pointer will reappear on the screen. The user can then repeat the above steps for further actions or exit from the on-screen interaction by clicking the right mouse button.

In the **FIXITY** mode, the active translational fixity condition is indicated by the current states of the **FIX\_X**, **FIX\_Y** and **FIX\_Z** menu options. An active **FIX\_X** option represents a translational fixity in the global x-direction and so on. If any node in the model has a translational fixity condition, the symbol of a small square enclosing a cross will be assigned to the node. In fact, the **FIXITY** mode is the default mode when the user enters into this menu page. In this mode, the square symbols associated with all the nodes having the active translational fixity condition are highlighted in red. For a node with a currently non-active translational fixity condition however, the square symbol attached to it is shown in white. It is therefore easy for the user to find out the fixity conditions which exist within the entire model. With an active **CHECK** option, the user can pick a node and the **FIX\_X**, **FIX\_Y** and **FIX\_Z** menu options will then switch to the appropriate states to reflect the current translational fixity condition at the node. With an active **ATTACH** option, the user can pick a node and the active translational fixity condition will then be assigned to the node. With an active **RELEASE** option, the user can pick a node and the current translational fixity condition at the node will then be removed.

In the **AXSYM** mode, there are various options which are available to the user. By activating the **NEW\_AXSYM** option, the user will initiate the task to define a new plane of symmetry. For this purpose, the coordinates of three points in space which will define the orientation of the symmetry plane, have to be specified into the editbox beneath the graphics window as shown in figure 7.10. In fact, if the above task is executed several times, the result will be a list of symmetry planes. When a new symmetry plane is defined, it is added to the end of the list. The active symmetry plane will be highlighted in red on the screen and on display in the editbox as shown in figure 7.10 will be information about the item in the list for this plane. This information will include the reference number of the item and the corresponding definition



data for the active symmetry plane. Any editing of this information can be done directly by the user within the editbox. The user can also inspect the list by using two further options. When the `NEXT` option is activated, the list is scrolled forwards to the next item and the information on display in the editbox will then switch to that corresponding to this next item. Similarly, by activating the `LAST` option, the list is scrolled backwards to the previous item. The user can also delete an existing symmetry plane by scrolling the list until the item corresponding to this plane appears in the editbox and then activates the `DELETE` option. If a node lies in a symmetry plane, the symbol of a small triangle will be assigned to the node. In the case of the active symmetry plane, the triangle symbols of the nodes lying in this plane will be highlighted in red. By activating the `NODE_SNAP` function, the user will map all the nodes given the restraint of the active symmetry plane, onto the plane itself. With an active `CHECK` option, the user can pick a node and the information corresponding to the current symmetry plane restraint at the node will then appear in the editbox. With an active `ATTACH` option, the user can pick a node and the active symmetry plane restraint will then be assigned to the node. With an active `RELEASE` option, the user can pick a node and the current symmetry plane restraint at the node will then be removed.

If the `RETURN` option is activated, the user will then move back into the 'master' menu page. The `BACK_UP` and `RESTORE` options in figure 7.10 are not functional at present.

As mentioned above, a node can be restrained by either giving it a fixity condition or attaching it to a plane of symmetry. However, in the case of a node given the restraints of both fixity and symmetry plane, the active restraint at the node is taken as that imposed most recently by the user. In the case of beam elements, in addition to translational fixities, there is the option of imposing rotational fixities from within the `BEAM ELEMENTS` menu page described later in section 7.21.

## 7.12 Elastic properties

All elements are given their default elastic properties when they are first generated either individually or within the mesh generator. The elastic properties are effective in resisting loads only when the elements are under elastic control. At the form-finding stage, fictitious elastic properties may be used to optimise the calculations as the critical time interval for the DR scheme is a function of the mass/stiffness ratio at each node in the model. In the case of line elements, fictitious elastic properties can also be used as a control for form adjustments. However, for load as well as dynamic analysis, the real elastic properties have to be used. The link, strut and slip cable elements have line element elastic properties which consist of their  $EA$  (ie. modulus of elasticity  $\times$  cross-sectional area) values and self-weights. The elastic properties of membrane elements are made up of their moduli of elasticity and Poisson's ratios in the warp and fill directions, shear moduli and self-weights. The line and membrane element properties are dealt with



RE_PAINT	EDIT_VIEW
BACK_UP	RESTORE

LINK	STRUT
S_CABLE	

ELEMENT	ZONE
BOUNDARY	FIELD
	ALL

L_Slack:	
RESET	NO_RESET

Props:	
ATTACH	CHECK

DELETE	
--------	--

LAST	NEW_PROP
NEXT	EDIT_PROP

RETURN	
--------	--

Figure 7.11

respectively in the LINE ELEMENT PROPS and the MEMBRANE PROPERTIES menu pages both of which are accessed from the 'master' menu page. Figure 7.11 shows the LINE ELEMENT PROPS menu page and figure 7.12 shows the MEMBRANE PROPERTIES menu page. Both these menu pages share the same menu and on-screen interaction styles. In the graphics window is a graphical image of the model in its current state. The RE\_PAINT option serves to refresh the current image display on the screen. If needed, the user can access the GRAPHIC DISPLAY menu page via the EDIT\_VIEW option in order to make adjustments to the current view setting for the on-screen image. The DUMP option is used to send a graphic dump of the on-screen image to the laser printer.

The NEW\_PROP option allows the user to define a new elastic property set and some default values will be assigned to this set. The repeated use of this option will result in a list of elastic property sets. When a new set is defined, it will be added to the end of the list. On display in the editbox will be information from the active property set in the list. This information will include the reference number of

the set and the associated elastic properties. The editbox in the LINE ELEMENT PROPS menu page is as given below

No	EA	Swt/L
1	1.310E+06	0.000E+00

while that in the MEMBRANE PROPERTIES menu page is as follows

No	Ew	Nw	Ef	Nf	Gwf	Swt/A
1	6.700E+04	0.00	4.000E+04	0.00	1.000E+03	0.000E+00

and all the elements with the active property set (ie. the elastic properties as shown in the editbox) will be highlighted in red on the screen. If the default elastic properties are not appropriate, the user can activate the EDIT\_PROP option and then directly edit the information given in the editbox. By activating the NEXT option, the list will be scrolled forward to the next set and the information in this set will then be shown in the editbox. Similarly, when the LAST option is activated, the list will be scrolled backward to the previous set. The user can also delete an existing elastic property set by scrolling the list until this set appears in the editbox and then activates the DELETE option.

The user can perform further operations using the CHECK and ATTACH options. These two options operate via the on-screen interaction mode. With either an active CHECK or ATTACH option, the user can subsequently enter into the on-screen interaction mode by clicking the right mouse button. In the LINE ELEMENT PROPS menu page, the user will then be prompted on the screen by either the



RE_PAINT	EDIT_VIEW
BACK_UP	RESTORE

MBRANE
--------

ELEMENT	ZONE
CLOTH	FIELD
	ALL

M_orient:	
SHADE_TOP	SHADE_OFF
G_ALIGN	NU_SIDE1
	INVERT

Props:	
ATTACH	CHECK

DELETE
--------

LAST	NEW_PROP
NEXT	EDIT_PROP

RETURN
--------

Figure 7.12

'link pick', 'strut pick' or 'slip cable pick' pointer depending on which one of the corresponding LINK, STRUT or S\_CABLE option is currently active. In the MEMBRANE PROPERTIES menu page, the user will be prompted on the screen by the 'membrane pick' pointer. The user can in turn use the corresponding pointer to pick an appropriate element and the 'picked' element will be highlighted in red. The subsequent operations will then depend on the current states of the CHECK and ATTACH options as described below.

For an active CHECK option, the current elastic property set of the 'picked' element will then appear in the editbox. For an active ATTACH option however, the accept/abort pointer will in turn appear. If the 'picked' element is accepted, the active elastic property set will then be assigned to the element.

Finally, when the user is ready to move back into the 'master' menu page, the RETURN option is activated. As before, the menu options in figures 7.11 and 7.12 besides those described above are not yet functional at the moment.

## 7.13 Stress/force and elastic controls

### 7.13.1 Membrane elements

For the form-finding purpose, tensile prestresses are assigned to the membrane elements in the model. By adjusting these prestresses, the user employs stress control to achieve the desired geometry of the model. In the fabric, the prestressing ensures that slack or wrinkling areas do not occur and preloads the fabric against the possible external loads. If the correct levels of prestress are used, the fabric will not become slack and flap about in a wind. For the membrane elements, the prestresses are prescribed in the warp and fill directions, ie. the two principal weave directions in the fabric material. The specified warp and fill stresses will govern the surface curvatures of the model as already discussed in chapter 6. For instance, if more curvature is desired in the warp or fill direction, the stress level in that direction should then be lowered. For the load analysis however, the membrane elements should be under the elastic control (ie. their elastic properties become active) so that their stiffnesses are effective in providing resistance to the applied loads.

The options for dealing with the stress and the elastic controls of the membrane elements are within the MEMBRANE CONTROL menu page shown in



figure 7.13. This menu page is accessible from the 'master' menu page. In the graphics window is a graphical image of the model in its current state. The `RE_PAINT` option is used to refresh the current image display on the screen. The `EDIT_VIEW` option allows the user to manipulate the view of the image shown on the screen. The functions for the `BACK_UP` and `RESTORE` menu options have yet to be implemented.

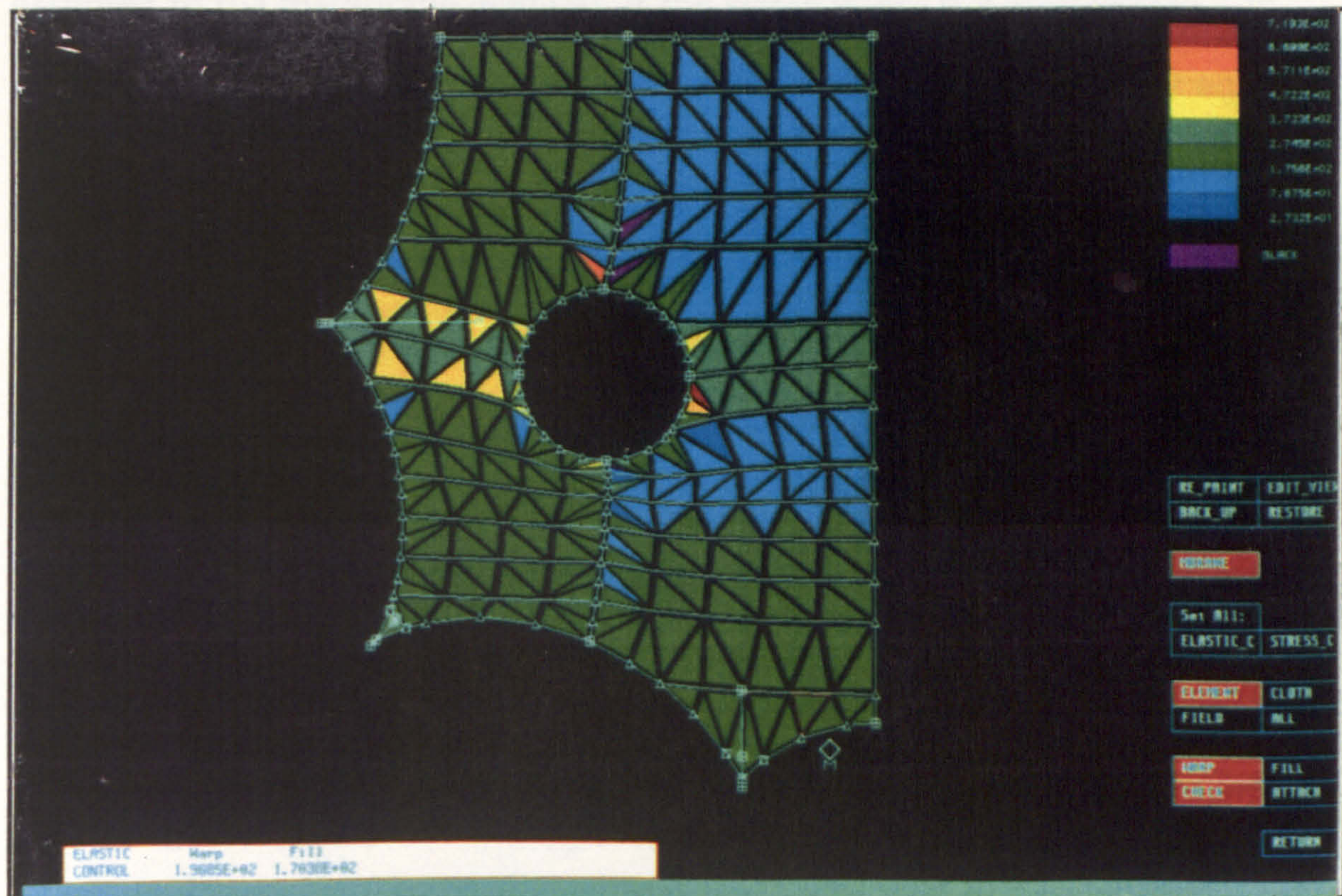


Figure 7.13

With an active `WARP` option, the user is then able to perform specific operations which concern the membrane stresses in the warp direction. On the other hand, an active `FILL` option indicates that the membrane stresses in the fill direction are under consideration instead. The membrane elements on the screen are shown filled in with colours which correspond to the element stresses. A colour chart displayed on the right hand side of the graphics window as shown in figure 7.13 gives the user an idea of the stress levels associated with the colours of the membrane elements.

There are two further options, ie. the `CHECK` and `ATTACH` options which operate in the on-screen interaction mode. The user will enter into this mode by clicking the right mouse button. This is followed by a switch of the on-screen arrow pointer into the 'membrane pick' pointer. The user can in turn use the 'membrane pick' pointer to pick a membrane element and the 'picked' membrane element will be highlighted in red.

With an active `CHECK` option, the warp and fill stresses in the 'picked' membrane element will then appear in the editbox. If the `WARP` option is active, the warp stress shown in the editbox will be taken as the active stress.



For an active `FILL` option, the active stress will instead be the fill stress shown in the editbox. The user can also directly edit the value of the active stress. The `ATTACH` option can only be used for membrane elements which are currently under stress control. For an active `ATTACH` option, the user will be prompted by the accept/abort pointer after picking a membrane element. If the user accepts the 'picked' membrane element, the active stress will be assigned to the membrane element. If the active stress is a warp stress, the membrane warp stress will be set equal to this stress. On the other hand, if the active stress is a fill stress, the membrane fill stress instead will be set equal to this stress. For an active `ELEMENT` option, it is only the 'picked' membrane element which will be attached with the active stress. In the case of an active `CLOTH` option however, all the membrane elements within the same cloth panel as the 'picked' membrane element will be assigned the active stress. Similarly, for an active `FIELD` option, all the membrane elements within the same field as the 'picked' membrane element will be assigned the active stress. With an active `ALL` option, all the membrane elements in the model will be set to the active stress. The colours of the membrane elements will be updated accordingly to account for the active stress attached to the elements.

By activating the `ELASTIC_C` option, the stress control of each membrane element in the model will be switched to the elastic control. Conversely, a switch from the elastic to the stress control of each membrane element in the model is initiated by activating the `STRESS_C` option.

If the `RETURN` option is activated, the user will then move back into the 'master' menu page.

### 7.13.2 Line elements

Further form-finding controls are given by the force and the elastic controls of the line elements. The force control of a cable involves the specification of a tensile force to one of the link elements which constitute the cable. The remaining link elements in the cable are then controlled by adjusting their slack lengths. An increase in the specified tensile force will lead to a lower curvature of the cable. For a cable under elastic control however, all the link elements in the cable are controlled by specifying the slack length of each element. The force and elastic controls can also be applied to the case of a slip cable. For a slip cable under force control, a tensile force is given to all the elements in the slip cable. On the other hand, the elastic control of a slip cable involves the adjustment of the slack length of the entire slip cable. The force and elastic controls mentioned above are further tools available to the user for achieving the desired geometry of the model.

The options for dealing with the force and elastic controls of the line elements are within the `LINK CONTROL` menu page shown in figure 7.14. This menu page is accessible from the 'master' menu page. In the graphics window is a graphical image of the model in its current state. The `RE_PRINT` option is used to refresh the current image display on the screen. The `EDIT_VIEW` option



allows the user to manipulate the view of the image shown on the screen. The functions for the BACK\_UP and RESTORE menu options have yet to be implemented.

RE_PRINT	EDIT_VIEW
BACK_UP	RESTORE
LINK	STRUT
S_CABLE	BOUNDARY
ELASTIC_C	FORCE_C
LAST	
NEXT	EDIT
RETURN	

Figure 7.14

In this menu page, the line elements under consideration are the link, strut and slip cable elements. There are specific operations which apply only to either the link, strut or slip cable elements at any one time. The choice of which line elements are to be operated on is decided by activating the LINK, STRUT or S\_CABL option accordingly. The chosen line elements will be given a specific colour on the screen. For instance, if the link elements are chosen, they will be shown in green while the remaining elements will be coloured in white. On the other hand, the chosen strut or slip cable elements will be shown in the magenta colour. Furthermore, the label in the menu option corresponding to the

activated option will be given the same colour as that for the chosen line elements on the screen. At the same time, the menu option labels for the other two line element options will be shown in white. Hence, it becomes obvious to the user which line elements are currently being operated on.

The user can subsequently enter into the on-screen interaction mode by clicking the right mouse button and the arrow pointer will in turn switch into either the 'link pick', 'strut pick' or 'slip cable pick' pointer depending on which one of the corresponding LINK, STRUT or S\_CABLE option is currently active. The user can then use the corresponding pointer to pick an appropriate line element. The 'picked' line element will be highlighted in red and taken as the active element. In addition, information about the active element will appear in the editbox located beneath the graphics window. If the active element is under the force control, the information shown will include the current tension and stressed length of the element. If desired, the user can directly edit the value of the tension shown by activating the EDIT option. Furthermore, an element which is under force control can be recognised by the yellow colour given to it. For an active element which is under elastic control however, the editbox information will include the current slack length, stressed length and tension of the element as shown below.

ELASTIC	Tension	:	5.9030E+02
CONTROL	L_current	:	0.836194
	L_SLACK	:	0.835817

If desired, the user can in this case directly edit the value of the slack length shown by activating the EDIT option. If the slack length value is edited, the tension of the element shown will automatically be updated accordingly. The link and slip cable elements can be given either force or elastic control. On the other hand, the strut elements can only have elastic control. As for the membrane elements, all the line elements will be given elastic control during the load analysis of the model.



Furthermore, the force control of the active element can be switched to elastic control by activating the `ELASTIC_c` option. Conversely, by activating the `FORCE_c` option, a switch from elastic to force control of the active element will take place. In both cases, the information in the editbox will be updated accordingly to account for the control change of the active element.

Lastly, by activating the `RETURN` option, the user will exit from this menu page and move back into the 'master' menu page.

### 7.14 Boundary control

SHOW_FLD	EDIT_VIEW
Bdy Pairs:	
COUPLE	UNCUPLE
ACT<>PASS	VERIFY
Node Posn:	
SCREEN	LISTING
EQ_SPACE	KEYB_ABS
	KEYB_PROP
	KEYB_INC
Bdy Prof:	
SCREEN	KEYB_DIP
	KEYB_RAD
	KEYB_S/D
	KEYB_Tau
Curve_fit:	
C_SPLINE	CIRCLE
LAST	ABORT
NEXT	ACCEPT
RETURN	

Figure 7.15

The menu options available within the `BOUNDARY CONTROL` menu page shown in figure 7.15 are used to perform specific operations which concern the boundaries in the model. This menu page is accessible from the 'master' menu page. On display in the graphics window area of the screen is a graphical image of the model in its current state. The `EDIT_VIEW` option allows the user to manipulate the view of the image shown in the graphics window. The `SHOW_FLD` option is used to check the field definitions within the model.

In the model, a field is defined by its enclosing boundaries. If more than one field are defined, then one field may have a boundary which coincides with that of the adjacent field. For the two coinciding boundaries, it is allowable for the nodes which lie along one boundary to be different from those along the other boundary. In addition, each of the two boundaries may consist of a series of link elements. The two coinciding boundaries share a common path over the surface of the model. It may be desired for the overall profile of the common path to be controlled predominantly by one of the two boundaries, ie. the active boundary. The user can decide which one of the two boundaries is to be taken as the active boundary and the other boundary

will then become the passive boundary. This can be done using the menu options grouped under the `Bdy Pairs:` label, ie. the `COUPLE`, `UNCUPLE`, `ACT<>PASS` and `VERIFY` options.

During the analysis, the nodes along a passive boundary except the node at either end of the boundary will be treated as fully restrained. The residual forces at these nodes will be redistributed accordingly to the appropriate nodes which belong to the active boundary. On the other hand, the nodes along the active boundary will be allowed to move to their equilibrium positions. The nodes along the passive boundary will be reset to appropriate locations along



the path of the active boundary. Hence, the two boundaries will follow a common path which is determined predominantly by the nodes along the active boundary.

The **COUPLE** option is used to couple together two coincident boundaries. When this option is activated, the user will automatically enter into the on-screen interaction mode and be prompted to pick the first boundary. The first 'picked' boundary will be highlighted in red and the accept/abort pointer will then appear. If the first 'picked' boundary is accepted, the user will then be prompted to pick the second boundary. The second 'picked' boundary which has to coincide with the first 'picked' boundary, will also be highlighted in red. The accept/abort pointer will then appear. If the second 'picked' boundary is accepted, then the first and second 'picked' boundaries will be coupled together. The first 'picked' boundary will be taken as the active boundary while the second 'picked' boundary will become the passive boundary. The two 'picked' boundaries will then be redrawn in their normal colour, ie. the yellow colour. It is noted that when picking the first boundary, the software only allows the user to pick a boundary which has not been coupled to another boundary. By repeating the above steps, further pairs of coincident boundaries can be coupled together using the **COUPLE** option.

Furthermore, the **UNCUPLE** option allows the user to uncouple (ie. undo the coupling) the pairs of coincident boundaries which have been previously coupled together using the **COUPLE** option described above. When this option is activated, the user will automatically enter into the on-screen interaction mode and be prompted to pick a boundary. In fact, the software only permits the user to pick a boundary which has previously been coupled to another boundary. The 'picked' boundary will be highlighted in red and the accept/abort pointer will then appear. If the 'picked' boundary is accepted, the coupling of this boundary to its coincident boundary will then be removed. These two coincident boundaries will both in turn be taken as active boundaries. The 'picked' boundary will then be redrawn in its normal colour, ie. the yellow colour. Further coupled pairs of coincident boundaries can similarly be uncoupled from each other using the **UNCUPLE** option.

For a coupled pair of coincident boundaries, the **ACT<PASS** option enables the user to switch the active boundary into the passive one and vice-versa. When this option is activated, the user will automatically enter into the on-screen interaction mode and be prompted to pick a boundary. The software will only permit the user to pick a boundary which has previously been coupled to another boundary. If the 'picked' boundary is the active boundary, this boundary will then be switched to become the passive boundary while the passive boundary coupled to the 'picked' boundary will in turn become the active boundary.

Under the **Node Posn:** label is the **SCREEN** option which allows the user to move a node along a boundary interactively on the screen. When this option is activated, the user will automatically enter into the on-screen interaction mode and be prompted to pick a boundary. In this case, the software allows



the user to pick any boundary in the model. The 'picked' boundary will be highlighted in red. If there is coupling between the 'picked' boundary and a second boundary, the accept/abort pointer will appear. If the 'picked' boundary is aborted, the second boundary will be taken as being accepted instead and highlighted in red. The 'picked' boundary will then be redrawn in its normal colour, ie. yellow. The following operations will apply to the 'picked' boundary. The user will be prompted to pick a node lying along the 'picked' boundary. The 'picked' node will be highlighted in the cyan colour. The pointer will then switch into a small cross symbol. The user will position the cross symbol at the new location along the boundary for the 'picked' node. This location will be indicated by a small cross marker coloured in cyan when the left mouse button is clicked. The software restricts this location to be somewhere along the boundary between the node before and the one after the 'picked' node. The accept/abort pointer will then appear. If the new location is accepted, the 'picked' node will then be moved to this location. Subsequently, the definition data of the boundary and the link elements along the boundary will be adjusted accordingly. If a link element connected to the 'picked' node is under the elastic control, the element slack length will reset with the element tension remaining the same. Hence, the `SCREEN` option provides an easy means of shuffling a node along a boundary to the desired location.

Under the `curve_fit` label are two further options, ie. the `c_spline` and `circle` options. By default, a boundary is displayed on the screen as a series of lines joining up the nodes which lie along the boundary. On the other hand, the user can enter into the `GRAPHIC DISPLAY` menu page and activates the option to display a boundary as a smooth curve. For such a case, a curve will be fitted through the nodes lying along the boundary. By default, the `c_spline` option is active and indicates that a cubic spline will be used for the curve fitting. With an active `circle` option however, a circle instead will be fitted through the nodes along the boundary.

When the user is ready to exit from this menu page and move back into the 'master' menu page, the `RETURN` option is activated. The menu options in figure 7.15 besides those described above are not functional at present.

## 7.15 Analysis

When the model is ready to be analysed, the user can then enter into the `ANALYSIS` menu page which is accessible from the 'master' menu page. The `ANALYSIS` menu page shown in figure 7.16 is used for analysing the model during both the form-finding and load analysis stages. In the graphics window are displayed a plan and two elevations of the model in its current state. This display is updated at regular intervals during the analysis of the model. In addition, the node with the current maximum residual (out-of-balance) force is identified by an on-screen marker. In this way, the user can monitor if the analysis is going as expected and any sign of possible physical instability is easily detected.



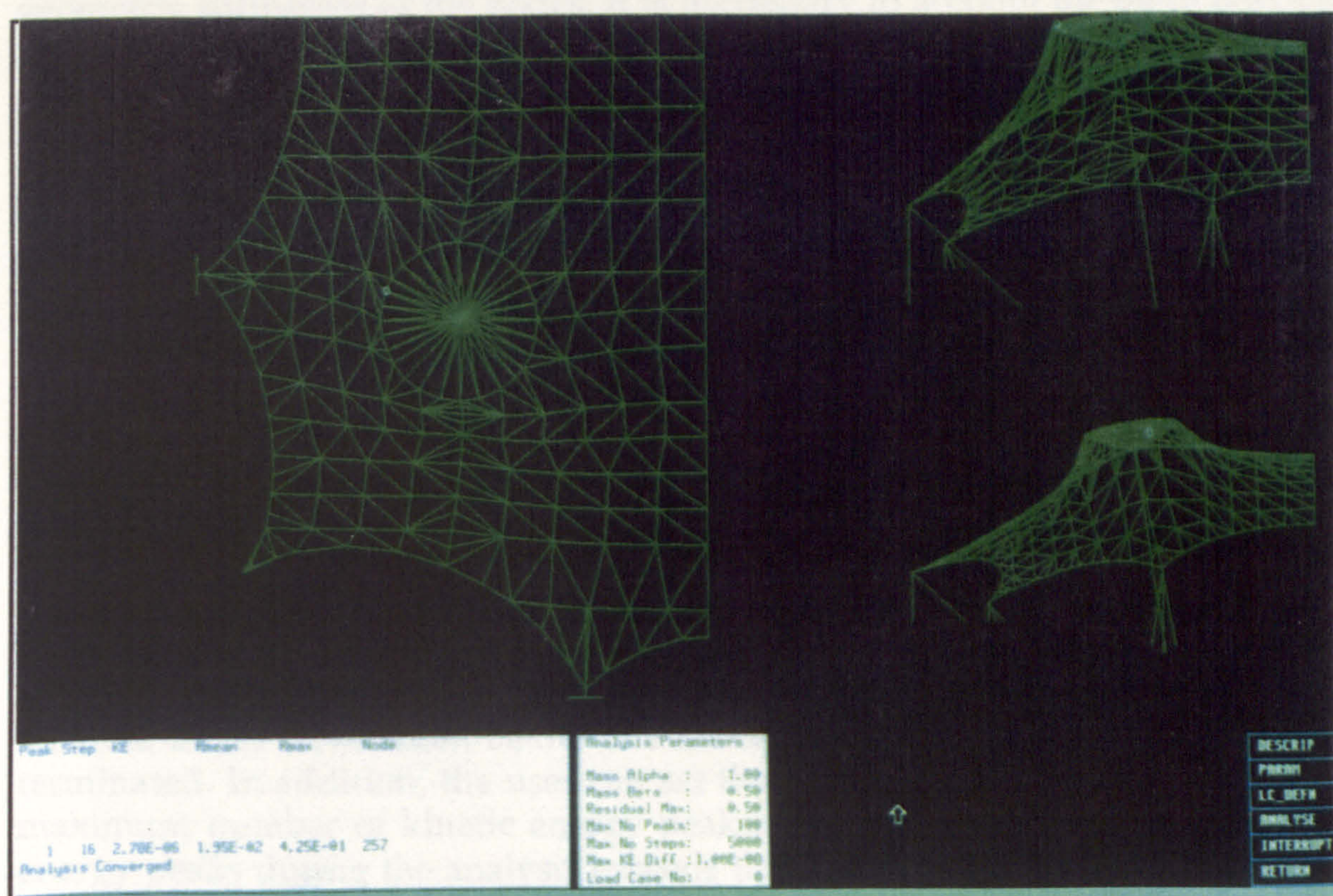


Figure 7.16

By activating the **PARAM** option, an editbox as shown below will appear beneath the graphics window. In the editbox will be displayed specific information about the various parameters which are used to control the analysis. The software gives a set of default values to these parameters. If the default values are inappropriate, the user can edit them directly in the editbox.

Peak	Step	KE	Rmean	Rmax	Node
1	16	2.78E-06	1.95E-02	4.25E-01	257
Analysis Converged					

Analysis Parameters		
Mass Alpha	:	1.00
Mass Beta	:	0.50
Residual Max	:	0.50
Max No Peaks	:	100
Max No Steps	:	5000
Max KE Diff	:	1.00E-08
Load Case No	:	0

The alpha and beta parameters are involved in the calculations of the nodal masses for the model. The dynamic relaxation method already outlined in the earlier chapters, is used for the analysis of the model. This method is a conditionally stable numerical scheme. In this method, the nodal masses are determined from the principal direct stiffnesses of the nodes. In the software, the nodal masses are calculated on the basis of the stiffnesses of the nodes at the start of the analysis. These nodal masses are then used throughout the analysis. By not having the nodal mass calculations at each time step, the computational effort involved and thus, the solution time of the analysis, will be reduced. During the form-finding of the model in its initial state, gross deformations may take place. This will result in large changes in the



geometric stiffnesses of the nodes. It is necessary to account for these possible deviations from the stiffnesses of the nodes at the start of the analysis. This is achieved by means of the alpha and beta parameters which are applied at the start of the analysis to increase the stiffnesses of the nodes sufficiently. If the appropriate values are given to the alpha and beta parameters, the resulting nodal masses will ensure that the analysis remains numerically stable throughout. At the start of the form-finding, it is normal to set larger values such as 2.00 and 1.00 for the alpha and beta parameters respectively. However, as the model approaches its equilibrium state, smaller values (and thus, larger time steps) can be used instead to speed up the analysis.

There are also parameters in the editbox which give the various criteria by which the analysis will be terminated. In the DR method, the model undergoes vibrations until it converges to an equilibrium state. The convergence criterion is given by the maximum limit on the residual forces in the model. This limit is a parameter which can be set by the user in the editbox. The model is taken to have reached convergence when all the residual forces have fallen below this maximum limit and the analysis will be terminated. In addition, the user can set the value of the parameter for the maximum number of kinetic energy peaks. When the total number of kinetic energy peaks during the analysis exceeds this value, the analysis will also be terminated. Hence, during the analysis, whenever either of the two criteria set by the above parameters is satisfied, the analysis will be terminated. In the editbox, a parameter is also used to set the maximum number of time steps between kinetic energy peaks during the analysis. This implies that if the current total of time steps until the next kinetic energy peak exceeds this maximum, it is taken that a peak has occurred and the analysis continues further to find the next peak. Another parameter is used to set a limit on the difference in kinetic energy levels between successive time steps during the analysis. If the current difference becomes less than the specified limit, it is assumed that a kinetic energy peak has occurred and the analysis continues further to find the next peak.

Furthermore, in the editbox is a parameter for the load case which will be applied to the model during the analysis. The default value of zero for the parameter indicates that no loads will be applied. In other words, there is no need for the user to edit this default value at the form-finding stage. For the load analysis however, it is presumed that a list of load cases have already been defined within another menu page which will be described later. Each of the load cases in this list will have a reference number. Hence, the corresponding parameter in the editbox will be given the appropriate load case number from the list if a load analysis is to be carried out.

With all the parameters in the editbox having the appropriate values, the analysis can then proceed by activating the ANALYSE option. Subsequently, on display in the editbox as shown above will be a trace of the kinetic energy peaks, mean and maximum residual forces during the analysis. If beam elements are present in the model, the trace will also include the mean and



maximum residual moments during the analysis. A trace of diminishing kinetic energy peaks indicate convergence of the analysis.

If the user decides to terminate the analysis at any time, the INTERRUPT option can be activated. When the analysis terminates, a summary of information about the analysis can be output to the laser printer. The summary will include a trace of the kinetic energy peaks, mean and maximum residual forces during the analysis. The residual forces at the nodal restraints will also be included in the output. If beam elements are present in the model, the residual moments at the nodal restraints will be output as well. From the results of the analysis, the model may be found to behave unsatisfactorily such as the presence of excessive stresses or wrinkling areas. Further adjustments to the model may be required to eliminate the deficiencies indicated by the analysis. This will then be followed by reanalysis of the model. When the results from the load analysis are acceptable, the resulting residual forces and moments will be used in the design of support structures and foundations.

The DESCRIP and LC\_DEFN options in this menu page are not functional at present. When the user is ready to exit from this menu page and move back into the 'master' menu page, the RETURN option is activated.

## 7.16 Loading definition

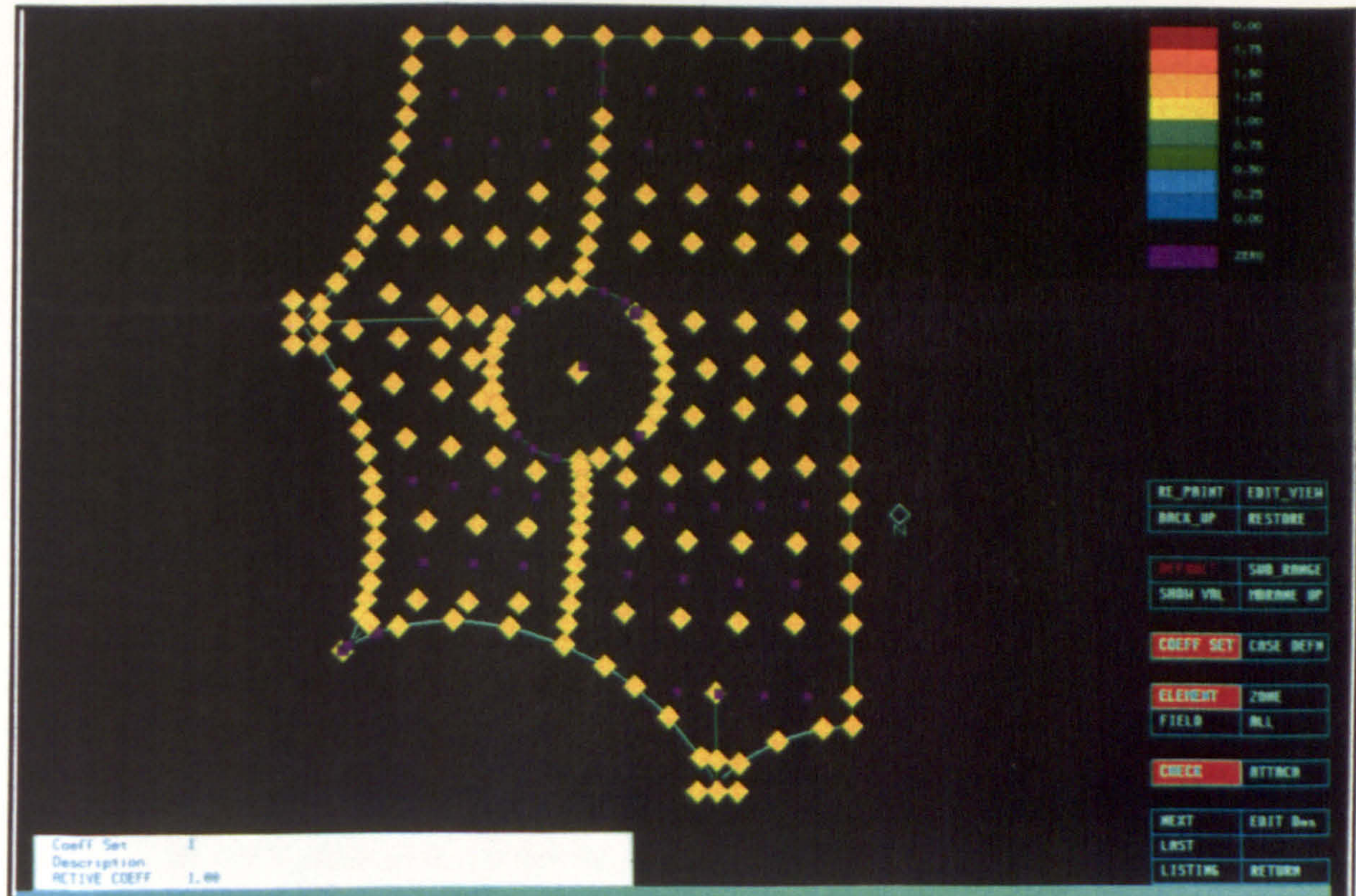


Figure 7.17



From the 'master' menu page, the user can enter into the **LOADING DEFINITION** menu page shown in figure 7.17 in which the applied loads on the model will be defined. In the graphics window is a graphical image of the model in its current state. The **RE\_PAINT** option serves to refresh the current image display on the screen. The **EDIT\_VIEW** option allows the user to manipulate the view of the image shown on the screen.

By activating the **COEFF SET** option, the user can then proceed to define the loading coefficients. An editbox as shown below will appear beneath the graphics window.

Coeff Set	1
Description	
ACTIVE COEFF	1.00

On display in the editbox will be the reference number for the current set of coefficients and a loading coefficient value which is taken as the active coefficient. The user can directly edit the value of the active coefficient.

The **CHECK** and **ATTACH** options both operate in the on-screen interaction mode. With an active **CHECK** or **ATTACH** option, the user can then initiate this mode by clicking the right mouse button. The on-screen arrow pointer will in turn switch into the 'node pick' pointer prompting the user to pick a node on display in the graphics window.

With the **COEFF SET** and **ATTACH** options both active, and when in the on-screen interaction mode, the user can subsequently use the 'node pick' pointer to pick a node. The active coefficient will be assigned to the 'picked' node. By continuing in a similar manner, the user can assign a loading coefficient to each of the nodes in the model. A positive loading coefficient assigned to a node will be shown on the screen as a diamond shaped symbol while a zero or negative loading coefficient will be represented by a rectangular symbol. Each symbol will also be filled in with a colour in accordance with a colour chart shown on the right hand side of the graphics window (see figure 7.17). The colour chart gives a band of colours which correspond to the entire magnitude range of the loading coefficients currently present in the model. This makes it easy to work out the distribution of the loading coefficients in the model. For an active **ELEMENT** option, it is only the 'picked' node which will be attached with the active coefficient. With an active **ALL** option however, all the nodes in the model will be attached with the active coefficient. In the case of an active **ZONE** option, the user can define a zone on the screen so that all the nodes which fall within this zone will be attached with the active coefficient. The symbols and their colours will also change accordingly to account for the new loading coefficients which have been attached to the nodes. The **FIELD** option is yet to be operational.

With both the **COEFF SET** and **CHECK** options active, and when in the on-screen interaction mode, the user can subsequently use the 'node pick' pointer to pick a node. The current loading coefficient at the 'picked' node will appear in



the editbox as shown above. The user can therefore in this way easily find out the loading coefficients which have been assigned throughout the model.

By activating the **NEXT** option when the **COEFF SET** option is still active, the user can then continue as described above to define another set of loading coefficients which can similarly be assigned to the entire model. A list of up to five sets of coefficients can be defined by the user. Conversely, by activating the **LAST** option, the user can scroll the list backwards to the previous set of loading coefficients. If desired, the user can scroll the list to the appropriate set and then edit the loading coefficients in that set. The **EXIT Des** option is yet to be operational.

The loading coefficients have to be multiplied by the corresponding loading intensities in order to set up a load case. The loading intensities in terms of the surface normal pressure, plan density and internal pressure can be applied. By activating the **CASE DEFN** option, the user can then proceed to set up the load cases. An editbox as shown below will appear beneath the graphics window.

Load	Normal:	PRESSURE	0.00	Plan:	DENSITY	60.00	Internal:	PRESSURE	0.00
Case		COEFF_SET	0		COEFF_SET	1			
2									

On display in the editbox will be the reference number for the current load case, the normal pressure and its associated set of loading coefficients, the plan density and its associated set of loading coefficients and the internal pressure. A normal pressure is taken as a loading per unit area acting in a direction normal to the surface, an example of which is the wind pressure. A plan density is taken as a loading per unit plan area of the surface, an example of which is the snow loading. The sign convention for the loading intensities should be consistent with that for the associated sets of loading coefficients. The user can subsequently specify in the editbox as shown above the appropriate values for the loading intensities and the reference numbers of the corresponding sets of loading coefficients. For an air-supported structure, it is necessary to consider the load case of a uniform inflation pressure. For this load case, an appropriate value will be given to the internal pressure while the remaining loading intensities will be set to zero.

By activating the **NEXT** option when the **CASE DEFN** option is still active, the user can then continue as described above to define another load case. A list of up to five load cases can be defined. Conversely, by activating the **LAST** option, the user can scroll the list backwards to the previous load case. If desired, the user can scroll the list to the appropriate load case and then edit the relevant information within that load case.

For the load analysis, the reference number of the appropriate load case will be specified accordingly by the user within the **ANALYSE** menu page described earlier.



By activating the RETURN option, the user will exit from this menu page and move back into the 'master' menu page. Besides those described above, the options which are not yet functional at the moment include the BACK\_UP, RESTORE, SUB\_RANGE, SHOW UAL and MBRANE UP options.

### 7.17 Patterning

When the results from the load analysis are acceptable, the user can proceed to the patterning stage in the design process of membrane structures. The CUTTING PATTERNS menu page shown in figure 7.18(a) is available to the user for precisely this task. The user can access this menu page from the 'master' menu page.

In the CUTTING PATTERNS menu page, the user will execute operations to develop the cutting patterns of the model. In this case, under consideration is the model derived from the form-finding stage, ie. in which the membrane elements are under stress control. A cutting pattern is the shape taken up by the triangular membrane elements in a cloth panel when unfolded onto a flat plane. This shape will be traced and cut out from a fabric roll on the shopfloor. It is obviously desirable to produce a cutting pattern of minimum width which will optimise the use of the fabric.

In the model, the individual cloth panels within a field are bound by a combination of ridge and boundary cables, and geodesic seams as shown in figure 7.18(a). The nodes lying along a seam line are constrained to follow a geodesic path over the surface during the form-finding. There are benefits in having geodesic seam lines in the model. Firstly, the common geodesic seam between two cloth panels has the advantage of being shear free. Secondly, a cloth panel with geodesic seams produces a cutting pattern which will optimise the use of the fabric material as shown in figure 5.8 (included in chapter 5).

On entry into the CUTTING PATTERNS menu page, a graphical image of the model in its current state will be shown in the graphics window. The RE\_PAINT option serves to refresh the current image display on the screen. If required, the user can also access the GRAPHIC DISPLAY menu page via the EDIT\_VIEW option in order to manipulate the view of the image shown in the graphics window. The BACK\_UP and RESTORE options are not yet functional at the moment.

Under the UNFOLD: label is the NEW\_FIELD option. By activating this option, the user will then be prompted on the screen by the 'field pick' pointer. The user can subsequently use the 'field pick' pointer to pick a field and the boundaries of the 'picked' field will be highlighted in red. The accept/abort pointer will then appear. If the user accepts the 'picked' field, the cloth panels in the field will then undergo the unfolding process. The 'picked' field will be taken as the active field. A zoom-in view of the active field will be displayed on the screen. All the unfolded cloths in the active field will be shown labelled with their cloth numbers. The top end of each of these unfolded cloths will also be



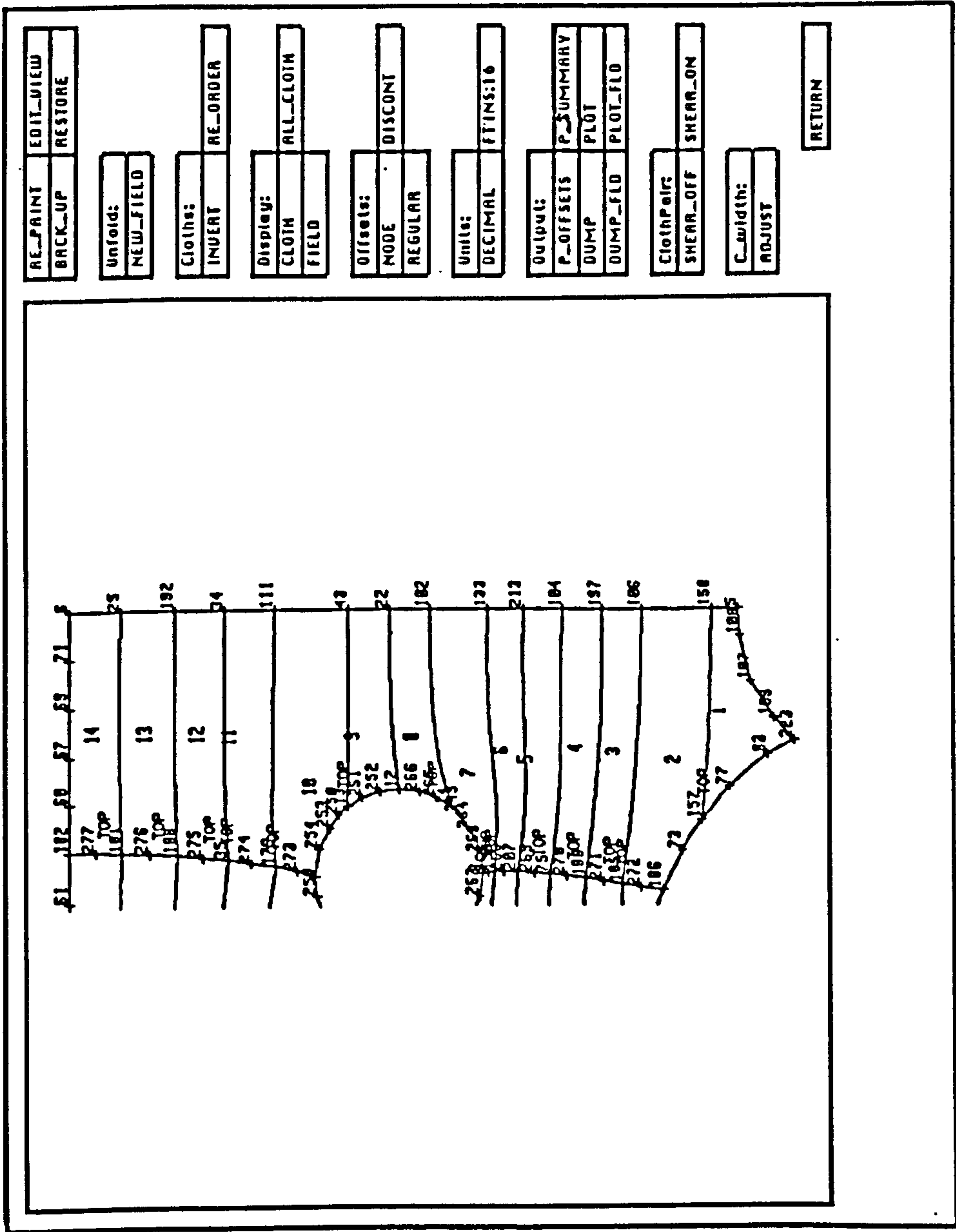


Figure 7.18(a)

FIELD No	Cloth Nos	Compensation		Stress	Max	Mean	Min	Active	Max Dimensions		Decomp	%	Length	Stress	Max	Min
2	Total	14	WARP_%	0.00	719	191	0	Cloth	Width	1.676	TOP	0	0.00	Warp	201	197
	Unfolded	14	FILL_%	0.00	485	195	54	1	Length	3.787	BASE	0	0.00	Fill	226	170

Figure 7.18(b)

indicated by the 'TOP' label as shown in figure 7.18(a). These unfolded cloths will be arranged so that the cloth top ends are orientated in a manner which is consistent with an ascending order of the cloth numbers (see figure 7.18(a)). An editbox as shown below will also appear beneath the graphics window.

There is much information on display in the editbox which includes the values (maximum, mean and minimum) of the warp and fill stresses in the active field, and the stretch compensation factors for the warp and fill directions of the fabric material. In the editbox is also information which will indicate if there is any cloth in the active field that cannot be unfolded. For such a cloth, the problem may be due to the incorrect way in which the membrane elements are sequenced within the cloth.

Under the Display: label are the CLOTH, ALL\_CLOTH and FIELD options. By activating the CLOTH option, the user will then be prompted on the screen by the 'cloth pick' pointer. The user can subsequently use the 'cloth pick' pointer to pick one of the unfolded cloths in the active field. The 'picked' cloth will be taken as the active cloth. The cutting pattern of the active cloth will in turn be displayed on the screen as shown below in figure 7.18(c).

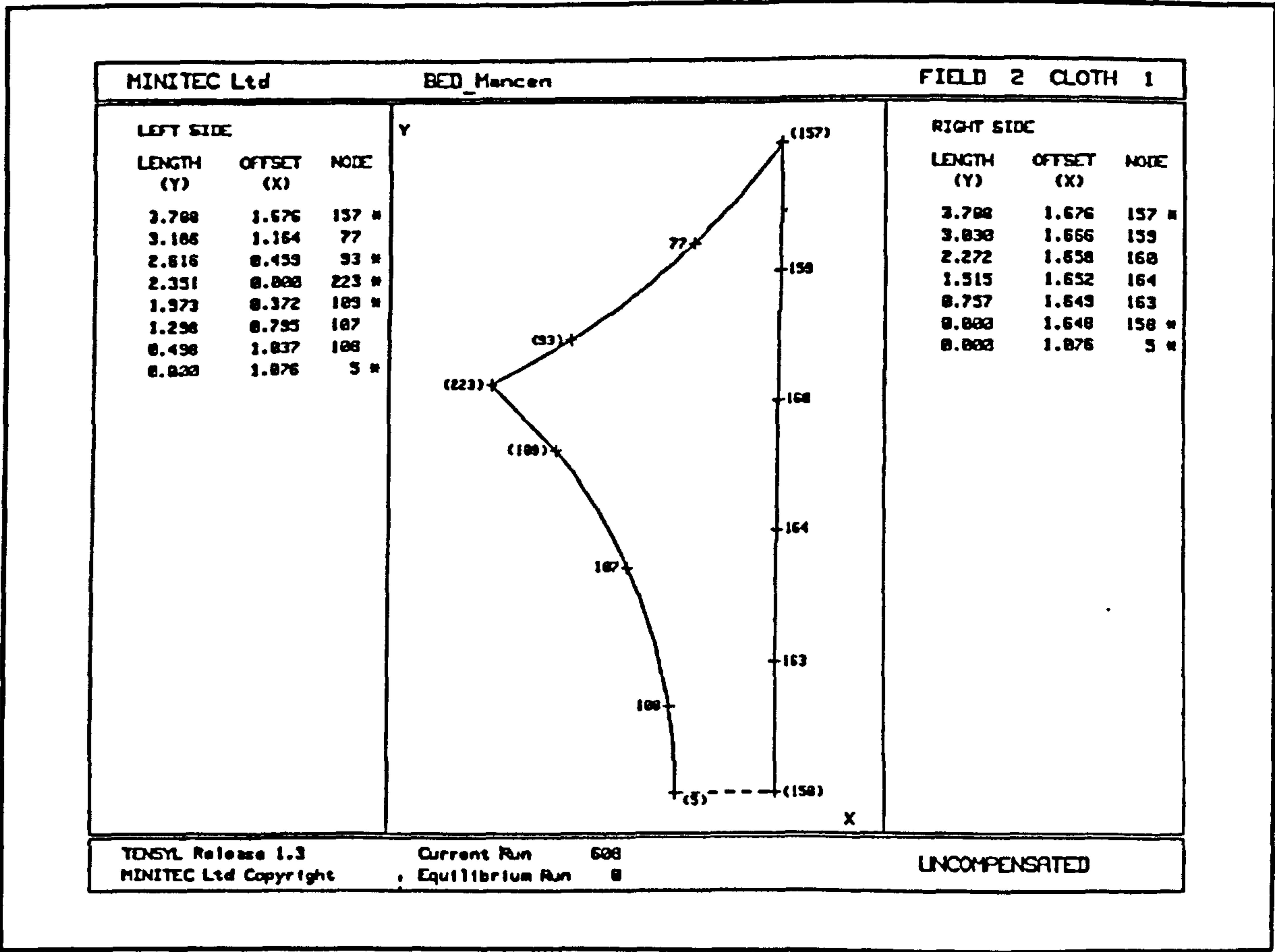


Figure 7.18(c)

The cutting pattern will be presented in an orientation which gives the minimum width. The node positions on the cutting pattern are marked and labelled with their node numbers. The discontinuities in the cloth are



annotated by the node numbers in brackets. The coordinates of the nodes along the left and right sides of the cloth are listed. These coordinates are relative to an origin of a local  $x$ - and  $y$ -axes system for the cloth as defined in figure 7.18(c).

If the cloth has an axis of symmetry, the corresponding cutting pattern will be orientated as shown in figure 7.18(c). The end of the cloth which lies along the axis of symmetry will be positioned along the local  $x$ -axis. On the shopfloor, by reflecting about the axis of symmetry, the cutting pattern for the whole cloth will in turn be obtained.

When the `DUMP` option is activated, the cutting pattern displayed on the screen as shown in figure 7.18(c) will be output to the laser printer. On the other hand, an activated `PLOT` option will send the cutting pattern to the plotter instead. The output from the laser printer or plotter can then be used on the shopfloor for marking out the cutting pattern on the fabric material. By activating the `DUMP_FLD` option, the cutting pattern in the format as shown in figure 7.18(c) for each of the unfolded cloths in the active field will be output to the laser printer. When the `PLOT_FLD` option is activated, the cutting patterns for all the unfolded cloths in the active field will be sent to the plotter instead.

Before the cutting pattern is finally ready for output to either the laser printer or plotter, the appropriate stretch compensation and decompensation factors are specified in the editbox as shown in figure 7.18(b). All these factors have the default value of zero which corresponds to the case of no compensation and decompensation of the cutting patterns. On the shopfloor, the cutting patterns are fabricated from the fabric roll in their stress free states. When these cutting patterns are assembled and then stretched out on site to achieve the desired surface geometry, the membrane stresses prescribed during the form-finding will in turn be induced into the fabric of the structure. The values of the stretch compensation and decompensation factors will be obtained from the laboratory tests on the fabric material. The stretch compensation factors are applied within the software to shrink the cutting patterns to their stress free states. In some situations such as in corner areas, it may be difficult to stretch the fabric fully to achieve the desired membrane stresses during the construction on site. In order to account for such situations, the decompensation factor will be applied to the appropriate cutting patterns. The decompensation factor is applied over a specified length at the top and/or bottom ends of a cloth. The compensated cutting patterns output from either the laser printer or plotter will be sent for fabrication on the shopfloor.

Under the `units:` label are the `DECIMAL` and `FTINS:16` options. With an active `DECIMAL` option, the cutting pattern information will be given in the metric units which are taken as the default units. If the user requires the cutting pattern information to be given in the imperial units, then the `FTINS:16` option is activated.



By activating the `ALL_CLOTH` option, all the unfolded cloths in the active field will be displayed side by side on the screen as shown in figure 7.18(d). The discontinuities in each cloth are annotated with the offset widths. In addition, given at the top and bottom of each cloth are the cloth number and length of the cloth respectively.

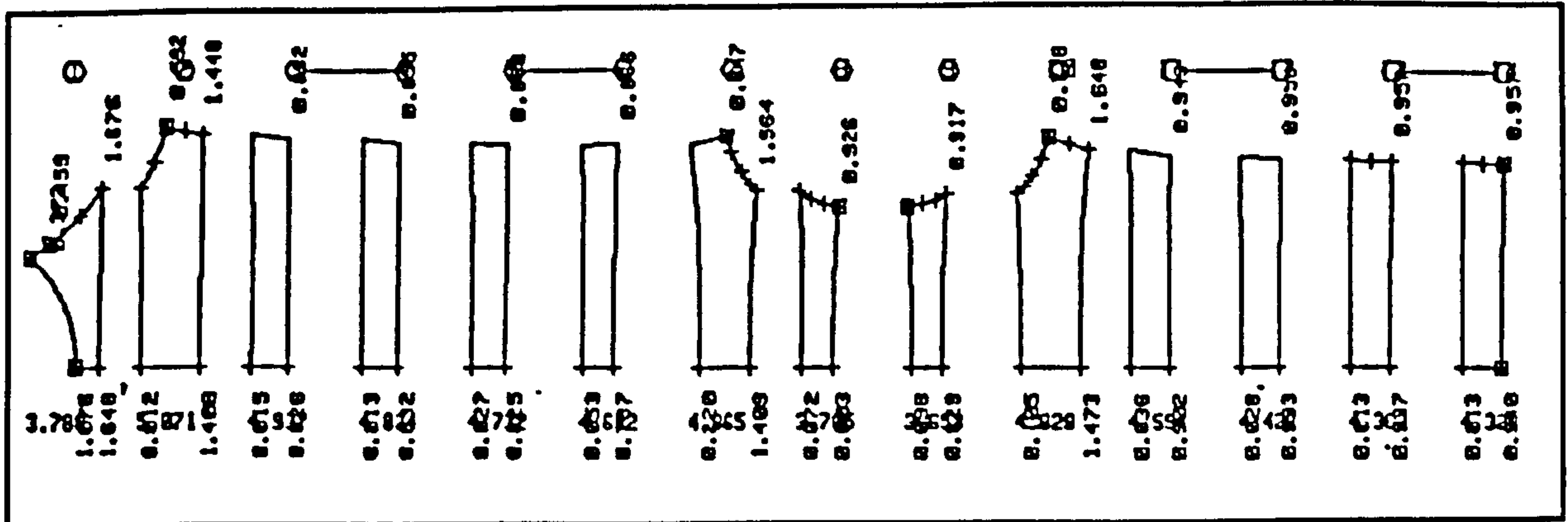


Figure 7.18(d)

The `FIELD` option when activated will result in the display of the active field on the screen as shown in figure 7.18(a). All the unfolded cloths in the active field are labelled with their cloth numbers. The top end of each of the unfolded cloths is also indicated by the 'TOP' label. The user can subsequently use the `CLOTH` option to display on the screen the cutting pattern of one of the unfolded cloths in the active field.

Both the `INVERT` and `RE_ORDER` options are grouped under the `cloths:` label. By activating the `INVERT` option, the user will then be prompted on the screen by the 'cloth pick' pointer. The user can subsequently use the 'cloth pick' pointer to pick one of the unfolded cloths in the active field. The 'picked' cloth will be highlighted in red. Further cloths can be picked until the user decides to exit from the on-screen interaction mode by clicking the right mouse button. This will then be followed by the inversion of all the 'picked' cloths such that their bottom ends now become the top ends and vice-versa. These new top ends will be marked with the 'TOP' labels.

The `RE_ORDER` option when activated allows the user to change the order of the unfolded cloths in the active field. The user will be prompted on the screen by the 'cloth pick' pointer. The user can subsequently use the 'cloth pick' pointer to pick one of the unfolded cloths in the active field. The sequence in which the user picks the cloths will decide how the unfolded cloths are to be reordered. The cloth which is picked first will have its cloth number reset to 1, the second 'picked' cloth will be given the cloth number 2 and so on. The 'picked' cloths will all be highlighted in red. The cloth numbers (and thus, order) of the remaining cloths in the active field will be readjusted accordingly. When the desired order of the cloths has been achieved, the user can then exit from the on-screen interaction mode by clicking the right mouse button.



Under the `output:` label are the `P_OFFSETS` and `P_SUMMARY` options. When the `P_OFFSETS` option is activated, a listing of the node numbers and local coordinates of the discontinuity nodes for all the unfolded cloths in the active field will be output to the laser printer. The `P_SUMMARY` option is not functional at the moment.

It is also noted that the options grouped under the `offsets:` label, ie. the `NODE`, `DISCONT` and `REGULAR` options are not functional at present.

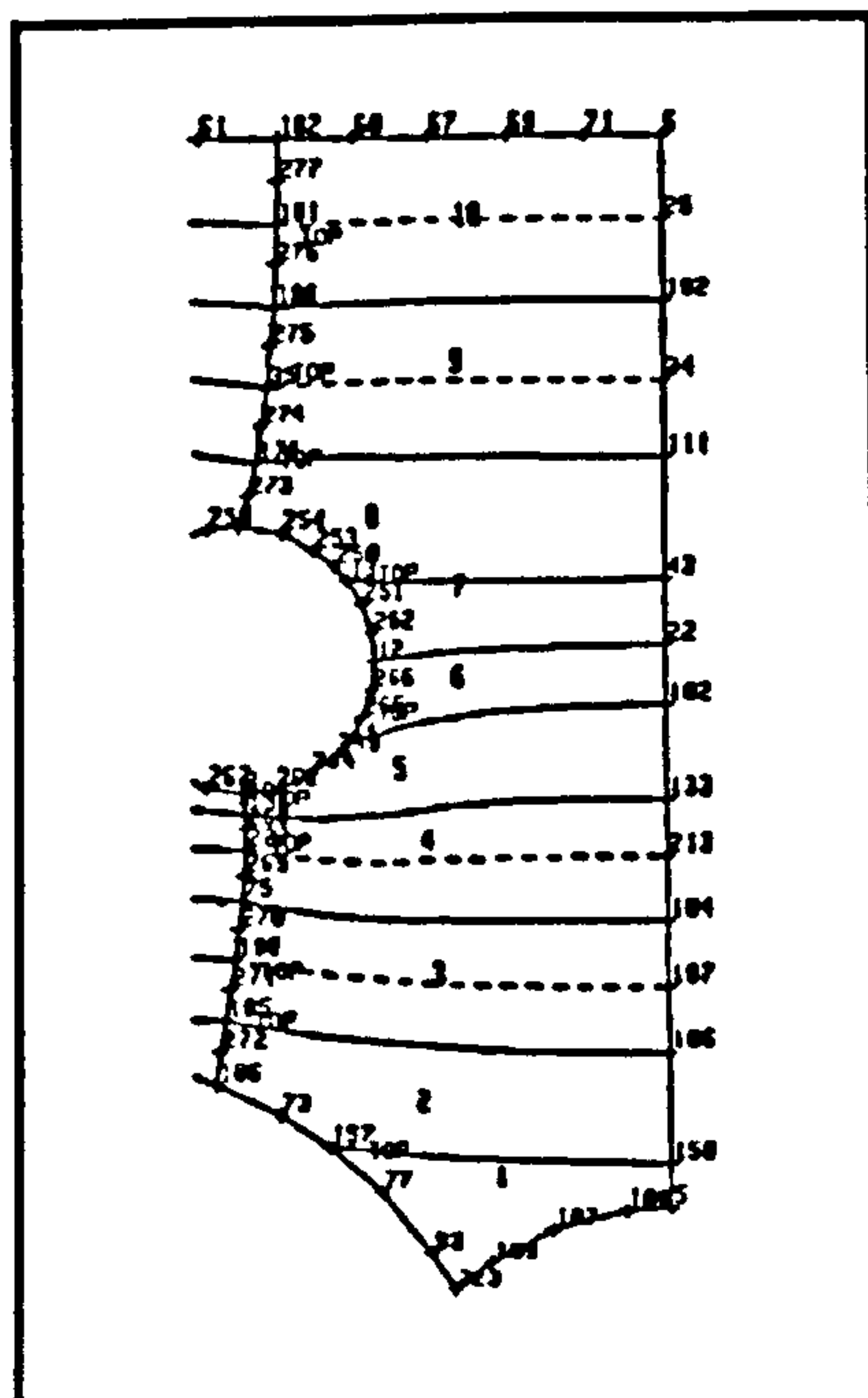


Figure 7.18(e)

When the user is ready to exit from this menu page and move back into the 'master' menu page, the `RETURN` option is activated.

7.18 Cloth width adjustments

Display:	
ALL	SUBSET

Adjust:	
NODE	SEAM
SNAP_OFF	SNAP_ON
SCREEN	KEYBD

ClothPair:	
COUPLE	DECOUPLE
SHEAR_OFF	SHEAR_ON

Topology:
CLOTH->2

DUMP
------

RETURN
--------

Furthermore, a cloth has an allowable width which is limited by the physical width of the fabric roll. Consequently, a problem arises if a cloth becomes too wide. The `ADJUST` option under the `c_width:` label in the `CUTTING PATTERNS` menu page shown in figure 7.18(a) is available to the user for solving this problem which involves width adjustments of cloths in the active field. By activating the `ADJUST` option, the user will then enter into the `ADJUST` menu page for cloth width adjustments shown in figure 7.19(a).

Figure 7.19(a)

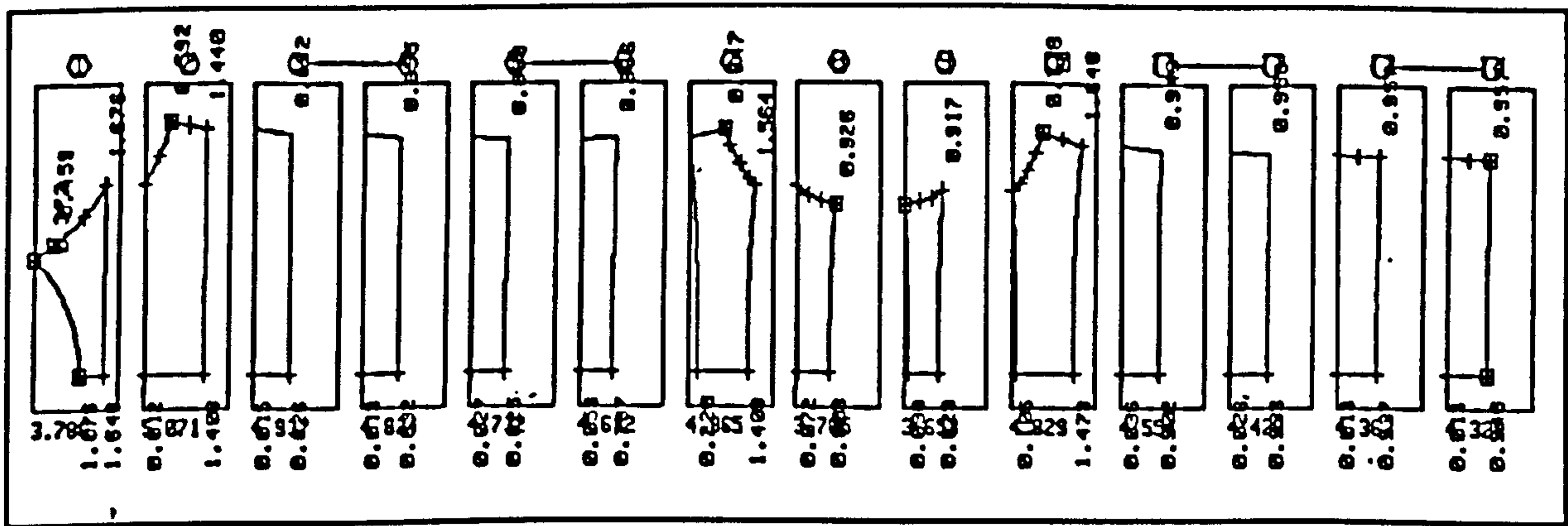


Figure 7.19(b)

In this menu page, all the unfolded cloths in the active field are displayed side by side on the screen as shown in figure 7.19(b). Each cloth is also framed by a box having a width that may be set equal to the physical width of the fabric roll. The discontinuities in each cloth are annotated with the offset widths. In addition, given at the top and bottom of each cloth are the cloth number and length of the cloth respectively. On display in the editbox located beneath the graphics window will be information which includes the cloth nominal width, and the stretch compensation and decompensation factors for the fabric material as shown below, ie.

Field	Cloth Nos	CLOTH	Compensation	Stress	Max	Mean	Min
No	Total	14	NOMINAL	Warp_ %	0.00	Warp	719
2	Unfolded	14	WIDTH	2.000	Fill_ %	0.00	Fill
							485
							195
							54



The cloth nominal width sets the width of the box which frames each of the cloths displayed on the screen. The user can directly edit the value of the cloth nominal width and therefore controls the width of the framing box. It is usual that the cloth nominal width is set equal to the physical width of the fabric roll with due allowance of the fabric material for the cloth seams. Hence, the user can find out directly from the screen display if there is any cloth width which exceeds the box width and therefore the width of the fabric roll.

At any stage, the DUMP option can be activated to output the current display on the screen directly to the laser printer.

Under the Display: label are the ALL and SUBSET options. When the SUBSET option is activated, the user will then be prompted on the screen by the 'cloth pick' pointer. The user can subsequently use the 'cloth pick' pointer to pick any two of the cloths displayed on the screen. The subset of cloths which are between and including the two 'picked' cloths will be highlighted in red. The accept/abort pointer will then appear. If the user accepts this subset of cloths, the screen display will then be updated to show only the cloths which belong to the subset as shown below in figure 7.19(c).

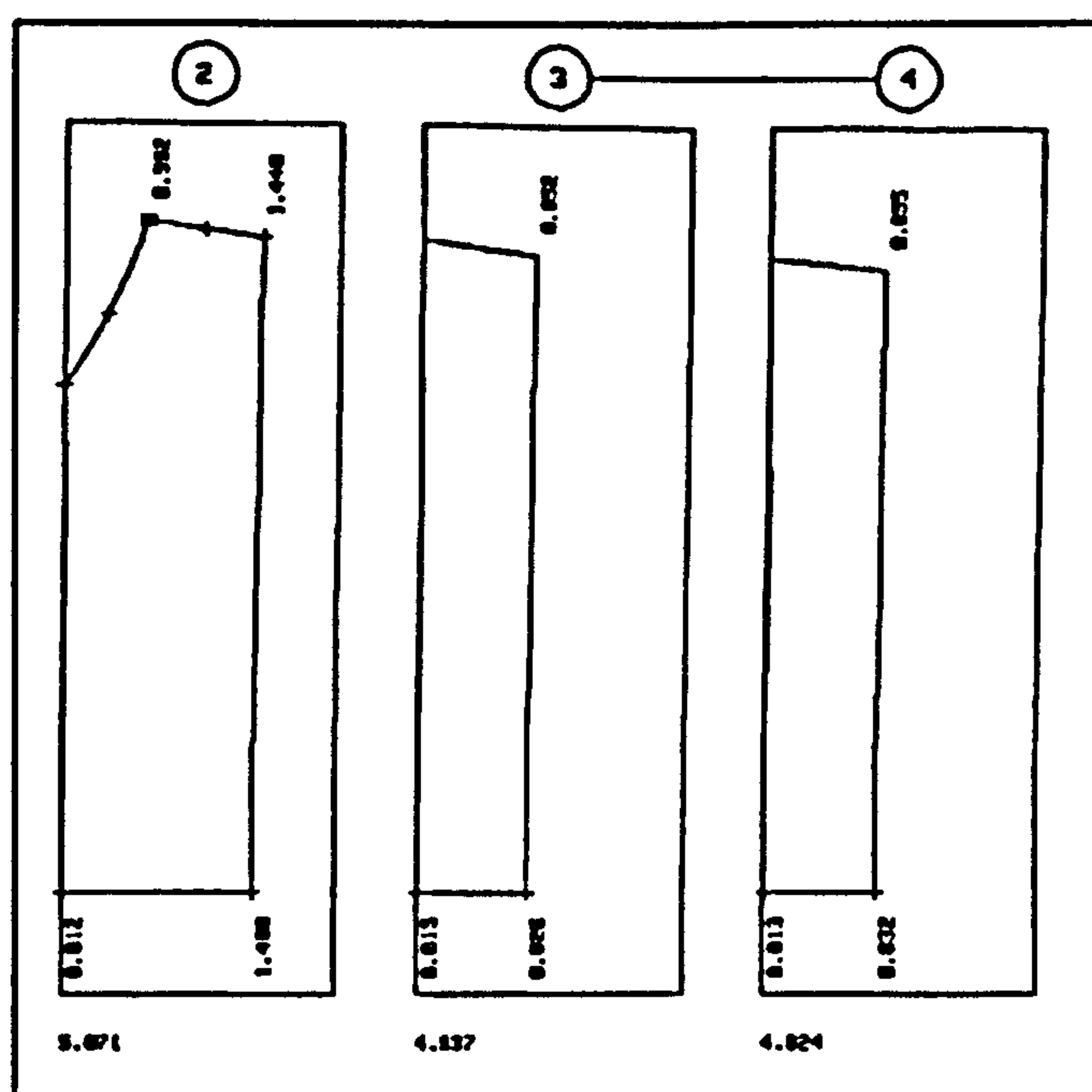


Figure 7.19(c)

With fewer cloths in the subset, these cloths will be shown enlarged on the screen which in turn is helpful when performing specific operations. By activating the ALL option, all the cloths in the active field will again be displayed on the screen as shown in figure 7.19(b).

The cloth widths should be adjusted so that they all fall eventually within their framing boxes. This can effectively be done by moving the nodes which are located at the ends of geodesic seams. These nodes are moved along the ridge or boundary cable in which they lie. In addition, along the cable are link

elements which are connected to these nodes. As a result of the node movements, the lengths of these link elements will change and have to be recalculated within the software.

The options grouped under the **Adjust:** label include the **NODE**, **SEAM**, **SNAP\_OFF**, **SNAP\_ON**, **SCREEN** and **KEYBD** options. With an active **NODE** option, the user can then proceed to adjust the cloth widths. Subsequently, by activating the **SCREEN** option, the user will be then prompted on the screen by the 'node pick' pointer. The user can then use the 'node pick' pointer to pick one of the cloth nodes on the screen. The user can only pick a node which is at the end of a geodesic seam of a cloth. This node should also lie along a ridge or boundary cable but not at the end of the cable. A cloth node located at the end of a cable will be marked by a symbol in the form of a small square enclosing a cross. If a valid node is picked, the 'picked' node will be marked by a cross symbol highlighted in red. This is followed by moving the 'picked' node to a new position on the screen. The user will in turn be prompted by a pointer in the form of a cross symbol to mark this new position on the screen. This pointer will be moved to the appropriate position and by clicking the left mouse button, this position will then be marked by a cross symbol in the cyan colour. As shown below in figure 7.19(d), the accept/abort pointer will then appear.

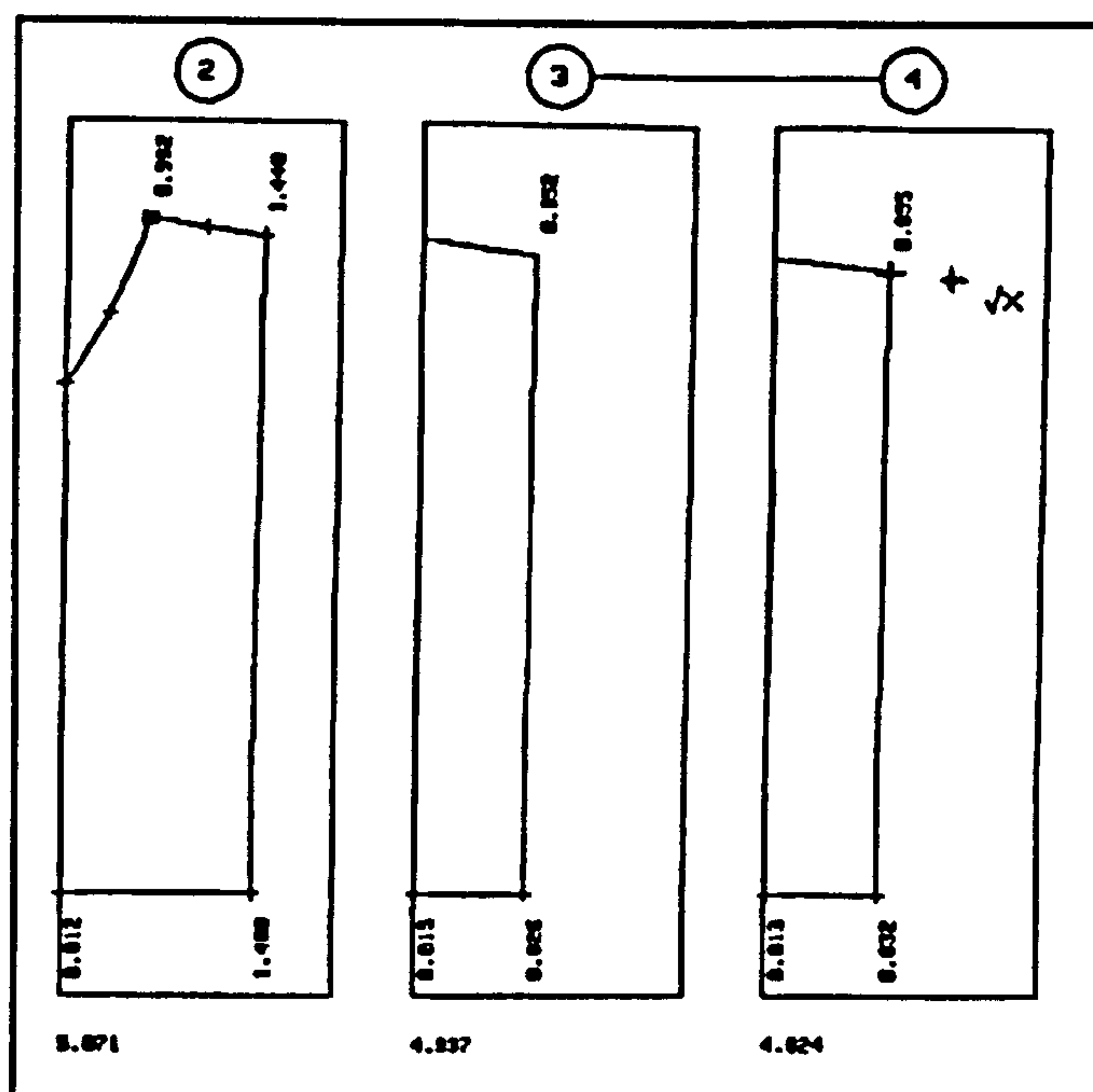


Figure 7.19(d)

If the user accepts the marked position, the 'picked' node will then be moved to this position on the screen and new spatial coordinates given to the node. This will in turn affect the link elements which are connected to the 'picked' node. The lengths of these link elements will be recalculated so that the current element tensions are maintained. Clearly, the adjoining cloth in the active field which shares the node that has just been moved will be adjusted accordingly as well. The seam which is common to the two cloths affected by the node movement is no longer geodesic and will be displayed as a straight line on the screen. In this way, the user can easily identify the cloths whose



nodes have been moved. The user can continue to make width adjustments to the different cloths in the active field. To exit from the `SCREEN` option, the user will click the right mouse button when prompted to pick the next node.

An active `SNAP_OFF` option applies in the case of the on-screen node movement described above. With an active `SNAP_ON` option however, there are additional conditions which apply to the on-screen node movement. If the marked position to which the 'picked' node will be moved is very close to either the left or right side of the box which frames the cloth concerned, the marked position will then snap onto the corresponding side of the box. The `SNAP_ON` option is therefore useful when the user intends to move a 'picked' node up to exactly the left or right side of the framing box. In this way, a cloth width which makes full use of the fabric roll may be achieved.

Furthermore, the `KEYBD` option is also available to the user for making cloth width adjustments. If the precise movement of a cloth node is desired, this option is used instead of the `SCREEN` option. When the `KEYBD` option is activated, the user will then be prompted on the screen by the 'node pick' pointer. The user can subsequently use the 'node pick' pointer to pick one of the cloth nodes on the screen. As in the case of the `SCREEN` option, the user can only pick a node which is located at the end of a geodesic seam of a cloth. This node should also lie along a ridge or boundary cable but not at the end of the cable. If a valid node is picked, the 'picked' node will be marked by a cross symbol highlighted in red. This is followed by moving the 'picked' node to a new position on the screen. In this case unlike the `SCREEN` option, the node movement is operated through the editbox as shown below located beneath the graphics window.

Cloth	Node	OFFSET	INCREMENT	[MOVE]	[DEFAULT]	[RETURN]
9	13	0.917	0.100			

The information shown in the editbox includes the cloth number, node number, offset value and increment value. In the editbox are also the `[MOVE]`, `[DEFAULT]` and `[RETURN]` command buttons. The number of the cloth which is shown connected to the 'picked' node on the screen will be the cloth number in the editbox. The absolute offset value refers to the local  $x$  coordinate of the 'picked' node. The increment value refers to a distance in the local  $x$ -axis direction (ie. horizontal distance) relative to the current offset of the 'picked' node. A positive increment value is a distance further to the right while a negative value indicates a distance further to the left of the current offset of the 'picked' node. In other words, the increment value can be considered as a relative offset value. The node number in the editbox will be that of the 'picked' node. The user can directly edit the offset and increment values currently shown in the editbox. If a new offset value is specified, a marker in the form of a cross symbol in the cyan colour will appear on the screen. This marker will be placed at the position which corresponds to the total offset value given by combining the new offset and current increment values. This marked position will be derived from an interpolation which involves the total offset value. If the marked position is to be shifted further to the left or



right, an appropriate increment value can be specified in the editbox. The marker will then be placed at the position indicated by the total offset value obtained from combining the new increment and current offset values. Hence, the user can continue to adjust the absolute and/or relative offset values until the marker is placed at the desired position on the screen. By activating the [MOVE] command button, the 'picked' node will then be moved to the current marked position. As a result of the node movement, specific related information will in turn be processed as in the case of the `SCREEN` option. The offset value in the editbox will be updated accordingly to that for the new position of the 'picked' node and the increment value will be reset to zero. On the other hand, when the [DEFAULT] command button is activated, there is no movement of the 'picked' node but instead default values are assigned to the offset and increment values in the editbox. The default increment value is zero while the default offset value is that for the current position of the 'picked' node. After moving the 'picked' node to the desired position, the user is then ready to operate on the next cloth node. By activating the [RETURN] command button, the user will exit from the editbox control and return to the menu control. Subsequently, the 'node pick' pointer will appear to prompt the user to pick the next cloth node on the screen. The user can then repeat the sequence of operations as described above. Alternatively, the user can exit altogether from the `KEYBD` option by clicking the right mouse button.

By using the `SCREEN` and/or `KEYBD` options, the user has a highly interactive and convenient means of performing the task of cloth width adjustments. There is also continuity between this task and the other operations involved at the patterning stage. This task has therefore been much simplified for the user and results in reduced cutting pattern production time.

In some cases however, a cloth cannot be trimmed to the required width purely through node adjustments. For such a cloth, the `CLOTH->2` option under the `Topology:` label will be used to split the cloth into two smaller ones. It may be desirable when performing this exercise, to have a subset of the cloths concerned displayed on the screen as shown in figure 7.19(c) using the `SUBSET` option. When the `CLOTH->2` option is activated, the user will then be prompted on the screen by the 'cloth pick' pointer. The user can then use the 'cloth pick' pointer to pick the cloth which is to be split. The 'picked' cloth will be highlighted in red. The user will then be prompted to pick a point along one end of the 'picked' cloth. This cloth end should be one which is part of a ridge or boundary cable. The 'picked' point will be marked by a small cross symbol in the cyan colour. This point may be at the location of an existing node. On the other hand, if this point falls between two nodes, a new node will be created. The accept/abort pointer will then appear. After accepting the first 'picked' point, the user will be prompted to pick another point along the opposite end of the 'picked' cloth. The second 'picked' point will similarly be highlighted. The two 'picked' points define the position of the new seam line which will divide the 'picked' cloth into two smaller ones. The accept/abort pointer will then appear. If the user accepts the two 'picked' points, the 'picked' cloth will then be split. The new nodes, elements and geodesic seam



for the two new cloths will automatically be generated within the software. The 'picked' cloth together with its membrane elements will also be deleted automatically from the model. The user can continue to pick and split another cloth which is displayed on the screen. On the other hand, the user may decide to exit from the CLOTH->2 option by clicking the right mouse button.

All the cloth width adjustments mentioned above will disturb the equilibrium of the model achieved from the previous form-finding. In order to reequilibrate the model, further form-finding is therefore necessary. After making all the necessary cloth width adjustments, the user can exit from the current menu page and return back to the CUTTING PATTERNS menu page. The user can in turn proceed to the ANALYSE menu page in order to perform an analysis of the model. During the analysis, the seam lines will take up new geodesic paths over the surface of the model. After the analysis, the user can return to the CUTTING PATTERNS menu page and then into the ADJUST menu page. If the unfolded cloths are still unacceptable, the whole process of cloth width adjustments followed by form-finding will be repeated until satisfactory results are achieved.

Furthermore, the ADJUST menu page provides another useful tool of allowing one actual cloth panel to be modelled as two cloths in the numerical model. Each cloth comprises of a sequence of triangular membrane elements along the length of the cloth. In addition, the length of each cloth is orientated in the warp direction of the fabric material. In areas of high surface curvature, it may not be possible to accurately represent the local curvature in the fill direction with just an element across the width of a cloth. For such a situation, using two cloths instead of one will obviously give a better modelling of the local fill curvature. This results from the fact that the local surface geometry will be represented by an increased number of node coordinates. On the shopfloor however, these two cloths can be combined together to produce a single panel to be fabricated from the fabric roll. In this way, economic use of the fabric roll can be achieved. For the above purpose, options have been implemented into this menu page in order to provide a fully interactive means of doing the job.

Under the CLOTHPAIR: label is a group of options which include the COUPLE, DECOUPLE, SHEAR\_OFF and SHEAR\_ON options. Firstly, the COUPLE option is used to select any two adjoining cloths to be coupled together. When this option is activated, the user will then be prompted on the screen by the 'cloth pick' pointer. The user can subsequently use the 'cloth pick' pointer to pick a cloth and the 'picked' cloth will be highlighted in red. The user will then be prompted to pick a second cloth which has to be adjacent (ie. either to the left or right) to the first 'picked' cloth. The second 'picked' cloth will again be highlighted in red. The accept/abort pointer will then appear. If the user accepts the pair of 'picked' cloths, these two cloths will then be grouped as a coupled pair within the software. A line will be drawn linking the cloth numbers displayed above the two coupled cloths as shown in figure 7.19(c) to denote the coupling between the two cloths. A cloth pair number will also be assigned to the coupled pair of cloths. The user can subsequently proceed to



pick and couple together another pair of adjoining cloths. In fact, the software will not allow the user to pick a cloth which is already part of a coupled cloth pair. On the other hand, the user may decide to exit from the on-screen interaction mode and therefore operation of the `COUPLE` option by clicking the right mouse button.

If a cloth in a coupled pair is split into two smaller ones using the `CLOTH->2` option described above, the cloth coupling information will be adjusted accordingly within the software, ie. one of the two split cloths will remain coupled to the other cloth of the coupled pair.

Later, if desired, any pair of adjoining cloths which have been coupled together using the `COUPLE` option can also be decoupled through the `DECOUPLE` option. A cloth which is not coupled to any other cloth is taken as an individual cloth. When the `DECOUPLE` option is activated, the user will then be prompted on the screen by the 'cloth pick' pointer. The software will only allow the user to pick a cloth which has been coupled to another cloth. The user can subsequently use the 'cloth pick' pointer to pick a cloth. The accept/abort pointer will appear when a valid cloth is picked. If the user accepts the pair of coupled cloths, this pair of cloths will then be decoupled from each other within the software. The line linking the cloth numbers displayed above the pair of cloths will also be removed to denote the loss of coupling between the two cloths. The user can proceed to pick and decouple another pair of coupled cloths. On the other hand, the user may decide to exit from the on-screen interaction mode and therefore operation of the `DECOUPLE` option by clicking the right mouse button.

Furthermore, the coupled cloth pairs which have been defined in the active field as described above can also be operated on by the `SHEAR_ON` and `SHEAR_OFF` options. When the `SHEAR_ON` option is activated, the two adjoining cloths in each coupled cloth pair will then be combined or sheared together to produce a single cloth panel. During the shearing process, each of the two adjoining cloths will be sheared across the cloth width to a common straight line, ie. the line which joins the nodes at the two ends of the geodesic seam common to the two coupled cloths. This line will be aligned along the local  $y$ -axis direction through rotations of the two cloths before they are being sheared together. It is assumed that the flexibility of the fabric material can accomodate the in-plane shear distortions caused by shearing two cloths together. Each sheared cloth will again be shown in an orientation which gives the minimum width. Furthermore, the `SHEAR_ON` option has no effect on the decoupled cloths in the active field. On the other hand, by activating the `SHEAR_OFF` option, each sheared cloth will then be converted back into the two component cloths which are coupled to each other. All these component and individual cloths in the active field will be displayed on the screen as shown in figure 7.19(b) which represents the case of an active `SHEAR_OFF` option. Figure 7.19(e) shows the case when the `SHEAR_OFF` option is active.



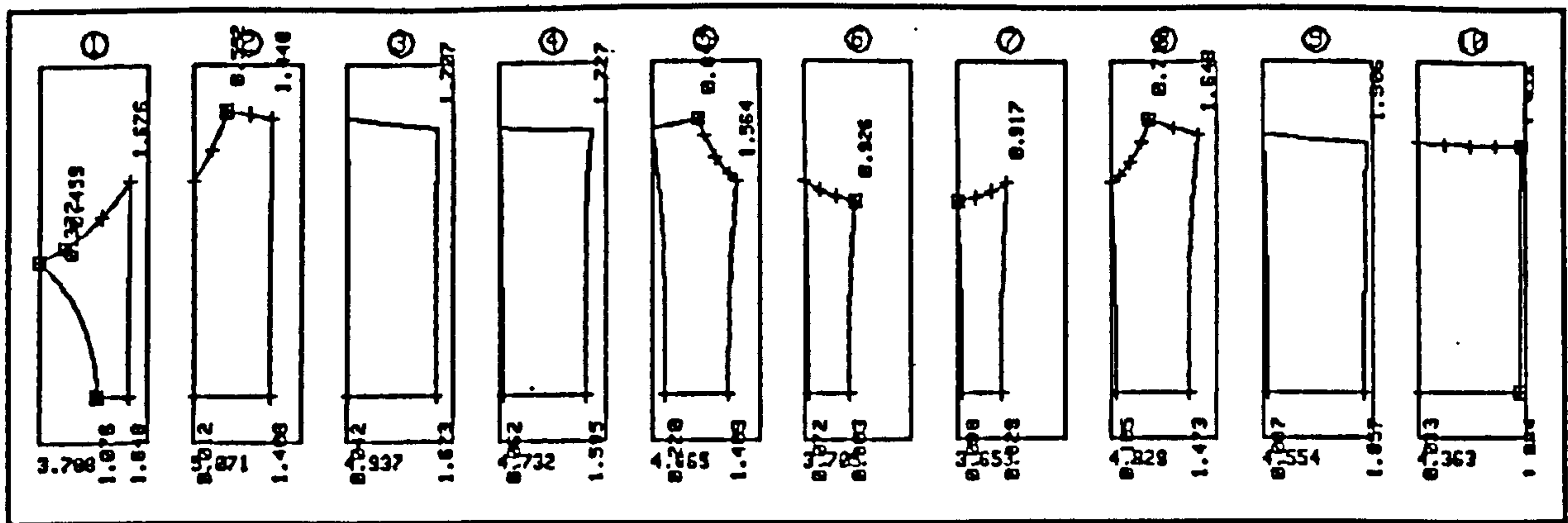


Figure 7.19(e)

By activating the RETURN option, the user will then move back into the CUTTING PATTERNS menu page shown in figure 7.18(a). The SHEAR\_ON and SHEAR\_OFF options are also available under the clothPair: label in the CUTTING PATTERNS menu page. These two options determine how the cloths will be displayed on the screen. With an active SHEAR\_ON option, each pair of coupled cloths will be shown on the screen as a single cloth panel (which is derived from shearing together the two coupled cloths). On the other hand, the two adjoining cloths in each coupled cloth pair will be shown on the screen as separated from each other when the SHEAR\_OFF option is active. The non-coupled cloths will always be displayed as separate cloths regardless of whether the SHEAR\_ON or SHEAR\_OFF option is currently active. Figure 7.18(a) shows the cloths in the active field when the SHEAR\_OFF option is active while figure 7.18(e) shows the case for an active SHEAR\_ON option in which the sheared cloths are each marked by a dashed line dividing the cloth. In this way, it becomes immediately obvious to the user which are the sheared cloths in the active field.

## 7.19 Structure visualisation

Tension structures often present complex surface curvatures which are difficult to comprehend without the help of a physical model. An excellent alternative is provided in the software by the use of high resolution computer graphics. An advanced structure visualisation module has been set up within the SURFACE\_M menu page shown in figure 7.20(a). This menu page is accessible from the GRAPHIC DISPLAY menu page already described earlier. The user can enter into the GRAPHIC DISPLAY menu page from the 'master' menu page as well as a number of other menu pages. The visualisation module fully exploits the SRX graphics coprocessors which have been incorporated into the workstation. These coprocessors provide the hardware implementation of hidden surface removal, smooth surface shading, multiple lighting sources, full surface texture and specular reflection modelling. The surface shading based upon the Gouraud shading model is used, and this gives smooth shading when illuminated by a lighting source. The description of complex surfaces is aided with the support of non-uniform rational spline surfaces. As a result, the surface shaded computer images can be generated at high speed, and therefore enabling the module to be highly responsive to the user. The



module provides an effective and fully interactive interface for the user to exploit the power offered by the hardware.

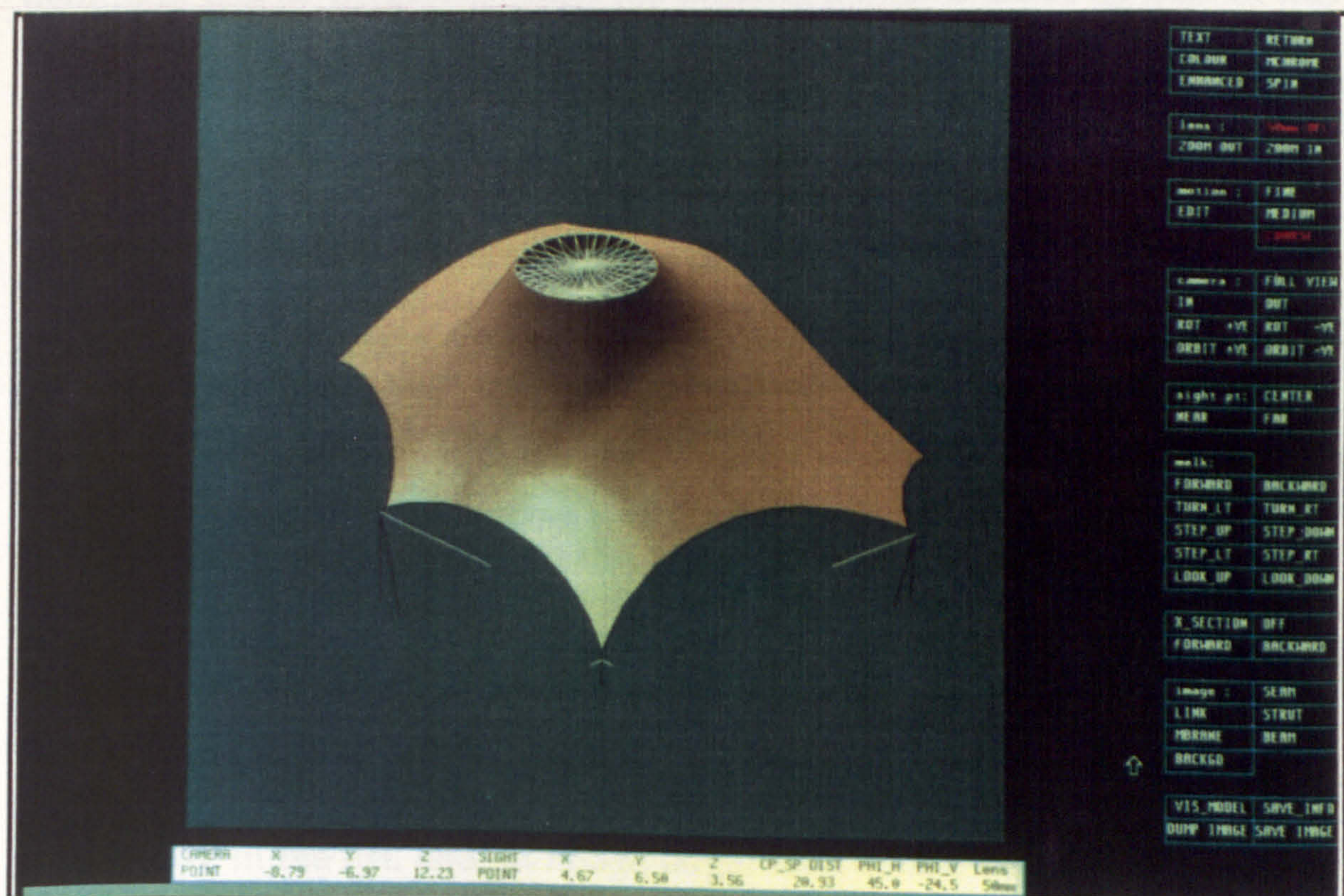


Figure 7.20(a)

In this menu page, the generation of images on display in the graphics window is based on the idea of a view as seen through a camera and thus, assumes an observer pointing the camera at an object. The active camera point refers to the current position of the camera (ie. observer) while the active sight point is the current position of a point on the object. A line can be drawn from the active camera point to the active sight point and this line is the sight line of the observer. Consequently, the observed view represented in the image display can be controlled by manipulating the active camera and sight points as will be described below.

An active **COLOR** option is the default setting in the **SURFACE\_M** menu page. This implies the display of images in colour on the screen. In the graphics coprocessors are 32 planes of memory allocated for the colour display, 24 of which are available for pixel colour definition. Within the software, this memory space is divided into a double buffer zone with 12 planes of memory in each buffer. While one buffer is being used for the current image display on the screen, the following image will be generated in the second buffer. When the image generation in the second buffer is complete, there will be a buffer switching to display the image on the screen. The first buffer will in turn be used to generate the following image. In this way, successive screen redraws will be continuous and flicker free as a result of using double buffering. In addition, a single buffer of 12 planes of memory enables over 16 million colours to be achieved simultaneously on a  $1280 \times 1024$  pixel



resolution screen. In other words, highly realistic computer images can be produced. Furthermore, colour computer images in even more enhanced definition will be generated when the **ENHANCED** option is active as well. In this case, all the 24 memory planes will be used to generate the image and the graphic processing speed will therefore be slowed down. It is customary to use this option only when the user is ready to photograph the current view of the screen image. On the other hand, an active **MCHROME** option is used to switch off the colours, and the computer images will then be displayed in black and white as well as the very fine shades of grey in between.

When the **SPIN** option is activated, the screen image will show the model going through a spinning motion. The user has to wait for the completion of the spinning motion before any other menu option can be used.

Under the **lens:** label are the **50mm DFLT**, **200M OUT** and **200M IN** options which allow the user to select a view as seen through a camera with varying lens sizes such as 28mm, 35mm, 50mm and so on. A list of these lens sizes are made available within the software. In this way, the degree of perspective in the image shown on the screen can be adjusted accordingly. The **200M OUT** option when activated will change the current lens size to the next larger size in the list, and an image smaller than before will then be produced. On the other hand, by activating the **200M IN** option, the lens size will be changed to the next smaller size in the list, and an image larger than before will in turn be achieved. If the **50mm DFLT** option is activated, the current lens size will be reset to the 50mm value and the corresponding image will then be shown on the screen.

Under the **motion:** label are the **FINE**, **MEDIUM**, **COARSE** and **EDIT** options. These options are used to define the size of the incremental step when moving either the camera or sight point. An active **FINE** option indicates that default values for the fine incremental steps will be used. There are separate values for the translational and rotational motions. The motion of either the camera or sight point will then be incremented in steps of the corresponding value. On the other hand, an active **MEDIUM** or **COARSE** option will in turn mean that default values for the medium or coarse incremental steps of the translational and rotational motions will be used. In addition, if the default values are inappropriate, these values can be changed by using the **EDIT** option. When this option is activated, an editbox as shown below will then appear beneath the graphics window.

		FINE	MEDIUM	COARSE	
motion increments	TRANSLATION	0.5	1.5	3.5	[DEFAULT]
	ROTATION	0.5	2.0	5.0	

Now, the values for the fine, medium and coarse incremental steps shown in the editbox can be edited directly. The new values will in turn be used for the subsequent motions of either the camera or sight point.

Under the **camera:** label are a group of options which include the **FULL VIEW**, **IN**, **OUT**, **ROT +VE**, **ROT -VE**, **ORBIT +VE** and **ORBIT -VE** options. These camera options allow



the user to manipulate the view of the screen image through positional adjustments of the camera point.

By activating the `FULL VIEW` option, the camera point will be positioned such that a full view of the entire image is displayed on the screen. This position will be computed within the module using certain default parameters.

When the `IN` option is activated, the camera point will be moved towards the sight point in incremental distances with each click of the left mouse button, and results in an increasing larger view of the image. In addition, if the button remains held down, the camera point will be moved continuously towards the sight point. Conversely, an activated `OUT` option results in the translational motion of the camera point in incremental distances further away from the sight point.

By activating the `ROT +VE` option, the camera point will be rotated by incremental angles about the active sight point. This rotational motion will be in a horizontal sense (ie. in the global  $x$ - $y$  plane) and the clockwise direction. Conversely, the `ROT -VE` option is activated to produce the rotational motion in the anti-clockwise direction.

The `ORBIT +VE` option when activated will result in the rotational motion of the camera point by incremental angles about the active sight point in a vertical sense (ie. in a plane normal to the global  $x$ - $y$  plane) and the clockwise direction. Conversely, the `ORBIT -VE` option is activated to produce the rotational motion in the anti-clockwise direction.

The options grouped under the `sight pt:` label allow the user to move the sight point instead of the camera point. Subsequently, the image corresponding to the view for the new position of the sight point will be displayed on the screen. By activating the `CENTRE` option, the sight point will be positioned at the centre of the entire model. When the `NEAR` option is activated, the sight point will be moved in incremental distances closer to the camera point. The reverse is true for an activated `FAR` option, ie. the sight point will instead be moved further away from the camera point.

Furthermore, if a view given by placing the camera and sight points at specific positions is desired, the user can specify directly in the editbox as shown in figure 7.20(a) the global coordinates for these two positions. The software adopts a right-handed cartesian coordinate system. The user can also edit the value of the distance from the camera point to the sight point. In addition, a view can also be selected by specifying the values of the horizontal and vertical angles in the editbox. The horizontal angle is an angle in the global  $x$ - $y$  plane and is positive when measured in the anti-clockwise sense. The vertical angle is an angle in a plane normal to the  $x$ - $y$  plane and is positive for an upward inclination. These angles will define the direction of the sight line from the camera point to the sight point. In the editbox is also a value for the lens size currently in use.



Under the **walk:** label are a group of options which allow a perceived view of the model on the basis of an observer walking about within the model. This view will be depicted in the image shown on the screen. The z coordinate of the camera point can be set to about the height of the observer. By activating the **FORWARD** option, the camera point will be moved in incremental distances towards the sight point. The z coordinate of the camera point will however be kept constant in order to simulate the situation of the observer walking forward. Conversely, the case of the observer walking backward is achieved by activating the **BACKWARD** option.

The **TURN\_LT** option when activated corresponds to the situation of an observer turning his/her head to the left. In this case, the camera point will be rotated by incremental angles about the current position of the sight point. This rotational motion will be in a horizontal sense and in the anti-clockwise direction. For the case of an observer turning his/her head to the right, the **TURN\_RT** option is activated instead.

By activating the **STEP\_UP** option, the z coordinate of the camera point is incremented in positive steps as in the case of an observer moving up a vertical height. On the other hand, the case of an observer descending a vertical height is simulated by activating the **STEP\_DOWN** option.

By activating the **STEP\_LT** option, the camera point will be moved in incremental distances to the left of and perpendicular to the sight line from the camera point to the sight point. The z coordinate of the camera point will be kept constant during the motion. Conversely, an activated **STEP\_RT** option will produce a motion of the camera point to the right instead.

The **LOOK\_UP** option when activated corresponds to the situation of an observer looking up. In this case, the camera point will be rotated by incremental angles about the current position of the sight point. This rotational motion will be in a vertical sense and in the clockwise direction. On the other hand, for the case of an observer looking down, the **LOOK\_DOWN** option is activated instead.

Consequently, these options offer an economic, convenient and effective means of obtaining a general impression of how the structure will look when actually built. This may be considered as a form of the so-called 'virtual reality'. By using these options, it is possible to simulate the situation of an observer walking through the model and a view inside the model can thus be perceived. With a physical model however, it may be difficult or often impossible to obtain an internal viewing of the model. In other words, the user can explore both the inside and outside of the entire model allowing for all the possible views of an observer. Hence, an overall assessment of the model will therefore be made much easier. If the model has any unsatisfactory features, they can be quickly identified and the appropriate actions taken.



For the SEAM option:

seam	FORM	WIDTH	TOP	LUM_FACTOR	BOTTOM	LUM_FACTOR	return
control	STRIP	0.050	ON	0.95	OFF	0.80	

For the LINK option:

link	HUE	SAT	LUM	ALL/FREE	default	return
control	0.00	1.00	0.00	ALL	colour	

For the STRUT option:

strut	HUE	SAT	LUM	LINE/TUBE	MATERIAL	default	return
control	0.00	1.00	0.00	LINE	STEEL	colour	

For the MBRANE option:

membrane	TOP:	HUE	SAT	LUM	SPEC_H	BOTTOM:	HUE	SAT	LUM	SPEC_H	MATERIAL	TRANSPARENCY	default	return
control		0.02	0.15	1.00	25		0.02	0.15	1.00	15	PLASTIC	0	colour	

For the BACKGD option:

background	HUE	SAT	LUM	default	return
control	0.60	0.26	0.70	colour	

For the TEXT option:

no	SWITCH	<TEXT (up to 60 characters)	----->	POSN:	XA	YA	HEIGHT	HUE	SAT	LUM	add	next	delete	return
1	OFF	???			0	0	0	0.00	0.00	0.00	0.00	last		

Figure 7.20(b)



By activating the `H_SECTION` option, a section will be made across the centre of the model. This sectional view can provide useful hints about the curvature variations over the surface and perhaps the height clearances at various locations of the model. In addition, the `FORWARD` and `BACKWARD` options will in turn allow the user to shift this sectional plane in incremental distances in the forward and backward directions respectively. When no longer required, the sectional view can be switched off by activating the `OFF` option.

Under the `image:` label are a group of options which provide the user with a few controls for the image of the analysis model. By activating one of these options, the corresponding editbox will appear beneath the graphics window, and the operational control will pass from the menu to the editbox. Subsequently, the 'return' button in the editbox when activated will allow the operational control to be passed from the editbox back to the menu.

The `SEAM` option is used for controlling the seam line display on the screen and the editbox which applies in the case of an activated `SEAM` option is given in figure 7.20(b). By default, the seam lines over the surface of the analysis model will be shown as solid black lines. The seam line display for the top and underside of the membrane are controlled separately. If the arrow pointer is positioned over the 'ON' label for the top side seam line display followed by a click of the left mouse button, the label will then switch to 'OFF'. The seam lines for the top side of the membrane will then not be shown. The display switch can be toggled between the 'ON' and 'OFF' states, and the seam line display will in turn be switched on and off accordingly. In addition, the 'LINE' label can be switched to 'STRIP' and the seam lines will then be displayed as strips over the surface. The default value for the strip width can be changed if desired. In this case, the colour for the seam strip display will be specified in terms of an intensity proportion of the membrane colour. The above controls provide a versatile means of adjusting the seam line display to achieve the desired effect.

The `LINK` option is used to manipulate the on-screen display of the link elements in the analysis model and the editbox which applies in the case of an activated `LINK` option is given in figure 7.20(b). By default, the link elements in the model will be shown as solid black lines. If desired, the default colour of the link elements can be changed by specifying the appropriate hue, saturation and luminosity values in the editbox. The 'ALL' label which is the default indicates that all the link elements are displayed on the screen. The 'ALL' label can be switched to 'FREE' in which case only those link elements not lying within the membrane are displayed.

The `STRUT` option operates in a similar manner to the `LINK` option but is used for the display of strut elements in the model which will be shown as solid black lines by default. The editbox which applies in the case of an activated `STRUT` option is given in figure 7.20(b). The 'LINE' label can be switched to 'TUBE' and the strut elements will then be displayed as surface shaded tubes with pointed ends. Each tube will be given a diameter which is decided within the software. The strut display can be toggled between the 'LINE' and 'TUBE' states. The



default colour for the line or tube display of strut elements can be changed if desired, ie. by specifying the appropriate hue, saturation and luminosity values. A further control is the material modelling in the tube display of strut elements. The software allows a list of materials such as aluminium, steel, plastic and rubber to be modelled. This list can be scrolled until the appropriate material label appears in the editbox. The scrolling is initiated by activating the material label. For each material is an associated surface texture which is modelled in the software on the basis of the specular reflection of light. For instance, a smooth surface texture is associated with the plastic material. The smooth surface texture is modelled by a specular reflection coefficient which will result in much light being reflected from the surface and therefore producing a shiny appearance. On the other hand, the rubber material has a dull appearance due to the reduced amount of light being reflected.

The **MBRANE** option provides the user with the controls for the on-screen display of the membrane elements in the model and the editbox which applies in the case of an activated **MBRANE** option is given in figure 7.20(b). The default colour of the membrane elements will be described by the hue, saturation and luminosity values in the editbox, and these values can be changed if desired. The colours given to the top and bottom sides of the membrane are defined separately. In addition, values can be specified for the surface texture and transparency of the membrane. Hence, a fabric material such as a translucent foil can be simulated by prescribing an appropriate transparency level.

The **BACKGD** option is used to control the background colour of the graphics window and the editbox which applies in the case of an activated **BACKGD** option is given in figure 7.20(b). The default background colour of the graphics window will be described by the hue, saturation and luminosity values in the editbox, and these values can be changed if desired.

The **TEXT** option provides the means to add annotation texts to the screen display and the editbox which applies in the case of an activated **TEXT** option is given in figure 7.20(b). The user is allowed to specify up to three lines of annotation texts into the editbox. The size, orientation, colour and position of each line of text can also be specified.

When the user is ready to exit from this menu page and move back into the **GRAPHIC DISPLAY** menu page shown in figure 7.5, the **RETURN** option is activated.

## **7.20 Further visualisation options**

Furthermore, in the **SURFACE\_M** menu page shown in figure 7.20(a) is the **VIS\_MODEL** option whose purpose is to implement further modelling primitives. This option when activated brings the user into the **VIS\_MODEL** menu page shown in figure 7.21(a). A comprehensive library of modelling primitives are available to the user. These primitives include the general



HIDE_MENU	
lighting:	DEFAULT
AMBIENT	MODELLING
DIRECTION	POSITION
READ_FILE	
SOLID	WIREFRAME
surfaces:	
COARSE	FINE
display:	
STRUCTURE	VIS_MODEL
BOTH	
limits:	
STRUCTURE	VIS_MODEL
ALL	
RETURN	

Figure 7.21(a)

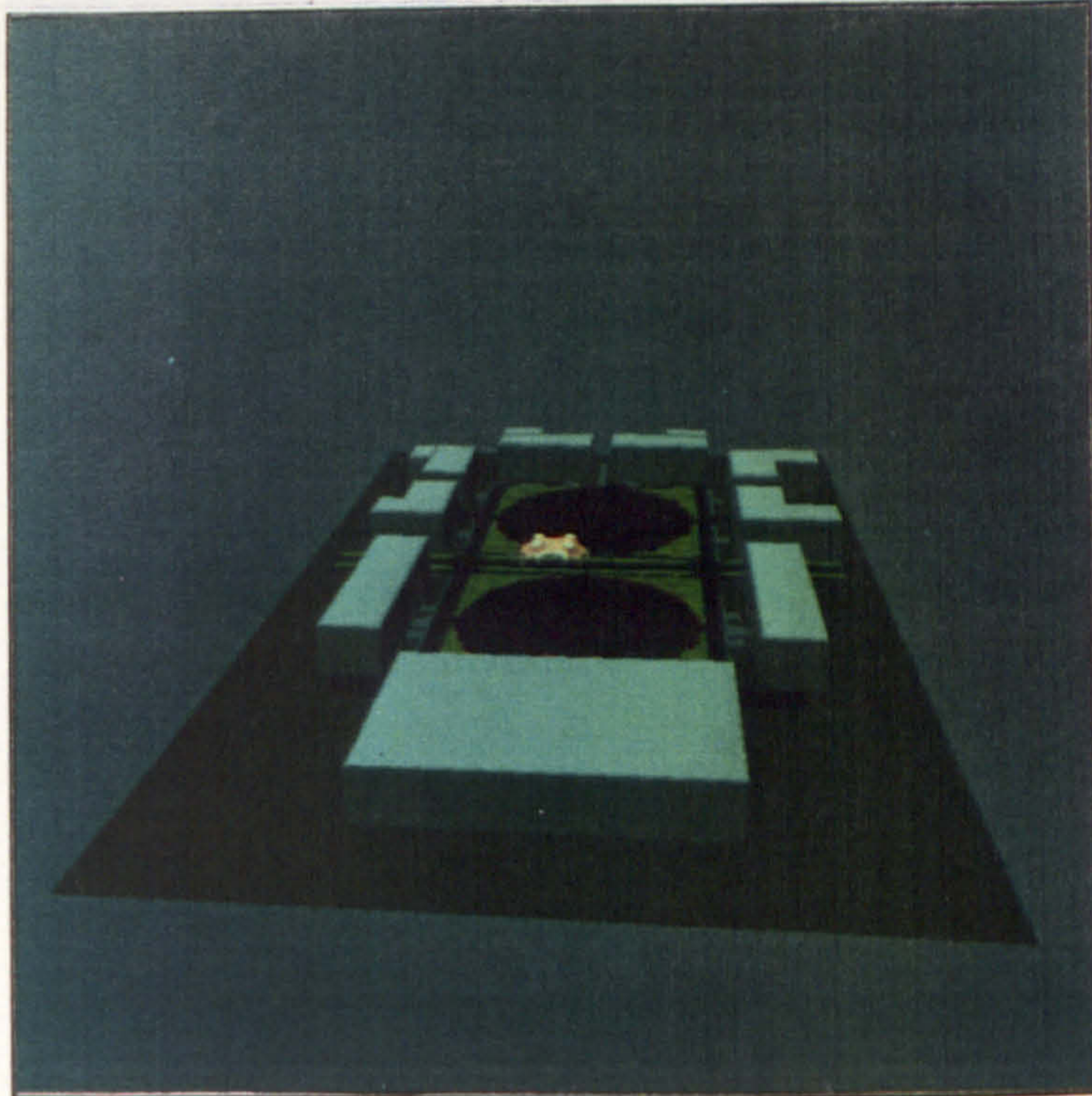
brick elements, ground planes, walls, floors, straight or curved circular tubes, straight or curved rectangular sections, I-beams of varying cross-sections and perforated sheets. These primitives provide the user with the building blocks from which objects of most shapes and sizes can be constructed. In fact, even objects of rather complex geometries can be built using these primitives as shown in figures 7.21(b), 7.21(c) and 7.21(d). It is also possible to model an object down to a high degree of detail. In this way, the existing and/or proposed features which surround the analysis model can be simulated in the computer graphics. This is of particular significance to an architect in order to make a reasonable assessment of how successful the analysis model will integrate with the surrounding features. Although a physical model can also be used to represent the analysis model as well as the surrounding features, there are a few benefits in using the structure visualisation module and hence, making it the preferred choice. Firstly, it is easy to add and delete the modelling primitives, and to study the effects of colours, surface textures and lighting conditions. In addition, the 'walk through'

facility mentioned above is useful for modelling for instance, the situation of a shopper walking about in a shopping complex.

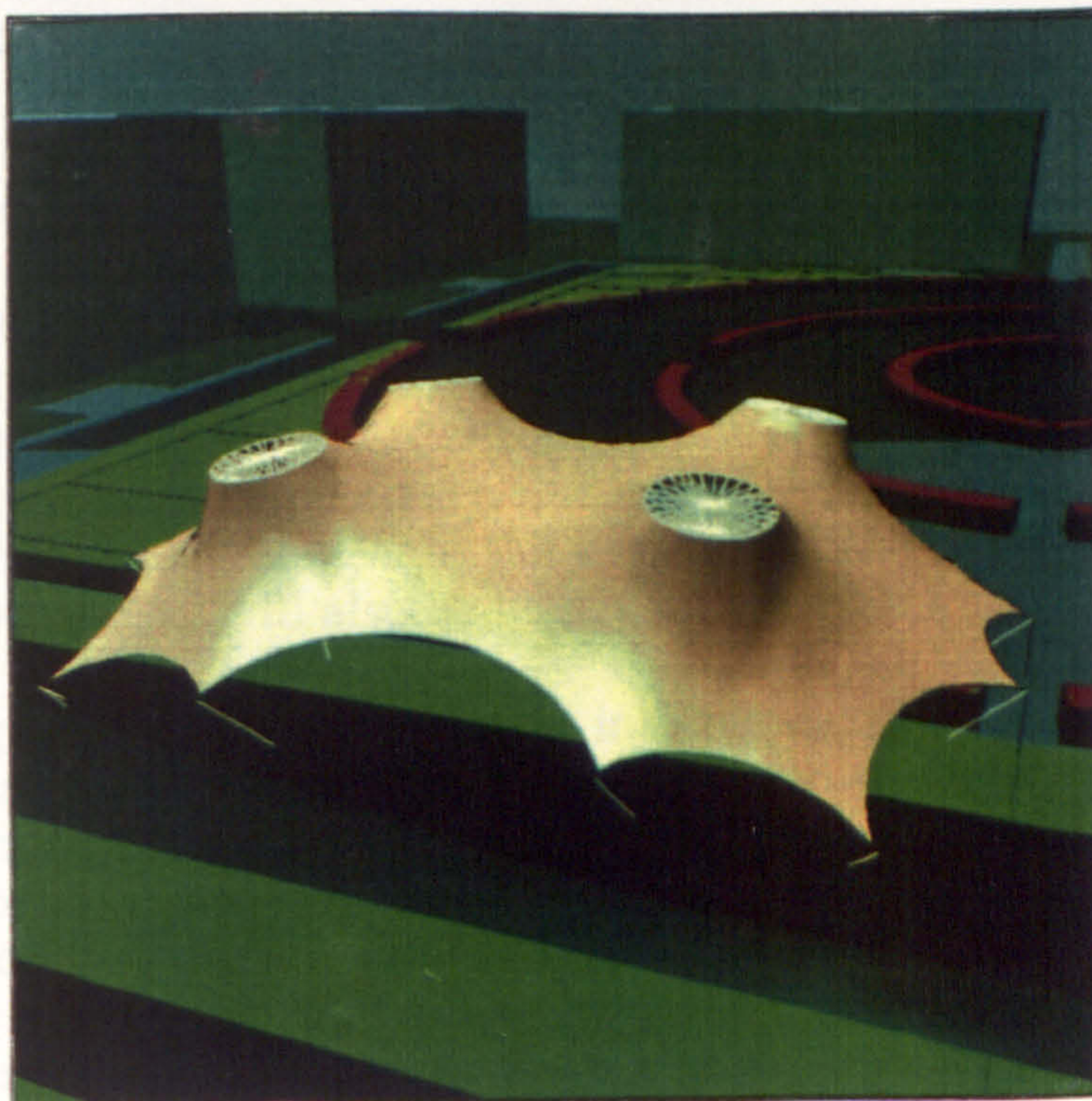
In this case, the user interface is based upon the setting up of a datafile. The software has been structured to accept a list of commands which will be entered into a datafile. Figure 7.21(e) shows an example of such a datafile. These commands serve to instruct the software on what input data to expect, and the actions to take and/or transformations to apply to the input data. The commands are simply code words, and a manual has been prepared which lists the available commands, their associated functions, the required input data and the format in which they should be specified. The user can refer to this manual for the details about the list of available commands. In the datafile should be a list of nodal data, ie. the node number and global coordinates for each node in the list. The modelling primitives will then be defined in terms of these node numbers. For instance, a general brick element is defined by giving the node numbers at each of the 8 vertices of the element. In addition, the required data for a curved tube include the node numbers of the three nodes which will define the plane of the tube in space and the tube diameter. Of the three required node numbers, two node numbers are those at the two ends of the tube. In fact, the three nodes will lie along the centre line of the tube.

The general brick elements can degenerate by node coalescing to some useful shapes such as the triangular blocks used to simulate pitched roofs. The brick elements can otherwise easily model buildings of various shapes and sizes,





Figures 7.21(b)



Figures 7.21(c)





Figures 7.21(d)

and even blocks with distorted surfaces. The ground plane can be used to represent various ground surfaces such as a field, road surface, water surface and so on. The perforated sheet is useful for modelling a wall with window openings. A wide range of primitives are available, and this adds flexibility and power to the structure visualisation module. These modelling primitives have been used to produce highly realistic and sophisticated images shown in figures 7.21(b), 7.21(c) and 7.21(d).

When the appropriate colour and surface texture are given to a modelling primitive, greater realism will be added to the image. Another useful description is the transparency level in varying degrees (from completely opaque to completely transparent) which can be assigned to the membrane elements and planar sheets in order to simulate fabrics such as translucent foils and glass windows respectively. Consequently, it is possible to study the impact of daylight penetrating into the structure through these materials. The transparency parameter will also be handy in modelling items such as water.

Besides having to enter the data directly into the datafile, the software also provides a data generation facility. This is achieved through the use of additional commands which will involve the simple combinations of translations, rotations about any node and reflections of modelling primitives about a defined plane as shown in figure 7.21(e). In many instances, a simple basic primitive will be set up and then by applying repeat transformation commands, reasonably complex shapes can be built up. The elements in the analysis model can similarly be duplicated for visualisation purposes without requiring extra information from the analysis section. The data generation facility can help to reduce considerably the amount of data which has to be



DATUM 1.00	42 0.0 2.0 3.0
WIRE_COLOUR 1.0 1.0 1.0	BRICK 3
COLOUR 6	1 2 3 3 0 0 0 0 1 1 3 2 1 2
1 0.00 0.00 0.70	5 6 7 8 0 0 0 0 1 1 4 2 1 2
2 0.50 1.00 1.00	9 10 11 12 13 14 15 16 1 1 2 2 1 2
3 0.83 1.00 1.00	FLOOR 1
4 0.17 1.00 1.00	17 18 19 20 0.30 5 1 2 1 2
5 0.50 0.00 0.20	WALL 1
6 0.00 0.00 0.90	21 0 0 22 0.50 6 1 1 2
TEXTURE 2	SHEET 1
1 15 0.50 0.50 1.00 0	23 24 25 26 3 2 1 2 1 2
2 25 0.50 0.50 1.00 0	0.50 0.50 1.50 1.50 5 1
NODE 42	LINE 1
1 0.0 0.0 5.0	1 40 3 3 1 2 3
2 4.5 0.0 5.0	ROUND_TUBE 2
3 5.5 5.0 6.0	17 21 0.5 0.5 3 2 2 2 1
4 0.0 4.5 5.0	2 17 0.5 0.5 3 2 1 2
5 4.5 0.0 3.5	RECT_TUBE 3
6 7.0 0.0 3.5	3 16 0.3 0.3 20.0 3 2 1 2
7 7.0 5.0 3.5	35 36 0.5 0.5 0.0 3 2 1 2
8 4.5 5.0 3.5	38 39 0.5 0.5 0.0 3 2 1 2
9 9.0 9.0 4.0	GROUND_PLANE 1
10 9.0 7.5 4.0	3 2 4 23 24 25 26 5 27 28 29 30 31 1 2
11 11.0 7.5 4.0	ROUND_ARCH 2
12 11.0 9.0 4.0	32 33 34 1.0 1 1 1 3
13 9.0 9.0 2.0	36 37 38 0.5 3 2 2 2 3
14 9.0 7.5 2.0	RECT_ARCH 1
15 11.0 7.5 2.0	36 37 38 0.50 0.50 3 2 1 1
16 11.0 9.0 2.0	2_NODE_BEAM 1
17 -2.0 12.0 0.0	1 3 5.0 0.6 0.8 4 1 2 1 2
18 -2.0 -2.0 0.0	4_NODE_BEAM 1
19 12.0 -2.0 0.0	5 6 7 8 0.50 3 2 2 2 3
20 12.0 12.0 0.0	STRUCTURE 2 2 4
21 -3.0 11.0 10.0	REPEAT 1
22 12.0 12.0 9.0	TRANS 0.50 0.75 -1.20
23 -1.0 11.0 1.0	ROT 40 -5.0 5.0 20.0
24 -1.0 -4.0 1.0	REFL 41 42 0.0
25 10.0 -4.0 1.0	END_REPEAT
26 10.0 11.0 1.0	REPEAT 2
27 0.0 5.0 0.5	TRANS 0.0 0.0 0.5
28 -0.5 3.0 1.0	ROT 1 10.0 0.0 0.0
29 6.0 1.0 0.5	TRANS 0.0 0.0 0.5
30 8.0 3.0 1.0	ROT 1 5.0 0.0 0.0
31 7.0 4.0 1.0	TRANS 0.0 0.0 0.5
32 2.0 6.0 5.0	ROT 1 0.0 0.0 5.0
33 4.0 6.0 15.0	REFL 41 42 0.0
34 10.0 6.0 5.0	END_REPEAT
35 0.0 5.0 1.0	REPEAT 3
36 0.0 5.0 5.0	ROT 1 30.0 0.0 0.0
37 5.0 5.0 10.0	END_REPEAT
38 10.0 5.0 5.0	REPEAT 4
39 10.0 5.0 1.0	ROT 41 30.0 0.0 0.0
40 5.0 5.0 5.0	END_REPEAT
41 0.0 0.0 0.0	END

Figure 7.21(e)



entered into the datafile. This is useful especially in the case of a datafile for highly complex images as shown in figures 7.21(b), 7.21(c) and 7.21(d).

The datafile of commands and input data will be created using the text editor of the Unix operating system. In addition, the datafile must be placed in the relevant project directory within the operating system.

The `READ_FILE` option when activated will cause an editbox as shown below to appear beneath the graphics window.

input data file ?  
???

The user will be prompted to enter the name of a datafile in the editbox. The software will know to go to the relevant directory, and open and read the datafile with the name specified by the user in the editbox. The commands and data in the datafile will subsequently be used to set up the modelling primitives. A certain amount of computational effort will be required to generate the information needed to produce the image shown on the screen.

If desired, the modelling primitives can also be shown in a wire-frame outline by activating the `WIRE_FRAME` option. The colour for the wire-frame outline will be specified in the datafile shown in figure 7.21(e).

Under the `lighting:` label are a group of options which provide the user with a few controls for the lighting conditions in the screen display. These options enable the modelling of different types of lighting conditions such as the ambient, parallel and point lighting. By activating one of these options, the corresponding editbox will appear beneath the graphics window, and the operational control will pass from the menu to the editbox. Subsequently, the 'return' button in the editbox when activated will allow the operational control to be passed from the editbox back to the menu.

The ambient lighting corresponds to the case of light shining onto an object from all directions. Hence, the ambient lighting will be the same at any location in the model. The `AMBIENT` option provides the user with the means of controlling the ambient lighting and the editbox which applies in the case of an activated `AMBIENT` option is given in figure 7.21(f).

By toggling the lighting switch label between the 'ON' and 'OFF' states, the ambient lighting will accordingly be switched on and off. For the default case, the ambient lighting will be switched on with a default value given to the light intensity. This default value can be changed to that which will give the ambient lighting as desired.

Parallel lighting corresponds to the case of light in parallel rays being emitted from a source. A far away light source such as the sun produces parallel lighting. Both the `MODELLING` and `DIRECTION` options are meant for the task of controlling parallel lighting. The editbox which applies in the case of either an activated `MODELLING` or `DIRECTION` option is given in figure 7.21(f).



For the AMBIENT option:

ambient	SWITCH	LEVEL	return
	ON	0.40	

For the MODELLING option:

modelling	SWITCH	LEVEL	DELTA_H	PHI_V	return
	OFF	0.20	30.0	0.0	

For the DIRECTION option:

directional	SWITCH	LEVEL	PHI_H	PHI_V	last	return
1	ON	0.50	-45.0	-74.2	next	

For the POSITION option:

positional	HUE	SAT	LUM	posn:	X	Y	Z	SPOT	LIGHT	ATTEN	LIGHT	CONE	LIGHT	dim:	PHI_H	PHI_V	last	return
1	ON	0.00	0.00	0.70		0.00	0.00	0.00	ON	1	ON	1000.0	ON	60.0	135.0	-45.0	next	

Figure 7.21(f)



For either option, the lighting switch label can be toggled between the 'ON' and 'OFF' states with the parallel lighting in turn being switched on and off accordingly with a default value given to the light intensity. The direction of the light rays is determined by the two angles in degrees which are specified in the editbox, and this direction is from the source outwards. This direction is taken as the light direction. These two angles consist of a horizontal angle in the  $x$ - $y$  plane and a vertical angle in a plane normal to the  $x$ - $y$  plane. A positive vertical angle measures an upward inclination from the  $x$ - $y$  plane while a negative value indicates a downward direction from the  $x$ - $y$  plane.

The sight line from the camera point to the sight point has a component in the  $x$ - $y$  plane. Let this component of the sight line be represented by the vector  $a$ . For the `MODELLING` option, the horizontal angle is measured relative to this vector  $a$ . A positive horizontal angle denotes a light direction orientated to the right of the vector  $a$  while a negative value indicates a light direction orientated to the left. Hence, the case of a miner's lamp (ie. lamp fixed above a miner's head) can be simulated by setting a zero value for the horizontal angle in the editbox. On the other hand, for the `DIRECTION` option, the horizontal angle is measured relative to the global  $x$ -axis. A positive horizontal angle is measured in the anti-clockwise sense while a negative value denotes an angle in the clockwise sense.

The `DIRECTION` option allows the setting up of two light sources of parallel lighting. By activating the 'next' button in the editbox as shown above, the list will be scrolled forward to the next light source. The information related to this light source will then be shown in the editbox. This light source can in turn be switched on or off. Conversely, the 'last' button when activated will scroll the list backward to the previous light source.

Next, the `POSITION` option deals with the point lighting condition which requires the use of point light sources, and these sources can be positioned anywhere in the model. The editbox which applies in the case of an activated `POSITION` option is given in figure 7.21(f).

A list of up to five point sources can be set up. The 'next' and 'last' buttons are used to scroll the list forward and backward until the information related to the appropriate point light source appears in the editbox. Subsequently, by toggling the switch label between the 'ON' and 'OFF' states, the light source will be switched on and off accordingly. The position of the light source has to be specified by giving its global coordinates in the editbox. The direction of the light will be determined by two specified angles in degrees, ie. the horizontal and vertical angles as for the `DIRECTION` option. This direction will be taken as from the source outwards. The colour of the light will be described by the hue, saturation and luminosity values. The intensity value of the light has to be specified as well.

A cone can also be defined around a point light source. The cone effect will be switched on and off accordingly by toggling the cone label between the 'ON' and 'OFF' states. If the cone label is in the 'ON' state, the included angle of the



cone has to be specified in the editbox. This angle will be centred on the direction of the light defined above. The light from the source will be cut off from the areas which fall outside the cone.

Furthermore, the point light source also permits the inclusion of the spot and attenuated lighting effects into the cone of light defined above. By toggling the spot label between the 'ON' and 'OFF' states, the spot lighting effect will be switched on and off accordingly. If the spot label is in the 'ON' state, a value for the degree or level of spot lighting has to be specified in the editbox. In the case of a higher value, the spot light will concentrate over a smaller area with an increased level of intensity. For a lower value however, the spot light will shine over a larger area with a reduced intensity level. For an area where the spot light is focussed on, the light intensity will decrease from the centre of the area outwards.

The attenuated lighting effect will be switched on and off accordingly by toggling the attenuated label between the 'ON' and 'OFF' states. The attenuation of light refers to the fall in the light intensity as the light travels further away from the source. If the attenuated label is in the 'ON' state, an attenuation parameter has to be specified in the editbox. This parameter gives the value of a distance from the light source. If an area is nearer to the light source than the attenuation parameter, the light intensity over this area will not be attenuated. On the other hand, the light intensity at a point will decrease as the point is further away beyond the attenuation parameter from the light source.

The user can set the various switches and parameter values described above for each of the five point sources in order to achieve the final point lighting conditions.

By activating the `DEFAULT` option, the ambient, parallel and point lighting conditions in the model will all be reset, ie. all the switches and parameter values for the different lighting options will be given their default states and values preset in the software.

The available lighting options enable the user to set up and control the lighting conditions until the desired effect is produced in the screen display. In addition, experiments can be carried out to study the impact of different lighting conditions on the display.

By activating the `RETURN` option, the user will then move back into the `SURFACE_M` menu page shown in figure 7.20(a). As indicated above, the `VIS_MODEL` menu page provides an effective, flexible and powerful tool for setting up the modelling primitives, and has proven its value in many projects. However, future work can be carried out to provide a more interactive user interface for setting up the modelling primitives. This interface will be such that the commands and data are input directly via the menu options, screen and/or editboxes as is the case for other parts of the software instead of through a datafile. The reason for the datafile approach was that a functional module



was needed as soon as possible for use in project work, and it would take a shorter time to develop the datafile approach than the more interactive interface used elsewhere in the software.

Furthermore, the `SAVE_INFO` option in the `SURFACE_M` menu page when activated will cause the current information such as parameter values, switch states and so on, pertaining to the various options in both the `VIS_MODEL` and `SURFACE_M` menu pages to be written to the database. Hence, these information will not be lost when the user exits from the `SURFACE_M` menu page and then from the software altogether. When the user returns to the `SURFACE_M` menu page at a later stage, the pertinent information stored in the database will then be used to produce the image shown on the screen.

## 7.21 Beam elements

On occasions, it may be necessary to introduce beam elements into the analysis model. The use of the beam elements to represent compression boundaries in the model has already been discussed in chapter 4. If the strut elements are used instead of the beam elements, structural mechanisms may occur during the analysis. The beam elements can also account for the bending deformations of the boundaries. The tensile membrane stresses by providing support to these boundaries means that slender compression members can be used. This makes it attractive to use compression boundaries rather than tension anchorages for providing supports to tension structures with very large spans. It has also been shown by Mollman [99], and Samuelli and Zingali [120] that erroneous results are produced if bending deformations of the supporting boundary (ring beam or arch) are not taken into account during the analysis of a tension structure.

As shown in figure 4.1, a local  $x$ -,  $y$ - and  $z$ -axes system can be defined for each of the beam elements. At each end node of a beam element are six degrees of freedoms, ie. the translations in the local  $x$ -,  $y$ - and  $z$ -axes directions and the rotations about the local  $x$ -,  $y$ - and  $z$ -axes. The three nodal translations apply to all the nodes in the model, but for a node connected to a beam element, the additional three nodal rotations are introduced. The nodal translations are measured from the current geometry of the beam element. On the other hand, the nodal rotations are displacements from a zero reference state (ie. the initially straight beam element) when the beam element is first defined.

The beam elements are analysed using the dynamic relaxation scheme applied to the analysis of all the other element types in the model. In this way, the same analysis section of the software can be used to deal with all the different elements in the model. This can only simplify the task of implementing the beam elements into the software. The dynamic relaxation analysis of the beam elements is an efficient means of dealing with the compression and bending elements in the model as already described in chapter 4. The underlying theory and advantages of the dynamic relaxation scheme have also been outlined in chapter 3.



For realistic modelling, the beam elements should be able to cope with various non-linear effects. In the dynamic relaxation scheme, the equilibrium and compatibility equations are considered for the current deformed state of the model. Consequently, any geometric non-linearity in the analysis will be automatically accounted for. The scheme has also been set up to deal with the following non-linearities, ie.

- the influence of the axial forces on the moment-curvature relations (this is taken into account by modifying the 's' and 'c' stability functions accordingly using the Livesley's power series method),
- the effects of bowing on the axial displacements (these are taken into account by applying correction factors),
- the fixed-end moments due to distributed loadings as a function of the axial forces.

A detailed account of the above non-linear effects has been given in chapter 4.

Furthermore, a future possibility is the inclusion of the ability to account for the on/off non-linearity which results from the formation of a plastic hinge. This will involve the introduction of a plastic hinge at a node where the plastic moment is exceeded during the analysis. The moment at the node will be reset to the plastic moment. The hinge rotation will then be given by the equilibrium equations for the resulting beam with one or two pin ends.

Within the dynamic relaxation solution scheme, the above non-linear effects are updated when a kinetic energy peak is reached, and the node coordinates are reset as well.

A few numerical examples have also been considered in chapter 4 as a confirmation the beam elements are behaving as expected and that reliable results are obtained.

The BEAM ELEMENTS menu page shown in figure 7.22(a) has been set up to implement the options for dealing with the beam elements in the model. The user can access this menu page from the 'master' menu page. On display in the graphics window will be a graphical image of the model in its current state. The RE\_PAINT option serves to refresh the current image display on the screen. The EDIT\_VIEW option allows the user to manipulate the view of the image shown on the screen. The BACK\_UP and RESTORE options are not yet functional at the moment.

The BEAMS option when activated allows the user to either add a new or delete an existing beam element interactively on the screen. With the ADD option active as well, the user can then enter into the on-screen interaction mode by clicking the right mouse button. The user needs to identify the two nodes which will define a new beam element. The user will be prompted on the



screen by the 'node pick' pointer. Subsequently, the user can use the 'node pick' pointer to pick a node and the 'picked' node will be highlighted in red. This will be followed by the picking of a second node and the second 'picked' node will also be highlighted in red. A line highlighted in red will be drawn between the two 'picked' nodes. The accept/abort pointer will then appear. If the new beam element defined by the two 'picked' nodes is accepted, the corresponding additional data will then be created in the database. For instance, the two 'picked' nodes will be flagged as being connected to a beam element and these nodes will be introduced with the additional rotational degrees of freedom. On the other hand, with the BEAMS and DELETE options both active, the user can then proceed to delete an existing beam element. The user will first enter into the on-screen interaction mode by clicking the right mouse button. The user will then be prompted on the screen by the 'beam pick' pointer. Subsequently, the user can use the 'beam pick' pointer to pick a beam element and the 'picked' element will be highlighted in red. The accept/abort pointer will then appear. If the 'picked' element is accepted, the data corresponding to this element will then be deleted from the database.

RE_PRINT	EDIT_VIEW
BACK_UP	RESTORE
BEAMS	ADD
	DELETE
FIXROT	FIX_RH
	FIX_RV
	FIX_RZ
BM_REL	LOCAL_X
	LOCAL_Y
	LOCAL_Z
BETA_ANGLE	
BM_PROPS	NEW_PROP
	EDIT_PROP
	DEL_PROP
LOADS	NLOAD
	UDL
Mode:	
CHECK	ATTACH
	RELEASE
RETURN	

An activated FIXROT option allows the user to check, attach or release rotational fixities from the nodes in the model using the CHECK, ATTACH OR RELEASE option accordingly. The rotational fixities are relevant only to nodes which have rotational degrees of freedom, ie. nodes which are connected to beam elements. The software ensures that only nodes with rotational degrees of freedom can be acted on by operations related to the rotational fixities. The active rotational fixity condition will be indicated by the current states of the FIX\_RH, FIX\_RV and FIX\_RZ menu options. An active FIX\_RH option represents a fixity condition for rotation about the global x-axis and so on for the active FIX\_RV and FIX\_RZ options. If any node in the model has a rotational fixity condition, the symbol of a small square enclosing a cross will be assigned to the node. Also, the square symbols associated with all the nodes having the active rotational fixity condition will be highlighted in red. For nodes with the non-active rotational fixity conditions however, the square symbols attached to them will be shown in yellow. This makes it easy for the user to find out the existing rotational fixity conditions throughout the entire model.

With either an active CHECK, ATTACH OR RELEASE option, the user can subsequently enter into the on-screen interaction mode by clicking the right mouse button. The user will then be prompted on the screen by the 'node pick' pointer. The user can in turn use the

'node pick' pointer to pick a node and the 'picked' node will be highlighted in

Figure 7.22(a)



red. The subsequent operations will then differ slightly depending on which is the currently active option as described below.

For an active **CHECK** option, the **FIX\_RH**, **FIX\_RV** and **FIX\_RZ** menu options will in turn switch to the appropriate states to reflect the current rotational fixity condition at the 'picked' node. The screen display will also be updated accordingly.

For an active **ATTACH** option, the accept/abort pointer will in turn appear. If the 'picked' node is accepted, the active rotational fixity condition will then be assigned to the node.

For an active **RELEASE** option, the accept/abort pointer will in turn appear. If the 'picked' node is accepted, the current rotational fixity condition at the node will be removed and the node will then be free of any rotational restraints.

The above functions of the **CHECK**, **ATTACH** and **RELEASE** options apply only in the case when the **FIXROT** option is active. The translational fixities are dealt with in a separate menu page, ie. the **FIXITY** menu page already outlined earlier.

The **BM\_PROPS** option when activated allows the user to perform operations related to the elastic properties of the beam elements in the model using the **NEW\_PROP**, **EDIT\_PROP** and **DEL\_PROP** options. The user interface implemented in these options are similar to that used in the **LINE ELEMENT PROPS** and **MEMBRANE PROPERTIES** menu pages already described previously. A default set of beam properties will automatically be assigned to a newly defined beam element.

Using the **NEW\_PROP** option, the user can create a new elastic property set and default values will be prescribed to this set. The repeated use of this option will produce a list of elastic property sets. When a new set is created, it will automatically be added to the end of the list. On display in the editbox as shown below will be information which include the reference number of the set and the associated elastic properties such as the **EA** (ie. modulus of elasticity  $\times$  cross-sectional area), **GJ** (ie. shear modulus of elasticity  $\times$  torsional constant), **EI<sub>y</sub>'** (ie. modulus of elasticity  $\times$  moment of inertia about the local *y*-axis), **EI<sub>z</sub>'** (ie. modulus of elasticity  $\times$  moment of inertia about the local *z*-axis) and self-weight values.

No	EA	GJ	EI <sub>y</sub> '	EI <sub>z</sub> '	Swt/L	last
1	2.783E+08	5.382E+07	7.064E+07	7.064E+07	0.000E+00	next

The property set whose values are currently shown in the editbox will be taken as the active property set. The beam elements prescribed with the active property set will be highlighted in red. If the default elastic properties are not appropriate, the user can activate the **EDIT\_PROP** option and then directly edit the information given in the editbox. By activating the 'next' button in the editbox, the list will be scrolled forward to the next set and the information in this set will then be shown in the editbox. Conversely, when the 'last' button is activated, the list will be scrolled backward to the previous set. The user can also delete an existing elastic property set by scrolling the list until this set



appears in the editbox and then activates the `DEL_PROP` option. The beam elements having the property set which has just been deleted will then be given the first property set in the list. The software does not allow the user to delete a property set if it is the only one in the list and hence, ensures that the case of beam elements having no elastic properties will never occur. The above functions of the `NEW_PROP`, `EDIT_PROP` and `DEL_PROP` options apply only in the case when the `BM_PROPS` option is active.

There are further facilities available to the user through the `CHECK` and `ATTACH` options. With either an active `CHECK` or `ATTACH` option, the user can subsequently enter into the on-screen interaction mode by clicking the right mouse button. The user will then be prompted on the screen by the 'beam pick' pointer. Using the 'beam pick' pointer, the user can pick a beam element and the 'picked' beam element will be highlighted in red. The subsequent operations will then differ slightly depending on which is the currently active option as described below.

For an active `CHECK` option, the current elastic property set assigned to the 'picked' beam element will then appear in the editbox.

For an active `ATTACH` option, the accept/abort pointer will in turn appear. If the 'picked' beam element is accepted, the active elastic property set will then be assigned to the element.

The above functions of the `CHECK` and `ATTACH` options apply only in the case when the `BM_PROPS` option is active.

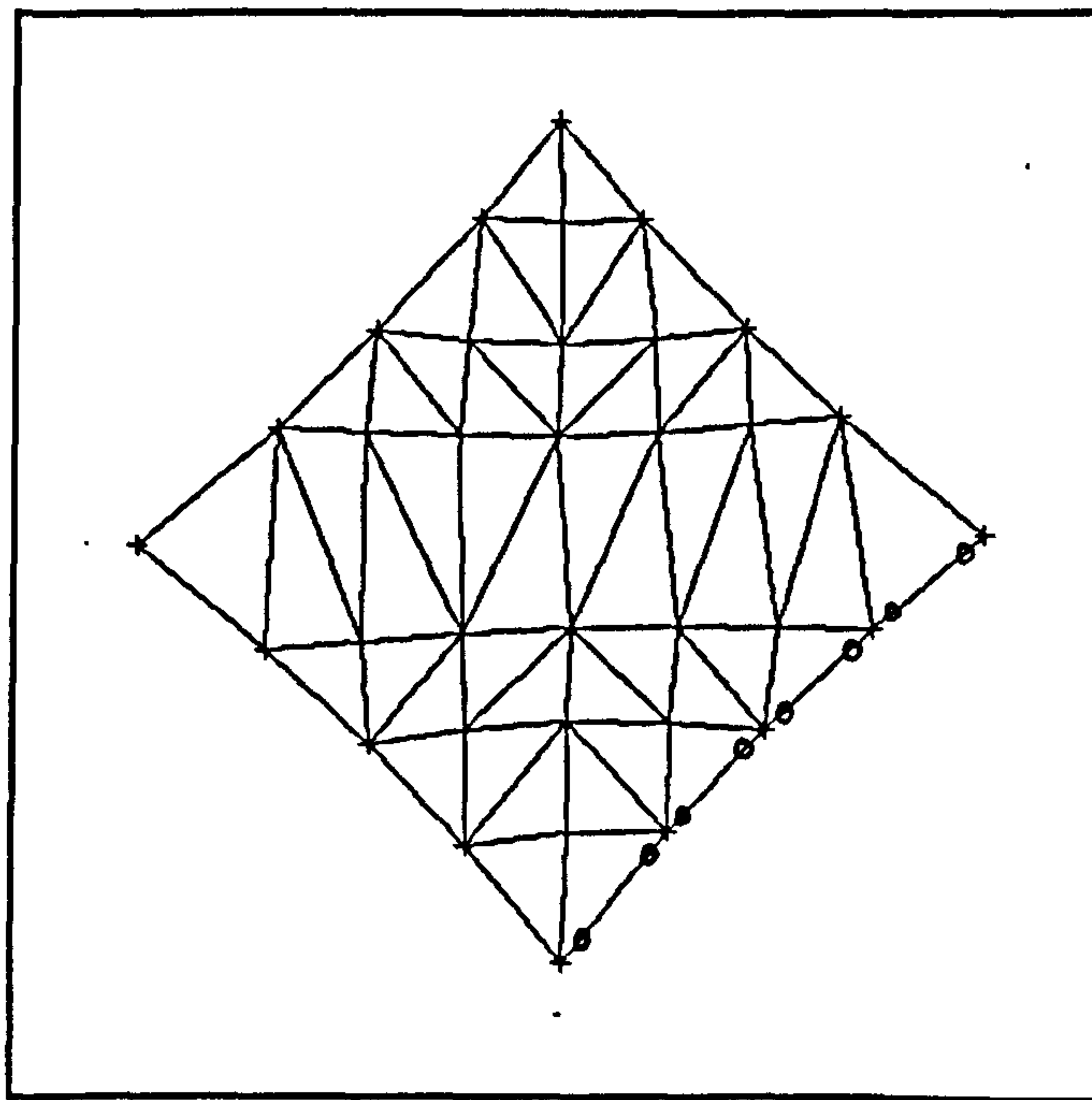


Figure 7.22(b)

Furthermore, the `BM_REL` option allows the user to introduce member releases about the element local  $x$ -,  $y$ - and  $z$ -axes to nodes which are connected to the beam elements. The member releases are used in the modelling of pin-ended



conditions, ie. where the bending moments are zero. The current setting of member releases about the element local x-, y- or z-axis or combination of these will be indicated by the current states of the `LOCAL_X`, `LOCAL_Y` and `LOCAL_Z` menu options. This setting of member releases will be taken as the active member release setting. An active `LOCAL_X` option represents a member release about the element local x-axis and so on for the active `LOCAL_Y` and `LOCAL_Z` options. A small circle marker drawn close to the node of a beam element will indicate that member releases have been assigned to the node as shown in figure 7.22(b). The circle markers associated with nodes having the active release setting will be highlighted in red while for nodes with member releases not represented by the active release setting, their associated circle markers will be shown in yellow. In this way, the user can easily establish the member releases which currently exist throughout the model.

The `CHECK`, `ATTACH` and `RELEASE` options are also available to the user to perform further operations related to the member releases. With either an active `CHECK`, `ATTACH` or `RELEASE` option, the user can subsequently enter into the on-screen interaction mode by clicking the right mouse button. The user will then be prompted on the screen by the 'beam pick' pointer. Using the 'beam pick' pointer, the user can pick a beam element and the 'picked' beam element will be highlighted in red. The 'node pick' pointer will then appear on the screen. The user can in turn use the 'node pick' pointer to pick either one of the two end nodes of the 'picked' beam element. The circle marker associated with the 'picked' node will be highlighted in red. The subsequent operations will then differ slightly depending on which is the currently active option as described below.

For an active `CHECK` option, the `LOCAL_X`, `LOCAL_Y` and `LOCAL_Z` menu options will switch to the appropriate states to reflect the current release setting at the 'picked' node which will in turn be taken as the active member release setting. The screen display will also be updated accordingly.

For an active `ATTACH` option, the accept/abort pointer will in turn appear. If the 'picked' node is accepted, the active release setting will then be assigned to the node.

For an active `RELEASE` option, the accept/abort pointer will in turn appear. If the 'picked' node is accepted, the current release setting at the node will be removed and the node will then be free of any member releases.

The above functions of the `CHECK`, `ATTACH` and `RELEASE` options apply only in the case when the `BM_REL` option is active.

The two end nodes of a beam element determine the position in space of the element but the unique definition of the element spatial orientation requires an additional parameter to be known. In this case, this parameter is taken to be the beta angle. For a beam element lying not parallel to the global z-axis, the beta angle is taken as the angle which the plane defined by the element local x- and z-axes makes with the global z-axis (see figure 4.2). On the other



hand, if the beam element lies parallel to the global z-axis, the beta angle is then the angle which the plane defined by the element local x- and y-axes makes with the global y-axis. The sign convention for the beta angle is such that the angle is positive if it is measured from the global z- or y-axis in a clockwise sense when looking in the direction of the element local x-axis. With the beta angle known, the spatial orientation and hence, the positions of the minor and major axes of the beam element can then be uniquely defined. The minor and major axes of the beam element are taken to be in the directions of the element local z- and y-axis respectively. The software assumes a default beta angle of zero degrees. An activated `BETA_ANG` option provides the user with the means to check or attach the beta angle to the beam elements in the model using the `CHECK` or `ATTACH` option accordingly. In the editbox as shown below located beneath the graphics window will be the value of a beta angle.

BETA ANGLE 0.000
---------------------

This value will be taken as the active beta angle. If desired, the user can directly edit the active beta angle shown in the editbox. The beam elements in the model with the active beta angle will be highlighted in red.

With either an active `CHECK` or `ATTACH` option, the user can subsequently enter into the on-screen interaction mode by clicking the right mouse button. The user will then be prompted on the screen by the 'beam pick' pointer. Using the 'beam pick' pointer, the user can pick a beam element and the 'picked' beam element will be highlighted in red. The subsequent operations will then differ slightly depending on which is the currently active option as described below.

For an active `CHECK` option, the current beta angle of the 'picked' beam element will be shown in the editbox. This beta angle will in turn be taken as the active beta angle. The screen display will also be updated accordingly.

For an active `ATTACH` option, the accept/abort pointer will in turn appear. If the 'picked' beam element is accepted, the active beta angle will then be assigned to the element.

The above functions of the `CHECK` and `ATTACH` options apply only in the case when the `BETA_ANG` option is active.

Furthermore, there is the `LOADS` option which when activated allows the user to check or attach applied loads to the beam elements in the model using the `CHECK` or `ATTACH` option accordingly. At the moment, the available load types which can be applied include point loads and uniformly distributed loads (udl).

An active `UDL` option indicates that the applied loads under consideration are the udl. An editbox as shown below will appear beneath the graphics window.



udl	Wx	Wy	Wz
	0.000E+00	0.000E+00	-1.000E+00

On display in the editbox will be the three component values of a udl, ie. the components in the directions of the global x-, y- and z-axes. These component values will form the active udl. If desired, the user can directly edit the active udl shown in the editbox. The beam elements in the model assigned with the active udl will be highlighted in red.

With either an active **CHECK** or **ATTACH** option, the user can subsequently enter into the on-screen interaction mode by clicking the right mouse button. The user will then be prompted on the screen by the 'beam pick' pointer. Using the 'beam pick' pointer, the user can pick a beam element and the 'picked' beam element will be highlighted in red. The subsequent operations will then differ slightly depending on which is the currently active option as described below.

For an active **CHECK** option, the current udl of the 'picked' beam element will be shown in the editbox. This udl will in turn be taken as the active udl. The screen display will also be updated accordingly.

For an active **ATTACH** option, the accept/abort pointer will in turn appear. If the 'picked' beam element is accepted, the active udl will then be assigned to the element.

The above functions of the **CHECK** and **ATTACH** options apply only in the case when both the **LOADS** and **UDL** options are active.

On the other hand, point loads will be considered when the **NLOAD** option is active. The three component values of a point load, ie. the components in the directions of the global x-, y- and z-axes will be displayed in the editbox as shown below.

point load	Wx	Wy	Wz
	0.000E+00	0.000E+00	-1.000E+00

These component values will form the active point load. If desired, the user can directly edit the active point load shown in the editbox. The nodes in the model assigned with the active point load will be highlighted in red.

With either an active **CHECK** or **ATTACH** option, the user can subsequently enter into the on-screen interaction mode by clicking the right mouse button. The user will then be prompted on the screen by the 'node pick' pointer. Using the pointer, the user can pick a node and the 'picked' node will be highlighted in red. The subsequent operations will then differ slightly depending on which is the active option as described below.

For an active **CHECK** option, the current point load assigned to the 'picked' node will be shown in the editbox. This point load will in turn be taken as the active point load. The screen display will also be updated accordingly.



For an active **ATTACH** option, the accept/abort pointer will in turn appear. If the 'picked' node is accepted, the active point load will then be assigned to the node.

The above functions of the **CHECK** and **ATTACH** options apply only in the case when both the **LOADS** and **NLOAD** options are active.

When the user is ready to exit from this menu page and move back into the 'master' menu page, the **RETURN** option is activated.

With the above relevant information set, the user can proceed to the **ANALYSE** menu page shown in figure 7.16 and runs an analysis of the beam elements. In this case, the analysis trace will display the additional data of mean and current maximum residual (ie. out-of-balance) moments in the model at each kinetic energy peak. At the end of the analysis, the user can proceed to the **LISTING** menu page and lists out to the laser printer the beam geometry data, bending moments and shear forces which are required for the subsequent design process.

## 7.22 Fabrication geometry

At the post-processing stage, of interest to the user will be the geometric data needed for designing the membrane and folded plate connections, and the relevant geometric data is obtainable from within the **FABRICATION GEOM'Y** menu page shown in figure 7.23. The user can access this menu page from the 'master' menu page. On display in the graphics window will be a graphical image of the model in its current state. The **RE\_PAINT** option serves to refresh the current image display on the screen. The **EDIT\_VIEW** option allows the user to manipulate the view of the image shown on the screen. The **BACK\_UP** and **RESTORE** options are not yet functional at the moment.

<b>RE_PAINT</b>	<b>EDIT_VIEW</b>
<b>BACK_UP</b>	<b>RESTORE</b>
<b>Bdy Coord:</b>	<b>ARC_LEN</b>
<b>Membrane</b>	<b>CLEARANCE</b>
	<b>AREA</b>
<b>Plate:</b>	<b>PLANE_ANG</b>
	<b>FOLD_ANG</b>
<b>RETURN</b>	

Under the **Boundary:** label is the **ARC\_LEN** option which is used to obtain the global coordinates of a specified point lying along a boundary. When this option is activated, an editbox as shown below will then appear beneath the graphics window.

Bdy	N1	N2	L_Arc	P_ARC	Xp	Yp	Zp
1	9	31	3.121	0.250	2.511	0.522	0.103

On display in the editbox will be the relevant boundary information. The user can enter into the on-screen interaction mode by clicking the right mouse button. This will be followed by a switch of the on-screen arrow pointer into the 'boundary pick'

pointer. The user can in turn use the 'boundary pick' pointer to pick a boundary and the 'picked' boundary will be highlighted in red. In addition, the information such as the reference number, the first and last nodes, and the total smooth arc length of the 'picked' boundary will be shown in the

Figure 7.23



editbox. The user can also specify an offset value in the editbox and this offset value will represent a distance along the 'picked' boundary measured from the start (ie. first node) of the boundary. The point along the 'picked' boundary corresponding to the specified offset value will be marked by a small cross symbol coloured in cyan. The global coordinates of the marked point will also be given in the editbox. In this way, the user can easily find out the global coordinates of any point along the 'picked' boundary by specifying the corresponding offset value in the editbox.

There are two options available under the **Membrane:** label, ie. the **CLEARANCE** and **AREA** options which are used respectively to obtain the surface clearance, and the surface and plan area information.

By activating the **CLEARANCE** option, an editbox as shown below will then appear beneath the graphics window.

POINT S: ???	[SOLVE POINT]	[RETURN]
Clearance < > Area_Ratio < >		
Points in Print File < >	[PRINT POINTS]	

The user can specify in the editbox the global coordinates of an arbitrary point in space. When the [SOLVE POINT] button in the editbox is activated, the surface clearance information for the specified point will be generated and then displayed in the editbox. This information will include the values of the 'Clearance' and 'Area\_Ratio' parameters. The surface clearance information is derived by considering the projection of the specified point onto the plane of each membrane element in the model. The projected point forms a triangle with each of the three sides of a membrane element and three triangles can thus be formed. The ratio of the total area of these three triangles to the area of the membrane element itself can be found. There is such a ratio for each of the membrane elements in the model. The minimum of all these ratios is taken to be the value of the 'Area\_Ratio' parameter. If this value is 1.0, the specified point has a projection which falls within the plane of a membrane element. On the other hand, if the 'Area\_Ratio' parameter has a value greater than 1.0, there is no projection of the specified point which falls within the plane of a membrane element. The 'Clearance' parameter is taken to be the shortest distance from the plane of a particular membrane element to the specified point. This particular membrane element is that upon which the value of the 'Area\_Ratio' parameter is also based. Then, by activating the [PRINT POINTS] button in the editbox, the surface clearance information of the specified point will be sent to the laser printer.

When the **AREA** option is activated, an editbox as shown below will then appear beneath the graphics window.

Surface Area	Plan Area	[PRINT]	[RETURN]
< >	< >		

On display in the editbox will be values of the total surface and plan areas of all the membrane elements in the model. In this case, the plan area refers to



the projection of the surface area onto the global  $x-y$  plane. By activating the [PRINT] button in the editbox, the surface and plan areas information of the membrane elements will then be sent to the laser printer.

Under the **Plate:** label are the **PLANE\_ANG** and **FOLD\_ANG** options which allow the user to obtain the geometric data needed for designing the membrane and folded plate connections.

By activating the **PLANE\_ANG** option, the editbox as shown below will then appear beneath the graphics window.

	n1	n2	L_Arc	P_ARC	[SOLVE]	angle(deg)	[PRINT]	[RETURN]
bdy 42	186	223	3.648	0.250		0.000		
bdy 43	223	5	2.668	0.250				

The user will enter into the on-screen interaction mode by clicking the right mouse button. The 'boundary pick' pointer will then appear on the screen. Using the 'boundary pick' pointer, the user can then pick the first boundary and the 'picked' boundary will be highlighted in red. The user can continue to use the 'boundary pick' pointer to pick the second boundary and the 'picked' boundary will again be highlighted in red. There should be a common node where both the first and second 'picked' boundaries will meet. The information such as the reference number, first and last nodes, and total smooth arc length for each of the two 'picked' boundaries will be shown in the editbox. In addition, for each of the two 'picked' boundaries, the user can specify an offset value in the editbox and this offset value will represent a distance along the boundary measured from the common node. The point along the boundary corresponding to the specified offset value will be marked by a small cross symbol coloured in white. These two marked points and the common node may be taken to represent a triangular membrane plate. Hence, from the common node to each of the two marked points, a vector can be defined. When the [SOLVE] button in the editbox is activated, the included angle (ie. the membrane plate angle) between these two vectors will be calculated and then displayed in the editbox. By repeating the above operations, a list of membrane plate angles can be calculated. The [PRINT] button when activated will then send to the laser printer information related to the list of membrane plate angles which have been calculated.

Similarly, when the **FOLD\_ANG** option is activated, an editbox as shown below will then appear beneath the graphics window.

	n1	n2	L_Arc	P_ARC	[SOLVE]	angle(deg)	[PRINT]	[RETURN]
bdy 42	186	223	3.648	0.250		0.000		
bdy 43	223	5	2.668	0.250				
bdy 44	75	223	3.120	0.250				

The user will enter into the on-screen interaction mode by clicking the right mouse button. In this case of deriving the fold angle between two adjoining membrane plates, the three boundaries which define the two planes of the membrane plates have to be identified. The 'boundary pick' pointer will then



appear on the screen. Using the 'boundary pick' pointer, the user can in turn pick the first boundary and the 'picked' boundary will be highlighted in red. The user can continue to use the 'boundary pick' pointer to pick the second and third boundaries, and these two 'picked' boundaries will again be highlighted in red. There should be a common node where these three 'picked' boundaries will meet. The second 'picked' boundary should lie along the fold line, ie. the line of intersection between the two planes of the membrane plates. The three boundaries should also be picked in an anti-clockwise sense looking from above the fold line. The information such as the reference number, first and last nodes, and total smooth arc length for each of the three 'picked' boundaries will be shown in the editbox. In addition, for each of the three 'picked' boundaries, the user can specify an offset value in the editbox and this offset value will represent a distance along the boundary measured from the common node. The point along the boundary corresponding to the specified offset value will be marked by a small cross symbol coloured in white. The marked points along the first and second 'picked' boundaries, and the common node may be taken to represent the first triangular membrane plate. Thus, the marked points along the second and third 'picked' boundaries, and the common node may be taken to represent the second triangular membrane plate. When the [SOLVE] button in the editbox is activated, the fold angle between the two membrane plates will be calculated and then displayed in the editbox. The adopted sign convention is such that a positive fold angle refers to the angle above the fold line while a negative angle is taken to be the angle below the fold line. By repeating the above operations, a list of fold angles can be calculated. The [PRINT] button when activated will then send to the laser printer information related to the list of fold angles which have been calculated.

When the user is ready to exit from this menu page and move back into the 'master' menu page, the RETURN option is activated.

### 7.23 Post-processing

When an analysis has terminated, the user can return back to the 'master' menu page from the ANALYSE menu page. The ELEMENT POST\_P menu page is available to the user to post-process the results from the analysis. The user can enter into this menu page shown in figure 7.24 from the 'master' menu page. On display in the graphics window will be a graphical image of the model in its current state. The EDIT\_VIEW option allows the user to manipulate the view of the image shown on the screen. The PLOT option is not yet functional at the moment.

In this menu page, the user can easily find out the forces in the line elements and the stresses in the membrane elements which result from the analysis. These forces and stresses will be displayed in colours which correspond to a colour chart located on the right hand side of the graphics window as shown in figure 7.24. The colour chart gives a band of colours which represent a specified magnitude range of the element forces or stresses in the model. In



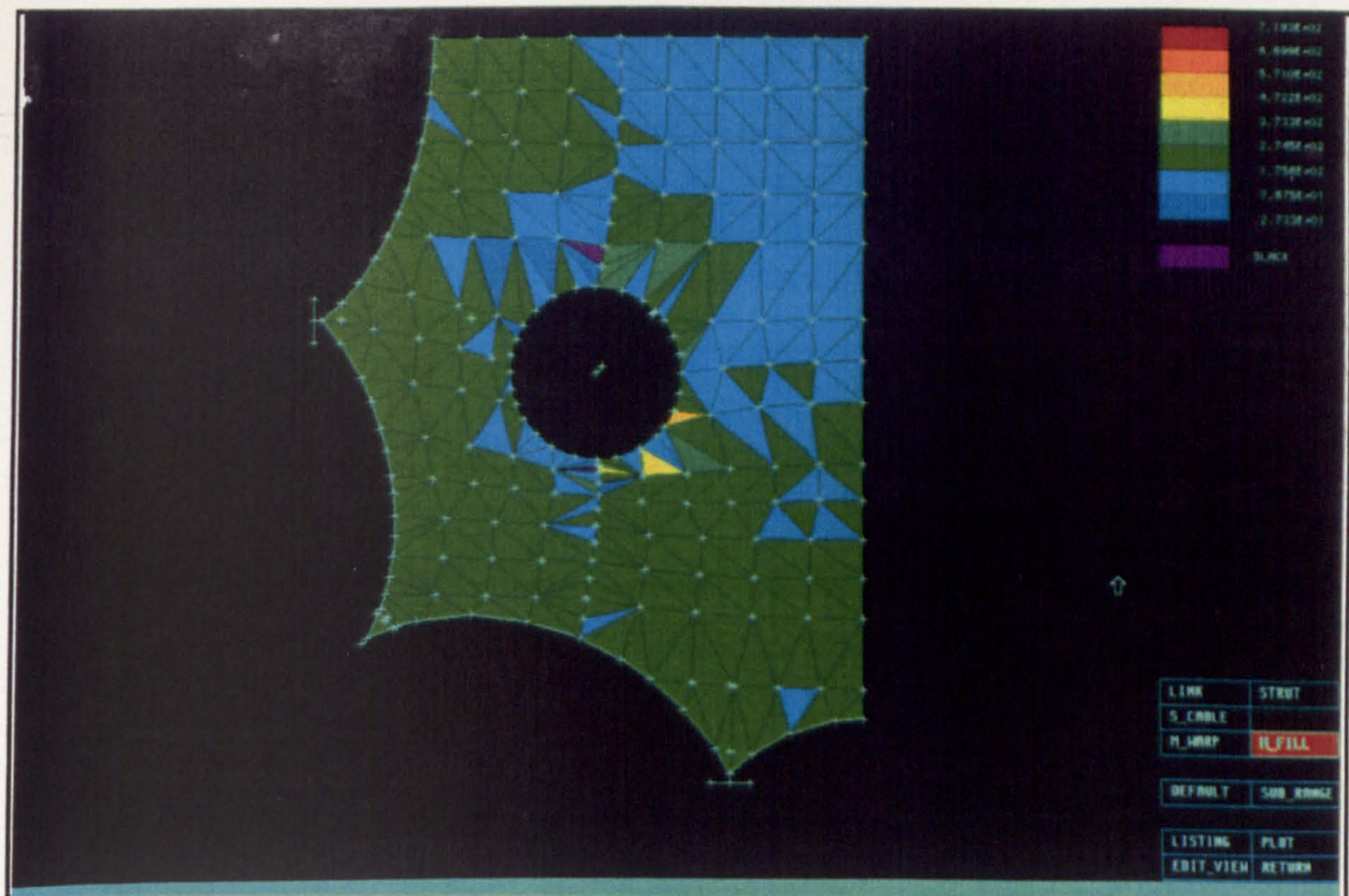


Figure 7.24

this way, the user will be able to make a quick assessment of the results presented visually on the screen. The line elements consists of the link, strut and slip cable elements. There are specific operations which apply to either the link, strut, slip cable or membrane elements at any one time. The choice of which line elements will be operated on is decided by activating the **LINK**, **STRUT** or **S\_CABLE** option accordingly.

By activating either the **M\_WARP** or **M\_FILL** option, the membrane elements will then be chosen as the active elements. With an active **M\_WARP** option, all the membrane elements in the model will be shown filled in with colours which represent the warp stress levels in the elements. The band of colours in the colour chart will correspond to the entire magnitude range of all the warp stresses in the model. On the other hand, by activating the **M\_FILL** option, the colour display for the fill stresses in the membrane elements will then be given on the screen as shown in figure 7.24. In this way, the user can easily find out the membrane stress distributions in the model, and identify the areas of excessive stresses and/or zero stresses (which indicate membrane slackening).

With an active **LINK** option, the link elements will then be chosen as the active elements. All the link elements in the model will in turn be shown in colours which indicate the force levels in the elements. The band of colours in the colour chart will correspond to the entire magnitude range of the link forces in the model. If information such as the exact force level in a particular link element is required, the user can obtain this through on-screen interrogation. This involves the user entering into the on-screen interaction



mode by clicking the right mouse button. The 'link pick' pointer will then appear on the screen. Using the 'link pick' pointer, the user can pick a link element and the 'picked' element will then be given a red marker at the mid-point of the element. An editbox as shown below will also appear beneath the colour chart located on the right hand side of the graphics window.

TENSION	5.903E+02
L_CURRENT	0.8362
L_SLACK	0.8358
NP 1 EA	1.310E+06

On display in the editbox will be the tension value, stressed length, slack length, material property set number and *EA* (ie. modulus of elasticity  $\times$  cross-sectional area) value of the 'picked' element. The above operations for the link elements will similarly apply to either the strut elements when the **STRUT** option is activated or the slip cable elements when the **s\_CABLE** option is activated. As the link and slip cable elements cannot resist compression, these elements are given zero force levels when they become slack.

Furthermore, the **DEFAULT** and **SUB\_RANGE** options apply only to the link and slip cable elements. By activating the **SUB\_RANGE** option while the **LINK** option is still active, the user will then be prompted on the screen by the 'link pick' pointer. The user can then use the 'link pick' pointer to pick two separate link elements. This will be followed by the resetting of the colour chart such that the band of colours correspond to a magnitude range given by the difference between the force levels in the two 'picked' elements. On the other hand, the **DEFAULT** option is used to reset the colour chart such that the band of colours correspond to the entire magnitude range of all the link forces in the model. For the above options, when the colour chart is reset, the colour display of the link elements on the screen will also be updated accordingly. With an active **s\_CABLE** option, the above operations of the **DEFAULT** and **SUB\_RANGE** options will in turn apply to the slip cable elements instead.

Lastly, the **LISTING** option allows the user to access the **LISTING** menu page which will be described in the following section.

By activating the **RETURN** option, the user will exit from this menu page and move back into the 'master' menu page.

## 7.24 Listing

At various stages during the design process, the user may need to extract certain information from the model. If desired, a listing of the required information can be obtained using the menu options available within the **LISTING** menu page shown in figure 7.25. This menu page is accessible from the 'master' menu page. Using the options within this menu page, the user can select the relevant information needed for design considerations, and then output them to the laser printer. This information may include a list of the node coordinates, nodal restraints, elastic properties, element forces and



RE_PRINT	EDIT_VIEW
BACK_UP	RESTORE

NODE	FIXITY
	AXSYM
LINK	STRUT
S_CABLE	CPROP
MBRANE	MPROP
BOUNDARY	G-STAG
BEAM	

Loads:	L_CASE
	L_COEFF

ELEMENT	ZONE
FIELD	ALL

Precision:	NORMAL
	FULL

Scope:	ALL
	STRESS
	MODEL

PRINTER	SCREEN
---------	--------

LIST DATA
-----------

RETURN
--------

stresses, and graphic dumps of screen images. In addition, for design considerations, the user may require a listing of the element forces and stresses for different load cases. A listing of the applied load intensities and their corresponding load coefficients for each node can also be obtained if required. The user will select the relevant information by switching the corresponding menu options to the active state. For instance, if a listing of the node coordinates is required, then the **NODE** option will be switched to the active state. Subsequently, by activating the **LIST DATA** option, a listing of the selected information will be output to the laser printer. When the user is ready to exit from this menu page and move back into the previous menu page, the **RETURN** option is activated.

Furthermore, at the end of each analysis run within the **ANALYSE** menu page, a listing of the analysis run trace can be output to the laser printer. Included in the trace will be information such as the residual forces, and the magnitude and sense of the corresponding resultant force at each restrained node (whether partially or fully fixed, or in a plane of symmetry). Later, this information can be fed into the analysis and design of structural components for a tension structure.

Figure 7.25

## 7.25 Conclusions

In this chapter, a detailed outline is given of the fully interactive graphical CAD system which has been developed for the design of membrane structures. It illustrates how the power and capabilities of the computer hardware have been fully exploited to benefit the user. The CAD system has proven to be a more effective, flexible and economic alternative to physical modelling which used to be the primary means of investigating the membrane structures until a few years ago.

Much effort and time have been expended to ensure that an effective and functional user interface to the CAD system is implemented. The user interface is based on the concept of the Graphical User Interface (GUI), ie. as much use as possible of graphical images on the screen to inform and guide the user. With such a user interface, the CAD system has been made fully interactive. A series of menu pages is available to implement the menu options designated for the operations involved at the various stages in the design of membrane structures. The menu options are driven into action by



means of a two button mouse. By using graphical images to represent the relevant information on the screen, the user can quickly grasp the information and respond to the CAD system accordingly. The user can enter into the on-screen interaction mode in order to interact directly with the graphical image for instance, the on-screen interrogation for specific information. An objective of the user interface is to take as much direct data handling as possible away from the user. The user interface used in the operations associated with the various menu options is clearly illustrated in the detailed discussion of the available menu pages given in this chapter. The discussion provides an insight into the procedures which are involved throughout the design process.

The complex behaviour of tension structures is often not within the grasp of most architects. As a result, unlike conventional buildings, it is customary for the engineer to become involved at the early stages of conceptual development with the architect. The `SURFACE_M` menu page shown in figure 7.20(a) provides the facility to generate highly realistic surface shaded graphical images. It is possible to set up a graphical image of the membrane structure complete with the surrounding features such as existing buildings, trees, roads and so on. In the menu page are menu options which allow the visual impressions from walking about in the model to be depicted in the graphical images. In the close co-operation between the architect and the engineer, these images serve as an effective means in the communication of ideas. In addition, the computer hardware is equipped to execute the computations involved in the analysis and graphic processing at high speed. Consequently, the CAD system allows the architect and engineer to investigate the effects on the model of various ideas and these effects will be quickly known. At the form-finding stage, it is possible for the architect and engineer to come together and use the CAD system interactively to explore the huge possibilities of surface shapes for the model.

The fully interactive graphical CAD system described in this chapter fulfills the principal objectives which have been laid down as the guidelines for the development of the system. Firstly, as it is intended for use in a design office environment, the user interface implemented ensures that the CAD system is highly user friendly. A new user to the CAD system will only require a short learning time. Indeed, the most significant benefit of the CAD system is the great reduction of the design time.

There are further enhancements which can be made to the CAD system and these will include

- (1) linking up the CAD system with a commercial draughting package such as 'Auto-Cad'; in this way, information from the CAD system can be used directly by 'Auto-Cad' to produce drawings of steelwork connections and other structural details;
- (2) integration of the CAD system into the cutting pattern production stage; in this way, a direct data transfer from the CAD system can be channelled



directly to fabricate the cutting patterns on the shopfloor; this reduces any errors which may be introduced in the process of sending the cutting pattern information output from the laser printer or plotter to the shopfloor;

- (3) the capability to analyse and design cable net structures; a large number of the facilities in the CAD system are equally applicable to cable net structures; consequently, this enhancement can be incorporated into the CAD system with minimal effort;
- (4) the capability to simulate the complex dynamic behaviour of membrane structures; at the moment, the theoretical basis for this enhancement is still under development as will be outlined in chapter 9; it is often necessary to investigate the wind induced dynamic effects on membrane structures; the present solution is to perform either a simple wind tunnel test followed by a quasi-static analysis or a full aeroelastic model test in a wind tunnel;
- (5) continued evolution of the CAD system; indeed, the practical approach is to use the CAD system for working on projects; the feedback from the user provides the key to the further refinements of the CAD system in order to keep up with the practical demands of the design process.

Finally, it must be said that the design process is not merely a matter of using the CAD system. The designer should have a thorough understanding of the structural behaviour and be aware of the limits of the computer modelling. The CAD system serves only as a useful tool to produce an efficient and practical design which meets the architectural, structural and other criteria which have been laid down.



## Part III

### Chapter 8

#### Loadings: static and dynamic

##### 8.1 Introduction

As mentioned in earlier chapters, the form of a tension structure established from a form-finding process should be evaluated for its behaviour under possible loads in the load analysis stage. Obviously, if these loads have not been assessed on a realistic basis, the results from the subsequent load analysis however sophisticated would be misleading. Consequently, an accurate estimation of the applied loads is critical for a structurally sound and economic design of the structure. It is also essential that the loads are defined in a form which can be easily applied in the structural analysis. The applied loads can range from a simple static load having a known magnitude and location to one of a dynamic nature which is a function of both space and time, and are notoriously difficult to predict in many instances. The discussion in this chapter will be concerned with the assessment of these loads.

##### 8.2 Design loads

For the load analysis, the self-weight of the cables, their clamps and fittings in cable nets may have to be considered while the self-weight of the lightweight membrane materials in membrane structures can be ignored. If access is provided for maintenance work to the structure, then some allowance has to be made for the possible imposed loads which may arise.

The critical loads for the design of tension structures are often those which arise from extreme weather conditions such as snowfall and storm winds. The codes of practice often contain information about the intensities of these loads and the risk levels associated with these intensities. For snow loads, the intensity is derived from the design ground snow accumulation. For wind loads, the intensity is a function of the design wind speed. The risk is measured in terms of the annual probability of exceedence or the return period. In addition, the coefficients which indicate how the snow or wind loads are distributed over the surface are determined from the codes of practice or other means. The load value applicable over an area is then given by the product of the load intensity and distribution coefficient for that area. As far as the determination of applied loads is concerned, the problem with tension structures is the highly individual and complex shapes present in many cases. Consequently, the appropriate load distribution coefficients may not be easily obtainable from the codes of practice which gives values more suitable for the simpler shapes of conventional structures. The flexible nature of tension structures also means that large deformations will take place in



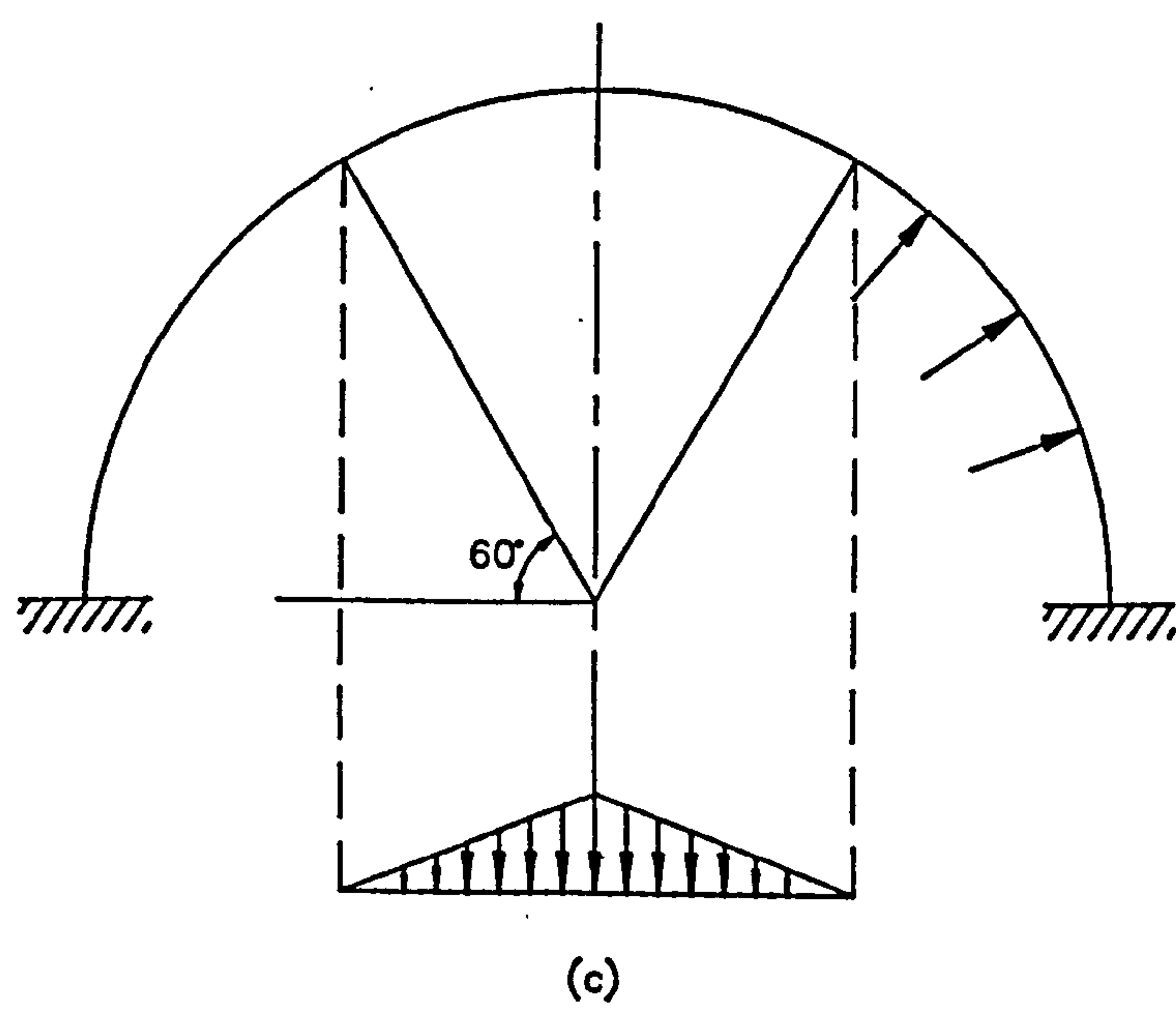
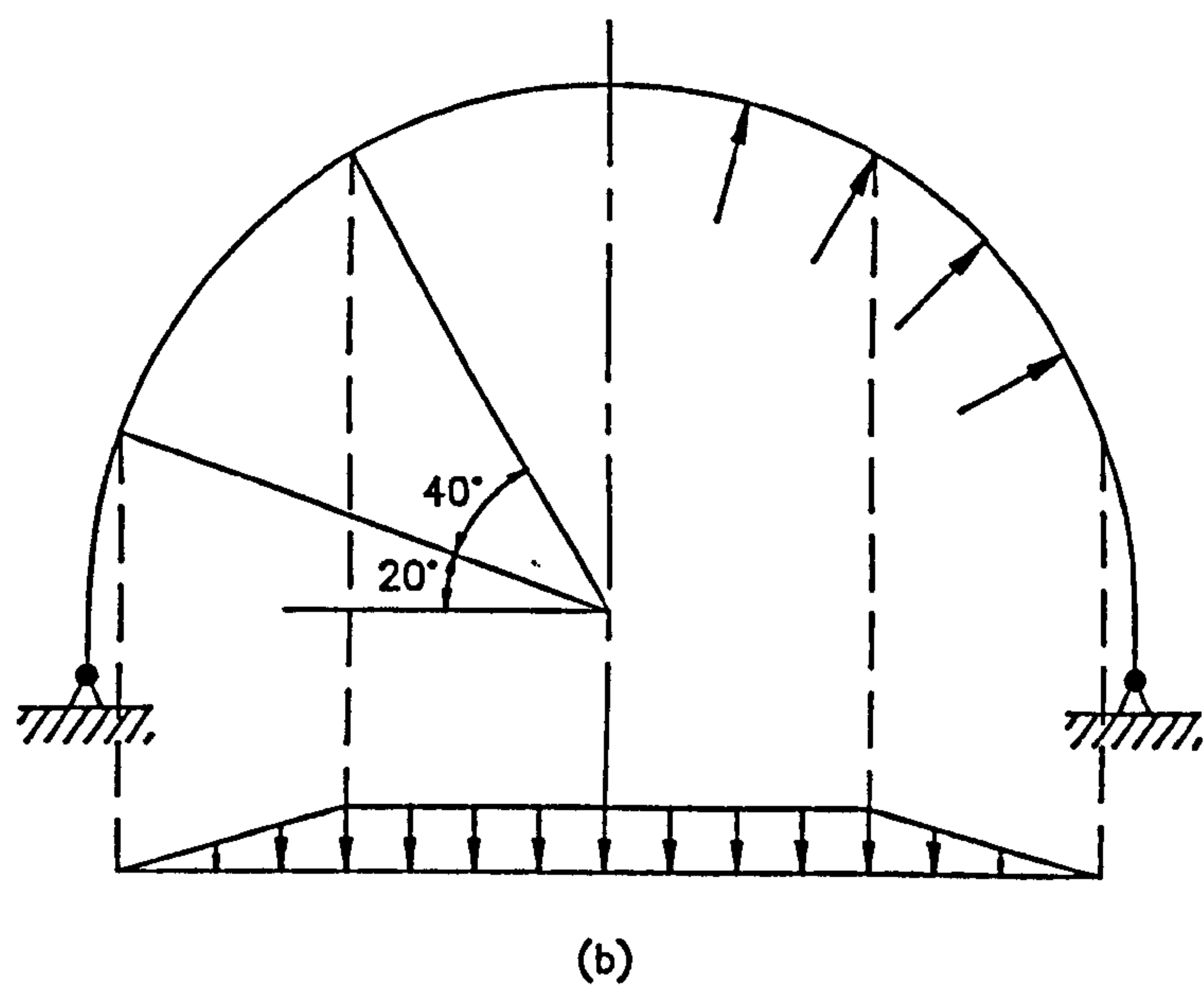
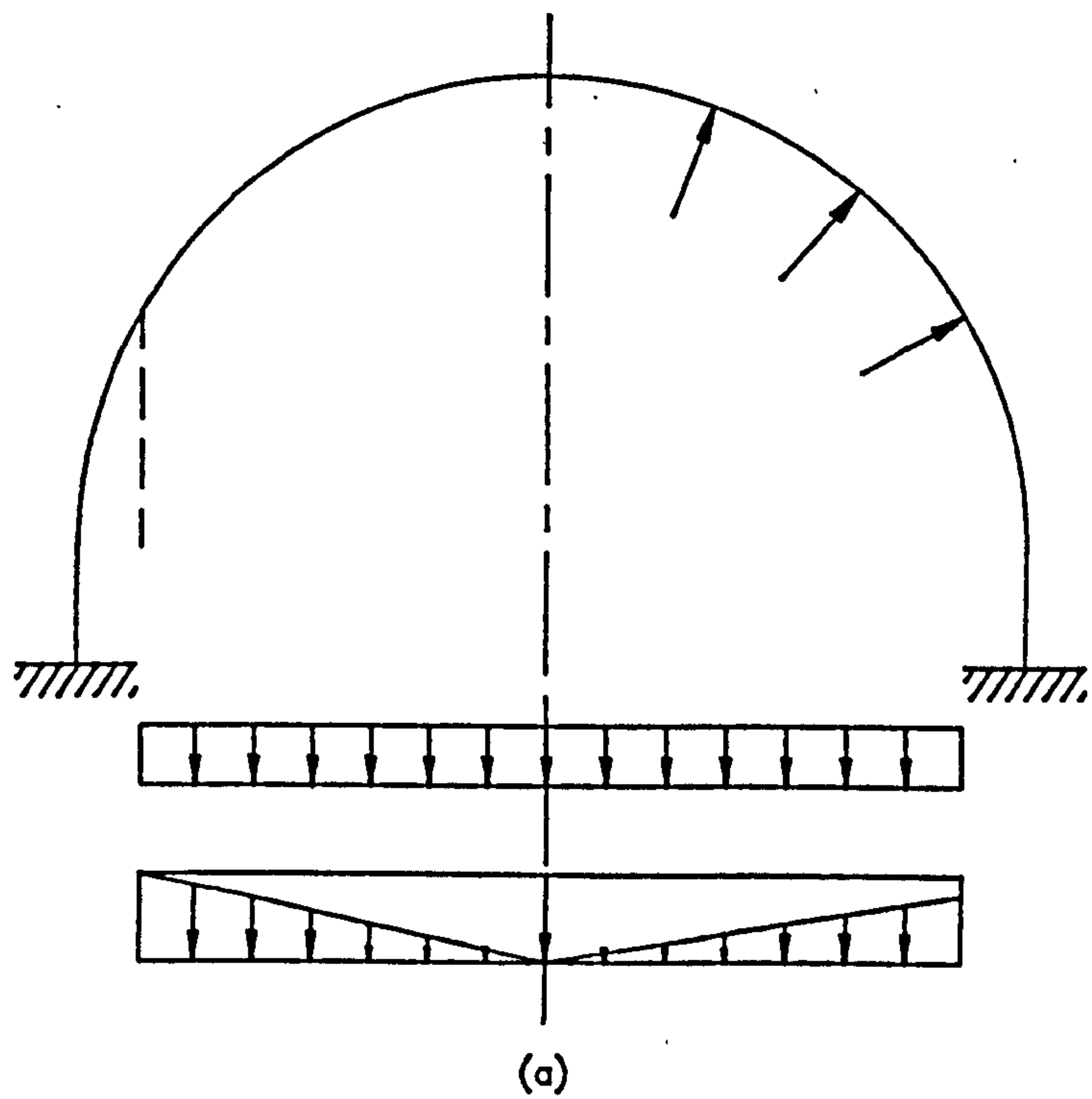


Figure 8.1



order to develop the forces for resisting the applied loads. As a result, the distribution coefficients may need updating during the analysis in order to be consistent with the current deformed geometry, ie. a case of non-linear load structure interaction. For a small scale tension structure however, a judgement may be required to simplify and make the derivation of the distribution coefficients more economic. It may be possible to guess the worst situation and then the corresponding set of distribution coefficients derived for use in the subsequent load analysis.

Before determining the applied loads, it is appropriate to decide on the nature of the load analysis. For instance, a static analysis alone may suffice in the preliminary study or routine design of a small scale structure. Consequently, the simple equivalent static loads are derived for the load analysis although the external loads may be of a dynamic nature. These static loads may be determined as outlined above from the load intensities and distribution coefficients given in the codes of practice. However, for large scale structures such as an air-supported stadium roof, a rigorous description of the external loads is necessary. The dynamic components if present in the external loads need to be considered and thus, a complete dynamic analysis of the structure is required.

### 8.2.1 Snow loads

The tendency of snow loads to slide down steep slopes and remain on the flatter slopes will result in high local patch loadings over the horizontal areas. For the large air-supported membrane roofs, a snow melt system may be in place to maintain an internal temperature level sufficient to avoid significant snow accumulation. Alternatively, allowance may be made for the snow to be removed mechanically. As a result, a reduced snow loading is to be designed for. The snow load is applied as a static load. The rate of snow accumulation hardly causes any vibrations in the tension structure. From the statistical assessment of snowfall records using extreme value theory, values of design snowfall intensities are established. The applied snow load is determined from a chosen design snowfall intensity and a distribution coefficient  $\mu$ .

There are disagreements over how the distribution coefficient  $\mu$  should be determined [76]. This is illustrated by a simple example shown in figure 8.1 (taken from [76]), ie. a roof of circular cross-section with different assumptions for the snow distributions. Figure 8.1(a) shows the possible snow accumulation away from the apex. Figure 8.1(b) takes into account the possibility of snow sliding off the roof at some angle. Figure 8.1(c) gives the possible case of low inflation pressure or a flat profile which may result in a snow filled dimple at the apex. The coefficient  $\mu$  also considers the effects of the surrounding topography. In the case of a structure in an exposed area with no shielding, a reduction in the value of  $\mu$  is allowed. In addition, the snow load cases to be considered should include the symmetric and asymmetric loading conditions. The critical forces in different parts of the structure may result from either the symmetric or asymmetric load case. For an air-



supported structure, a possible strategy is the increase of inflation pressure to balance the snow load. This will result in reduced internal forces for the subsequent design. It is also possible for the snow to build up as the structure deforms.

### 8.2.2 Wind loads

As evident from one's experience of conditions on a windy day and examination of wind records from meteorological stations, a natural wind consists of components which vary instantaneously, and in a highly complex and irregular manner. In other words, the natural wind has a turbulent nature. This suggests that it is only possible to specify in terms of probability that a particular wind speed will occur within a certain period of time. At present, it is not possible to derive a complete description of the wind at any instant. By means of a statistical approach however, an indication of the turbulence in the wind can be obtained as will be described shortly.

#### 8.2.2.1 Gust spectrum

At any instant, the wind velocity at a point can be taken to consist of a hourly mean velocity component plus random fluctuating components. For instance, the velocity in the  $x$ -direction is given by

$$u(t) = \bar{u} + u'(t) \quad (8.2.1)$$

where  $\bar{u}$  is the hourly mean value of the velocity and  $u'$  is the instantaneous value of the velocity fluctuation about the mean value. In this case, the  $x$ -direction is taken to be in a horizontal sense (ie. parallel to the ground). In addition,  $v'$  and  $w'$  are the velocity fluctuations about the mean value in the  $y$ - and  $z$ -directions respectively.

Subsequently, the total pressure at any point  $(x, y, z)$  on the structure is given by

$$p(t) = \frac{1}{2} \rho C_p(x, y, z) [\bar{u}(x, y, z) + u'(x, y, z)]^2 \quad (8.2.2)$$

in which  $\rho$  is the density of air and  $C_p$  is the normal wind pressure coefficient. The mean pressure component is then given by

$$\bar{p} = \frac{1}{2} \rho C_p \bar{u}^2 \quad (8.2.3)$$

which may form a quasi-static load vector, and the fluctuating pressure component is given by



$$p'(t) = \frac{1}{2} \rho C_p (2\bar{u}u' + u'^2). \quad (8.2.4)$$

On average, the fluctuations on either side of the mean velocity component will cancel out so that

$$\bar{u}' = 0. \quad (8.2.5)$$

The fluctuating velocity component  $u'$  gives rise to the gustiness in the wind and is therefore termed as the gust velocity. The intensity of turbulence due to the gustiness is defined as follows

$$I = \sqrt{\overline{(u')^2}}. \quad (8.2.6)$$

At a point, the wind velocity  $u$  at any time can be resolved into a number of sinusoidal fluctuations of different frequencies and amplitudes about the mean velocity  $\bar{u}$ . The cumulative value of the composite fluctuations can be resolved into components according to their frequencies. The 'strength' of a contributory fluctuation can be given by the sum of squares of the velocity. It is necessary to square the velocities since a summation of velocities alone with time for a sinusoidal fluctuation gives a zero value over a whole period.

It follows that the variance of the wind velocity  $u$  is given by

$$\sigma^2(u) = \bar{u}^2 - \overline{u^2} = \int_0^{\infty} S(f) df \quad [= \overline{(u')^2}] \quad (8.2.7)$$

where  $S(f)$  is a function of frequency known as the spectrum or power spectral density which indicates the change of variance of the fluctuations in the wind with respect to the frequency  $f$  of the contributory fluctuation. A plot of  $S(f)$  against frequency will give some indication of the relative size of each of the contributions. In addition,

$$\int_0^{\infty} S(f) df = \int_0^{\infty} f S(f) d(\ln f). \quad (8.2.8)$$

Subsequently, a plot of the product of  $S(f)$  and  $f$  (which has the same dimensions as the variance, ie.  $(\text{m/s})^2$ ) against the logarithm of the frequency gives the horizontal or longitudinal gust spectrum of the wind velocity  $u$ . The advantage of such a plot is that the area under the curve between any two frequencies will give a true measure of the energy in that frequency range. Hence, the longitudinal gust spectrum can give a measure of the turbulence in the wind in terms of the energy content of the fluctuating components as a function of the frequencies of these components. The gust spectra for the  $v$



and  $w'$  components can be derived in a similar manner. However, it has been observed from experimental data that the variance associated with  $u'$  in the direction of the mean velocity  $\bar{u}$  is much greater than those associated with  $v'$  and  $w'$  [40]. Consequently, it is adequate to use the longitudinal gust spectrum in most practical wind-loading problems. Another important consideration in the modelling of a turbulent wind is the need to account for the spatial correlation of the fluctuating velocity components in the wind.

Davenport [50] has developed a mathematical expression which fits the longitudinal gust spectrum for strong winds and established a procedure of using the spectrum for design purposes. This entails the derivation of an empirical and linear relationship between the gust spectrum and the response of the structure, and such a relationship is the basis of a means of assessing the wind loading on a structure (ie. quasi-static assessment in the frequency domain) as will be described later.

#### 8.2.2.2 Quasi-static wind loads

Cook [48] suggested that there are three fundamental aspects to consider when deriving the wind loading for a structure in general, ie.

- (1) the wind climate which consists of the weather conditions leading to strong winds,
- (2) the atmospheric boundary layer which consists of the lower layer of the atmosphere in which the wind is modified by the rough surface terrain,
- (3) the structure which is immersed in the boundary layer and is itself a part of the terrain.

The interaction between the three aspects can be assessed in terms of either the physical scale or frequency range which corresponds to each aspect. The results from consideration in either way lead to similar conclusions which are as follows

- (1) the interaction between the wind climate and the boundary layer is negligible, and
- (2) there exists interaction between the boundary layer and the structure although insignificant in most cases.

Consequently, the effects of the wind climate and the boundary layer can be considered independently. The characteristics of the atmospheric boundary layer over different types of terrain can be assessed without reference to any particular structure. Subsequently, the wind loads which act on the structure should reflect the fluctuations in the wind flow caused by the turbulence in the boundary layer and those generated by the wake behind the structure.



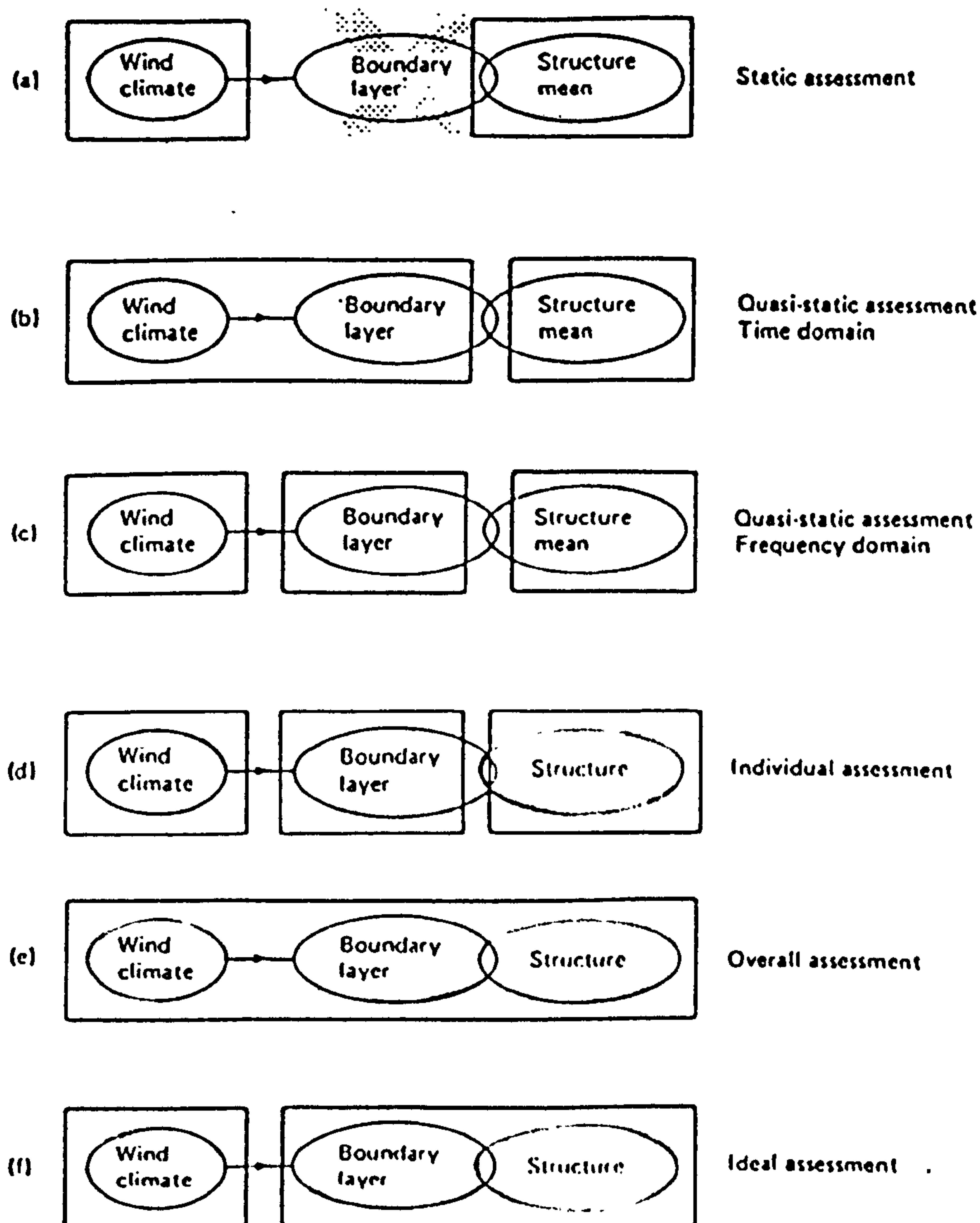


**Figure 8.2**

Based upon the above mentioned three aspects, Cook [48] suggested six ways of arriving at the wind loads for a structure as given in figure 8.2. The three aspects are depicted as individual ellipses. The possible interaction between the boundary layer and the structure is indicated by the overlap of the ellipses which correspond to the boundary layer and the structure. The manner in which the aspects are grouped as indicated by the boxes shown in figure 8.2 gives the various ways of assessing the wind loading on a structure as follows

**(a) Static assessment**

Under this approach, the design wind speed is decided and used in conjunction with the design static loading coefficient to give the full design load. The wind tunnel test of the structure to obtain the loading coefficient is based on a smooth uniform air flow. This is generally no longer used.



(b) Quasi-static assessment (Time domain)

(Current code of practice for wind loadings on structures in the UK (ie. CP3: 1972), France and Australia)

Under this approach, the wind turbulence generated by the structure is suppressed. All the fluctuations in the wind loading are taken to be caused by the gusts in the boundary layer. The structure is assumed to respond in exactly the same manner to gusts as it does to the mean flow and the maximum incident gust imposes the maximum load on the structure. This design approach is termed the equivalent static gust method. The accuracy of this approach is quite good in terms of the overall forces and movement of the structure where ignoring the wind turbulence generated by the structure causes only little discrepancy. However, for local forces on cladding, particularly in regions of separated flow near the periphery of a roof, the accuracy of this approach is poor. Under this approach, the design wind speed is assessed as the maximum gust speed likely to occur during the lifetime of the structure. The gust duration is usually taken as one second. The design gust wind speed is combined with a design mean loading coefficient (given in CP 3: 1972 only for very simple shapes of buildings) to produce a design load.

(c) Quasi-static assessment (Frequency domain)

(Current code of practice for wind loadings on structures in Canada, Australia and USA)

The previous approach is adequate in the case of a stiff structure in which its response follows the quasi-static loading. On the other hand, if the structure is flexible such that its response assumes a dynamic nature, the previous approach should be modified. Under this modified approach, the action of the turbulence in producing loads on the structure is quantified in terms of an admittance function, and the response of the structure to the loads is quantified by a frequency response function. The design method using this approach is the admittance method which operates entirely in the frequency domain in the following manner. A design mean wind speed determines the turbulence spectrum over any given terrain; the admittance function corresponding to the aerodynamic shape of the structure acts on this turbulence spectrum to produce a quasi-static load spectrum; and the frequency response function of the structure operates on the quasi-static load spectrum to produce the dynamic response spectrum.

The accuracy of this approach is reasonable, and can be used for the design of structures with linear dynamic characteristics.

(d) Individual assessment

(Calculations of local pressures in the current code of practice in the UK, Australia, Canada and USA)

Under this approach, the fluctuations in the wind loading due to the turbulence generated by the structure are taken into account unlike in the previous approaches. The turbulence generated by the structure is considered



together with those from the boundary layer as considering them separately would cause difficulties. This approach largely empirical, is used as a correction to an otherwise quasi-static method.

(e) Overall assessment

This approach is based on measuring the performance of a structure exposed to the wind conditions which prevail at a particular site over a long period of time. The problem is not considered in terms of its individual aspects.

This approach was used by BRE (British Research Establishment) to perform a damage survey of the entire range of building types in the UK over 20 years, from 1962 to 1982 and the details of which are outlined in [48]. The survey was conducted in terms of how the buildings performed when exposed to strong winds. The actual damage sustained by the buildings was assessed without the use of any instrumentation. The results obtained are thus only qualitative.

(f) Ideal assessment

This form of assessment ideally reflects the observed behaviour of the three fundamental aspects of the problem. Only the design methods for stiff structures which respond statically to the fluctuations of load, have been developed from this form of assessment (ie. the approach given in (2)). No suitable design methods have yet been developed for dynamic structures to replace the quasi-static admittance approach other than wind tunnel testing.

However, it is noted that the admittance approach (which operates in the frequency domain) is suitable only to be used for structures with linear dynamic characteristics. Consequently, it is not appropriate to apply this approach to tension structures in which the load structure interaction is generally non-linear.

In deriving the wind loads, a judgement is required on their forms suitable for use in the load analysis. In general, a full dynamic analysis is too costly for the routine design of a small scale structure. In such a case, the wind loading may be treated as an equivalent static force system using the approach of quasi-static assessment (time domain) described in (2) above. This is the common practice for dealing with most small scale tension structures. It is required that the structure has a high level of damping which ensures that only limited dynamic response may occur. In addition, the natural frequency of the structure should be much higher than the frequencies of the fluctuating components in the wind flow. This avoids the possible occurrence of the resonance situation. The design gust wind speed can be obtained from the relevant codes of practice in which the basic hourly mean wind speeds have been derived from statistical analysis of wind records using extreme value theory. In deciding the design gust wind speed, the level of risk appropriate for the design life of the structure and the consequences of collapse should be considered.



The distribution of the wind pressure over the surface is given in terms of the  $C_p$  coefficients. Until quite recently, the values of  $C_p$  are obtained from wind tunnel tests of rigid models in smooth flow or in turbulent shear flow [76]. According to Howell [76], these values so obtained are commonly assumed to be generally conservative. This may be the case if the deformations of the structure do not significantly affect the flow pattern or there is no interaction between the structure and the fluctuating wind load which leads to dynamic magnification of the wind pressures. The results from wind tunnel tests in smooth flow could not always be relied upon to predict the form of the instability in the natural wind or the wind speed at which it might occur. The  $C_p$  values should be determined from wind tunnel tests in which the turbulent boundary layer is suitably modelled. This often implies the use of so-called boundary layer wind tunnels.

At the moment, the idea of setting up a sufficiently large database of reference data from wind tunnel tests on tension structures of various kinds has been suggested by Dr. Michael Barnes and David Sykes of City University, London and Buro Happold. This database can in turn be used to predict the  $C_p$  coefficients for any new surface. *could*

The maximum snow load is unlikely to occur at the same time as the maximum wind load. It is reasonable to expect a strong wind to remove the snow which has accumulated and deposit it in the leeward areas. Hence, the case of maximum snow load or maximum wind load can often be taken as acting individually.

### 8.2.2.3 Fluctuating wind loads

For a major tension structure in which any structural failure will result in disastrous consequences, it is inadequate to use the equivalent quasi-static wind loads. In the design of such a structure, it is important to investigate the dynamic response of the structure caused by the action of the fluctuating components in the wind. In other words, there is a need to perform a full dynamic analysis of the structure. This in turn gives rise to two difficult problems which are outlined below.

Firstly, there is a need to devise a simple means of modelling a turbulent wind which can be easily applied in the dynamic analysis. A suggestion by Barnes [20] is as follows, ie. an analysis is first carried out to obtain the static equilibrium geometry and membrane stresses on the basis of the hourly mean velocity and  $C_p$  distributions (ie. for the quasi-static load vector given in equation (8.2.3)), and then to traverse across the structure at the mean velocity a plane wave (of length equal to the turbulence length) a gust wind band of locally higher speed. This is based on the Taylor's hypothesis that the velocity fluctuations recorded at a point travel unchanged in the direction of the mean wind at mean velocity [82]. An improved representation of the wind, with more random correlation, might be obtained by dividing the structure into several strips parallel to the mean wind direction, with each strip having



its own wind record assumed to obey the Taylor's hypothesis [85]. A further suggestion for the turbulent wind modelling is given in [40] which involves the generation of correlated wind histories for different points on the structure based upon power or autopower spectra of the wind at the appropriate levels above the ground.

The second problem is concerned with the complex nature of the dynamic response of a tension structure. The wind flow over the surface of the structure will alter the natural frequencies of the structure. In addition, the relationship between the fluctuating components in the wind and the deformations of the structure is grossly non-linear. Due to the dynamic response itself, additional aerodynamic effects will also be produced. Further detail on these effects will be given in chapter 9. Hence, it is a difficult task to analyse for the dynamic response of the structure. For the dynamic analysis, there is no available solution method which can account for all the aerodynamic effects arising from the dynamic response. The wind tunnel testing of an aeroelastic model with mass, damping and stiffness which have been properly scaled to simulate the real structure is the current procedure used to study the dynamic responses of tension structures. Dimensional analysis is used to establish the correct modelling parameters. Deflections and strains can be measured directly on the model without the need for structural analysis. In the wind tunnel, there should also be appropriate modelling of the turbulence in the wind. Examples of large scale tension structures for which such wind tunnel tests have been conducted include the Hajj terminal at Jeddah, the Riyadh Stadium, the Calgary Olympic Stadium and the Montreal Olympic Stadium. A detailed discussion on the complex task of analysing for the dynamic responses of tension structures will be given in chapter 9.

### 8.3 Conclusions

In this chapter, the possible loads which tension structures have to be designed for are discussed. In most cases, the design loads are those due to snow and wind. An accurate assessment of these loads is essential in order to achieve a structurally sound and economic design. It should also be possible for the loads to be represented in a form which can be easily applied in the structural analysis. However, there are a few characteristics of a tension structure in general which make the prediction of the applied loads difficult. Firstly, the load distribution coefficients which are appropriate for the highly individual and complex shapes often found in tension structures, may not be easily obtainable from the codes of practice. In addition, tension structures are likely to undergo gross deformations under applied loads as a result of their flexible nature, which in turn means that the possible non-linear load structure interaction has to be considered. Consequently, the load distribution coefficients may need to be updated during the load analysis.

For the preliminary study or routine design of a small scale structure, it may suffice to consider static load analysis alone. In this case, an equivalent quasi-



static form of the wind load (ie. that due to the design gust wind speed) can be applied in the analysis. This approach is adopted in the current code of practice for wind loadings on structures in the UK (ie. CP3: 1972). For a large scale structure however, it is necessary to design for the possible dynamic response which is caused by the fluctuating components (ie. turbulence) in the wind. As outlined in this chapter, a full dynamic analysis of the structure in such a case will involve two basic problems, ie. (i) the need to find a simple means of modelling a turbulent wind which can be easily applied in the dynamic analysis and (ii) the complex nature of the dynamic response. A few approaches of dealing with the problem in (i) have been suggested, but a great deal more work is required to verify these approaches in terms of accuracy, computational effort and general use in practice, and also to find other possible approaches. This problem is designated as an area for future research and will not be considered further in this thesis. The problem in (ii) will however be discussed in detail in chapter 9 and in which an outline will be given of a numerical approach developed to solve such a problem.



## Chapter 9

### Dynamic responses of tension structures

#### 9.1 Introduction

In chapter 8, it was pointed out that the action of a natural wind can result in the dynamic responses of tension structures. This is due to the fluctuating components in the wind flow. In the design of tension structures such as an air-supported stadium roof in which a structural failure can lead to disastrous consequences, the dynamic response of the structure should be properly understood and accounted for. It is essential to identify the situations during the dynamic response in which the serviceability or more seriously the stability of the structure may be adversely affected. The appropriate measures should then be taken to avoid such possible situations. In this case, the approach of using an equivalent quasi-static wind load and treating the structure statically may be inadequate.

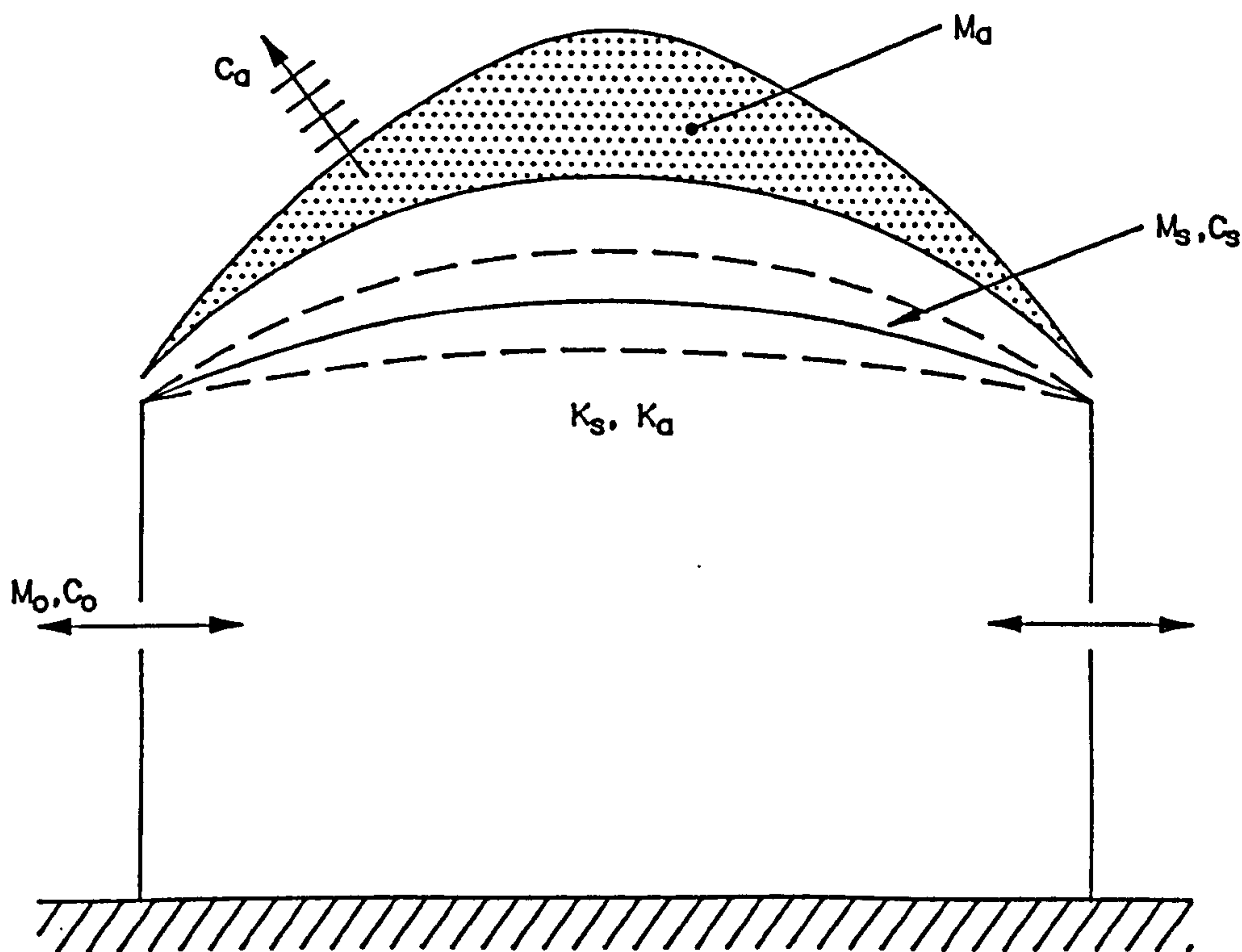


Figure 9.1 Sources of mass, stiffness and damping

A tension structure is in general both lightweight and flexible in nature. This gives rise to a few difficulties in the solution for its dynamic response. First of all, the structure will deform in a highly non-linear manner in relation to the fluctuating wind forces. Secondly, the gross structural deformations caused by the wind load may induce additional aerodynamic forces into the dynamic



response of the structure. These additional forces may produce further deformations which will in turn lead to further aerodynamic forces. The causes of these aerodynamic forces are the aerodynamic mass, stiffness and damping terms which arise from the movement of the structure as shown in figure 9.1 (taken from [51]).

The aerodynamic mass refers to the air mass,  $M_a$  which is accelerated by the motion of the roof as well as the air mass,  $M_o$  which is accelerated through openings by the bellows action of the roof. The aerodynamic stiffness,  $K_a$  is due to the pressurisation of the internal air which results from the volume changes. The aerodynamic damping is contributed by the movement against external pressures,  $C_a$  as well as the resistance through openings,  $C_o$ . The presence of these aerodynamic effects have made the dynamic analysis of a tension structure into a highly complex problem. There is no available solution method which can model all these aerodynamic effects during the dynamic analysis. This problem is solved at the moment by the aeroelastic model testing in a boundary layer wind tunnel. An aeroelastic model has scaled mass, stiffness and damping values which reflect the corresponding properties of the real structure. The deflections and strains of the aeroelastic model are measured directly during the wind tunnel testing. According to Williams [136, 137], even the most rudimentary aeroelastic model test is more accurate and should be used rather than a sophisticated rigid model test followed by non-linear dynamic analysis. This is because the results from the wind tunnel testing of a rigid model will be unrealistic as the rigid model is unable to account for the aerodynamic effects and aeroelastic instabilities. However, the aeroelastic model construction may be difficult and the whole procedure of aeroelastic model testing in a boundary layer wind tunnel can be costly justifiable perhaps only in the design of very large structures.

Consequently, there is a need to develop a numerical approach which can realistically predict the dynamic responses of tension structures. This will give the advantages of much economy in terms of the design costs and time. In addition, such an approach may be more readily applicable in the routine design of most tension structures. The numerical approach should be sufficiently general, accurate and reliable for it to be considered as a suitable alternative to the wind tunnel testing of an aeroelastic model. There has been some work done to achieve such a numerical approach by Krakowska [86] and Williams [136].

For an air-supported structure, there are three main types of dynamic responses which may occur, ie. the responses due to buffeting, vortex shedding and aeroelastic instability [76, 137]. In addition, the response due to aeroelastic instability may take one of the following forms:

- (i) Flutter: This arises as a result of the aerodynamic damping becoming effectively negative.
- (ii) Divergence: This is the loss of static stability of the structure as a result of the wind inducing a condition of negative stiffness in the structure.



One of the main tasks during the dynamic analysis of a structure is to determine the natural frequencies of the structure. If the frequencies of the wind forces acting on the structure are known, it is therefore possible to establish if there is a danger of resonance taking place, ie. if any of the frequencies of the wind forces is close to a natural frequency of the structure. A classic failure which has been caused by resonance is the Tacoma Narrows bridge disaster. The resonance problem may be solved in the design by providing adequate levels of damping and/or modifying the natural frequencies of the structure which in the case of an air-supported structure is most simply achieved by changing the inflation pressure. The maximum deflections and stresses in the structure during the dynamic analysis will also be required for design considerations. It may also be possible to find out from the dynamic analysis if there is any likelihood of aeroelastic instabilities such as flutter and divergence.

In this chapter, an attempt has been made to gain a better understanding of the dynamic responses of tension structures. The primary objective is to establish the theoretical basis for the development of a practical numerical approach which can realistically predict such responses. The work in this chapter is mainly concerned with the case of an air-supported structure of membrane construction. The use of internal air pressure to support all or part of a structure can be economically attractive. In particular, this concept is attractive for supporting roofs over a large column free area and several large sports stadia constructed in recent years have utilised air-supported roofs. However, many of the underlying principles discussed in the following sections in the context of an air-supported structure, are equally applicable to a tension structure in general.

The dynamic response of a structure can be described by the following fundamental equation

$$m\ddot{x} + c\dot{x} + kx = f(\ddot{x}, \dot{x}, x, t) \quad (9.1.1)$$

in which  $m$ ,  $c$  and  $k$  are the mass, damping and stiffness terms respectively, and  $f(\ddot{x}, \dot{x}, x, t)$  is the external loading which may be a function of  $\ddot{x}$ ,  $\dot{x}$  and  $x$  (ie. the acceleration, velocity and displacement terms respectively), and also time  $t$ .

Unlike conventional structures, the solution of equation (9.1.1) for tension structures is complicated by the need to model the aerodynamic effects mentioned above. There are many available solution schemes for solving equation (9.1.1) with no provision for the aerodynamic effects. There are specific dynamic problems for which these solution schemes may be most suited. In many cases, the presence of both geometric and material non-linearities will not give rise to any problem. A brief review of these schemes is given in the next section. Subsequently, the adopted strategy is to choose one of the available solution schemes and then modify the scheme accordingly to model the aerodynamic effects. The chosen solution scheme



should be efficient in dealing with tension structures. The scheme should also be able to easily accommodate the necessary modifications for taking the aerodynamic effects into account. It is desired to produce a reasonably simple means of modelling the aerodynamic effects and that the resulting solution scheme will be relatively easy to apply.

The modelling of the aerodynamic effects requires some knowledge of fluid mechanics. As a preliminary exercise, it is necessary to establish the basic principles within the vast body of well established work on fluid mechanics which are relevant to the problem under consideration here.

The lightweight construction of a tension structure in general implies that the structural mass has no significant influence on the dynamic response. As a result, a more dominant role is played by the added mass of the surrounding air when set into motion by the vibrations of the structure. The total effective mass multiplied by the acceleration term then gives the inertia force in equation (9.1.1). In general, the aerodynamic damping also exerts a strong influence on the response due to the often small values of the structural damping. The values of the aerodynamic damping terms are likely to be close to or above the critical damping level, particularly for very light fabric roofs [51]. The resonant effects are thus minimal. However, if the aerodynamic damping terms are negative, then aeroelastic instability such as flutter (or flapping) can arise. The total effective damping multiplied by the velocity term constitutes the damping force in equation (9.1.1). Due to its flexible nature, the structure will probably undergo large deformations during the dynamic analysis. The membrane material itself may also experience non-linear behaviour such as on/off buckling and creep deformations. The total effective stiffness consists of the non-linear geometric and elastic stiffnesses as well as the aerodynamic stiffness. A negative contribution may come from the aerodynamic stiffness and lead in turn to the membrane losing static stability (ie. divergence). The total stiffness multiplied by the displacement term gives the elastic force in equation (9.1.1).

## 9.2 A brief review of available solution schemes

Equation (9.1.1) is basically a set of second order ordinary differential equations, and many analytical and numerical methods exist for solving the equation in different ways. In general, these methods can be divided into two basic classes, ie. the mode superposition method and the direct step-by-step time integration methods. The direct integration methods can be further subdivided into the explicit and implicit schemes. Each class of solution method is best suited for solving specific problems dependent on the degree of non-linearity in each problem. The mode superposition method is often applied to situations in which only slight non-linearities are observed. In addition, the method requires that there are no large fluctuations in the wind pressures acting on the structure. Conversely, the explicit direct integration methods may be more appropriate in dealing with highly non-linear problems such as which involve on/off non-linearities caused by cable or membrane buckling.



They are also efficient in cases where the high frequency responses are of much interest.

### 9.2.1 The mode superposition method

The mode superposition method is an analytical solution procedure and provides an insight into the overall dynamic behaviour of a structure which may not be clearly understood when strictly numerical schemes are applied. This method is well suited to solve problems in which only the first few modes of vibration are sufficient to give a good approximation to the true dynamic response. However, in order to use this method, it has to be assumed that the oscillations due to buffeting wind loads are linear about the quasi-static equilibrium configuration defined by the mean component of wind loading [79, 82].

The basis of this method is that the displacement vector  $\delta(t)$  may be expressed as a linear combination of vibration mode shapes, ie.

$$\delta(t) = \sum_{n=1}^N \varphi_n x_n \quad (9.2.1)$$

in which  $N$  is the number of modes to be considered,  $\varphi_n$  is the  $n$ th mode shape vector and  $x_n$  is the  $n$ th modal response. The idea is to transform the element nodal degrees of freedom to the generalised degrees of freedom of the vibration mode shapes. As a preliminary step in this method, the free vibration frequencies and corresponding mode shapes of the structure have to be determined, for instance by the subspace iteration method.

As mentioned earlier, the mode superposition method is inefficient and often unable to cope with the highly non-linear dynamic responses of tension structures. As such a problem has no true vibration modes, it is therefore more appropriate to use the direct integration methods.

### 9.2.2 The direct step-by-step time integration methods

The direct time integration methods are essentially numerical solution schemes. In these methods, equation (9.1.1) is integrated directly by a numerical step-by-step procedure in which the time history is divided into a series of finite time intervals. The response at the end of any time interval is evaluated in terms of the initial conditions and the loading during the interval. In general, the direct integration methods can be divided into the following two classes [22]

- (i) the implicit scheme in which the equilibrium conditions at time  $t_{i+1}$  are used to solve for the response at time  $t_{i+1}$ ,



- (ii) the explicit scheme in which the response at time  $t_{i+1}$  is computed based on the equilibrium conditions at time  $t_i$ .

The implicit schemes which are widely used include the Houbolt, Wilson- $\theta$  and Newmark methods. These methods differ in terms of the finite difference expressions used to derive the acceleration, velocity and displacement terms in equation (9.1.1). The implicit schemes are unconditionally stable for linear problems. The full stiffness matrix has to be assembled and a set of simultaneous equations solved at each time step. Furthermore, for non-linear solutions, iterations may be necessary at each time step or several time steps with an updated stiffness matrix. The Newton-Raphson or modified Newton-Raphson method may be used for these iterations. As the implicit schemes are inherently more stable, comparatively large time steps can be used in tracing the dynamic response.

Although numerical instability may not arise when larger time steps are used in the implicit schemes, the high frequency responses tend to be filtered out. The reason for this filtering-out effect is the presence of artificial damping which leads to amplitude decay and period elongation [22, 23]. This occurs for example in the Houbolt and Wilson- $\theta$  methods. In the Newmark method, period elongation is present but not amplitude decay [106]. In other words, the high frequency responses are in general not accurately determined in the implicit methods.

The explicit schemes are conditionally stable whether the solution is linear or non-linear, ie. the time step used should be less than a critical value to avoid numerical instability. The critical time step is governed by the mass and stiffness at each node of the element idealisation of the structure. If a diagonal mass matrix is used, the equilibrium and compatibility equations can be satisfied at the element level. The assembly of the full stiffness matrix and the solution of simultaneous equations can therefore be avoided. This makes the explicit schemes computationally more efficient than the implicit schemes. Both geometric and material non-linearities can also be easily taken into account within the explicit schemes. The central difference method is the most widely used explicit scheme. In terms of accuracy and complexity, this method lies between the simple Euler method and the higher order or predictor-corrector methods. The central difference method has no artificial damping which can suppress the mode responses.

The mode frequencies are often overestimated when consistent mass matrices are used whereas lumped masses underestimate the mode frequencies. The explicit central difference method tends to overestimate the mode frequencies. Hence, lumped masses (ie. a diagonal mass matrix) are used in the explicit central difference method so that both accuracy as well as computational efficiency can be achieved.

The highest frequency of the dynamic response determines the maximum time step allowed in the conditionally stable methods. On the other hand, the overall dynamic response may be governed largely by the lower dominant



modes in the response. This leads to the idea of having fictitious masses in the directions of the highest frequency and true masses for the more flexible degrees of freedom in the structural idealisation [12, 14]. As a result, larger time steps can be used in the explicit central difference scheme.

For the analysis of flexible membrane structures, Oden, Key and Fost [108] suggested that the advantage of unconditional stability in some implicit methods is outweighed by the need to solve a complete set of simultaneous equations at each time step, and that the time step required for accurate modelling is usually as small as that required for numerical stability of explicit schemes.

There are also investigations into the possible use of mixed time integration schemes such as mixed explicit-implicit schemes [22].

### 9.3 Dynamic analysis by an explicit numerical scheme

The explicit central difference scheme is the basis of the dynamic relaxation (ie. DR) method applied in earlier chapters to the static analysis of tension structures. The same explicit numerical scheme can be used to investigate the dynamic responses of tension structures as well. Such an explicit numerical scheme has been applied to the dynamic analysis of an impulsively loaded pneumatic dome [11].

For the dynamic relaxation method as outlined earlier in chapter 3, the damping constant is set to zero and the kinetic damping procedure implemented to control the solution process until it converges to an equilibrium static state. In addition, there are artificial controls such as fictitious masses and fictitious elastic properties which can be used to improve the convergence of the solution. Only few changes to the explicit numerical scheme are necessary when used for the purpose of dynamic analysis. The kinetic damping procedure being an efficient numerical tool for achieving static solutions, is not appropriate for the dynamic analysis. The viscous damping procedure should be adopted instead with a suitable value chosen for the damping constant. It is usual that light structural damping is used. The explicit numerical scheme traces the damped dynamic response of the structure. The actual values have to be assigned to the nodal masses and the elastic properties. However, as mentioned above, fictitious nodal masses may be used in directions where they do not significantly influence the overall dynamic response and yet allow the use of larger time steps. With these considerations in mind, the basic mechanics of the explicit numerical scheme outlined in chapter 3 are applied here to study the dynamic response of a pneumatic dome. During the dynamic analysis, the actual trace of the structural vibrations is followed from which the vibration characteristics such as the natural frequencies can be determined. Of interest are also the structural displacements at each time step and in order to obtain the high frequency responses, small time steps are required.



On the basis of the explicit numerical scheme described above, further considerations are needed to account for the creep effects, on/off buckling and aerodynamic effects, and are discussed in the sections which follow. A few modifications or extensions will be added to the basic scheme to incorporate these considerations.

#### 9.4 Visco-elastic material behaviour

A visco-elastic material exhibits the combined characteristics of a viscous liquid and an elastic solid. Visco-elastic properties are present in most membrane materials. The essential difference between a visco-elastic material and a purely elastic one is the introduction of time dependence. A visco-elastic material experiences creep, ie. deformation which occurs with time at constant stress. In general, a flexible membrane structure has very little damping capacity by itself. Vibrations are dissipated mainly through the creep effects in the membrane material. Consequently, it is important to include the modelling of visco-elastic material behaviour into the dynamic analysis of membrane structures.

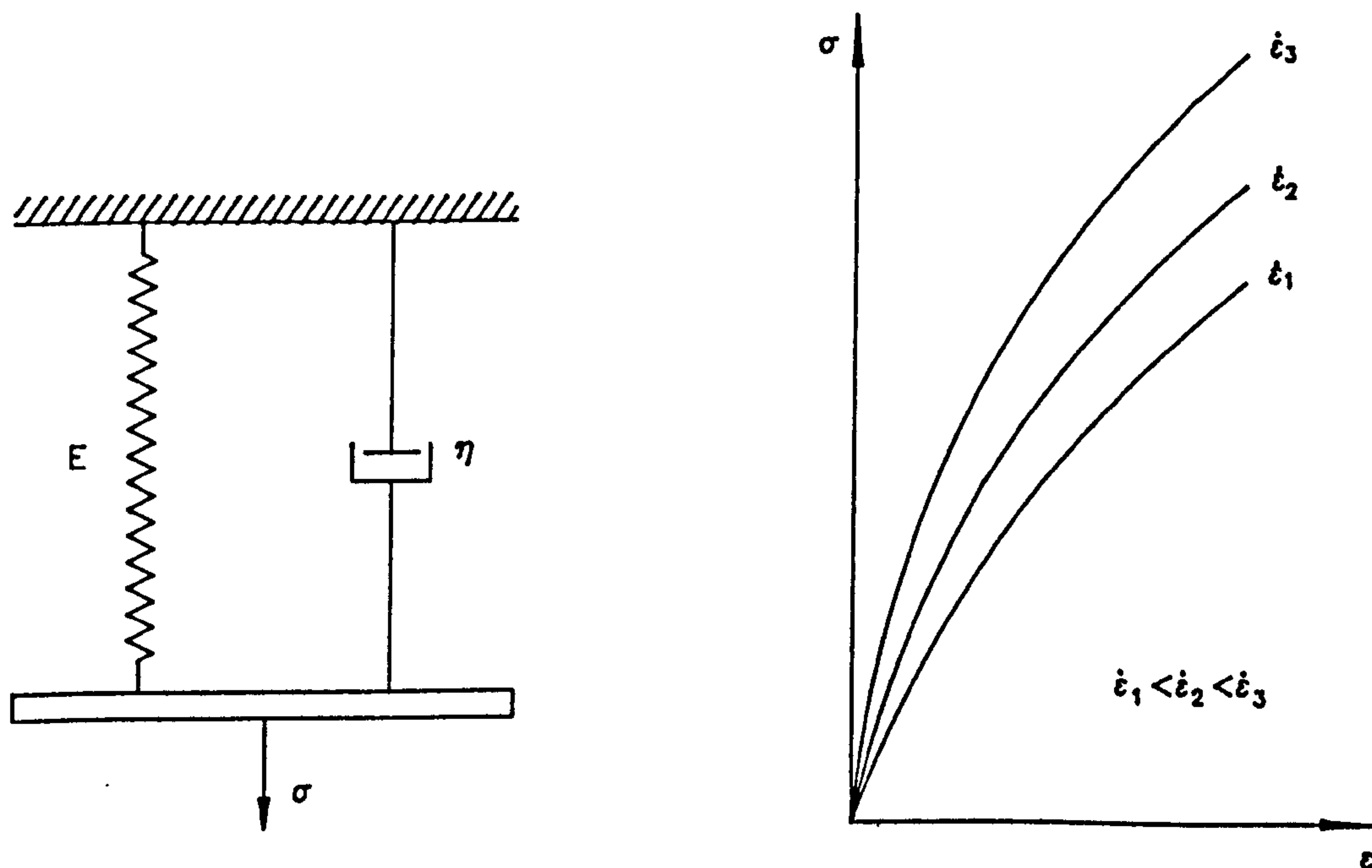


Figure 9.2

The visco-elasticity effect is characterised by the fact that the rate at which creep strains develop depends not only on the current state of stresses and strains, but in general, on the full history of their development as well. The visco-elastic materials show a clear dependence on the rate of loading; the strain being larger if the stress has grown more slowly to its final value. Several models are available to describe the visco-elasticity effects in materials. Basically, they are derived from the Kelvin solid and Maxwell fluid



combined together either in series or in parallel. For the purpose of tracing the dynamic response over a short period, it may suffice to use a single Kelvin model. Essentially, this simple model may be idealised by a dashpot (which models a viscous liquid) connected in parallel with a spring (which models an elastic solid) as shown in figure 9.2.

The spring represents a Hookean solid with an elastic modulus  $E$  and in which the stress varies linearly with the strain. For the dashpot however, the stress is proportional to the strain rate and the constant of proportionality is  $\eta$ , ie. the coefficient of viscosity of the liquid resisting the piston as it moves in the dashpot. This model is known as a Voigt-Kelvin model with a stress-strain-time relationship which will be described shortly.

From figure 9.2, for the same  $\varepsilon$  in both the spring and dashpot, the total stress in the model is given by the sum of the contributions,  $\sigma'$  and  $\sigma''$  as follows

$$\begin{aligned}\sigma' &= E\varepsilon_c, & \sigma'' &= \eta\dot{\varepsilon}_c, \\ \Rightarrow \sigma &= \sigma' + \sigma'' = E\varepsilon_c + \eta\dot{\varepsilon}_c, \\ \Rightarrow \dot{\varepsilon}_c &= \frac{1}{\eta}\sigma - \frac{1}{\eta}E\varepsilon_c = a\sigma - b\varepsilon_c\end{aligned}\tag{9.4.1}$$

in which  $\sigma$  is the current stress level,  $\varepsilon_c$  is the total accumulated creep strain,  $\dot{\varepsilon}_c$  is the creep strain rate, and  $a$  and  $b$  are the visco-elastic constants for the material.

For a more accurate modelling of the visco-elastic material behaviour,  $n$  Kelvin elements connected in series may be used and thus,

$$\dot{\varepsilon}_c = \sum_{r=1}^n \dot{\varepsilon}_c^r = \left(\sum_{r=1}^n a_r\right)\sigma - \sum_{r=1}^n b_r \varepsilon_c^r\tag{9.4.2}$$

in which the first summation leads to a constant, and the second gives the sum of accumulated creep strains due to the individual Kelvin elements.

Assuming that  $\varepsilon_c$  varies linearly during the time intervals  $(t - n\Delta t/2) \rightarrow (t + n\Delta t/2)$ , equation (9.4.2) can be rewritten in the case of a single Kelvin element as follows

$$\frac{(\varepsilon_c^{t+n\Delta t/2} - \varepsilon_c^{t-n\Delta t/2})}{n\Delta t} = a\sigma^t - b\frac{(\varepsilon_c^{t+n\Delta t/2} + \varepsilon_c^{t-n\Delta t/2})}{2}\tag{9.4.3}$$



in which  $n\Delta t$  is the number of time steps between updating of the creep strain  $\epsilon_c$  and on rearranging,

$$\begin{aligned}
 (\epsilon_c^{t+n\Delta t/2} - \epsilon_c^{t-n\Delta t/2}) &= an\Delta t \sigma^t - bn\Delta t \frac{(\epsilon_c^{t+n\Delta t/2} + \epsilon_c^{t-n\Delta t/2})}{2}, \\
 \Rightarrow (1 + \frac{bn\Delta t}{2}) \epsilon_c^{t+n\Delta t/2} &= an\Delta t \sigma^t + (1 - \frac{bn\Delta t}{2}) \epsilon_c^{t-n\Delta t/2}, \\
 \Rightarrow \epsilon_c^{t+n\Delta t/2} &= \frac{an\Delta t \sigma^t}{(1 + \frac{bn\Delta t}{2})} + \frac{(1 - \frac{bn\Delta t}{2})}{(1 + \frac{bn\Delta t}{2})} \epsilon_c^{t-n\Delta t/2} \\
 &= a' \sigma^t + b' \epsilon_c^{t-n\Delta t/2}
 \end{aligned} \tag{9.4.4}$$

$$\text{in which } a' = \frac{an\Delta t}{(1 + \frac{bn\Delta t}{2})}, \quad b' = \frac{(1 - \frac{bn\Delta t}{2})}{(1 + \frac{bn\Delta t}{2})}. \tag{9.4.5}$$

The creep strain  $\epsilon_c^{t+n\Delta t/2}$  obtained from equation (9.4.4) is assumed constant throughout the interval  $n\Delta t$ .

From equation (9.4.4), the vector of creep strains which corresponds to a membrane element used in modelling the material can be written as follows

$$\begin{Bmatrix} \epsilon_{xc} \\ \epsilon_{yc} \\ \gamma_{xyc} \end{Bmatrix}^{t+n\Delta t/2} = [a'] [\Psi] \{\sigma\}^t + [b'] \{\epsilon_c\}^{t-n\Delta t/2} \tag{9.4.6}$$

in which  $[\Psi]$  is a function of the Poisson's ratio only. In equation (9.4.6), it is assumed that the material is isotropic and the creep is therefore associated only with the deviatoric stress components [143]. Furthermore, the Poisson's ratio for creep in an isotropic material can be taken as 0.5 and that the matrix  $[\Psi]$  can in turn be written as follows [143], ie.

$$[\Psi] = \begin{bmatrix} 1 & -0.5 & 0 \\ -0.5 & 1 & 0 \\ 0 & 0 & 3 \end{bmatrix}. \tag{9.4.7}$$

For a membrane element with a two-dimensional state of stress, equation (9.4.6) then becomes



$$\begin{Bmatrix} \varepsilon_{xc} \\ \varepsilon_{yc} \\ \gamma_{xyc} \end{Bmatrix}^{t+n\Delta t/2} = \begin{bmatrix} a_x' & 0 & 0 \\ 0 & a_y' & 0 \\ 0 & 0 & a_{xy}' \end{bmatrix} [\Psi] \{\sigma\}^t + \begin{bmatrix} b_x' & 0 & 0 \\ 0 & b_y' & 0 \\ 0 & 0 & b_{xy}' \end{bmatrix} \{\varepsilon_c\}^{t-n\Delta t/2} \quad (9.4.8)$$

in which

$$a_x' = a_y' = a_{xy}' = a \frac{n\Delta t}{(1 + \frac{bn\Delta t}{2})},$$

$$b_x' = b_y' = b_{xy}' = \frac{(1 - \frac{bn\Delta t}{2})}{(1 + \frac{bn\Delta t}{2})}, \quad (9.4.9)$$

and the values of  $a$  and  $b$  are determined from material tests. In the case of an isotropic material, the  $[\Psi]$  matrix is given by equation (9.4.7).

The choice of which Kelvin model to adopt is dependent on the type of loading. For short term dynamic loading, a single element model may suffice particularly if of interest is a qualitative study of the damping effect of the visco-elastic membrane material. A more complex model may be necessary for long term quasi-static creep investigations of a membrane under prestress.

In this chapter, the creep effects in the membrane material will be considered on the basis of a single Kelvin model. Besides simplifying the calculations for the creep effects, the use of a single Kelvin model will also enable the membrane dynamic properties to be assessed with relative ease. In his analysis of a pneumatic dome subjected to suddenly applied dynamic loading, Barnes [11] used a single Kelvin model to obtain numerical results of dynamic response which agree closely with the experimental values.

## 9.5 Incremental procedure to account for on/off buckling

A membrane material has strength only by being in tension. Under compression, it buckles and loses its load carrying capacity. During the dynamic analysis, the stresses in the membrane can go from the tensile into the compressive state or vice versa. This means that the membrane will undergo on/off buckling. A procedure of modelling the on/off buckling has to be implemented into the explicit dynamic analysis. At the moment, a general formula which describes the stress-strain relation during on/off buckling is still unknown and further research is required to derive such a formula. However, a practical solution can be found in the procedure which will be outlined shortly. The procedure is based on an elastic stress-strain relationship. It will involve checking for the presence of negative or compressive stresses during the dynamic analysis and resetting any compressive stresses to zero. The checks for the presence of compressive



stresses, ie. buckling checks need not be carried out at each time interval, but can be coupled with the creep strain calculations.

The incremental procedure to allow for on/off buckling consists of the following three stages [11], ie.

### Stage I

At the start of the dynamic analysis, the initial stress level  $\{\sigma\}^i$  for each element is established. The material elastic and visco-elastic properties corresponding to this stress level are obtained. The initial force vector  $\{T\}^i$  and natural stiffness matrix  $[K]$  for each element are also set up as follows

$$\{T\}^i = [G]^T \{\sigma\}^i, \quad [K] = [G]^T [D] [G] \quad (9.5.1)$$

in which  $[G]$  and  $[D]$  are the strain and elasticity matrices respectively. The vector of creep strains,  $\{\epsilon_c\}$  for each element are measured relative to the geometry of the structure at this stage.

### Stage II

The dynamic analysis is iterated through  $n$  time intervals  $\Delta t$  with the current force vector  $\{T\}$  for each element updated in the following manner

$$\{T\} = \{T\}^i + [K] \{\Delta e\} \quad (9.5.2)$$

in which  $\{\Delta e\}$  is the vector of element side extensions relative to the geometry of the structure at the start of each period of  $n\Delta t$ .

### Stage III

For each element:

(1) determine stresses relative to chosen local  $x$ - and  $y$ -axes, ie.

$$\{\sigma\}^t = \{\sigma\}^i + [D][G]\{e\}^t - [D]\{\epsilon_c\}^{t-n\Delta t/2} \quad (9.5.3)$$



in which  $\{e\}^t$  is the vector of total side extensions relative to the geometry of the structure at stage I;

- (2) determine principal stress vector  $\{\sigma_p\}$  and their inclinations to the local  $x$ - and  $y$ -axes;
- (3) if any of the principal stresses is negative (ie. compressive), set to zero and modify principal stress vector to give  $\{\sigma_p'\}$ ;
- (4) the elasticity matrix relative to the principal axes, ie.  $[D_p]$  is modified with the elastic constants reset to account for buckling, to give  $[D_p']$  which in turn is transformed as follows

$$[D'] = [C]^T [D_p'] [C] \quad (9.5.4)$$

in which  $[C]$  is the transformation matrix between the local and the principal axes, and  $[D']$  is the modified elasticity matrix relative to the local axes;

- (5) determine modified stresses:

$$\{\sigma'\}^t = [C]^T \{\sigma_p'\}, \quad \{\Delta\sigma'\}^t = \{\sigma'\}^t - \{\sigma\}^i; \quad (9.5.5)$$

- (6) determine new creep strains:

$$\{\epsilon_c\}^{t+n\Delta t/2} = [a'] [\Psi] \{\Delta\sigma'\}^t + [b'] \{\epsilon_c\}^{t-n\Delta t/2}; \quad (9.5.6)$$

- (7) determine new initial force vector:

$$\{T\}^i = [G]^T \{\sigma'\}^t - [G]^T [D'] (\{\epsilon_c\}^{t+n\Delta t/2} - \{\epsilon_c\}^{t-n\Delta t/2}); \quad (9.5.7)$$

- (8) form new  $[G]$  matrix and new natural stiffness matrix:

$$[K] = [G]^T [D'] [G]. \quad (9.5.8)$$

Return to stage II

Figure 9.3

If a principal stress is found to be zero or negative in step (3) above, the material becomes highly anisotropic in behaviour. In the direction of compression, the elastic stiffness becomes effectively negligible and can be assumed to be zero. As a result, the  $[D_p]$  matrix has to be modified accordingly in step (4) above in the following manner

$$\{\sigma_p\} = [D_p] \{\epsilon_p\},$$



$$\Rightarrow \begin{Bmatrix} \sigma_x \\ \sigma_y \\ 0 \end{Bmatrix} = \begin{bmatrix} d_{11} & d_{12} & 0 \\ d_{21} & d_{22} & 0 \\ 0 & 0 & d_{33} \end{bmatrix} \begin{Bmatrix} \varepsilon_x \\ \varepsilon_y \\ 0 \end{Bmatrix} \quad (9.5.9)$$

in which if

- (i)  $\sigma_x \leq 0 \Rightarrow d_{11} = d_{12} = d_{21} = d_{33} = 0$  and  $d_{22} = E_y$ ,
- (ii)  $\sigma_y \leq 0 \Rightarrow d_{12} = d_{21} = d_{22} = d_{33} = 0$  and  $d_{11} = E_x$ ,
- (iii)  $\sigma_x \leq 0$  and  $\sigma_y \leq 0 \Rightarrow d_{11} = d_{12} = d_{21} = d_{22} = d_{33} = 0$ , (9.5.10)

where  $E_x$  and  $E_y$  are the moduli of elasticity in the local  $x$ - and  $y$ -directions respectively. The  $[D']$  matrix derived from the modified matrix  $[D_p']$  will in turn be used in all subsequent computations until it is reset when the analysis next returns to stage III. However, the  $[D]$  matrix should always be used in step (1) above as it will not be sensible to assume an element has already buckled before a buckling check.

The  $[C]$  matrix mentioned above can be defined as follows

$$[C] = \begin{bmatrix} \cos^2\theta & \sin^2\theta & \cos\theta\sin\theta \\ \sin^2\theta & \cos^2\theta & -\cos\theta\sin\theta \\ -2\cos\theta\sin\theta & 2\cos\theta\sin\theta & \cos^2\theta - \sin^2\theta \end{bmatrix} \quad (9.5.11)$$

in which  $\theta$  is the angle between the local  $x$ -axis and the direction of maximum principal stress.

The incremental procedure outlined above will be simplified when the local axes of each element are aligned to coincide with the warp and fill directions of the membrane material which are also the directions of the principal membrane stresses. By doing so, any transformation between the local axes and the principal stress directions can therefore be avoided. In such a case, the  $[C]$  matrix is effectively an identity matrix. The incremental procedure with the above simplification is implemented into the explicit dynamic analysis considered in this chapter.

In the above incremental procedure, the creep and buckling effects are both considered in stage III after each period of  $n\Delta t$  in stage II. In this way, the explicit dynamic analysis will be made more efficient. A larger value of  $n$  may be allowed if a very small time interval  $\Delta t$  is used. In some cases however, it may be required to perform the buckling checks at a frequency different from that at which the creep effects are considered.



## 9.6 Pneumatic stiffness and damping

Under investigation in this chapter is a pneumatic dome pressurised by air on the inside. The internal (ie. inflation) pressure is maintained at an operating level by means of mechanical fans. At the start of the dynamic analysis, the dome will be caused to undergo vibrations. As the dome vibrates, the internal (or enclosed) volume of the dome will increase or decrease accordingly, ie. volume-displacing modes of motion. These volume changes gives rise to the pneumatic stiffness and damping in the dome. The pneumatic stiffness is due to the increase in internal pressure as the internal volume decreases. On the other hand, the pneumatic damping is due to the increase in internal pressure in direct proportion to the rate of volume decrease. As the dome under consideration here is essentially sealed with negligible air leakage, the pneumatic stiffness will be significant and thus, has to be taken into account within the dynamic analysis. The pneumatic damping however is important only if there is quite high air leakage from the dome which is not the case here. Consequently, the pneumatic damping can be ignored in the dynamic analysis of the dome.

Furthermore, the internal pressure can be assumed to be uniform throughout the dome at any instant because the time taken for an acoustic wave to propagate across the dome is typically several times less than the period of major membrane vibrations [81]. The air in the dome is also assumed to behave isentropically as would be the case in a dynamic situation. The pneumatic stiffness of the dome is considered using the following relationship between pressure  $P$  and volume  $V$  assuming isentropic ideal gas behaviour, ie.

$$PV^\alpha = \text{constant} \quad (9.6.1)$$

in which  $\alpha$  is a coefficient which can be taken as 1.4 for air. In the explicit dynamic analysis, equation (9.6.1) is expressed in the following form

$$P_{in}^t = (P_{in}^{t-\Delta t} + P_{ex}) \left( \frac{V^{t-\Delta t}}{V^t} \right)^\alpha - P_{ex} \quad (9.6.2)$$

in which  $V^{t-\Delta t}$  and  $V^t$  are the internal volumes at times,  $(t - \Delta t)$  and  $t$  respectively,  $P_{in}^{t-\Delta t}$  and  $P_{in}^t$  are the internal pressures at times,  $(t - \Delta t)$  and  $t$  respectively, and  $P_{ex}$  is the external (ie. atmospheric) pressure.

Subsequently, for each membrane element, the internal pressure at time  $t$  gives rise to the following forces

$$\begin{Bmatrix} P_x \\ P_y \\ P_z \end{Bmatrix}^t = \frac{1}{6} \times P_{in}^t \times \{u_n\}^t \quad (9.6.3)$$



in which  $\{u_n\}^t$  is an outward normal vector of the element, and  $P_x$ ,  $P_y$  and  $P_z$  are the forces in the global  $x$ -,  $y$ - and  $z$ -directions respectively at each node of the element.

### 9.7 Added mass effects

A membrane encounters more resistance when oscillating in air than in a vacuum. The resistance comes from having to mobilise the surrounding air attached to the membrane into motion as well. The mass of air which is set into motion can be termed as the added mass. It has been found from experiments and theoretical work that for a sphere, the added mass is approximately equal to one half of the mass of fluid displaced by the sphere. As would be expected, the shape and stiffness of the body, the nature of its motion, and the density of the fluid are all factors which will have an influence on the added mass.

For an air-supported structure, the added mass of the surrounding air will have an effect on how the membrane will behave and therefore deserves much attention particularly so considering the lightweight nature of the membrane. The membrane motion induces pressure perturbations in the surrounding air. These pressure changes are proportional to the normal accelerations of the membrane. If the pattern of these changes is in phase with the membrane motion, no energy is added to or lost from the membrane. However, if they either lead or lag behind the membrane motion, then the air acts as an exciter which may lead to instability, or as a damper respectively.

Jensen [79] conducted a series of tests on suspended cable structures with and without membrane cladding, and concluded that the added mass effects are significant for the membrane-clad nets. He concluded that the added mass  $m''$  could be approximated by the following formula, ie.

$$m'' = c_m \rho_a a^3 \quad (9.7.1)$$

in which  $c_m$  ( $= 2.7 \rightarrow 7.5$ ) is a coefficient dependent on the shape and vibration mode of the structure,  $\rho_a$  is the density of air, and  $a$  is a typical dimension of the structure such as the radius for a dome.

For the membrane dome with a radius of 2.37m considered here, equation (9.7.1) gives an added mass which ranges from 44.1kg to 122.4kg, ie. 44 to 122 times the membrane mass which is about 1.0kg. In addition, Irwin, et. al. [77] using an almost flat two-dimensional membrane to study the roof of the Montreal Olympic Stadium (with a 180m  $\times$  120m elliptical membrane roof) found that the added mass due to the attached air was about 37 times the membrane mass. Clearly, the added mass has a much more significant influence on the dynamic response of the dome than the membrane mass. As a result, the exclusion of the added mass effects from the explicit dynamic analysis will only lead to unrealistic prediction of the dynamic response.



Krakowska [86] suggested that there are three different approaches of handling the problem of modelling the effects of the surrounding air within the dynamic analysis:

- (1) the behaviour of surrounding air can be modelled numerically using equations from fluid mechanics, and coupled with the structural dynamic analysis;
- (2) the influence of surrounding air on the structural response is accounted for by means of additional terms in the mass, damping and external force matrices of the equations of motion; this may be derived from theoretical models and/or simple relations from fluid mechanics;
- (3) an approach similar to (2), but with the additional terms obtained from simple theories combined with experimental coefficients.

In general, the least amount of computations will be involved if the approach in (3) is adopted, but at the same time, a large number of experiments also need to be carried out; experiments are required for the different types and shapes of membrane structures. For instance, Jensen [79] derived equation (9.7.1) from the results obtained through a series of experiments.

The approach in (1) in theory, has the potential of giving the most accurate solution. However, this approach probably requires an enormous amount of computations to solve the time dependent equations from fluid mechanics. This approach has been used by Krakowska [86] in the form of a coupled fluid-structure numerical scheme to investigate the dynamic response of a suddenly unloaded air-supported dome. A formulation of the Lagrangian type was used for the fluid, ie. the motion of every particle of the fluid is traced historically [90]. The independent variables are the initial position vectors of the fluid particles and time. The internal air was divided into triangular elements for a two-dimensional case, and into tetrahedral elements for a three-dimensional case. Each air element was assumed to have a constant mass, and to undergo translations and distortions due to compressibility. The influence of the external air was not considered. The behaviour of the internal air was described by equations from fluid mechanics. The motions of the air elements were coupled with the dynamic response of the membrane. However, a very fine mesh and thus, a very small time step was required for the explicit dynamic analysis. The enormous amount of computing time needed to achieve converged solutions means that this method is currently impractical. A similar method has been used by Barnes [19] to analyse the dynamic response of a cylindrical membrane structure subjected to a suddenly applied patch loading. Both the internal and external air were discretised into finite air elements. Again, extremely slow convergence was observed even though the problem considered was only a simple two-dimensional one. Until much more powerful computers become available in future, the approach in (1) is at present not a practical solution.



On the other hand, the approach in (2) seems a practical one, ie. it involves finding an acceptable solution which demands much less computational effort than the approach in (1). Consequently, this approach is adopted for implementation into the explicit dynamic analysis being considered here.

Furthermore, for the approach in (2), the modelling of the influence of surrounding air on the dynamic response will require the application of a few concepts from the field of fluid mechanics. There has been much theoretical work done in this vast field, and the classic text by Lamb [90] is the primary source for the basic concepts of fluid mechanics outlined in the discussion which follows. These concepts are those relevant for modelling the added mass effects under investigation here.

### 9.8 Basic assumptions

As mentioned earlier, the solution for the dynamic response of a tension structure is a complex aeroelastic problem. Subsequently, a few assumptions have to be made in order to simplify the problem and make it solvable with the available means. The basic assumption is that the air flow is irrotational, ie. it has zero vorticity. The definition of vorticity can be illustrated using figure 9.4 in which  $u$  and  $v$  are the fluid velocities in the  $x$ - and  $y$ -directions respectively.

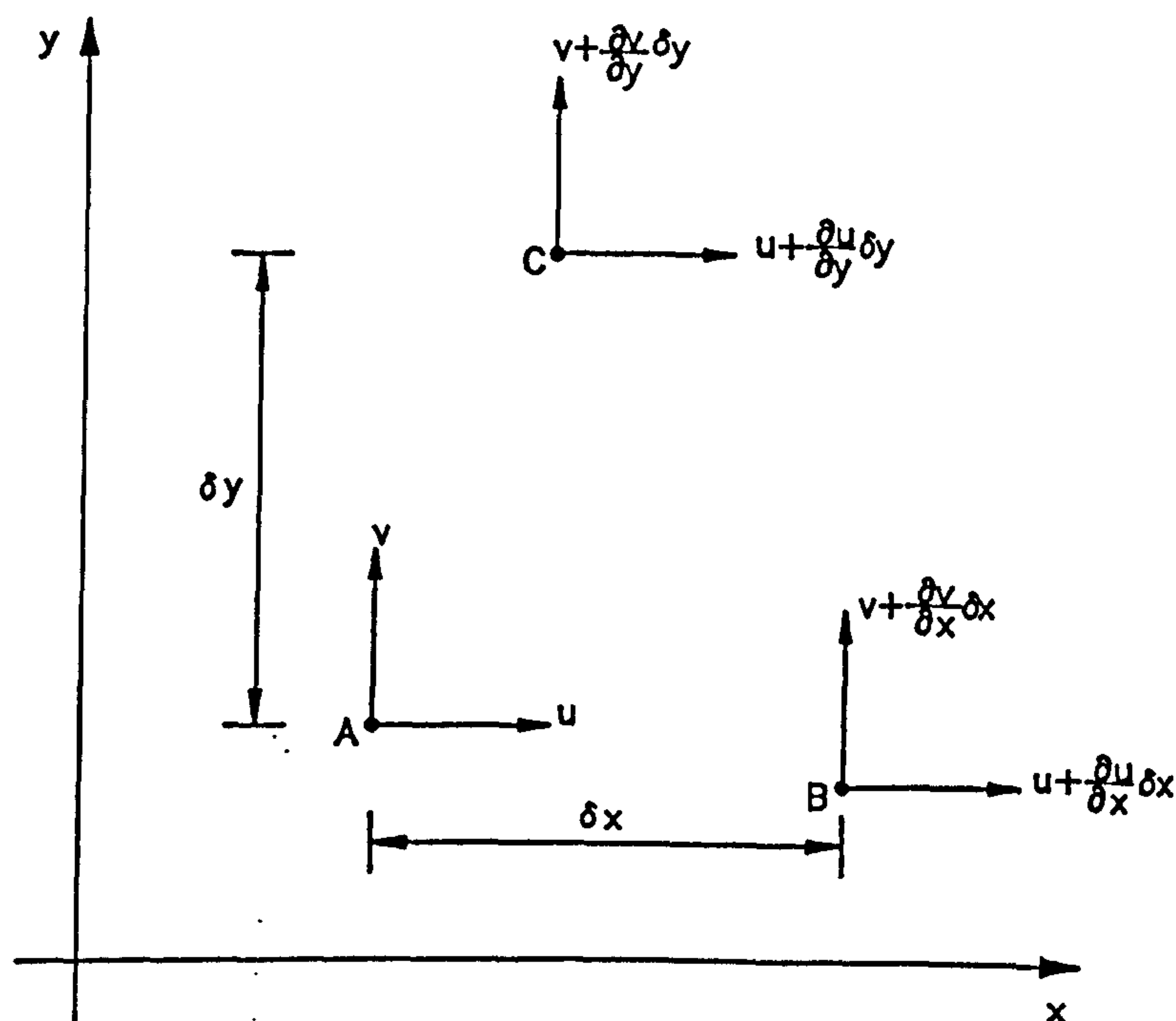


Figure 9.4

In general,  $u$  and  $v$  will be functions of  $x$  and  $y$ , and also time, if the flow is unsteady.  $A$ ,  $B$  and  $C$  are three fluid 'particles' moving with the fluid. Figure



9.4 shows an instant in which the line  $AB$  is horizontal and the line  $AC$  is vertical. The anti-clockwise angular velocity of the line  $AB$  is given by

$$\frac{\text{vertical velocity of } B - \text{vertical velocity of } A}{\text{distance } AB} = \frac{(v + \delta v) - v}{\delta x} = \frac{\delta v}{\delta x} = \frac{\partial v}{\partial x} \quad (\text{as } \delta x \rightarrow 0).$$

Similarly, the clockwise angular velocity of the line  $AC$  is  $\frac{\partial u}{\partial y}$ . The vorticity or mean angular velocity about a line parallel to the  $z$ -axis is given by

$$\frac{1}{2} \left[ \frac{\partial v}{\partial x} - \frac{\partial u}{\partial y} \right]. \quad (9.8.1)$$

The minus sign occurs because  $\frac{\partial v}{\partial x}$  is anti-clockwise and  $\frac{\partial u}{\partial y}$  is clockwise. In addition, the rate of shear strain is defined by

$$\frac{1}{2} \left[ \frac{\partial v}{\partial x} + \frac{\partial u}{\partial y} \right]. \quad (9.8.2)$$

A perfect fluid is a fluid (liquid or gas) with no viscosity (ie. inviscid), and if the vorticity of the flow of a perfect fluid is initially zero, it will always remain so. Therefore, viscosity is necessary to generate vorticity and since the viscosity of air is very low, it seems reasonable to assume that the flow of air is irrotational (ie. has zero vorticity). However, the intense rates of shear strain which occur when a fluid flows past a solid surface means that vorticity is generated in the boundary layer and if the flow separates from the surface, the vorticity is shed into the main flow to form a turbulent wake.

From the studies by Hess and Smith [72], the neglect of viscosity is justified except at points in or very near regions of catastrophic separation, for example, wakes. Local regions of separation and reattachment do not normally invalidate the calculations. Even when catastrophic separation is present, the calculations are valid a moderate distance forward of the separation point.

It is virtually impossible to proceed ahead with the theory without the assumption of irrotational flow, even with the most powerful computers. Hence, the theory will only produce results which correspond to the assumption made, and according to Williams [136, 137, 141], aeroelastic wind tunnel tests should still be used for accurate quantitative predictions.

Furthermore, the air is assumed to be incompressible. This assumption is reasonable since pressures associated with the wind are of the order of magnitude of  $1 \text{ kNm}^{-2}$  whereas the atmospheric pressure is approximately  $100 \text{ kNm}^{-2}$  so that the volumetric strains will be of the order of 1% as given by equation (9.6.1).



The assumption of incompressibility of air can also be viewed in terms of the sound waves, ie. is justified if the wavelength of sound is much larger than the wavelengths of movements in the membrane as is usually the case for an air-supported structure.

### 9.9 Potential flow theory

In the following discussion, the symbolic vector operator

$$\nabla = i \frac{\partial}{\partial x} + j \frac{\partial}{\partial y} + k \frac{\partial}{\partial z} \quad (9.9.1)$$

is used, in which  $i$ ,  $j$  and  $k$  are unit vectors in the global  $x$ -,  $y$ - and  $z$ -directions respectively. If

$$q = f(x, y, z)$$

is a differentiable scalar function, then  $\nabla q$  is the gradient of  $q$ , ie.

$$\text{grad } q = \nabla q = i \frac{\partial q}{\partial x} + j \frac{\partial q}{\partial y} + k \frac{\partial q}{\partial z}. \quad (9.9.2)$$

In addition, for a vector field such as

$$\varphi(x, y, z) = i \varphi_x(x, y, z) + j \varphi_y(x, y, z) + k \varphi_z(x, y, z), \quad (9.9.3)$$

the divergence is then defined as follows

$$\text{div } \varphi = \nabla \cdot \varphi = \frac{\partial \varphi_x}{\partial x} + \frac{\partial \varphi_y}{\partial y} + \frac{\partial \varphi_z}{\partial z}. \quad (9.9.4)$$

For the case of zero viscosity and constant density, the general Navier-Stokes equations reduce to the well known Eulerian equation of motion, ie.

$$\frac{\partial V}{\partial t} + (V \cdot \nabla) V = -\frac{1}{\rho} \nabla p \quad (9.9.5)$$

in which  $V$  is the fluid velocity at any point and time  $t$ ,  $p$  is the fluid pressure, and  $\rho$  is the fluid density which is constant, and the equation of continuity becomes

$$\nabla \cdot V = 0 \quad (9.9.6)$$

or, in Cartesian notation

$$\frac{\partial V_x}{\partial x} + \frac{\partial V_y}{\partial y} + \frac{\partial V_z}{\partial z} = 0 \quad (9.9.7)$$



in which  $V_x$ ,  $V_y$  and  $V_z$  are the component velocities in the global  $x$ -,  $y$ - and  $z$ -directions respectively. The equation of motion (equation (9.9.5)) accounts for the system of forces acting in the fluid, and the equation of continuity (equation (9.9.6)) ensures that there is conservation of mass throughout the fluid.

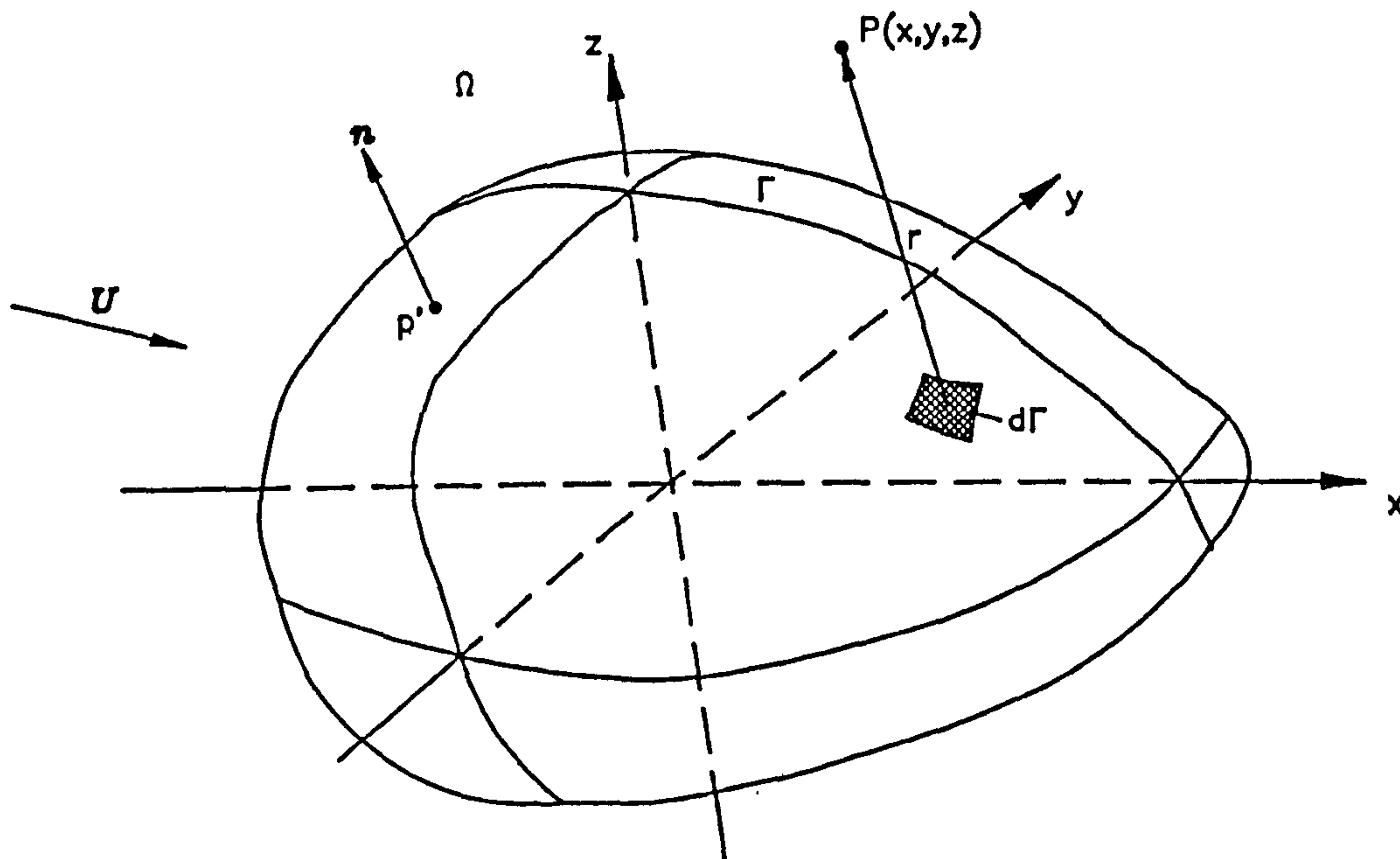


Figure 9.5

It is assumed that the locations of all boundary surfaces are known, possibly as functions of time, and the normal component of fluid velocity is prescribed on these boundaries. Let  $\Gamma$  denotes the boundary of  $\Omega$  which is the region of flow as shown in figure 9.5 and the boundary condition is given by

$$V \cdot n|_{\Gamma} = F \quad (9.9.8)$$

in which  $n$  is the unit outward normal vector at a point on  $\Gamma$ , and  $F$  is a known function of position on  $\Gamma$  and possibly also a known function of time.

The velocity field  $V$  can be expressed as the sum of two velocities, ie.

$$V = U + v. \quad (9.9.9)$$

The vector  $U$  is the velocity of the onset flow, which is defined as the velocity field that would exist in the fluid in the absence of all boundaries. The vector  $v$  is the disturbance velocity field which exists as a result of the boundaries. The velocity  $v$  is assumed to be irrotational and may thus be written as follows



$$\mathbf{v} = -\nabla \phi = -\mathbf{i} \frac{\partial \phi}{\partial x} - \mathbf{j} \frac{\partial \phi}{\partial y} - \mathbf{k} \frac{\partial \phi}{\partial z} \quad (9.9.10)$$

in which  $\phi = \phi(x, y, z)$  is a scalar function which in this case is the velocity potential. The existence of a velocity potential depends on the condition of irrotationality assumed for the velocity  $\mathbf{v}$ . By using equation (9.9.10), the number of dependent variables in the problem considered here is reduced by two. However, it is not necessary to apply the assumption of irrotationality to the velocity  $\mathbf{U}$ . Since  $\mathbf{U}$  is the velocity of an incompressible flow, it satisfies equation (9.9.6), and thus, so does  $\mathbf{v}$ , ie.

$$\nabla \cdot \mathbf{v} = 0. \quad (9.9.11)$$

Using  $\mathbf{v}$  from equation (9.9.10) in equation (9.9.11) leads to the following

$$\nabla^2 \phi = 0 \quad (9.9.12)$$

in which  $\nabla^2 = \nabla \cdot \nabla$  is the Laplacian operator. Equation (9.9.12) is the Laplace equation for the region  $\Omega$  shown in figure 9.5, and expresses the continuity condition for an incompressible potential flow. From equations (9.9.8), (9.9.9) and (9.9.10), the boundary condition on  $\phi$  is then given by

$$\nabla \phi \cdot \mathbf{n} \big|_{\Gamma} = \frac{\partial \phi}{\partial n} \big|_{\Gamma} = \mathbf{U} \cdot \mathbf{n} \big|_{\Gamma} - F. \quad (9.9.13)$$

The essential simplicity of potential flow is that the velocity field is determined by the equation of continuity (equation (9.9.11)) and the condition of irrotationality (equation (9.9.10)). Thus, the equation of motion (equation (9.9.5)) is not used, and the velocity may be determined independently of the pressure. Once the velocity field is known, the pressure is calculated from equation (9.9.5). The problem is essentially reduced to the solution of equation (9.9.12) subject to the boundary condition given by equation (9.9.13).

For a steady potential flow (ie. both  $\mathbf{U}$  and  $\mathbf{v}$  assumed to be steady and irrotational), equation (9.9.5) then reduces to

$$(\mathbf{V} \cdot \nabla) \mathbf{V} = -\frac{1}{\rho} \nabla p \quad (9.9.14)$$

which can then be integrated to give one of the forms of the Bernoulli equation, ie.

$$\frac{p}{\rho} = G - \frac{1}{2} |\mathbf{V}|^2 \quad (9.9.15)$$

in which  $G$  is a constant from the integration. In most cases, the onset flow is a uniform stream, ie.  $\mathbf{U}$  is a constant vector. Under these conditions, equation (9.9.15) can be used in an expression for the pressure coefficient  $C_p$  given as follows



$$C_p = \frac{p - p_\infty}{\frac{1}{2}\rho |U|^2} = 1 - \frac{|v|^2}{|U|^2} \quad (9.9.16)$$

in which  $p_\infty$  is the pressure at infinity. The assumption of steady flow implies that conditions of instability such as flutter cannot be modelled directly.

The boundary condition given by equation (9.9.8) may be prescribed in different forms. For a fluid mass which is unbounded, the boundary conditions at infinity and on the surface of a body submerged in the fluid are considered. It is often that the fluid is taken to be at rest at infinity. On the surface of a submerged body, the boundary condition may be such that in a direction normal to the surface, both the fluid and the surface have the same velocities. On the surface of a solid body, the fluid velocity normal to the surface is taken to be zero, ie. the function  $F$  in equation (9.9.8) is equal to zero.

### 9.10 Solution of the Laplace equation

As shown above, the main concern in the potential flow problem comes down to solving the Laplace equation, ie. equation (9.9.12). Despite the fact that the Laplace equation is one of the simplest and best known of all partial differential equations, there are only a few useful exact analytic solutions. This is because equation (9.9.12) can be solved analytically only for an extremely limited class of boundary surfaces  $\Gamma$ . It is therefore likely that the exact solution of the potential flow problem for arbitrary boundaries has to be found in a numerical approach. Furthermore, it is efficient in the numerical approach to reduce the problem to an integral equation over the boundary surface. For the adopted approach in this chapter, it will involve sources and doublets distributed over the boundary surface.

A source is a point from which fluid is imagined to flow out uniformly in all directions. If the total flux outwards across a small closed surface surrounding the point is  $\omega$ , then  $\omega$  is called the strength of the source. A negative source is called a sink.

A combination of two equal and opposite sources  $\pm\omega$ , at a distance  $\delta s$  apart, where, in the limit,  $\delta s$  is taken to be infinitely small, and  $\omega$  infinitely large, but so that the product  $\omega\delta s$  is finite and equal to  $\mu$  (say), is called a doublet of strength  $\mu$ , and the line  $\delta s$ , considered as drawn in the direction from  $-\omega$  to  $+\omega$ , is called its axis.

Although the sources and doublets defined above are purely abstract conceptions which do not occur in nature, they are nevertheless useful, as will be shown, for describing the motion of a fluid.



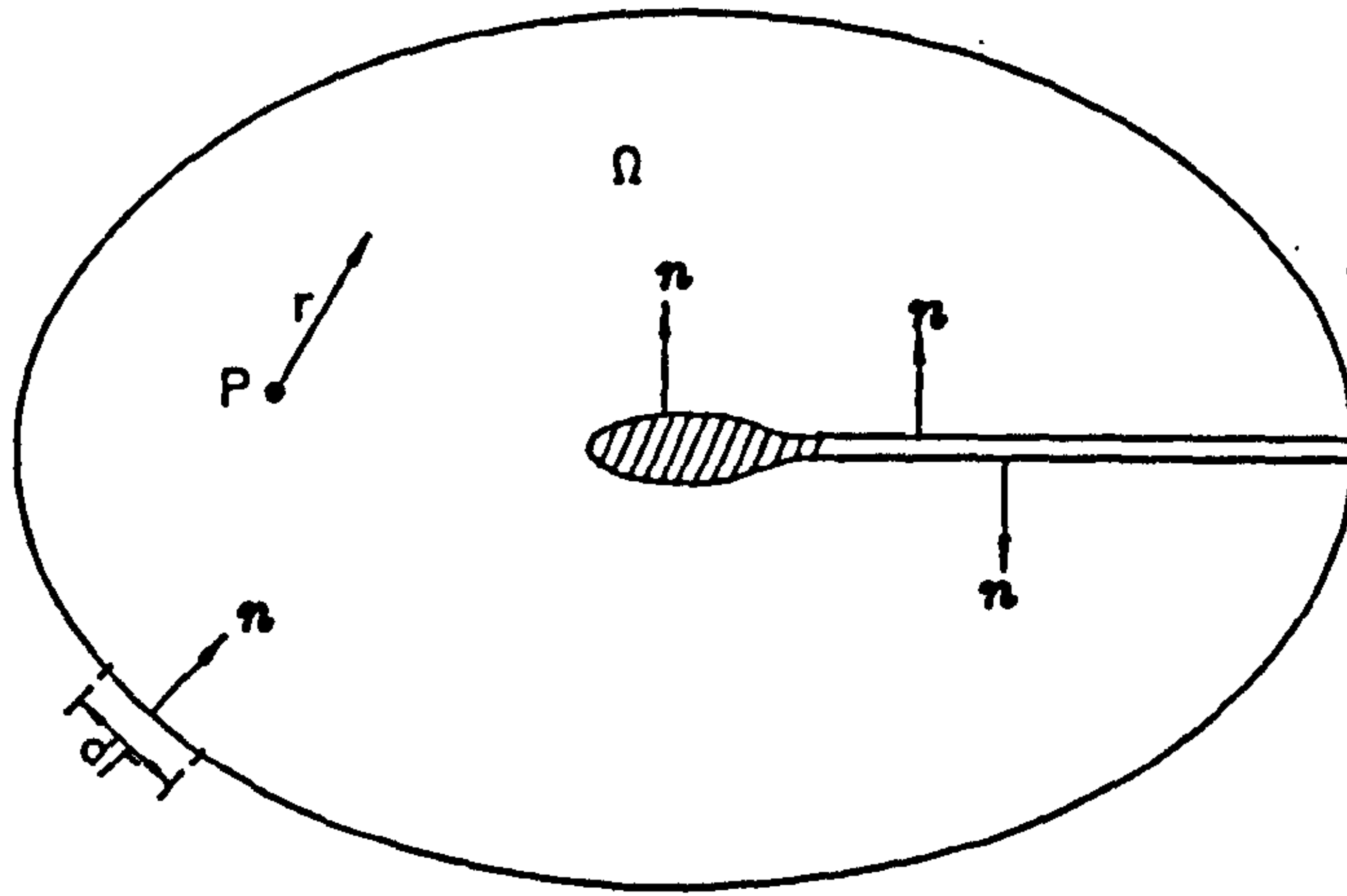


Figure 9.6

According to Lamb [90], any continuous acyclic irrotational motion of a fluid mass may be regarded as associated with a distribution of sources and doublets over the boundary surface. This can be proved using the divergence theorem (Gauss's theorem) which states that the volume integral of the divergence of a vector field  $\varphi$  taken over any volume  $\Omega$  is equal to the surface integral of  $\varphi$  taken over the closed surface surrounding the volume  $\Omega$  (see figure 9.6), ie.

$$\int_{\Omega} \nabla \cdot \varphi \, d\Omega = - \int_{\Gamma} n \cdot \varphi \, d\Gamma \quad (9.10.1)$$

or, in Cartesian notation

$$\iiint_{\Omega} \left( \frac{\partial \varphi_x}{\partial x} + \frac{\partial \varphi_y}{\partial y} + \frac{\partial \varphi_z}{\partial z} \right) dx dy dz = - \iint_{\Gamma} (l \varphi_x + m \varphi_y + n \varphi_z) d\Gamma \quad (9.10.2)$$

in which the volume  $\Omega$  refers to a region in space occupied by the flow field,  $\Gamma$  is the surface which bounds  $\Omega$ ,  $n$  is a unit vector (with direction cosines given by  $l$ ,  $m$  and  $n$ ) normal to  $\Gamma$  and directed into  $\Omega$ , and  $\varphi$  is a continuous function of position inside  $\Omega$ . The minus sign in equation (9.10.1) is due to the fact that  $n$  is directed into  $\Omega$ .

The vector  $\varphi$  in equation (9.10.1) can be defined as follows

$$\varphi = \phi \nabla \phi_s - \phi_s \nabla \phi \quad (9.10.3)$$

in which  $\phi$  is the velocity potential of the flow in  $\Omega$ , so that



$$\mathbf{v} = -\nabla \phi \quad (9.10.4)$$

is the fluid velocity in  $\Omega$ . On the other hand,  $\phi_s$  is the potential of a source of unit strength at some arbitrary point  $P(x, y, z)$  in  $\Omega$ , and

$$\begin{aligned} \phi_s &= -\frac{1}{2\pi} \ln(r) && \text{in two dimensions,} \\ &= \frac{1}{4\pi} \frac{1}{r} && \text{in three dimensions.} \end{aligned} \quad (9.10.5)$$

in which  $r$  is the distance from  $P$  to the point at which  $\phi$  is to be evaluated, as shown in figure 9.6. For a continuous function  $\phi$  in  $\Omega$ , the terms  $\phi$ ,  $\nabla \phi$ ,  $\phi_s$  and  $\nabla \phi_s$  should be continuous as well. However,  $\phi_s$  and its derivatives are singular when  $\phi$  is evaluated at  $P$  (ie.  $r = 0$ ). Hence, before integrating over  $\Omega$ , a small circle (in two dimensions) or sphere (in three dimensions) with radius  $\varepsilon$  and centred at  $P$  is defined, as shown in figure 9.7. Let  $\Omega_\varepsilon$  be the part of  $\Omega$  outside that excluded region, and  $\Gamma_\varepsilon$  be the surface of the circle or sphere. For the same reason, such entities as the vortex sheet should be excluded from  $\Omega$  since the velocity  $\mathbf{v}$  is discontinuous across such a sheet.

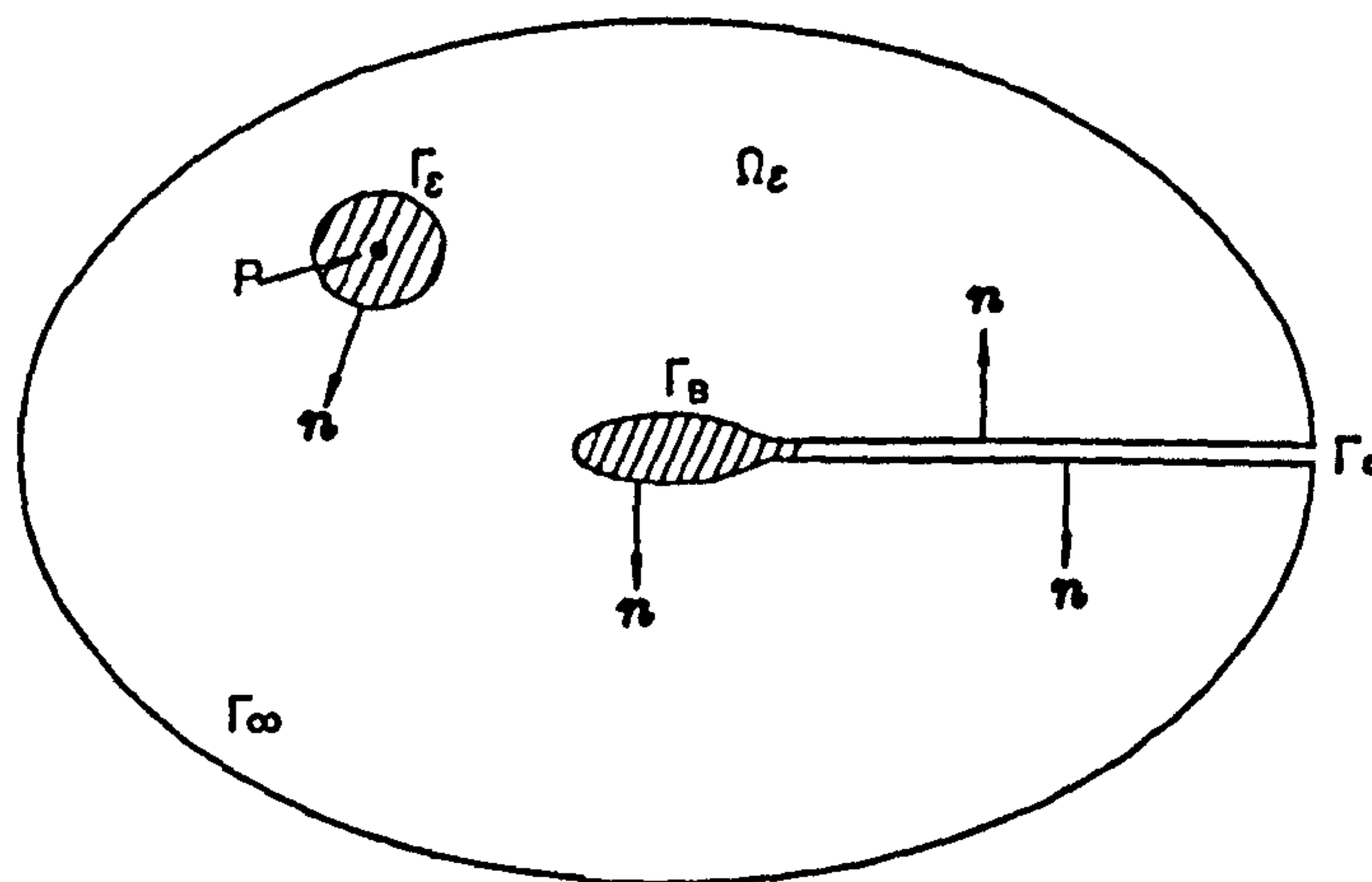


Figure 9.7

Generally, the surface  $\Gamma$  has the following three components [100], ie.

- (i)  $\Gamma_B$ , the surface of the body immersed in the flow,
- (ii)  $\Gamma_\infty$ , a surface far from  $\Gamma_B$ ,
- (iii)  $\Gamma_C$ , a two-sided surface that runs between  $\Gamma_B$  and  $\Gamma_\infty$ , and which sandwiches discontinuities in  $\phi$  and/or  $\nabla \phi$ .



The terms  $\phi_s$  and  $\phi$  satisfy the Laplace equation everywhere in  $\Omega_\epsilon$ . Hence, from equation (9.10.3),

$$\begin{aligned}\nabla \cdot \phi &= \nabla \phi \cdot \nabla \phi_s + \phi \nabla \cdot \nabla \phi_s - \nabla \phi_s \cdot \nabla \phi - \phi_s \nabla \cdot \nabla \phi \\ &= \phi \nabla^2 \phi_s - \phi_s \nabla^2 \phi \\ &= 0 \quad \text{in } \Omega_\epsilon.\end{aligned}\tag{9.10.6}$$

Applying equation (9.10.1) to the region  $\Omega_\epsilon$  then gives

$$\int_{\Omega_\epsilon} \nabla \cdot \phi \, d\Omega = 0 = - \int_{\Gamma + \Gamma_\epsilon} n \cdot (\phi \nabla \phi_s - \phi_s \nabla \phi) \, d\Gamma.\tag{9.10.7}$$

Equation (9.10.7) can in turn be written as

$$\int_{\Gamma_\epsilon} n \cdot (\phi \nabla \phi_s - \phi_s \nabla \phi) \, d\Gamma = - \int_{\Gamma} n \cdot (\phi \nabla \phi_s - \phi_s \nabla \phi) \, d\Gamma.\tag{9.10.8}$$

If ( $\epsilon \rightarrow 0$ ), then  $\phi$  and  $\nabla \phi$  approach their values at  $P$ , ie.  $\phi_P$  and  $-v_P$  respectively, and thus, the left hand side of equation (9.10.8) becomes

$$\int_{\Gamma_\epsilon} n \cdot (\phi \nabla \phi_s - \phi_s \nabla \phi) \, d\Gamma \approx \phi_P \int_{\Gamma_\epsilon} n \cdot \nabla \phi_s \, d\Gamma + v_P \cdot \int_{\Gamma_\epsilon} n \phi_s \, d\Gamma.\tag{9.10.9}$$

The first integral on the right hand side of equation (9.10.9) is just the volume rate of flow through  $\Gamma_\epsilon$ , which equals the strength of the source inside, namely, unity and thus,

$$\phi_P \int_{\Gamma_\epsilon} n \cdot \nabla \phi_s \, d\Gamma = \phi_P \int_{\Gamma_\epsilon} \frac{\partial \phi_s}{\partial n} \, d\Gamma = \phi_P (-1) = -\phi_P.\tag{9.10.10}$$

As for the second integral on the right hand side of equation (9.10.9),  $r$  is constant (ie.  $\epsilon$ ) on  $\Gamma_\epsilon$  and so is  $\phi_s$  from equation (9.10.5). Taking  $\phi_s$  outside the integral leaves

$$\int_{\Gamma_\epsilon} n \, d\Gamma$$



which in turn vanishes by symmetry, and thus, in the limit, equation (9.10.8) reduces to

$$\phi_P = - \int_{\Gamma} (n \cdot \nabla \phi) \phi_s - \phi (n \cdot \nabla \phi_s) d\Gamma \quad (9.10.11)$$

which is known as the Green's third identity. Equation (9.10.11) gives the value of  $\phi$  at any point  $P$  in  $\Omega$ , a region in which  $\phi$  is a continuous solution of the Laplace equation, in terms of the values of  $\phi$  and  $(-n \cdot \nabla \phi)$  on the boundary of  $\Omega$ .

Although the derivation of equation (9.10.11) is rather mathematical, there is a physical interpretation to the result. The term  $\phi_s$  in the first right integral, ie.

$$- \int_{\Gamma} (n \cdot \nabla \phi) \phi_s d\Gamma \quad (9.10.12)$$

depends only on the distance  $r$  between  $P$  and the  $d\Gamma$  whose contribution to the integral is under consideration. Therefore, although in equation (9.10.5),  $\phi_s$  is the potential of a source of unit strength at point  $P$ , evaluated at a point on  $\Gamma$  a distance  $r$  away, it could also be taken as the potential of a source of unit strength at  $d\Gamma$ , evaluated at  $P$ . As such, the term in equation (9.10.12) can be interpreted as the potential of a source distribution on  $\Gamma$  whose strength per unit area is  $(-n \cdot \nabla \phi)$ , ie. the component normal to  $\Gamma$  of the local fluid velocity.

For the second right integral in equation (9.10.11), ie.

$$\int_{\Gamma} \phi (n \cdot \nabla \phi_s) d\Gamma \quad (9.10.13)$$

in which the term  $(n \cdot \nabla \phi_s)$  is the rate of change of  $\phi_s$  in the direction of  $n$  at the element  $d\Gamma$ . This can be interpreted as follows.

As shown in figure 9.8, let  $g_1$  and  $g_2$  be two points  $\delta$  apart, on either side of  $d\Gamma$ , and arranged so that the vector from  $g_2$  to  $g_1$  is given by  $\delta n$ . Let  $\phi_1$  and  $\phi_2$  be the values of potential at  $g_1$  and  $g_2$  respectively due to a source of unit strength at  $P$ , and thus,



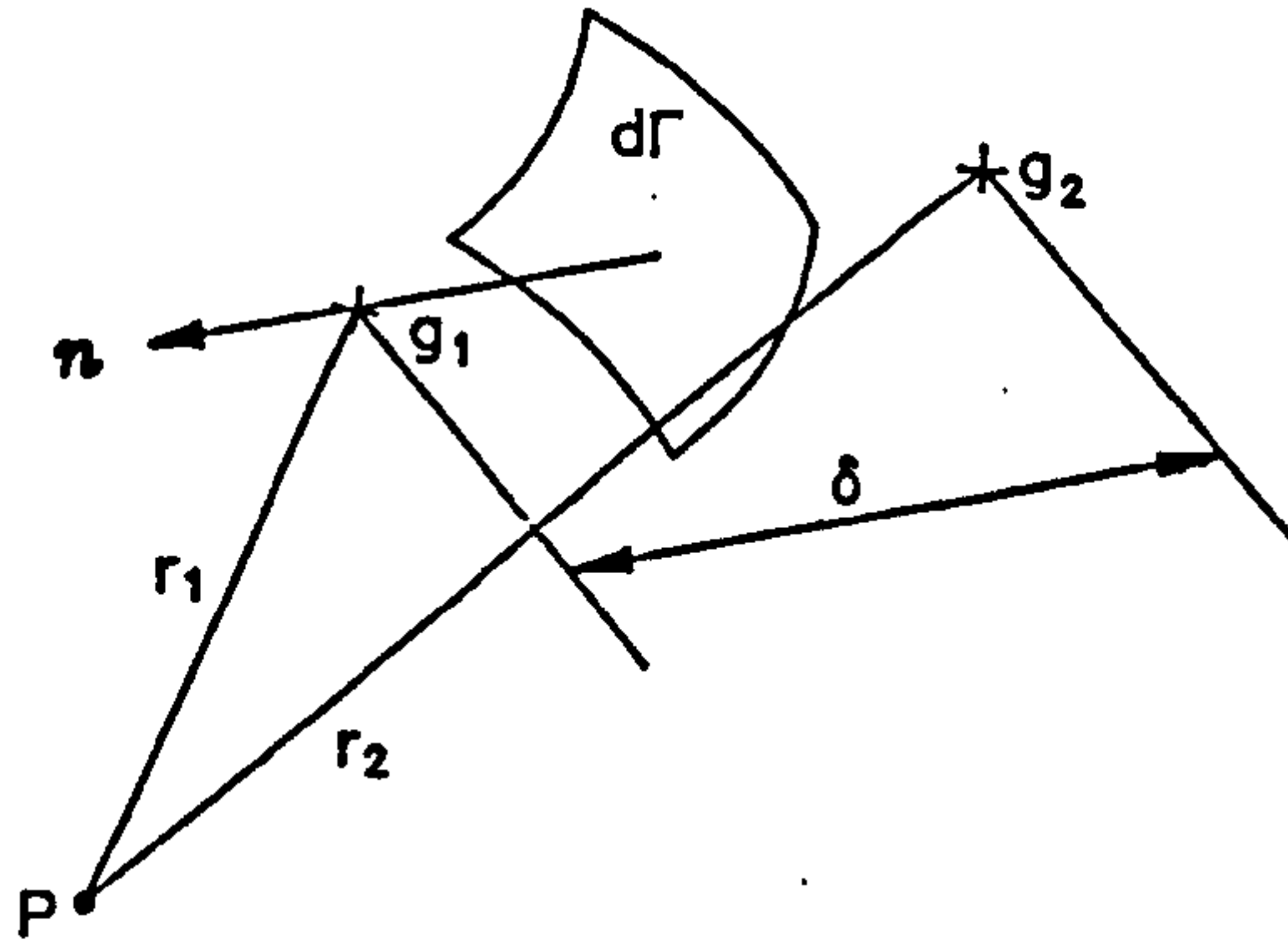


Figure 9.8

$$n \cdot \nabla \phi_s = \lim_{\delta \rightarrow 0} \frac{\phi_1 - \phi_2}{\delta}. \quad (9.10.14)$$

As demonstrated above,  $\phi_1$  and  $\phi_2$  can also be taken as the potentials at  $P$  due to unit-strength sources at  $g_1$  and  $g_2$  respectively. Consequently, the term  $(\phi_1/\delta - \phi_2/\delta)$  refers to the difference in potentials at  $P$  due to two sources of strength  $1/\delta$  with one at  $g_1$  and another at  $g_2$ . As  $(\delta \rightarrow 0)$ , the two sources coalesce into a doublet of strength given by the product of the source strength and the distance between the sources, which in this case equals to unity. Hence, equation (9.10.13) can be viewed as the potential at  $P$  due to a doublet distribution over the surface  $\Gamma$ . The axes of the doublets are normal to  $\Gamma$ , and the strength per unit area of the distribution is given by  $\phi$ , ie. the local velocity potential.

It has been shown that the velocity potential of any irrotational flow can be given by a distribution of sources and doublets over its bounding surfaces. The strength of the source and doublet distributions per unit area are in turn given by the boundary values of  $(-\partial\phi/\partial n)$  and  $\phi$  respectively.

Subsequently, equation (9.10.11) can be rewritten as follows

$$\phi_P = -\frac{1}{4\pi} \int_{\Gamma} \frac{1}{r} \frac{\partial\phi}{\partial n} d\Gamma + \frac{1}{4\pi} \int_{\Gamma} \phi \frac{\partial}{\partial n} \left( \frac{1}{r} \right) d\Gamma. \quad (9.10.15)$$

According to Lamb [90], equation (9.10.15) is only one out of an infinite number of surface distributions which will give the same value of  $\phi$  throughout the region  $\Omega$ . It is shown below that the distribution in equation (9.10.15) can further be replaced by one of sources only, or of doublets only, over the boundary.



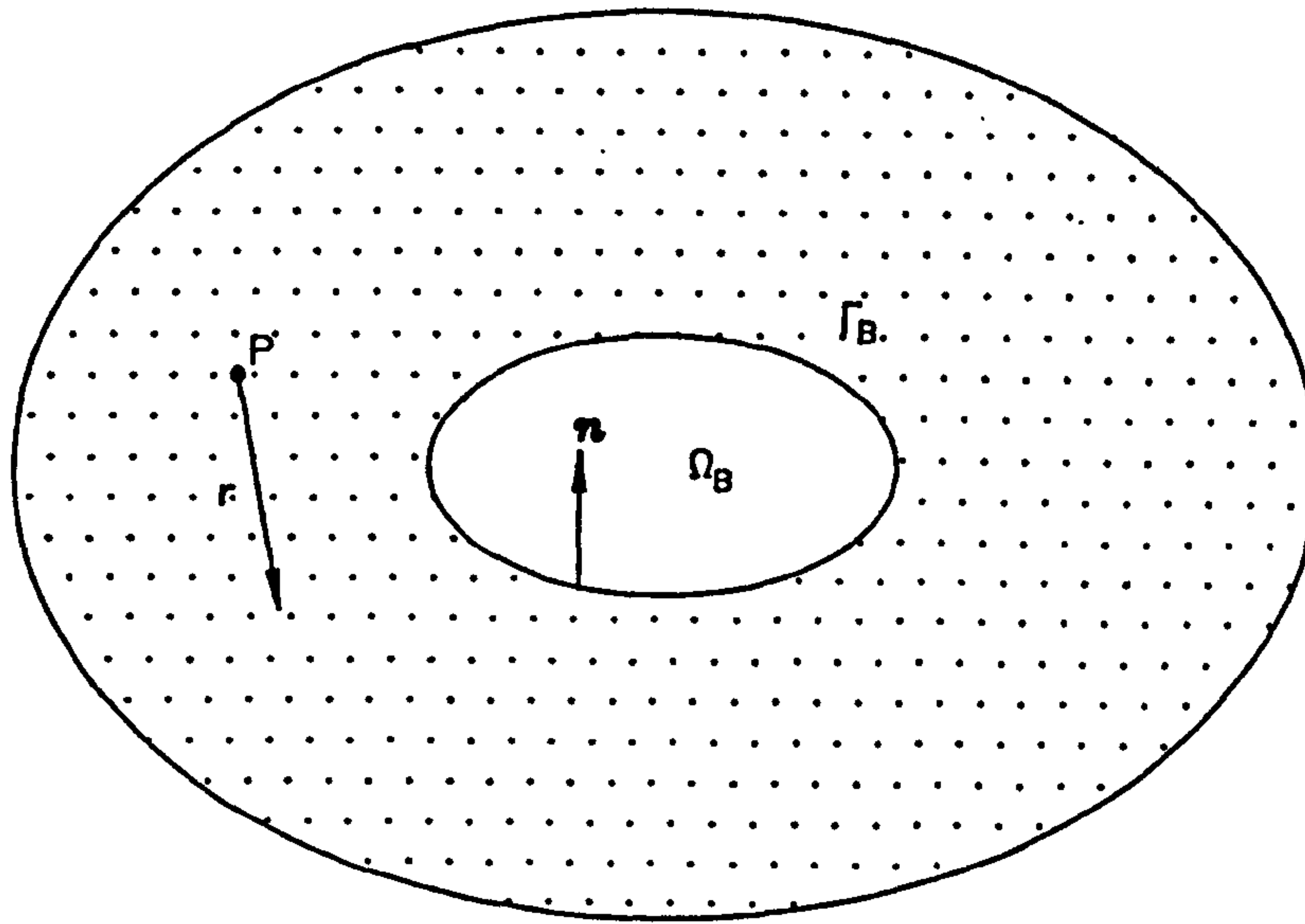


Figure 9.9

Let  $\phi^*$  be the potential in the region  $\Omega_B$  that is inside the body surface  $\Gamma_B$ , as shown in figure 9.9. The term  $\phi_s$  is still the potential of a point source outside the body surface, and from equation (9.10.3),

$$\phi^* = \phi^* \nabla \phi_s - \phi_s \nabla \phi^*, \quad (9.10.16)$$

and from equation (9.10.6),

$$\nabla \cdot \phi^* = 0 \quad \text{in } \Omega_B. \quad (9.10.17)$$

Hence, from equations (9.10.1) and (9.10.16),

$$0 = - \int_{\Gamma_B} n^* \cdot (\phi^* \nabla \phi_s - \phi_s \nabla \phi^*) d\Gamma \quad (9.10.18)$$

in which the unit normal  $n^*$  is directed into  $\Omega_B$  and so is equal and opposite to the  $n$  in equation (9.10.11) at the same point on  $\Gamma_B$ , ie.  $n^* = -n$ . By addition of equations (9.10.11) and (9.10.18), and assuming no contributions from the surfaces  $\Gamma_\infty$  and  $\Gamma_C$ ,

$$\phi_P = - \int_{\Gamma_B} (\sigma \phi_s - \mu n \cdot \nabla \phi_s) d\Gamma \quad (9.10.19)$$



in which

$$\sigma = n \cdot \nabla(\phi - \phi^*),$$

and

$$\mu = \phi - \phi^*. \quad (9.10.20)$$

Firstly, consider the case of  $\phi = \phi^*$  at the surface. The tangential velocities on the two sides of the boundary are then continuous, but the normal velocities are discontinuous. This may be illustrated by considering a fluid which fills infinite space, and to be divided into two portions by an infinitely thin vacuum sheet within which an impulsive pressure  $\rho\phi$  is applied, so as to generate the given motion from rest [90]. The last integral in equation (9.10.19) vanishes, so that

$$\phi_P = -\frac{1}{4\pi} \int_{\Gamma_B} \frac{1}{r} \left( \frac{\partial \phi}{\partial n} - \frac{\partial \phi^*}{\partial n} \right) d\Gamma, \quad (9.10.21)$$

and the motion (on either side) is the result of a surface distribution of sources, of density

$$-\left( \frac{\partial \phi}{\partial n} - \frac{\partial \phi^*}{\partial n} \right).$$

Secondly, consider the case of  $n \cdot \nabla \phi = n \cdot \nabla \phi^*$  over the boundary. This gives continuous normal velocity, but discontinuous tangential velocity over the boundary. This motion may be imagined to be generated by giving the prescribed normal velocity ( $-\partial\phi/\partial n$ ) to every point of an infinitely thin membrane coincident in position with the boundary [90]. In this case, the first integral in equation (9.10.19) vanishes, so that

$$\phi_P = \frac{1}{4\pi} \int_{\Gamma_B} (\phi - \phi^*) \frac{\partial}{\partial n} \left( \frac{1}{r} \right) d\Gamma, \quad (9.10.22)$$

and the motion (on either side) is due to a surface distribution of doublets, of density

$$(\phi - \phi^*).$$

According to Lamb [90], the above results for  $\phi$  in terms of sources alone, or of doublets alone, are unique; whereas the representation in equation (9.10.11) is indeterminate.

In equation (9.10.19), the assumption of no contribution from the surface  $\Gamma_\infty$  is justified if the fluid is at rest at infinity. In addition, the surface  $\Gamma_C$  can be



excluded if there are no discontinuities in  $\phi$  and/or  $\nabla\phi$  within the region  $\Omega$  considered. However, if the stated conditions are present, then the effects of the surfaces  $\Gamma_\infty$  and  $\Gamma_C$  have to be taken into account.

### 9.11 Kinetic energy considerations

An estimation of the added mass of the surrounding air when set into motion can be obtained by considering the kinetic energy of the moving air. For a potential flow, the total kinetic energy  $T_f$  of the fluid (in this case, moving air) is given by [90]

$$T_f = -\frac{1}{2}\rho \int_{\Gamma} \phi \frac{\partial \phi}{\partial n} d\Gamma \quad (9.11.1)$$

in which the integral is taken over the bounding surface  $\Gamma$  of the fluid. This result has a simple physical interpretation. The term  $(-\partial\phi/\partial n)$  is the normal velocity of the fluid inwards, and  $\rho\phi$  is the impulsive pressure necessary to generate the motion. In addition, the work done by an impulse is equal to the product of the impulse into half the sum of the initial and final velocities, resolved in the direction of the impulse at the point to which it is applied. Hence, the surface integral gives the work done by the impulsive pressures which, applied to the surface  $\Gamma$ , would generate the actual motion [90].

In the case of fluid extending to infinity and is at rest there, and is limited internally by one or more closed surfaces  $\Gamma$ , equation (9.11.1) holds only if the total flux across the internal boundary is zero, ie.

$$\int_{\Gamma} \frac{\partial \phi}{\partial n} d\Gamma = 0 \quad (9.11.2)$$

with the integration extending over the whole boundary. This may be regarded as a generalised form of the equation of continuity (ie. equation (9.9.12)). Equation (9.11.2) simply implies that the source or doublet distribution does not contribute to the flux. This is certainly a physical requirement for flow of an incompressible fluid. It is important to bear in mind the condition given in equation (9.11.2) when considering cases in which one or more closed surfaces are present, as otherwise the resulting kinetic energy becomes infinite [90].

A simple relationship between the kinetic energy of the fluid and the added mass is given by

$$T_f = \frac{1}{2} \times m_a \times (w_m)^2 \quad (9.11.3)$$



in which  $m_a$  is the added mass and  $w_m$  is a typical or representative velocity of the membrane. Furthermore, if the kinetic energy of the membrane is  $T_m$ , then the following ratio of the kinetic energies, ie.

$$\frac{T_f}{T_m} = \Lambda_{am} \quad (9.11.4)$$

gives a measure of the added mass of the surrounding fluid relative to the membrane total mass, and  $\Lambda_{am}$  is termed the added mass coefficient.

The kinetic energy considerations discussed above give rise to a relatively simple procedure of estimating the added mass of the surrounding air as will be shown. This procedure can also be incorporated into the explicit dynamic analysis with relative ease.

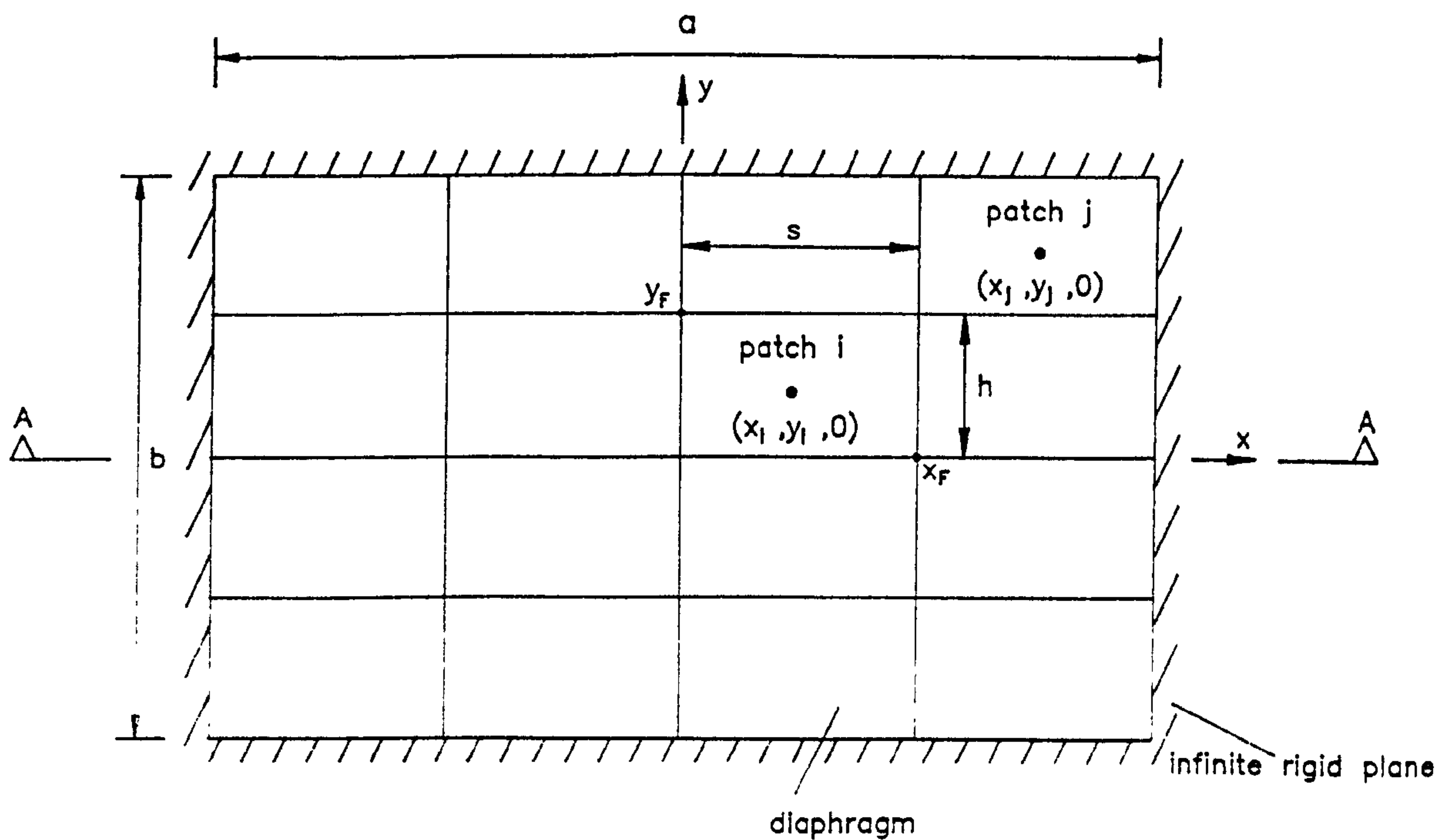
### 9.12 A diaphragm embedded in an infinite rigid plane

The concepts discussed above have been applied to the case of a diaphragm embedded in an infinite rigid plane by Campbell [42], and a brief account of his work is given below.

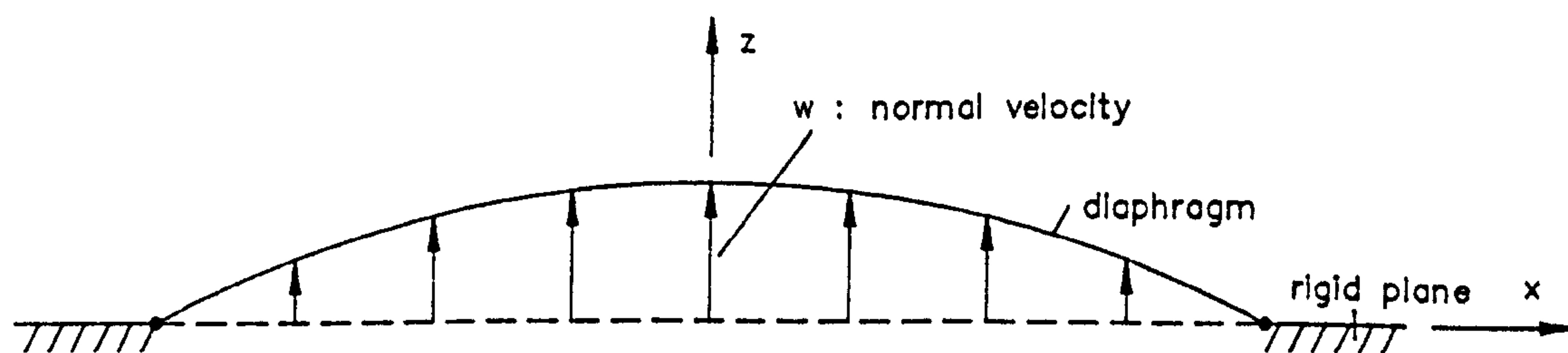
The diaphragm is sealed into a rectangular opening ( $a \times b$  in plan) in an infinite rigid plane, completely separating the semi-infinite body of fluid on one side of the diaphragm from that on the other side (see figure 9.10). This corresponds to the 'closed edge' case in which there is no mixing of fluid between the two sides of the diaphragm. The 'open edge' case corresponds to a diaphragm oscillating on its own and isolated in an unlimited mass of fluid, and in which there is mixing of fluid between the two sides of the diaphragm. The normal displacement out of plane of the diaphragm is assumed to be small and that the normal velocity distribution is known. The choice of using either a distribution of sources or doublets is governed by the boundary conditions on and off the body. Using a surface distribution of doublets gives continuous normal velocity but discontinuous tangential velocity over the diaphragm. On the other hand, a surface distribution of sources implies the tangential velocities on the two sides of the diaphragm are continuous, but the normal velocities are discontinuous. For the 'closed edge' case, the requirement of no mixing of fluid between the two sides of the diaphragm favour the use of sources. Furthermore, the sign of the normal velocity does not affect the value of the kinetic energy which depends on the square of the velocity. Hence, a distribution of sources is used over the diaphragm which is lying in the  $z=0$  plane as shown in figure 9.10. On the other hand, a distribution of doublets is used for the 'open edge' case. However, only the 'closed edge' case will be discussed further in this section.

The diaphragm can be imagined to consist of two sides; the upper side represents the top surface of the membrane with the attached air moving in the same direction as the membrane; and the lower side models the under surface of the membrane. As a result of using a source distribution, the

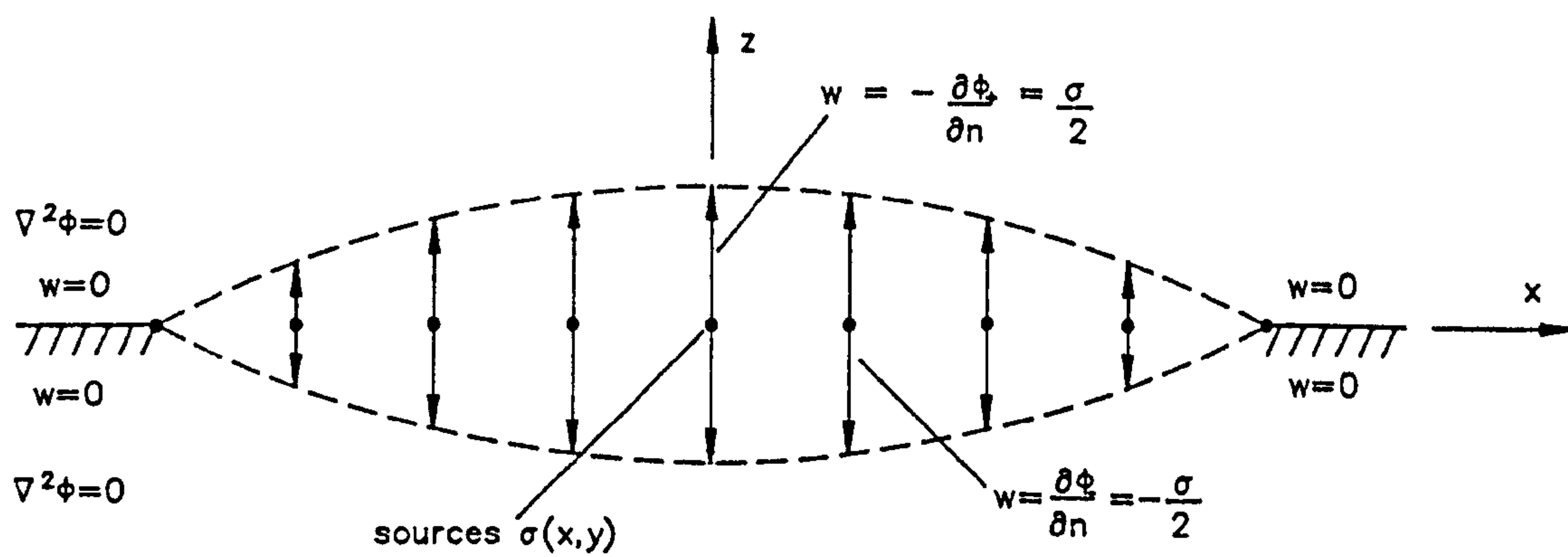




(a) Plan



(b) Section A-A



(c) Distribution of discrete sources

Figure 9.10



internal and external air move in opposite directions normal to the diaphragm. As indicated above, this is acceptable as far as kinetic energy considerations are concerned. There are various ways in which to distribute the sources. In this case, the diaphragm is divided into rectangular patches with a discrete source placed at the centre of each patch.

From equation (9.10.5), the potential  $\phi$  at any point  $P$  with coordinates  $(x, y, z)$  due to a source of strength  $\omega$  placed at the origin is given by

$$\phi = \frac{\omega}{4\pi r} \quad (9.12.1)$$

in which  $r$  is the distance of  $P$  from the source and thus,  $r = \sqrt{x^2 + y^2 + z^2}$ . As mentioned earlier, the strength of the source can be taken as the total flux outwards across a small closed surface surrounding the source.

The velocity  $w$  in the  $z$ -direction is then given by

$$w = -\frac{\partial \phi}{\partial z} = \frac{\omega}{4\pi} \frac{z}{(x^2 + y^2 + z^2)^{3/2}}. \quad (9.12.2)$$

Hence, for a source in the  $z=0$  plane, the flow out of this plane vanishes everywhere except at the location of the source. Considering a small circle of radius  $\varepsilon$  centred at the source, the average upward velocity  $w_{av}$  can be written as follows

$$\begin{aligned} w_{av} &= \frac{1}{\pi \varepsilon^2} \frac{\omega}{4\pi} \lim_{z \rightarrow 0^+} \int_0^\varepsilon \frac{z}{(\theta^2 + z^2)^{3/2}} 2\pi \theta d\theta \\ &= \frac{1}{\pi \varepsilon^2} \frac{\omega}{2} \lim_{z \rightarrow 0^+} \left. \frac{-z}{(\theta^2 + z^2)^{1/2}} \right|_0^\varepsilon \\ &= \frac{1}{\pi \varepsilon^2} \frac{\omega}{2}. \end{aligned} \quad (9.12.3)$$

For  $(z \rightarrow 0^-)$ , equation (9.12.3) gives the average downward velocity as expected from the fact that half of the flux from the source flows downward.

Similarly, for a source of strength  $\omega_i$  placed at the centre of a rectangular patch  $i$  ( $s \times h$ , see figure 9.10) of area  $A_i$  in the  $z=0$  plane,

$$w_{avi} = \frac{1}{A_i} \frac{\omega_i}{2}. \quad (9.12.4)$$

Subsequently, consider the potential in patch  $i$  which is contributed by the sources at the centres of all other patches. The average potential over the area of patch  $i$  due to a source at point  $(x_j, y_j, 0)$ , ie. the centre of patch  $j$ , can be obtained as follows



$$\begin{aligned}
\phi_{avij} &= \frac{1}{A_i} \frac{\omega_j}{4\pi} \int_0^{x_F} \left( \int_0^{y_F} \frac{dy}{\sqrt{x^2 + y^2}} \right) dx \\
&= \frac{1}{A_i} \frac{\omega_j}{4\pi} \int_0^{x_F} \ln \left( \frac{y_F + \sqrt{x^2 + y_F^2}}{x} \right) dx \\
&= \frac{1}{A_i} \omega_j C_{ij}
\end{aligned} \tag{9.12.5}$$

in which the terms  $x$ ,  $y$ ,  $x_F$  and  $y_F$  are as defined in figure 9.10, and  $C_{ij}$  is a coefficient which can be found numerically such as by the trapezoidal rule. Considering the distribution of sources over the entire diaphragm, the total average potential of patch  $i$  is then given by

$$\phi_{avi} = \frac{1}{A_i} \sum_{j=1}^n \omega_j C_{ij} \tag{9.12.6}$$

where  $n$  is the total number of patches, and from equation (9.12.4),

$$\omega_j = 2 \times w_{avj} \times A_j. \tag{9.12.7}$$

In order to determine the added mass coefficient  $\Lambda_{am}$  (given in equation (9.11.4)), it is required to find the kinetic energy of air on both sides of the diaphragm. Subsequently, equation (9.11.1) which gives the kinetic energy of the fluid, can in this case be written as follows

$$T_f = \rho_a \iint_{\Gamma z^+} \phi_u w_u dx dy \tag{9.12.8}$$

in which  $\rho_a$  is the density of air,  $\phi_u$  and  $w_u$  are respectively the potential and normal velocity over the top surface of the diaphragm, and the  $z^+$  term indicates that the integration is for the case of  $(z \rightarrow 0^+)$  over the diaphragm. As both  $\phi$  and  $(-\partial\phi/\partial n)$  are symmetrical about the  $z=0$  plane for a source distribution, equation (9.12.8) gives the total kinetic energy of air on both sides of the diaphragm.

For a sufficiently large number of patches, the integration can be approximated by a summation as follows

$$T_f = \rho_a \sum_{i=1}^n (\phi_{avi}) (w_{avi}) (A_i). \tag{9.12.9}$$

The kinetic energy of the diaphragm in turn can be expressed as



$$T_m = \frac{1}{2} \rho_m \sum_{i=1}^n (w_{avi})^2 (A_i) (th) \quad (9.12.10)$$

in which  $\rho_m$  and  $th$  are the density and thickness of the diaphragm material respectively. The ratio of  $(T_f/T_m)$  then gives an indication of the added mass effects of the diaphragm (see equation (9.11.4)).

Using the above equations, Campbell [42] calculated the added mass effects of the diaphragm for various normal velocity distributions prescribed over the diaphragm. In each case, convergence was achieved as the number of patches were increased. The results obtained includes the case of an aspect ratio (ie. length to width of diaphragm) equal to 100. These results were then extrapolated to the limit of  $(n \rightarrow \infty)$ , and when compared with the two-dimensional theoretical results, there was close agreement.

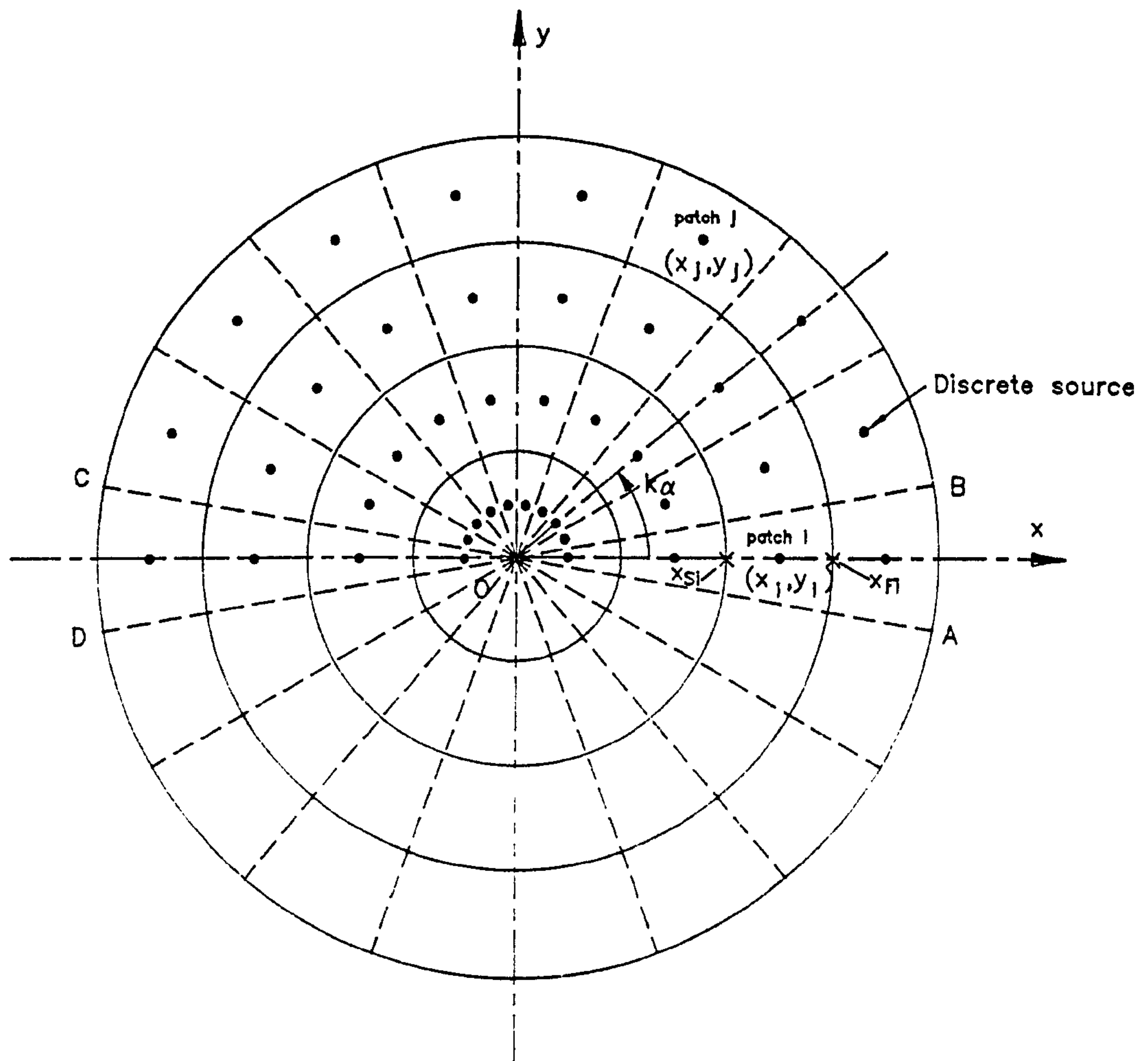
### 9.13 A shallow pneumatic dome

In the previous section, an account is given of an approach (termed here as the discrete source method) applied by Campbell [42] to calculate for the added mass effects of a 'closed edge' diaphragm. This approach has been further applied to assess the added mass effects of a shallow pneumatic dome by Krakowska [86], and an account of her work is given in this section.

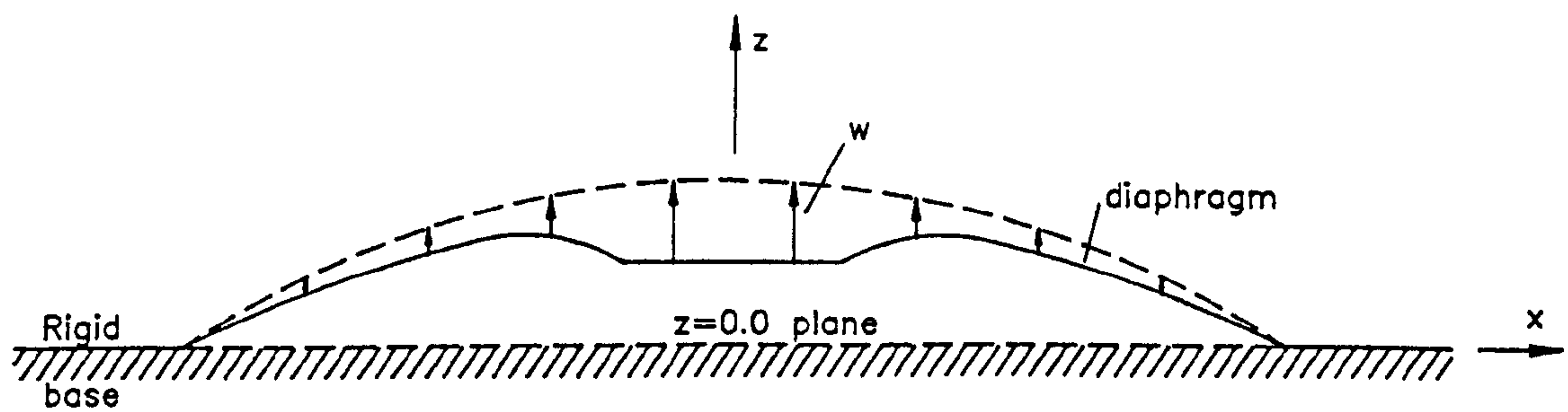
The dome is constructed from a light membrane material. In addition, the dome has a ratio of maximum dynamic height to span of less than 1:20 and hence, can be taken as a shallow structure. Furthermore, the normal displacements (ie. in the  $z$ -direction) both observed during experiment and determined from theory, are small when compared with the dome diameter. The average potentials are calculated for a mesh of triangular and trapezoidal patches which lie in the  $z=0$  (or  $x-y$ ) plane as shown in figure 9.11, with a discrete source placed at the centre of each patch. On the other hand, the structural analysis is based on the idealisation of the dome into a mesh of constant strain triangular elements which lie over the membrane. In the plan view of the dome, the node positions of the patches coincide with those of the elements.

As a result of the uniform division of the dome into patches and elements, certain variables which are functions of the radius need only be determined for the patches and elements in a single slice of the dome. In this case, the chosen slice is that represented by the region  $AOB$  of the dome as shown in figure 9.11(a). Using the normal nodal velocities of the elements obtained from the explicit dynamic analysis and assuming a linear variation, the velocities  $w_{avi}$  at the centres of the corresponding patches can be found. With all the patches lying in the  $z=0$  plane, the  $r$  term in equation (9.12.1) can be taken as  $\sqrt{x^2 + y^2}$ .

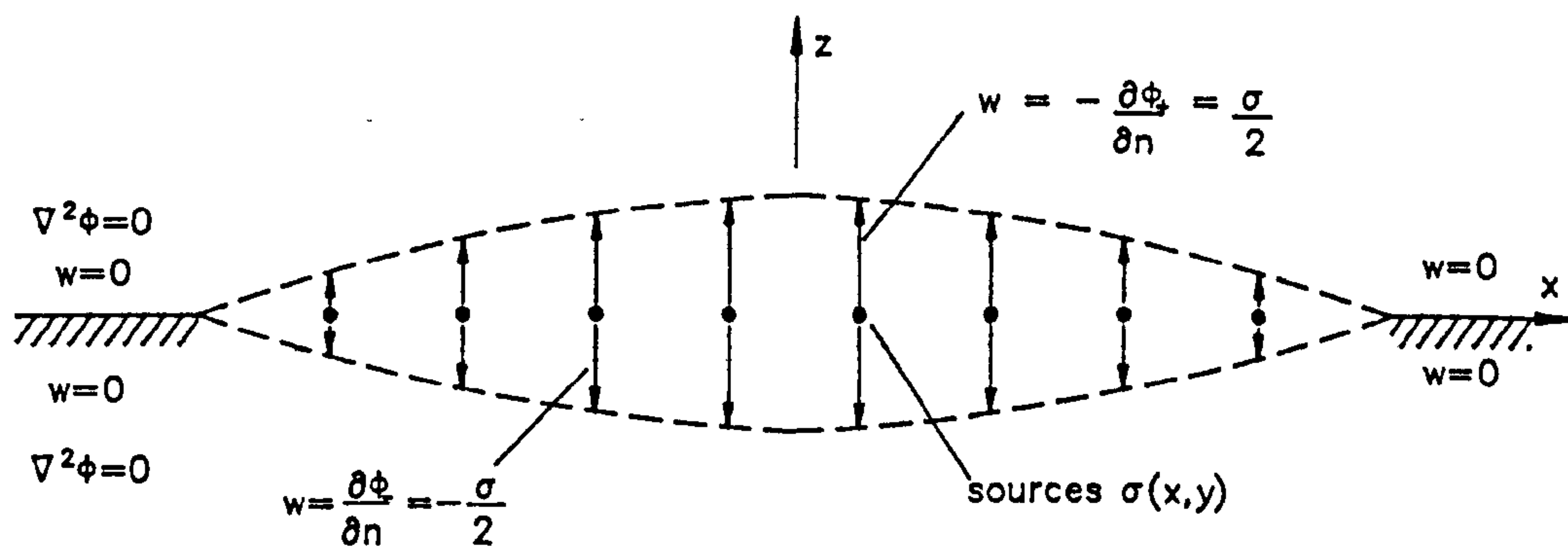




(a) Plan of dome



(b) Section



(c) Distribution of discrete sources

Figure 9.11



Using equation (9.12.7), the strength of a source at the centre of patch  $j$  can be obtained as follows

$$\omega_j = 2 \times w_{avj} \times A_j. \quad (9.13.1)$$

As in equation (9.12.5), the average potential over the area of patch  $i$  due to a source at the centre of patch  $j$  is given by

$$\begin{aligned} \phi_{avij} &= \frac{\omega_j}{4\pi A_i} \int_{x_{Si}}^{x_{Fi}} \int_{-x \tan \alpha}^{x \tan \alpha} \frac{dy}{\sqrt{(x-x_j)^2 + (y-y_j)^2}} dx \\ &= \frac{\omega_j}{4\pi A_i} \int_{x_{Si}}^{x_{Fi}} \ln \frac{|x \tan \alpha - y_j + \sqrt{(x-x_j)^2 + (x \tan \alpha - y_j)^2}|}{|-x \tan \alpha - y_j + \sqrt{(x-x_j)^2 + (x \tan \alpha + y_j)^2}|} dx \\ &= \frac{\omega_j}{A_i} C_{ij}. \end{aligned} \quad (9.13.2)$$

For a patch  $j$  within the  $AOB$  region in figure 9.11(a), equation (9.13.2) simplifies to

$$\begin{aligned} \phi_{avij} &= \frac{\omega_j}{2\pi A_i} \int_{x_{Si}}^{x_{Fi}} \ln \frac{|x \tan \alpha + \sqrt{(x-x_j)^2 + (x \tan \alpha)^2}|}{|x-x_j|} dx \\ &= \frac{\omega_j}{A_i} C_{ij}. \end{aligned} \quad (9.13.3)$$

The coordinates  $(x_j, y_j)$  at the centre of a patch which is outside the  $AOB$  region can be found from the coordinates  $(x'_j, 0)$  of the corresponding patch within the region in the following manner

$$x_j = x'_j \times \cos(k\alpha), \quad y_j = x'_j \times \sin(k\alpha)$$

in which the  $(k\alpha)$  term is as defined in figure 9.11(a).

Subsequently, the total average potential in patch  $i$  is obtained by summing the contributions from all patches, ie.

$$\phi_{avi} = \frac{1}{A_i} \sum_{j=1}^n \omega_j C_{ij} \quad (9.13.4)$$

in which  $n$  is the number of discrete sources distributed over the  $z=0$  plane. As the problem has axisymmetry, the average potentials are calculated for patches within the  $AOB$  region only (see figure 9.11(a)). The potential



coefficients  $C_{ij}$  due to patches within the COB region of the dome are approximately the same as those from the DOA region. Hence, only one set of coefficients are determined and then multiplied by two to account for both the regions mentioned. Using equations (9.12.7), (9.12.9) and (9.13.4), the kinetic energy of the surrounding air is then given by

$$T_f = 2\rho_a \sum_{i=1}^{n_s} \sum_{j=1}^n (w_{avj} A_j C_{ij}) w_{avi} \quad (9.13.5)$$

in which  $n_s$  is the number of patches in the AOB region (see figure 9.11(a)), and from equation (9.12.10), the kinetic energy of the dome is determined as follows

$$T_m = \frac{1}{2} \rho_m \sum_{i=1}^{n_s} (w_{avi})^2 A_i \quad (9.13.6)$$

in which  $\rho_m$  is the membrane mass per unit area.

#### 9.14 A generalised discrete source method

In the work by Krakowska [86] considered above, based on the assumption of a shallow pneumatic dome, a distribution of sources is prescribed over the  $z=0$  plane. As a result, the mathematics involved are much simplified with the  $z$ -dimension omitted from various equations. The above assumption however, also limits the applicability of the discrete source method to only pneumatic domes of low rise-to-span ratios.

In addition, equations (9.13.2) and (9.13.3) have been derived for the arrangement of patches shown in figure 9.11(a). In other words, the use of these equations will require the patches to be arranged in such a manner, and a restriction will thus be imposed on the idealisation of the dome to give a suitable element layout such that the nodes of the elements and patches coincide in the  $x$ - $y$  plane. As a result, there may be a limitation on the shape of the structure which can be considered. It is also inconvenient to use a mesh of patches for the average potential calculations which is separate from the element idealisation adopted for the structural analysis.

Furthermore, the use of the trapezoidal rule (or other method) to solve the integrals in equations (9.13.2) and (9.13.3) numerically means that there is a need to decide on a suitable division of the integral range which will give a reasonably accurate result, and a few trials may be required in order to establish such a level of division.

A further consideration is the calculation of the average potential over the area of a patch due to a source at the centre of the same patch (ie. for the case of  $(i=j)$  in equation (9.13.3)). For such a case, there will be rapid variations of



the integrand value in equation (9.13.3) as the position of the source is approached (ie. as  $r \rightarrow 0$ ). Consequently, very close intervals are required in the vicinity of the source in order to trace these rapid variations as will be shown later.

In this section, it is intended to generalise the discrete source method so that the limitations and difficulties mentioned above will be removed. By doing so, much more enhancement and power will be added to the method as a result. The generalised discrete source method will not be restricted in its application to a shallow pneumatic dome, but can in fact be applied to a closed membrane structure of any shape.

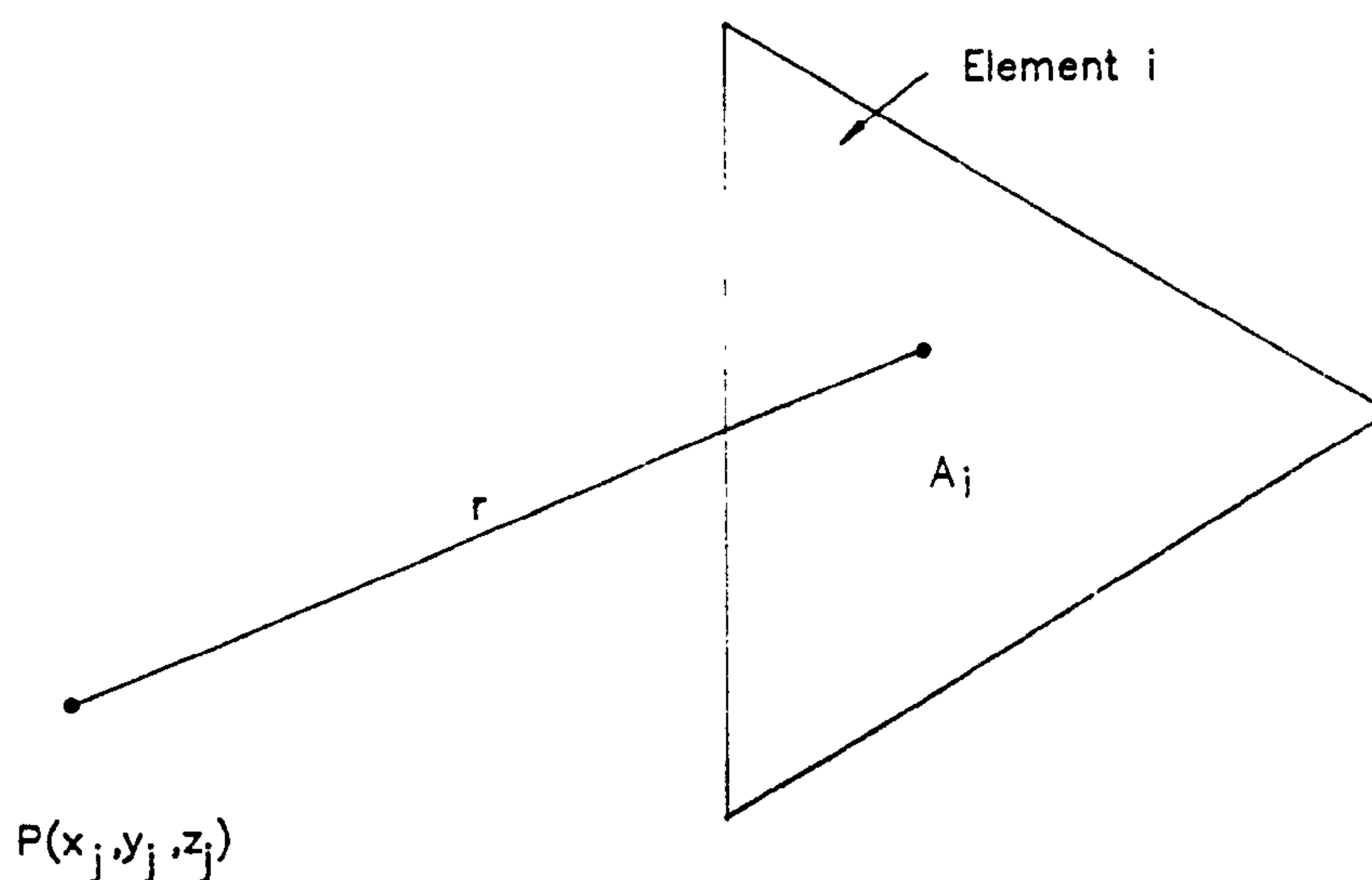


Figure 9.12

In the generalised method, the sources are placed at the centroids of the triangular elements which constitute the structural idealisation of the dome; the sources are therefore distributed over the dome instead of the  $z=0$  plane as in the case of Krakowska [86]. The centroid of a triangular element is calculated using the strategy given in figure 9.12. Although the source distribution itself has no bearing on how the dome is to be idealised into the triangular elements, the approximation of using discrete sources means that sufficiently small element sizes should be used. Furthermore, there is no need to use a separate mesh of patches to represent the dome for the average potential calculations. This is because the average potentials are calculated for the element idealisation of the dome.

It follows from equation (9.13.2) that

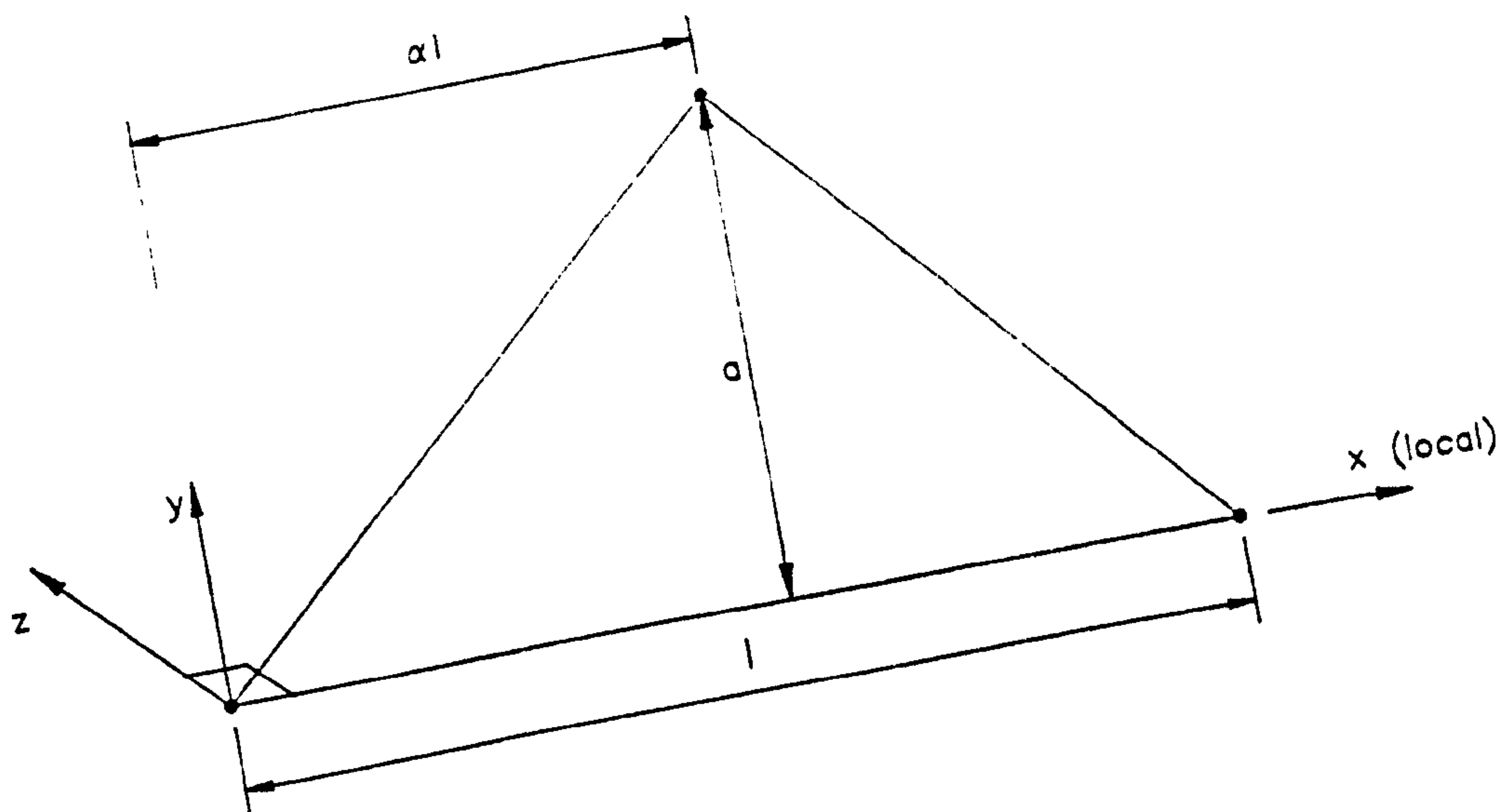
$$\phi_{avij} = \frac{1}{A_i} \frac{\omega_i}{4\pi} \iint_{A_i} \frac{dA}{r}$$



$$= \frac{\omega_i}{4\pi A_i} \Psi_{ij} \quad (9.14.1)$$

in which  $r$  is the distance from any point  $P(x_j, y_j, z_j)$  to a point within element  $i$  as shown in figure 9.13. A discrete source of strength  $\omega_i$  is placed at point  $P(x_j, y_j, z_j)$ , and this position of the source is referred to as the control point. On comparing equations (9.13.2) and (9.14.1), it can be seen that the  $\Psi_{ij}$  coefficient is related to the potential coefficient  $C_{ij}$  in the following manner

$$C_{ij} = \frac{\Psi_{ij}}{4\pi}. \quad (9.14.2)$$



$$\text{Centroid : } \bar{x} = \frac{1}{3} (\alpha l + l)$$

$$\bar{y} = \frac{a}{3}$$

Figure 9.13

The integral in equation (9.14.1) is carried out over the area  $A_i$  of triangular element  $i$  shown in figure 9.13, and the strategy here is to find an analytic solution for this integral.

A local cylindrical coordinate system is introduced with the axis parallel to the  $z$ -axis and origin at the point  $(x_j, y_j, 0)$  as shown in figure 9.14. For each element, such a coordinate system is used with the element lying in a local  $x$ - $y$  plane, ie. the normal to the element is in the direction of the local  $z$ -axis. The polar angle  $\theta$  is measured clockwise from any convenient reference direction, in this case the negative  $x$ -axis. From equation (9.14.1),



$$\Psi_{ij} = \iint_{A_i} \frac{dA}{r}. \quad (9.14.3)$$

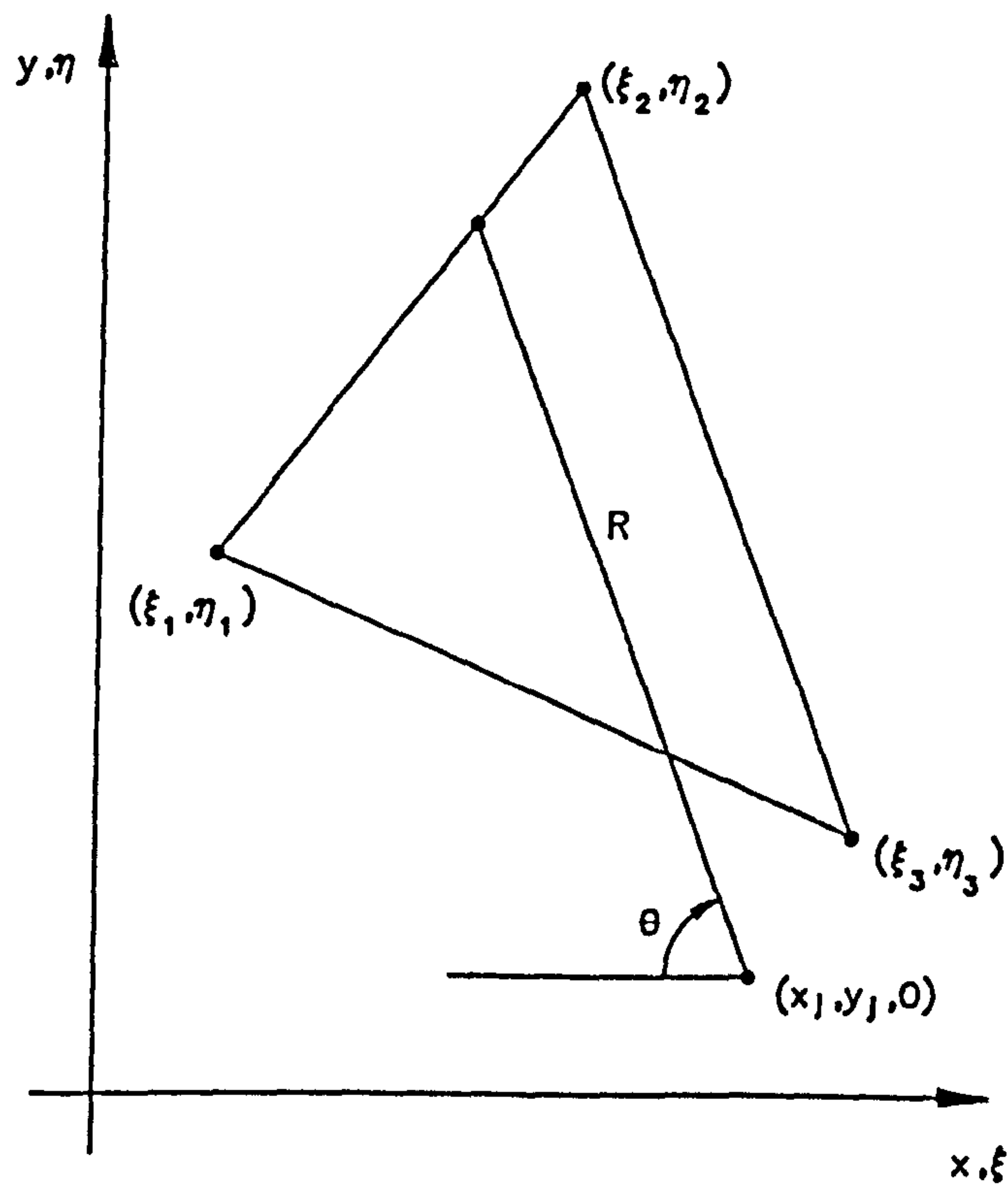


Figure 9.14

Subsequently, with  $r = \sqrt{R^2 + z^2}$  and  $dA = R dR d\theta$  (see figure 9.14), equation (9.14.3) can in turn be written as follows

$$\begin{aligned} \Psi_{ij} &= \int_0^R \int \frac{R dR d\theta}{\sqrt{R^2 + z^2}} \\ &= \int_{|z|}^r dr d\theta \\ &= \int r d\theta - |z| \Delta\theta \end{aligned} \quad (9.14.4)$$



in which the  $R$  integration is taken from  $R = 0$  to a point on the perimeter of element  $i$ , and the  $\theta$  integration is taken in the clockwise sense around the perimeter of the element.

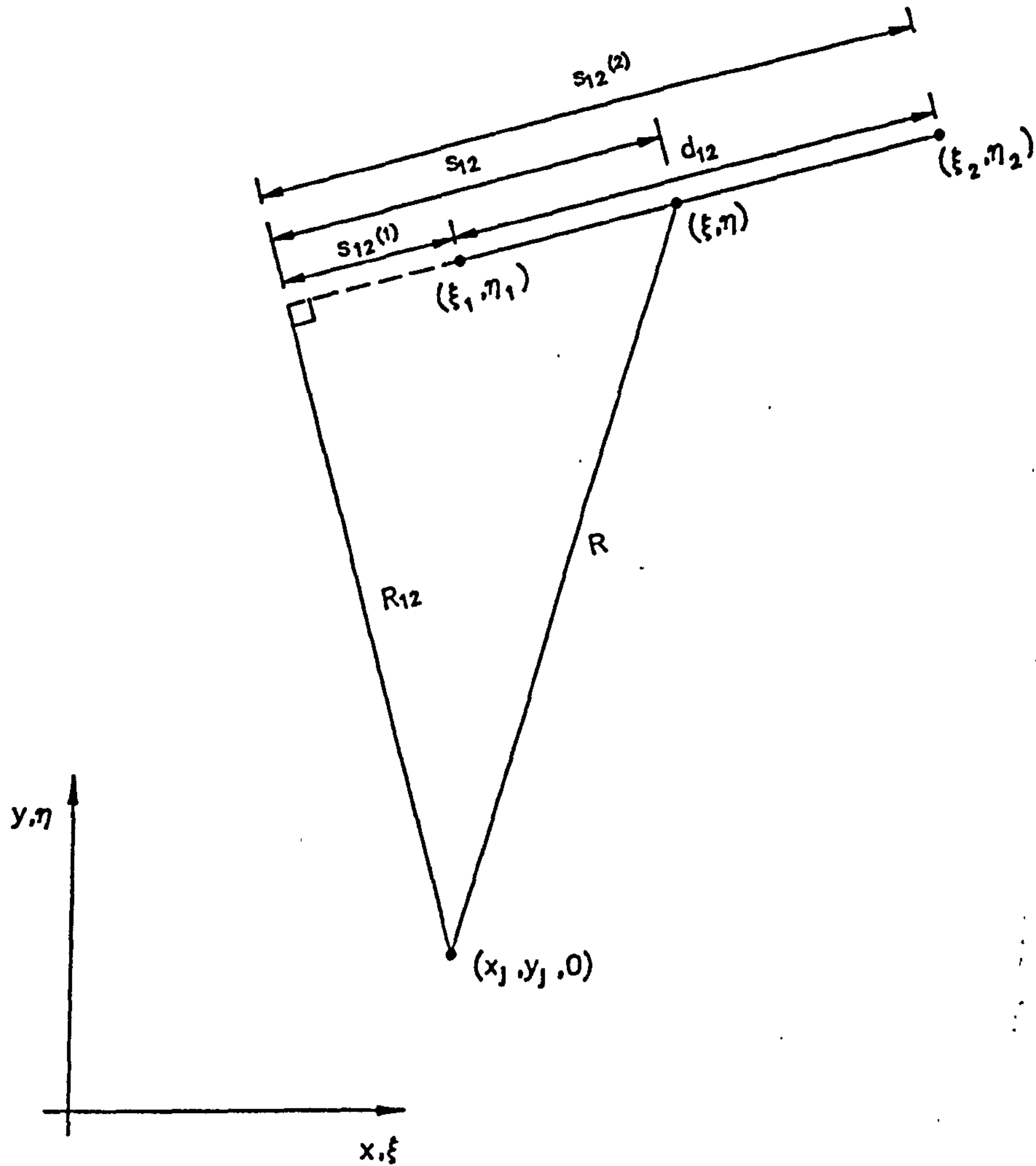


Figure 9.15

For the first term in equation (9.14.4), there is a contribution from each of the three sides of triangular element  $i$ . For instance, consider side 1 between the points  $(\xi_1, \eta_1, 0)$  and  $(\xi_2, \eta_2, 0)$  as shown in figure 9.15, and its contribution  $\varphi_{12}$  can in turn be calculated using the following formulas. From equation (9.14.4),

$$\begin{aligned}\varphi_{12} &= \int_1^2 r d\theta \\ &= R_{12} Q_{12} + |z| J_{12}\end{aligned}\tag{9.14.5}$$



in which  $Q_{12} = \ln \left( \frac{r_1 + r_2 + d_{12}}{r_1 + r_2 - d_{12}} \right),$

$$J_{12} = \tan^{-1} \left[ \frac{R_{12} |z| (r_1 s_{12}^{(2)} - r_2 s_{12}^{(1)})}{r_1 r_2 R_{12}^2 + z^2 s_{12}^{(2)} s_{12}^{(1)}} \right],$$

$$r_1 = \sqrt{(x - \xi_1)^2 + (y - \eta_1)^2 + z^2},$$

$$r_2 = \sqrt{(x - \xi_2)^2 + (y - \eta_2)^2 + z^2},$$

$$d_{12} = \sqrt{(\xi_2 - \xi_1)^2 + (\eta_2 - \eta_1)^2},$$

$$R_{12} = (x - \xi_1) S_{12} - (y - \eta_1) C_{12},$$

$$S_{12} = \frac{\eta_2 - \eta_1}{d_{12}}, \quad C_{12} = \frac{\xi_2 - \xi_1}{d_{12}},$$

$$s_{12}^{(1)} = (\xi_1 - x) C_{12} + (\eta_1 - y) S_{12},$$

$$s_{12}^{(2)} = (\xi_2 - x) C_{12} + (\eta_2 - y) S_{12}. \quad (9.14.6)$$

The terms used above in equations (9.14.5) and (9.14.6) are as shown in figure 9.15. The above equations are expressed in a compact form which may seem a bit complicated, but they are easy to use in practice. In addition, the above equations have been derived to apply in a general situation which is obviously desirable.

Similarly, the contributions from the remaining two sides of element  $i$  are evaluated. The geometric terms corresponding to the side under consideration are substituted into equations (9.14.5) and (9.14.6). From equations (9.14.4), (9.14.5) and (9.14.6), the  $\Psi_{ij}$  term in equation (9.14.1) can then be given by

$$\Psi_{ij} = \varphi_{12} + \varphi_{23} + \varphi_{31} - |z| \Delta \theta \quad (9.14.7)$$

in which  $\varphi_{12}$ ,  $\varphi_{23}$  and  $\varphi_{31}$  are the contributions from sides 1, 2 and 3 respectively of element  $i$ , and

$$\Delta \theta = 0 \quad \text{if the control point lies outside element } i, \text{ and}$$

$$\Delta \theta = 2\pi \quad \text{if the control point lies within element } i. \quad (9.14.8)$$

Using equation (9.14.7), the total potential in element  $i$  contributed by each of the discrete sources distributed over the membrane of the dome and its



imaginary mirror image, can be calculated. It is also noted that the singularity situation of the source placed at element  $i$  own control point does not cause any difficulty. Using equation (9.14.8), this situation is dealt with by simply assigning a value of  $2\pi$  to the  $\Delta\theta$  term in equation (9.14.7). In equation (9.14.6), the  $Q$  terms in are singular only on the sides of the element, and for  $z$  (local) = 0, all the  $J$  terms vanish. The above equations provide an analytic solution for the integrations involved in the average potential calculations.

The analytic solution derived above requires fewer computations than the numerical integrations considered previously. Consequently, the savings in computation time can be quite significant especially for a fine element idealisation of the membrane. By using the analytic solution, there is also no need to perform trials as required in the numerical integrations in order to establish the appropriate intervals to use. The analytic solution is also exact while the results given by numerical integrations are only approximate.

By differentiating the  $\Psi_{ij}$  term with respect to the local  $z$  coordinate, the result is

$$V_z = -\frac{\partial \Psi_{ij}}{\partial z} = \text{sgn}(z) [\Delta\theta - J_{12} - J_{23} - J_{31}] \quad (9.14.9)$$

as can be gathered from equations (9.14.5) and (9.14.7), and  $\text{sgn}(z)$  refers to the sign of the  $z$  coordinate of the control point. For the case of  $z$  (local) = 0,

$$V_z = \text{sgn}(z)\Delta\theta. \quad (9.14.10)$$

From equation (9.14.8), it follows that

$$V_z = \text{sgn}(z)2\pi \quad \text{for a control point on the element,}$$

$$\text{and} \quad V_z = 0 \quad \text{for a control point outside.} \quad (9.14.11)$$

Subsequently, the average normal velocity over element  $i$ , ie.  $w_{avi}$  due to the distribution of discrete sources over the membrane, can be found. This refers to the velocity in the direction of the local  $z$ -axis of the element, ie. normal to the plane of the element. From the potential flow theory, and equations (9.14.1), (9.14.9) and (9.14.11),

$$w_{avi} = -\frac{\partial \phi_{avi}}{\partial z} = \frac{\omega_i}{4\pi A_i} \times \left( -\frac{\partial \Psi_{ij}}{\partial z} \right) = \frac{\omega_i}{4\pi A_i} \text{sgn}(z)2\pi = \text{sgn}(z) \frac{1}{A_i} \frac{\omega_i}{2}. \quad (9.14.12)$$

For a control point defined to have  $z=0^+$ , the following relationship can be obtained from equation (9.14.12), ie.



$$\omega_i = \text{sgn}(z)(2 \times w_{avi} \times A_i) \quad (9.14.13)$$

as was derived before in an alternative manner (see equation (9.12.7)). This simple but useful relationship enables  $\omega_i$ , the strength of the source placed at the centroid of element  $i$  to be determined from the  $w_{avi}$  and  $A_i$  terms once they are known. The use of the 'sgn(z)' term in equation (9.14.13) ensures that the strength  $\omega_i$  is always positive.

The above equations automatically account for the effects of all the details of the shape of the triangular element. In other words, these equations can be applied in general to any triangular element and thus, impose no constraint on how the membrane is to be idealised into the triangular elements. In fact, these equations apply equally to an element of any polygonal shape. It is just a matter of taking the integration in equation (9.14.5) along each side of the element, and the equations adjusted to allow for the contribution from each side. For a control point which is far from the element  $i$ , the details of the shape of the element are not significant. In such an instance, an approximation may be allowed based upon the use of a multi-pole expansion. This may lead to some savings in computation time. However, it is not the intention here to explore this possibility any further. It is an area for some future work.

With the attractive features described above, the generalised method developed has widened the scope of application of the discrete source method used by Krakowska [86]. It offers a practical solution to use for the added mass calculations within the explicit dynamic analysis.

### 9.15 Comparison of $\Psi_{ij}$ coefficients calculated numerically and analytically

As an effort to clarify a few ideas discussed in the previous section, these ideas are applied to the two simple cases shown in figures 9.16 and 9.18. From equation (9.14.3),

$$\Psi_{ij} = \iint_{A_i} \frac{dA}{r} \quad (9.15.1)$$

and the task here is to calculate the  $\Psi_{ij}$  values for these two cases.

First of all, consider the case of a single triangular element shown in figure 9.16 with the element lying in the  $z=0$  plane. A discrete source is placed at the point  $P(25.0, 0.0, 0.0)$  (ie. point  $P$  is the control point). The  $\Psi_{ij}$  values are calculated in three separate ways and compared in figure 9.17. From equations (9.13.2) and (9.14.2),



$$\Psi_{ij} = \int_{x_{Si}}^{x_{Fi}} \ln \frac{|x \tan \alpha - y_j + \sqrt{(x-x_j)^2 + (x \tan \alpha - y_j)^2}|}{|-x \tan \alpha - y_j + \sqrt{(x-x_j)^2 + (x \tan \alpha + y_j)^2}|} dx. \quad (9.15.2)$$

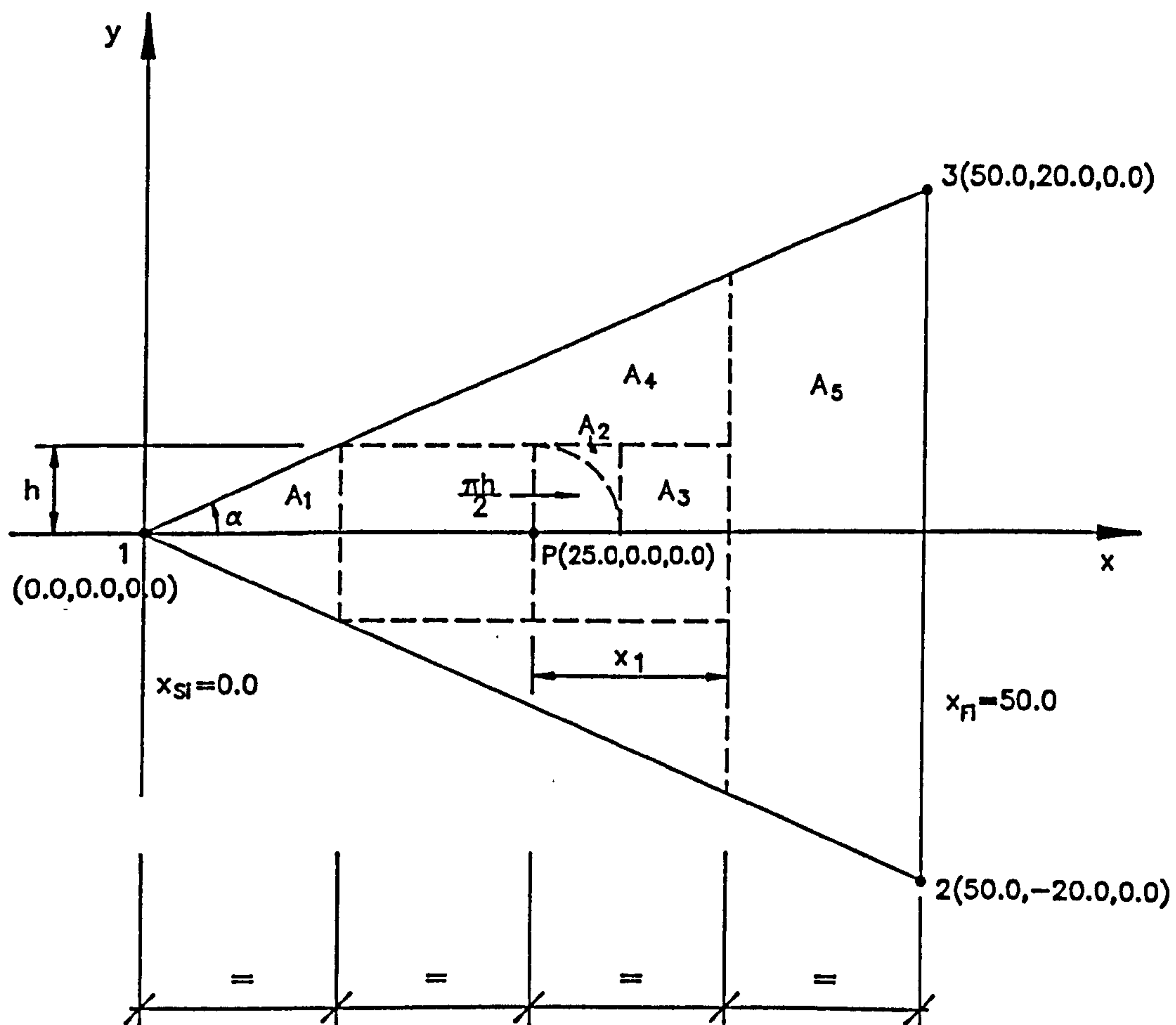


Figure 9.16

The area integral in equation (9.14.3) has now been simplified to the form given in equation (9.15.2), ie. an integral along the  $x$ -axis. The integral in equation (9.15.2) can in turn be solved numerically using the simple trapezoidal rule. This strategy is used in schemes (a) and (b) which will be described shortly, to obtain the  $\Psi_{ij}$  values tabulated in figure 9.17.

For the triangular element in figure 9.16,

$$x_j = 25.0, \quad y_j = 0.0, \quad z_j = 0.0,$$

and under consideration is the integral over the area of the element in which the source is placed (ie.  $i=j$ ) in equation (9.15.1)). Consequently, the singularity problem of ( $r \rightarrow 0$ ) (as the source is approached) will arise. In scheme (a), this singularity problem is solved by dividing the element into a



number of areas as shown in figure 9.16. A rectangular zone of  $(2x_1 \times 2h)$  is defined with its centre at the location of the discrete source, ie.  $P(25.0, 0.0, 0.0)$ . The integral in equation (9.15.2) can be evaluated over this rectangular zone in the following manner

$$\begin{aligned} \Psi_{ij}' &= 4.0 \times \int_0^{x_1 h} \int_0^h \frac{1}{\sqrt{x^2 + y^2}} dx dy \\ &= 4.0 \times \left\{ \frac{\pi h}{2} + 2h \int_{1/\sqrt{2}}^1 \ln \frac{k(1 + \sqrt{2})}{1 + \sqrt{1 - k^2}} dk + \int_0^h \ln \frac{x_1 + \sqrt{x_1^2 + y^2}}{h + \sqrt{h^2 + y^2}} dy \right\}. \end{aligned} \quad (9.15.3)$$

The first and second integrals in equation (9.15.3) correspond to the areas  $A_2$  and  $A_3$  of the element in figure 9.16. By having an analytic solution for a small circular region enclosing the discrete source, no singularity problem will then arise for the integral over the remainder area of the element. The integrals in equation (9.15.3) can in turn be solved numerically using the trapezoidal rule. The same applies to the integral in equation (9.15.2) for the areas  $A_1$ ,  $A_4$  and  $A_5$  of the element in figure 9.16. The total contributions from the areas  $A_1$ ,  $A_4$  and  $A_5$  are then multiplied by two to account for the similar areas in the other half of the element. For each of the numerical integrations in scheme (a), the integral range is divided into 12 equal intervals (ie.  $n = 12$  as indicated in figure 9.17). The main purpose of setting up scheme (a) is to highlight the difficulty of using scheme (b) to calculate the  $\Psi_{ij}$  value in the case of the element shown in figure 9.16.

For scheme (b) however, the integral in equation (9.15.2) is solved numerically using the trapezoidal rule over the entire area of the element in figure 9.16. The  $\Psi_{ij}$  values obtained from various divisions of the integral range, ie.  $n = 12, 100, 1000$  and  $5000$  are tabulated in figure 9.17. In addition, scheme (b) is used for the average potential calculations in the work by Krakowska [86].

For scheme (c), the  $\Psi_{ij}$  value is obtained by solving equation (9.15.1) analytically using the corresponding equations given in section 9.14. In scheme (c), there is no need for any special consideration to cope with the singularity problem which is dealt with automatically without any difficulty. In addition, scheme (c) is used for the average potential calculations in the generalised method.

From the results in figure 9.17, it can be seen that scheme (a) gives a  $\Psi_{ij}$  value close to that given by scheme (c), using a much smaller number of intervals compared with scheme (b). This is because a large number of intervals is



needed in scheme (b) in order to account for the rapid variations in the integral values corresponding to the intervals close to and around point  $P$ . The use of an analytic solution in scheme (a) for a small circular region around point  $P$  avoids the need to use a large number of intervals. This also means that scheme (b) involves much more computational effort than scheme (a). Apart from requiring the least computational effort, the  $\Psi_{ij}$  value given by scheme (c) is exact while those values given by schemes (a) and (b) are only approximate.

It is noted that schemes (a) and (b) are applicable only to two-dimensional situations in which all the quantities involved in the calculations for the  $\Psi_{ij}$  values, are in the same plane such as the  $z=0$  plane for the cases shown in figures 9.16 and 9.18, and the shallow dome considered earlier. On the other hand, scheme (c) imposes no such constraint and can therefore be applied to three-dimensional situations; by using scheme (c) in the generalised source method, the sources are allowed to be distributed over the membrane instead of the  $z=0$  plane.

	(a)	(b)				(c)
	$n = 12$	$n = 12$	$n = 100$	$n = 1000$	$n = 5000$	
$\Psi_{ij}$	102.6978	802.0112	184.4845	110.6271	104.2334	102.6761

Figure 9.17

With the discrete source placed at the point  $P(50.0/3, 0.0, 0.0)$  (ie. centroid of the triangular element shown in figure 9.16), scheme (c) gives a  $\Psi_{ij}$  value of 89.5619.

Subsequently, schemes (b) and (c) are used to obtain the  $\Psi_{ij}$  values (tabulated in figure 9.19) for the quadrilateral element shown in figure 9.18. In this case, the discrete source is placed at the point  $P(25.0, 0.0, 0.0)$  which is outside the element (ie. the case of  $(i \neq j)$  in equation (9.15.1)) and thus, scheme (a) is not applicable here. This is because no singularity problem will be encountered in integrating numerically over the area of the quadrilateral element. For scheme (b), only the case of the quadrilateral element is considered. For scheme (c) however, two cases (ie. (i) and (ii)) are considered; case (i) is based on the quadrilateral element and case (ii) is based on the two triangular elements into which the quadrilateral element can be divided as shown in figure 9.18. For case (ii), the  $\Psi_{ij}$  value tabulated in figure 9.19 is given by the sum of the contributions from the areas  $A_1$  and  $A_2$  shown in figure 9.18. From the results in figure 9.19, it can be seen that scheme (b) requires a much



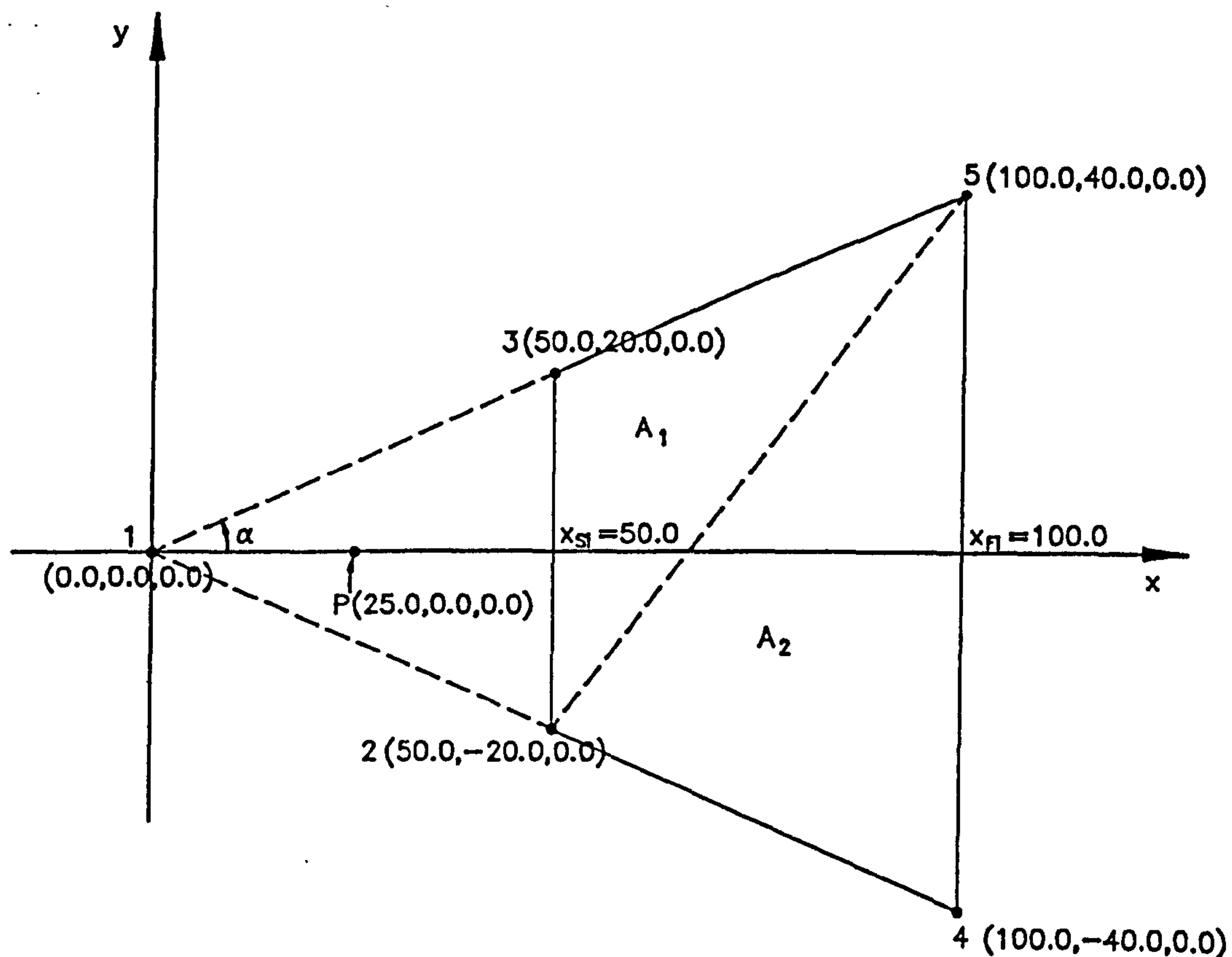


Figure 9.18

smaller number of intervals compared with the previous case shown in figure 9.16, in order to obtain a  $\Psi_{ij}$  value sufficiently close to that given by scheme (c). This is as expected because the numerical integrations involved in this case do not have to cope with any singularity problem. In the calculations for the  $\Psi_{ij}$  values, fewer computations are involved in scheme (c) than in scheme (b).

	(b)			(c)	
	$n = 12$	$n = 100$	$n = 1000$	(i)	(ii)
$\Psi_{ij}$	58.50148	58.47040	58.46999	58.46997	58.46999

Figure 9.19

The use of scheme (c) to calculate the  $\Psi_{ij}$  values for cases (i) and (ii) gives an indication of the general nature of the scheme in terms of its ability to be



applied easily to both triangular and quadrilateral elements. In fact, scheme (c) can be easily applied to an element of any polygonal shape.

It is clear from the above discussion that scheme (c) has a few advantages which make it well suited for the task of calculating the  $\Psi_{ij}$  coefficients, and this scheme is therefore chosen to be implemented into the generalised source method.

### 9.16 The shallow pneumatic dome and its imaginary mirror image

The shallow pneumatic dome shown in figure 9.11 has a boundary condition of zero normal velocity of the air across the rigid base (in the  $z=0$  plane) of the dome. This boundary condition is satisfied by reflecting the dome about the base to give an imaginary mirror image. A source distribution similar to that over the dome is prescribed over the surface of the imaginary mirror image as shown in figure 9.20. This is achieved by first calculating the control points for the source distribution over the dome. By taking these control points with the  $z$  coordinates given their negative values, the control points for the source distribution over the imaginary image will then be obtained. The air velocities normal to the  $z=0$  plane due to the source distribution over the dome will be equal and opposite to those air velocities due to the source distribution over the imaginary image. As a result, the effect of zero normal velocity of the air across the rigid base of the dome will be achieved.

The source distributions over the dome and its imaginary image are then used to calculate for the total kinetic energy of the air on both sides of the dome which is given by equation (9.11.1). For ease of reference, equation (9.11.1) is written here again

$$T_f = -\frac{1}{2}\rho \int_{\Gamma} \phi \frac{\partial \phi}{\partial n} d\Gamma. \quad (9.16.1)$$

Using equation (9.12.9), equation (9.16.1) can then be approximated as follows

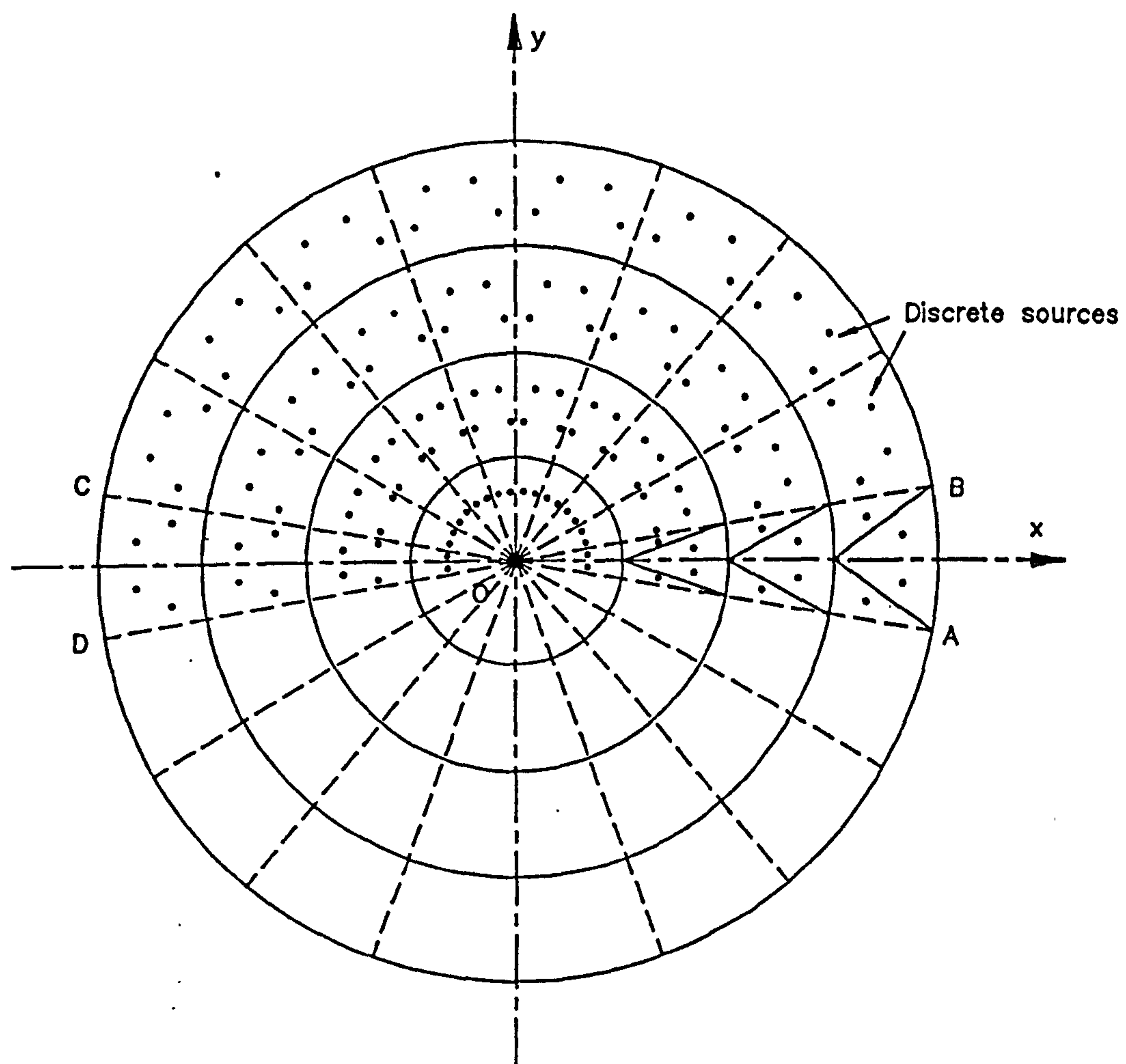
$$T_f = \frac{1}{2}\rho_a \sum_{i=1}^{n_s} (\phi_{avi})(w_{avi})(A_i). \quad (9.16.2)$$

in which  $n_s$  is the number of elements in the structural idealisation of the dome.

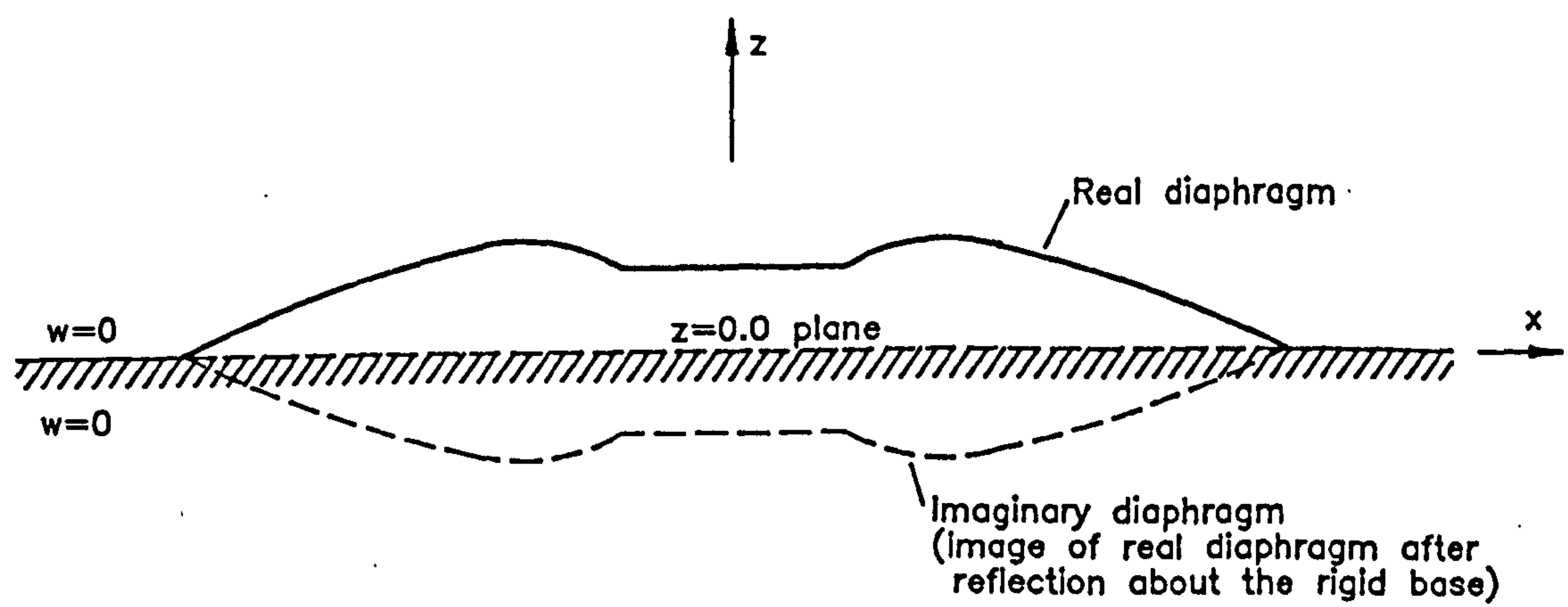
Using equations (9.13.4) and (9.14.13), equation (9.16.2) can in turn be written as follows

$$T_f = \rho_a \left\{ \sum_{i=1}^{n_s} \left\{ \sum_{j=1}^n (\text{sgn}(z)w_{avj})(A_j)(C_{ij}) \right\} (w_{avi}) \right\} \quad (9.16.3)$$





(a) Plan of dome



(b) Section

Figure 9.20



in which  $n$  is the number of discrete sources distributed over the dome and its imaginary image. From equation (9.13.6), the kinetic energy of the dome is then determined as follows

$$T_m = \frac{1}{2} \rho_m \left\{ \sum_{i=1}^{n_s} (w_{avi})^2 (A_i) \right\}. \quad (9.16.4)$$

Using equation (9.11.4), the added mass coefficient  $\Lambda_{am}$  can subsequently be established.

As discussed in section 9.13, a distribution of sources is used over the  $z=0$  plane in the work by Krakowska [86] (see figure 9.11). As such a source distribution gives rise to air velocities normal to the  $z=0$  plane (and with no corresponding equal and opposite air velocities), the boundary condition of zero normal velocity of the air across the rigid base of the dome will be not satisfied.

### 9.17 Explicit dynamic analysis with added mass calculations

A procedure of incorporating the added mass calculations into the explicit numerical scheme for the dynamic analysis, is described below. It is intended to achieve this with the least and yet simple changes to the scheme bearing in mind to preserve the existing advantages of the scheme.

The basic strategy is to introduce an additional step of calculating the added mass coefficient  $\Lambda_{am}$  (see equation (9.11.4)) at each time step. Assuming that the added mass effects are uniform over the membrane of the dome, the added mass of the attached air is then distributed to each node in the following manner

$$m_t = m_n (1 + \Lambda_{am}) \quad (9.17.1)$$

in which  $m_n$  and  $m_t$  are the nodal mass due to the membrane and the total nodal mass respectively.

If there are no added mass calculations in the dynamic analysis, the nodal masses due to the membrane are computed based on the starting geometry, and these values are then used throughout the analysis. With the added mass taken into account however, the nodal masses have to be calculated at each time step including the added mass of the attached air by means of the  $\Lambda_{am}$  coefficient.

Subsequently, the nodal velocities in the explicit numerical scheme are updated according to the following recurrence equation (see equation (3.3.6) given in chapter 3)



$$V_{ix}^{t+\Delta t/2} = V_{ix}^{t-\Delta t/2} + \frac{\Delta t}{M_i} R_{ix}^t. \quad (9.17.2)$$

For the added mass calculations at each time step, a further consideration as described below is needed. This involves expressing the Newton's second law in a vector form relating the impulse due to the internal and external forces,  $R$  to the resulting change of linear momentum (ie. mass  $m \times$  velocity  $V$ ) of the system as follows

$$R dt = d(mV). \quad (9.17.3)$$

Equation (9.17.3) can in turn be expressed in the central finite difference form, and for any node  $i$  in direction  $x$  at time  $t$ , the result is as follows

$$\Delta t R_{ix}^t = m_i^{t+\Delta t/2} V_{ix}^{t+\Delta t/2} - m_i^{t-\Delta t/2} V_{ix}^{t-\Delta t/2}. \quad (9.17.4)$$

On rearranging equation (9.17.4), the following recurrence equation for the nodal velocities is obtained, ie.

$$V_{ix}^{t+\Delta t/2} = \frac{\Delta t R_{ix}^t + m_i^{t-\Delta t/2} V_{ix}^{t-\Delta t/2}}{m_i^{t+\Delta t/2}}. \quad (9.17.5)$$

In the explicit numerical scheme, the nodal velocities are calculated at the middle of each time step, and the coordinates and forces at the end/start of time steps. After calculating the nodal velocity  $V_{ix}^{t-\Delta t/2}$  at time  $(t - \Delta t)$ , the added mass coefficient  $A_{am}$  and hence, the nodal mass  $m_i^{t-\Delta t/2}$  (taken to be the same in the  $x$ -,  $y$ - and  $z$ -directions) can then be determined. In order to find the nodal velocity at the next time step,  $V_{ix}^{t+\Delta t/2}$  using equation (9.17.2), an initial approximation of  $m_i^{t+\Delta t/2} = m_i^{t-\Delta t/2}$  is made. With the velocity  $V_{ix}^{t+\Delta t/2}$  known, the mass  $m_i^{t+\Delta t/2}$  can in turn be determined. Subsequently, the above steps can be repeated to produce further velocities and masses. However, this procedure leads to a change in mass from  $m_i^{t-\Delta t/2}$  to  $m_i^{t+\Delta t/2}$  at time  $(t + \Delta t/2)$ . Hence, this suggests a jump in the value of the linear momentum at time  $(t + \Delta t/2)$ , ie.

$$m_i^{t-\Delta t/2} V_{ix}^{t+\Delta t/2} \Rightarrow m_i^{t+\Delta t/2} V_{ix}^{t+\Delta t/2}.$$

As a result, errors will begin to accumulate. A strategy is thus needed to avoid the problem of discontinuity in linear momentum.

A procedure of dealing with the above problem is outlined as follows

- (1) At the end of the time step  $t \rightarrow t + \Delta t$ , the forces  $R_{ix}^t$ , masses  $m_i^{t-\Delta t/2}$ ,



velocities  $V_{ix}^{t+\Delta t/2}$  and coordinates  $x_i^{t+\Delta t}$  are determined.

(2) With the above information, the masses  $m_i^{t+\Delta t/2}$  can then be found.

(3) This is followed by the resetting of the coordinates  $x_i^t$  (see equation (3.3.8) given in chapter 3) and velocities  $V_{ix}^{t+\Delta t/2}$  (see equation (9.17.2)) as follows

$$x_i^t = x_i^{t+\Delta t} - \Delta t V_{ix}^{t+\Delta t/2},$$

$$V_{ix}^{t-\Delta t/2} = V_{ix}^{t+\Delta t/2} - \frac{\Delta t}{m_i^{t-\Delta t/2}} R_{ix}^t.$$

(4) The velocities  $V_{ix}^{t+\Delta t/2}$  are then calculated using equation (9.17.5), and the coordinates  $x_i^{t+\Delta t}$  and forces  $R_{ix}^{t+\Delta t}$  in turn obtained.

(5) Assuming that  $m_i^{t+3\Delta t/2} = m_i^{t+\Delta t/2}$ , the velocities  $V_{ix}^{t+3\Delta t/2}$  can subsequently be found and the whole cycle repeated.

A small discrepancy in the above strategy arises from the fact that the masses  $m_i^{t+\Delta t/2}$  are calculated from the velocities  $V_{ix}^{t+\Delta t/2}$  found in step (1).

However, the actual velocities in the subsequent analysis are determined from step (4). Hence, the procedure, where necessary, may be further improved by iterating the above steps until the values of  $m_i^{t+\Delta t/2}$  between successive iterations differ to within a specified tolerance.

The added mass calculations based on the considerations discussed above, will only require a relatively small amount of computations and solution time. As a result, this offers a practical means of modelling the added mass effects in the dynamic response unlike the approach proposed by Barnes [19] which involves the discretisation of the surrounding air into elements. The added mass calculations can be implemented with relative ease involving only few and simple changes to the basic numerical scheme. The is also the case when incorporating the procedures to account for the creep effects and on/off buckling, into the explicit dynamic analysis. In this way, the essential simplicity and efficiency of the basic numerical scheme are retained.

In summary, the added mass calculations are incorporated into the dynamic analysis by the inclusion of the following additional steps:

(1) determine the control points and potential coefficients  $C_{ij}$  (these values are then taken to apply throughout the dynamic analysis);



(2) in the main loop:

- (a) calculate the fluid and membrane kinetic energies, and then the added mass coefficients, and finally the total nodal masses;
- (b) implement the procedure outlined above for dealing with the problem of discontinuity in linear momentum.

The explicit numerical scheme implemented with the various procedures to account for the creep effects, on/off buckling, added mass effects and so on, is applied to the dynamic analysis of a pneumatic dome and the results from the analysis are discussed in the following section.

### 9.18 Numerical examples and discussions

The shallow pneumatic dome already mentioned above and used by Krakowska [86] in her investigations, is chosen as the test problem to be solved by the explicit numerical scheme developed in this chapter for the dynamic analysis. The results obtained from both experiments and dynamic analysis by Krakowska [86] are compared with those given by the dynamic analysis carried out here. This dome as shown in figure 9.20 has a diameter of 4.74 m at its base and is constructed from a light, isotropic polythene material of 0.06 mm thick.

The test problem includes various stages which can be briefly described as follows. First, an initially flat and uniformly prestressed dome is being inflated to a desired shape. This is the form-finding stage of the analysis. It is important to achieve an inflated dome which is as close as possible to the form produced by Krakowska [86]. Subsequently, the inflated dome is loaded in two ways, ie. centrally and asymmetrically. In the experiment, the loading was carried out by placing the applied load on a circular platen of 0.58 m diameter which was then lowered onto the inflated dome. Under the applied loads, the dome undergoes deformations until it reaches a stable and static state. The deformed geometry and resulting membrane stresses of the dome from the load analysis provide the initial conditions for the dynamic analysis to follow. In this case, under investigation is the dynamic response of the dome initiated by the sudden removal of the applied loads. This situation may be taken as one of no or zero wind since it is desirable to keep the problem as simple as possible. In a real situation however, a likely cause of the dynamic response of the pneumatic dome comes from the action of a fluctuating wind. As mentioned previously, a complete description of a fluctuating wind load can be highly complex or may even be impossible. The main objective here is to find a practical numerical approach which can give a reasonable prediction of the dynamic response of the dome accounting purely for the effects of creep, on/off buckling, internal air stiffening and added mass. After having achieved this, the problem of dynamic response induced by a fluctuating wind load can in turn be investigated. During the form-finding and static loaded state, the internal pressures of the dome are assumed to be



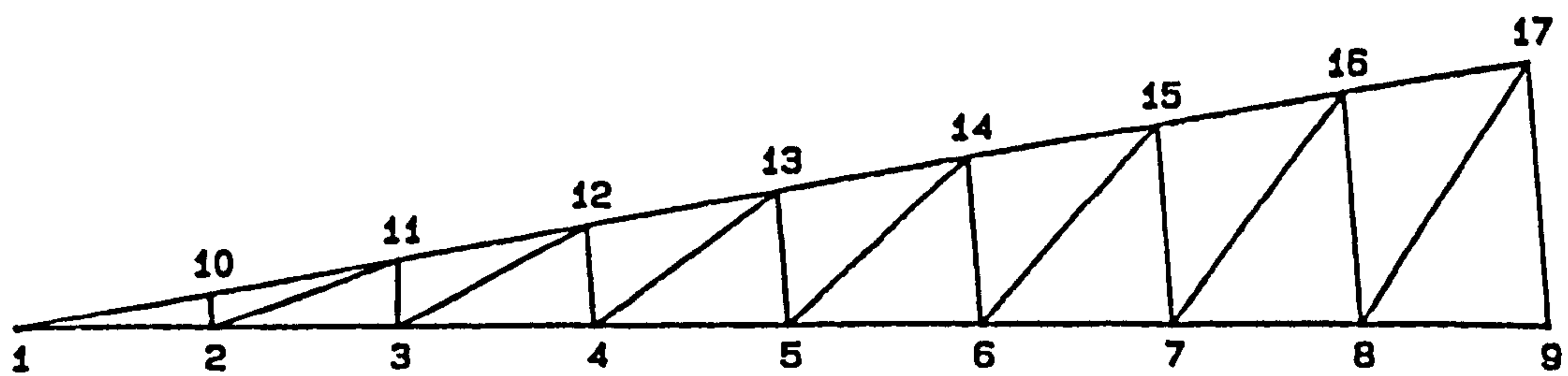
maintained at values obtained from the experiments conducted by Krakowska [86].

The membrane of the dome is discretised into a mesh of constant strain triangular elements as shown in figure 9.21. There is no division of the surrounding air into elements. It is convenient to use the same triangular elements for both the structural modelling and added mass calculations. This helps to simplify the organisation of the computer program. Subsequently, a sensible strategy is to place a discrete source at the centroid of each triangular element on the membrane (see figure 9.20(a)). An alternative strategy may be to have a discrete source assigned to the centroid of each trapezoidal panel derived from combining two triangular elements together (see figure 9.11(a)). But although this may lead to fewer computations, the resulting solution will be less accurate due to the fewer number of discrete sources distributed over the membrane. An additional effort would also be required within the computer program to deal with information related to the trapezoidal elements. Consequently, the source distribution adopted above, ie. with a discrete source at the centroid of each triangular element is a better choice. In addition, the discrete sources are distributed over the membrane and its image (see figure 9.20(b)) instead of the  $z=0$  plane as in the numerical analysis by Krakowska [86].

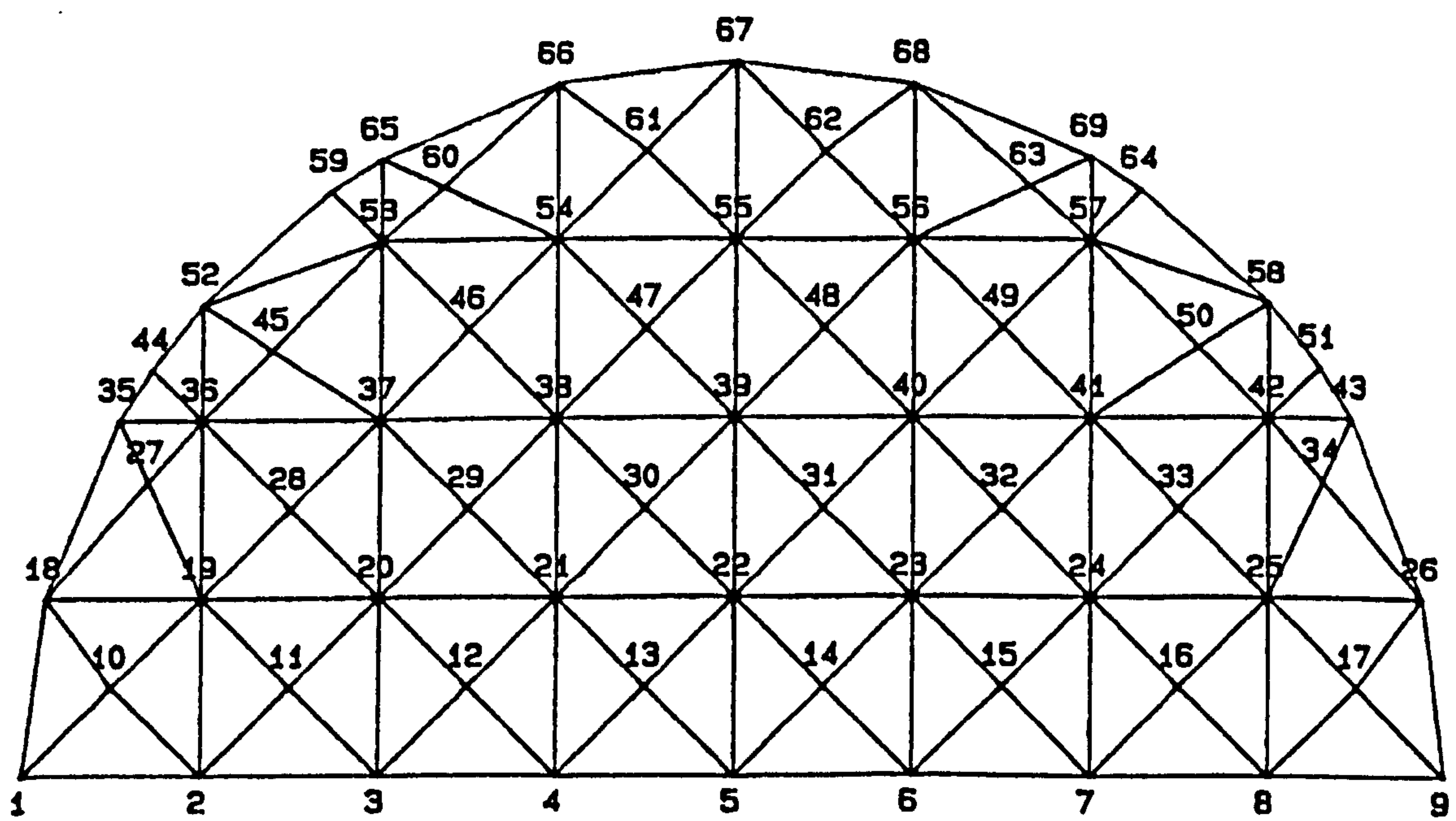
In the case of the centrally loaded dome, ie. load applied to the crown of the dome, it is noted that there is axisymmetry in terms of both geometry and loading. Consequently, the problem size can be reduced by considering only a slice of the dome with the appropriate boundary conditions prescribed along the two axes of symmetries. A slice with a  $10^\circ$  included angle (ie. region AOB in figure 9.20(a)) is the choice for the subsequent analysis. This slice is discretised into a mesh of elements. A sufficiently fine mesh is used in order that a reasonably accurate modelling will be achieved. However, this in turn means that a small time step has to be used in the explicit dynamic analysis as required when the element size is small. The  $10^\circ$  slice is divided uniformly in the radial direction into 15 triangular elements as shown in figure 9.21(a). For estimation of the added mass effects, the influence of each of the discrete sources distributed over the entire membrane and its image on the average potential within the  $10^\circ$  slice is calculated. However, the calculation of the kinetic energy ratio (ie.  $\Lambda_{am}$ ) is required for this slice only. On the other hand, for the asymmetrically loaded dome, half of the dome has to be considered instead as shown in figure 9.21(b), ie. having only one axis of symmetry in this case.

For the form-finding stage, a uniform prestress of  $37 \text{ Nm}^{-1}$  is assigned to the initially flat membrane and then an inflation pressure of  $15.4 \text{ Nm}^{-2}$  is applied to raise the dome to the desired shape. During the form-finding, the membrane elements undergo gross changes in geometries from their initial flat states. It is therefore necessary to reset the element stiffness matrices at frequent intervals during the form-finding. At the same time, there is a need to update the normal pressure vectors to account for the current geometry of the dome.





(a) Centrally applied load



(b) Asymmetrically applied load

Figure 9.21 Idealisations of dome



After the dome has achieved an equilibrium shape during the form-finding, a comparison is made with the inflated dome geometries obtained by Krakowska [86] from experiment and numerical analysis. This is based on the values of the  $z$  coordinate at a few selected nodes on the inflated dome as tabulated in figure 9.23. In this case, the  $z$  coordinate at a node indicates the vertical height of the node above the base plane of the dome. As given in figure 9.23, the values obtained here agree very closely with those determined by Krakowska [86]. Hence, this inflated dome can then be used for the subsequent static load analysis.

### 9.18.1 Static load analysis

The following stage is the analysis of the inflated dome for a static load case. The elastic properties of the membrane material used in the static load analysis are as follows

$$E = 5260 \text{ Nm}^{-1}, \quad \nu = 0.52$$

in which  $E$  and  $\nu$  are the elastic modulus and Poisson's ratio respectively. These values are taken from the tests carried out on the membrane material by Krakowska [86]. The membrane material is isotropic, ie. has the same elastic properties in both the warp and fill directions.

#### 9.18.1.1 Centrally applied load

In the experiment by Krakowska [86], the load was applied by means of a platten to the crown of the inflated dome. Hence, for the numerical load analysis, all the nodes at the crown of the dome should show the same vertical deflection. In order to achieve this, the idealisation of the dome for this load case as shown in figure 9.21(a) is such that the platten load  $P_a$  of 80 N is represented in the analysis by the following equivalent vertical loads applied at nodes 1, 2 and 10 [86]:

$$P_1 = 0.00084 \times P_a,$$

$$P_2 = 0.0136 \times P_a,$$

$$P_{10} = 0.0133 \times P_a.$$

During the load analysis, the internal pressure of the dome is kept at  $28 \text{ Nm}^{-2}$ . In the experiment, this internal pressure was maintained in the dome by means of a high pressure air pump.

Under the above applied nodal loads and internal pressure, the inflated dome derived earlier deforms to a new equilibrium geometry (see figure 9.22(a)). The results at nodes 3, 5 and 6 of the dome (see figure 9.21(a)) in the



prestressed and static loaded states are obtained for comparison with those determined by Krakowska [86] in figure 9.23(a). Under comparison are the values of the z coordinate and vertical deflection from the initial inflated state of the dome.

#### 9.18.1.2 Asymmetrically applied load

For the asymmetrically loaded dome, half of the dome as shown in figure 9.21(b) has to be considered. In this case, the idealisation of the dome is such that the platten load  $P_a$  of 80 N is represented in the analysis by the following vertical loads applied at nodes 6, 7 and 15 in figure 9.21(b):

$$P_6 = 0.0633 \times P_a,$$

$$P_7 = 0.1984 \times P_a,$$

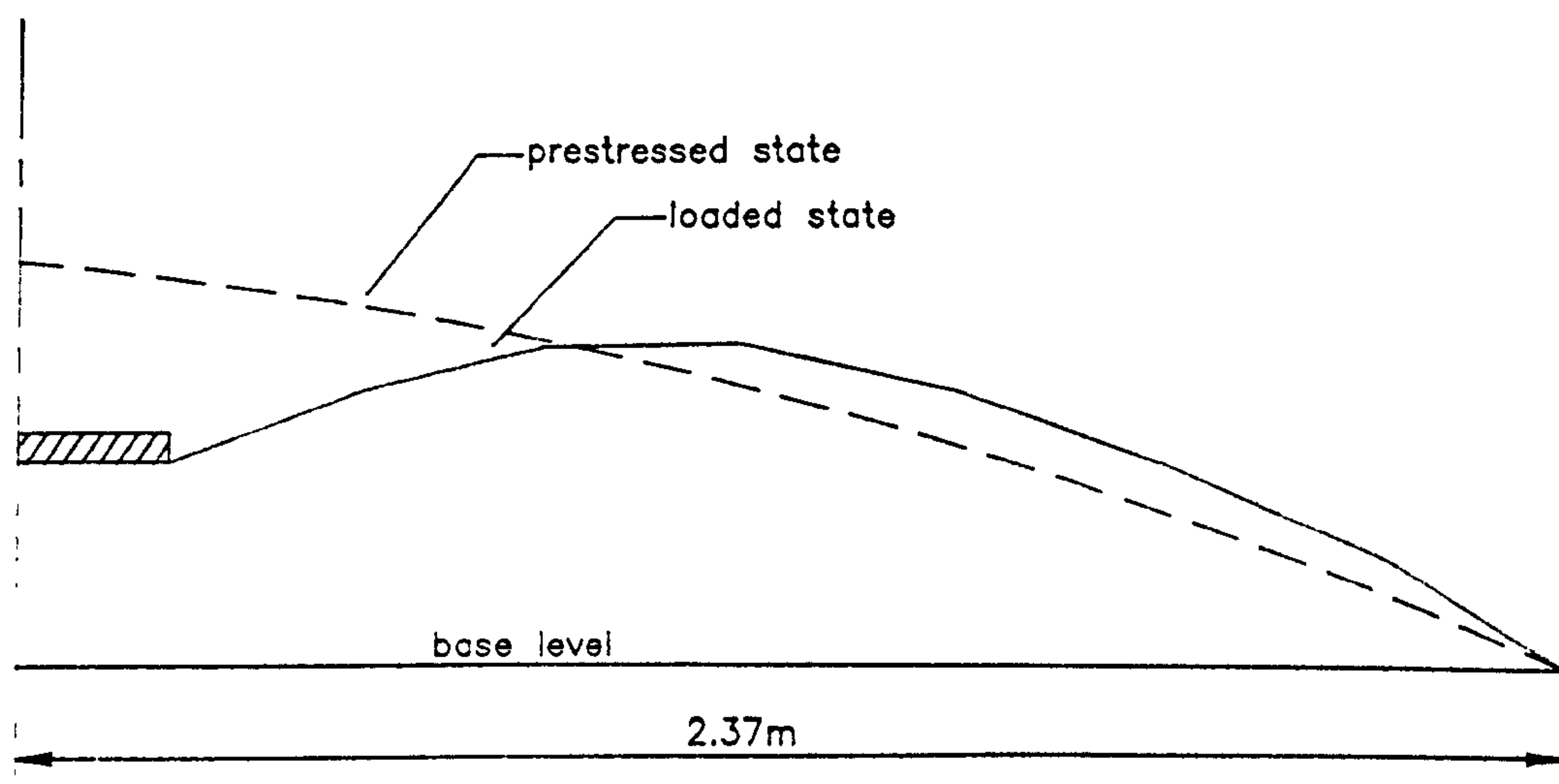
$$P_{15} = 0.2383 \times P_a.$$

The internal pressure of the dome during the load analysis is kept at 26 Nm<sup>-2</sup>.

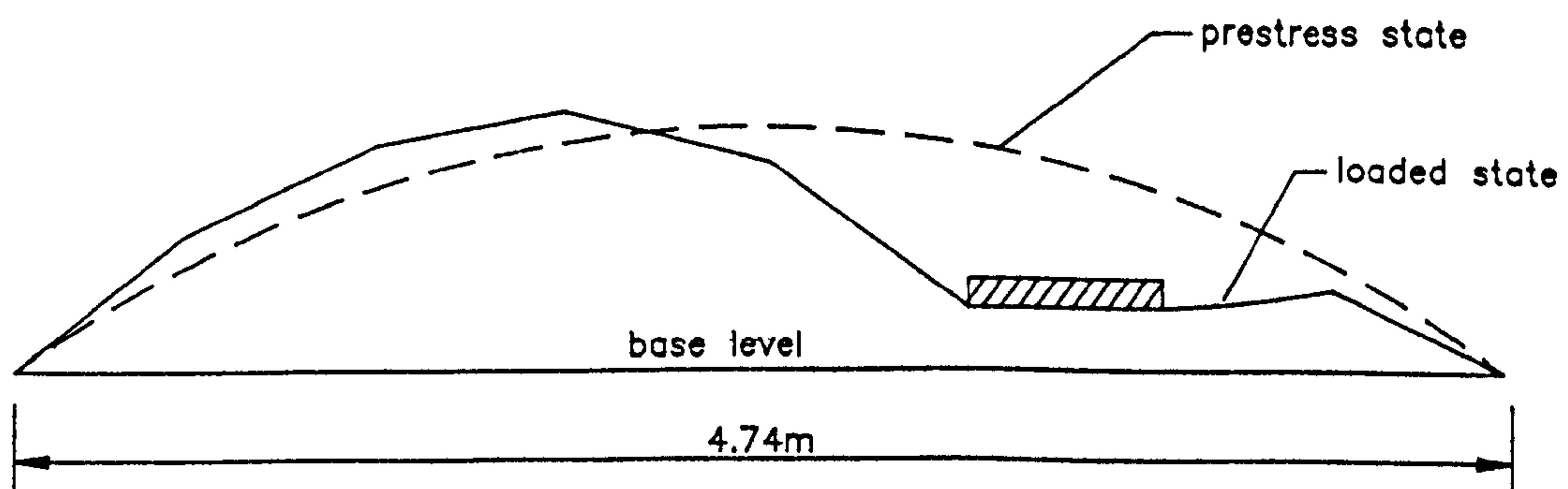
The deformed geometry of the asymmetrically loaded dome is shown in figure 9.22(b). In this case, the results at nodes 20, 21 and 29 of the dome (see figure 9.21(b)) in the prestressed and static loaded states are obtained for comparison with those determined by Krakowska [86] in figure 9.23(b).

In both cases of the centrally and asymmetrically applied loads, there is good agreement between the values obtained here and those determined by Krakowska [86]. The resulting membrane stress states from the load analysis here are also compared in figure 9.24 with the corresponding values obtained by Krakowska [86] and there are again very close agreements between the results. The current geometry and corresponding stress state of the loaded dome are then taken as the starting basis for the explicit dynamic analysis which follows.





(a) Centrally applied load



(b) Asymmetrically applied load

Figure 9.22 Static deflections of dome



Node Number	Inflated Dome			Loaded Dome			Deflection		
	(i)	(ii)	(iii)	(i)	(ii)	(iii)	(i)	(ii)	(iii)
3	0.217	0.214	0.214	0.172	0.172	0.177	-0.045	-0.042	-0.037
5	0.173	0.173	0.173	0.183	0.185	0.187	0.010	0.012	0.014
6	0.140	0.142	0.142	0.159	0.162	0.163	0.019	0.020	0.021

(a) Centrally applied load

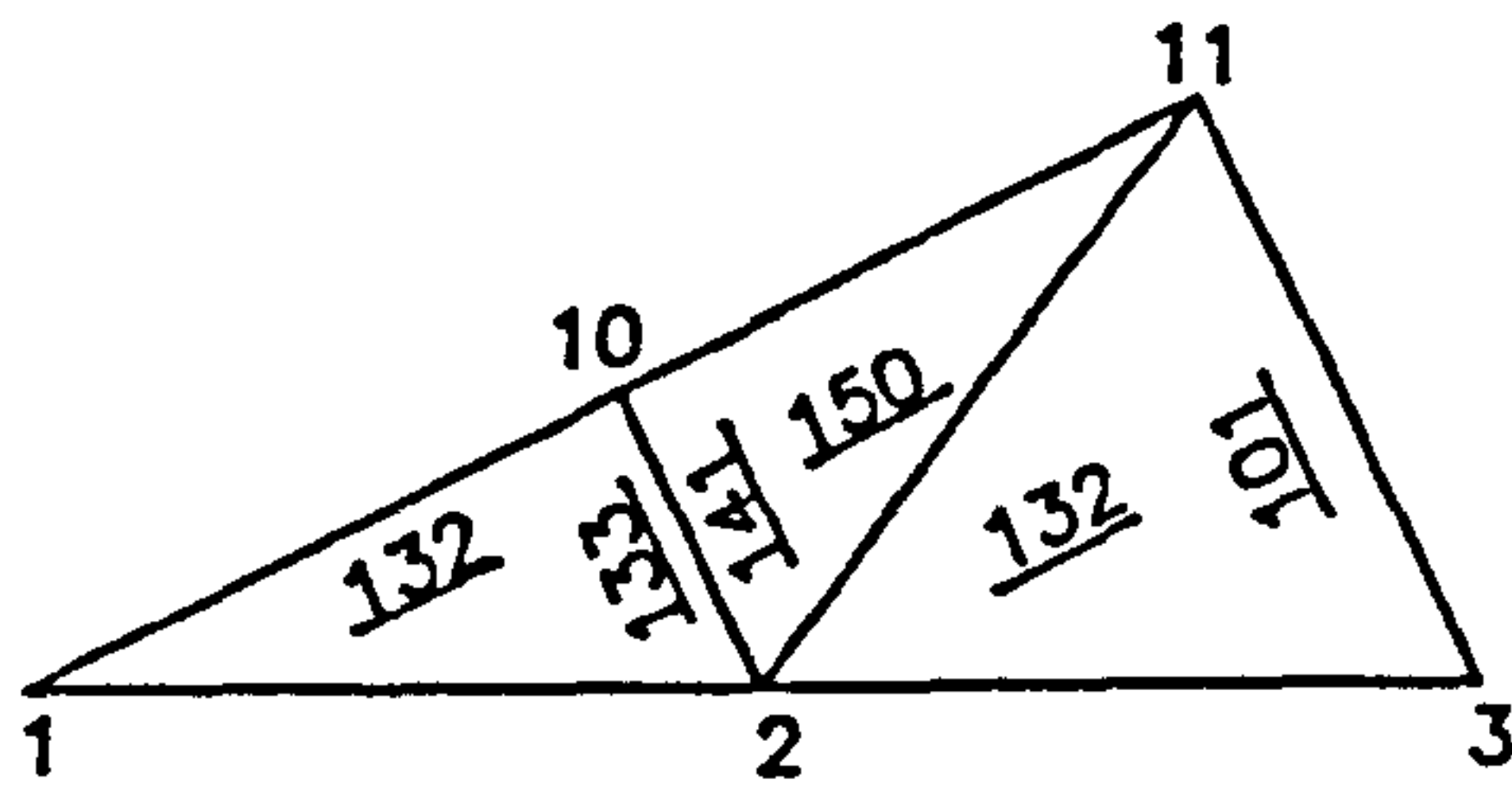
Node Number	Inflated Dome			Loaded Dome			Deflection		
	(i)	(ii)	(iii)	(i)	(ii)	(iii)	(i)	(ii)	(iii)
20	0.163	0.163	0.160	0.198	0.197	0.196	0.035	0.034	0.036
21	0.203	0.203	0.201	0.226	0.227	0.234	0.023	0.024	0.033
29	0.169	0.168	0.165	0.202	0.198	0.198	0.033	0.030	0.033

(b) Asymmetrically applied load

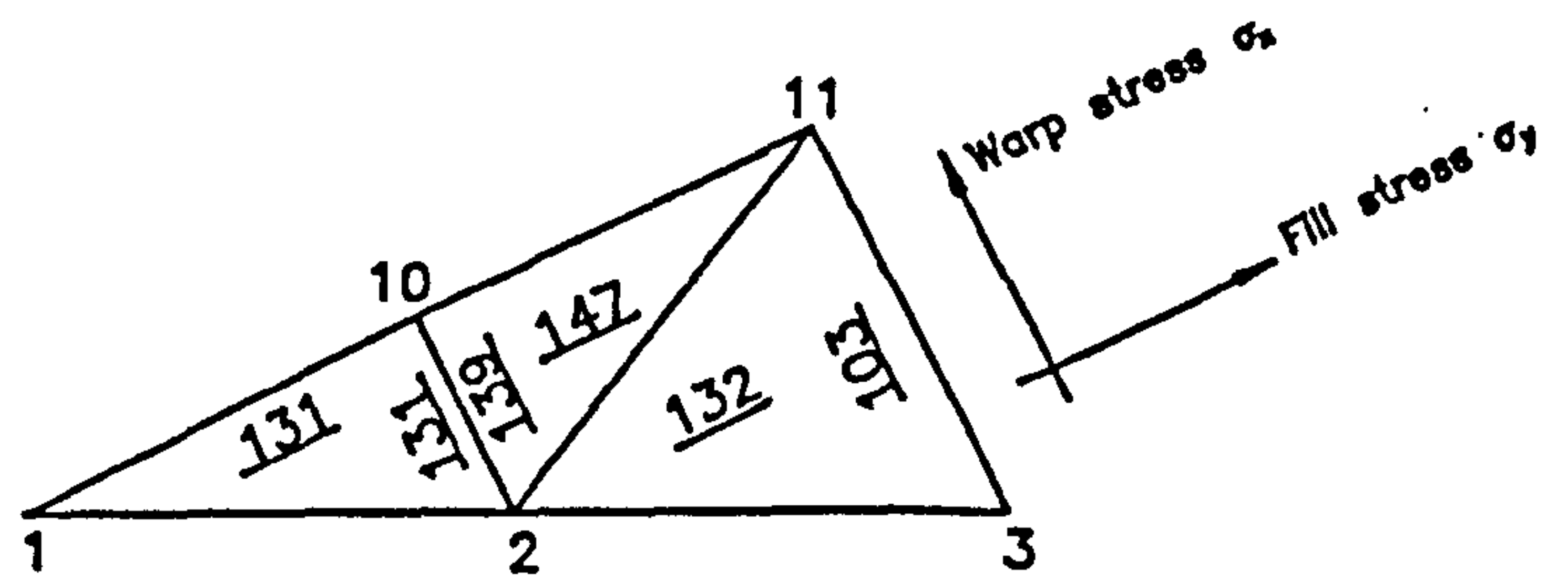
In the above,  
column (i) contains the experimental results obtained by Krakowska [86],  
column (ii) contains the numerical results obtained by Krakowska [86],  
column (iii) contains the numerical results obtained from present work.

Figure 9.23



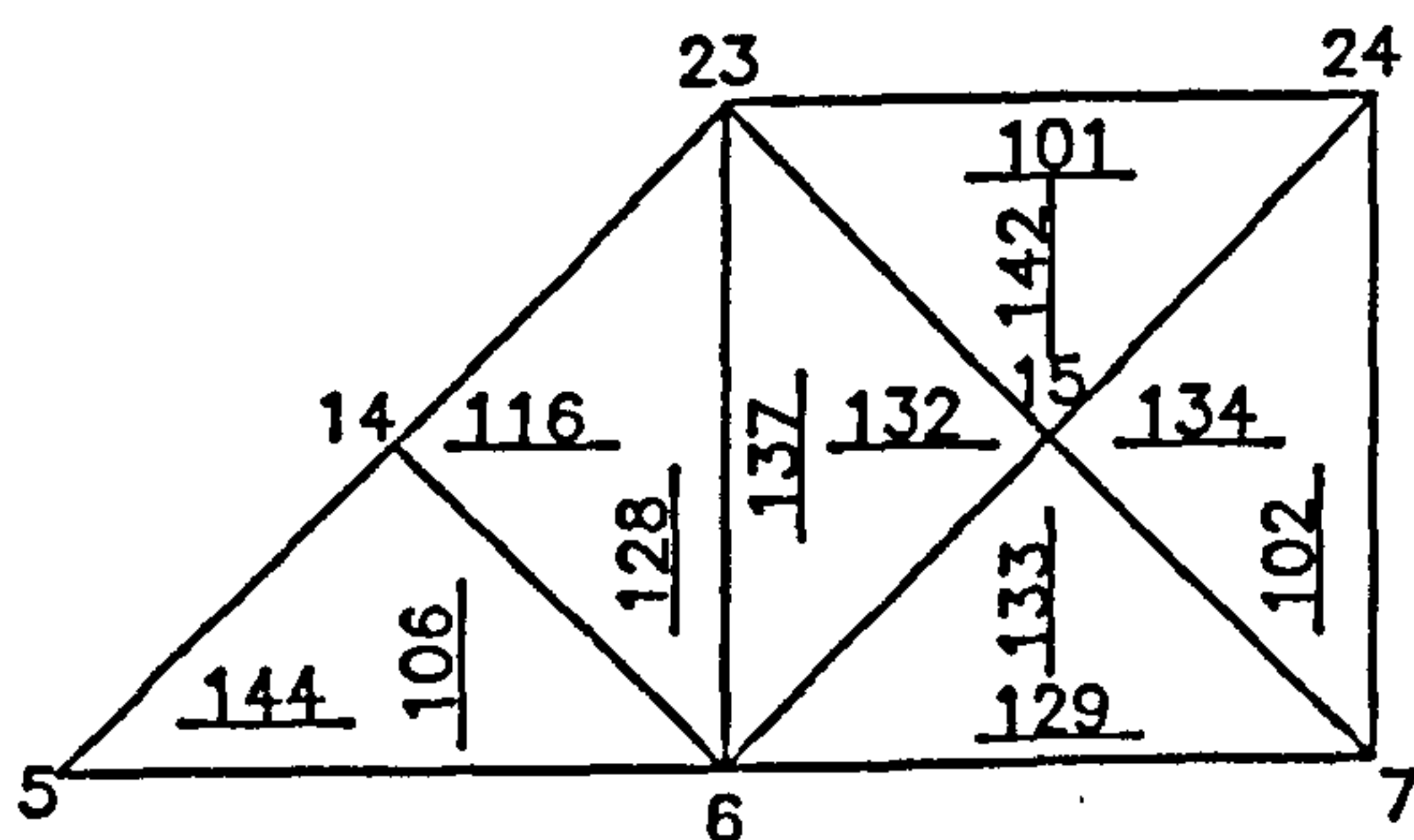


Results obtained by Krakowska [86]

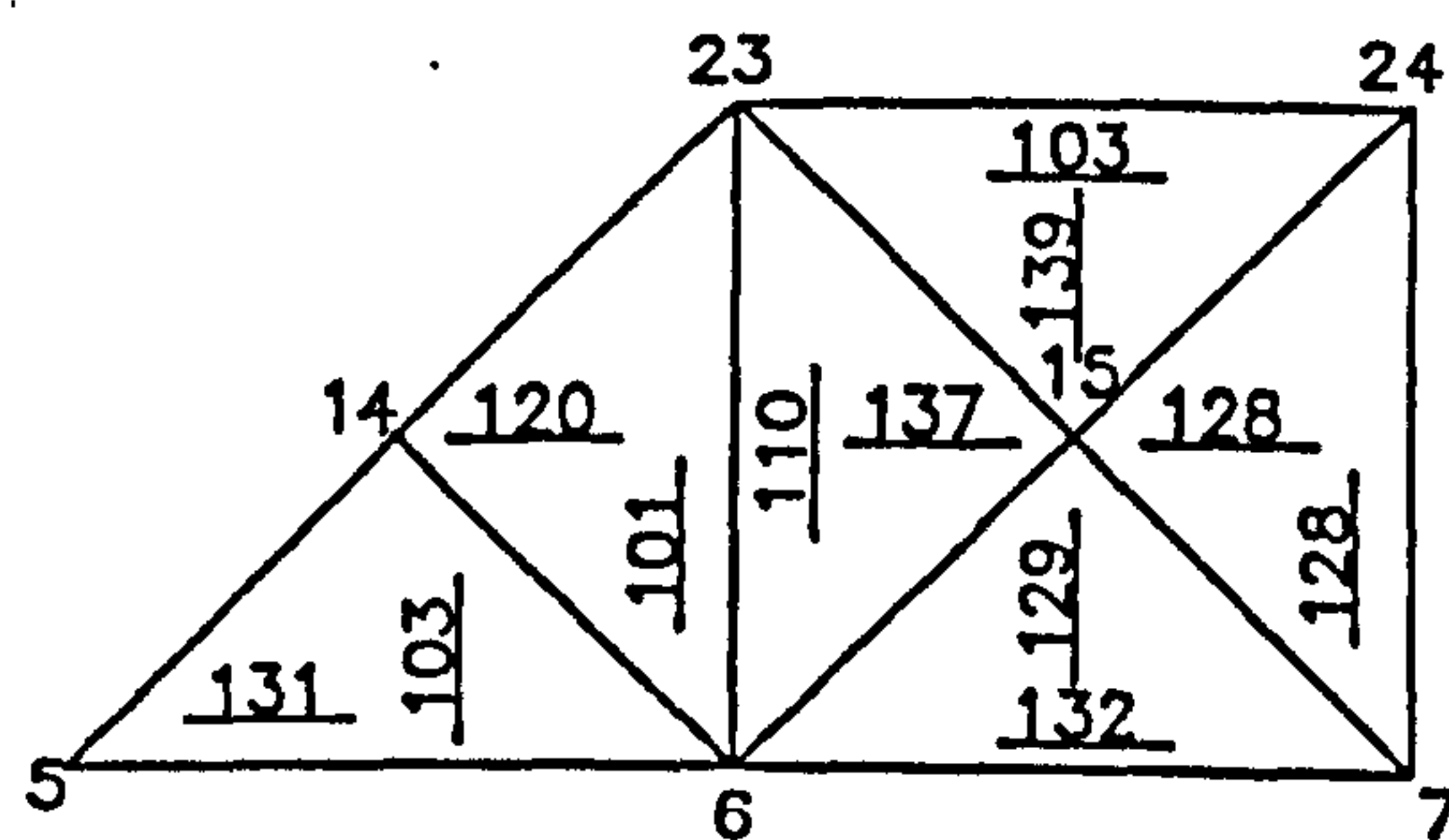


Results from present work

(a) Centrally applied load



Results obtained by Krakowska [86]



Results from present work

(b) Asymmetrically applied load

Figure 9.24 Comparison of membrane stress states

### 9.18.2 Dynamic analysis

At the end of the above static load analysis, the membrane is set into motion by suddenly removing the applied load. By doing so, the vibrations of the membrane will cause movement in the surrounding air. In the absence of any significant mass acting on the lightweight membrane, the moving air will then greatly influence the dynamic response of the dome. The resulting dynamic response of the dome will be analysed using the explicit numerical scheme implemented with the various procedures outlined earlier. Of particular significance is the inclusion of the added mass calculations into the dynamic analysis (in addition to the modelling of the visco-elastic membrane material properties, on/off buckling and internal air stiffening due to overall volume changes). The vibrations of the membrane will eventually be damped out by the structural and aerodynamic damping until the dome reaches static equilibrium again.



The dynamic response of the dome is traced over a short period only from the instant the applied load is removed. As a result, it may suffice to use a single Kelvin model to account for the visco-elasticity in the membrane material. For this purpose, the values of the visco-elastic constants for the membrane material have to be determined from the material tests by Krakowska [86]. The following values are found for the dynamic properties of the membrane material:

immediate elastic modulus  $E = 36500 \text{ Nm}^{-1}$ ,

Poisson's ratio  $\nu = 0.52$ ,

Kelvin model constants:  $a = 0.00024 \text{ m(Nsec)}^{-1}$ ,  $b = 10.5 \text{ sec}^{-1}$ .

The mass per unit area of the membrane material is equal to  $0.057 \text{ kgm}^{-2}$ . Subsequently, for each triangular element, the membrane mass can be found and distributed equally as a lumped mass to each node of the element. The critical time step for the explicit dynamic analysis is dependent on the mass to stiffness ratio at each node. Hence, from the highest mass to stiffness ratio estimated at the start of the dynamic analysis, the critical time step can be determined. However, a value smaller than this critical time step is used as the actual time step in the dynamic analysis in order to account for the possible variations in stiffnesses at the nodes during the analysis.

Within the explicit numerical scheme is an incremental procedure to allow for the on/off buckling which may occur in each element during the dynamic analysis. In the case of the impulsively unloaded dome being considered here, the dynamic analysis is sensitive to the frequency of buckling checks within the scheme. The reason is that element buckling occurs at almost all stages of the dynamic analysis. The incremental procedure for on/off buckling described earlier in section 9.5 can be taken as a 'force' scheme (see figure 9.3) in which the calculations involve the setting up of element force vectors, with the check for on/off buckling being carried out at intervals of  $n$  time steps (ie.  $n\Delta t$ ). For some problems, it may be acceptable to have buckling checks at infrequent intervals with a fairly large value assigned to  $n$ . For the dome under consideration here however, it is necessary to have a buckling check at every time step, ie.  $n = 1$ . For such a case, the use of a 'stress' scheme instead of the 'force' scheme will lead to a more efficient solution in terms of computation time. An outline of this 'stress' scheme is given below in figure 9.25 (refer to the 'force' scheme described in section 9.5 for the definitions of terms used here).

#### Stage I

At the start of the dynamic analysis:

(1) establish  $[D]$ ,  $[\Psi]$ ,  $[a']$  and  $[b']$ ;



(2) establish  $\{\sigma\}^i$ ,  $[G]$  and  $[G]^T$  for each element;

(3) set  $\{\sigma^*\} = \{\sigma\}^i$  for each element.

### Stage II

The explicit dynamic analysis is iterated through  $n$  time steps of  $\Delta t$ .

Within each time step:

(1) update the current stress vector  $\{\sigma\}$  for each element as follows

$$\{\sigma\}^t = \{\sigma^*\} + [D][G]\{e^*\} \quad (9.18.1)$$

in which  $\{e^*\}$  is the vector of element side extensions relative to the geometry of the structure at the start of each period of  $n\Delta t$ ;

(2) check for on/off buckling; if any components of  $\{\sigma\}^t$  is negative (ie. compressive), it is reset to zero and modify the stress vector, ie.  $\{\sigma\}^t \Rightarrow \{\sigma'\}^t$ .

### Stage III

For each element:

(1) calculate the stress vector as follows

$$\{\sigma\}^t = \{\sigma\}^i + [D][G]\{e\}^t - [D]\{\epsilon_c\}^{t-n\Delta t/2} \quad (9.18.2)$$

in which  $\{e\}^t$  is the vector of total side extensions relative to the geometry of the structure at stage I;

(2) check for on/off buckling; if any components of  $\{\sigma\}^t$  is negative (ie. compressive), it is reset to zero and modify the stress vector, ie.  $\{\sigma\}^t \Rightarrow \{\sigma'\}^t$ ;

(3) calculate  $\{\Delta\sigma\}^t = \{\sigma'\}^t - \{\sigma\}^i$ ;

(4) calculate new creep strains:



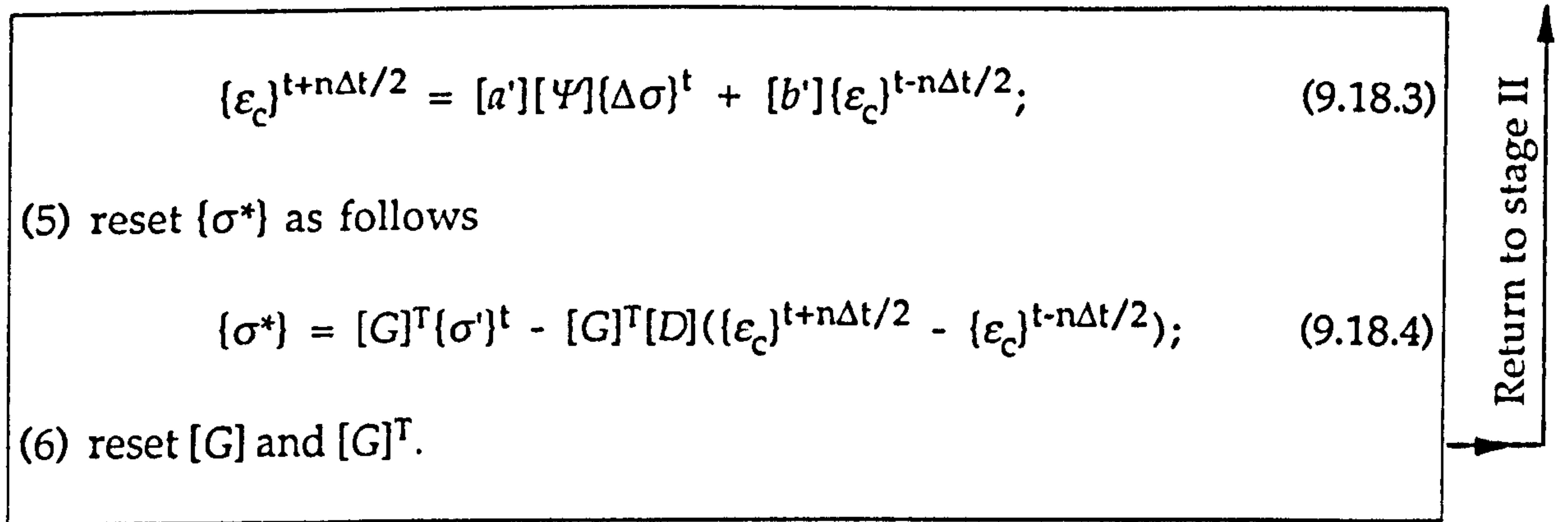


Figure 9.25

In the 'stress' scheme, the idea is to base all calculations on the element stresses except when equilibrating forces at the nodes. Hence, from figure 9.25, instead of the initial force vectors and stiffness matrices in the 'force' scheme, the  $\{\sigma^*\}$ ,  $[G]$  and  $[G]^T$  terms are updated, and passed from stage III to stage II. It is noted that the side extensions  $\{e^*\}$  at step (1) in stage II is relative to the element geometry when returning from stage III to stage II. On the other hand, at step (1) in stage III, the side extensions  $\{e\}$  are relative to the initial element geometry at the start of the dynamic analysis.

In the 'force' scheme, a buckling check is implemented into the same secondary loop as calculations for the current element stiffness matrices, creep strains, initial force vectors and unit pressure vectors. All these operations within the secondary loop are executed at intervals of  $n$  time steps and in this case, a value of  $n = 1$  is required for a stable dynamic analysis. In the 'stress' scheme however, there is a check for on/off buckling at each time step in the main and secondary loops. As a result, it is permissible to increase the value of  $n$  up to 30. The result is a reduction in computation time due to fewer resets of the  $[G]$  and  $[G]^T$  matrices, creep strains and unit pressure vectors in the secondary loop. For the 'stress' scheme, the value of  $n$  is decided by the possible changes in geometry and stress levels, but not directly influenced by the on/off buckling checks within the scheme.

In summary, the 'force' and 'stress' schemes differ mainly in the following aspects:

- (i) The 'stress' scheme implements buckling checks within each cycle of the main and secondary loops, ie. at each time step. As a result, there is no need to modify the  $[D]$  matrix during the analysis.
- (ii) The calculations in the 'stress' scheme are based on the element stress vectors instead of the force vectors. This means that there is no need to set up the element stiffness matrices. In stage III, the  $[G]$  and  $[G]^T$  matrices are reset, and new initial stress vectors  $\{\sigma^*\}$  and unit pressure vectors are calculated. These quantities are then passed to stage II.



The dome under investigation here is a shallow one; the low rise of the dome means that the membrane is close to the base plane, ie. the  $x$ - $y$  plane. The mass to stiffness ratio at each node is largest for displacements in the plane of the membrane as a result of the in-plane membrane stiffness being much higher than the out-of-plane membrane stiffness. Consequently, it is a good approximation to take the critical time step for the explicit dynamic analysis as decided by the mass to stiffness ratios in the  $x$ - and  $y$ -directions of the dome. However, the dominant dynamic responses of the unloaded dome are the displacements normal to the membrane, ie. can approximately be taken as those in the  $z$ -direction of the dome. It has been suggested by Krakowska [86] that the masses in the  $x$ - and  $y$ -directions, ie.  $m_x$  and  $m_y$  respectively can be artificially increased up to a certain limit with only minimal effect on the  $z$ -displacements. In this way, the mass to stiffness ratios in the  $x$ - and  $y$ -directions are magnified and thus, allowing a larger time step to be used in the explicit dynamic analysis. It has been shown by Krakowska [86] in a numerical analysis that with the masses  $m_x$  and  $m_y$  increased by a factor of two, no significant change (from the case in which the masses are not factored) is observed in the response produced. At the same time, a time step larger by a factor of 1.4 can be used which in turn leads to a reduction in computation time. However, in the dynamic analysis carried out here, no magnification factor has been applied to the nodal masses of the membrane and the case of  $m_x = m_y = m_z$  is assumed in the analysis. These nodal masses refer only to the lumped masses derived from the mass density of the membrane material and do not include the added mass of the surrounding air.

#### 9.18.2.1 Centrally unloaded dome

A time step  $\Delta t = 0.00005$  sec is used in the explicit dynamic analysis. This time step is less than half the calculated value of the critical time step based on conditions at the start of dynamic analysis.

It is useful to assess the significance of including the added mass calculations into the explicit dynamic analysis. In order to do this (for comparative purposes), it is required to consider the dynamic response of the unloaded dome with no account of the added mass effects. A dynamic analysis for such a case is carried out. Of interest is the dynamic response of node 3 (ie. a point at a horizontal distance of 0.584 m from the centre of the dome - see figure 9.21(a)). An indication of this dynamic response is given by a trace of the vertical deflection at node 3 as a function of time, ie.  $\Delta z_3(t)$  calculated as follows

$$\Delta z_3(t) = z_3(t) - z_3(t_0)$$

in which  $z_3(t)$  and  $z_3(t_0)$  are the  $z$  coordinates of node 3 at times  $t$  and  $t_0$  respectively. The time  $t$  refers to the current time and time  $t_0$  is the instant when the applied load is suddenly removed. The result of  $\Delta z_3(t)$  obtained



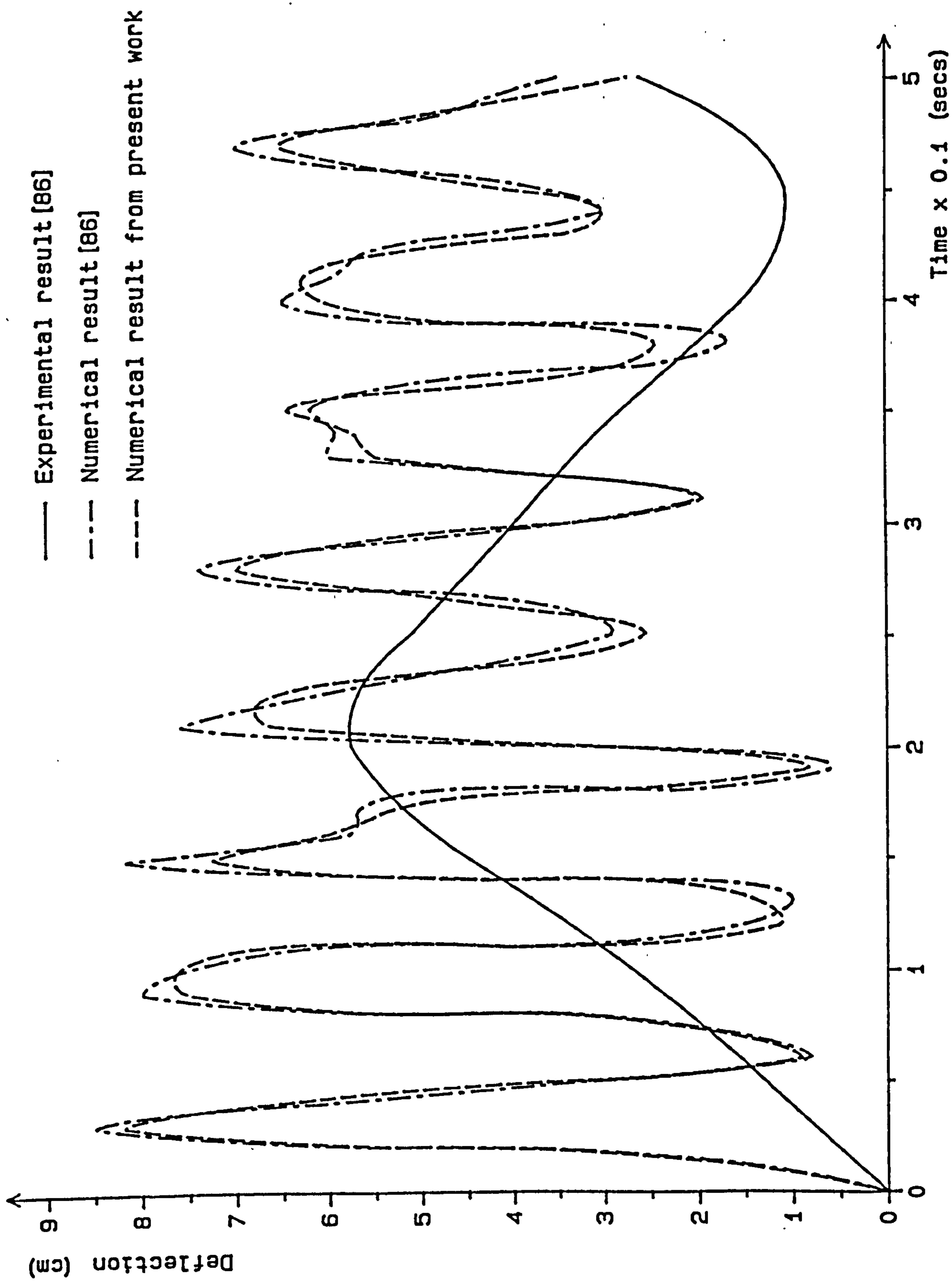


Figure 9.26 Deflection vs time trace of node 3 for the centrally unloaded dome



here for the period ( $t=0 \rightarrow 3$  secs) is compared in figure 9.26 with that determined from the dynamic analysis of the same case by Krakowska [86], and the results agree closely. In these results, there is modelling for the effects of internal air stiffening, creep strains and on/off buckling, but the added mass calculations are excluded. The result of  $\Delta z_3(t)$  determined from experiment is also given in figure 9.26. It can be seen that the experimental result differs significantly in terms of frequencies and maximum deflections from both sets of numerical results.

When additionally accounting for the added air mass effects, the stability of the solution process is influenced by the way in which the added mass calculations are implemented into the explicit dynamic analysis. Furthermore, in order to study parameters related to the added mass calculations, the results of  $\Delta z_3(t)$  are obtained from a series of explicit dynamic analyses carried out for the various schemes ((a) to (f)) outlined below.

Scheme (a) is set up to be similar to the 'two-dimensional' source scheme used in the dynamic analysis by Krakowska [86] to account for the added mass effects, and is based on equations given in section 9.13. The average potentials are calculated for a mesh of triangular and trapezoidal patches which is in the  $z=0$  plane as shown in figure 9.11(a). A source is placed at the centre of each patch. With the source distribution in the same plane as the mesh of patches, the  $z$ -dimension is eliminated and thus, simplifying the calculations to those corresponding to a two-dimensional case. For the structural analysis, the dome is idealised into a mesh of constant strain triangular elements which lie over the membrane.

The difference between schemes (a) and (b) is in the calculation of the kinetic energy of the fluid,  $T_f$  using equation (9.13.5). In scheme (a), the average velocity terms in equation (9.13.5) are used without taking their absolute values while in scheme (b), the absolute values of these terms are used. In schemes (c) to (f), the kinetic energy of the fluid is also calculated by taking the absolute values of the average velocity terms which seems clearly appropriate. Firstly, the  $w_{avj}$  term in equation (9.13.5) is related to the corresponding source strength by equation (9.13.1). As a source strength is always positive, the absolute value of the  $w_{avj}$  term should be used. Secondly, as can be deduced from equation (9.12.9), the kinetic energy of the fluid is not dependent on the sign of the  $w_{avj}$  term in equation (9.13.5) and thus, the absolute value of this term should be used. Consequently, the use of scheme (a) will lead to an underestimation of the kinetic energy of the fluid. It is also likely that Krakowska [86] used equation (9.13.5) to calculate the kinetic energy of the fluid without taking the absolute values of the average velocity terms as will be evident from the results in figure 9.27 discussed later.

In scheme (c), the same distribution of sources as used in scheme (b), ie. as shown in figure 9.11, is used. In this case however, the potential coefficients  $C_{ij}$  are calculated using the equations given in section 9.14, and this applies to schemes (d) to (f) as well.



In scheme (d), the average potentials are calculated for a mesh of triangular patches which is in the  $z=0$  plane. These patches are given simply by the projection of the element idealisation of the dome onto the  $z=0$  plane. A source is placed at the centroid of each patch. The structural analysis is still based on the triangular elements.

In scheme (e), the sources are distributed in a similar manner to that used in scheme (d). In this case however, the average potentials are calculated for the triangular elements instead of the triangular patches.

In scheme (f), the sources are distributed over the dome, ie. with a source placed at the centroid of each triangular element as shown in figure 9.20(a). A distribution of sources similar to that over the dome is prescribed over an imaginary image which is the mirror reflection of the dome about the base. By doing so, the boundary condition of zero normal velocity of the air across the base is satisfied as discussed in section 9.16. In this scheme, the average potentials are calculated for the triangular elements and there is no use of a separate mesh of patches. Hence, scheme (f) corresponds to the generalised source method.



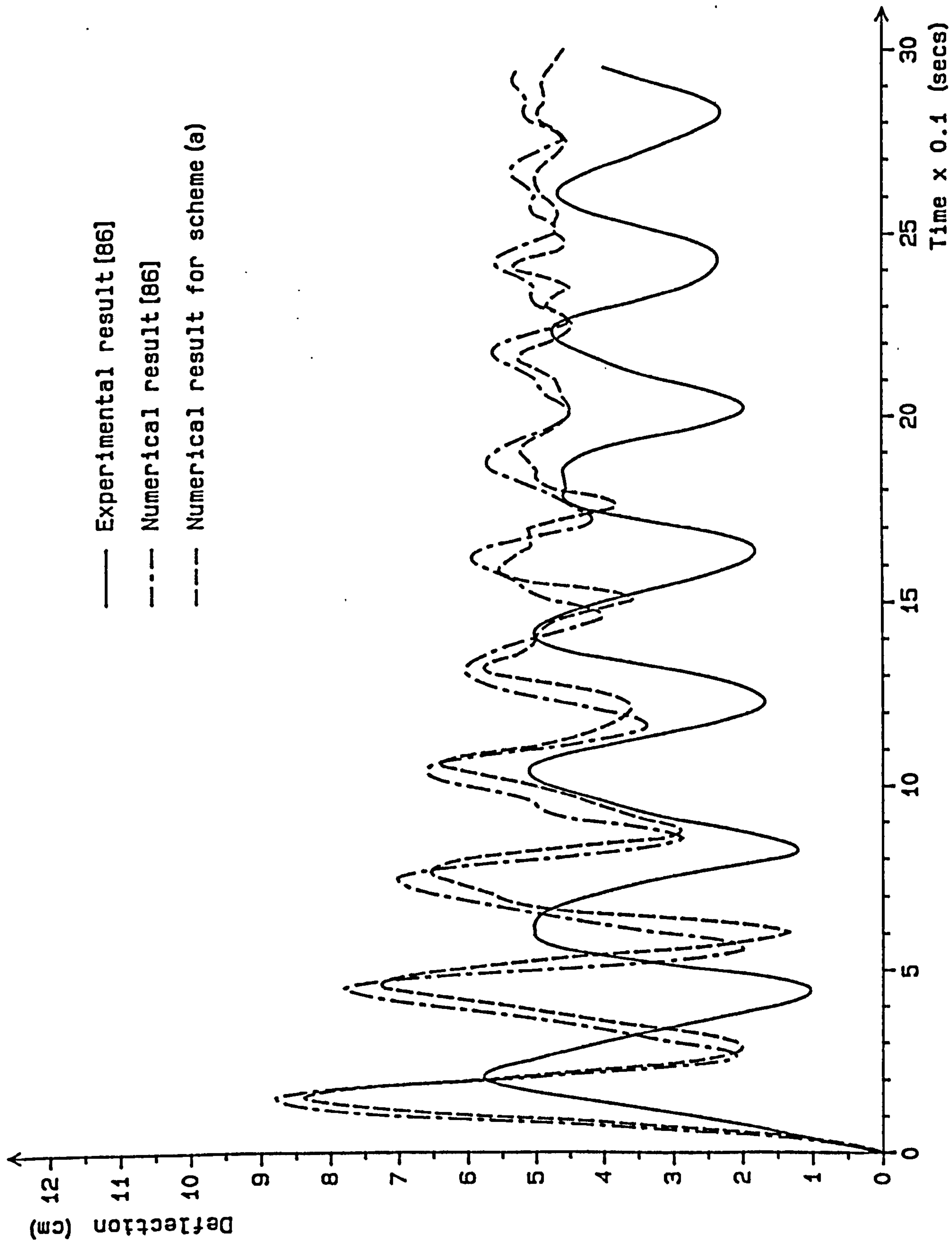


Figure 9.27 Deflection vs time trace of node 3 for the centrally unloaded dome



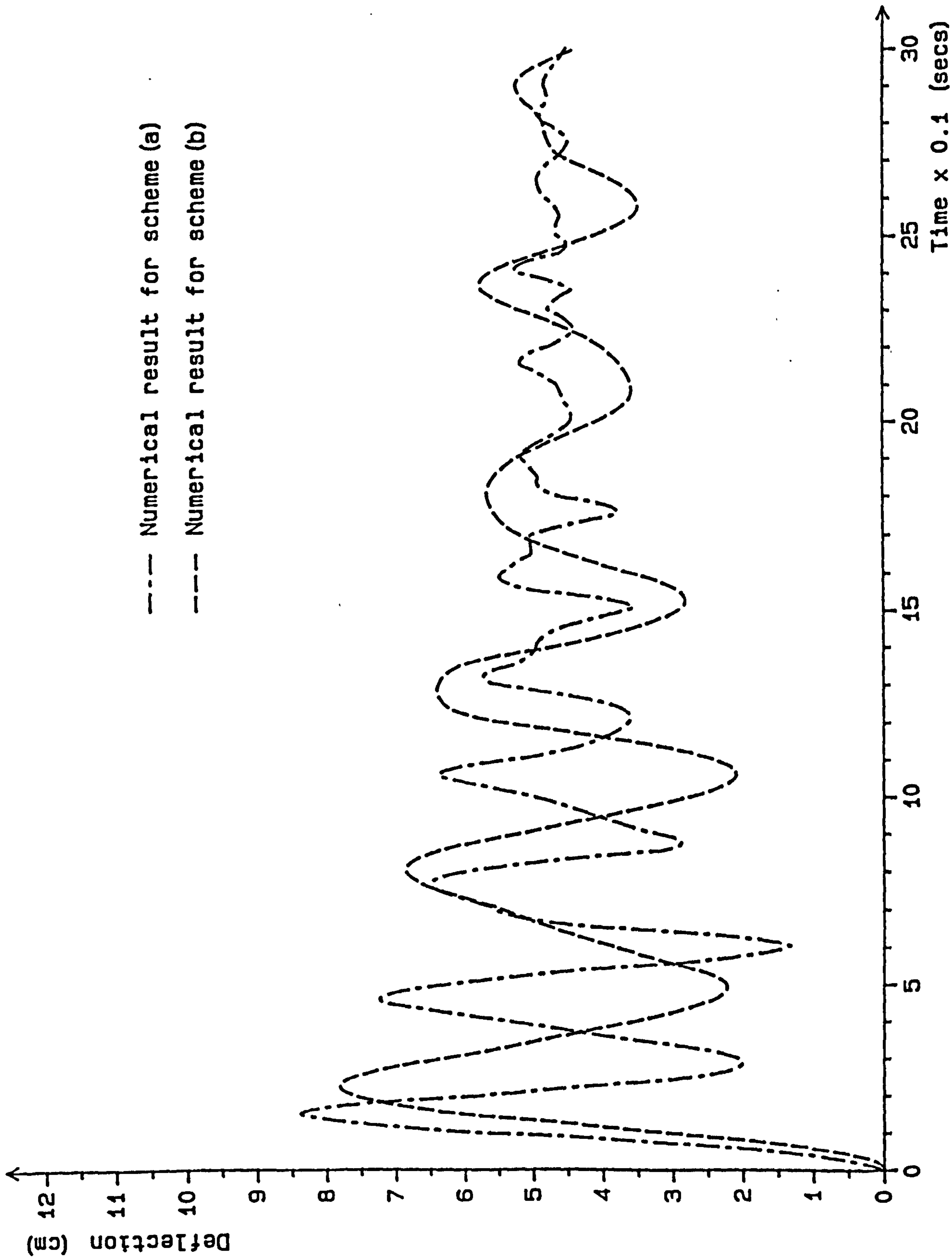


Figure 9.28 Deflection vs time trace of node 3 for the centrally unloaded dome



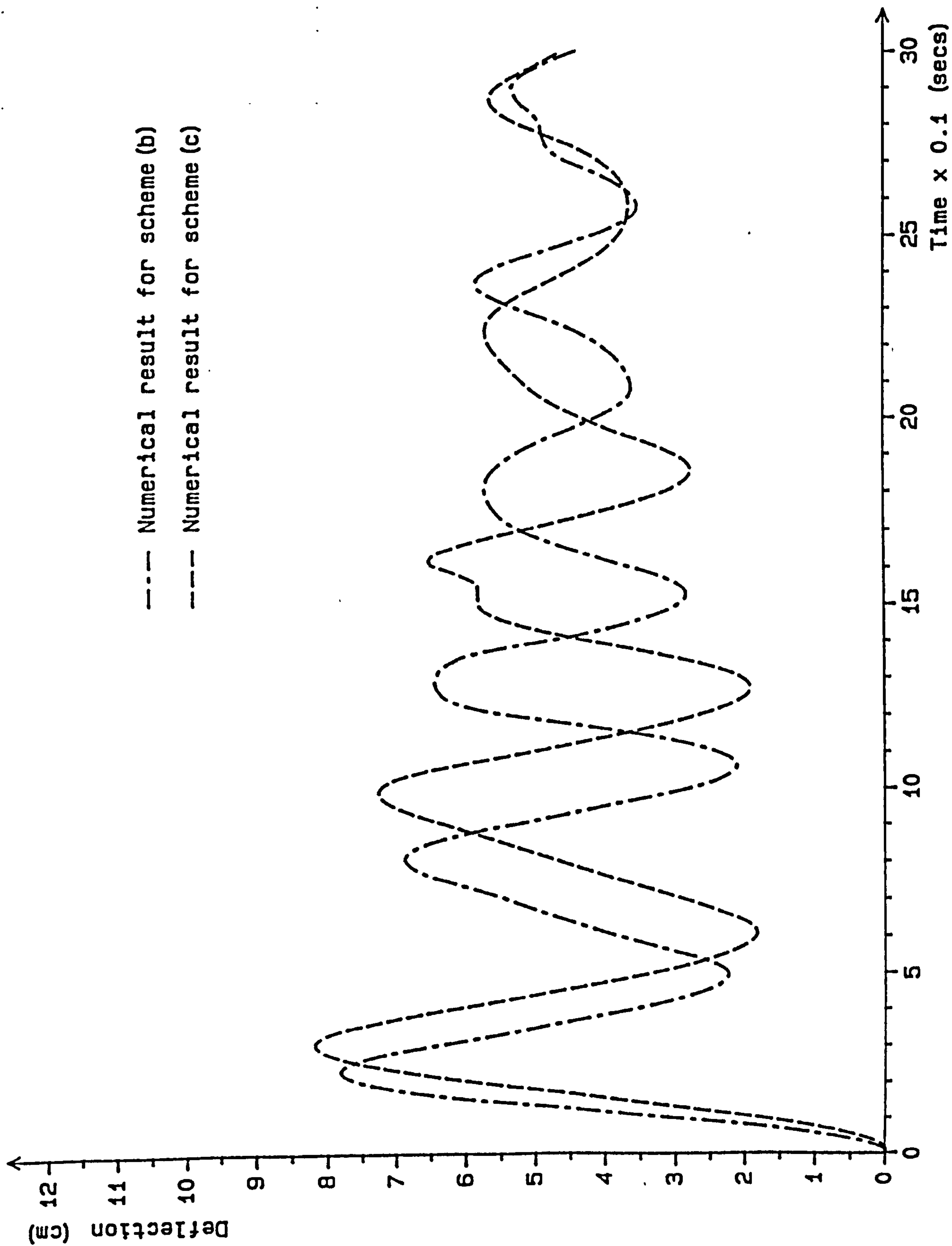


Figure 9.29 Deflection vs time trace of node 3 for the centrally unloaded dome



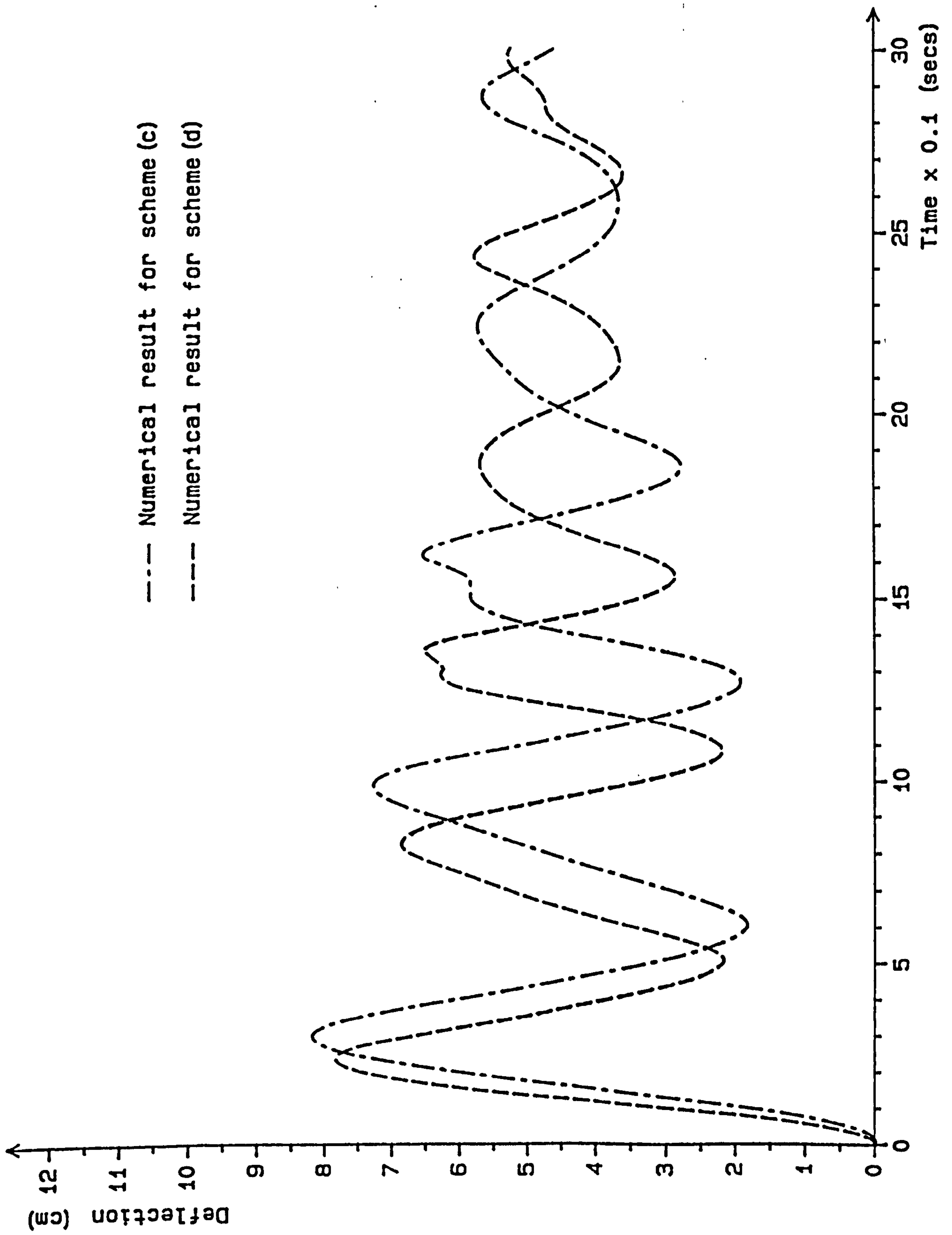


Figure 9.30 Deflection vs time trace of node 3 for the centrally unloaded dome



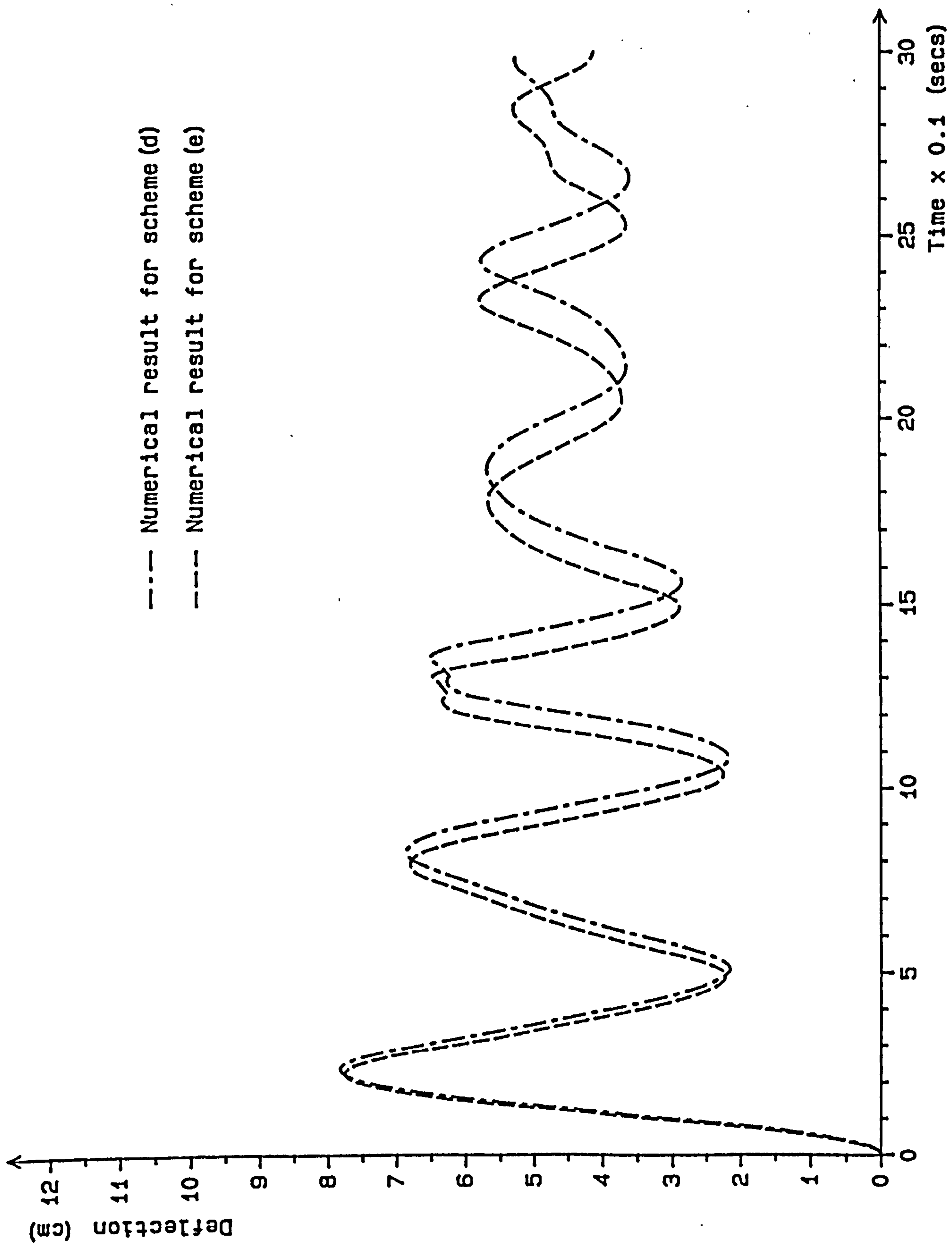


Figure 9.31 Deflection vs time trace of node 3 for the centrally unloaded dome



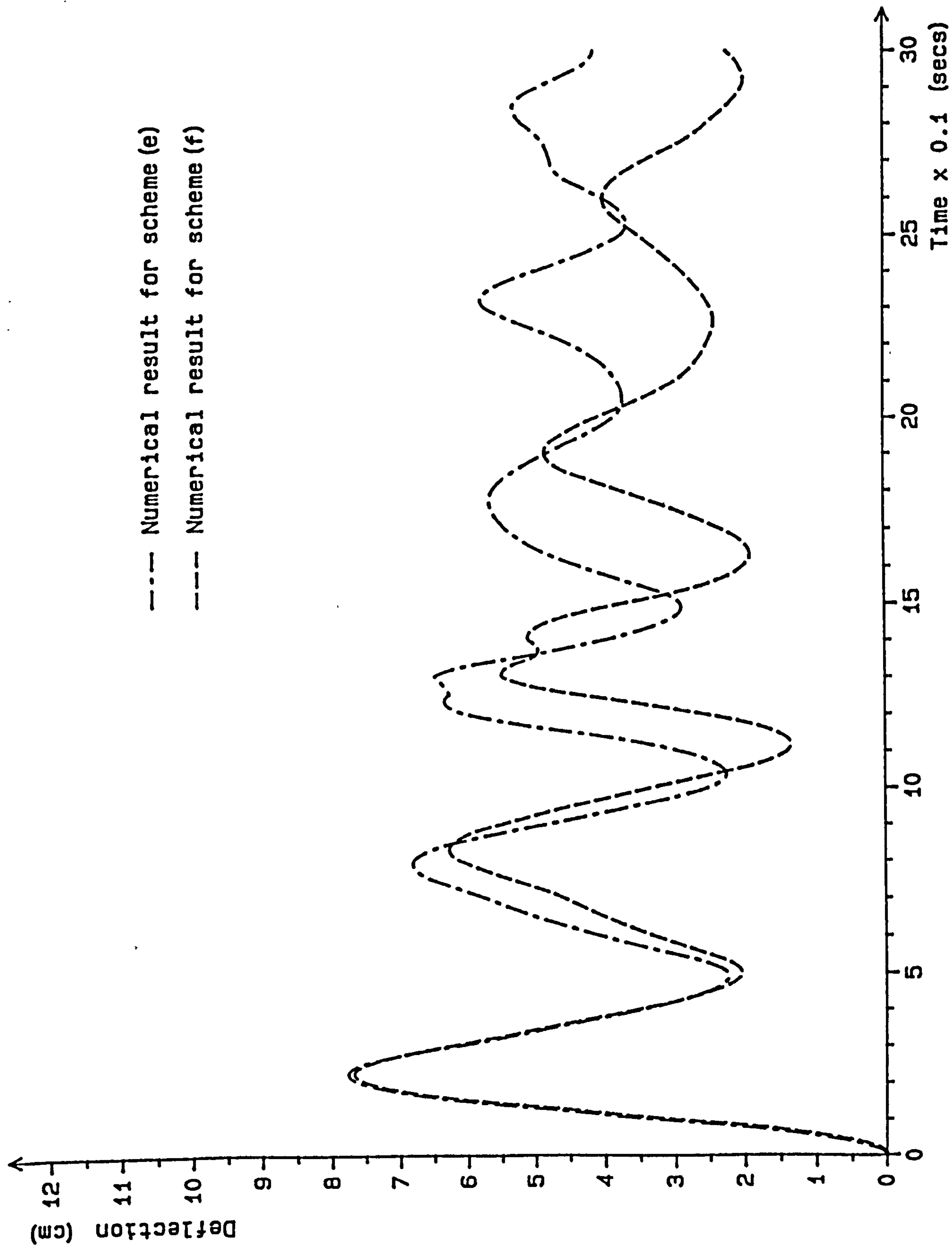


Figure 9.32 Deflection vs time trace of node 3 for the centrally unloaded dome



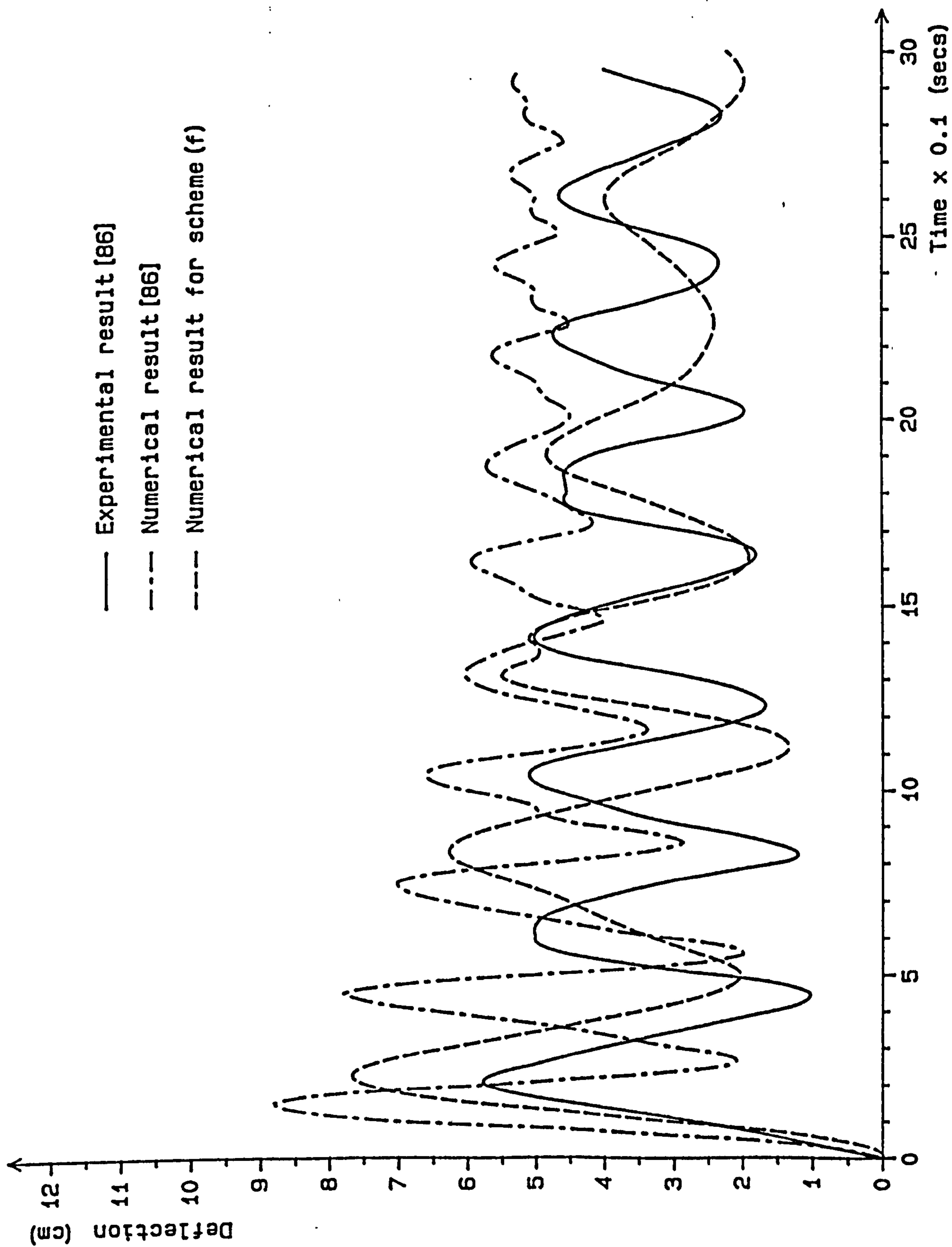


Figure 9.33 Deflection vs time trace of node 3 for the centrally unloaded dome



The result of  $\Delta z_3(t)$  obtained from dynamic analysis based on scheme (a) is given in figure 9.27. The results obtained from experiment and dynamic analysis by Krakowska [86] are also given in figure 9.27. As scheme (a) is similar to the scheme used in the dynamic analysis by Krakowska [86] to account for the added mass effects, there should be close agreement between the two sets of numerical results as illustrated in figure 9.27. It can be seen that the numerical results in figure 9.27 are much closer to the experimental result than those given in figure 9.26. This improvement comes from inclusion of the added mass calculations into the dynamic analysis.

The effect of the difference between schemes (a) and (b) on the result of  $\Delta z_3(t)$  is shown in figure 9.28. The underestimation of the kinetic energy of fluid and thus, the attached added air mass results in the higher frequency of the dynamic response given by scheme (a).

In figure 9.29, the results of  $\Delta z_3(t)$  obtained from dynamic analyses based on schemes (b) and (c) are compared. In both schemes, the same distribution of sources as shown in figure 9.11 is used. The difference between the schemes is that in scheme (b), the added mass calculations are based on equations given in section 9.13 while in scheme (c), they are carried out using the generalised source method described in section 9.14. A dynamic response of higher frequency is given by scheme (c).

It is noted that scheme (b) involves numerical integrations which in this case are evaluated using the trapezoidal rule. This requires the divisions of elements into sufficiently fine intervals in order to ensure that reasonably accurate integrations are achieved. The generalised source method used in schemes (c) to (f) involves exact analytic integrations instead. Hence, this avoids the errors which arise from using numerical integrations in scheme (b). The evaluation of the analytic integrations also requires much less computational effort than in the case with the numerical integrations. Hence, scheme (c) requires a shorter solution time than scheme (b). In fact, the implementation of scheme (c) into the basic explicit numerical scheme for the dynamic analysis leads to only a small increase in computational effort (about 20%) compared with when there is no account whatever of the added mass effects.

In figure 9.30, the results of  $\Delta z_3(t)$  obtained from dynamic analyses based on schemes (c) and (d) are compared. In both schemes, the sources are distributed over the  $z=0$  plane. However, while the sources in scheme (c) are placed at the centroids of triangular and trapezoidal elements as shown in figure 9.11(a), the sources in scheme (d) are placed at the centroids of triangular elements as shown in figure 9.20(a). In both schemes, the average potentials are calculated with the elements taken to lie in the  $z=0$  plane. The effect on the result of  $\Delta z_3(t)$  of the difference between the source distributions in schemes (c) and (d) is illustrated in figure 9.30. It is more convenient and general to adopt the strategy of placing sources at the centroids of triangular elements as implemented in scheme (d). It is also reasonable to suggest that



Parameters	Krakowska[86]	Present Work
air density	unavailable	$1.2256 \text{ kgm}^{-3}$
atmospheric pressure	unavailable	$100500 \text{ Nm}^{-2}$
mass density of membrane material	$0.057 \text{ kgm}^{-3}$	$0.057 \text{ kgm}^{-3}$
immediate elastic modulus E	$36500 \text{ Nm}^{-1}$	$36500 \text{ Nm}^{-1}$
Poisson's ratio	0.52	0.52
Kelvin model constants:	$a = 0.00024 \text{ m(Nsec)}^{-1}$ $b = 10.5 \text{ sec}^{-1}$	$a = 0.00024 \text{ m(Nsec)}^{-1}$ $b = 10.5 \text{ sec}^{-1}$
n	20	30
$\Delta t$	0.00007 sec	0.00005 sec

Figure 9.34(a) Parameters used in the dynamic analyses of the centrally unloaded dome.



the higher density of sources used in scheme (d) should give a more accurate result.

In figure 9.31, the results given by schemes (d) and (e) are compared. The sources in both schemes are distributed over the  $z=0$  plane. For the average potential calculations, the relatively little effect of taking the triangular elements to be on the membrane in scheme (e) instead of in the  $z=0$  plane in scheme (d) is indicated by the results shown in figure 9.31.

In figure 9.32, the results given by schemes (e) and (f) are compared. The aim is to investigate the effect of distributing the sources over the membrane and its mirror image in scheme (f) instead of the  $z=0$  plane in scheme (e). This results in the dynamic response given by scheme (f) having an increased attached added air mass and thus, a lower frequency, and also a lower long term (or average) deflection.

The results obtained by Krakowska [86] from experiment and dynamic analysis (given earlier in figure 9.27) are compared in figure 9.33 with the result given by scheme (f). The basic differences in added mass calculations between the dynamic analysis by Krakowska [86] and that based on scheme (f) are summarised below in figure 9.34.

Dynamic analysis by Krakowska [86] (cf: SCHEME (a))	Dynamic analysis based on schemes (b) → (f)
Kinetic energy of fluid calculated without taking absolute values of the average velocity terms.	Kinetic energy of fluid calculated using absolute values of the average velocity terms. (b)
Based on equations given in section 9.13, and involves numerical integrations.	Based on equations given in section 9.14, and involves exact analytic integrations. (c)
Sources are placed at the centres of triangular and trapezoidal patches as shown in figure 9.11(a).	Sources are placed at the centroids of triangular elements as shown in figure 9.20(a). (d)
Average potentials are calculated for these triangular and trapezoidal patches which lie in the $z=0$ plane.	Average potentials are calculated for these triangular elements which constitute the structural idealisation of the dome. (e)
Distribution of sources is over the $z=0$ plane as shown in figure 9.11(c).	Distribution of sources is over the membrane and its imaginary mirror image as shown in figure 9.20(b). (f)

Figure 9.34



In the right hand column of figure 9.34 are the five main differences listed in the order in which each of them is investigated separately in schemes (b), (c), (d), (e) and (f) respectively. The results in figures 9.28 to 9.32 illustrate the varying degrees of effect which these differences have on the dynamic response of the centrally unloaded dome. The one with the least significant effect is that related to the average potential calculations.

As shown in figure 9.33, when compared with the numerical result obtained by Krakowska [86], the dynamic analysis based on scheme (f) gives a dynamic response of lower frequency and with longer term average deflections closer to that of the experimental result.

	(i)	(ii)	(iii)	(iv)	
No. of cycle	Frequency	Frequency	Frequency	Frequency	Added mass coefficient
1	2.5	3.5	16.4	1.7	64.3
2	2.5	3.5	16.1	1.7	61.3
3	2.5	3.4	15.6	1.8	48.0
4	2.5	3.4	15.9	1.4	60.0

Figure 9.35

Under comparison in figure 9.35 are the following results for the first few cycles of the dynamic response  $\Delta z_3(t)$ :

- (i) frequencies obtained from experiment by Krakowska [86],
- (ii) frequencies obtained from dynamic analysis by Krakowska [86],
- (iii) frequencies obtained from dynamic analysis which excluded the added mass calculations (the result of  $\Delta z_3(t)$  for this case is given in figure 9.26),
- (iv) frequencies and added mass coefficients  $\Lambda_{am}$  (calculated as average values) obtained from dynamic analysis based on scheme (f).

By averaging the results in figure 9.35 over the first four cycles of the dynamic response, the added mass coefficient is 58.4, and (iv) gives a frequency value



of 1.65 which is much closer to the experimental value of 2.5 than the value of 16.0 given by (iii). By accounting for the added mass effects within the dynamic analysis, the prediction of frequency is vastly improved with the discrepancies being reduced from 540% to 34%. Hence, a very significant factor for a realistic modelling of dynamic response of the dome is to account for the added mass effects within the analysis. The average frequency of 3.45 given by (ii) is 38% higher than the experimental value. Hence, the explicit dynamic analysis based on scheme (f) gives an average frequency which is marginally closer to the experimental value. As shown in figure 9.33, the result given by scheme (f) still differs noticeably from the experimental result in terms of the rate of decay.

As mentioned earlier, the added mass of the attached air can also be approximated using equation (9.7.1) derived by Jensen [79]. Equation (9.7.1) gives an added mass which ranges from 44 to 122 times the membrane mass. However, equation (9.7.1) is given in terms of  $a^3$  with 'a' being a typical dimension of the structure. For some complex airhouses, it may be difficult to decide upon which structural dimension to use for the variable 'a'. The explicit dynamic analysis based on scheme (f) outlined above offers more flexibility; it has been developed to eliminate a few of the limitations of the 'two-dimensional' source scheme used in the dynamic analysis by Krakowska [86] so that it is applicable more generally to a pneumatic dome of any shape. It is also fair to consider the dynamic response determined from the explicit dynamic analysis based on scheme (f) as reasonable bearing in mind the underlying assumptions of the potential flow theory and added mass calculations which have been discussed in this chapter.

#### 9.18.2.2 Asymmetrically unloaded dome

In the case of the asymmetric load suddenly lifted off the dome, a time step  $\Delta t = 0.0002$  sec is used in the dynamic analysis. This time step is approximately 55% of the value of critical time step calculated on the basis of conditions at the start of dynamic analysis. In addition, this time step is larger than that used in the case of the centrally unloaded dome. This is due to the use of larger elements and that the maximum deflections are smaller in the case of the asymmetrically unloaded dome. Although a rather coarse mesh of elements as shown in figure 9.21(b) is used in the analysis, the improvement in prediction of the dynamic response especially in terms of frequency which can be gained by using a finer mesh of elements will be much less significant compared with that which can result from inclusion of the added mass calculations into the analysis.

As for the centrally unloaded dome, the dynamic analysis is based on the 'stress' scheme already described earlier. Of interest is the z-deflection trace of node 4 versus time, ie.  $\Delta z_4(t)$  which is given by the following

$$\Delta z_4(t) = z_4(t_o) - z_4(t).$$



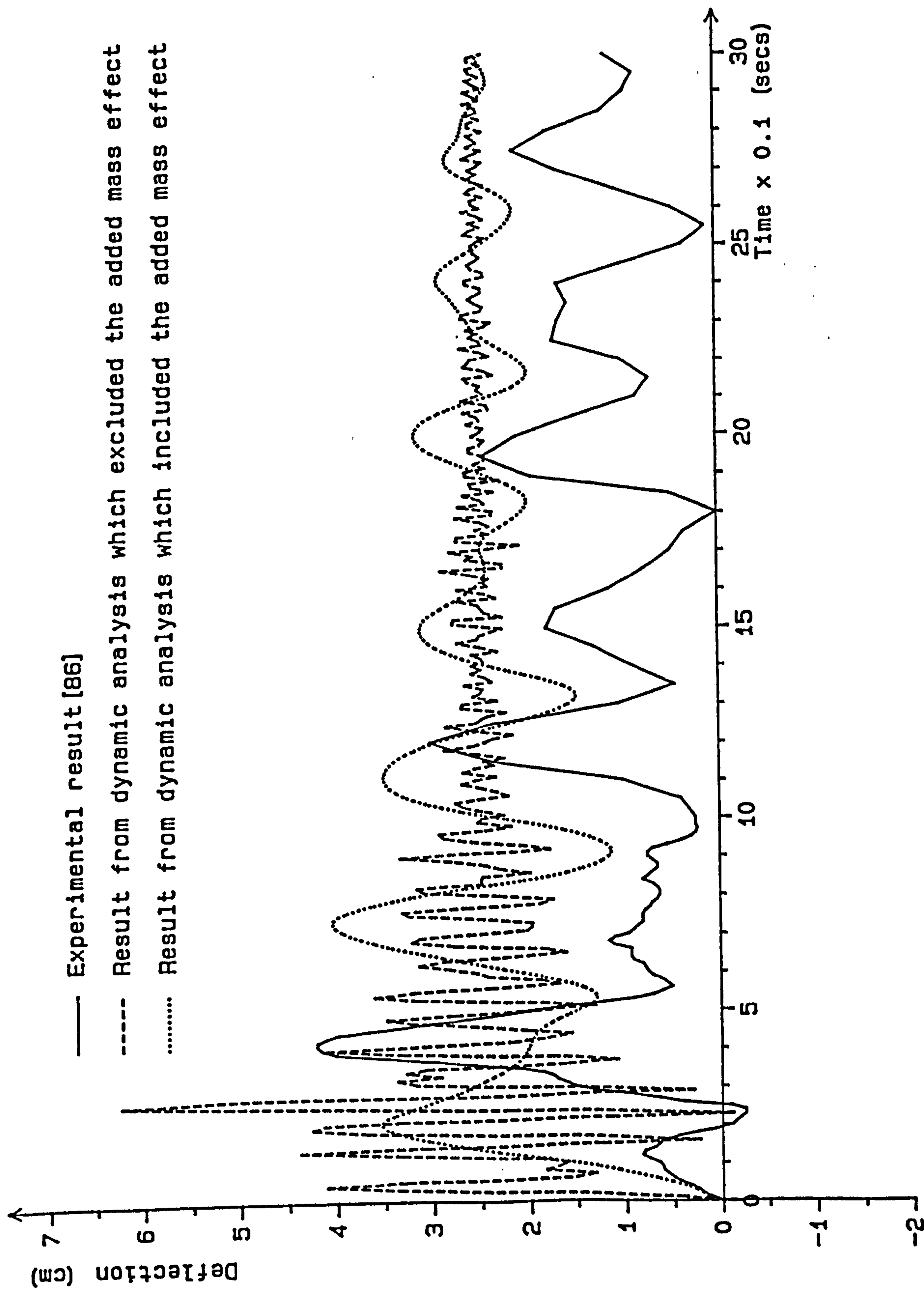


Figure 9.36 Deflection vs time trace of node 4 for the asymmetrically unloaded dome



As shown in figure 9.21(b), node 4 lies on the axis of symmetry but on the opposite side of the dome to the point where the load is released. The results of  $\Delta z_4(t)$  obtained from schemes (a) and (b) for the period ( $t = 0 \rightarrow 3$  secs) are compared in figure 9.36 with the experimental result determined by Krakowska [86] (no numerical results were available). In scheme (a), the added mass effects are excluded from the dynamic analysis while in scheme (b), the added mass effects are accounted for in a similar manner as in scheme (f) used for the dynamic analysis of the centrally unloaded dome discussed earlier. For the asymmetrically unloaded dome however, half of the dome has to be considered in the explicit dynamic analysis.

	(i)	(ii)	(iii)	
No. of cycle	Frequency	Frequency	Frequency	Added mass coefficient
1	5.0	11.1	2.1	29.0
2	3.3	16.4	2.5	30.6
3	3.3	14.9	2.5	30.8
4	2.2	14.1	2.0	31.5

Figure 9.37

Under comparison in figure 9.37 are the following results for the first few cycles of the dynamic response  $\Delta z_4(t)$ :

- (i) frequencies obtained from experiment by Krakowska [86],
- (ii) frequencies obtained from dynamic analysis which excluded the added mass calculations (ie. scheme (a)),
- (iii) frequencies and added mass coefficients  $\Lambda_{am}$  (calculated as average values) obtained from dynamic analysis based on scheme (b).

In figure 9.37, the results of (ii) and (iii) are those for the first four cycles which are easily identifiable from the deflection traces given in figure 9.36; for (i) however, the first four cycles are not so clearly defined. For (i), the frequencies in figure 9.37 for the first two cycles are those over the period ( $t \approx 0 \rightarrow 0.6$  sec) and for the next two cycles are those over the period



( $t \approx 1.1 \rightarrow 1.9$  secs) (see figure 9.36). By averaging the results in figure 9.37 over four cycles of the dynamic response, the added mass coefficient is 30.5, and (iii) gives a frequency value of 2.3 which is much closer to the experimental value of 3.45 than the value of 14.1 given by (ii). The discrepancies in the prediction of frequency is reduced from 309% to 33% by including the added mass calculations into the dynamic analysis. However, this improvement has to be viewed in relation to the fact of not considering the experimental result over the period ( $t \approx 0.6 \rightarrow 1.1$  secs) in calculating the average frequency. As shown in figure 9.36, the result given by scheme (b) still differs quite noticeably from the experimental result in terms of the overall shape of the deflection trace, long term deflection and rate of decay.

In the experiment by Krakowska [86], it was observed that the membrane in the area of the asymmetric load moved upwards to balance a new pattern of loading, creating a local area of low pressure underneath when the load was suddenly raised. The air in a different part of the pneumatic dome, having higher pressure, then surged towards this lower pressure region. This movement can be associated with the first peak of the experimental results in figure 9.35. Subsequently, the air rebounded and returned to the previous position, thus creating again lower pressure in the local area under the membrane, where the platten rested. The air mass continued to 'slosh' about caused more by impinging on the membrane and rebounding than by differences in pressure. The peaks in the experimental results became successively lower as the air momentum decreased.

The 'sloshing' (or momentum) effect described above may be a significant factor in terms of influence on the dynamic response of the asymmetrically unloaded dome. There is no account of this momentum effect (as distinct from the 'attached' added air mass effects) in the explicit dynamic analysis considered so far. This may be the reason for the differences in the overall shape of the deflection trace, and to a lesser extent, the frequency between the experimental result and that given by scheme (b). Further research is required to find a simple and practical means which can model the 'sloshing' (or momentum) effect due to a moving mass of air.

In the comparison between the experimental and numerical results considered above, a point worth noting is that which concerns the dynamic properties assumed for the membrane material in the explicit dynamic analysis. In the experiment by Krakowska [86], the applied load remained on the dome for a short period of time. However, this may already give sufficient time for viscous strains to accumulate in the membrane until the applied load is suddenly removed from the dome. On the other hand, the membrane dynamic properties were established from material tests in which viscous strains have not been allowed to accumulate in the membrane. A further consideration may be the limitation of the single Kelvin model used in the explicit dynamic analysis to give a precise modelling of the visco-elasticity in the membrane material.



Bearing in mind the limitations of the potential flow theory and the factors discussed above, the comparison of the experimental and theoretical results seems reasonable; particularly at the later stages of the dynamic trace. In the earlier stages, some transient dynamic responses are likely to have been caused in the experimental results by the manner and time duration of the sudden removal of the platten load.

### 9.19 The dynamic response in the presence of wind

In the above discussions, the main emphasis has been on the consideration of the added mass effects. For the dome considered, the dynamic response is initiated by the sudden removal of the applied load. In this case, due to the lightweight of the membrane material, the significance of the added mass of the surrounding air set into motion by the vibrations of the dome can be clearly illustrated. In addition, the condition of zero or no wind simplifies the problem to a certain extent. When the applied load is suddenly lifted off the dome, the resulting out-of-balance forces in the membrane then cause the dome to vibrate in order to reestablish its equilibrium. The surrounding air adjacent to the membrane is set into motion with the same velocity as that of the vibrating membrane in the direction normal to the membrane. The work carried out above, however, can also provide a good basis for considering the situation when there is a wind flow over the dome, ie. when the dynamic response is initiated by the action of wind, which will normally be the case in practice. It is necessary to make simplifying assumptions of potential flow for the fluctuating components of wind speed over the surface of the membrane.

As given in equation (9.9.9), the velocity field  $V$  of a wind flow over a structure can be expressed as the sum of two velocities, ie.

$$V = U + v \quad (9.19.1)$$

in which  $U$  is the velocity of the onset flow and  $v$  is the disturbance velocity due to the presence of the structure. (For the dome considered above under the no wind condition, the velocity  $U$  is null).

The irrotationality condition is applied to the velocity  $v$  but not necessarily to the velocity  $U$ . Subsequently, from equation (9.9.13),

$$\nabla \phi \cdot n|_{\Gamma} = \frac{\partial \phi}{\partial n}|_{\Gamma} = U \cdot n|_{\Gamma} - F. \quad (9.19.2)$$

By solving the Laplace equation (ie. equation (9.9.12)), the velocity potential  $\phi$  is then determined. As outlined above, a solution for  $\phi$  can be given by a distribution of simple sources over the real membrane and its imaginary image of the dome. The membrane is discretised into triangular elements for the purpose of structural analysis. A convenient strategy is to take the centroids of the triangular elements as the control points and place the discrete sources at these control points. Subsequently, with  $N$  control points



in the dome considered earlier, the following relation for element  $i$  can be derived from equation (9.9.13), ie.

$$\frac{1}{2}\omega_i + \sum_{j=1, j \neq i}^N B_{ij}\omega_j = -n_i \cdot U_i + F_i. \quad (9.19.3)$$

in which  $\frac{1}{2}\omega_i$  is the outward velocity normal to element  $i$  due to the discrete source of strength  $\omega_i$  at the control point of element  $i$ . The term  $B_{ij}\omega_j$  is the outward velocity normal to element  $i$  due to the discrete source of strength  $\omega_j$  at the control point of element  $j$  and  $B_{ij}$  is the corresponding influence coefficient, ie. gives the normal velocity at the control point of element  $i$  due to a source of unit density at the control point of element  $j$ . The contributions of  $B_{ij}\omega_j$  from the  $N$  control points (except for that at element  $i$ ), have to be summed. The velocity  $U_i$  is the velocity of the wind flow at the control point of element  $i$  in the absence of the dome and  $n_i$  is the unit outward normal vector of element  $i$ . It is noted that the values of  $U_i$  and  $F_i$  may vary over the body surface. Furthermore, the condition of no flow normal to the surface has to be satisfied at each control point, ie.  $F = 0$  in equation (9.19.3). Hence,

$$\frac{1}{2}\omega_i + \sum_{j=1, j \neq i}^N B_{ij}\omega_j + n_i \cdot U_i = 0. \quad (9.19.4)$$

The equation (9.19.4) can be set up for each of the control points in the problem to form a set of linear algebraic equations. In the case of the dome, the problem size can be reduced by making use of axisymmetry of the dome and the symmetry across the rigid base. Hence, from equation (9.19.4),

$$[B]\{\omega\} = \{U\} \quad (9.19.5)$$

in which  $[B]$  is the matrix of influence coefficients,  $\{\omega\}$  is the vector of unknown source densities and  $\{U\}$  is the vector of velocities of the onset flow. The equation (9.19.5) can in turn be readily solved for the source densities using both direct and iterative methods. The set of  $N$  linear algebraic equations given in equation (9.19.5) is the desired approximation of equation (9.19.2).

For the impulsively unloaded dome considered previously, the source densities  $\omega_j$  can be found directly from the average normal velocities of the elements as given in equation (9.14.13), ie.

$$\omega_i = \text{sgn}(z)(2 \times w_{avi} \times A_i) \quad (9.19.6)$$

in which  $w_{avi}$  and  $A_i$  are respectively the average normal velocity and area of element  $i$  with the local  $z$ -axis normal to the plane of the element. The velocity  $w_{avi}$  is in the direction of the local  $z$ -axis. For a control point at  $z = 0^+$  (ie. outward), then



$$w_{avi} = \frac{1}{A_i} \frac{1}{2} \omega_i \quad (9.19.7)$$

and this relationship has been used in equation (9.19.4).

After the source densities  $\omega_j$  have been found by solving equation (9.19.5), the other flow quantities of interest can be determined by rapid direct calculation. Of interest is the flow over the membrane of the dome. The flow quantities on the membrane are computed only at the control points of the element. The potential and velocity at a control point on the membrane are obtained as follows

$$\phi_i = \sum_{j=1}^N \Phi_{ij} \omega_j, \quad (9.19.8)$$

$$V_i = \sum_{j=1}^N v_{ij} \omega_j + U_i \quad (9.19.9)$$

in which  $\Phi_{ij}$  and  $v_{ij}$  are respectively the potential and velocity that are induced at the control point of element  $i$  by a discrete source of unit density at the control point of element  $j$ . The values of  $\phi_i$  and  $V_i$  for  $(i = 1, 2, \dots, N)$  can therefore be determined. It is noted that  $\phi_i$  is the perturbation potential due to the body surface and  $V_i$  is the total velocity which includes the effects of the onset flow. The magnitude of the velocity  $V_i$  can be found and then used to compute the local pressure coefficient  $C_{pi}$  using equation (9.9.16), ie.

$$C_{pi} = 1 - \frac{|V_i|^2}{|U|^2}. \quad (9.19.10)$$

Subsequently, the local force which arises from the local pressure can be determined as follows

$$R_i = \int p_i ds_i = q \int C_{pi} ds_i \quad (9.19.11)$$

in which  $R_i$  and  $p_i$  are respectively the force and pressure over the area  $s_i$  of element  $i$ , and  $q$  is the dynamic pressure ( $= \frac{1}{2} \rho |U|^2$ ). With the  $C_{pi}$  taken to apply over the element  $i$ , then

$$R_i = \frac{1}{2} \rho |U|^2 \times C_{pi} \times s_i \quad (9.19.12)$$

and the force  $R_i$  acts normally to element  $i$ , and is assumed to be distributed equally to the nodes of the element. These resulting nodal forces are then applied to the next time step (or group of time steps) in the explicit dynamic analysis of the dome.



A description is given above of a relatively simple scheme which has been proposed to deal with the case when there is a wind flow over the dome. The scheme attempts to model how the presence of the dome has disturbed the wind flow. It is anticipated that the scheme can be incorporated without much difficulty into the explicit dynamic analysis considered earlier.

In the above, for the simple case of a uniform and steady wind flow, the velocity  $U$  is simply a constant vector. For the non-uniform and steady onset flows, the values of the velocity  $U$  are specified at the control points of the elements. In the case of a steady wind flow, the structure will deform changing the pressure distribution until an equilibrium state is reached. A steady wind flow is flow in which the velocity depends only on position and not on time, and may correspond to the wind with a hourly mean speed relevant to the site of the structure. The natural atmospheric boundary layer may be simulated by using a wind flow having a mean speed which increases with height according to a power law.

During the dynamic analysis, the information of interest will be the resulting maximum deflections and stresses in the membrane.

In the design of an air-supported structure, the necessary pressure differential across the membrane has to be provided and maintained. The inflation pressure (together with the average suction loading on the membrane due to the mean wind flow) must ensure that the structure does not become unstable in a wind. Williams [141] has applied the classical theory of travelling and standing waves to study the stability of fabric structures in a wind. The discussion is limited to a two-dimensional situation or model. In addition, it is assumed that the fabric structures have low profiles (ie. low rise-to-span ratios). A few useful results for the design of fabric structures have been obtained. For instance, the critical wind velocity,  $V_c$  at which a one-way spanning low profile air-supported roof loses static stability (ie. divergence) is given by

$$V_c = \sqrt{\frac{\pi p_i}{4\mu\rho}} \quad (9.19.13)$$

in which  $p_i$  is the sum of the inflation pressure and mean suction acting on the surface,  $\rho$  is the density of air and  $\mu$  is the rise-to-span ratio. This result gives an idea of the inflation pressure which is required in order to avoid divergence for the design wind velocity. Furthermore, the natural frequency  $f_o$  under zero wind is given by

$$f_o = \sqrt{\frac{\pi p_i}{8\mu\rho S^2}} \quad (9.19.14)$$

in which  $S$  is the span of the air-supported structure. The wind tunnel testing of an aeroelastic model of an air-supported structure has been carried out by



Davies [52] to verify the above formulas. The results obtained agree reasonably well with those values calculated using the above formulas.

An extension of the above work by Williams [141] to a three-dimensional situation has been carried out by Barnes [20]. The case of a rectangular membrane or region of a membrane is considered. The following results are obtained:

$$V_{xc} = \sqrt{\frac{2\pi}{\rho} \left( \frac{T_x}{\lambda_x} + \frac{T_y \lambda_x}{\lambda_y^2} \right)}, \quad V_{yc} = \sqrt{\frac{2\pi}{\rho} \left( \frac{T_x \lambda_y}{\lambda_x^2} + \frac{T_y}{\lambda_y} \right)} \quad (9.19.15)$$

in which  $V_{xc}$  is the critical wind velocity for a wind blowing in the  $x$ -direction while  $V_{yc}$  is the corresponding value if the wind is blowing in the  $y$ -direction. The terms  $T_x$  and  $T_y$  are the membrane tensions per unit width in the  $x$ - and  $y$ -directions respectively, and  $\lambda_x$  and  $\lambda_y$  are the wavelengths of the mode shapes in the  $x$ - and  $y$ -directions respectively of the membrane. In addition, for a travelling wave in the  $x$ -direction of the membrane under zero wind,

$$f_o = \sqrt{\frac{T_x}{m' \lambda_x^2} + \frac{T_y}{m' \lambda_y^2}} \quad (9.19.16)$$

in which  $m' = (m + \frac{\lambda_x \rho}{\pi})$  is the effective mass per unit area. The term  $m$  refers to the mass per unit area of the membrane, and  $\frac{\lambda_x \rho}{\pi}$  is the added mass per unit area of the air affected by the mode shapes in the membrane. A similar natural frequency can be found for the travelling wave in the  $y$ -direction of the membrane under zero wind. From the critical wind velocities given by equation (9.19.15), the required inflation pressures can then be worked out.

The above results derived by Williams [141] and Barnes [20] are based on the potential flow theory. These results apply only to the case of a steady wind flow over the surface of an air-supported structure of simple shape. As further work, a dynamic analysis based on the discrete source method discussed earlier can be carried out to produce results for comparison with those given by the equations (9.19.13), (9.19.14), (9.19.15) and (9.19.16).

## 9.20 Summary and conclusions

In this chapter, the problem of analysing the dynamic responses of tension structures is examined. The most common cause of the dynamic response is the natural wind. The lightweight and flexible nature of a tension structure makes it highly susceptible to wind loading and it is therefore important for the design process to include a reliable assessment of the dynamic response which may occur. A tension structure has the tendency to interact strongly with the wind which then causes additional aerodynamic mass, damping and stiffness terms to be introduced into the dynamic analysis. The additional forces arising from these aerodynamic terms have to be considered and the



dynamic analysis therefore becomes a complex aeroelastic problem. The creep effects of the membrane material and on/off element buckling which may occur during the dynamic analysis, also have to be taken into account.

For this complex problem, the adopted approach is to first decide on an efficient solution scheme for the basic dynamic analysis and then implement into the scheme, procedures which account for the creep effects, on/off buckling and aerodynamic effects. The various available solution schemes for the dynamic analysis of structures in general include the mode superposition method and direct step-by-step time integration methods (which can be classified as either implicit or explicit schemes). In this chapter, the chosen solution scheme is an explicit scheme based on the central difference approximation of Newton's second law of motion. This scheme when applied in earlier chapters to the static analysis of tension structures is known as the dynamic relaxation method; the basic mechanics and advantages of this method have already been outlined in chapter 3.

The chosen explicit scheme is applied to investigate the dynamic response of a pneumatic dome. The membrane of the dome is constructed from a light, isotropic polythene material which exhibits visco-elastic behaviour. A single Kelvin model is used in the dynamic analysis to calculate for the accumulated creep strains arising from the visco-elasticity in the membrane material. In addition, the membrane material cannot sustain any compression and thus, undergoes buckling when subject to compressive forces. An incremental procedure is implemented in order to allow for this on/off buckling. For the pneumatic dome being considered here, on/off buckling occurs at almost all stages of the dynamic analysis. In such a case, it is more efficient in terms of computation time to implement an incremental procedure based on the 'stress' scheme given in figure 9.25 instead of that based on the 'force' scheme given in figure 9.3. The pneumatic stiffness (or internal air stiffening) of the dome is modelled using the pressure-volume relationship given in equation (9.6.1).

A procedure is developed to model the aerodynamic mass, ie. the added mass of surrounding air attached to the membrane of the dome. This procedure is based on the potential flow theory and involves the solution of the Laplace equation, ie. equation (9.9.12). For the dome in question here, Laplace equation is solved by prescribing a distribution of sources over the membrane. The ratio of the kinetic energy of the surrounding air when set into motion to that of the vibrating membrane is determined. This ratio known as the added mass coefficient gives a measure of the added mass of the attached air relative to the membrane mass. Proceeding in this way, Campbell [42] calculated the added mass effects of a diaphragm embedded in an infinite rigid  $z=0$  plane for various normal velocity distributions prescribed over the diaphragm. The diaphragm is divided into rectangular patches with a discrete source placed at the centre of each patch. The above scheme used by Campbell [42] known as the discrete source method, is further applied by Krakowska [86] to assess the added mass effects of a shallow pneumatic dome in which a distribution of sources over the  $z=0$  plane as shown in figure 9.11(c) is used.



For the average potential calculations, the membrane is represented by a mesh of triangular and trapezoidal patches lying in the  $z = 0$  plane, ie. in the same plane as the source distribution. The sources are placed at the centres of the triangular and trapezoidal patches. The problem is simplified with the  $z$ -dimension omitted from the various equations concerned. This 'two-dimensional' approach has been derived on the assumption of a shallow dome. The need to use a mesh of triangular and trapezoidal patches as shown in figure 9.11(a) also imposes a constraint on the element idealisation of the dome. In addition, this approach involves numerical integrations which require sufficiently fine divisions of the patches for reasonably accurate integrations to be achieved, and special attention is needed to deal with the integrations used in calculating the average potential over the area of a patch due to a source at the centre of the same patch.

In this chapter, a generalised source method has been developed to eliminate the above mentioned limitations and difficulties of the 'two-dimensional' approach. In the generalised method, there is no restriction of having to assume a shallow dome. The sources are placed at the centroids of triangular elements which constitute the structural idealisation of the dome and there is no use of a separate mesh of patches for the purpose of calculating the average potentials. The generalised method can deal with triangular elements of any shapes and thus, imposes no constraint on the element idealisation of the dome. In this method, exact analytic integrations are used and this leads to the advantages illustrated by the simple numerical examples considered in section 9.15. As a result of these features, the generalised method is sufficiently flexible and powerful to be applied generally in the dynamic analysis of a closed membrane structure of any shape.

The boundary condition of zero normal velocity of the air across the rigid base of the dome has to be satisfied. In the generalised method, this boundary condition is satisfied by reflecting the dome about the base to give an imaginary mirror image, and prescribing over this image a distribution of sources similar to that over the dome. In the case of the 'two-dimensional' approach, this boundary condition is not satisfied with the sources distributed over the  $z = 0$  plane.

In using the generalised source method to account for the added mass effects, a further consideration is the need to avoid the problem of discontinuity in linear momentum within the dynamic analysis. This is achieved by incorporating a strategy which involves the Newton's second law expressed in a vector form.

The explicit numerical scheme implemented with the various procedures to model the visco-elastic material behaviour, on/off buckling, internal air stiffening and added mass effects, has been applied to investigate the dynamic response of a pneumatic dome for which experimental results [86] were available for comparison. These experiments were carried out for the cases of both centrally (symmetric) and asymmetric initial loadings applied to the dome in its initial state; the dynamic response of the dome being initiated by



the sudden removal of these initial applied loadings. Due to the absence of any significant mass acting on the lightweight membrane, the dynamic response of the dome is greatly influenced by the added mass of the attached air as is evident from the following results obtained from the dynamic analyses:

- (i) For the centrally unloaded dome, the added mass coefficient (averaged over the first four cycles of the dynamic response) is 58.4, and that for the asymmetrically unloaded dome is 30.5.
- (ii) For the centrally unloaded dome, the dynamic analysis in which the added mass effects are taken into account gives a frequency (averaged over the first four cycles of the dynamic response) much closer to the experimental value than that given by the dynamic analysis in which the added mass calculations are excluded. By accounting for the added mass effects within the dynamic analysis, the discrepancies in the prediction of the experimental frequency is reduced from 540% to 34%. For the asymmetrically unloaded dome, the discrepancies in the prediction of the experimental frequency is reduced from 309% (with no account of the added mass effects within the dynamic analysis) to 33% (with the added mass calculations included).

In the experiment, it was observed that the air mass in the dome was caused to 'slosh' about when the asymmetrically applied load was suddenly lifted off the dome. There is no account of this 'sloshing' (or momentum) effect as distinct from the added mass effects of the attached air, in the dynamic analysis considered so far. Further research is required in order to find a simple and practical means of modelling this momentum effect.

In view of the difficulties in obtaining accurate transient dynamic experimental results, and the limitations in the theory for the dynamic analysis, the numerical results for both the centrally and asymmetrically unloaded dome seem quite reasonable and encouraging.

The cases of both the centrally and asymmetrically unloaded dome correspond to a situation where there is no wind flow over the dome. In section 9.19, the case when there is a wind flow over the dome is considered and a proposed procedure for dealing with such a case is outlined; this procedure is yet to be implemented into the explicit numerical scheme. It is also noted that there is a critical wind speed at which the dome will lose static stability (ie. divergence). Williams [141] derived a formula for calculating such a critical wind speed for the case of a low profile air-supported structure, and Barnes [20] derived a corresponding formula which applies to a shallow, rectangular membrane structure.

In this chapter, an explicit numerical scheme is developed for the dynamic analysis of a closed membrane structure of any shape. This scheme is efficient in terms of computational effort and solution time, and also relatively simple to use. There are however a few important points about this scheme which



should be noted. Firstly, the use of the potential flow theory means that the scheme may not be appropriate in situations where the assumptions in the theory lead to gross misrepresentations such as in a situation where there is catastrophic flow separation. For the cases of both the centrally and asymmetrically unloaded dome, flow separation may not occur until after the first few cycles of the dynamic response. In addition, the scheme has no procedure to account for the aerodynamic damping and hence, cannot predict the instability condition of flutter which arises if the aerodynamic damping becomes effectively negative. Further research is required in order to derive a simple means of modelling the aerodynamic damping. A further approximation is that the added mass effects of the attached air are assumed to be uniform over the membrane of the dome. There is also no modelling of the possible air momentum effect within the scheme.



## Chapter 10

### Summary, conclusions and recommendations

#### 10.1 Summary and conclusions

In this chapter, a summary is given of the work which has been covered in this thesis. The main conclusions are discussed and some possible areas of further research are also outlined.

The work in this thesis has been mainly concerned with the development of a CAD system for tension structures in general and a detailed discussion of the difficult task of analysing their highly complex dynamic behaviour. Much of the software development work for the CAD system which forms part of this thesis, has been carried out under the Teaching Company Scheme (1988-1990) set up between Buro Happold, Bath and City University, London. This CAD system is now in operation for project work at the Lightweight Structures Division of Buro Happold.

For tension structures, it is essential to apply numerical modelling at both form-finding (architectural design) and engineering analysis stages. A review of appropriate numerical schemes which are available can be found in chapter 2. In general, these numerical schemes come under the following groups: (a) iterative methods, (b) incremental methods, (c) minimisation methods and (d) relaxation methods. Both the iterative and incremental methods are implicit schemes as they involve setting up the overall or tangent stiffness matrix of the structure in their solutions. Examples of the implicit iterative methods are the Newton-Raphson, modified Newton-Raphson and secant stiffness methods. The incremental methods are used in the solution of path dependent problems, in which the applied loads are increased in small increments. On the other hand, both the minimisation and relaxation methods are explicit schemes as no formation of the overall or tangent stiffness matrix is required in their solutions. In the minimisation methods, the idea is to reach an equilibrium solution by minimising the total potential energy function of the structure. This involves the searching along a descent direction until the local minimum in that particular direction is found. The search then continues along a different descent direction and the process is repeated until the global minimum is reached. The minimisation methods have mainly been applied to solve cable net problems. The various ways of finding the minimum of the total potential energy function result in the different minimisation schemes which are available. The direct minimisation methods include the random search and the Monte-Carlo methods, and in these methods, there is no need for the explicit evaluation of any partial derivatives of the total potential energy function. The gradient minimisation methods include the method of steepest descent and the conjugate gradient method, and in these methods, the partial derivatives of the total potential energy function are required. The convergence rate of the conjugate gradient method can be improved by the scaling of certain terms



which results in the scaled conjugate gradient method. Examples of explicit relaxation methods are the Point-Jacobi, Gauss-Seidel, Successive Over-Relaxation (SOR) and Dynamic Relaxation (DR) methods. These relaxation methods except for the dynamic relaxation method, may encounter difficulties when dealing with situations such as on/off element buckling which can often occur during the analysis of a tension structure. However, the dynamic relaxation method can easily cope with on/off buckling and in general, is much better suited to solve highly non-linear problems involving both geometric and material non-linearities.

In chapter 3, the dynamic relaxation method is described in further detail. The underlying principle of the method is the time-step integration of Newton's second law of motion for a structure with high damping imposed to obtain convergence to a static solution. The dynamic relaxation method is only conditionally stable, ie. if a time step which exceeds a critical value is used, then numerical instability will result. This stability criterion is satisfied through a strategy of using fictitious nodal masses which also leads to an increased convergence rate. There are various means of establishing the appropriate fictitious nodal masses. In this case, it is convenient to have for each node, a diagonal matrix of fictitious masses. At the start of the analysis, certain parameters can be easily chosen which are factors to be applied to the diagonal mass matrix in order to compensate for the coupling effects between the various degrees of freedom at each node. This gives the advantage of an automatic control of the fictitious nodal masses. For the form-finding and static analysis of tension structures, the kinetic damping procedure is effective in dealing with suddenly imposed high residuals which can often arise during form adjustments. For modelling the dynamic behaviour, the true structural damping has to be used instead. Furthermore, within the dynamic relaxation method, the natural stiffness relations are used in the calculations for the natural forces from the corresponding basic displacements. The natural forces are then transformed to the global coordinate system and added to the nodal residual forces. This proves an efficient means of deriving the nodal residual forces and therefore produces much saving in computation time. A further advantage of the dynamic relaxation method is the uncoupling of the equations of equilibrium and continuity/compatibility. This allows the strain components to be updated independently of stresses. Hence, complex stress/strain relations can be readily implemented and on/off buckling easily dealt with. In addition, geometric non-linearity is automatically taken into account within the method. During the analysis, any signs of physical instabilities which may be present in the structure are easily detected and hints often given about their causes. This is particularly advantageous at the form-design stage of tension structures.

Chapter 4 gives an account of the case in which a tension structure is bounded by compression boundaries. Instead of tension anchorages, a compression boundary can prove to be an efficient alternative means of providing support to a large span structure. It is often adequate to use slender sections in the compression boundary as a result of the stability support contributed by the tension elements in the structure. Instead of being taken as a fixed support,



the compression boundary has flexibility and can undergo finite deformations, and is properly modelled using beam elements. The beam elements are easily implemented into the dynamic relaxation scheme used for all the analysis work in this thesis. The natural stiffness relations are used in deriving the moment-curvature relations of the beam element. Hence, a local axes system is defined for each element. In the dynamic relaxation analysis which uses kinetic damping, the stiffnesses and non-linear effects of the beam element are updated when an energy peak is detected. These non-linearities include the influences which the axial force have on the moment-curvature relations and fixed-end moments, and the element bowing effects. In addition, any geometric non-linearity is automatically taken into account. The sway angles are determined in order to account for the rigid body motions in the calculations for the beam displacements. An end release can be prescribed to impose a pin-ended condition for bending about any of the local axes. All the above features have been implemented to enable a realistic modelling of the interaction between the tension structure and the compression boundaries. Within the dynamic relaxation scheme, the rotational degrees of freedom are treated as decoupled from the translational degrees of freedom. Hence, for each node of a beam element, a  $(3 \times 3)$  mass matrix is set up for the rotational degrees of freedom separately from the  $(3 \times 3)$  mass matrix for the translational degrees of freedom. The beam elements as formulated above provide an efficient means of dealing with compression boundaries in a tension structure.

A discussion is given in chapter 5 concerning the topics of differential geometry which are applicable to the various procedures involved in the design of tension structures. It is common to find complex surface curvatures in a tension structure; even for one of relatively simple shape. This makes it relevant to have a useful knowledge of differential geometry which is the study of space curves and surfaces. In fact, differential geometry provides the basis for some of the fundamental concepts which have been applied to the form-finding and patterning procedures. For instance, the condition of a seam line following a geodesic path over the surface is often imposed during the form-finding of a membrane structure. This has the advantage of producing fabric panels which optimise the width use of a fabric roll. In addition, it has been shown how the warp and weft yarns in a fabric panel will undergo distortions by continuously changing the angle between them in order to achieve the desired Gaussian curvature of the surface. Furthermore, the equilibrium equations of the surface acted on by applied loads are derived which give the relationships between the stresses in the surface and its geometry. The unknowns in the solution of the equilibrium equations can either be the stresses or geometry of the surface. In the discussion, the treatment of the various topics of differential geometry is rather mathematical, and the use of tensor notation has been convenient.

In chapter 6, the form-finding and static analysis of tension structures are discussed. During the form-finding, an equilibrium geometry and the corresponding stress state in the structure are determined. As mentioned earlier, the unknowns in the problem can theoretically either be the geometry



or the stresses (provided that any stress states are allowed). In this thesis, the adopted approach is to find the unknown equilibrium geometry given the stress distributions, the initial and boundary conditions. Hence, for a membrane structure, the form-finding controls are derived from the adjustments of the prescribed uniform or anisotropic membrane stresses, or initial and/or boundary conditions, or any combination of the former controls. During the form-finding, the seam lines between fabric panels are constrained to follow geodesic paths over the surface to yield appropriate geometry for subsequent fabrication patterning. The form-finding is followed by load analysis in which the possible loads are applied to the form which has been achieved. If the load analysis results in unsatisfactory behaviour (for instance, the fabric becomes overstressed or wrinkled or inverts under wind load) or the model becomes structurally unstable, then the geometry derived from the form-finding may have to be revised in order to alleviate the problem. Hence, there is an iterative process between the form-finding and load analysis. When a satisfactory form has been found, the corresponding cutting patterns are developed. This is then followed by the detailed design of the supporting steelwork, connections and so on. X

A fully interactive graphical CAD system for tension structures is the subject developed in chapter 7. Within the software for the CAD system are implemented the theoretical concepts which have been described in the previous chapters. The system fully exploits the capabilities which can be offered by the computer hardware and is far more effective than physical modelling in many aspects such as form-finding, load analysis and patterning. In the design office, the CAD system has already produced much saving in design time. The system has also been a useful tool for the communication of ideas between the engineer and the architect since it is an excellent means for exploring the huge possibilities of shapes at the form-finding stage. Much thought has gone into achieving an effective and functional human user interface for the CAD system. The user interface has been designed to be fully interactive and based on the concept of the Graphical User Interface (GUI), ie. as much use as possible of graphical images on the screen to inform and guide the user. The command line interface (CLI) style is avoided if possible. In fact, the user is not required to learn any command entry through the keyboard as far as the software execution is concerned. In addition, the graphical images, symbols and labels which are always displayed on the screen during the software execution, serve as useful guides to the possible actions which the user can take. In consequence, a new user of the CAD system should only need a short learning time. It is effective to present information in the form of graphical images rather than numbers on the computer screen. The user interacts with the software mainly by means of the on-screen menus which are activated using a mouse, and can interrogate and interact directly with the image on the screen. The CAD system comprises of individual modules designated for the tasks of form-finding, load analysis and patterning. These modules are integrated together to make the design process into a smooth and continual one. A common database is maintained throughout the software and is updated regularly to reflect the current state of the numerical model. An outline is given in chapter 7 of the menu options



for the numerous functions which are available to the user during the execution of the software. These functions begin with the setting up of the model together with assignment of all the necessary prerequisites, followed by the analysis and then post-processing of the results. The beam elements have been implemented into an individual module within the CAD system, and the same style of interaction as the rest of the software is imposed on the module. In addition, an advanced structure visualisation module has been set up to provide a solid modelling capability. This enables a good appreciation of the complex surface geometry commonly found in a tension structure.

In chapter 8, consideration is given to the possible loads which a tension structure may have to resist during its service life. The primary design loads are often the snow and wind loads. The lightweight and flexibility of a tension structure make it highly susceptible to wind, and an accurate assessment of these loads is essential to enable a structurally sound and economic design of the structure. It is also sensible that the loads can be expressed in a form easily applicable within the structural analysis. As a result of its flexible nature, a tension structure is likely to undergo gross deformations during load analysis. This may in turn lead to the problem of non-linear load structure interaction. The complex surface shapes often found in a tension structure implies that the appropriate load distribution coefficients may not be easily obtainable from the codes of practice which contain values applicable more to the simpler shapes of conventional structures. Although the natural wind consists of fluctuating components, a quasi-static form of the wind load is often used for preliminary studies or routine designs of small scale structures. According to (CP3: 1972), this quasi-static wind load is taken as that due to the maximum gust which will act on the structure. The wind load distribution coefficients given in the codes of practice are obtained from wind tunnel tests of rigid models. This approach can provide some design information such as maximum deflections and stresses. However, no account is taken of the oscillatory nature of the structural response due to the action of the wind. On the other hand, the above quasi-static approach can be modified to include the possible loading caused by the turbulence in the wind. This modified approach leads to the admittance design method which produces a dynamic response spectrum from a quasi-static load assessment. This method can be applied to the design of structures with linear dynamic characteristics. However, for a large tension structure such as an air-supported stadium roof, a detailed description of the wind load taking into account the randomly varying components and the spatial correlation of wind gusts, is required. A possible approach is to use statistical analysis. The dynamic response of the structure itself produces additional mass, damping and stiffness terms which in turn give rise to aerodynamic forces on the structure. Hence, the dynamic analysis of the structure is a complex aeroelastic problem. In the above approaches which use the quasi-static form of the wind load, there is no account of these aerodynamic forces. In addition, vortex shedding may occur along the free edges of the structure which in turn gives rise to additional dynamic forces.



The problem under examination in chapter 9 is the dynamic analysis of tension structures. In most instances, the dynamic response of a tension structure is initiated by the action of the natural wind. A reliable assessment of this dynamic response is necessary so that the structure can be designed to avoid any possible resonance situation. As mentioned earlier, the dynamic analysis of a tension structure is much complicated by the presence of aerodynamic mass, stiffness and damping terms. At present, this problem is solved by an aeroelastic model test in a boundary layer wind tunnel. In this chapter, the objective is to derive a numerical approach, even though an elementary one at this stage, for the dynamic analysis of the structure. It is hoped that eventually with further research, a numerical approach is found which is sufficiently general, accurate and reliable to be considered an attractive alternative to aeroelastic wind tunnel testing. A brief review is given of the solution schemes which are available for the dynamic analysis of structures in general. The explicit numerical scheme (based on central difference approximation of Newton's second law of motion) previously used for the form-finding and static load analysis, is conveniently applied to the dynamic analysis as well. A few points to note when using the explicit numerical scheme for dynamic analysis are the use of viscous structural damping instead of kinetic damping, and real nodal masses instead of fictitious values. In addition, the creep effects of the visco-elastic membrane material are taken into account by means of a single Kelvin element model. An incremental procedure based upon a 'stress' scheme is employed to allow for the on/off element buckling. Implemented into the explicit numerical scheme is a proposed strategy to include the aerodynamic mass (ie. added mass) of the surrounding air into the dynamic analysis. A simple means is also suggested to model the aerodynamic stiffness (ie. pneumatic stiffness). However, there is no account of the aerodynamic damping and possible momentum effect in the dynamic analysis. For the investigation in this chapter, the case of the dynamic analysis as applied to an air-supported dome is considered.

A generalised source method is developed for the task of calculating the added mass effects. This method is an enhancement of the scheme proposed by Krakowska [86] such that it can be applied to any closed membrane structure of arbitrary shape. The underlying basis of the generalised method is the potential flow theory and hence, primarily involves the solution of the Laplace equation. This solution can be obtained in terms of either a distribution of sources or doublets over the structure. For the dome under consideration, a distribution of sources is prescribed over the membrane. For the structural modelling, the membrane of the dome is discretised into constant strain triangular elements. In the generalised method, a discrete source is placed at the centroid of each triangular element. The boundary condition of zero normal velocity across the rigid base of the dome is satisfied by having a distribution of sources over the surface of an imaginary mirror image of the dome. This image is the reflection of the dome across the base and the source distribution for the image should be similar to that for the dome. The added mass calculations are based on kinetic energy considerations



involving the use of the source distributions in finding the kinetic energy due to the motion of surrounding air.

The experimental test cases used for comparison with the developed theory are based on the traces of unloading deformations of a very light pneumatic dome. These experiments were previously carried out by Krakowska [86] for the cases of both initially applied central (symmetric) loading and asymmetric loading; the dynamic responses being initiated by the sudden removal of these initial loadings. In consequence, the contained air mass is quite high in comparison with the membrane mass yet the dynamic deformations of the dome are large. The theoretical results were found to be in reasonable agreement with the corresponding results determined from experiment by Krakowska [86]. As confirmed from the theoretical results in each case in terms of the average added mass coefficient and the significant improvement in the prediction of the experimental frequency compared with when there is no account of the added mass effects, the added mass of the attached air has a dominant influence on the dynamic response of the dome.

The explicit numerical scheme developed for the dynamic analysis of the impulsively unloaded dome is still under development. More research is needed in a few areas as will be outlined in the following section, in order to further improve the scheme so that it can eventually be applied in practice to provide relevant design information concerning the dynamic responses of tension structures and until then, the practical solution at present is to perform wind tunnel testing of an aeroelastic model of the structure.

## 10.2 Recommendations

From the work which has been considered in this thesis, particular areas can be identified where there is scope for further research work.

For the beam elements considered in chapter 4, a possible area of future work is the inclusion of the ability to allow for the plastic hinge formation during the analysis of the structure. This will enable the modelling of the elastic-plastic behaviour which may be expected under certain circumstances (ie. ultimate load capacity checks).

The discussion in chapter 5 has shown that the ideas from differential geometry do contribute to the development of the numerical schemes applied to the form-finding and patterning procedures. The condition of prescribed principal tensile stresses following the sense of a geodesic coordinate system on the surface is imposed on the form-finding process of a membrane structure. This requirement is not necessary but does offer a convenient means of producing different surface forms, the choice of which can be enormous. Further investigations can be carried out to find alternative approaches, using ideas from differential geometry, to the form-finding in particular of cable nets such as principal curvature and constant tension coefficient nets.



For the CAD system described in chapter 7, there are areas where further developments can be made to enhance the capability of the system. These include the following:

- (1) additional module for the analysis and design of cable net structures;
- (2) direct linking of the system to the cutting pattern production stage on the shopfloor (ie. linking of the engineering design output with CNC systems for laser cutting of the fabric patterns);
- (3) linking of the system to a commercial draughting package such as 'Auto-Cad' and to alternative architectural visualisation packages;
- (4) additional module for the dynamic analysis of tension structures.

As discussed in chapter 8, further research is needed to obtain a more accurate description of the loading due to a turbulent wind. This description should give an indication of the random fluctuating components in the wind rather than a quasi-static assessment as is the common practice at present. It is only practical that this loading can be expressed in a form which is easily applied in the dynamic analysis.

For the dynamic analysis of tension structures, further improvement can be made to the generalised source method in order to model the distribution of the added mass effects over the structure. The assumption that these effects are uniform over the structure introduces an error of yet undetermined magnitude. Furthermore, more work can be carried out to devise a practical means of modelling the aerodynamic damping within the dynamic analysis. An empirical formula for the aerodynamic damping has been suggested by Davenport [51] which requires the determination of an aerodynamic coefficient for the structure under consideration. In addition, a means has to be found of modelling the momentum effect of a body of air when set into motion. This will require a formulation which takes into account how the motion of the membrane (ie. boundary) is translated into the momentum of the surrounding air. Obviously, the behaviour of the external air will differ from that of the air enclosed within the dome. A suggestion is to discretise the surrounding air into finite elements and formulate a finite element scheme to model the momentum effect. In a sense, this may involve the coupling of the boundary solution determined from the potential flow theory with the finite element field for the surrounding air. A scheme which follows this line of thought has been proposed by Barnes [19] which has yet to be verified numerically. Hence, further investigation can be carried out in order to determine if this scheme can suitably be used within the above numerical approach for the dynamic analysis. Another area of further work is the implementation and verification of the proposed procedure outlined in section 9.19 of chapter 9 for dealing with the case of dynamic response in the presence of wind.



## References

- [1] Abu-Sitta, S. H. and Elashkar, I. D., 'The dynamic response of tension roofs to turbulent wind', Int. Conf. on Tension Structures, London, 1974.
- [2] Argyris, J. H. and Scharpf, D. W., 'Some general considerations on the natural mode technique', J. R. Ae. S., Vol. 73, 1969.
- [3] Argyris, J. H., Angelopoulos, T. and Bichat, B., 'A general method for the shape finding of lightweight structures', Int. Conf. on Tension Structures, London, 1974.
- [4] Barnes, M. R., 'Dynamic relaxation analysis of tension structures', Int. Conf. on Tension Structures, London, 1974.
- [5] Barnes, M. R., 'Applications of dynamic relaxation to the design and analysis of cable, membrane and pneumatic structures', 2nd Int. Conf. on Space Structures, Guilford, 1975.
- [6] Barnes, M. R., 'An investigation of vibration decay in a model pneumatic dome', Int. Symp. on Wide Span Surface Structures, Stuttgart, 1976.
- [7] Barnes, M. R., 'Explicit dynamic analysis of tension structures', Int. Symp. on Wide Span Surface Structures, Stuttgart, 1976.
- [8] Barnes, M. R., 'Form-finding of minimum surface membranes', IASS Congress on Structures for Space Enclosure, Montreal, 1976.
- [9] Barnes, M. R., Topping, B. H. V. and Wakefield, D. S., 'Aspects of form-finding by dynamic relaxation', Int. Conf. on Slender Structures, London, 1977.
- [10] Barnes, M. R., 'Form-finding and analysis of tension space structures by dynamic relaxation', Ph.D. thesis, The City University, London, 1977.
- [11] Barnes, M. R., 'Explicit dynamic analysis of an impulsively loaded pneumatic dome', Symposium on Air-Supported Structures: the State of the Art, IStructE, London, 1980.
- [12] Barnes, M. R., 'Non-linear numerical solution methods for static and dynamic analysis of tension structures', Symposium on Air-Supported Structures: the State of the Art, IStructE, London, 1980.
- [13] Barnes, M. R., 'Form-finding, analysis and patterning of tension structures', 3rd Int. Conf. on Space Structures, Guildford, 1984.



- [14] Barnes, M. R., 'Review of solution methods for static and dynamic analysis of tension structures', Conf. on the Design of Air-Supported Structures, IStructE, Bristol, 1984.
- [15] Barnes, M. R. and Wakefield, D. S., 'Dynamic relaxation applied to interactive form-finding and analysis of air-supported structures', Conf. on the Design of Air-Supported Structures, IStructE, Bristol, 1984.
- [16] Barnes, M. R., 'Form-finding and analysis of prestressed nets and membranes', Int. Conf. on the Design and Construction of Non-Conventional Structures, London, 1987.
- [17] Barnes, M. R., 'Form-finding and analysis of prestressed nets and membranes', Computers and Structures, Vol. 30, No. 3, 1988.
- [18] Barnes, M. R. and Wakefield, D. S., 'Form-finding, analysis and patterning of surface-stressed structures', 1st Oleg Kerensky Memorial Conf., London, 1988.
- [19] Barnes, M. R., 'The response of air-supported structures to gust loading', Proc. 4th Int. Conf. on Civil and Structural Eng. Computing, Civil-Comp Press, Vol. 2, 1989.
- [20] Barnes, M. R., 'Wind load validation of low rise air structures', IABSE Colloquium on Air-Supported Structures, Cambridge, July 1992.
- [21] Baron, F. and Venkatesan, M. S., 'Non-linear analysis of cable and truss structures', J. Struct. Div., ASCE, Vol. 97, 1971.
- [22] Bathe, K. J. and Wilson, E. L., 'Numerical methods in finite element analysis', Prentice-Hall, Inc., New Jersey, 1976.
- [23] Bathe, K. J. and Wilson, E. L., 'Stability and accuracy analysis of direct integration methods', Int. J. Meth. in Earthquake Eng. and Struct. Dynamics, Vol. 1, 1973.
- [24] Belytschko, T. and Hsieh, B. J., 'Non-linear transient finite element analysis with convected coordinates', Int. J. Num. Meth. in Engng., Vol. 7, 1973.
- [25] Belytschko, T., Chiappetta, R. L. and Bartel, H. D., 'Efficient large scale non-linear transient analysis by finite element', Int. J. Num. Meth. in Engng., Vol. 10, 1976.
- [26] Bergan, P. G. and Soriède, T., 'A comparative study of different numerical solution techniques as applied to a non-linear structural problem', Comp. Meth. in Appl. Mech. and Eng., Vol. 2, 1973.



- [27] Bisplinghoff, R. L., Ashley, H. and Halfmann, R. L., 'Aeroelasticity', Addison-Wesley, Massachusetts, 1955.
- [28] Brew, J. S. and Brotton, D. M., 'Non-linear structural analysis by dynamic relaxation', Int. J. Num. Meth. in Engng., Vol. 3, 1971.
- [29] Buchholdt, H. A., 'Prestressed cable nets with finite displacements', Ph.D. thesis, University of London, 1967.
- [30] Buchholdt, H. A., 'The configuration of prestressed cable nets', Acta Polytechnica Scandinavica, Ci54, Trondheim, 1968.
- [31] Buchholdt, H. A., Davies, M. and Hussey, M. J. L., 'The analysis of cable nets', J. Inst. of Mathematics and its Applications, Vol. 4, 1968.
- [32] Buchholdt, H. A., 'A non-linear deformation theory applied to 2-dimensional pretensioned cable assemblies', Proc. ICE, Vol. 42, 1969.
- [33] Buchholdt, H. A., 'Tension structures', The Structural Engineer, 1970.
- [34] Buchholdt, H. A., 'Pretensioned cable girders', Proc. ICE, Vol. 45, 1970.
- [35] Buchholdt, H. A., 'The Newton-Raphson approach to skeletal assemblies having significant displacements', Acta Polytechnica Scandinavica, Ci72, Trondheim, 1971.
- [36] Buchholdt, H. A. and McMillan, B. R., 'Iterative methods for the solution of pretensioned cable structures and pin-jointed assemblies having significant geometrical displacements', IASS Symp. on Tension Structures and Space Frames, Tokyo and Kyoto, 1971.
- [37] Buchholdt, H. A. and McMillan, B. R., 'A non-linear vector method for the analysis of vertically and laterally loaded cable assemblies', Proc. ICE, Vol. 55, 1973.
- [38] Buchholdt, H. A., Das, N. K., and Al-Hilli, A., 'A gradient method for the analysis of cable structures with flexible boundaries', Int. Conf. on Tension Structures, London, 1974.
- [39] Buchholdt, H. A., 'The behaviour of circular saddle shaped nets with flexible boundaries', Int. Symp. on Wide Span Surface Structures, Stuttgart, 1976.
- [40] Buchholdt, H. A., 'Introduction to cable roof structures', Cambridge University Press, 1985.
- [41] Calladine, C. R., 'Gaussian curvature and shell structures', The mathematics of surfaces, Gregory, J. A. ed., OUP, Oxford, 1986.



- [42] Campbell, W. F., 'The added mass of some rectangular and circular flat plates and diaphragms', National Research Council of Canada, LTR-LA-223, 1982.
- [43] Cassell, A. C. and Hobbs, R. E., 'Numerical stability of dynamic relaxation analysis of non-linear structures', Int. J. Num. Meth. in Engng., Vol. 10, 1976.
- [44] Clough, R. W. and Penzien, J., 'Dynamics of structures', McGraw-Hill, New York, 1975.
- [45] Coates, R. C., Coutie, M. G. and Kong, F. K., 'Structural analysis', ELBS and Nelson, 2nd ed., 1980.
- [46] Cook, M., 'The design of air-supported structures to resist wind loading', Ph.D. thesis, University of Bath, 1983.
- [47] Cook, M., 'The use of physical models in the design of air-supported structures', Conf. on the Design of Air-Supported Structures, IStructE, Bristol, 1984.
- [48] Cook, N. J., 'The designer's guide to wind loading of building structures', Part 1, BRER, Butterworths, 1985.
- [49] Cundall, P., 'Explicit finite difference methods in geomechanics', Proc. Conf. Numerical Methods in Geomechanics, Blacksburg, Va., 1976.
- [50] Davenport, A. G., 'The relationship of wind structure to wind loading', Proc. Conf. on Wind Effects on Buildings and Structures, NPL, Teddington, 1963.
- [51] Davenport, A. G., 'The response of tension structures to turbulent wind: the role of aerodynamic damping', 1st Oleg Kerensky Memorial Conference, London, 1988.
- [52] Davies, P. J., 'Aeroelastic wind tunnel testing of an air-supported structure', BEng thesis, University of Bath, 1990.
- [53] Day, A. S., 'An introduction to dynamic relaxation', The Engineer, Jan. 1965.
- [54] Dowell, E. H., 'Aeroelasticity of plates and shells', Leyden, Noordhoff, 1975.
- [55] Eng, S. H., 'The use of the boundary element method to include the mass of the surrounding air in the dynamic analysis of membrane structures', M.Sc. thesis, University of Bath, 1984.



- [56] Fletcher, R. and Reeves, C. M., 'Function minimisation by conjugate gradients', *Computer Journal*, Vol. 7, 1964.
- [57] Foley, J. D. and Van Dam, A., 'Fundamentals of Interactive Computer Graphics', Addison Wesley, 1982.
- [58] Frieze, P. A., 'Elasto-plastic buckling in short thin-walled beams and columns', *Proc. ICE*, Vol. 65, 1978.
- [59] Frieze, P. A., Hobbs, R. E. and Dowling, P. J., 'Application of dynamic relaxation to the large deflection elasto-plastic analysis of plates', *Computers and Structures*, Vol. 8, 1978.
- [60] Gauss, K. F., 'Disquisitiones generales circa superficies curvas', Gottingen, 1828 (English translation by J. C. Morehead and A.M. Hiltebeitel, Princeton, 1902; reprinted with introduction by R. Courant, Raven Press, Hewlett, New York, 1965).
- [61] Green, A.E. and Zerna, W., 'Theoretical Elasticity', 2nd ed., Oxford University Press, 1968.
- [62] Greenberg, D. P., 'Inelastic analysis of suspension roof structures', *J. Struct. Div.*, ASCE, Vol. 96, 1970.
- [63] Haber, R. B., 'Computer-aided design of cable reinforced membrane structures', Ph.D. thesis, Cornell University, New York, 1980.
- [64] Happold, E. and Dickson, M. G. T., 'Introductory paper: review of the current state of the industry', *Symposium on Air-Supported Structures: the State of the Art*, IStructE, London, 1980.
- [65] Harris, R. I., 'The classification of structures for wind effects', *Proc. Conf. on Wind Engineering in the Eighties*, CIRIA, 1980.
- [66] Harris, R. I. and Deaves, D. M., 'The structure of strong wind', *Proc. Conf. on Wind Engineering in the Eighties*, CIRIA, 1980.
- [67] Haug, E. and Powell, G. H., 'Finite element analysis of non-linear membrane structures', *IASS Symp. on Tension Structures and Space Frames*, Tokyo and Kyoto, 1971.
- [68] Haug, E., 'Finite element analysis of pneumatic structures', *Int. Symp. on Pneumatic Structures*, Delft, 1972.
- [69] Haug, E. and Powell, G. H., 'Analytical shape finding for cable nets', *IASS Pacific Symposium Part II on Tension Structures and Space Frames*, Tokyo and Kyoto, 1972.



- [70] Haug, E., 'Remarks on unsymmetric coefficient matrices in implicit non-linear finite element membrane and cable analyses', Int. Symp. on Wide Span Surface Structures, Stuttgart, 1976.
- [71] Haug, E., 'Numerical design and analysis of lightweight structures', Symposium on Air-Supported Structures: the State of the Art, IStructE, London, 1980.
- [72] Hess, J. L. and Smith, A. M. O., 'Calculation of potential flow about arbitrary bodies', Progress in Aeronautical Sciences, Vol. 8, 1967.
- [73] Hestenes, M. R. and Steifel, E., 'Methods of conjugate gradients for solving linear systems', J. Res. of the Nat. Bureau of Standards, Vol. 49, 1952.
- [74] Houghton, E. L. and Carruthers, N. B., 'Wind forces on buildings and structures: an introduction', Edward Arnold Ltd, London, 1976.
- [75] Howell, J. F. and Novak, M., 'Vortex shedding from circular cylinders in turbulent flow', 5th Int. Conf. on Wind Effects on Buildings and Structures, Fort Collins, Colorado, USA, 1979.
- [76] Howell, J. F., 'Definition of external forces', Symposium on Air-Supported Structures: the State of the Art, IStructE, London, 1980.
- [77] Irwin, H. P. A. H., et al., 'A wind tunnel investigation of the Montreal Olympic Stadium Roof', National Research Council of Canada, LTR-LA-228, 1979.
- [78] Isaacson, E. and Keller, H. B., 'Analysis of numerical methods', J. Wiley and Sons, 1966.
- [79] Jensen, J. J., 'Dynamics of tension roof structures', Int. Conf. on Tension Structures, London, 1974.
- [80] Jonatowski, J. J., 'Tensile roof structures: an inelastic analysis', Int. Conf. on Tension Structures, London, 1974.
- [81] Kind, R. J., 'Pneumatic stiffness and damping in air-supported structures', J. Wind Eng. Aerodyn., 1984.
- [82] Knudson, W. C., 'Response of cable-net structures under dynamic loads', Proc. IASS Symp. on Tension Structures and Space Frames, Tokyo and Kyoto, 1971.
- [83] Knudson, W. C., 'Static and dynamic analysis of cable-net structures', Ph.D. thesis, University of California, Berkeley, 1971.



- [84] Knudson, W. C., and Scordelis, A. C., 'Cable forces for desired shapes in cable-net structures', Proc. IASS Pacific Symp. (Part II) on Tension Structures and Space Frames, Tokyo and Kyoto, 1972.
- [85] Knudson, W. C., 'Some aspects of the response of cable nets to wind loadings', Int. Symp. on Wide Span Surface Structures, Stuttgart, 1976.
- [86] Krakowska, T. L., 'Wind loading and dynamic response of air-supported roof structures', Ph.D. thesis, City University, London, 1989.
- [87] Krieg, R. D. and Key, S. W., 'Transient shell response by numerical time integration', Int. J. Num. Meth. Engng, Vol. 17, 1973.
- [88] Krishna, P., 'Theoretical analysis of pretensioned cable networks', Proc. IASS Symp. on Tension Structures and Space Frames, Tokyo and Kyoto, 1971.
- [89] Kunieda, H., et al., 'Cylindrical pneumatic membrane structures subject to wind', ASCE Proc., Eng. Mech. Division Journal, Vol. 107, 1981.
- [90] Lamb, H., 'Hydrodynamics', 6th ed., Cambridge University Press, 1932.
- [91] Leonard, J. W., 'Chapter 3 - Static structural analysis', State-of-the-Art Report on Air-Supported Structures, ASCE, 1979.
- [92] Livesley, R. K. and Chandler, D. B., 'Stability functions for structural frameworks', Manchester, 1956.
- [93] Lynch, R. D., Kelsey, S. and Saxe, H. C., 'The application of dynamic relaxation to the finite element method of structural analysis', Tech. Report No. THEMIS-UND-68-1, University of Notre Dame, 1968.
- [94] Mallett, R. H. and Berke, L., 'Automated method for the finite displacement analysis of 3-dimensional truss and frame assemblies', AFFDL-TR-102, 1966.
- [95] Mallett, R. H. and Schmidt, L. A., 'Non-linear structural analysis by energy search', J. Struct. Div., ASCE, Vol. 93, 1967.
- [96] Milne-Thomson, L. M., 'Theoretical hydrodynamics', 5th ed., Macmillan, London, 1972.
- [97] Mollman, H., 'A study in the theory of suspension structures', Akademisk Forlag, 1965.
- [98] Mollman, H. and Mortensen, P. L., 'The analysis of prestressed suspended cable nets', Int. Conf. on Space Structures, Guilford, 1966.



- [99] Mollmann, H., 'Analysis of hanging roofs by means of the displacement method', Polyteknisk Forlag, Lyngby, Denmark, 1974.
- [100] Moran, J., 'An introduction to theoretical and computational aerodynamics', Wiley, Chichester, New York, 1984.
- [101] Morris, N. F., 'Chapter 4 - Dynamic structural analysis', State-of-the-Art Report on Air-Supported Structures, ASCE, 1979.
- [102] Nakanishi, H. and Namita, Y., 'Shape determination analysis of cable structures for optimization problem', Contribution No. 3.6 in the work documents to the International Symposium on Wide Span Surface Structures, Stuttgart, 1976.
- [103] Newman, B. G. and Tse, M. C., 'Flow past a thin, inflated lenticular aerofoil', J. Fluid Mech., Vol. 100, Part 4, 1980.
- [104] Newman, B. G. and Golland, D., 'Two-dimensional inflated buildings in a cross wind', J. Fluid Mech., Vol. 117, 1982.
- [105] Newman, B. G., et al., 'Flow over spherical inflated buildings', J. Wind Eng. Ind. Aerodyn., 1984.
- [106] Newmark, N. M., 'A method of computation for structural dynamics', J. Engng. Mech. Div., ASCE, Vol. 85, EM3, 1959.
- [107] Oden, J. T. and Kubitza, W. K., 'Numerical analysis of non-linear pneumatic structures', Proc. Int. Colloquim on Pneumatic Structures, IASS, Stuttgart, 1967.
- [108] Oden, J. T., Key, J. E. and Fost, R. B., 'A note on the analysis of non-linear dynamics of elastic membranes by the finite element method', Computers and Structures, Vol. 4, 1974.
- [109] Ohyama, H. and Kawabata, S., 'A problem of surface design for prestressed cable nets', IASS Pacific Symposium Part II on Tension Structures and Space Frames, Tokyo and Kyoto, 1972.
- [110] Ong, C. F., 'Finite element analysis of linear transient dynamic analysis', M.Sc. thesis, The City University, London, 1987.
- [111] Ong, C. F., Wakefield, D. S. and Barnes, M. R., 'Interactive graphic CAD for tension structures', Proc. 4th Int. Conf. on Civil and Structural Eng. Computing, Civil-Comp Press, Vol. 2, 1989.
- [112] Otter, J. R. H., 'Dynamic relaxation compared with other iterative finite difference methods', Nuclear Eng. and Design, Vol. 3, 1966.



- [113] Otter, J. R. H., Cassell, A. C. and Hobbs, R. E., 'Discussion on dynamic relaxation', Proc. ICE, Vol. 36, 1967.
- [114] Otto, F., 'Tensile Structures', MIT Press, 1973.
- [115] Papadrakakis, E. M., 'Gradient and relaxation non-linear techniques for the analysis of cable supported structures', Ph.D. thesis, The City University, London, 1978.
- [116] Poskitt, T. J., 'Numerical solution of non-linear structures', J. Struct. Div., ASCE, ST4, 1967.
- [117] Rushton, K. R., 'Dynamic relaxation solutions of elastic plate problems', J. Strain Analysis, Vol. 3, No. 1, 1968.
- [118] Rushton, K. R., 'Large deflection analysis of variable thickness plates', Int. J. Mech. Sci., Vol. 10, 1968.
- [119] Saafan, S. A., 'Non-linear behaviour of structural plane frames', J. Struct. Div., ASCE, Vol. 89, 1963.
- [120] Samuelli Ferretti, A. and Zingali, A., 'A large span hanging roof: The Palasport in Milan', Prelim. Report 9th IABSE Congress, Amsterdam, 1972.
- [121] Schek, H. J., 'The force density method for form-finding and computations of general networks', Computer Methods in Applied Mechanics and Engineering, Vol. 3, 1974.
- [122] Siev, A., 'A general analysis of prestressed nets', Publs. Int. Assoc. Bridge Struct., 1963.
- [123] Siev, A. and Eidelman, J., 'Shapes of suspended roofs', Proc. IASS Colloquium on Hanging Roofs, Continuous Metallic Shell Roofs and Superficial Lattice Roofs, 1962.
- [124] Siev, A. and Eidelman, J., 'Stress analysis of prestressed suspended roofs', J. Struct. Div., ASCE, ST4, 1964.
- [125] Struik, D.J., 'Lectures on classical differential geometry', 2nd ed., Addison-Wesley, Reading, Massachusetts, 1961.
- [126] Tan, K. Y., 'Dynamic analysis of a model pneumatic dome', M.Sc. thesis, The City University, London, 1983.
- [127] Tan, K. Y. and Barnes, M. R., 'Numerical representation of stress/strain relations for coated fabrics', Conf. on the Design of Air-Supported Structures, IStructE, Bristol, 1984.



- [128] Thomas, G. and Finney, R., 'Calculus and analytic geometry', 5th ed., Addison-Wesley, 1983.
- [129] Thornton, J., 'Skin tight', World Architecture Issue No. 8, 1990.
- [130] Turner, J. J., Dill, E. H., Martin, H. C. and Melosh, R. J., 'Large deflections of structures subjected to heating and external loads', J. Aero. Sci., Vol. 27, 1960.
- [131] Turvey, G. J., 'Large deflection of tapered annular plates by dynamic relaxation', J. Eng. Mech. Div. ASCE, Vol. 104, 1978.
- [132] Varga, R. S., 'Matrix iterative analysis', Prentice-Hall, 1962.
- [133] Wakefield, D. S., 'Dynamic relaxation analysis of pretensioned networks supported by compression arches', Ph.D. thesis, The City University, London, 1980.
- [134] Williams, C. J. K., 'Form-finding and cutting patterns for air-supported structures', Symposium on Air-Supported Structures: the State of the Art, IStructE, London, 1980.
- [135] Williams, C. J. K., 'Form-finding and cutting patterns for air-supported structures', Conf. on the Design of Air-Supported Structures, IStructE, Bristol, 1984.
- [136] Williams, C. J. K., 'Methods of including the effect of the surrounding air in the dynamic analysis of air-supported structures', Conf. on the Design of Air-Supported Structures, IStructE, Bristol, 1984.
- [137] Williams, C. J. K., 'The integration of wind tunnel testing and structural analysis of air-supported structures', Conf. on the Design of Air-Supported Structures, IStructE, Bristol, 1984.
- [138] Williams, C. J. K., 'Defining and designing curved flexible tensile surface structures', The mathematics of surfaces, Gregory, J. A. ed., OUP, Oxford, 1986.
- [139] Williams, C. J. K., 'Use of structural analogy in generation of smooth surfaces for engineering purposes', Computer Aided Design, Vol. 15, No. 6, 1987.
- [140] Williams, C. J. K., 'The generation of a class of structural forms for vaults and sails', The Structural Engineer, Vol. 68, No. 12, 1990.
- [141] Williams, C. J. K., 'Travelling waves and standing waves on fabric structures', The Structural Engineer, Vol. 68, No. 21, 1990.
- [142] Williams, C. J. K., Private communication, 1991.



- [143] Zienkiewicz, O. C., Watson, M. and King, I. P., 'A numerical method of visco-elastic stress analysis', Int. J. Mech. Sci., Vol. 10, 1968.
- [144] Zienkiewicz, O. C., 'The finite element in engineering science', McGraw-Hill, London, 1971.
- [145] Davenport, A. G., 'Gust loading factors', J. Struct. Div. ASCE, 1967.
- [146] Anthony, K. C., 'The background to the statistical approach', Paper 2, The Modern Design of Wind Sensitive Structures, CIRIA, 1971.
- [147] Liddell, I., 'The engineering of surface stressed structures', Patterns 5, Buro Happold Consulting Engineers, 1989.